THE ROLE OF MAGNETIC FIELDS IN THE FORMATION OF STARS

EDITED BY: Derek Ward-Thompson, Ray S. Furuya, Yusuke Tsukamoto and Christopher F. McKee

PUBLISHED IN: Frontiers in Astronomy and Space Sciences

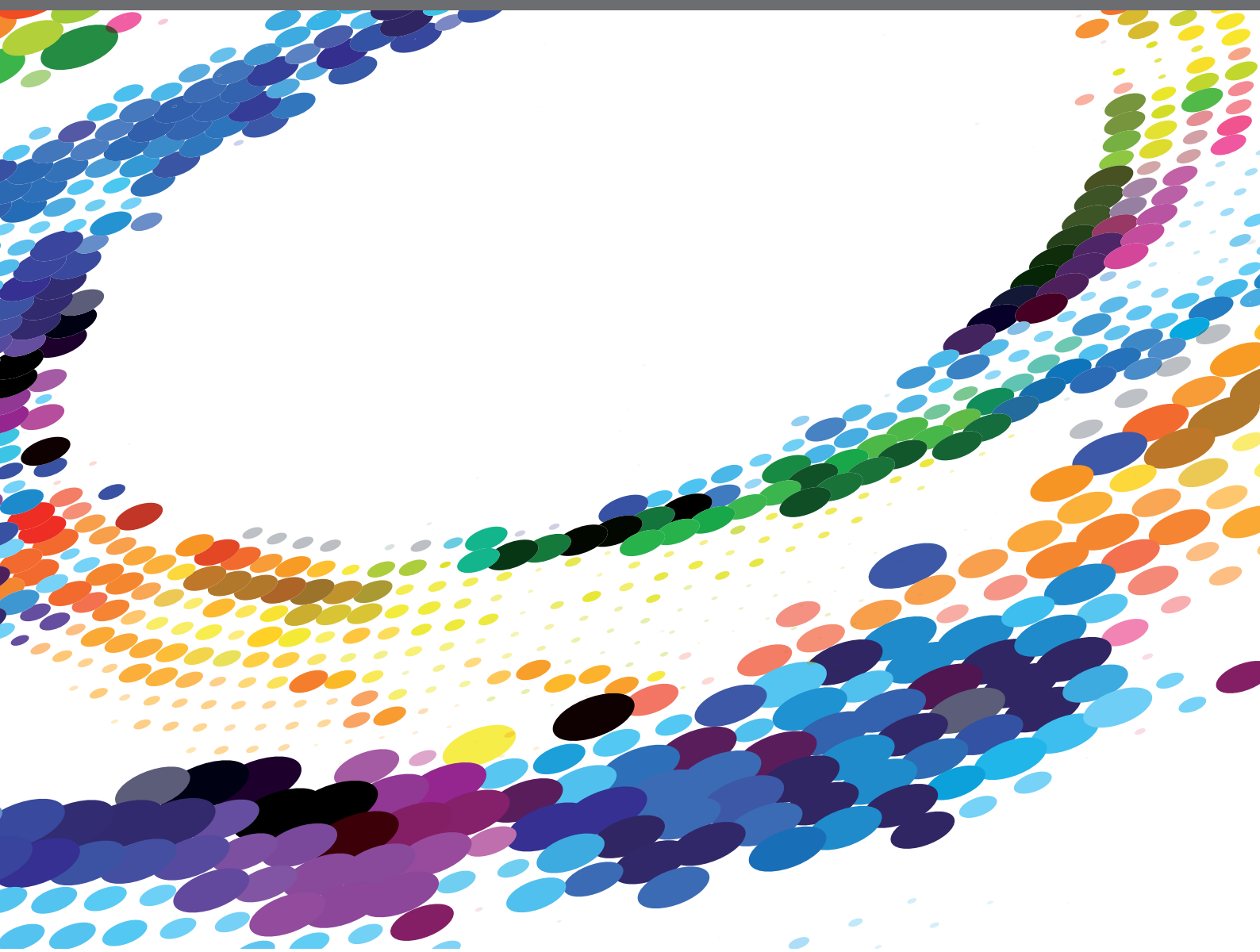

frontiers Research Topics

frontiers

ISSN 1664-8714
ISBN 978-2-88963-772-0
DOI 10.3389/978-2-88963-772-0

About Frontiers

Frontiers is more than just an open-access publisher of scholarly articles: it is a pioneering approach to the world of academia, radically improving the way scholarly research is managed. The grand vision of Frontiers is a world where all people have an equal opportunity to seek, share and generate knowledge. Frontiers provides immediate and permanent online open access to all its publications, but this alone is not enough to realize our grand goals.

Frontiers Journal Series

The Frontiers Journal Series is a multi-tier and interdisciplinary set of open-access, online journals, promising a paradigm shift from the current review, selection and dissemination processes in academic publishing. All Frontiers journals are driven by researchers for researchers; therefore, they constitute a service to the scholarly community. At the same time, the Frontiers Journal Series operates on a revolutionary invention, the tiered publishing system, initially addressing specific communities of scholars, and gradually climbing up to broader public understanding, thus serving the interests of the lay society, too.

Dedication to Quality

Each Frontiers article is a landmark of the highest quality, thanks to genuinely collaborative interactions between authors and review editors, who include some of the world's best academicians. Research must be certified by peers before entering a stream of knowledge that may eventually reach the public - and shape society; therefore, Frontiers only applies the most rigorous and unbiased reviews.
Frontiers revolutionizes research publishing by freely delivering the most outstanding research, evaluated with no bias from both the academic and social point of view. By applying the most advanced information technologies, Frontiers is catapulting scholarly publishing into a new generation.

What are Frontiers Research Topics?

Frontiers Research Topics are very popular trademarks of the Frontiers Journals Series: they are collections of at least ten articles, all centered on a particular subject. With their unique mix of varied contributions from Original Research to Review Articles, Frontiers Research Topics unify the most influential researchers, the latest key findings and historical advances in a hot research area! Find out more on how to host your own Frontiers Research Topic or contribute to one as an author by contacting the Frontiers Editorial Office: researchtopics@frontiersin.org

THE ROLE OF MAGNETIC FIELDS IN THE FORMATION OF STARS

Topic Editors:
Derek Ward-Thompson, University of Central Lancashire, United Kingdom
Ray S. Furuya, Tokushima University, Japan
Yusuke Tsukamoto, Kagoshima University, Japan
Christopher F. McKee, University of California, Berkeley, United States

Citation: Ward-Thompson, D., Furuya, R. S., Tsukamoto, Y., McKee, C. F., eds. (2020). The Role of Magnetic Fields in the Formation of Stars. Lausanne: Frontiers Media SA. doi: 10.3389/978-2-88963-772-0

Table of Contents

frontiers in Astronomy and Space Sciences

EDITORIAL
published: 16 April 2020
doi: 10.3389/fspas.2020.00013

Editorial: The Role of Magnetic Fields in the Formation of Stars

Derek Ward-Thompson[1]*, *Christopher F. McKee*[2], *Ray Furuya*[3] and *Yusuke Tsukamoto*[4]

[1] Jeremiah Horrocks Institute, University of Central Lancashire, Preston, United Kingdom, [2] Departments of Physics and of Astronomy, University of California, Berkeley, Berkeley, CA, United States, [3] Institute of Liberal Arts and Sciences, Tokushima University, Tokushima, Japan, [4] Department of Physics and Astronomy, Faculty of Science, Kagoshima University, Kagoshima, Japan

Keywords: star formation, magnetic fields, inter-stellar medium, molecular clouds, protostars, circumstellar disks

Editorial on the Research Topic

The Role of Magnetic Fields in the Formation of Stars

The subject of how stars and planets form is one of the most fundamental outstanding questions in astronomy. Many theories have been proposed to explain the various processes involved. One of the key unanswered aspects of this whole question is exactly what role magnetic fields play in the overall process. It has been known for many years that magnetic fields exist in the interstellar medium, although their role is hotly debated.

Some theories have magnetic fields as the key agents of evolution, whilst other theories ignore magnetic fields altogether, as being only a minor perturbation on an otherwise turbulent picture. However, the recent advent of new telescopes capable of measuring inter-stellar magnetic fields, with previously unheard-of sensitivity and resolution, such as ALMA, NOEMA, CARMA, SMA, and new instruments on existing ground-based telescopes such as JCMT, Nobeyama and IRAM, and airborne/space-based telescopes such as SOFIA and Planck, has meant that it is now possible to revisit this question with fresh eyes, based on new data. In addition, the huge increase in the power of High-Performance Computers (HPCs) means that the current generation of simulations can include more details of more aspects of astrophysics than ever before.

In this Research Topic we revisit the question of the role of magnetic fields in the star formation process and bring together the latest observations with the latest theories to see what progress can now be made in addressing this question. The ordering of this Editorial follows the broad theme of observations followed by theory, with each scaling roughly from large scales to small—from entire molecular clouds to individual protostars.

Crutcher and Kemball begin the observation section with a discussion of the use of the Zeeman Effect to measure the line-of-sight strength of magnetic fields in molecular clouds and the general inter-stellar medium (ISM). This has only been detected in three species in the general ISM, HI, OH and CN, and in three species in masers, OH, CH_3OH, and H_2O. The Zeeman Effect calculates the line-of-sight field strength from measurements of the hyper-fine splitting of a degenerate line, where the amount of splitting is directly proportional to the field strength, with the constant of proportionality relating to the Bohr magneton. The magnetic field strength can then be used to derive the mass to magnetic flux ratio to determine whether a cloud is magnetically super-critical (prone to collapse) or sub-critical (supported by the magnetic field) using a version of the magnetic virial theorem. The magnetic field strength shows a behavior with respect to the column density as follows (see their Figures 4, 5): below a column density of order 10^{21-22} cm^{-2} the field is essentially independent of column density (at around 10–20 μG); above this column density the field strength increases with increasing column density (with a relation of $B \propto n^{0.65}$). In terms of volume density this transition occurs at roughly 300 cm^{-3}. This can be interpreted in a way that says that low-density gas is sub-critical and high-density gas is super-critical.

Edited and reviewed by:
Scott William McIntosh, National Center for Atmospheric Research (UCAR), United States

***Correspondence:**
Derek Ward-Thompson
dward-thompson@uclan.ac.uk

Specialty section:
This article was submitted to Stellar and Solar Physics, a section of the journal Frontiers in Astronomy and Space Sciences

Received: *13 March 2020*
Accepted: *19 March 2020*
Published: *16 April 2020*

Citation:
Ward-Thompson D, McKee CF, Furuya R and Tsukamoto Y (2020) Editorial: The Role of Magnetic Fields in the Formation of Stars. Front. Astron. Space Sci. 7:13. doi: 10.3389/fspas.2020.00013

Pattle and Fissel move onto single-dish millimeter and far-infrared observations. Here again the dominant source of polarization is thermal emission from partially aligned dust grains. They discuss the currently popular radiative alignment torque mechanism for grain alignment, and the causes of depolarization, such as decreasing alignment efficiency and changes in magnetic field geometry on scales smaller than the beam. They go on to describe various techniques for inferring magnetic field strengths from linear polarization measurements. The polarization can be used to infer the magnetic field strength most commonly via the DCF method, for comparison with the Zeeman measurements. Interestingly, a very similar result is seen (see their Figure 2) to that discussed above in the Crutcher and Kemball paper. In fact, the agreement between these totally different methods is quite striking, especially given that the Zeeman effect measures the line-of-sight magnetic field and polarization can only probe the plane-of-sky field. They discuss observations in a variety of environments, such as ionized regions, infrared-dark clouds, filaments, isolated globules and molecular cloud complexes. There appears to be growing evidence for bimodality in the alignment between fields and filaments, with the fields lying preferentially either parallel to, or perpendicular to filaments. The observations can be interpreted as either a magnetic field passing through a filament, or else as a magnetic field being helically wound around a filament until it runs virtually parallel to the filament. In the former case it would be predicted that the filament would fragment, while in the latter case the filament might be predicted to be longer-lived. Magnetic fields in more isolated cores are seen to typically lie at 30 degrees to the projected short axis of the core. This can be explained as an ensemble of tri-axial asymmetric ellipsoids with the magnetic field parallel to the shortest axis. Projection effects then statistically favor this projected offset.

Hull and Zhang round up the observations section by discussing interferometric observations of magnetic fields in star-forming regions. Clearly, these observations cover the smallest scales currently observable, of protostars and their circum-stellar discs at resolutions of 100 au or less in nearby regions. The polarization observed by interferometers at millimeter wavelength scale is dominated by preferential thermal emission from partially aligned dust grains. Field strengths are estimated from these observations to be in the region of fractions of a mGauss to a few mGauss. The authors claim that the most recent observations appear to show that the popular quasi-static, magnetically-dominated core collapse model is an over-simplification in all but a few cases. This model produces the classic hour-glass field morphology, but it appears that only a few such cases are seen. The apparent random alignment of magnetic fields and outflows suggests that the fields do not determine the angular momentum direction during collapse. The small virial parameters seen in many cases also throw into question virialized collapse models, although the authors mention that strong fields could account for the low virial parameter.

Krumholz and Federrath begin the theory section by studying the effect of the magnetic field on the star formation rate (SFR) and the initial mass function (IMF) of stars. The authors claim that the most significant effects of the magnetic field on the SFR are all indirect. They provide examples, including: magnetic fields provide support against gravitational collapse; they give additional support against shock compression, making it more difficult to shock gas to very high densities; it is also possible that magnetic fields inhibit the decay rate of the turbulence that is driven by the self-gravitational compression of the gas. They finish by looking at the effects of the magnetic field on the stellar IMF. They discuss the two-component IMF: log-normal plus power-law tail. The former comes from the general turbulence in the ISM generating a log-normal distribution of pre-stellar core masses, while the latter has been attributed to a linear scaling of post-shock gas density with shock Mach number. The authors claim that the latter effect does not match the observations after the introduction of magnetic fields. The authors themselves have made a series of models of MHD-turbulence-regulated star formation, using a Press-Schechter formalism, and claim to find better agreement with observations, such as the Salpeter power-law tail of the IMF.

Hennebelle and Inutsuka explore the role of magnetic fields in the formation and evolution of molecular clouds. They start from ideal MHD and incorporate the first non-ideal correction, namely ion-neutral drift. They return to the topic introduced observationally in an earlier chapter of magnetic fields and filaments, but this time consider the theoretical implications. They deduce that the magnetic field is probably responsible for shaping the inter-stellar gas by generating a multitude of filaments, and for reducing the overall star formation efficiency by a factor of a few. Furthermore, they could indirectly lower the star formation efficiency by a further factor by enhancing the stellar feedback in higher-mass stars.

Wurster and Li continue the theoretical section by considering magneto-hydrodynamic (MHD) simulations of protostellar discs. Velocity data indicate that typical pre-stellar cores have enough angular momentum to generate a protostellar disc of scale of order 100 au. However, what is not known is to what extent magnetic braking helps to dissipate this angular momentum and hence suppress disc formation. Ideal MHD simulations can prevent disc formation in some cases, although disks can form in the presence of turbulence, which leads to the misalignment of the field and the angular momentum. Theorists have turned to non-ideal MHD to salvage disc formation and form the hundreds of discs and thousands of planets that have been observed. Non-ideal MHD includes both charged and neutral species, allowing for a weakly-ionized ISM. Non-ideal processes help to diffuse and weaken the magnetic field, hence reducing the magnetic braking effect and allowing discs of sizes of tens of au to form. The authors find that by misaligning the B-field and angular momentum vectors, larger or smaller discs can form, depending on environmental conditions.

Pudritz and Ray move on from circum-stellar discs to protostellar outflows. Bipolar outflows are observed right across the stellar mass spectrum and are fundamental to the star formation process. They are one of the key processes invoked to inject turbulence into the ISM, as well as often being invoked to carry away excess angular momentum from collapsing protostars. Observations now confirm that the jets at the centers of outflows do, in fact, rotate. Of the two main theoretical outflow

launching mechanisms that have been proposed, the magneto-rotational instability (MRI) turbulence model has recently run into problems relating to damping, and so the authors claim that the magnetized disc wind model is the more likely to transport angular momentum from the disc to the jet and explain the observations of rotating jets. Recent multi-scale MHD observations can now trace star formation evolution from giant molecular cloud (GMC) scales of tens of pc down to circumstellar disc scales of tens of au for the first time in a single code. The authors conclude that feedback from magnetized outflows plays a key role in regulating the star-formation efficiency of a molecular cloud.

Teyssier and Commerçon round up the volume by reviewing numerical schemes for MHD and radiation transfer for the modeling of star-formation regions in environments where the turbulence is both super-sonic and super-Alfvenic and include the effects of radiation and self-gravity. They describe the most popular types of numerical schemes: smoothed particle hydrodynamics (SPH); finite difference methods; and finite volume methods; including various implementations of non-ideal MHD effects; Ohmic and ambipolar diffusion, and the Hall Effect. They discuss how to overcome the major numerical problems both for SPH and grid methods: divergence-free magnetic fields; numerical diffusion; and resolution requirements. For the avoidance of infinitesimally small time-stepping, they discuss sink particles and sub-grid models, although these are not without their drawbacks. Multi-fluid, multi-phase approaches have recently been all but abandoned due to their prohibitive computational cost. They conclude that there is still much work to do, given that all existing models have been forced to cover only a limited portion of the full parameter space needed in this field.

Overall, this volume puts together all the many aspects of the role of magnetic fields in the formation of stars from both observational and theoretical perspectives and presents the reader with numerous challenges and issues for future work in many different directions. It is hoped that proposed new instrumentation, such as SPICA-Pol and the new imaging polarimeter under construction for JCMT will continue to move this field forwards. Progress in this field touches on so many other areas of astrophysics, from planet formation, to the evolution of whole galaxies. Within the next decade it could be possible to determine the complete energy balance of entire disk galaxies.

AUTHOR CONTRIBUTIONS

All authors listed have made a substantial, direct and intellectual contribution to the work, and approved it for publication.

ACKNOWLEDGMENTS

The Editors wish to thank all the authors and reviewers of the submitted papers for their time, their careful work, and their patience. We gratefully acknowledge the assistance of the people in the Editorial Office of Frontiers who helped immensely, especially Christiane Ranke, Marta Brucka, Mathew Williams, Caroline Lasfargeas, and Claudio Bogazzi. UK STFC ST/R000786/1 (DW-T) and JSPS KAAKENHI grant number 18H05437, 18K13581, 18K03703 (YT).

Conflict of Interest: The authors declare that the research was conducted in the absence of any commercial or financial relationships that could be construed as a potential conflict of interest.

frontiers in Astronomy and Space Sciences

REVIEW
published: 17 October 2019
doi: 10.3389/fspas.2019.00066

Review of Zeeman Effect Observations of Regions of Star Formation

Richard M. Crutcher and Athol J. Kemball*

Department of Astronomy, University of Illinois, Urbana, IL, United States

The Zeeman effect is the only observational technique available to measure directly the strength of magnetic fields in regions of star formation. This chapter reviews the physics of the Zeeman effect and its practical use in both extended gas and in masers. We discuss observational results for the five species for which the Zeeman effect has been detected in the interstellar medium—H I, OH, and CN in extended gas and OH, CH_3OH, and H_2O in masers. These species cover a wide range in density, from $\sim$10 cm^{-3} to $\sim 10^{10}$ cm^{-3}, which allows magnetic fields to be measured over the full range of cloud densities. However, there are significant limitations, including that only the line-of-sight component of the magnetic field strength can usually be measured and that there are often significant uncertainties about the physical conditions being sampled, particularly for masers. We discuss statistical methods to partially overcome these limitations. The results of Zeeman observations are that the mass to magnetic flux ratio, which measures the relative importance of gravity to magnetic support, is subcritical (gravity dominates magnetic support) at lower densities but supercritical for $N_H \gtrsim 10^{22}$ cm^{-2}. Above $n_H \sim 300$ cm^{-3}, which is roughly the density at which clouds typically become self-gravitating, the strength of magnetic fields increases approximately as $B \propto n^{2/3}$, which suggest that magnetic fields do not provide significant support at high densities. This is consistent with high-density clouds being supercritical. However, magnetic fields have a large range in strengths at any given density, so the role of magnetic fields should differ significantly from one cloud to another. And for maser regions the dependence of field strength on density may have a slightly lower slope. Turbulent reconnection theory seems to best match the Zeeman observational results.

Keywords: Zeeman effect, magnetic fields, molecular clouds, mass/flux ratio, star formation, masers

OPEN ACCESS

Edited by:
Derek Ward-Thompson, University of Central Lancashire, United Kingdom

Reviewed by:
Sebastian Wolf, University of Kiel, Germany
Tyler Bourke, Square Kilometre Array Organisation, United Kingdom

****Correspondence:***
Richard M. Crutcher
crutcher@illinois.edu

Specialty section:
This article was submitted to Stellar and Solar Physics, a section of the journal Frontiers in Astronomy and Space Sciences

Received: *23 March 2019*
Accepted: *30 September 2019*
Published: *17 October 2019*

Citation:
Crutcher RM and Kemball AJ (2019) Review of Zeeman Effect Observations of Regions of Star Formation. Front. Astron. Space Sci. 6:66. doi: 10.3389/fspas.2019.00066

1. INTRODUCTION

What governs or regulates star formation has been a crucial question in astrophysics for many decades. The two extreme positions are: (1) that magnetic fields support clouds against gravitational collapse and that star formation can occur only when magnetic support is removed, through a process such as ambipolar diffusion, e.g., Mouschovias and Ciolek (1999) or (2) that interstellar turbulence governs the formation of self-gravitating clouds that once formed can collapse and form stars, e.g., Mac Low and Klessen (2004). Theory alone cannot answer this question; required are observations of magnetic fields.

There are several observational techniques for the study of magnetic fields in the interstellar medium, with the two most prominent being (1) linear polarization of continuum radiation emitted or absorbed by dust grains aligned by magnetic fields and (2) the Zeeman effect that produces frequency-shifted polarized spectral lines. This chapter is concerned with the Zeeman effect.

The Zeeman effect was discovered by Dutch physicist Pieter Zeeman in 1896 in a laboratory experiment. In his discovery paper Zeeman suggested that the effect he had discovered could be important in measuring magnetic fields in astrophysics. The Zeeman effect was first applied in astrophysics in 1908 by George Ellery (Hale, 1908), who measured magnetic fields in sun spots. Although interstellar magnetic fields were first detected by Hiltner (1949) by observing linear polarization of starlight passing through the intervening interstellar medium, the first detection of the Zeeman effect in the interstellar medium came only after almost another 20 years. The first indication of an interstellar Zeeman effect came from observations of polarization in OH masers by Weinreb et al. (1965); although they suggested that the polarization might be due to the Zeeman effect, that interpretation was not certain because the standard pattern of the classical Zeeman effect was not seen in the polarized maser emission. Following intense observational work by several workers, Verschuur (1968) first detected the Zeeman effect in the extended interstellar medium in the 21 cm hyperfine line of H I. It was another 15 years before Zeeman splitting in extended molecular gas was detected, in OH by Crutcher and Kazès (1983), and yet another 15 years before detection in the third (and so far last) species, CN, by Crutcher et al. (1996, 1999b). Interstellar maser observations of the Zeeman effect have been extended from OH to additional species: H_2O (Fiebig and Guesten, 1989) and CH_3OH (Vlemmings, 2008b).

The Zeeman effect is used to study magnetic fields in the diffuse and dense (molecular) interstellar medium. In this chapter we review Zeeman observations in the interstellar medium and discuss how observations of the Zeeman effect can test models of star formation, the present state of such tests, and possible future developments. Crutcher (2012) previously reviewed observations (by all techniques) of magnetic fields in molecular clouds. This article is specific to the Zeeman effect; it expands discussion of the effect itself, summarizes the discussion in the above review, adds the (very limited) new Zeeman data that have become available, and discusses some more recent controversies about the astrophysical interpretation of the observational results.

2. THE ZEEMAN EFFECT

Immediately after Zeeman's discovery, Hendrik Lorentz explained the Zeeman effect in terms of classical physics—an electrical charge moving in a circular orbit in a magnetic field. The predicted frequencies for the Zeeman-split lines are then:

$$\nu = \nu_0 \pm \frac{eB}{4\pi m_e c}, \tag{1}$$

where ν_0 is the unshifted line frequency, e is the charge of an electron, B is the magnetic field strength, m_e is the mass of an electron, and c is the speed of light.

The above might suggest that in the presence of a magnetic field, an atom would emit two spectral lines at the frequencies given by Equation (1). However, only the vector component of the electron acceleration perpendicular to the line of sight will produce electromagnetic radiation along the line of sight. For atoms with electron orbital planes perpendicular to the line of sight, as the electrons accelerate in their circular orbits they will emit circularly polarized radiation along the magnetic field direction. Since electrons are negatively charged, right circularly polarized radiation has the higher frequency and left circularly polarized radiation the lower frequency. On the other hand, if one observes perpendicular to the magnetic field vector **B** with the electron orbits perpendicular to **B**, then only the acceleration of the electron perpendicular to **B** will emit radiation along the line of sight, and this radiation will be linearly polarized perpendicular to **B**. In practice one could not observe a single atom but an ensemble of atoms with electron orbital planes randomly distributed with respect to **B**. In the case of observations along the magnetic field direction, the projection of these orbits onto the plane perpendicular to **B** would produce the same two circularly polarized Zeeman components as described above. For observations perpendicular to **B**, however, a frequency of radiation different from the two Zeeman components is introduced. Electron orbits parallel to **B** will produce linearly polarized radiation parallel to **B** but unshifted in frequency since the electron acceleration that produces the radiation is parallel to **B**, hence there is no additional force produced by the magnetic field.

However, with higher spectral resolution it was soon found that the triplet of lines predicted by classical physics was actually a more complicated pattern of more than three lines. This "anomalous" Zeeman effect is not explicable by classical physics, for it is only the angular momentum of the electron in its orbit that produces the classical Zeeman effect. Electron spin means that it is the total angular momentum, both orbital and spin angular momenta, that produces the Zeeman effect. The various coupling modes of the two angular momenta produce the more complicated anomalous effect with more than the three classical line components when the net spin of the electrons is an odd half integer. Therefore, atomic hydrogen is in general a case of anomalous Zeeman splitting. However, since the 21 cm line of H I arises from the two hyperfine energy levels in the ground $S_{1/2}$ state with $m_J = \pm 1/2$, the Zeeman pattern is the classical three-line one. The "anomalous" Zeeman effect is in fact THE Zeeman effect; the "normal" Zeeman effect with a triplet of lines is simply a subset of the complete situation. With a single electron moving in a magnetic field, the prediction is the same as the classical one:

$$\nu = \nu_0 \pm \frac{\mu_B B}{h}, \tag{2}$$

where the Bohr magneton $\mu_B \equiv eh/4\pi m_e c = 9.2732 \times 10^{-21}$ erg/G, which means that the frequency shift due to the Zeeman effect for the 21 cm H I line is 1.4 Hz/μG.

The atoms and molecules that are most useful in studying magnetic fields in the interstellar medium are hydrogenic, with an odd number of electrons. The unpaired electron in hydrogenic systems will lead to large Zeeman splittings, approximately equal to the Bohr magneton, and hence to detectable Zeeman splittings at the relatively low ($\sim$10 μG in H I, e.g., Heiles and Troland, 2005) magnetic field strengths in the interstellar medium. Even for systems with all electrons paired, there may still be a Zeeman effect, but this time due to the nuclear spin rather than the electron spin. However, the Zeeman splitting is now approximately equal to the nuclear magneton, $\mu_N = eh/4\pi m_p c = \mu_B/1836$. Only for very strong magnetic fields and very strong spectral lines is the Zeeman effect detectable in the interstellar medium for this case; examples are the CH_3OH and H_2O masers.

Figure 1 (upper) illustrates the above discussion of the Zeeman effect. The lower part of **Figure 1** shows the polarizations of the frequency unshifted (π) and shifted (σ) Zeeman components, with their polarization states depending on the viewing angle.

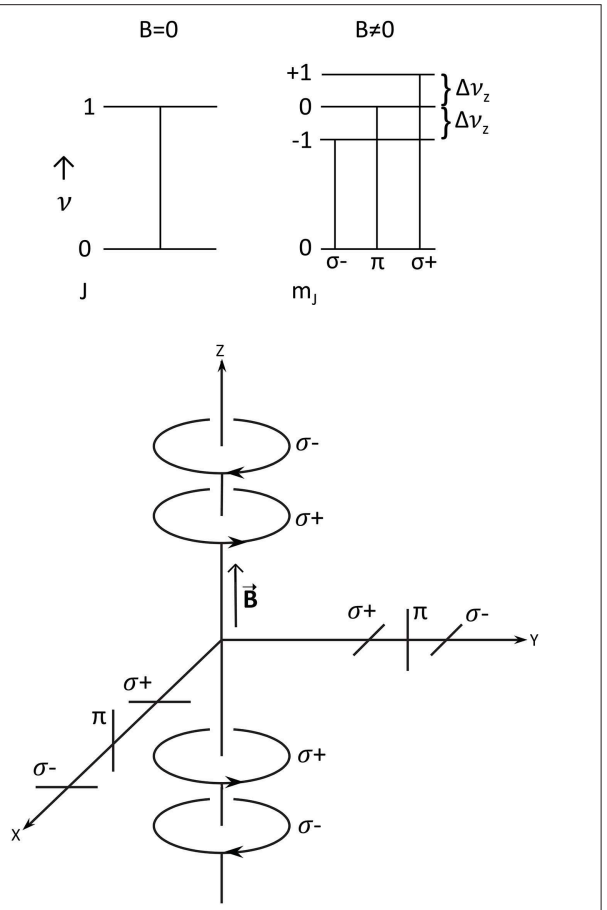

FIGURE 1 | Top: Energy level diagram showing Zeeman splitting. **Bottom**: Polarizations that would be observed from different angles with respect to the magnetic field.

3. OBSERVING THE ZEEMAN EFFECT

Figure 2 illustrates what will be observed for the classical Zeeman effect. **Figure 2A** shows a Gaussian Stokes I spectral line with unit intensity and unit sigma-width $\Delta\nu_\sigma$ (i.e., FWHM = 2.355). **Figure 2B** shows the three Zeeman components when the Zeeman splitting is sufficiently large that the Zeeman components are cleanly separated, with the total intensity of each component being in the ratio 1:2:1. **Figure 2C** shows what would be observed with a instrument sensitive to circular polarization with a 1% Zeeman splitting. **Figure 2D** shows what would be observed with a instrument sensitive to linearly polarization perpendicular to the magnetic field in the plane of the sky with a large Zeeman splitting, such as might occur in mainline OH masers. In these cases, one would observe the Zeeman components with their full separations $\Delta\nu_z$ and be able to infer the full magnetic field strength. However, if the Zeeman splitting were only 1% of the line width, **Figure 2E** shows the Stokes Q and/or U spectra that would be observed. Note the very small amplitude of the signal. Finally, **Figure 2F** complements (**Figure 2D**) and shows the spectrum that would be observed in linear polarization observing parallel to a field in the plane of the sky.

The strength of the π component is proportional to the strength of the magnetic field in the plane of the sky parallel to the magnetic vector **B**. The σ components are generally elliptically polarized, since the magnetic field will in general be at an angle to the line of sight. The elliptical polarization is a combination of linear polarization perpendicular to **B** in the plane of the sky and circular polarization proportional to the strength of the magnetic field along the line of sight. The sense of the circular polarization of the two σ components reverses depending on whether the line-of-sight component B_{LOS} is toward or away from us. From $\Delta\nu_z$, the degree of elliptical polarization of the σ components, and the relative amplitudes of the σ and π components, it is possible in principle to infer full information about **B** (Crutcher et al., 1993).

However, in the extended (non-masing) interstellar medium, the Zeeman splitting is generally much smaller than the line width, and it is possible to infer only the amplitude and direction of the line-of-sight component B_{LOS} of **B**. We can see why this is if we consider a magnetic field with components both along the line of sight and in the plane of the sky. If an instrument is sensitive only to (for example) left-circular polarization, it could detect (say) 100% of the $\sigma-$ (or equivalently red-shifted σ_r) Zeeman component and 0% of the $\sigma+$ (or equivalently blue-shifted σ_b) component. But the linearly polarized $\sigma-$, π, and $\sigma+$ Zeeman components would also be detected by this instrument at a fraction of their full intensity (depending on θ, the angle between the line of sight and **B**). This would increase the detected strength of the $\sigma+$ Zeeman component, but would shift the centroid of the observed left-circularly polarized spectrum toward the unshifted line frequency ν_0. Hence, the observed Zeeman frequency shift would be less than $\Delta\nu_z$. When the right circularly polarized spectrum was observed, a similar shift toward the central unshifted frequency would occur. The result would

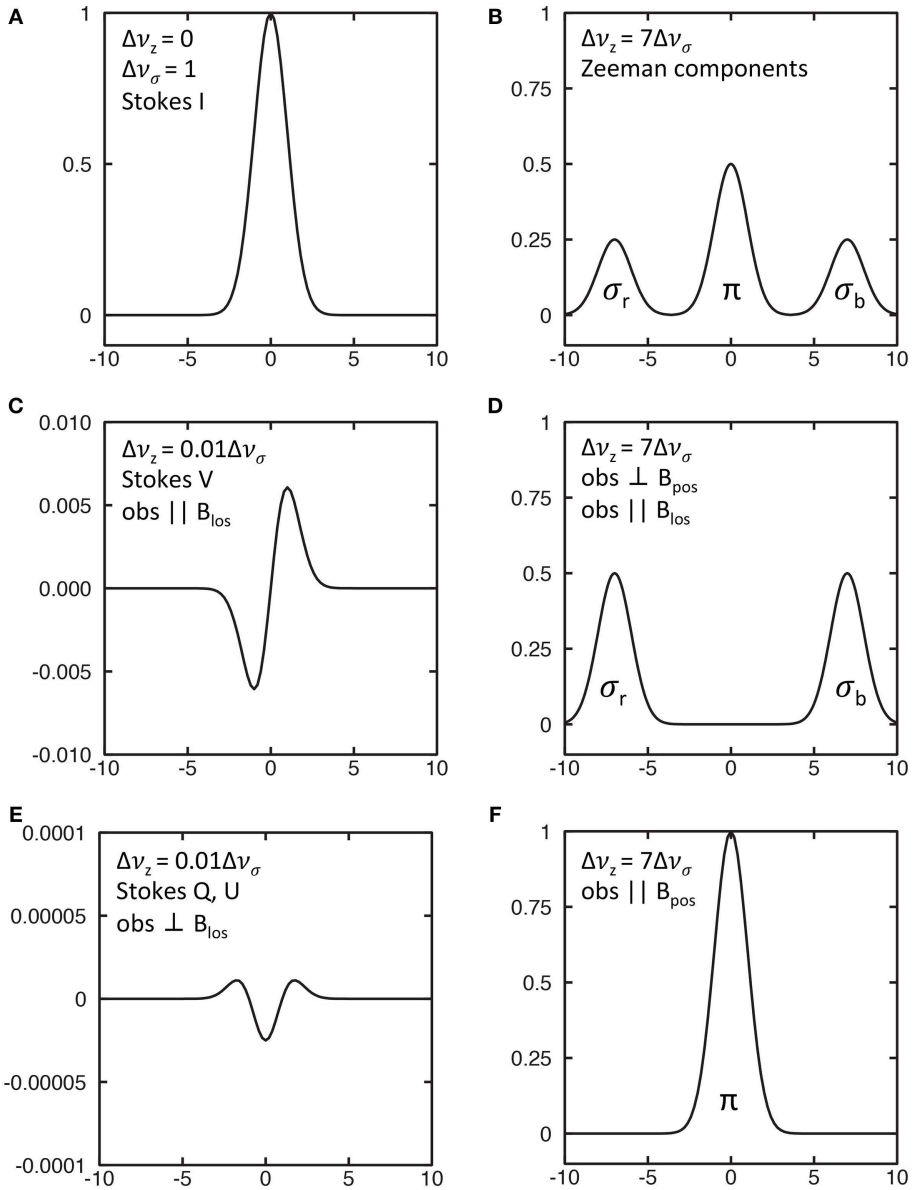

FIGURE 2 | Simulated Zeeman profiles for a Gaussian line profile. Units are relative with respect to peak of the Stokes I profile = 1. **(A)** Stokes I profile. **(B)** Zeeman-split components. **(C)** Stokes V profile for small Zeeman splitting. **(D)**: Stokes σ profile for large Zeeman splitting. **(E)** Stokes Q or U profiles for small Zeeman splitting. **(F)** Stokes π profile for large Zeeman splitting.

be an "observed" Zeeman splitting less than $\Delta\nu_z$, by an amount $cos\theta$. Hence, observation of the Stokes parameter V spectrum yields only $B\cos\theta = B_{LOS}$, the line-of-sight component of **B**. As illustrated in **Figure 2C**, when the Zeeman splitting is 1/100th the width of the spectral line ($\Delta\nu_z = 0.01\Delta\nu_\sigma$), the shape of the Stokes V spectrum is that of the first derivative with respect to frequency of the Stokes I spectrum and the total amplitude of the Stokes V spectrum is about 1/100 that of the Stokes I spectrum.

In principle, information about the field in the plane of the sky (POS) would come from the Stokes Q and U spectra, with strengths proportional to $(\Delta\nu_z/\Delta\nu_\sigma)^2 \times B_{POS}$. The reason for this second-order dependence of the strengths of the Stokes Q and U spectra on the strength of the magnetic field comes from the fact that there is not just the Zeeman-split linearly-polarized σ components, but also the linearly polarized and non-shifted π Zeeman component. **Figure 2E** illustrates this for a Zeeman splitting of 1/100th the width of the spectral line. The magnitude of the Stokes Q or U spectrum (depending on the orientation of the magnetic field on the plane of the sky) is much too small to be detected as a practical matter.

To date the Zeeman effect has been detected unambiguously in non-masing interstellar gas only in H I, OH, and CN lines and in maser lines of OH, CH_3OH, and H_2O. The Zeeman splitting factor $Z = 2\Delta\nu_z$, which is the separation between the two σ components or twice the Zeeman frequency shift, is specific to the spectral transition. The Zs for transitions with interstellar

Zeeman detections are given in **Table 1** (maser lines of CH_3OH and H_2O are blends of several ΔF transitions, and Z factors are somewhat uncertain). In this table R.I. is the relative intensity and Z is the Zeeman splitting factor of each line, so R.I. $\times$ Z is the relative sensitivity to B_{LOS}. Other promising species are C_2H, SO, C_2S, and CH. Unfortunately, most of the common interstellar molecules have all their electrons paired (non-paramagnetic species) and therefore do not have strong Z factors. Because Z does not depend on spectral-line frequency, sensitivity to the Zeeman effect decreases with increasing spectral-line frequency, so cm-wavelength transitions like those of H I and OH are sensitive to much lower field strengths than those of mm-wavelength transitions like those of CN.

Zeeman radio spectral-line observations are generally not reported as right and left circularly polarized spectra (RCP and LCP), but as Stokes parameter spectra I = RCP + LCP and V = RCP-LCP (for technical reasons telescope software sometimes returns I and V as 1/2 the above). As noted above, for the limit of Zeeman splitting much smaller than the spectral-line width, the "theoretical" Stokes V spectrum is $V \approx dI/dv \times Z \times B\cos\theta$. The analysis technique followed is to calculate the derivative of the I spectrum by numerically differentiating the observed I spectrum, and to fit (usually by least squares) this to the observed V spectrum. Because there may be a gain difference "g" between the left and right circular polarization due to instrumental effects, generally one also includes a term to fit for this. So the general equation fitted to the observed Stokes V spectrum is:

$$V \approx dI/dv \times Z \times B\cos\theta + g \times I. \quad (3)$$

The mean error in $B\cos\theta$ is also given by the least-squares fitting process.

Very small instrumental polarization effects can be very important for Zeeman work; hence, observers must be very careful that instrumental polarization effects are not mistaken for the Zeeman effect. The most significant instrumental effect in single-dish Zeeman observations is the phenomenon of "beam squint", for which the left and right circularly polarized beams of the telescope point in different directions. Beam squint is important for Zeeman work because the combination of beam squint and a velocity gradient in a cloud will produce a V spectrum identical to the one expected for the Zeeman effect. Heiles and Troland (2004) have extensively described the possible instrumental effects and techniques for mitigating these effects when performing Zeeman observations. The technical challenges of high-accuracy Stokes V interferometric observations and analysis are described by Sault et al. (1990) and Kemball and Richter (2011).

When only one component of **B** is measurable, the Zeeman effect gives directly only a lower limit to the total magnetic field strength. However, a statistical study of a large number of clouds can yield information about total field strengths, e.g., Heiles and Crutcher (2005). Most of the earlier statistical studies assumed that the measured B_{LOS} in a set of clouds were uniformly distributed between $-B_0$ and B_0, where B_0 is the total field strength that is assumed to be the same in all lines of sight observed. Then the median and mean of the set of measured $|B_{LOS}| = \frac{1}{2}B_0$. Hence, one simply determines the mean of $|B_{LOS}|$ to infer B_0. However, the approaches that deal only with mean or median values ignore the possibly large variation in total field strength (B_{TOT}) in the sample. A more sophisticated approach is to measure the probability distribution function (PDF) of B_{LOS} over a sample of clouds and to infer the PDF of the total magnitude of the magnetic field strength. An application of this approach will be discussed in detail below.

4. ZEEMAN OBSERVATIONAL RESULTS—EXTENDED GAS

4.1. H I, OH, and CN Zeeman Observations

The Zeeman effect in the ISM was first detected—after multiple attempts—in absorption lines of H I toward the Cassiopeia A supernovae remnant (Verschuur, 1968). Over the next 5 years only three more detections were made, toward Orion A, M 17, and Taurus A. Three of these were in the H I associated with molecular clouds, while the Taurus A line is not.

Troland and Heiles (1982a,b) and Heiles and Troland (1982) achieved the first H I Zeeman detections beyond Verschuur's original four souces, 14 years after that first detection. Further emission-line H I Zeeman observations and maps were toward the dark cloud filament L204 (Heiles, 1988), H I filaments associated with supernova or super-bubble shells (Heiles, 1989), the Ophiuchus dark cloud (Goodman and Heiles, 1994), and four dense H I clouds (Myers et al., 1995). Heiles (1997) mapped H I Zeeman toward 217 positions in the Orion-Eridanus region and carried out an extensive analysis. Finally, Heiles and Troland (2004) carried out a large H I Zeeman survey in absorption lines toward continuum sources.

The first detection was of OH absorption toward the NGC 2024 molecular cloud (Crutcher and Kazès, 1983). The OH Zeeman effect was later mapped with the VLA (e.g., **Figure 3**) toward several molecular clouds.

Crutcher et al. (1993) carried out a survey of OH Zeeman toward dark clouds, achieving mostly upper limits. Bourke et al. (2001) extended attempts to detect the OH Zeeman effect, and obtained one definite and one probable new detection out of the 23 molecular clouds observed. Then, Troland and Crutcher (2008) carried out a major survey toward dark clouds, with 9 detections out of 34 positions.

Crutcher et al. (1996, 1999b) detected the Zeeman effect in a second molecular species, CN. Finally, Falgarone et al. (2008) extended the earlier work on CN Zeeman with a survey of dense molecular cores. The combined total was 14 positions observed and eight detections.

Figures 4, **5** show results for the Zeeman observations of H I, OH, and CN in extended gas.

4.2. Interpretation of Zeeman Observations

The three species (H I, OH, and CN) with Zeeman detections in extended gas have resulted in measurements of B_{LOS} that cover a large range of densities. H I emission samples the cold neutral atomic medium over densities between 1 and 100 cm^{-3}. H I in absorption toward molecular clouds can sample densities $\sim 10^2$-10^4 cm^{-3}; the ground-state 18 cm lines of OH sample roughly

TABLE 1 | Zeeman splitting factors Z.

Species	Transition	ν (GHz)	R.I.	Z (Hz/μG)	R.I. × Z	References
H I	$F = 1 - 2$	1.420406	1	2.80	–	1
CH	$J = {}^3/_2, F = 2 - 2$	0.701677	5	1.96	16.4	1
	$J = {}^3/_2, F = 1 - 1$	0.7724788	9	3.27	17.6	1
OH	$J = {}^3/_2, F = 1 - 1$	1.665402	5	3.27	16.4	1
	$J = {}^3/_2, F = 2 - 2$	1.667359	9	1.96	17.6	1
	$J = {}^3/_2, F = 2 - 1$	1.720530	1	1.31	1.31	1
	$J = {}^5/_2, F = 2 - 2$	6.030747	7	1.58	11.1	1
	$J = {}^5/_2, F = 3 - 3$	6.035092	10	1.13	11.3	1
	$J = {}^7/_2, F = 3 - 3$	13.434637	27	1.03	28	2
	$J = {}^7/_2, F = 4 - 4$	13.441417	35	0.80	28	2
CH_3OH	$J_N = 5_1 - 6_0$	6.668519	1	–0.00114	–	3
CCS	$J_N = 1_0 - 0_1$	11.119446	1	0.81	0.81	4
	$J_N = 2_1 - 0_1$	22.344033	1	0.77	0.77	4
	$J_N = 3_2 - 2_1$	33.751374	1	0.70	0.70	4
	$J_N = 4_3 - 3_2$	45.379033	1	0.63	0.63	4
H_2O	$F = 6_{16} - 5_{23}$	22.23508	1	0.003	–	5
SO	$J_N = 1_0 - 0_1$	30.001630	1	1.74	1.74	4
	$J_N = 1_2 - 0_1$	62.931731	1	0.93	0.93	4
	$J_N = 1_1 - 2_2$	86.094	1	1.38	1.38	6
	$J_N = 3_2 - 2_1$	99.299875	1	1.04	1.04	4
	$J_N = 4_3 - 3_2$	138.178548	1	0.80	0.80	4
	$J_N = 3_2 - 4_3$	158.972	1	0.81	0.81	6
CCH	$N = 1 - 0, J = {}^3/_2 - {}^1/_2, F = 2 - 1$	87.31723	42	0.70	29	7
	$N = 1 - 0, J = {}^3/_2 - {}^1/_2, F = 2 - 1$	87.32892	21	2.3	48	7
	$N = 1 - 0, J = {}^3/_2 - {}^1/_2, F = 2 - 1$	87.40234	21	0.93	20	7
CN	$J = {}^1/_2 - {}^1/_2, F = {}^1/_2 - {}^3/_2$	113.1442	8	2.18	17.4	8
	$J = {}^1/_2 - {}^1/_2, F = {}^3/_2 - {}^1/_2$	113.1705	8	–0.31	2.5	8
	$J = {}^1/_2 - {}^1/_2, F = {}^3/_2 - {}^3/_2$	113.1913	10	0.62	6.2	8
	$J = {}^3/_2 - {}^1/_2, F = {}^3/_2 - {}^1/_2$	113.4881	10	2.18	21.8	8
	$J = {}^3/_2 - {}^1/_2, F = {}^5/_2 - {}^3/_2$	113.4910	27	0.56	15.1	8
	$J = {}^3/_2 - {}^1/_2, F = {}^1/_2 - {}^1/_2$	113.4996	8	0.62	5.0	8
	$J = {}^3/_2 - {}^1/_2, F = {}^3/_2 - {}^3/_2$	113.5089	8	1.62	13.0	8

References: 1. Heiles et al. (1993), 2. Uchida et al. (2001), 3. Lankhaar et al. (2018), 4. Shinnaga and Yamamoto (2000), 5. Nedoluha and Watson (1992), 6. Cazzoli et al. (2017), 7. Bel and Leroy (1998), 8. Crutcher et al. (1996).

the same density range. Finally, the 3 mm emission lines of CN, which have a critical density $\sim 10^5$ cm^{-3}, sample densities $\sim 10^5$–10^6 cm^{-3}.

The astrophysical significance of Zeeman results requires determination of N_H and/or n_H in the regions where magnetic field strengths have been measured. For H I in absorption N_H may be determined by also observing the line in emission off the continuum source so that the spin temperature and optical depth can be inferred, e.g., Heiles and Troland (2003). The associated n_H may then be estimated from the mean interstellar pressure in the cold neutral diffuse medium and the spin temperature, e.g., Crutcher et al. (2010b). Since the OH line optical depths are generally small, N_{OH} can be estimated from the observed line strengths, e.g., Crutcher (1979). To obtain N_H one then uses the [OH/H] ratio determined by Crutcher (1979). To obtain n_H for the regions in which OH is found one divides N_H by the mean diameter of the OH region. For CN (Falgarone et al., 2008), the methods are similar to those for OH. The CN hyperfine-line ratios imply that the lines are optically thin, so $N(CN)$ may be calculated from observed line strengths. N_H then comes from [CN/H] based on studies by Turner and Gammon (1975) and Johnstone et al. (2003). The n_H in the CN emitting regions must be fairly close to the critical density of the transition, since the lines are observed to be much weaker than kinetic temperatures and optically thin (no line photon trapping). Unfortunately few excitation analyses of CN excitation have been carried out, but since CN and CS have similar critical densities and map similarly, n_H in the CN regions can be assumed to be about the same as obtained from CS excitation analyses. Finally, a second, independent method for determining n_H comes by dividing N_H by the estimated thickness of clouds from the mean extent of the CN distribution on the sky. There are certainly significant uncertainties in the estimates of n_H especially, particularly as applied to individual clouds, where estimates may be off by

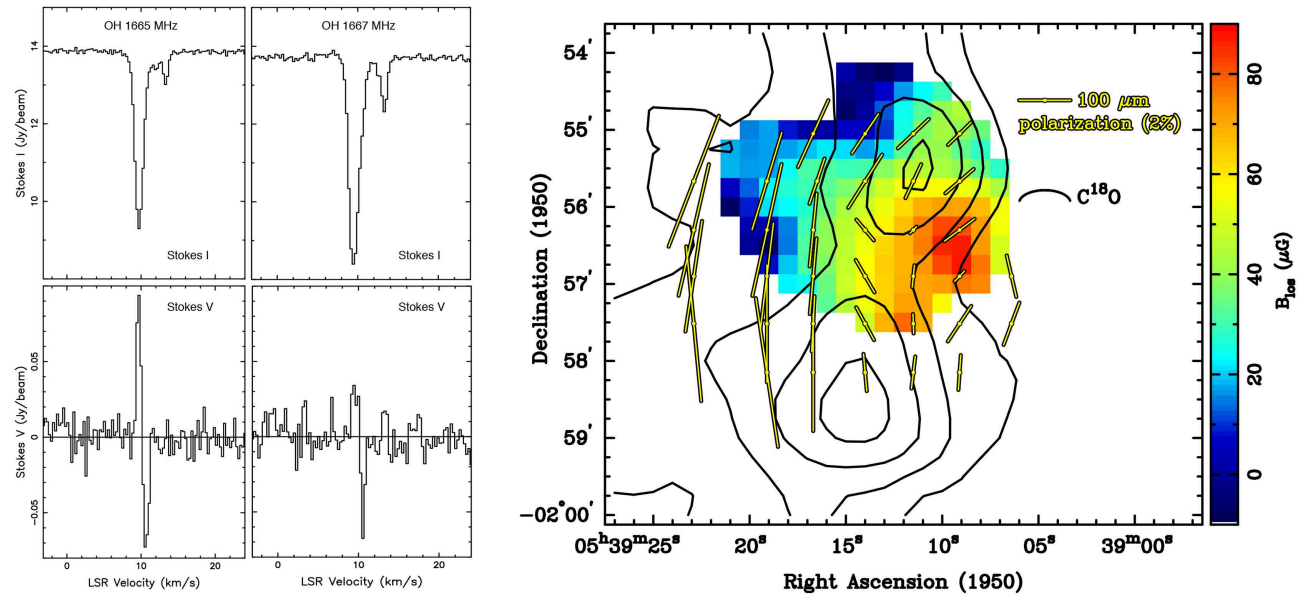

FIGURE 3 | Left: OH Zeeman Stokes I and V profiles toward NGC2024 at the peak B_{LOS} position from VLA mapping (Crutcher et al., 1999a). **Right**: Map of B_{LOS} (color) from OH Zeeman. Contours are $C^{18}O$ intensities and yellow line segments are dust polarization directions (Hildebrand et al., 1995). The magnetic field in the plane of the sky is perpendicular to the dust polarization, hence roughly along the minor axis of the molecular cloud defined by $C^{18}O$ (horizontal in the figure).

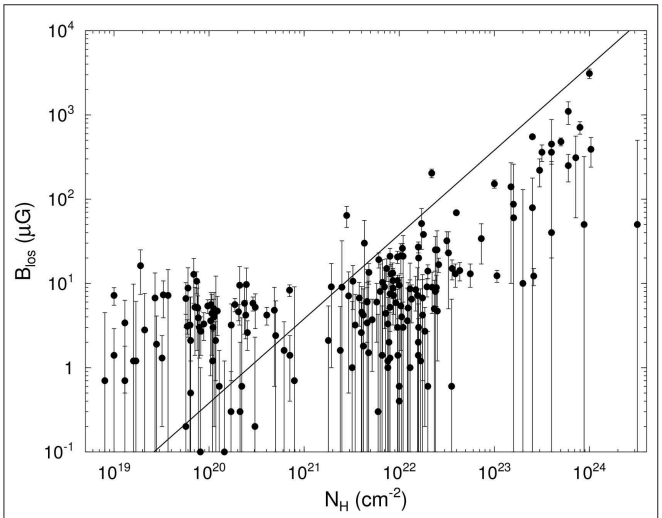

FIGURE 4 | H I, OH, and CN Zeeman measurements of B_{LOS} vs. $N_H = N_{H\,I} + 2N_{H_2}$. The straight line is for a critical $M/\Phi = 3.8 \times 10^{-21} N_H/B$. Measurements above this line are subcritical, those below are supercritical.

an order of magnitude. However, in statistical studies such as those described in this paper, more important is the ensemble uncertainty. Crutcher et al. (2010b) found a statistical uncertainty of about a factor of two in n_H.

Two important quantities than can be inferred from the Zeeman data are the mass to magnetic flux ratio M/Φ ($\propto N_H/B$) and κ (in the $B \propto n_H^{\kappa}$ relation (see Crutcher, 2012 for a detailed discussion). M/Φ is proportional to the ratio of gravity to magnetic pressure and informs whether magnetic fields are sufficiently strong to support clouds against gravitational contraction. A simple way to derive the expression for the critical M/ΦA at which magnetic and gravitational energies are in equilibrium is to equate the virial terms: $3GM^2/5R = B^2R^3/3$. Since magnetic flux $\Phi = \pi R^2 B$, the critical M/Φ is:

$$\left(\frac{M}{\Phi}\right)_{critical} = \frac{1}{3\pi}\sqrt{\frac{5}{G}}. \quad (4)$$

The precise numerical value differs slightly for detailed models depending on geometry and density structure. A supercritical ratio means that magnetic pressure alone is insufficient to prevent gravitational collapse, while a subcritical ratio means collapse is prevented by magnetic pressure. The scaling of magnetic field strength with density is a prediction of many theoretical studies of the evolution of the interstellar medium and star formation. Simple examples include (1) mass accumulation along field lines without change in magnetic field strength, for which $\kappa = 0$; compression of mass perpendicular to the field with flux freezing, for which $\kappa = 1$; and spherical collapse with flux freezing and weak field strength, for which $\kappa = 2/3$ (Mestel, 1966).

4.2.1. B vs. N

First, we discuss field strength vs. column density. Bourke et al. (2001) plotted this for their OH observations and discussed the implication. **Figure 4** shows B_{LOS} vs. N_H with data from the compilation by Crutcher (1999) and four later major Zeeman surveys of H I, OH, and CN (Bourke et al., 2001; Heiles and Troland, 2004; Falgarone et al., 2008; Troland and Crutcher, 2008). The data are clearly separated into three ranges in N_H,

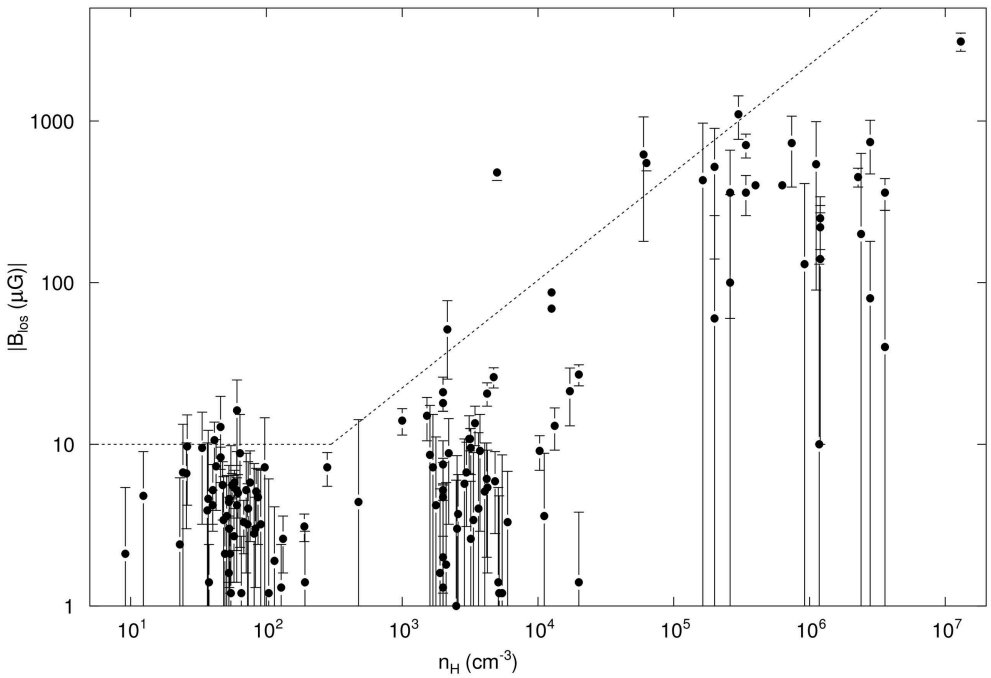

FIGURE 5 | The set of diffuse cloud and molecular cloud Zeeman measurements of the magnitude of the line-of-sight component B_{LOS} of the magnetic vector **B** and their 1σ uncertainties, plotted against $n_H = n(H\,I)$ or $2n(H_2)$ for H I and molecular clouds, respectively. Different symbols denote the nature of the cloud and source of the measurement: H I diffuse clouds, filled circles (Heiles and Troland, 2004); dark clouds, open circles (Troland and Crutcher, 2008); dark clouds, open squares (Crutcher, 1999), molecular clouds, filled squares (Crutcher, 1999); and molecular clouds, stars (Falgarone et al., 2008). Although Zeeman measurements give the direction of the line-of-sight component as well as the magnitude, only the magnitudes are plotted. The dotted line shows the most probable maximum values for $B_{TOT}(n_H)$ determined from the plotted values of B_{LOS} by the Bayesian analysis of Crutcher et al. (2010b).

corresponding to the tracers H I, OH, and CN. The straight line is the critical M/Φ line.

An essential point in interpreting **Figure 4** is that only one component of the total magnetic vector **B** is measured. Hence, all points are lower limits on what the total magnetic field strength would be. However, for $N_H \lesssim 10^{21}$ cm^{-2}, most of the points are above the critical line, showing that at low column densities the diffuse H I and lower column density molecular gas is subcritical. In contrast, for $N_H \gtrsim 10^{22}$ cm^{-2}, all but one of the points are below the critical line. It is possible that some of these clouds are subcritical with the magnetic field close to the plane of the sky. However, that fact that all of the points are below the critical line suggests strongly that a transition occurs at $N_H \sim 10^{22}$ cm^{-2} from subcritical to supercritical M/Φ. Clouds with $N_H \gtrsim 10^{22}$ cm^{-2} have a mean M/Φ that is supercritical by a factor of 2–3. The data strongly suggest that subcritical self-gravitating clouds are the exception and in fact none may exist. These self-gravitating clouds are the ones in the ambipolar diffusion model that should be subcritical at early stages of gravitational contraction.

Figure 4 might appear to support the ambipolar diffusion model of cloud evolution, in which initially subcritical clouds become supercritical by gravitational contraction of neutral matter through magnetic fields. However, the points with $N_H \lesssim 10^{21}$ cm^{-2}, are lower density H I clouds. These cold H I clouds are confined by pressure from the surrounding warm ISM and are not self-gravitating, so they could not gravitationally collapse as envisioned by the ambipolar diffusion model. Heiles and Troland (2005) found that the mean B_{TOT} is approximately the same in the cold H I medium and the warm neutral medium. Hence, the magnetic field strength does not systematically change during transitions of gas between the lower density warm and the higher density cold neutral medium. Possible explanations for this are that diffuse clouds form by flows along magnetic flux tubes or that they form preferentially from regions of lower magnetic field strength. Another process that could be important in keeping field strengths fairly constant is turbulent magnetic reconnection (Vishniac and Lazarian, 1999).

N_H in the range 10^{21-22} cm^{-2} marks a clear transition between magnetic field strengths being statistically independent of N_H and an increase in strength with column density. A similar transition is seen in **Figure 5** (discussed below) at $n_H \approx 300$ cm^{-3}. Assuming that these N_H and n_H correspond to the same clouds, the typical diameters of these clouds is 0.1–1 pc. These are roughly the parameters for an interstellar cloud to become self-gravitating. Gravitational contraction with flux freezing would then cause the magnetic field strength to increase with increasing N_H and n_H. We also note that $N_H \approx 10^{22}$ cm^{-2} is also roughly the column density where the orientation of magnetic fields in the plane of the sky as mapped with polarized dust emission changes (statistically) from parallel to perpendicular with respect to the

elongated mass structures on the plane of the sky (Ade et al., 2016).

Probably the main uncertainty in **Figure 4** comes from the column densities. For H I the N_H are very well determined, since both the line optical depths and spin temperatures are directly measured. However, for OH and CN the N_H come from determinations of N_{OH} and N_{CN} and studies of OH/H and CN/H, which introduce possible errors. A major issue is exactly what N_H the OH and CN Zeeman results sample. On the basis of ambipolar diffusion models with time-dependent astrochemistry, Tassis et al. (2012) argue that OH and CN are heavily depleted at higher densities due to chemistry and hence tend to sample the lower density outer layers of clouds rather than the cores, and that therefore the Zeeman results underestimate the magnetic field strengths in cores. If the true field strengths are higher at each N_H than those plotted in **Figure 4**, many of the points with $N_H > 10^{22}$ cm^{-2} should be plotted at stronger field strengths. Such points would then lie above the critical M/Φ line, and would represent subcritical self-gravitating clouds. One issue with this conclusion is that ambipolar diffusion driven evolution is significantly slower than those for which the magnetic flux problem has been resolved by other physics such as turbulent reconnection (Vishniac and Lazarian, 1999; Lazarian et al., 2012); the chemical depletion at high densities may not have had sufficient time to be as significant as Tassis et al. (2012) find. A more direct problem with their argument is that the interpretation of **Figure 4** does not depend on OH and CN sampling the highest densities of molecular cores. The Zeeman effect estimates the magnetic field strength in the regions sampled by the Zeeman tracer (OH or CN), and the relevant N_H and n_H for estimating M/Φ are those sampled by the Zeeman species. There is no claim that either species samples the highest densities of cores. Ideally one might use a variety of Zeeman species that sample a range of densities in order to measure the change in M/Φ from envelope to core in clouds. The fact that all Zeeman species do not trace the field in the cores, while true, does not invalidate our interpretation of **Figure 4**.

4.2.2. B vs. n

The above discussion was limited by the fact that only the line-of-sight component of the vector **B** is measured with the Zeeman effect. However, with a large number of Zeeman measurements, it is possible to infer statistical information about the total field strength. One can assume a PDF of the total field strength, $P(B_{TOT})$, and compute $P(B_{LOS})$, the PDF of the observable line-of-sight field strengths, assuming a random distribution of the θ. Comparison between the two lets one infer the most probable (of those assumed) $P(B_{TOT})$. Heiles and Crutcher (2005) attempted this for H I Zeeman data with a frequentist approach, but found that the observations did not allow a strong discrimination among possible PDFs for the total field strength.

Crutcher et al. (2010b) used a Bayesian approach, and expanded the Zeeman data set to include H I, OH, and CN surveys (Crutcher, 1999; Heiles and Troland, 2004; Falgarone et al., 2008; Troland and Crutcher, 2008). Their model for B_{TOT} vs. n_H had $B_{TOT,max} = B_0$ at lower densities, based on the most probable result from Heiles and Crutcher (2005). For higher densities the maximum B_{TOT} had a power-law dependance, $B_{TOT,max} = B_0(n/n_0)^\kappa$. The PDF of B_{TOT} at each density was assumed to be flat, with the B_{TOT} equally distributed between the $B_{TOT,max}$ at that n_H and a lower limit $B_{TOT} = f \times B_0$, with $0 \leq f \leq 1$. A delta function PDF (all B_{TOT} at each n_H being the same) would have $f = 1$, while $f = 0$ would be the flat PDF between $B_{TOT,max}$ and 0. The results for the four free parameters in the Bayesian model (**Figure 5**) were $B_0 \approx 10$ μG, $n_0 \approx 300$ cm^{-3}, $\kappa \approx 0.65$, and $f \approx 0$.

For $n_H > n_o$ interstellar magnetic field strengths increase with density. Possible explanations are that diffuse clouds form by accumulation of matter along magnetic field lines, which would increase the density but not the field strength, or that there is a physical process such as turbulent magnetic reconnection that acts to keep fields from increasing with density (Vishniac and Lazarian, 1999; Lazarian et al., 2012). Once densities become large enough for clouds to be self-gravitating, gravitational contraction with flux freezing may lead to the increase in field strength with increasing density.

The Bayesian analysis of the PDFs of the total field strength leads to the same result for the importance of magnetic fields with respect to gravity that was discussed above: for lower densities (where clouds are predominately not self-gravitating), the mass-to-flux ratio is subcritical. At higher densities it is supercritical.

The statistical increase in field strengths with density, parameterized by the power law exponent κ, may be compared with theoretical predictions. The ambipolar diffusion theory has κ near zero at early stages when contraction of neutrals increases density but not field strengths; as evolution proceeds, κ gradually increases to a maximum of 0.5, e.g., Mouschovias and Ciolek (1999). The Bayesian analysis value of $\kappa \approx 0.65 \pm 0.05$ does not agree with the ambipolar diffusion prediction. It does agree with the value $\kappa = 2/3$ found by Mestel (1966) for a spherical cloud with flux freezing. However, while spherical collapse does produce $\kappa = 2/3$, finding that clouds have κ near this value does not require that clouds be spherical. It only means that collapse is approximately self-similar. The Bayesian result does imply that magnetic fields in self-gravitating clouds are generally too weak to dominate gravity in a large fraction of molecular clouds. However, the Bayesian analysis is a statistical one that does not rule out ambipolar diffusion being dominant in a small proportion of molecular clouds.

Tritsis et al. (2015) have questioned the results of the Bayesian analysis described above on several grounds, including: (i) that the clouds are not observed to be spherical; (ii) that the Bayesian analysis included both H I and molecular cloud data; a non-Bayesian analysis by Tritsis et al. (2015) of molecular cloud detections only yielded $\kappa \approx 0.5$; and, (iii) that they found inferred cloud densities in a separate literature search often differing from those used by Crutcher et al. (2010b), particularly higher CN cloud densities, and argued that the CN points in **Figure 5** should move further right thus lowering κ. Collectively, these are open questions for which countervailing arguments and considerations exist; both are important to our full understanding of the scientific interpretation of Zeeman observations. On (i) it can be argued that real clouds invariably have significantly non-spherical morphologies due to other forces

such as bulk flows and turbulence. Regarding (ii), omitting clouds with Zeeman non-detections (and accordingly smaller inferred magnetic field strengths) in a non-Bayesian analysis can bias the estimation of κ downwards; the subset of clouds with larger field strengths may well have a smaller κ than the total set. On the final point (iii), it is required to estimate the density of the Zeeman tracer as opposed to the highest density for each cloud. Further, high excitation lines of other molecular species may sample higher densities that the N = 1–0 CN transition due to excitation and astrochemical depletion. As current and future telescopes provide further data, as described in section 6, these questions will undoubtedly be further constrained.

4.2.3. Radial Dependence of Mass/Flux

Study of M/Φ such as that illustrated by **Figure 4** compare different clouds. Also of interest is the variation of M/Φ within a cloud, for that can be indicative of the role of the magnetic field in the structure and evolution of a cloud. This is a very difficult observational task because spectral lines will generally be weaker away from cloud centers. However, Crutcher et al. (2009) reported such a study toward four dark clouds. Although determination of actual values of M/Φ requires knowledge of the unknown angle θ between the magnetic field vector and the line of sight, it is possible to map the variation from point to point within a cloud if one assumes that the magnetic field direction is the same at the various positions. This is a reasonable assumption if the magnetic field is strong and dominates turbulence, as in the standard ambipolar diffusion model of star formation. That model requires that M/Φ increase from envelope to core as collapse of neutrals through the magnetic field increases the mass but not (so much) the field strength in the core.

The Crutcher et al. (2009) result was that in all four clouds, M/Φ decreases from envelope to core—the opposite of the ambipolar diffusion prediction. This observational result agreed with results from a weak field, turbulence dominated simulation (Lunttila et al., 2009). The observed result could also be due to magnetic reconnection (Lazarian, 2005), since loss of magnetic flux due to turbulent reconnection will proceed more rapidly in envelopes that in cores, since in envelopes have larger spatial scales and in general stronger turbulence.

Mouschovias and Tassis (2009, 2010) reviewed the above results and conclusion, and argued that (1) motion of cores through surrounding more diffuse gas could lead to **B** in cores and their envelopes not being essentially parallel and (2) that since B_{LOS} was not detected in the envelopes only upper limits should be considered. Crutcher et al. (2010a) discussed these arguments. The first point may have some validity, but observed correlation of B_{POS} directions in cores and surrounding gas argues against it. In any case, such a process would sometimes increase and sometimes decrease the observed radial dependence of M/Φ. Four clouds is not a large number, but all four did show the same result. On the second point, it is certainly true that at the 3σ upper-limit level, M/Φ constant or even decreasing slightly with radius is consistent with the data for each cloud individually, but the probability that this is true for all four clouds is $\sim 3 \times 10^{-7}$. None the less, clear observational evidence for the ambipolar diffusion theory was not provided by the results in Crutcher et al. (2009).

4.2.4. Models of Specific Clouds

Ambipolar diffusion models for specific clouds, B1 and L1544, have been produced for comparison with observational data including OH Zeeman detections (Crutcher et al., 1994; Ciolek and Basu, 2000). In both cases the models could agree with observations, but both required that the fields be mainly in the plane of the sky, since the field strengths required by the models were much larger than the line-of-sight strengths obtained from Zeeman observations. While this could be true for the very small sample of two, in the larger sample of dark clouds with OH Zeeman observations one might expect to find examples of the field lying mainly along the line of sight, such that very large B_{LOS} would be found from Zeeman observations. Such large fields are not found.

5. ZEEMAN OBSERVATIONAL RESULTS—MASERS

Astrophysical maser components, due to their intrinsic nature as compact objects of high brightness temperature, are critical probes of magnetic fields in intermediate- and high-mass star forming regions (HMSFR) and are of unique importance in the study of the magnetic field over spatial scales of 10–100 AU (Vlemmings et al., 2010; Surcis et al., 2013). Hydroxyl (OH), water (H_2O), and methanol (CH_3OH) maser species have widespread association with HMSFR; each probes different physical conditions in these regions. SiO masers are rare toward SFR (Elitzur, 1992), and we do not discuss them in this review. Broad reviews of maser observations of star forming regions (SFR) are provided in the monographs by Elitzur (1992) and Gray (2012). Polarization-specific observations of masers toward SFR are reviewed by Vlemmings (2008a) and Vlemmings (2012). In this article we seek to synthesize the current status of maser polarization observations of SFR, the impact of such observations on magnetic field estimates in these regions, and their relationship to open questions in star formation theory. All magnetic field values cited in this section are B_{LOS} unless otherwise specified.

5.1. OH Masers

Hydroxyl masers are common in SFR and are believed to lie in the enclosing dusty molecular envelope, arising during the development of the associated ultra-compact HII (UCHII) region and within the period when the UCHII is within ∼30 milliparsec in size (Caswell, 2001). Several sources are known to be somewhat larger in extent including OH 330.953–0.182 (Caswell et al., 2010) and OH 337.705–0.053 (Caswell et al., 2011b), the latter source perhaps approaching the end of its evolutionary maser-emitting phase.

5.1.1. Main Line OH Masers

OH maser emission toward SFR is detected most frequently in the ground-state main line transitions $^2\Pi_{\frac{3}{2}}, J = \frac{3}{2}, \{F = 1 \rightarrow 1, F = 2 \rightarrow 2\}$ at 1,665 and 1,667 MHz, respectively, and in the

excited-state transitions $^2\Pi_{\frac{3}{2}}, J = \frac{5}{2}, \{F = 2 \rightarrow 2, F = 3 \rightarrow 3\}$ at 6,031 and 6,035 MHz, respectively. The Zeeman effect is readily detected in OH maser transitions due to the paramagnetic nature of the hydroxyl radical (Cook, 1977; Elitzur, 1992). In the formalism of the foundational theory of maser polarization (Goldreich et al., 1973) the Zeeman splitting will exceed the maser linewidth if the magnetic field $B > 0.5$ mG (Slysh et al., 2002). The Zeeman pattern is as discussed above; as noted in that discussion, fully-separated Zeeman components allow inference of the total magnetic field B_{TOT}. The π components are not frequently observed (Slysh et al., 2002) but are not completely absent; Green et al. (2015) find an incidence of $\sim$ 16% in excited state OH transitions.

OH Zeeman pairs are frequently detected toward SFR in interferometric observations sensitive to circular or full polarization. In this paragraph we consider such observations of the main line 1,665 and 1,667 MHz OH masers. The contemporary MAGMO survey of the Carina-Saggitarius tangent in these OH transitions toward methanol maser sites and previously-known OH sources using the Australia Telescope Compact Array (ATCA) by Green et al. (2012) detected 11 Zeeman components and found OH maser fractional linear polarization m_l $\sim$22–95% and fractional circular polarization m_c $\sim$6–100%. These observations and prior aggregated OH Zeeman measurements in this region span a B-field range: –1.5 mG < B < +8.9 mG. Interferometric studies of individual sources find broadly comparable magnetic field magnitudes, including Very Long Baseline Array (VLBA) observations of G23.01–0.41 (Sanna et al., 2010) and W75(N) (Slysh et al., 2002), Long Baseline Array (LBA) observations of OH 337.705–0.053 (Caswell et al., 2011b), OH 330.953–0.182 (Caswell et al., 2010), OH 300.969+1.147 (Caswell et al., 2009), and 323.459–0.079 (Caswell and Reynolds, 2001), and MERLIN observations of IRAS 20126+4104 (Edris et al., 2005). A recent extensive Parkes single-dish polarization spectroscopic survey found that approximately one third of the main-line OH masers toward SFR have a feature that is at least 50% linearly polarized (Caswell et al., 2013). Single-dish observations with the Nançay Radio Telescope (NRT) detected several Zeeman features with inferred magnetic fields consistent with the interferometric results cited above (Bayandina et al., 2014).

5.1.2. Excited State OH Masers

Excited-state OH masers at 6 GHz are usually strongly associated with 1,665 MHz OH masers toward SFR, although at perhaps one third the incidence to the same sensitivity level (Caswell, 2001). Caswell (2004) note that this is consistent with pumping models predicting similar conditions (Pavlakis and Kylafis, 2000; Cragg et al., 2002). Ground-state OH masers have representative dust temperatures $\geq$ 100 K, gas temperatures $\leq$ 100 K, and density $10^4 < n_H < 10^{8.3}$ cm^{-3} (Cragg et al., 2002). Excited-state OH masers trace somewhat cooler gas, at higher density $10^{6.5} < n_H < 10^{8.3}$ cm^{-3} (Cragg et al., 2002; Green et al., 2007).

In this paragraph we consider recent interferometric Zeeman or full polarization observations of 6 GHz excited state OH maser emission toward SFR. A contemporary survey of 30 source positions using the ATCA by Green et al. (2015) detected 94 Zeeman pairs and 18 Zeeman triplets with inferred magnetic fields –10.4 mG < B < 11.4 mG. Interferometric observations of individual sources find Zeeman pairs with a comparable range of magnetic field magnitudes including European VLBI Network (EVN) observations of W3(OH) (Fish and Sjouwerman, 2007), MERLIN observations of W51 (Etoka et al., 2012), W3(OH) (Etoka et al., 2005), and ON1 (Green et al., 2007), ATCA observations of OH 353.410–0.360 (Caswell and Reynolds, 2001), LBA observations of G351.417+0.645 and G353.410–0.360 (Caswell et al., 2011a), and Very Large Array (VLA) observations of NGC 6334I (Hunter et al., 2018).

5.1.3. 1,720 MHz OH Masers

The $^2\Pi_{\frac{3}{2}}, J = \frac{3}{2}, F = 2 \rightarrow 1$ OH maser transition at 1,720 MHz is less frequently observed and detected toward SFR. They are believed to be $\sim$1/6th as prevalent as 1,665 MHz OH masers toward SFR when surveyed to the same sensitivity limit (Caswell, 2004). Observationally 6,035 and 1,720 MHz OH masers are known to have correlated association (Caswell, 2001); at high resolution (Fish and Sjouwerman, 2007) find components in these transition to be co-spatial within 10–20 mas. An ATCA interferometric survey of 1,720 MHz OH masers associated with 1,665 and 6,035 MHz OH maser sites found Zeeman pairs with associated magnetic field magnitudes as high as $\sim$ 16 mG (Caswell, 2004). These authors argue that the 1,720 MHz OH masers toward SFR trace regions of higher densities and higher associated magnetic fields ($\sim$1.5–2$\times$) accordingly.

5.1.4. Detection of Zeeman Pairs

OH Zeeman pairs can be difficult to identify unambiguously due to flux density or positional offsets between the two σ components (Cook, 1977), likely due to differing maser amplification paths for the two separated components. This effect is more pronounced for the main line OH maser transitions as they have larger Zeeman splitting coefficients Z than the 1,720 MHz OH transition and 6 GHz excited state OH transitions. These values are 0.113 km/s/mG at 1,720 MHz (Caswell, 2004), 0.079 km/s/mG at 6,030 MHz and 0.056 km/s/mG at 6,035 MHz (Caswell et al., 2011a); cf. **Table 1**.

5.2. Methanol Masers

Methanol masers have emerged as particularly powerful probes of star formation. The 6.7 GHz $5_1 \rightarrow 6_0 A^+$ methanol transition is associated only with HMSFR (Minier et al., 2003; Green et al., 2007). It is difficult to infer local magnetic field structure in high-resolution observations of ground-state OH masers toward SFR due to significant external Faraday rotation (Surcis et al., 2009); methanol maser transition frequencies are far less affected.

Methanol masers are classified as either Class I or Class II (Menten, 1991a,b). Class I methanol masers trace shocked gas at the interfaces of outflows from HMSFR (Cyganowski et al., 2009). A comprehensive review of Class I methanol masers and their excitation is provided by Leurini et al. (2016). Class II methanol masers are found closer to massive protostars within HMSFR. Wiesemeyer et al. (2004) cites W3(OH) as the prototype Class II methanol maser source. The two strongest Class II methanol maser transitions are the $2_0 \rightarrow 3_{-1} E$ 12.2 GHz transition (Batrla

et al., 1987) and the $5_1 \rightarrow 6_0A^+$ 6.7 GHz transition (Menten, 1991b). Typical physical conditions for Class II methanol maser excitation are cited by Wiesemeyer et al. (2004) as $n \sim 10^{5-8}$ cm^{-3} with a gas temperature less than the dust temperature (both $\leq$ 100 K).

The methanol molecule is non-paramagnetic and expected to have low linear and circular polarization in an external magnetic field (Green et al., 2007; Vlemmings, 2008b) particularly if partially saturated, as described in the general maser theory summarized by Watson (2009). A further complication for Zeeman polarimetry of methanol masers was immediately presented once these observations became technically feasible: no accurate laboratory measurement existed for the Landé g-factor for the transitions of interest. The community relied on an uncertain extrapolation of laboratory measurements of 25 GHz methanol transitions (Jen, 1951), and the extrapolation calculation may have been in error by an order of magnitude (Vlemmings et al., 2011). Recently a full quantum mechanical derivation has been performed (Lankhaar et al., 2018) resulting in an accurate Zeeman coefficient. Accordingly we do not cite inferred magnetic fields from work using earlier Landé g-factors than (Lankhaar et al., 2018), but only note Zeeman velocity or frequency splitting for those results accordingly.

5.2.1. 6.7 GHz Methanol Masers

In this paragraph we confine our discussion to polarization observations of the 6.7 GHz methanol maser transition toward HMSFR. Ellingsen (2002) reported the detection of linear polarization at levels of up to 10% toward NGC6334F using the ATCA. MERLIN observations of W3(OH) by Vlemmings et al. (2006) detected a median linear polarization fraction $m_l \sim 1.8\%$ and set an upper limit to the fractional circular polarization $m_c < 2\%$; the upper limit to the Zeeman splitting was $v_z < 1.1 \times 10^{-3}$ km/s. Dodson (2008) reported linear polarization $m_l \sim 0.5 - 10.1\%$ toward G339.88–1.26 using the LBA. The first systematic survey for Zeeman components was performed by Vlemmings (2008b) using the Effelsberg single-dish telescope to observe a sample of 24 sources; 17 Zeeman components were detected with an average Zeeman splitting of 0.56 m/s. **Figure 6** shows an example of a Zeeman detection Stokes I and V profile. Zeeman splitting toward the period flaring source G09.62+0.20 was reported by Vlemmings et al. (2009) using similar Effelsberg observations. As more telescopes and interferometer arrays became equipped with receivers in this band the scope of observations of this transition toward HMSFR increased significantly. MERLIN observation of DR21(OH) and DR21(OH)N were completed by Harvey-Smith et al. (2008), of Cepheus A HW2 by Vlemmings et al. (2010), and of IRAS 18089–1732 by Dall'Olio et al. (2017). Dodson and Moriarty (2012) undertook a survey of ten SFR using the ATCA; and the Mount Pleasant 26 m single dish telescope was equipped for polarimetry in this transition by Stack and Ellingsen (2011), who detected Zeeman splitting in the periodic flaring source G9.62+0.20. A significant systematic survey campaign of HMSFR using the EVN is reported by Surcis et al. (2009, 2012, 2013, 2015); these authors report Zeeman v_z splitting spanning the range from –9.7 m/s to +7.8 m/s and fractional linear polarization in the range $m_l \sim 0.4 - 17\%$. We do not imply that the data are uniformly distributed in these ranges; an approximate summation here suggests a mean unsigned $|v_z| \sim 3.2$ m/s and a mean fractional linear polarization $\bar{m}_l \sim 3.6\%$. Vlemmings et al. (2011) cite a fitted Zeeman splitting dispersion $\langle \triangle V_Z \rangle \sim$ 0.62 m/s from their Effelsberg single-dish Zeeman survey. Lankhaar et al. (2018) report that this translates to a mean magnetic field magnitude $\sim$ 12 mG using the correct Zeeman splitting coefficient.

5.2.2. 36 and 44 GHz Methanol Masers

The Class I $4_{-1} \rightarrow 3_0E$ 36 GHz methanol maser transition was detected toward the HMSFR M8E using the VLA by Sarma and Momjian (2009); these authors resolved two Zeeman components with splitting $v_z = 34.4 \pm 5.9$ Hz and $v_z = -53.2 \pm 6.0$ Hz, respectively. Zeeman splitting has also been detected in the Class I $7_0 \rightarrow 6_1A+$ 44 GHz methanol maser transition toward the SFR OMC-2 (Sarma and Momjian, 2011; Momjian and Sarma, 2012) and DR21(OH) (Momjian and Sarma, 2017). In DR21(OH) the authors find $v_z = 53.5 \pm 2.7$ Hz and for OMC-2 report $v_z = 18.4 \pm 1.1$ Hz and $v_z = 17.7 \pm 0.9$ Hz over two epochs.

Using the correct Landé g-factors computed for these transitions and the most likely hyperfine transitions, Lankhaar et al. (2018) infer a magnetic field magnitude of 20–75 mG for the reported 36 and 44 GHz methanol maser Zeeman observations. Momjian and Sarma (2017) note that these masers sample densities $n \sim 10^{7-8}$ cm^{-3} (Leurini et al., 2016). As noted by Lankhaar et al. (2018) the B-field magnitudes $\sim 20 - 75$ mG are not inconsistent with shock compression.

5.2.3. Other Millimeter Wavelength Transitions

Wiesemeyer et al. (2004) conducted single-dish polarimetry of methanol masers at higher frequencies using the IRAM 30 m telescope. They observed the Class I transitions: $5_{-1} \rightarrow 4_0E$ (85 GHz), $8_0 \rightarrow 7_1A+$ (95 GHz), $6_{-1} \rightarrow 5_0E$ (132 GHz); and Class II transitions: $3_1 \rightarrow 4_0A+$ (107 GHz) and $6_0 \rightarrow 6_{-1}E$ (157 GHz). The authors report fractional linear polarization in the range $m_l \sim 2.8 - 39.5\%$ and fractional circular polarization $m_c \sim -7.1 - 3.52\%$. They argue that the masers are unsaturated and that the theory of Nedoluha and Watson (1992) applies; specifically that the linear polarization arises from anisotropic pumping and anisotropic radiation losses and the circular polarization from non-Zeeman effects (Watson, 2009). Kang et al. (2016) present a survey of linear polarization in 44 and 95 GHz Class I masers conducted with a single dish from the Korean VLBI Network (KVN). Their results yielded a lower fractional linear polarization and they argue accordingly for a diminished influence of anisotropic pumping and losses than (Wiesemeyer et al., 2004).

5.3. Water Masers

The advent of the VLBA was accompanied by the development of observing techniques that allowed VLBI polarimetry of 22 GHz water masers (Leppänen et al., 1998). VLBI observations of the Zeeman effect in 22 GHz water masers were first reported by Vlemmings et al. (2006) and Sarma et al. (2008); such observations allow the magnetic field in SFR to be measured

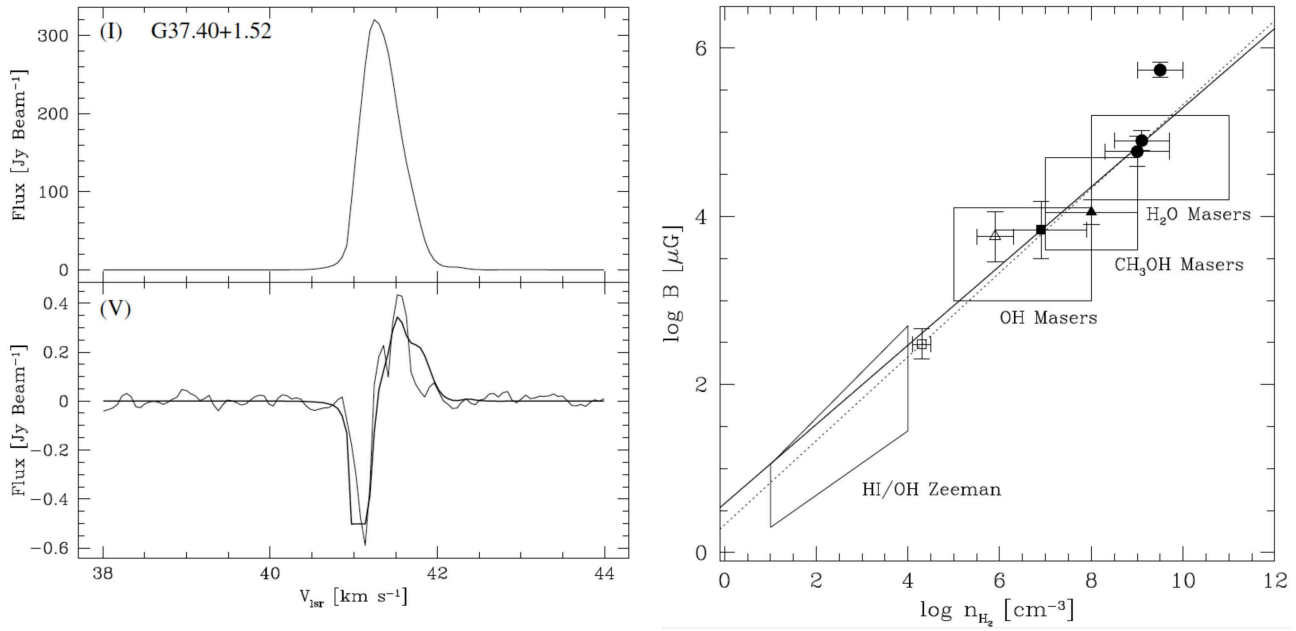

FIGURE 6 | Maser Zeeman results from Vlemmings (2008b). **Left**: Example of 6.7 GHz methanol maser Zeeman observation. Inferred $B_{LOS} = 15.4 \pm 0.4$ mG. **Right**: Points with error bars show maser Zeeman inferred values of magnetic field strength in the massive star forming region Cepheus A. Boxes show literature values for maser and extended regions for other regions. Solid line show $B \propto n^{0.5}$ relation while dotted line shows fit to Cepheus A data. Although the slope from this figure seems different from the 0.65 from **Figure 5**, the maser slope does not allow for the constant value of field strength for H I Zeeman data. When this is included, the slope for the maser gas is reasonably compatible with 0.65 given the large uncertainties in the gas densities in the maser regions.

in high-density regions $n \sim 10^9$ cm^{-3}. Contemporary VLBI observations of W75N are reported by Surcis et al. (2011). Their analysis leads to an inferred magnetic field of 200 to 1,000 mG in the shocked outflow region where the water masers arise. Modeling suggests that the shock is a C-shock. As part of their comprehensive observations of the HMSFR G23.01–0.41 (Sanna et al., 2010) included VLBA observations of H_2O masers, confirming that the water masers trace fast outflows from the massive YSO in this source.

5.4. Relationship of Maser Polarization Observations to Star Formation Theory

There remain broad open questions in both the micophysics and macrophysics of star formation theory (McKee and Ostriker, 2007). Maser polarization observations in SFR probe the fine-scale magnetic field in dense regions $n \sim 10^{5-11}$ cm^{-3} of obscured HMSFR (Kang et al., 2016) and therefore provide constraints on the theory of high-mass as opposed to low-mass star formation (Zinnecker and Yorke, 2007). In addition, masers are confined to certain evolutionary phases of HMSF, specifically between the formation of hot dense molecular cores (HDMC) (Zinnecker and Yorke, 2007), equivalently high-mass protostellar objects (HMPO) (McKee and Ostriker, 2007), and their subsequent evolution into ultra-compact HII regions (UCHII) (Churchwell, 2002). The hot molecular core phase is associated with the emergence of outflows, jets, and water and methanol maser emission (McKee and Ostriker, 2007; Zinnecker and Yorke, 2007) with the later emergence of OH maser emission during the development of an UCHII region (Churchwell, 2002). HMPOs have high extinction, complex spatial structure due to clustered HMSF, and may lie at large distances (McKee and Ostriker, 2007). Maser observations can mitigate these observational challenges however and provide unique probes of the fine-scale kinematics and magnetic fields in HMPO regions. However, it is critical to locate the maser emission within the broader kinematic and dynamical picture of high-mass star formation regions as accurately as possible in order to assess the physical meaning of the magnetic field measurements inferred from maser observations and their overall role as probes of HMSF in general.

Class II methanol masers lie closer to the central HMPOs but there has been debate as to their exact location and kinematics; we consider the available evidence here. Early interferometric imaging of 6.7 and 12.2 GHz methanol masers toward SFR revealed frequent linear or arc-like features, which were interpreted as Keplerian disks (Norris et al., 1993, 1998). However, as described by Dodson and Moriarty (2012) competing interpretations have arisen, including shocks (Walsh et al., 1998), disk infall or outflow (Bartkiewicz et al., 2009), and shock interaction with rotating molecular clouds (Dodson et al., 2004). Dodson and Moriarty (2012) conducted a survey of 10 SFR in the 6.7 GHz methanol transition using the ATCA in order to distinguish these cases by comparing the gross polarization morphology and the structural morphology of the maser distribution; this statistical test was inconclusive. Using a larger sample of SFR observed in full polarization in the 6.7 GHz methanol transition using the EVN, Surcis et al. (2013, 2015) have synthesized all external information on outflow

direction from other molecular or dust polarization observations for their sample and searched for correlations between structural maser distribution and polarization EVPA and outflow direction. They find a statistically significant correlation supporting the alignment of the inferred magnetic field direction and the large-scale outflow direction. This is not universal but is clearly indicated in several sources studied in detail in the 6.7 GHz methanol transition. Cepheus A HW2 shows methanol masers in an elliptical ring of size $\sim$ 650 AU that probe material being accreted onto the disk (Vlemmings et al., 2010). There is no clear sign of rotation and the magnetic field is aligned with the outflow. The HMSFR G23.01-0.41 observed by Sanna et al. (2010) using VLBI shows methanol masers in a toroid consistent with expansion and rotation about a massive YSO; this is confirmed in an associated proper motion analysis. MERLIN observation of W51 by Etoka et al. (2012) show the methanol masers around e2-W51 to be in a velocity-coherent structure perpendicular to the CO outflow; the maser spots appear to trace the magnetic field lines elsewhere in the source. Harvey-Smith et al. (2008) find a methanol maser distribution toward DR21(OH) consistent with a Keplerian disk toward DR21(OH)N. The preceding results show that methanol masers are unique probes of disks or toroids surrounding HMPOs and that there is significant potential in future observations. These inner regions are critical to understanding key issues in HMSF including accretion mechanisms (Krumholz et al., 2007), angular momentum transport, disks (Cesaroni et al., 2007) and outflows. The physics of low- and high-mass star formation differ in key respects, as summarized by Zinnecker and Yorke (2007).

In several sources it is particularly clear that the measured methanol maser magnetic fields sample an overall coherent magnetic field and not isolated regions of dense shocked material. This is argued for Cepheus A HW2 by Vlemmings et al. (2010) who also cite additional supporting evidence for the source W75N (Surcis et al., 2009). There is a particularly strong alignment between the methanol maser magnetic field orientation and the field derived from dust polarization in W51-e2 (Surcis et al., 2012 in particular see their Figure 10). The evidence that maser polarization observations sample the global field is particularly valuable constraining HMSF collapse, accretion, and angular momentum transport mechanisms (McKee and Ostriker, 2007).

5.5. Magnetic Fields and Density Relation

Using Zeeman magnetic field measurements made possible for different maser species in the past decade, particularly with the addition of methanol and water masers, Vlemmings (2008b) compared the resulting magnetic field—density relation for Cepheus A against the relation $B \propto n^{0.47}$ derived by Crutcher (1999) finding excellent agreement; see **Figure 6**. This is confirmed after revisions accounting for the more accurate Landé g-factor for the methanol molecule (Lankhaar et al., 2018). The agreement with this relation has been used as an independent consistency check on measurements of maser magnetic fields (Surcis et al., 2011; Momjian and Sarma, 2017). However, note that the Crutcher (1999) study has been superceded by a more complete and statistically improved study that yields an exponent of ≈ 0.65. With the uncertainties in especially densities sampled by masers, in addition of other uncertainties discussed above, the Vlemmings (2008b) result is not inconsistent with the higher exponent. But it is also true that the physics governing the relationship between field strength and density may be completely different in the extended gas and the regions with the special conditions that give rise to masers; there is no strong astrophysical argument that the same exponent hold in both regions.

Future observations offer the potential of extending measurement of the magnetic field—density relation at maser densities over a larger sample of individual sources. It is challenging to aggregate these data but new instrumental capabilities increasingly make this a possibility. A larger ensemble of sources will offset the inherent uncertainty in maser excitation density and provide tighter constraints on the $B \propto n^{\kappa}$ exponent in maser regions and better understanding of the underlying physics. We refer the reader to the discussion in section 4.2 concerned the physical meaning of different exponent values.

6. SUMMARY AND CONCLUSIONS

Interstellar Zeeman detections have been made in five species, H I, OH, CN, CH_3OH, and H_2O, that sample densities n_H over about 10 orders of magnitude (10^{0-10} cm^{-3}). Hence, information about magnetic field strengths is available over the full range of densities from diffuse atomic clouds to very dense gas in regions of star formation. There are, however, a number of limitations in the data. Zeeman detections generally involve high sensitivity observations that require long telescope observation time, which limits the quantity of data available. In most cases the Zeeman effect provides only the field strength along the line of sight (with the exception of OH masers with fully separated Zeeman components), so statistical analysis is necessary. Obtaining astrophysical information such as the mass/flux ratio and the scaling of field strength with density requires knowledge of the column densities and volume densities traced by the Zeeman species. Particularly for masers, where the range of physical conditions under which masing may occur can be broad, this introduces significant uncertainties. Nonetheless, since the Zeeman effect provides the only direct technique for measurement of interstellar magnetic field strengths, Zeeman observations are crucial for our understanding of the role of magnetic fields in the evolution of interstellar clouds and in star formation.

At the lower densities sampled by H I, field strengths do not appear to be systematically dependent on volume density, with maximum strengths of 10-20 μG. At densities starting at about 300 cm^{-3}, field strengths increase with density, following a scaling $B \propto n^{0.65}$, based on Bayesian analysis of OH and CN Zeeman data in extended gas. At higher densities, $\gtrsim 10^6$ cm^{-3}, results come from masers, and density estimates are less certain than for extended gas. Nonetheless, it is clear that field strengths continue to increase as a power law of density; early results suggested an exponent of 0.5 in this regime but on inspection

current data are not inconsistent with a 0.65 exponent. Further analysis over a larger source sample is needed.

The observed ratio of column density to field strength is directly proportional to the mass/flux ratio M/Φ, which measures whether gravitational or magnetic energy dominates. At lower densities M/Φ is subcritical; magnetic fields dominate gravity. Again at about densities of 300 cm^{-3} the situation changes, and M/Φ becomes supercritical.

These two measures of the relative importance of gravity and magnetic fields give the same result. At about the density at which clouds become self-gravitating, the importance of magnetic fields changes. The Zeeman data are consistent with a picture in which a cloud forms by flows along magnetic flux tubes (sometimes described as converging flows), increasing the local mass and density but not the field strength, until the cloud becomes magnetically supercritical and contracts gravitationally and eventually forms stars. Turbulent magnetic diffusion probably plays a large role in moderating field strengths during the evolutionary process. While this broad picture appears generally to satisfy data constraints, cloud evolution and star formation is a very complex process and this broad picture may not (always) be correct.

Although there have been extensive Zeeman observations in molecular clouds, conclusions remain tentative. Additional observational work that should lead to more definitive conclusions are: (1) measurement of the overall M/Φ of molecular cloud complexes to study the degree of magnetic support; (2) additional Zeeman measurements at high densities in order to solidify κ in the $B \propto \rho^{\kappa}$ relation; (3) additional studies of the magnetic field morphology and strength both within cores and between cores and between GMCs.

Progress in interstellar Zeeman observations, particularly in non-masing lines, has slowed considerable in the last decade, due to the requirement of very large amounts of telescope time and instrumental polarization problems with important telescopes such as the IRAM 30-m and the ALMA telescopes that have prevented Zeeman observations in recent years. Hopefully these instrumental problems will be overcome so Zeeman data can be significantly extended in coming years. Being able to measure the Zeeman effect in protostellar disks with (for example) CN transitions would add significantly to information about magnetic fields. There has however been significant progress in maser observations of SFR in the past decade, particularly VLBI polarimetry sensitive to the Zeeman effect in receiver bands allowing observations of important tracers of HMSFR such as the 6.7 GHz methanol maser transition. This work has been facilitated both by improvements in observing and analysis techniques and advancement in the application of the theory polarized maser radiation transport. It has become clear that methanol masers in particular trace coherent magnetic field structures in HMSFR, provide important Zeeman probes of the magnetic field near massive YSOs, and add particular value to understanding star formation when considered with all other molecular and dust tracers.

As noted above, the commissioning of circular polarization capability on ALMA has been technically challenging, however recent results are highly encouraging (Vlemmings et al., 2017, 2019). The latter work presents an upper limit on the magnetic field in the disk of TW Hya based on, at present, the non-detection of the Zeeman effect in CN. The feasibility of Zeeman observations of CN emission in protostellar disks was considered earlier by Brauer et al. (2017). A review of the potential of ALMA for linear polarization maser observations is provided by Pérez-Sánchez and Vlemmings (2013); the linear polarization capabilities of ALMA have been realized much earlier in telescope operation due to their lower technical complexity than circular polarization for ALMA.

The ngVLA[1] science case for the study of magnetic fields in SFR is presented by Hull et al. (2018). The science case includes Zeeman observations of a range of Galactic thermal and maser emission, including maser emission from the near environments of YSOs, OH masers to study the large-scale magnetic field distribution in the Milky Way, and Zeeman observations to detect magnetic fields in extragalactic OH masers sources. The ngVLA offers significantly increased sensitivity, a key consideration along with instrumental polarization purity in the technical feasibility of Zeeman observations, and nearly continuous coverage of the useful frequency spectrum from 1 to 116 GHz. The potential for Zeeman observations using the Square Kilometer Array (SKA[2]) is described by Robishaw et al. (2015). The high sensitivity of the SKA similarly enhances the technical feasibility of Zeeman observations; the authors note specific opportunities for significantly improved Zeeman observations to measure magnetic field densities in SFR with both OH and methanol masers, HI absorption studies toward background continuum sources as well as diffuse HI emission, OH masers tracing the Galactic magnetic field structure, and extragalactic masers. The SKA precursor projects MeerKAT[3] and ASKAP http://www.atnf.csiro.au/projects/askap/index.html have lower sensitivity and reduced frequency coverage relative to the full SKA, but will make important contributions to the areas of SKA Zeeman science mentioned above.

AUTHOR CONTRIBUTIONS

RC was primarily responsible for sections 1–4 and AK for section 5. Section 6 is the responsibility of both.

FUNDING

RC receives support from NSF AST 18-15987.

ACKNOWLEDGMENTS

RC and AK acknowledge with thanks the many colleagues with whom they have worked on Zeeman observations.

[1] https://ngvla.nrao.edu
[2] https://www.skatelescope.org
[3] https://www.ska.ac.za

REFERENCES

Ade, P. A. R., Aghanim, N., Alves, M. I. R., Arnaud, M., Arzoumanian, D., Ashdown, M., et al. (2016). Planck intermediate results. XXXV. Probing the role of the magnetic field in the formation of structure in molecular clouds. *Astron. Astrophys.* 586:A138. doi: 10.1051/0004-6361/201525896

Bartkiewicz, A., Szymczak, M., van Langevelde, H. J., Richards, A. M. S., and Pihlström, Y. M. (2009). The diversity of methanol maser morphologies from VLBI observations. *Astron. Astrophys.* 502, 155–173. doi: 10.1051/0004-6361/200912250

Batrla, W., Matthews, H. E., Menten, K. M., and Walmsley, C. M. (1987). Detection of strong methanol masers towards galactic H II regions. *Nature* 326, 49–51.

Bayandina, O. S., Alakoz, A. V., and Val'tts, I. E. (2014). Magnetic fields in methanol maser condensations based on data for related regions. Seven sources: astrophysical parameters. *Astronomy Rep.* 58, 462–470. doi: 10.1134/S1063772914070026

Bel, N., and Leroy, B. (1998). Zeeman splitting in interstellar molecules. II. The ethynyl radical. *Astron. Astrophys.* 335, 1025–1028.

Bourke, T. L., Myers, P. C., Robinson, G., and Hyland, A. R. (2001). New OH zeeman measurements of magnetic field strengths in molecular clouds. *Astrophys. J.* 554, 916–932. doi: 10.1086/321405

Brauer, R., Wolf, S., and Flock, M. (2017). Magnetic fields in circumstellar disks. The potential of Zeeman observations. *Astron. Astrophys.* 607:A104. doi: 10.1051/0004-6361/201731140

Caswell, J. L. (2001). Maser emission from OH at the 6035-MHz transition. *Month. Notices Roy. Astron. Soc.* 326, 805–820. doi: 10.1046/j.1365-8711.2001.04745.x

Caswell, J. L. (2004). OH 1720-MHz masers in southern star-forming regions. *Month. Notices R. Astron. Soc.* 349, 99–114. doi: 10.1111/j.1365-2966.2004.07472.x

Caswell, J. L., Green, J. A., and Phillips, C. J. (2013). Parkes full polarization spectra of OH masers - I. Galactic longitudes 350° through the Galactic Centre to 41°. *Month. Notices R. Astron. Soc.* 431, 1180–1219. doi: 10.1093/mnras/stt239

Caswell, J. L., Kramer, B. H., and Reynolds, J. E. (2009). Maser maps and magnetic field of OH 300.969+1.147. *Month. Notices R. Astron. Soc.* 398, 528–534. doi: 10.1111/j.1365-2966.2009.14952.x

Caswell, J. L., Kramer, B. H., and Reynolds, J. E. (2011a). Magnetic fields from OH maser maps at 6035 and 6030 MHz at Galactic sites 351.417+0.645 and 353.410-0.360. *Month. Notices R. Astron. Soc.* 414, 1914–1926. doi: 10.1111/j.1365-2966.2011.18510.x

Caswell, J. L., Kramer, B. H., and Reynolds, J. E. (2011b). Maser maps and magnetic field of OH 337.705-0.053. *Month. Notices R. Astron. Soc.* 415, 3872–3878. doi: 10.1111/j.1365-2966.2011.18998.x

Caswell, J. L., Kramer, B. H., Sukom, A., and Reynolds, J. E. (2010). LBA observations of the maser cluster OH 330.953-0.182. *Month. Notices R. Astron. Soc.* 402, 2649–2656. doi: 10.1111/j.1365-2966.2009.16076.x

Caswell, J. L., and Reynolds, J. E. (2001). Maser maps and magnetic field of OH 323.459-0.079. *Month. Notices R. Astron. Soc.* 325, 1346–1352. doi: 10.1046/j.1365-8711.2001.04479.x

Cazzoli, G., Lattanzi, V., Coriani, S., Gauss, J., Codella, C., Ramos, A. A., et al. (2017). Zeeman effect in sulfur monoxide. A tool to probe magnetic fields in star forming regions. *Astron. Astrophys.* 605:A20. doi: 10.1051/0004-6361/201730858

Cesaroni, R., Galli, D., Lodato, G.,Walmsley, C. M., and Zhang, Q. (2007). "Disks around young O-B (proto)stars: observations and theory," in *Protostars and Planets V*, eds B. Reipurth, D. Jewitt, and K. Keil (Tucson, AZ: University of Arizona Press), 197.

Churchwell, E. (2002). Ultra-compact HII regions and massive star formation. *Ann. Rev. Astron. Astrophys.* 40, 27–62. doi: 10.1146/annurev.astro.40.060401.093845

Ciolek, G. E., and Basu, S. (2000). Consistency of ambipolar diffusion models with infall in the L1544 protostellar core. *Astrophys. J.* 529, 925–931. doi: 10.1086/308293

Cook, A. H. (1977). *Celestial Masers*. Cambridge: Cambridge University Press.

Cragg, D. M., Sobolev, A. M., and Godfrey, P. D. (2002). Modelling methanol and hydroxyl masers in star-forming regions. *Month. Notices Roy. Astrono. Soc.* 331, 521–536. doi: 10.1046/j.1365-8711.2002.05226.x

Crutcher, R. M. (1979). Nonthermal OH main lines and the abundance of OH in interstellar dust clouds. *Astrophys. J.* 234, 881–890.

Crutcher, R. M. (1999). Magnetic fields in molecular clouds: observations confront theory. *Astrophys. J.* 520, 706–713.

Crutcher, R. M. (2012). Magnetic fields in molecular clouds. *Ann. Rev. Astron. Astrophys.* 50, 29–63. doi: 10.1146/annurev-astro-081811-125514

Crutcher, R. M., Hakobian, N., and Troland, T. H. (2009). Testing magnetic star formation theory. *Astrophys. J.* 692, 844–855. doi: 10.1088/0004-637X/692/1/844

Crutcher, R. M., Hakobian, N., and Troland, T. H. (2010a). Self-consistent analysis of OH Zeeman observations. *Month. Notices Roy. Astrono. Soc.* 402, L64–L66. doi: 10.1111/j.1745-3933.2009.00802.x

Crutcher, R. M., and Kazès, I. (1983). The magnetic field of the NGC 2024 molecular cloud - Detection of OH line Zeeman splitting. *Astron. Astrophys.* 125, L23–L26.

Crutcher, R. M., Mouschovias, T. C., Troland, T. H., and Ciolek, G. E. (1994). Structure and evolution of magnetically supported molecular clouds: evidence for ambipolar diffusion in the Barnard 1 cloud. *Astrophys. J.* 427, 839–847.

Crutcher, R. M., Roberts, D. A., Troland, T. H., and Goss, W. M. (1999a). The magnetic field of the NGC 2024 molecular cloud. *Astrophys. J.* 515, 275–285.

Crutcher, R. M., Troland, T. H., Goodman, A. A., Heiles, C., Kazès, I., and Myers, P. C. (1993). OH Zeeman observations of dark clouds. *Astrophys. J.* 407, 175–184.

Crutcher, R. M., Troland, T. H., Lazareff, B., and Kazès, I. (1996). CN Zeeman observations of molecular cloud cores. *Astrophys. J.* 456:217.

Crutcher, R. M., Troland, T. H., Lazareff, B., Paubert, G., and Kazès, I. (1999b). Detection of the CN zeeman effect in molecular clouds. *Astrophys. J. Lett.* 514, L121–L124.

Crutcher, R. M., Wandelt, B., Heiles, C., Falgarone, E., and Troland, T. H. (2010b). Magnetic fields in interstellar clouds from zeeman observations: inference of total field strengths by bayesian analysis. *Astrophys. J.* 725, 466–479. doi: 10.1088/0004-637X/725/1/466

Cyganowski, C. J., Brogan, C. L., Hunter, T. R., and Churchwell, E. (2009). A class I and class II CH_3OH maser survey of EGOs from the GLIMPSE survey. *Astrophys. J.* 702, 1615–1647. doi: 10.1088/0004-637X/702/2/1615

Dall'Olio, D., Vlemmings, W. H. T., Surcis, G., Beuther, H., Lankhaar, B., Persson, M. V., et al. (2017). Methanol masers reveal the magnetic field of the high-mass protostar IRAS 18089-1732. *Astron. Astrophys.* 607:A111. doi: 10.1051/0004-6361/201731297

Dodson, R. (2008). First VLBI observations of methanol maser polarisation, in G339.88-1.26. *Astron. Astrophys.* 480, 767–773. doi: 10.1051/0004-6361:20078670

Dodson, R., and Moriarty, C. D. (2012). Probing the magnetic fields of massive star-forming regions with methanol maser polarization. *Month. Notices R. Astron. Soc.* 421, 2395–2406. doi: 10.1111/j.1365-2966.2012.20472.x

Dodson, R., Ojha, R., and Ellingsen, S. P. (2004). High-resolution observations of 6.7-GHz methanol masers with the Long Baseline Array. *Month. Notices Roy. Astrono. Soc.* 351, 779–790. doi: 10.1111/j.1365-2966.2004.07844.x

Edris, K. A., Fuller, G. A., Cohen, R. J., and Etoka, S. (2005). The masers towards IRAS 20126 + 4104. *Astron. Astrophys.* 434, 213–220. doi: 10.1051/0004-6361:20041872

Elitzur, M. (ed.). (1992). "Astronomical masers," in *Astrophysics and Space Science Library* (Berlin: Springer).

Ellingsen, S. P. (2002). "Polarization properties of 6.7 GHz methanol masers in NGC6334F," in *Cosmic Masers: From Proto-Stars to Black Holes, Vol 206*, eds V. Migenes and M. J. Reid (Cambridge: IAU Symposium), 151.

Etoka, S., Cohen, R. J., and Gray, M. D. (2005). The association of OH and methanol masers in W3(OH). *Month. Notices R. Astron. Soc.* 360, 1162–1170. doi: 10.1111/j.1365-2966.2005.09130.x

Etoka, S., Gray, M. D., and Fuller, G. A. (2012). Methanol and excited OH masers towards W51 - I. Main and South. *Month. Notices R. Astron. Soc.* 423, 647–662. doi: 10.1111/j.1365-2966.2012.20900.x

Falgarone, E., Troland, T. H., Crutcher, R. M., and Paubert, G. (2008). CN Zeeman measurements in star formation regions. *Astron. Astrophys.* 487, 247–252. doi: 10.1051/0004-6361:200809577

Fiebig, D., and Guesten, R. (1989). "Magnetic fields in interstellar water masers," in *The Physics and Chemistry of Interstellar Molecular Clouds - mm and Sub-mm Observations in Astrophysics, Vol 331*, eds G. Winnewisser J. T. Armstrong (Berlin: Lecture Notes in Physics, Berlin Springer Verlag), 93–96.

Fish, V. L., and Sjouwerman, L. O. (2007). Structure of W3(OH) from very high spectral resolution observations of 5 centimeter OH masers. *Astrophys. J.* 668, 331–347. doi: 10.1086/521096

Goldreich, P., Keeley, D. A., and Kwan, J. Y. (1973). Astrophysical Masers. 11. Polarization Properties. *Astrophys. J.* 179, 111–134.

Goodman, A. A., and Heiles, C. (1994). The magnetic field in the Ophiuchus dark cloud complex. *Astrophys. J.* 424, 208–221.

Gray, M. (2012). *Maser Sources in Astrophysics*. Cambridge: Cambridge University Press.

Green, J. A., Caswell, J. L., and McClure-Griffiths, N. M. (2015). Excited-state hydroxyl maser polarimetry: who ate all the πs? *Month. Notices R. Astron. Soc.* 451, 74–92. doi: 10.1093/mnras/stv936

Green, J. A., McClure-Griffiths, N. M., Caswell, J. L., Robishaw, T., and Harvey-Smith, L. (2012). MAGMO: coherent magnetic fields in the star-forming regions of the Carina-Sagittarius spiral arm tangent. *Month. Notices R. Astron. Soc.* 425, 2530–2547. doi: 10.1111/j.1365-2966.2012.21722.x

Green, J. A., Richards, A. M. S., Vlemmings, W. H. T., Diamond, P., and Cohen, R. J. (2007). A MERLIN study of 6-GHz excited-state OH and 6.7-GHz methanol masers in ON1. *Month. Notices R. Astron. Soc.* 382, 770–778. doi: 10.1111/j.1365-2966.2007.12418.x

Hale, G. E. (1908). On the probable existence of a magnetic field in sun-spots. *Astrophys. J.* 28:315.

Harvey-Smith, L., Soria-Ruiz, R., Duarte-Cabral, A., and Cohen, R. J. (2008). First images of 6.7-GHz methanol masers in DR21(OH) and DR21(OH)N. *Month. Notices R. Astron. Soc.* 384, 719–726. doi: 10.1111/j.1365-2966.2007.12737.x

Heiles, C. (1988). L204 - A gravitationally confined dark cloud in a strong magnetic environment. *Astrophys. J.* 324, 321–330.

Heiles, C. (1989). Magnetic fields, pressures, and thermally unstable gas in prominent H I shells. *Astrophys. J.* 336, 808–821.

Heiles, C. (1997). A holistic view of the magnetic field in the eridanus/orion region. *Astrophys. J. Suppl.* 111, 245–288.

Heiles, C., and Crutcher, R. (2005). "Magnetic fields in diffuse HI and molecular clouds," in *Cosmic Magnetic Fields, Vol 664*, eds R. Wielebinski and R. Beck (Berlin: Lecture Notes in Physics, Berlin Springer Verlag), 137.

Heiles, C., Goodman, A. A., McKee, C. F., and Zweibel, E. G. (1993). "Magnetic fields in star-forming regions - observations," in eds E. H. Levy and J. I. Lunine (Tucson, AZ: Protostars and Planets III), 279.

Heiles, C., and Troland, T. H. (1982). Measurements of magnetic field strengths in the vicinity of Orion. *Astrophys. J. Lett.* 260, L23–L26.

Heiles, C., and Troland, T. H. (2003). The millennium arecibo 21 centimeter absorption-line survey. II. properties of the warm and cold neutral media. *Astrophys. J.* 586, 1067–1093. doi: 10.1086/367828

Heiles, C., and Troland, T. H. (2004). The millennium arecibo 21 centimeter absorption-line survey. III. techniques for spectral polarization and results for stokes V. *Astrophys. J. Suppl.* 151, 271–297. doi: 10.1086/381753

Heiles, C., and Troland, T. H. (2005). The millennium arecibo 21 centimeter absorption-line survey. IV. statistics of magnetic field, column density, and turbulence. *Astrophys. J.* 624, 773–793. doi: 10.1086/428896

Hildebrand, R. H., Dotson, J. L., Dowell, C. D., Platt, S. R., Schleuning, D., Davidson, J. A., et al. (1995). "Far-infrared polarimetry," in eds M. R. Haas, J. A. Davidson,and E. F. Erickson, *From Gas to Stars to Dust*, Vol 73 (San Francisco, CA: Astronomical Society of the Pacific Conference Series), 97–104.

Hiltner, W. A. (1949). Polarization of light from distant stars by interstellar medium. *Science* 109:165.

Hull, C. L. H., Carrasco-González, C., Williams, P. K. G., Girart, J. M., Robishaw, T., Galván-Madrid, R., et al. (2018). "Magnetic fields in forming stars with the ngVLA," in *Science with a Next Generation Very Large Array Vol 517*, ed E. Murphy (San Francisco, CA: Astronomical Society of the Pacific Conference Series), 357.

Hunter, T. R., Brogan, C. L., MacLeod, G. C., Cyganowski, C. J., Chibueze, J. O., Friesen, R., et al. (2018). The extraordinary outburst in the massive protostellar system NGC 6334i-MM1: emergence of strong 6.7 GHz methanol masers. *Astrophys. J.* 854:170. doi: 10.3847/1538-4357/aaa962

Jen, C. K. (1951). Rotational magnetic moments in polyatomic molecules. *Phys. Rev.* 81, 197–203.

Johnstone, D., Boonman, A. M. S., and van Dishoeck, E. F. (2003). Astrochemistry of sub-millimeter sources in Orion. Studying the variations of molecular tracers with changing physical conditions. *Astron. Astrophys.* 412, 157–174. doi: 10.1051/0004-6361:20031370

Kang, J.-h., Byun, D.-Y., Kim, K.-T., Kim, J., Lyo, A.-R., and Vlemmings, W. H. T. (2016). Linear polarization of class I methanol masers in massive star-forming regions. *Astrophys J. Suppl. Ser.* 227:17. doi: 10.3847/0067-0049/227/2/17

Kemball, A. J., and Richter, L. (2011). Circular polarization measurement in millimeter-wavelength spectral-line VLBI observations. *Astron. Astrophys.* 533:A26. doi: 10.1051/0004-6361/201117337

Krumholz, M. R., Klein, R. I., and McKee, C. F. (2007). Radiation-hydrodynamic simulations of collapse and fragmentation in massive protostellar cores. *Astrophys. J.* 656, 959–979. doi: 10.1086/510664

Lankhaar, B., Vlemmings, W., Surcis, G., van Langevelde, H. J., Groenenboom, G. C., and van der Avoird, A. (2018). Characterization of methanol as a magnetic field tracer in star-forming regions. *Nat. Astronomy* 2, 145–150. doi: 10.1038/s41550-017-0341-8

Lazarian, A. (2005). "Astrophysical implications of turbulent reconnection: from cosmic rays to star formation," in *Magnetic Fields in the Universe: From Laboratory and Stars to Primordial Structures, American Institute of Physics Conference Series, Vol 84*, eds E. M. de Gouveia dal Pino, G. Lugones, and A. Lazarian (College Park, MD: American Institute of Physics), 42–53.

Lazarian, A., Esquivel, A., and Crutcher, R. (2012). Magnetization of cloud cores and envelopes and other observational consequences of reconnection diffusion. *Astrophys. J.* 757:154. doi: 10.1088/0004-637X/757/2/154

Leppänen, K., Liljeström, T., and Diamond, P. (1998). Submilliarcsecond linear polarization observations of water masers in W51 M. *Astrophys. J.* 507, 909–918.

Leurini, S., Menten, K. M., and Walmsley, C. M. (2016). Physical characteristics of bright Class I methanol masers. *Astron. Astrophys.* 592:A31. doi: 10.1051/0004-6361/201527974

Lunttila, T., Padoan, P., Juvela, M., and Nordlund, Å. (2009). The super-alfvénic model of molecular clouds: predictions for mass-to-flux and turbulent-to-magnetic energy ratios. *Astrophys. J. Lett.* 702, L37–L41. doi: 10.1088/0004-637X/702/1/L37

Mac Low, M.-M., and Klessen, R. S. (2004). Control of star formation by supersonic turbulence. *Rev. Mod. Phys.* 76, 125–194. doi: 10.1103/RevModPhys.76.125

McKee, C. F., and Ostriker, E. C. (2007). Theory of star formation. *Ann. Rev. Astron. Astrophys.* 45, 565–687. doi: 10.1146/annurev.astro.45.051806.110602

Menten, K. M. (1991a). Methanol masers and submillimeter wavelengthWater masers in star-forming regions. in *Atoms, Ions and Molecules: New Results in Spectral Line Astrophysics*, vol 16, eds A. D. Haschick, and P. T. P. Ho (San Francisco, CA: Astronomical Society of the Pacific Conference Series), 119–136.

Menten, K. M. (1991b). The discovery of a new, very strong, and widespread interstellar methanol maser line. *Astrophys. J. Lett.* 380, L75–L78.

Mestel, L. (1966). The magnetic field of a contracting gas cloud. I,Strict flux-freezing. *Month. Notices Roy. Astrono. Soc.* 133:265.

Minier, V., Ellingsen, S. P., Norris, R. P., and Booth, R. S. (2003). The protostellar mass limit for 6.7 GHz methanol masers. I. A low-mass YSO survey. *Astron. Astrophys.* 403, 1095–1100. doi: 10.1051/0004-6361:20030465

Momjian, E., and Sarma, A. P. (2012). Comparison of two epochs of the zeeman effect in the 44 GHz class I methanol (CH3oh) maser line in OMC-2. *Astron. J.* 144:189. doi: 10.1088/0004-6256/144/6/189

Momjian, E., and Sarma, A. P. (2017). The Zeeman Effect in the 44 GHz Class I Methanol Maser Line toward DR21(OH). *Astrophys. J.* 834:168. doi: 10.3847/1538-4357/834/2/168

Mouschovias, T. C., and Ciolek, G. E. (1999). "Magnetic fields and star formation: a theory reaching adulthood," in *NATO Advanced Science Institutes (ASI) Series C*, vol 540, eds C. J. Lada and N. D. Kylafis (Berlin: NATO Advanced Science Institutes (ASI) Series C), 305.

Mouschovias, T. C., and Tassis, K. (2009). Testing molecular-cloud fragmentation theories: self-consistent analysis of OH Zeeman observations. *Month. Notices Roy. Astrono. Soc.* 400:L15–L19. doi: 10.1111/j.1745-3933.2009.00752.x

Mouschovias, T. C., and Tassis, K. (2010). Self-consistent analysis of OH-Zeeman observations: too much noise about noise. *Month. Notices Roy. Astrono. Soc.* 409, 801–807. doi: 10.1111/j.1365-2966.2010.17345.x

Myers, P. C., Goodman, A. A., Gusten, R., and Heiles, C. (1995). Observations of magnetic fields in diffuse clouds. *Astrophys. J.* 442, 177–185.

Nedoluha, G. E., and Watson, W. D. (1992). The Zeeman effect in astrophysical water masers and the observation of strong magnetic fields in regions of star formation. *Astrophys. J.* 384, 185–196.

Norris, R. P., Byleveld, S. E., Diamond, P. J., Ellingsen, S. P., Ferris, R. H., Gough, R. G., et al. (1998). Methanol masers as tracers of circumstellar disks. *Astrophys. J.* 508, 275–285.

Norris, R. P., Whiteoak, J. B., Caswell, J. L., Wieringa, M. H., and Gough, R. G. (1993). Synthesis images of 6.7 GHz methanol masers. *Astrophys. J.* 412, 222–232.

Pavlakis, K. G., and Kylafis, N. D. (2000). 5 centimeter OH masers as diagnostics of physical conditions in star-forming regions. *Astrophys. J.* 534, 770–780. doi: 10.1086/308763

Pérez-Sánchez, A. F., and Vlemmings, W. H. T. (2013). Linear polarization of submillimetre masers. Tracing magnetic fields with ALMA. *Astron. Astrophys.* 551:A15. doi: 10.1051/0004-6361/201220735

Robishaw, T., Green, J., Surcis, G., Vlemmings, W. H. T., Richards, A. M. S., Etoka, S., et al. (2015). "Measuring magnetic Fields Near and Far with the SKA via the Zeeman Effect," in *Advancing Astrophysics with the Square Kilometre Array (AASKA14)* (Trieste), 110.

Sanna, A., Moscadelli, L., Cesaroni, R., Tarchi, A., Furuya, R. S., and Goddi, C. (2010). VLBI study of maser kinematics in high-mass star-forming regions. II. G23.01-0.41. *Astron. Astrophys.* 517:A78. doi: 10.1051/0004-6361/201014234

Sarma, A. P., and Momjian, E. (2009). Detection of the zeeman effect in the 36 GHz class I CH3oh maser line with the EVLA. *Astrophys. J. Lett.* 705, L176–L179. doi: 10.1088/0004-637X/705/2/L176

Sarma, A. P., and Momjian, E. (2011). Discovery of the zeeman effect in the 44 GHz class I methanol (CH3oh) maser line. *Astrophys. J. Lett.* 730:L5. doi: 10.1088/2041-8205/730/1/L5

Sarma, A. P., Troland, T. H., Romney, J. D., and Huynh, T. H. (2008). VLBA Observations of the Zeeman Effect in H_2O Masers in OH 43.8-0.1. *Astrophys. J.* 674, 295–303. doi: 10.1086/524939

Sault, R. J., Killeen, N. E. B., Zmuidzinas, J., and Loushin, R. (1990). Analysis of zeeman effect data in radio astronomy. *Astrophys. J. Suppl.* 74:437.

Shinnaga, H., and Yamamoto, S. (2000). Zeeman effect on the rotational levels of CCS and SO in the $^3\sigma^-$ ground state. *Astrophys. J.* 544, 330–335. doi: 10.1086/317212

Slysh, V. I., Migenes, V., Val'tts, I. E., Lyubchenko, S. Y., Horiuchi, S., Altunin, V. I., et al. (2002). Total linear polarization in the OH maser W75 N: VLBA polarization structure. *Astrophys. J.* 564, 317–326. doi: 10.1086/324152

Stack, P. D., and Ellingsen, S. P. (2011). Polarisation of class II methanol masers. *Public. Astron. Soc. Aust.* 28, 338–356. doi: 10.1071/AS11029

Surcis, G., Vlemmings, W. H. T., Curiel, S., Hutawarakorn Kramer, B., Torrelles, J. M., and Sarma, A. P. (2011). The structure of the magnetic field in the massive star-forming region W75n. *Astron. Astrophys.* 527:A48. doi: 10.1051/0004-6361/201015825

Surcis, G., Vlemmings, W. H. T., Dodson, R., and van Langevelde, H. J. (2009). Methanol masers probing the ordered magnetic field of W75n. *Astron. Astrophys.* 506, 757–761. doi: 10.1051/0004-6361/200912790

Surcis, G., Vlemmings, W. H. T., van Langevelde, H. J., and Hutawarakorn Kramer, B. (2012). EVN observations of 6.7 GHz methanol maser polarization in massive star-forming regions. *Astron. Astrophys.* 541:A47. doi: 10.1051/0004-6361/201118658

Surcis, G., Vlemmings, W. H. T., van Langevelde, H. J., Hutawarakorn Kramer, B., Bartkiewicz, A., and Blasi, M. G. (2015). EVN observations of 6.7 GHz methanol maser polarization in massive star-forming regions. III. The flux-limited sample. *Astro. Astrophys.* 578:A102. doi: 10.1051/0004-6361/201425420

Surcis, G., Vlemmings, W. H. T., van Langevelde, H. J., Hutawarakorn Kramer, B., and Quiroga-Nuñez, L. H. (2013). EVN observations of 6.7 GHz methanol maser polarization in massive star-forming regions. II. First statistical results. *Astron. Astrophys.* 556:A73. doi: 10.1051/0004-6361/201321501

Tassis, K., Willacy, K., Yorke, H. W., and Turner, N. J. (2012). Non-equilibrium chemistry of dynamically evolving prestellar cores. II. Ionization and magnetic field. *Astrophys. J.* 754:6. doi: 10.1088/0004-637X/754/1/6

Tritsis, A., Panopoulou, G. V., Mouschovias, T. C., Tassis, K., and Pavlidou, V. (2015). Magnetic field-gas density relation and observational implications revisited. *Month. Notices Roy. Astrono. Soc.* 451, 4384–4396. doi: 10.1093/mnras/stv1133

Troland, T. H., and Crutcher, R. M. (2008). Magnetic fields in dark cloud cores: arecibo OH zeeman observations. *Astrophys. J.* 680, 457–465. doi: 10.1086/587546

Troland, T. H., and Heiles, C. (1982a). Magnetic field measurements in two expanding H I shells. *Astrophys. J. Lett.* 260, L19–L22.

Troland, T. H., and Heiles, C. (1982b). The Zeeman effect in 21 centimeter line radiation - Methods and initial results. *Astrophys. J.* 252, 179–192.

Turner, B. E., and Gammon, R. H. (1975). Interstellar CN at radio wavelengths. *Astrophys. J.* 198, 71–89.

Uchida, K. I., Fiebig, D., and Güsten, R. (2001). Zeeman line splitting measurements sampling dense gas in dark cloud and star-forming cores. *Astron. Astrophys.* 371, 274–286. doi: 10.1051/0004-6361:20010329

Verschuur, G. L. (1968). Positive determination of an interstellar magnetic field by measurement of the zeeman splitting of the 21-cm hydrogen line. *Phys. Rev. Lett.* 21, 775–778.

Vishniac, E. T., and Lazarian, A. (1999). Reconnection in the interstellar medium. *Astrophys. J.* 511, 193–203.

Vlemmings, W. H. T. (2008a). "Maser polarization and magnetic fields during massive star formation," in *Massive Star Formation: Observations Confront Theory: ASP Conference Series, Vol. 387*, eds H. Beuther, H. Linz, and T. H. Itor (San Francisco, CA: Astronomical Society of the Pacific), 117.

Vlemmings, W. H. T. (2008b). A new probe of magnetic fields during high-mass star formation. Zeeman splitting of 6.7 GHz methanol masers. *Astron. Astrophys.* 484, 773–781. doi: 10.1051/0004-6361:200809447

Vlemmings, W. H. T. (2012). "Maser polarization and magnetic fields," in *Cosmic Masers: from OH to H_0: Proceedings IAU Symposium, Vol 287*, eds R. S. Booth, E. M. L Humphreys, and W. V (San Francisco, CA), 31–40.

Vlemmings, W. H. T., Diamond, P. J., van Langevelde, H. J., and Torrelles, J. M. (2006). The magnetic field in the star-forming region Cepheus A. from H_2O maser polarization observations. *Astron. Astrophys.* 448, 597–611. doi: 10.1051/0004-6361:20054275

Vlemmings, W. H. T., Goedhart, S., and Gaylard, M. J. (2009). Possible magnetic field variability during the 6.7 GHz methanol maser flares of G09.62+0.20. *Astron. Astrophys.* 500, L9–L12. doi: 10.1051/0004-6361/200912298

Vlemmings, W. H. T., Harvey-Smith, L., and Cohen, R. J. (2006). Methanol maser polarization in W3(OH). *Month. Notices R. Astron. Soc.* 371, L26–L30. doi: 10.1111/j.1745-3933.2006.00201.x

Vlemmings, W. H. T., Khouri, T., Martí-Vidal, I., Tafoya, D., Baudry, A., Etoka, S., et al. (2017). Magnetically aligned dust and SiO maser polarisation in the envelope of the red supergiant VY Canis Majoris. *Astron. Astrophys.* 603:A92. doi: 10.1051/0004-6361/201730735

Vlemmings, W. H. T., Lankhaar, B., Cazzoletti, P., Ceccobello, C., Dall'Olio, D., van Dishoeck, et al. (2019). Stringent limits on the magnetic field strength in the disc of TW Hya. ALMA observations of CN polarisation. *Astron. Astrophys.* 624:L7. doi: 10.1051/0004-6361/201935459

Vlemmings, W. H. T., Surcis, G., Torstensson, K. J. E., and van Langevelde, H. J. (2010). Magnetic field regulated infall on the disc around the massive protostar CepheusAHW2. *Month. Notices R. Astron. Soc.* 404, 134–143. doi: 10.1111/j.1365-2966.2010.16297.x

Vlemmings, W. H. T., Torres, R. M., and Dodson, R. (2011). Zeeman splitting of 6.7 GHz methanol masers. On the uncertainty of magnetic field strength determinations. *Astron. Astrophys.* 529:A95. doi: 10.1051/0004-6361/201116648

Walsh, A. J., Burton, M. G., Hyland, A. R., and Robinson, G. (1998). Studies of ultracompact HII regions - II. High-resolution radio continuum and methanol maser survey. *Month. Notices Roy. Astrono. Soc.* 301, 640–698.

Watson,W. D. (2009). "*Magnetic fields and the polarization of astrophysical maser radiation: a review," in Magnetic Fields in the Universe II: From Laboratory and Stars to the Primordial Universe: Revista Mexicana de Astronomia y Astrofisica Conference Series, Vol. 36*, eds A. Esquivel, J. Franco, G. García-Segura, E. M. de Gouveia Dal Pino, A. Lazarian, S. Lizano, 113.

Weinreb, S., Meeks, M. L., and Carter, J. C. (1965). Observations of polarized OH emission. *Nature* 208, 440–441.

Wiesemeyer, H., Thum, C., and Walmsley, C. M. (2004). The polarization of mm methanol masers. *Astron. Astrophys.* 428, 479–495. doi: 10.1051/0004-6361:20040343

Zinnecker, H., and Yorke, H. W. (2007). Toward understanding massive star formation. *Ann. Rev. Astron. Astrophys.* 45, 481–563. doi: 10.1146/annurev.astro.44.051905.092549

Conflict of Interest: The authors declare that the research was conducted in the absence of any commercial or financial relationships that could be construed as a potential conflict of interest.

frontiers in Astronomy and Space Sciences

REVIEW
published: 05 April 2019
doi: 10.3389/fspas.2019.00015

Submillimeter and Far-Infrared Polarimetric Observations of Magnetic Fields in Star-Forming Regions

Kate Pattle[1]* *and Laura Fissel*[2]

[1] National Tsing Hua University, Hsinchu, Taiwan, [2] National Radio Astronomy Observatory, Charlottesville, VI, United States

Observations of star-forming regions by the current and upcoming generation of submillimeter polarimeters will shed new light on the evolution of magnetic fields over the cloud-to-core size scales involved in the early stages of the star formation process. Recent wide-area and high-sensitivity polarization observations have drawn attention to the challenges of modeling magnetic field structure of star forming regions, due to variations in dust polarization properties in the interstellar medium. However, these observations also for the first time provide sufficient information to begin to break the degeneracy between polarization efficiency variations and depolarization due to magnetic field sub-beam structure, and thus to accurately infer magnetic field properties in the star-forming interstellar medium. In this article we discuss submillimeter and far-infrared polarization observations of star-forming regions made with single-dish instruments. We summarize past, present and forthcoming single-dish instrumentation, and discuss techniques which have been developed or proposed to interpret polarization observations, both in order to infer the morphology and strength of the magnetic field, and in order to determine the environments in which dust polarization observations reliably trace the magnetic field. We review recent polarimetric observations of molecular clouds, filaments, and starless and protostellar cores, and discuss how the application of the full range of modern analysis techniques to recent observations will advance our understanding of the role played by the magnetic field in the early stages of star formation.

Keywords: molecular clouds, far-infrared (FIR), magnetic fields, star formation, submillimeter astronomy, polarimetry

OPEN ACCESS

Edited by:
Derek Ward-Thompson, University of Central Lancashire, United Kingdom

Reviewed by:
Tim M. Gledhill, University of Hertfordshire, United Kingdom
Sven Van Loo, University of Leeds, United Kingdom

***Correspondence:**
Kate Pattle
kpattle@gapp.nthu.edu.tw

Specialty section:
This article was submitted to Stellar and Solar Physics, a section of the journal Frontiers in Astronomy and Space Sciences

Received: *02 October 2018*
Accepted: *01 March 2019*
Published: *05 April 2019*

Citation:
Pattle K and Fissel L (2019) Submillimeter and Far-Infrared Polarimetric Observations of Magnetic Fields in Star-Forming Regions. Front. Astron. Space Sci. 6:15. doi: 10.3389/fspas.2019.00015

1. INTRODUCTION

In this chapter we discuss single-dish polarimetric observations of star-forming regions made at far-infrared and submillimeter wavelengths. These observations make use of the tendency for asymmetric dust grains to align with their long axis perpendicular to the local magnetic field direction (Davis and Greenstein, 1951; Andersson et al., 2015). Measurement of linearly polarized thermal radiation from dust is a technique which is now coming into its own: the current and forthcoming generation of polarimeters are permitting wide-area surveys in polarized light across the far-infrared and submillimeter wavelength regime. Such surveys represent a significant

improvement over previous observations, and open up the properties of magnetic fields in a variety of star-forming environments to statistically rigorous analysis.

Polarized dust emission is a key tool for understanding the role of magnetic fields in star-forming regions, being a direct measurement of magnetic field morphology on most size scales and at most densities, from the diffuse ISM to the highest densities found in gravitationally bound cores, at which the coupling between magnetic field orientation and grain alignment is thought to break down (e.g., Jones et al., 2015). Emission polarimetry can also provide indirect measurements of magnetic field strength, most commonly through the (Davis-)Chandrasekhar-Fermi method (Davis, 1951; Chandrasekhar and Fermi, 1953), and of the dynamical importance of magnetic fields to molecular clouds (e.g., Soler et al., 2013).

Interpretation of emission polarization observations requires care, due to the degenerate plane-of-sky polarization patterns produced by various combinations of three-dimensional magnetic field geometry and variable efficiency of alignment of dust grains with the magnetic field. Breaking such degeneracies in order to accurately interpret polarization observations often requires comparison to models. However, few simulations of magnetized star formation to date have produced synthetic observations with which comparisons can be made, in part due to the past paucity of observations. In this chapter we discuss comparison of data to models where such comparisons exist. For in-depth discussion of numerical simulations of star formation, we refer the reader to Teyssier and Commerçon (under review).

In this chapter we focus on observations made with single-dish instrumentation. For a discussion of recent advances in interferometric polarimetry, we refer the reader to Hull and Zhang (2019). Discussion in this chapter is restricted to observations of polarized continuum emission from dust grains aligned with their local magnetic field direction. Polarization induced by scattering from dust grains is discussed by Hull and Zhang (2019).

This chapter is structured as follows: in section 2 we discuss past, current and forthcoming instrumentation. In section 3 we discuss methods by which polarization observations are interpreted. In section 4 we discuss observations of magnetic fields on the scale of molecular clouds. In section 5, we discuss observations of magnetic fields in Bok globules; in section 6 we discuss observations of magnetic fields in filaments; and in section 7 we discuss observations of magnetic fields in starless, prestellar and protostellar cores. Section 8 summarizes this chapter.

2. AN OVERVIEW OF POLARIMETERS

Thermal emission from dense molecular clouds is typically a few percent polarized, making the detection of their polarized radiation challenging. Determining linear polarization requires measurement of differential power for light with different orientations of $\vec{E}$, and is typically characterized by the Stokes parameters I, Q, and U:

$$Q = I_0 - I_{90} \tag{1}$$

$$U = I_{45} - I_{135}, \tag{2}$$

where I_x indicates the polarized component of total intensity I, with $\vec{E}$ parallel to the on-sky angle x. The polarization angle θ and fraction of the radiation that is polarized p can be measured from the Stokes parameters with

$$\theta = \frac{1}{2}\arctan(U, Q) \tag{3}$$

and

$$p = \frac{\sqrt{Q^2 + U^2}}{I} \tag{4}$$

respectively. Here we have used the IAU convention that a polarization angle of 0° is aligned North-South and that θ increases when rotated toward the East of North.

In this section we discuss design and observation strategies of different types of polarimeters. We also briefly review polarimeters past, currently operating or being constructed, and proposed for next-generation far-IR/sub-mm satellites.

2.1. Polarimeter Design and Observation Strategies

Measurements of linear polarization with incoherent detectors, such as bolometers, require a method of measuring total power at different E-field orientations. Fast modulation of the polarized signal is also required so that Q and U can be measured on timescales faster than noise drifts associated with the instrument and/or observations. Finally, the background signal contributed from sky emission must be removed from the observations.

Table 1 summarizes all single-dish polarimeters that have operated between 100 μm to 1.2 mm and have resolution $< 10'$ FWHM, in addition to polarimeters that are being constructed, or have recently been proposed. The development of sub-mm and far-IR polarimeters has been driven by a quest for improvements in mapping speed, by increasing the number of detectors and operating at better observing sites. Ground-based polarimeters built for large-aperture telescopes such as the James Clerk Maxwell Telescope (JCMT, 15-m), Caltech Sub-mm Observatory (CSO, 10.4-m), Atacama Pathfinder EXperiment (APEX, 12-m), Institut de Radioastronomie Millimétrique (IRAM, 30-m), and the Large Millimeter Telescope (LMT, 50-m), can be used to make high-resolution maps of magnetic field morphology in star-forming regions. However, this resolution comes at the cost of observing through the atmosphere, requiring these polarimeters to observe through narrow windows in the sub-mm atmospheric transmission spectrum, or at millimeter bands away from the spectral peak of molecular cloud dust. The atmosphere also emits radiation at far-IR, sub-mm, and millimeter wavelengths, resulting in additional power absorbed by the detectors, or "loading," and reduces the overall detector responsivity.

Ideally, one would put sub-mm polarimeters in space (for example the *Planck* Surveyor); however, such satellites are

TABLE 1 | Listing of past, current, and proposed Sub-mm polarimeters.

Instrument (Telescope)	Platform	Start date	Status	Bands [μm]	N_{pixels}	FWHM [arcsec]	Polarization strategy	Key References
UCL Polarimeter	Balloon	1980	Finished	77	1	300	RP, Chopping	Cudlip et al., 1982
KAO	Airborne	1983	Finished	270	1	60	S-HWP, K-mirror	Dragovan, 1986
POLY (KAO)	Airborne	1986	Finished	100	1	55, 40	S-HWP	Novak et al., 1989
MILLIPOL (NRAO-12m)	Ground	1987	Finished	1300	1	30	S-HWP, linear feed	Barvainis et al., 1988, Clemens et al., 1990
UKT-Polarimeter (JCMT)	Ground	1989	Finished	450, 850, 1100	1	8–18	S-HWP, F-A	Flett and Murray, 1991
Stokes (KAO)	Airborne	1990	Finished	100	2 × 32	35	S-HWP, P-G, Chop	Platt et al., 1991
HERTZ (CSO)	Ground	1995	Finished	353	2 × 32	20	S-HWP, P-G, Chop	Schleuning et al., 1997, Dowell et al., 1998
SCUPOL (JCMT)	Ground	1997	Finished	850	37	14	S-HWP, F-A, Chop	Murray et al., 1997, Greaves et al., 2003
SPARO (VIPER)	Ground	2000	Finished	450	2 × 9	∼300	S-HWP, P-G, Chop	Dotson et al., 1998 Renbarger et al., 2004
BLASTPol	Balloon	2010	Finished	250, 350, 500	266	150	S-HWP, P-G, Scan	Galitzki et al., 2014b
SHARP/SHARC (CSO)	Ground	2005	Finished	350 and 450		9	X-Grid, S-HWP, chopping	Li et al., 2008
PolKa/LABOCA (APEX)	Ground	2011	Not Currently Offered	870	295	20	RPM	Siringo et al., 2012, Wiesemeyer et al., 2014
HAWC+ (SOFIA)	Airborne	2016	Active	53, 62 , 89, 154, 214	1,280	4.8–18.2	S-HWP, Dual-Pol, Chop	Dowell et al., 2018
Planck	Space	2009	Finished	850	8	300	Scan	Lamarre et al., 2010, Planck Collaboration VIII, 2016
PILOT	Balloon	2015	Last Flight 2017	214	2048	120	S-HWP, dual-analyzer, Scan	Foënard et al., 2018
POL2 (JCMT)	Ground	2016	Active	450, 850	5120 (each)	10, 14	Sp-HWP, Dual-Pol	Bastien et al., 2011, Friberg et al., 2016
BLAST-TNG	Balloon	2019	Integration	250, 350, 500	759, 475, 230	31, 41, 59	S-HWP, Dual-Pol, Scan	Galitzki et al., 2014a
TolTEC (LMT)	Ground	2019	Construction	1100, 1400, 2100	900, 1800, 3600	5.0, 6.3, 9.8	Sp-HWP, Dual-Pol	Bryan et al., 2018
NIKA-2 (IRAM)	Ground	2019	Integration	1150, 2000	1140 × 2616	11, 18	Dual-Pol, HWP	Adam et al., 2018
A-MKID (APEX)	Ground	2019	Integration	350, 850	3520 (350), 21600 (850)	19 (at 850)	Dual-Pol, Sp-HWP	Otal, 2014
POL (SPICA)	Space	∼2030	Proposed	100, 200, 350	32 × 32, 16 × 16, 8 × 8	9, 18, 32	S-HWP, Dual-Pol, Scan	Gaspar Venancio et al., 2017 Roelfsema et al., 2018
PICO	Space	∼2030	Proposed	375, 450, 541, 649 779, 935, 1124	10000 total	66–192	Dual-Pol, Scan	Sutin et al., 2018 Young et al., 2018
FIP (OST)	Space	∼2030	Proposed	50, 250	26000/6500	2–10	Dual-Pol, Sp-HWP, Scan	Staguhn et al., 2018 (Concept-2)

Polarization Strategy Abbreviations: S-HWP, Stepped HWP; Sp-HWP, Continuously Spinning HWP; P-G, Polarizing Grid; X-Grid, Cross-Grid Splitter; RP, Rotating Polarizing Grid; RPM, Reflecting Polarization Modulator; F-A, Fixed Analyzer/Polarizing Grid; Dual-Pol, Dual Polarization Detectors; Scan, Scan Modulation; Chop, Chopping.

very expensive. Alternatively, polarimeters can operate in the stratosphere. Polarimeters on an aircraft, such as the Kuiper Airborne Observatory (KAO) or Stratospheric Observatory for Infrared Astronomy (SOFIA), typically operate at 10–13 km above sea-level (∼90 % of the atmosphere), which greatly decreases the atmospheric loading and allows observations at wavelengths $< 300\,\mu m$. Stratospheric balloons offer an even more lofty platform at 35–50 km above sea-level (above $>$ 99% of the atmosphere). Such balloon-borne polarimeters can operate in near-space conditions, at a fraction of the cost of a satellite. However, stratospheric balloon flights are currently limited to several weeks' length, reducing the amount of polarization data obtainable.

2.1.1. Measuring Differential Power

The most basic requirement of a polarimeter is to measure the intensity of the component of incoming radiation at different polarization angles. This has often been accomplished by placing a polarizing grid in the light path detector focal plane, such that component of the radiation with $\vec{E}$-orientation parallel to the grid wires is reflected while radiation with $\vec{E}$ perpendicular to the wires is transmitted. The reflected orthogonal polarization component can be directed to different focal plane arrays. This method is somewhat inefficient: either half the light is discarded before reaching the detector focal plane (e.g., BLASTPol), or one part of the array is used to detect one polarization component, and a separate part of the array is required to detect the orthogonal component (e.g., SHARP, SPARO polarimeters).

Most modern polarimeters now use dual-polarization detectors, which can measure both orthogonal polarization components at the same location on the focal plane, for example Transition Edge-Sensors (TES), and Kinetic Inductance Detectors (KIDs) (see Mauskopf, 2018 for a recent review).

2.1.2. Polarization Modulation

For ground-based polarimeters, the dominant source of noise comes from short-timescale fluctuations in the thermal emission of atmosphere and telescope. High-frequency referencing to an off-source sky position or fast ($>>$ 1 Hz) modulation of the polarization orientation measured by the instrument is therefore crucial.

2.1.2.1. Chopping

The noise of a polarization measurement can be reduced by high-frequency "chopping" of an optical element, commonly the secondary mirror, to a nearby location on the sky assumed to be free of polarized emission (see Hildebrand et al., 2000). The size of the pointing offset, or chop-throw, severely limits the largest angular scales that can typically be recovered. Also, if there is polarized emission at the reference locations then this will add a systematic error to the polarization measured at the target location (see Appendix A of Matthews et al., 2001b).

2.1.2.2. Rotation of a half-wave plate

Birefringent half-wave plates (HWP) rotate the polarization angle of incoming light by 2α, where α is the angle of HWP rotation. These HWPs can serve two purposes: if spun continuously they can modulate the polarization such that all Stokes parameters can be measured on timescales faster than the low-frequency drifts of the telescope (e.g., POL2, TolTEC). In contrast, a stepped HWP can be used to rotate the polarization, in order to measure both Stokes Q and U with each individual detector, and thereby correct for differences in detector beam shape or gains, and characterize the instrumental polarization (IP).

HWPs are an important tool for modulating polarization. However, their disadvantages include modulation of polarization from the optical path between the source and the HWP, preventing their use to characterize IP caused by optical elements earlier in the light path, such as the primary and secondary mirrors. Also, any differences in transmission across the HWP can cause the signal incident to the detectors to vary. It is thus advisable to place a HWP before the re-imaging optics, and far from a focus point of the instrument.

2.1.2.3. Modulation by scanning

For instruments where the time-scale associated with low-frequency ($1/f$) noise is long, polarization can be modulated by scanning the telescope such that Stokes Q and U can be measured at a given location on the sky on timescales faster than ($1/f$).

This was the strategy adopted by the BLASTPol balloon-borne polarimeter (Galitzki et al., 2014b), which utilized a patterned polarization grid such that each adjacent bolometer sampled an orthogonal polarization component. As the telescope scanned across a target region, the time between when a source was measured with one detector and a detector sampling an orthogonal polarization component was $\ll$1 s. The largest recoverable scale was therefore bounded by the scan speed/(1/f). For BLASTPol a typical scan speed was $0.2^\circ\,s^{-1}$, and the characteristic 1/f knee frequency was ∼50 mHz, so polarized emission on the scales of several degrees could be recovered.

2.2. Previous Polarimeters

2.2.1. Early Detections of Polarized Emission

The first successful observation of linearly-polarized emission was by Cudlip et al. (1982), using the UCL 60 cm telescope, which operated from a stratospheric balloon platform, and used a fast-rotating polarized grid (32 Hz), combined with telescope chopping at 4 Hz. Cudlip et al. (1982) found a polarization level of 2.2% for the Orion Nebula integrated over a frequency band with an effective central wavelength of 77 μm for a 70 K blackbody spectral shape, and measured a polarization angle that was roughly orthogonal to the polarization angle measured from the polarization of extincted starlight, suggesting that the polarized signal was indeed due to emission from dust grains aligned with long axes perpendicular to the magnetic field.

Later Hildebrand et al. (1984) made the first detection of sub-mm polarization centered at 270 μm, also of Orion-KL, using a ^{3}He-cooled bolometer system on the KAO. They detected 1.7 ± 0.4 % polarization, with a polarization orientation that agreed with the angle from Cudlip et al. (1982), using two different methods of modulating polarization: a rotating sapphire HWP and a rotating K-mirror, and found consistent polarization levels. This polarimeter was later reconstructed to operate at 100 μm, closer to the spectral peak of hot dust in bright active star-forming regions (Novak et al., 1989).

The first ground-based detection was made with the 1.3 mm MILLIPOL instrument on the NRAO 12-m telescope (Barvainis et al., 1988). MILLIPOL used a HWP rotating at 1.6Hz to modulate polarization signal directed to a linearly-polarized feed, and again observed Orion-KL, finding polarization angles consistent with previous far-IR and sub-mm stratospheric observations. A polarimeter was also constructed for the UKT-14 single bolometer instrument on the JCMT (Flett and Murray, 1991).

2.2.2. Improvements in Polarimeters, 1990–2017

In the 1990s use of low-noise amplifiers, combined with the ability to construct large focal plane arrays of bolometers, made observations of larger areas and fainter sources possible. The first polarimeter using an array of bolometers was the STOKES instrument, which was built for the KAO. STOKES began operations in 1991 and had two arrays of 32 bolometers that simultaneously measured orthogonal polarization components (Platt et al., 1991). STOKES made over 1,100 individual polarization measurements during its 5 year operational period (Dotson et al., 2000).

Ground-based polarimeters also took advantage of sub-mm bolometer arrays, such as the Hertz instrument for the CSO (Schleuning et al., 1997; Dowell et al., 1998), and SCUPOL, built for the SCUBA camera at the JCMT (Murray et al., 1997; Greaves et al., 2003). Over a decade these two polarimeters observed dense sub-regions within molecular clouds, protostars, supernova remnants and bright nearby galaxies (see Matthews et al., 2009; Dotson et al., 2010 for summaries of the observations).

However, the necessity of instrument chopping to remove atmospheric noise made recovering polarization on scales larger than a few arcminutes difficult. The SPARO instrument, which operated on the 2-m VIPER telescope at the Amundsen-Scott South Pole station, took advantage of the atmospheric stability from the extremely cold and dry conditions during the Antarctic winter to use a much larger chop throw of 0.5°, and therefore make the first large-scale polarization maps across entire molecular clouds (Li et al., 2006).

Later polarimeters were built with even larger detectors arrays, such as SHARP, which used a cross-grid to direct horizontally and vertically polarized light to opposite sides of the SHARC-II camera on the CSO, such that a 12×12 bolometer array would measure each polarization component (Li et al., 2008). The PolKa instrument on the Atacama Pathfinder Experiment (APEX, Güsten et al., 2006), was built for the LABOCA instrument, operating at 870 μm with 295 pixels (Wiesemeyer et al., 2014).

Sub-mm polarimetry from sub-orbital platforms on stratospheric balloon-borne telescopes also saw major advances. BLASTPol (the Balloon-borne Large Aperture Sub-mm Telescope for Polarimetry), simultaneously imaged the sky in three wide frequency ($\Delta f/f = 0.3$) passbands centered at 250, 350, and 500 μm (Galitzki et al., 2014b). During Antarctic science flights in 2010 and 2012 BLASTPol was been able to recover polarized emission on degree-scales, impossible for ground-based telescopes. The PILOT balloon-borne polarimeter, which operates at 214 μm and has even more detectors than BLASTPol, has flown from both Canada and Australia (Foënard et al., 2018).

Finally the *Planck* Surveyor, launched in 2007, was the first satellite polarimeter to both provide all-sky observations in the sub-mm (at 850 μm) and to have sufficient resolution to make fairly detailed (FWHM $\sim 5'$) maps of molecular clouds (Lamarre et al., 2010; Planck Collaboration VIII, 2016).

2.3. Current Instrumentation

Current polarimeters benefit from new technology which allows for the automated construction of large focal-plane arrays of detectors, such as the super-conducting transition-edge sensor (TES) bolometers, or kinetic inductance detectors (KIDs). In **Figure 1**, we compare the spatial-scale and instrument sensitivity to cold dust (left panel) and warm dust (right panel) for several recent, upcoming, and proposed polarimeters.

An exciting new instrument is the POL-2 polarimeter, which operates simultaneously at 450 and 850 μm and uses a half wave plate spinning at 2 Hz to measure linear polarization with the 10,000 pixels SCUBA-2 camera on the JCMT (Bastien et al., 2005; Friberg et al., 2016).

Additionally, the HAWC+ instrument on SOFIA has recently begun science operations (Harper et al., 2018). With 1280 TES bolometers and a best resolution of $5''$ at 53 μm HAWC$^+$ is producing high resolution maps of protostars and active star-forming regions.

2.4. Future Polarimeters

Several new polarimeters will be coming online in the next few years. One is the TolTEC camera on the newly-upgraded 50-meter Large Millimeter Telescope (LMT) in Puebla, Mexico, which should begin commissioning in early 2019 (Bryan et al., 2018). TolTEC uses microwave kinetic inductance detectors (mKIDs, Austermann et al., 2018) and operates simultaneously at 1.1, 1.4, and 2.1 mm. With $5''$ FWHM resolution at 1.1 mm TolTEC will have a factor of two improvement in resolution compared to any other single-dish sub-mm or millimeter polarimeter. Commissioning is also underway for the NIKA-2 (Adam et al., 2018) and A-KIDs (Otal, 2014) mKID array mm/sub-mm cameras on the IRAM/APEX telescopes, with instruments expected to include polarimetry capability. These new higher-mapping-speed, high-resolution instruments will be extremely important for mapping magnetic fields within filaments and dense cores.

High-detail maps of magnetic fields covering entire molecular clouds are the goal of the next-generation BLAST telescope (BLAST-TNG; Galitzki et al., 2014a). BLAST-TNG is expected to launch in December 2019 from McMurdo Station, Antarctica for a $\sim$28 day flight, and will map dozens of molecular clouds. The new version of BLAST-TNG also uses large-format mKID arrays, with an expected >10 times increase in mapping speed and $\sim$5 times increase in resolution compared to BLASTPol.

Finally, several satellite telescopes have been proposed that include far-IR, sub-mm, and mm linear polarization sensitivity. These telescopes would be cooled to $\leq$6 K, and consequently the instrumental loading would be much lower than that of ground-based or stratospheric polarimeters. The design for the SPICA satellite currently includes a sub-mm polarimeter which

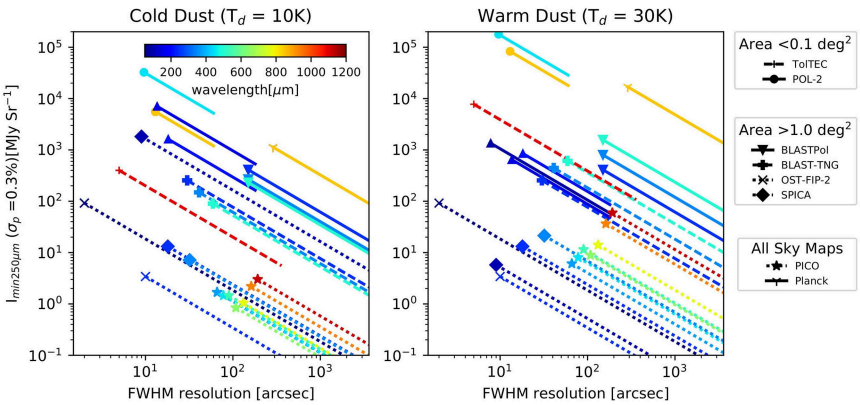

FIGURE 1 | Sensitivity vs. resolution for selected recent (solid lines), upcoming (dashed lines) and proposed (dotted lines) polarimeters. The sensitivity is quantified in terms of the minimum total intensity for which the uncertainty in fractional polarization is less than 0.3%, scaled to the equivalent intensity at 250 μm, ($I_{min\,250\,\mu m}$), assuming a single temperature dust population with β = 1.8, and T_d = 10 K **(left)** or 30 K **(Right)**. The line color indicates the effective central wavelength for each frequency band. For all-sky coverage polarimeters (*Planck* and the proposed PICO satellite) the average expected depth is quoted. For large mapping area experiments (BLASTPol, BLAST-TNG and the proposed SPICA and OST satellites) a mapping speed of 1 deg^2 h^{-1} was assumed, while small area instruments (POL-2, HAWC+, TolTEC) assume a map of one instrument FOV in an hour. The symbols show the depth expected at full polarimeter resolution, lines show how the sensitivity changes with smoothing assuming $I_{min\,250}$ decreases linearly with the ratio of the smoothed beam FWHM to the intrinsic instrument resolution. References: POL-2/JCMT https://proposals.eaobservatory.org/jcmt/calculator/scuba2/time, Friberg et al. (2016), we assumed El = 45°, $\tau_{225\,GHz}$ = 0.05; BLASTPol, BLAST-TNG: Marsden et al. (2009), Galitzki et al. (2014b), Fissel et al. (2016); HAWC+/SOFIA (Harper et al., 2018); TolTEC/LMT Bryan et al. (2018); *Planck*: Lamarre et al. (2010); Planck Collaboration VIII (2016); FIP/OST (Concept-2) Staguhn et al. (2018); POL/SPICA: Gaspar Venancio et al. (2017); PICO: Sutin et al. (2018).

would operate at 100, 200, and 350 μm (Gaspar Venancio et al., 2017; Roelfsema et al., 2018), while the Concept-2 design for the proposed Origins Space Telescope includes a Far-infrared Polarimeter (FIP), which would operate in both the far-IR and sub-mm (Staguhn et al., 2018). Both satellites would map hundreds of square degrees, with $\sim$10″, at 100 and 250 μm, respectively. A satellite targeting the entire sky, the Probe for Inflation and Cosmic Origins (PICO), has also been proposed (Sutin et al., 2018; Young et al., 2018). PICO would provide coverage in 10 frequency bands between 375 μm to 2 mm, with a best resolution of 1.1′. While this resolution is considerably lower than that of SPICA and OST, PICO would map every molecular cloud in the Galaxy, with thousands of molecular clouds mapped to a resolution better than 1 pc.

3. TECHNIQUES FOR INTERPRETATION OF POLARIZATION OBSERVATIONS

In this section we summarize techniques for interpreting polarization observations, particularly in terms of determining the strength and energetic importance of the magnetic field. We discuss degeneracies between grain alignment, line-of-sight and sub-beam effects which complicate determination of magnetic field properties from polarization observations.

3.1. (Davis-)Chandrasekhar-Fermi Analysis and Its Variations

The most widely-used method of estimating magnetic field strength from continuum polarization data is the (Davis-)Chandrasekhar-Fermi (DCF) method (Davis, 1951; Chandrasekhar and Fermi, 1953). DCF assumes perturbations in the magnetic field to be Alfvénic, i.e., deviation in angle from the mean field direction results from distortion by small-scale non-thermal motions, such that $\delta v \propto \delta B/\sqrt{\rho}$. The plane-of-sky magnetic field strength is estimated as

$$B_{pos} = Q\sqrt{4\pi\rho}\frac{\sigma_v}{\sigma_\theta}, \tag{5}$$

where ρ is volume density, σ_v is velocity dispersion, σ_θ is dispersion in angle, and Q is a correction factor discussed below. DCF further assumes that turbulence is statistically isotropic, i.e., $\sigma_{v,los} = \sigma_{v,pos}$ (LOS – line of sight; POS – plane of sky).

Numerous attempts at improving the DCF method exist, falling into two camps: (1) better estimation of σ_θ and Q, (2) direct measurement of the ratio of turbulent to ordered magnetic energy through structure function analyses.

3.1.1. Classical DCF Method

Classical DCF assumes that the turbulent-to-ordered magnetic field strength ratio $\frac{B_t}{B_o} \sim \sigma_\theta/Q$, and that variation about the mean field direction is Gaussian and results from turbulent fluctuations about the mean field direction (the effect of measurement uncertainty on the measured dispersion in angle can where necessary be accounted for; see Pattle et al., 2017).

3.1.1.1. Q parameter

Classical DCF overestimates magnetic field strength due to two integration effects, (1) of ordered structure on scales smaller than the telescope beam, and (2) of emission from multiple turbulent cells within the telescope beam, including those along the line of sight. These effects are parameterized as a correction factor, $0 < Q < 1$ (Zweibel, 1990; Myers and Goodman, 1991; Ostriker et al., 2001).

Heitsch et al. (2001) found, based on numerical simulations, that for strong magnetic fields with well-resolved field structure, DCF results are typically correct to within a factor of 2, but strengths of weak and/or poorly-resolved fields could be overestimated by a factor $\lesssim$ 10. Padoan et al. (2001) found that in low- to intermediate-density regions, $Q \sim 0.3 - 0.4$, while Ostriker et al. (2001) found $Q \sim 0.5$ at high densities. Crutcher et al. (2004) thus suggested that in dense, self-gravitating filaments and cores in which little field substructure is expected, $Q \sim 0.5$ is a reasonable value.

DCF will overestimate field strength by a factor $\sqrt{N}$, where N is the number of turbulent cells enclosed within the volume sampled by the telescope beam (e.g., Houde et al., 2009). Where the linear resolution of the telescope beam is smaller than the scale of a turbulent cell, this overestimation reduces to the square root of the number of turbulent cells along the line of sight: $\sim \sqrt{L_{los}/L_{turb}} \sim \sqrt{N}$, where L_{los} is the length of the optically thin column along the line of sight and L_{turb} is the driving length scale of the turbulence (e.g., Cho and Yoo, 2016). Cho and Yoo (2016) proposed a measure of N, and so correction specifically for line-of-sight variations,

$$\frac{\delta V_c}{\delta v_{los}} \sim \frac{1}{\sqrt{N}}, \tag{6}$$

where δV_c is the standard deviation of centroid velocities across the area to which the DCF method is applied, and δv_{los} is the average line-of-sight velocity dispersion across the same region. While a correction for sub-beam effects is also necessary, an independent estimate of N provides a useful check on other methods of parameterizing line-of-sight effects, as described below.

Interferometric results show complex magnetic field structure on small scales within molecular clouds (e.g., Hull et al., 2017), suggesting that DCF analyses using single-dish data need a good understanding of the effect of sub-beam field structure—particularly, ordered structure with size scales potentially smaller than the turbulent dissipation scale of the system—on measured angular dispersion.

3.1.1.2. Large-scale ordered field structure

DCF assumes that all variation in the magnetic field direction results from perturbations driven by Alfvénic turbulence, i.e., that the underlying field geometry is linear, which is not generally the case.

Pillai et al. (2015) introduced a "spatial filtering" method to account for ordered field structure, in which at each position the ordered field component is approximated by a distance-weighted mean of the angle at neighboring positions. The residual angle is given by

$$\theta_{i,res} = \theta_i - \frac{\sum_{j=1}^{N} w_{i,j}\theta_j}{\sum_{j=1}^{N} w_{i,j}}, \tag{7}$$

where the weighting function $w_{i,j} = \sqrt{1/d_{i,j}}$, and $d_{i,j}$ is the separation between positions i and j. The angular dispersion σ_θ is determined from the standard deviation of these residuals.

Similarly, Pattle et al. (2017) introduced an "unsharp masking" method, in which the map of magnetic field angles is smoothed with a 3 × 3-pixel boxcar filter. This smoothed map—a model of the underlying ordered field—is subtracted from the original map, and the angular dispersion σ_θ is determined from the standard deviation of the residuals.

These methods require a separate estimate of the Q parameter.

3.1.1.3. Restrictions on angular dispersion

Classical DCF is valid in the small-angle limit, found to be $\sigma_\theta \lesssim 25°$ (Ostriker et al., 2001; Padoan et al., 2001). Heitsch et al. (2001) present a correction for the small-angle approximation, $\sigma_\theta \rightarrow \sigma(\tan\theta)$, in Equation (5); this requires further correction in order to avoid anomalous behavior as $\theta \rightarrow \pm 90°$. Falceta-Gonçalves et al. (2008) present a more generalized DCF equation,

$$B_{pos}^{ext} + \delta B \simeq \sqrt{4\pi\rho}\frac{\sigma_v}{\tan\sigma_\theta}, \tag{8}$$

where B_{pos}^{ext} is the plane-of-sky projected component of the mean (ordered) magnetic field and δB is the turbulent field component, taking $\sigma(\tan\theta) \approx \tan\sigma_\theta$ to avoid discontinuities.

3.1.2. Structure-Function DCF Method

An alternative approach is to invoke structure function analysis to determine the ratio of the turbulent to the total magnetic field strength. This was first applied to the DCF method by Falceta-Gonçalves et al. (2008) and expanded upon by Hildebrand et al. (2009) (accounting for large-scale field structure), and Houde et al. (2009) (additionally accounting for sub-beam and line-of-sight effects).

In structure function analyses, the DCF equation is modified to become

$$B_{pos} = \sqrt{4\pi\rho}\sigma_v \left(\frac{\langle B_t^2\rangle}{\langle B_o^2\rangle}\right)^{-\frac{1}{2}} \tag{9}$$

where B_t is the turbulent component of the magnetic field and B_o is the ordered component of the magnetic field, such that

$$\langle B^2\rangle = \langle B_t^2\rangle + \langle B_o^2\rangle, \tag{10}$$

with B being total magnetic field strength.

The structure function under consideration is the average difference in angle between pairs of measured polarization vectors at positions $\vec{r}$ and $\vec{r} + l$ as a function of the distance l between them,

$$\langle \Delta\theta(l)\rangle = \langle \theta(\vec{r}) - \theta(\vec{r} + \vec{l})\rangle. \tag{11}$$

Houde et al. (2009) fit the function

$$1 - \langle \cos[\Delta\theta(l)]\rangle \simeq \frac{1}{N(\delta, W, \Delta')}\frac{\langle B_t^2\rangle}{\langle B_o^2\rangle}\left(1 - \exp\left[\frac{l^2}{2(\delta^2 + 2W^2)}\right]\right) + al^2 \tag{12}$$

where N is given by

$$N(\delta, W, \Delta') = \Delta'\frac{\delta^2 + 2W^2}{\delta^3\sqrt{2\pi}}. \tag{13}$$

See Hildebrand et al. (2009) and Houde et al. (2009) for the derivation of this result. This function is fitted for $\langle B_t^2\rangle/\langle B_o^2\rangle$, the mean ratio of the turbulent and ordered field components; δ, the turbulent length scale; and a, the first term in the Taylor expansion of the autocorrelation function. Fixed quantities are W, the telescope beam width ($FWHM = W\sqrt{8\ln 2}$), and Δ', the effective cloud thickness, which is assumed by Houde et al. (2009) to be the FWHM of the autocorrelation function of the polarized flux emission as a function of distance l.

This method requires the turbulent length scale δ to be resolved by the observations in order to determine N and $\langle B_t^2\rangle/\langle B_o^2\rangle$. Where δ is not resolved ($\delta \lesssim W$), the maximum value of N can be constrained, for an assumed cloud thickness Δ' (Pillai et al., 2015).

3.1.3. Correction for Total Field Strength

Total magnetic field strength can be estimated by combining DCF plane-of-sky measurements with line-of-sight field strengths determined from Zeeman splitting (e.g., Kirk et al., 2006), requiring the Zeeman-split line emission and the polarized dust emission to trace the same material. Kirk et al. (2006) combine JCMT/SCUPOL-data-derived DCF estimates with Zeeman splitting of the high-density tracer CN to estimate total field strength in a dense core. However, as Zeeman splitting is most easily detected in HI and OH (e.g., Crutcher, 2012), this analysis is more easily applicable at low-to-intermediate densities. Comparison of DCF and Zeeman measurements is discussed in detail in section 3.2.

The total magnetic field strength can alternatively be estimated statistically. Crutcher et al. (2004) argue that for a magnetic field geometry without a preferred axis, on average,

$$B_{pos} = \frac{\pi}{4}|\vec{B}|, \tag{14}$$

where $|\vec{B}|$ is the magnitude of the total magnetic field strength. While this correction is useful when considering an ensemble of DCF measurements (e.g., Crutcher et al., 2004), its applicability to any individual case is uncertain.

Heitsch et al. (2001) proposed a statistical correction for line-of-sight effects, where the full magnetic field strength is estimated as

$$|\vec{B}| = \left[4\pi\rho\frac{\sigma_v}{\sigma(\tan\theta)}\left(1+3\sigma(\tan\theta)^2\right)\right]^{0.5}. \tag{15}$$

3.1.4. Comparison and Testing of DCF Methods

Only classical DCF has been fully tested against synthetic observations generated from MHD simulations including self-gravity (Heitsch et al., 2001; Ostriker et al., 2001; Padoan et al., 2001), thus determining $Q \sim 0.5$. The principle of the structure function method has been tested against non-self-gravitating simulations (Falceta-Gonçalves et al., 2008), but its practical realizations (Hildebrand et al., 2009; Houde et al., 2009) have not been. Additionally, Pattle et al. (2017) performed limited testing of their "unsharp masking" variant of the classical DCF method against model field geometries.

Some direct comparisons have been made of the various DCF methods. Poidevin et al. (2013), using JCMT/SCUPOL data, compared the Falceta-Gonçalves et al. (2008) classical modification to the Hildebrand et al. (2009) structure function method, finding Hildebrand et al. (2009) field strengths to be consistently higher, typically by a factor ~ 5, across a range of densities ($\sim 10^3$—$10^6\,\mathrm{cm}^{-3}$), a difference ascribed both to high angular dispersions affecting the Falceta-Gonçalves et al. (2008) estimates and to the lack of correction for line-of-sight or beam signal integration effects in the Hildebrand et al. (2009) method. Planck Collaboration Int. XXXV (2016) compared the classical DCF method to the Houde et al. (2009) structure function method, finding that at low densities ($n \sim 100\,\mathrm{cm}^{-3}$) and high angular dispersions ($\sigma_\theta > 25°$), the Houde et al. (2009) method gives field strengths approximately twice those of classical DCF.

Hildebrand et al. (2009) and Pattle et al. (2017) found comparable values for magnetic field strength in OMC 1, of 3.8 mG (CSO/Hertz data) and 6.6 ± 4.7 mG (JCMT/POL-2 data), respectively. Houde et al. (2009) found 0.76 mG (CSO/SHARP) for the same region, inferring $N \sim 21$ independent turbulent cells along the line of sight. Using the Cho and Yoo (2016) method and $C^{18}O$ line data, Pattle et al. (2017) found $N \lesssim 2$.

A self-consistent comparison of the various classical and structure-function DCF methods, using both observational data and synthetic observations from self-gravitating MHD simulations, would be of significant value. Comparison of the values of N determined by the structure-function method and by the Cho and Yoo (2016) parameterization would also be useful.

In **Figure 2** we collate DCF-estimated magnetic field strengths from single-dish emission measurements over the last two decades. This plot suggests that the systematic differences between the different methods are comparable to the uncertainties on individual measurements, although most DCF measurements are unfortunately given without formal uncertainties. Structure function measurements are typically amongst the higher magnetic field strengths, for a given density.

3.2. Comparison of DCF and Zeeman Measurements

The DCF method provides only an indirect measurement of magnetic field strength. The only direct method of measuring magnetic field strengths in molecular clouds is through Zeeman splitting of line emission from paramagnetic molecules (e.g., Crutcher, 2012). However, measuring the Zeeman effect in the environments of molecular clouds is extremely technically challenging, and unambiguous detections remain sparse (Crutcher, 2012), making indirect methods the only practical means of measuring magnetic fields in many ISM environments. However, in order to verify that the DCF method produces reasonable results, comparison must be made to Zeeman measurements where possible. Zeeman measurements of magnetic field strength are discussed in detail by Crutcher and Kemball (under review).

Crutcher et al. (2010) proposed an upper-limit relationship between gas density n and total magnetic field strength B in which $B = 10\mu\mathrm{G}$ at $n(\mathrm{H}) < 300\,\mathrm{cm}^{-3}$, and $B \propto n^{0.65}$

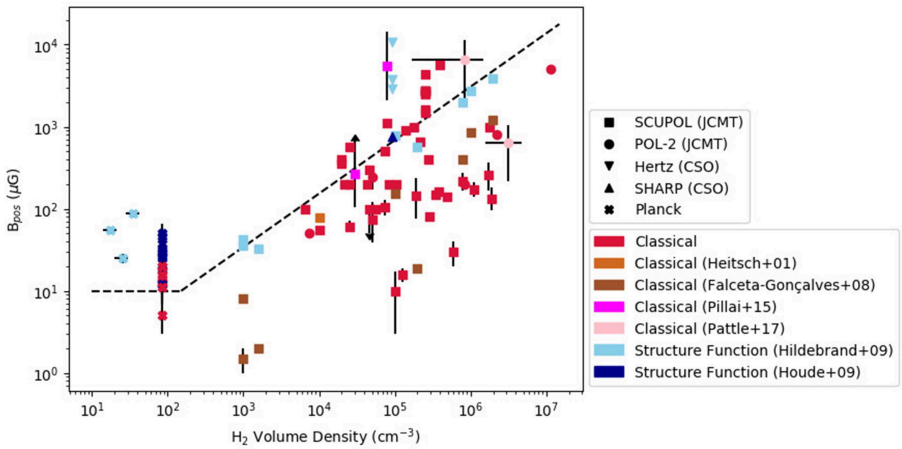

FIGURE 2 | A collation of DCF magnetic field strength measurements from single-dish emission polarimetry as a function of volume density. Note that some sources appear more than once on this plot. Dashed line marks the Crutcher et al. (2010) magnetic field/density relation, scaled to $n(H_2)$. All volume densities are converted to $n(H_2)$ if not given as such in the original work, assuming $n(H_2) = 0.5\,n(H)$, and mean molecular weight $\mu = 2.8$ (i.e., $n(H_2) = \frac{5}{6}\,n_{total}$), unless another value of μ is given in the original work. References: Davis et al. (2000), Henning et al. (2001), Matthews et al. (2002), Wolf et al. (2003), Vallée et al. (2003), Crutcher et al. (2004), Curran et al. (2004), Kirk et al. (2006), Curran and Chrysostomou (2007), Vallée and Fiege (2007), Hildebrand et al. (2009), Houde et al. (2009), Poidevin et al. (2013), Pillai et al. (2015), Planck Collaboration Int. XXXV (2016), Pattle et al. (2017), Kwon et al. (2018), Liu et al. (2018), Pattle et al. (2018), Soam et al. (2018), and Soler et al. (2018).

at higher densities. This result was determined by Bayesian modeling of Zeeman measurements made in molecular clouds to that date. The estimated power-law index of 0.65 supports models in which the magnetic field is not strong enough to dominate over gravity in most environments considered. We show the Zeeman-derived Crutcher et al. (2010) $B - n$ relation (scaled to $n(H_2)$) on **Figure 2**. The DCF B_{pos} measurements are broadly consistent with the Crutcher et al. (2010) relation, suggesting that DCF-derived field strength estimates are comparable to Zeeman measurements at these densities. While Crutcher et al. (2010) give their relation as an upper limit on magnetic field strength, some DCF-derived values significantly in excess of this relation are seen. These excesses could be caused by shortcomings in the DCF method, particularly failure to properly account for line-of-sight/sub-beam variations (cf. Hildebrand et al., 2009, although this method also gives values in excess of the Crutcher et al., 2010 relation), or by unaccounted-for uncertainties (as discussed by Pattle et al., 2017), or by genuinely highly magnetically-dominated systems (as claimed by, e.g., Pillai et al., 2015).

Figure 2 shows that on average, DCF field strengths are comparable to those derived from Zeeman measurements. A more direct check on DCF results is comparison with Zeeman measurements in individual sources. However, such comparisons are complicated by the requirement that the species in which the Zeeman effect is observed traces the same material as the dust emission upon which the DCF analysis is performed (see discussion in Crutcher et al., 2004), and by the fact that DCF and Zeeman measurements trace orthogonal components of the magnetic field (cf. Heiles and Robishaw, 2009).

Ground-based submillimeter data sets typically trace volume densities $\geq 10^4\,cm^{-3}$, and so CN and CCS are generally the only suitable tracers for direct comparison (cf. Crutcher et al., 1996). Comparisons of individual CN/CCS Zeeman measurements to SCUPOL-, Hertz-, SHARP-, and POL-2-derived DCF measurements generally find DCF field strengths to be the same order of magnitude as, but somewhat larger than, those determined from Zeeman measurements—see Kirk et al. (2006), Curran and Chrysostomou (2007), Hildebrand et al. (2009), Houde et al. (2009), Pillai et al. (2016), and Pattle et al. (2017).

Space-based and stratospheric instruments are less restricted in the volume densities which they can trace, and so allow direct comparison to the more easily detectable OH and HI Zeeman effects—for example, Soler et al. (2018) directly compare HI Zeeman measurements to Planck DCF measurements of the Eridanus superbubble, finding $B_{pos,DCF}/B_{los,HI} \sim 2.5 - 13$. In more distant and higher-mass regions, some comparisons can usefully be made between DCF measurements and Zeeman measurements from OH and H_2O maser emission (e.g., Curran and Chrysostomou, 2007; Pattle et al., 2017), although care must be taken as maser emission traces only the extremely dense material surrounding the emitting source.

Poidevin et al. (2013) discuss comparison of CN and OH Zeeman and SCUPOL-derived DCF measurements in detail, finding that on average, $B_{pos}/B_{los} = 4.7 \pm 2.8$. They suggest several causes for this discrepancy: (1) line-of-sight field reversals to which Zeeman measurements are sensitive and DCF is not, (2) systematic differences in material traced, (3) the spatial averaging effects to which both methods are subject, (4) the possibility that DCF-inferred field strengths may be systematically overestimated due to integration effects (see discussion above), and (5) statistical differences between line-of-sight and plane-of-sky field strengths, noting that B_{pos} will on average be larger than B_{los}, and a better tracer of total magnetic field strength (Heiles and Robishaw, 2009). Poidevin et al. (2013) argue that, in general, DCF-derived

B_{pos} provides an upper limit on the true magnetic strength, while Zeeman-measured B_{los} provides a lower limit.

3.3. Intensity Gradient Technique

Koch et al. (2012a) proposed a method of measuring magnetic field strength based on the measured angle between magnetic field direction and gradient in emission intensity (see also Koch et al., 2012b, 2013). This method assumes that an emission intensity gradient is representative of the resultant direction of motion of material due to magnetic, pressure and gravitational forces. The "significance of the magnetic field"—the ratio of magnetic to gravitational and pressure forces—Σ_B, is given by

$$\Sigma_B \equiv \frac{F_B}{|F_G + F_P|} = \frac{\sin\psi}{\sin\alpha}, \tag{16}$$

where α is the angle between polarization direction and intensity gradient direction, ψ is the angle between the direction of the local center of gravity and the intensity gradient direction, and F_B, F_G, and F_P are the magnetic, gravitational and pressure forces, respectively. Σ_B provides an estimate of whether the magnetic field is sufficiently strong to prevent gravitational collapse, with $\Sigma_B > 1$ indicating that the region under consideration is magnetically supported (Koch et al., 2012a).

Equation (16) can be rearranged to give magnetic field strength,

$$B = \sqrt{\frac{\sin\psi}{\sin\alpha}(F_G + F_P)4\pi R}, \tag{17}$$

where R is the radius of curvature of the magnetic field. Note that this equation is given in cgs units.

This method requires estimation of a large-scale magnetic field curvature, and treats any deviation of polarization vector angles from the mean direction due to turbulent effects as a contaminant effect on the large-scale, ordered field. This method has the advantage of being able to provide a point-to-point estimate of magnetic field strength across a map, while DCF analysis provides an average value across a region. The method is also applicable to any measure of magnetic field direction, including, e.g., Faraday rotation. However, its applicability is limited to situations in which self-gravity is important, and is most applicable to the weak-field case in which magnetic fields are regulated by gravity (Koch et al., 2012a).

3.4. Velocity Gradient Technique

The velocity gradient technique (VGT; González-Casanova and Lazarian, 2017) indirectly estimates magnetic field strength and morphology in low-density, turbulent regions. VGT proposes that turbulence mixes magnetic field lines perpendicular to the local magnetic field direction, producing velocity gradients from which the magnetic field strength and morphology can be inferred. The VGT method works in simulations (González-Casanova and Lazarian, 2017), and predicts comparable magnetic field morphologies to those observed in dust polarization by Planck when applied to HI data (Yuen and Lazarian, 2017). This approach may usefully complement polarization measurements in the environments in which its assumptions can be expected to hold.

3.5. Histogram of Relative Orientations (HRO)

The Histogram of Relative Orientations (HRO; Soler et al., 2013) characterizes the dynamic importance of the magnetic field in molecular clouds through the distribution of angles between the projected magnetic field vectors on the plane of the sky and the column density gradient (indicative of the preferred direction of density structure) at each position. Simulations suggest that a weak magnetic field and/or non-self-gravitating density structure result in magnetic fields aligned along the preferred axis of the density structure, whereas a strong magnetic field and self-gravitating structure result in preferential alignment of high density structures orthogonal to the magnetic field direction (e.g., Soler et al., 2013; Wareing et al., 2016; Klassen et al., 2017). HROs provide a qualitative but powerful diagnostic of the relative importance of the magnetic field to a region. By restricting the analysis to progressively higher column densities, a threshold at which self-gravity becomes important can be identified (Chen et al., 2016).

The local orientation of cloud structure projected on the sky can be characterized by calculating the gradient field of the column density map $N_{\rm H}$. Since the gradient angle is normal to the local iso-$N_{\rm H}$ contour lines and the inferred magnetic field direction is perpendicular to the polarization orientation $\vec{E}$ the relative orientation angle between the local cloud orientation and the magnetic field is:

$$\phi = \arctan\left(|\nabla N_{\rm H} \times \vec{E}|, \nabla N_{\rm H} \cdot \vec{E}\right), \tag{18}$$

where ϕ is only unique within the range $0 \leq \phi \leq 90^\circ$ (Soler et al., 2017). From this set of relative orientation angles a preference for parallel vs. perpendicular alignment can be calculated either from the HRO parameter,

$$\xi = \frac{N_{||} - N_{\perp}}{N_{||} + N_{\perp}}, \tag{19}$$

where $N_{||}$ and $N_{\perp}$ are the number of cloud sightlines where the local cloud orientation is parallel or perpendicular to the inferred magnetic field direction (Soler et al., 2013), or with the projected Rayleigh statistic,

$$Z_x = \frac{\sum_i^n \cos 2\phi_i}{\sqrt{n/2}}, \tag{20}$$

(Jow et al., 2018). For both relative orientation statistics ξ or $Z_x > 0$ implies that the cloud structure is more often aligned parallel rather than perpendicular to the magnetic field, while ξ, $Z_x < 0$ indicates that the relative alignment is more often perpendicular than parallel.

3.6. Interpretation of Polarization Fraction

In the relatively low-density environments of molecular clouds and cores, it can reasonably be assumed that where a preferred polarization direction exists, it is perpendicular to the local magnetic field direction (Davis and Greenstein, 1951). Various theories of how this alignment comes about exist, although recently the radiative alignment torques (RAT) mechanism

(Dolginov and Mitrofanov, 1976; Draine and Weingartner, 1996; Lazarian and Hoang, 2007) has become increasingly favored (Andersson et al., 2015). The analyses described above assume that grains are aligned with their long axes perpendicular to the local magnetic field, and that polarization observations accurately trace this alignment. It is of great importance to know the conditions under which this assumption holds.

Depolarization—a decrease in observed polarization fraction—is often seen toward high-column-density regions (e.g., Alves et al., 2014; Kwon et al., 2018). Depolarization could result from geometrical effects (vector cancelation of the magnetic field due to integration along the line of sight and/or within the telescope beam in the plane of the sky), or from grains becoming misaligned with the magnetic field at high optical depths. In the RAT paradigm, this would occur due to the increasing attenuation of short-wavelength radiation with increasing depth into the cloud preventing progressively larger grains from being aligned (e.g., Andersson et al., 2015).

Interferometric measurements indicate highly ordered magnetic field structures on small scales in protostellar systems (Hull et al., 2017). Thus, there are at least some circumstances in which grain alignment can persist to very high optical depths. However, interferometric measurements to date have focussed on systems with some internal source of radiation, the photons from which could aid the alignment of grains. Whether grain alignment persists to the centers of starless cores is not yet clear.

A useful measure of how well grains are aligned—on the assumption that the underlying magnetic field is linear—is polarization efficiency, ϵ_p (Whittet et al., 2008). For optically thin polarized emission, polarization efficiency is identical to polarization fraction (e.g., Jones et al., 2015). In extinction polarimetry, polarization efficiency is defined as polarization fraction normalized by optical depth in the relevant band (Andersson et al., 2015, and refs. therein).

Typically, $\epsilon_p \propto A_V^{-\alpha}$, with $0.5 \lesssim \alpha \lesssim 1$ (Alves et al., 2014, 2015; Jones et al., 2015), suggesting that grains become progressively less well-aligned at higher optical depths. There is some indication of a break in behavior at $A_V \sim 20$, beyond which the power-law index steepens significantly, suggesting very poorly-aligned or entirely unaligned grains (Jones et al., 2015), as shown in **Figure 3**. This would put an upper limit on the column densities at which dust polarimetry can trace magnetic fields. Fissel et al. (2016) explore this relation in detail using BLAST-Pol observations of Vela C, investigating the dependence of P on both column density ($\propto A_V$) and dispersion in polarization angle. Fissel et al. (2016) also discuss the degeneracy between depolarization, sub-beam effects, and integration along long sight-lines in such analyses.

It should be noted that the standard selection of polarization vectors by their signal-to-noise ratio in polarization fraction, $p/\delta p$ may create bias in the recovered value of α. The sensitivity of recent observations allows the implementation of Bayesian analyses of the ϵ_p-A_V relationship (Wang et al., 2018), which should better inform future discussions of the limits of applicability of submillimeter polarization observations.

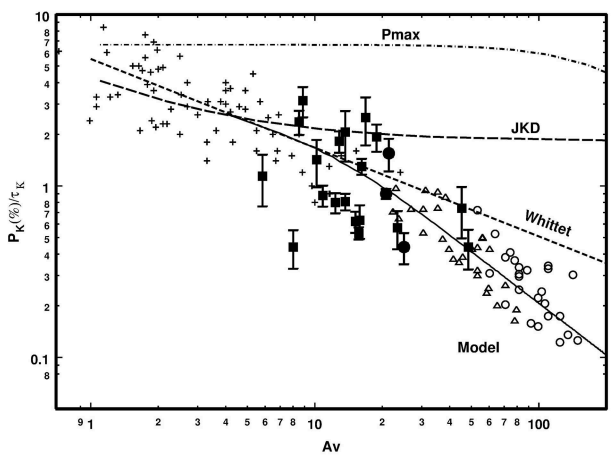

FIGURE 3 | A plot of polarization efficiency (ϵ_p), here defined as the K-band ratio of polarization fraction to optical depth (p_K/τ_K), as a function of visual extinction A_V in a starless core—Jones et al. (2015), Figure 5 © AAS. Reproduced with permission. Crosses and closed symbols show extinction polarimetric measurements; open symbols show submillimeter emission measurements. Note that polarization efficiency is defined in extinction as $\epsilon_p = p/\tau$ and in optically-thin emission as $\epsilon_p = p$; here, submillimeter emission points have been arbitrarily scaled to match extinction data. How effectively grains are aligned with the magnetic field is indicated by the gradient of the $\log \epsilon_p - \log A_V$ relation: the submillimeter data show a steeper gradient than the extinction data, suggesting that grains are less well-aligned at high optical depths.

4. OBSERVATIONS OF MOLECULAR CLOUDS

Molecular clouds represent the largest structures associated with star formation that may be gravitationally bound. In this section we discuss polarization observations on large scales (>1 pc) within clouds, and discuss what these data reveal about both the properties of cloud magnetic fields, and the role of the magnetic field in influencing cloud formation and evolution.

The importance of magnetic fields in molecular clouds is typically parameterized by two quantities. The first is the Alfvén Mach number $\mathcal{M}_\mathrm{A}$, which is the ratio of the turbulent velocity to the Alfvén speed $v_\mathrm{A} = |B|/\sqrt{4\pi\rho}$, where the ratio of turbulent to magnetic energy $E_K/E_B \approx \mathcal{M}_\mathrm{A}^2$. The second is the mass-to-flux ratio Φ, the ratio of the cloud mass to the maximum mass that be supported by the magnetic flux through the cloud against cloud self-gravity.

As discussed in section 2 observing magnetic fields within molecular clouds is challenging: the fraction of dust emission that is polarized is typically less than 10%, and in some cases can be less than 1% (Planck Collaboration Int. XIX, 2015). Observations with ground-based telescopes have been mostly limited to observing the bright, high-column density regions of molecular clouds (e.g., Matthews et al., 2009; Dotson et al., 2010), with the exception of the maps from the SPARO instrument, which produced the first large scale polarization maps covering entire giant molecular clouds (Li et al., 2006).

A major recent advance is the release of all-sky polarization maps from the *Planck* satellite (Planck Collaboration Int. XIX, 2015). *Planck* had 4.8′ FWHM resolution at its 353 GHz (850 μm) frequency band, but due to sensitivity constraints *Planck* polarization maps typically require smoothing to at least 10′ FWHM resolution (∼0.4 pc resolution for the nearest molecular clouds at d ∼150 pc). In addition, the balloon-borne polarimeter BLASTPol (best FWHM resolution of 2.5′), has published extremely detailed polarization maps of the nearby giant molecular cloud Vela C at 250, 350, 500 μm (Fissel et al., 2016; Soler et al., 2017). With the Planck and BLASTPol polarization maps it is now possible to apply the statistical analysis techniques discussed in section 3 to a large number of molecular cloud observations.

4.1. Where Does Polarized Dust Emission Best Trace Cloud Magnetic Fields?

Dust grains are thought to be aligned with respect to their local magnetic field due to radiative torques from relatively high energy photons (see discussion in section 3.6), and so the grain alignment is expected to be more efficient in the outer layers of molecular clouds. Since dust grains in the outer layers of clouds absorb more photons from the local interstellar radiation field (ISRF) they will also be warmer. These grains are therefore likely responsible for a larger fraction of both the total and polarized intensity, compared to colder, more shielded dust grains. Both of these factors imply that the magnetic field inferred from polarized dust emission is weighted toward the outer layers of molecular clouds.

Using BLASTPol 500 μm observations of the Vela C giant molecular cloud Fissel et al. (2016) found that peaks in polarized intensity generally coincide with high column density regions, indicating that the polarization maps are tracing the cloud structure (see **Figure 4B**). However, polarization "holes" are observed toward several high column density regions. Fissel et al. (2016) modeled the decrease in fractional polarization with increasing column density, for the limiting case where all of the observed depolarization is caused by a decrease in grain alignment efficiency for more deeply embedded regions. They found that for moderate column density sightlines ($A_V \sim 10$) polarization measurements trace magnetic fields of all densities, while for high column density sightlines ($A_V \sim 40$) roughly half of the embedded dust contributes little to the polarized emission. This finding is in agreement with a study of polarization efficiency within a starless core by Alves et al. (2014), where it was found that grains remain largely aligned up to $A_V \sim 30$ mag.

Lower-resolution *Planck* maps of both molecular cloud envelopes and the diffuse ISM, also show regions of low polarization (Planck Collaboration Int. XIX, 2015). However, these observations can be explained entirely by turbulence and changes of the magnetic field geometry with respect to the line of sight, and do not appear to be caused by changes in grain alignment efficiency (Planck Collaboration Int. XX, 2015; Planck Collaboration et al., 2018).

As many techniques for analyzing magnetic fields using polarization data require comparison with simulations, it will be important to create realistic synthetic polarization maps from numerical simulations of star formation. Post-processing software such as POLARIS (Reissl et al., 2016), which can include calculations of grain alignment efficiency and variations in dust temperature, are now available. Seifried et al. (2019) applied POLARIS post-processing to the large scale SILCC-Zoom simulations, and found that the inferred magnetic field orientation from polarization maps with $\lambda \geq 160\,\mu m$ typically agrees with the density averaged magnetic field angle to better than 10°.

4.2. Correlations Between Cloud Structure and Magnetic Field Orientation

Optical and near-infrared polarimetry observations show that high column density filamentary structures are often (e.g., B213 in Taurus, Goldsmith et al., 2008; Serpens South, Sugitani et al., 2011) but not always (e.g., L1495, Chapman et al., 2011) aligned perpendicular to the magnetic field. In contrast, lower density gas sub-filaments or "striations" seen in nearby clouds are often oriented parallel to the magnetic field direction (Goldsmith et al., 2008; Palmeirim et al., 2013).

Tassis et al. (2009) compared the orientation of cloud elongation to the inferred magnetic field orientation using archival CSO/Hertz polarization observations of structures ranging from nearby clumps to distant GMCs. They found a weak statistical preference for the cloud long axis to be oriented close to perpendicular to the magnetic field.

More recently, *Planck* and BLASTPol have produced large-scale polarization maps covering entire molecular clouds. These maps have been used to statistically analyze the relationship between cloud column density and magnetic field structure over many orders of magnitude in density and spatial scale. Planck Collaboration Int. XXXV (2016) studied 10 nearby clouds (d < 450 pc) with 10′ FWHM resolution (**Figure 5**) using the histogram of relative orientations (HRO) method discussed in section 3.5. They found that at low column densities (N_H) the cloud structure is more likely to align parallel than perpendicular to the magnetic field, while at N_H greater than $\sim 10^{22}$ cm^{-2}, the clouds structure is more likely to align perpendicular or have no preferred orientation to the magnetic field. This same trend is seen in synthetic polarization maps of numerical simulations only where the magnetic field is in equilibrium with or stronger than turbulence (Soler et al., 2013).

Using BLASTPol polarization maps of Vela C at 250, 350, and 500 μm Soler et al. (2017) studied the relative orientation of the inferred magnetic field, which has resolution ∼0.6 pc, to the higher resolution (0.16 pc FWHM) column density maps derived from *Herschel* data. Similar to the results from Planck Collaboration Int. XXXV (2016), small-scale cloud structure of Vela C is preferentially aligned parallel to the cloud-scale magnetic field at low N_H, and perpendicular to the magnetic field at high N_H (Soler et al., 2017; Jow et al., 2018). Furthermore, the slope of this transition from parallel to perpendicular is

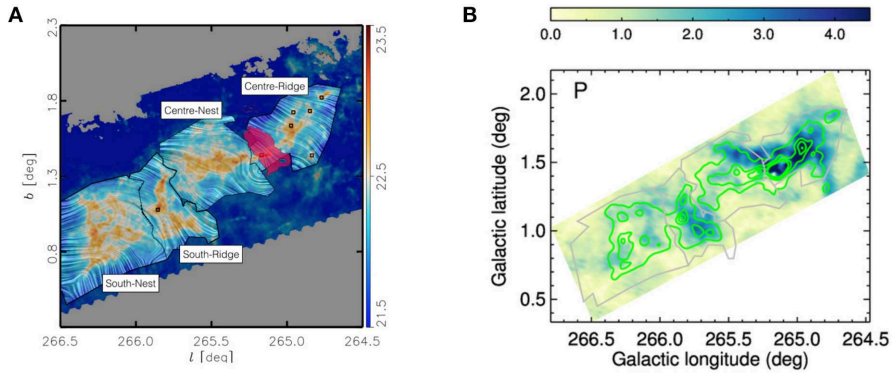

FIGURE 4 | Polarization observations of the Vela C cloud from the BLASTPol telescope. **(A)** Magnetic field orientation (texture) inferred from the BLASTPol 500 μm data overlaid on a *Herschel*-derived column density (N_H) map—Soler et al. (2017), reproduced with permission © ESO. Four sub-region are labeled, while the shaded pink region indicates where the dust is heated by a compact H_{II} region. **(B)** Map of polarized intensity with contours of total intensity (green) overlaid (from Figure 3 of Fissel et al., 2016 © AAS. Reproduced with permission).

observed to be stronger in two cloud sub-regions dominated by dense, high-column density "ridge"-like structures, compared to the other two "nest"-like sub-regions where lower-N_H filaments extend in many directions (**Figure 4**). Comparisons of the inferred magnetic field with orientation of structure in integrated molecular line intensity maps of Vela C show that low volume density molecular gas tracers (such as ^{12}CO and ^{13}CO) show structures aligned parallel to the magnetic field, while intermediate or high density gas shows a weak preference for alignment perpendicular to the large-scale magnetic field, with the transition occurring at $n_{H2} \sim 10^3$ cm^{-3} (Fissel et al., 2018). These results show that in Vela C the cloud-scale magnetic field appears to have played an important role in the formation of small-scale and high density cloud sub-structure.

Applying relative orientation analysis to synthetic polarization observations of numerical simulations, indicates that the slope and intercept of the relative orientation parameter, may encode information about the geometry of the flows that created the cloud (Soler and Hennebelle, 2017; Wu et al., 2017), or the magnetic field strength (Soler et al., 2013; Chen et al., 2016; Wu et al., 2017).

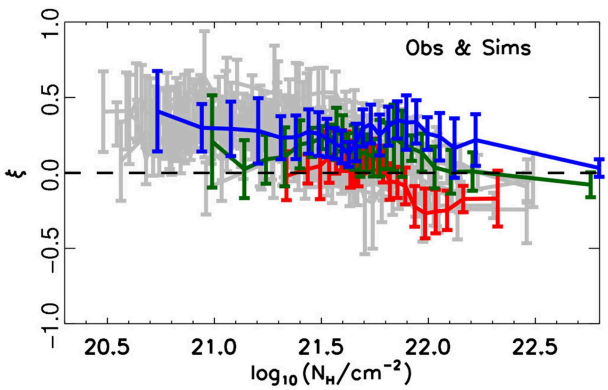

FIGURE 5 | Relative orientation between cloud structure and the magnetic field orientation with increasing column density adapted from Figure 11 of Planck Collaboration Int. XXXV (2016), reproduced with permission © ESO. Gray lines show *Planck* polarization maps of nearby molecular clouds, while colored lines show synthetic observations of MHD simulations of Soler et al. (2013). Planck observations show a change in relative orientation from preferentially parallel ($\xi > 0$) at low N_H, to no preferred orientation ($\xi = 0$) or perpendicular ($\xi < 0$) at high N_H, similar to the simulations where the magnetic field is strong compared to the turbulent gas motions (red), or equal in energy to turbulence (green), but not the simulation where the magnetic field is weak compared to turbulence (blue).

4.3. Magnetic Field Direction vs. Scale in Molecular Clouds

Molecular clouds are created from compressive flows in the more diffuse interstellar medium (ISM). One question of interest is whether magnetic fields preserve a "memory" of the local galactic magnetic field orientation. If the magnetic fields of molecular clouds are weak compared to turbulence then the field directions are expected to be decoupled from the field direction of the ISM.

Observations of the correspondence of molecular cloud fields and Galactic fields in the Milky Way are complicated by the long integration path of polarization observations through the Galactic disk. A study using CSO/Hertz polarization data by Stephens et al. (2013) found that while an average cloud magnetic field direction could be determined for most star forming regions (indicating relatively ordered fields), there was no clear correlation between the average cloud magnetic field direction and location on the Galactic plane, whereas the Galactic magnetic field is thought to be aligned parallel to the spiral arms (Heiles, 1996). However, many of the molecular clouds observed by Stephens et al. (2013) are high mass star forming regions, so the orientation of the magnetic field may have been modified by interactions with photo-ionized regions. Li and Henning (2011) compared the CO line polarization of six giant molecular clouds in the nearby galaxy M33 to the spiral arm orientation, and found a bi-modal relative orientation distribution consistent with alignment between the cloud magnetic field and the galactic field.

In an earlier study by Li et al. (2009), the authors compared the orientation of the magnetic field in dense cloud sub-regions (1 pc or less) inferred from CSO/Hertz and JCMT/SCUPOL sub-mm polarization observations to the orientation of the magnetic field in the diffuse ISM surrounding the cloud from optical polarimetry. They found that 84% of all dense clumps have a difference in orientation of the clump vs. ISM field direction of less than 45°, and estimate that the probability of this occurring by chance is less than 0.01%. Attempts to reproduce this result in simulations by Li et al. (2015) indicate that the magnetic field in molecular clouds must be fairly strong; simulations with the magnetic field energy weaker than that of turbulence ($\mathcal{M}_A >> 1$) cannot reproduce the correspondence between the observed core and large scale field direction.

4.4. Estimates of the Magnetic Field Strength Within Molecular Clouds

Estimates of magnetic field strength on cloud scales with the Davis-Chandrasekhar-Fermi (DCF) method discussed in section 3.1 are challenging because the available cloud scale sub-mm polarization maps from SPARO, BLASTPol, and *Planck* all typically have coarse resolution of several arcminutes. Any disordered field component on scales smaller than the telescope beam will not be observed, and this would lead to an overestimate of the POS magnetic field strength. Most estimates of large scale magnetic fields in molecular clouds with the DCF method use near-IR extinction polarimetry, since cloud envelopes typically have $A_V << 10$, such that background stars can still be observed (see for example Cashman and Clemens, 2014; Kusune et al., 2016).

SPARO observed four giant molecular clouds, with $4'$ resolution, finding well ordered fields in two clouds, NGC6334 and G333.6-0.2, and two clouds where the magnetic field morphology appears to have been altered by feedback, the Carina Nebula and G331.5-0.1 (Li et al., 2006). Novak et al. (2009) used SPARO data and higher resolution CSO/Hertz follow-up observations to correct for the dispersion lost due to beam smoothing, and argue that the magnetic field strength must be at least as strong as turbulence in both NGC6334 and G333.6-0.2.

In Appendix D of Planck Collaboration Int. XXXV (2016), both the DCF method discussed in section 3.1.1 and the modified DCF modeling of the polarization structure function discussed in section 3.1.2 were applied to 10 nearby clouds observed with $10'$ FWHM resolution *Planck* observations. Their estimated values of plane-of-sky magnetic field $B_{\rm POS}$ range from 5 to 20 μG for the DCF method alone, and 12 to 50 μG using the DCF method combined with structure function analysis. Both methods of estimating magnetic field strength are consistent with mass-to-flux ratios $\Phi < 1$, which would imply that the magnetic field is strong enough to support the clouds against gravity. However, the authors of Planck Collaboration Int. XXXV (2016) caution that the measured dispersion in polarization angles is larger than the $\sigma_\theta \sim 25°$ threshold found in synthetic observations of numerical turbulence simulations by Ostriker et al. (2001), below which the DCF method can be used to estimate the magnetic field strength. They also note that the assumptions required for the structure function method of Hildebrand et al. (2009) and Houde et al. (2009) of a scale invariant random magnetic field component are not applicable to the Planck observations, and suggest that the values of magnetic field strength should be interpreted with caution.

4.5. Magnetic Fields in Photo-Ionized Regions

Giant molecular clouds often produce high mass stars, which then form photo-ionized regions that can alter both the structure of the parent cloud, and the morphology of the cloud magnetic field. Observations of magnetic fields in dense gas affected by feedback from high-mass stars remain scarce. Interpreting magnetic fields in such regions requires care, in order to distinguish between the effects of self-gravity and of external pressure on field geometry. For example the BLASTPol map of Vela C in **Figure 4B** shows a pinched field geometry toward the high density ridge associated with the cluster powering the RCW 36 HII region; however, it is unclear whether the field geometry is caused by a dragging of field lines by gravitational collapse or by the field geometry being shaped by the bipolar compact HII region (Soler et al., 2017).

The closest high-mass star-forming region, Orion, has been observed extensively with ground-based polarimeters. Polarization observations of Orion are discussed in detail in section 6.2.2.

Pattle et al. (2018) observed the photo-ionized columns (elephant trunks) known as the "Pillars of Creation" in M16 using POL-2 (**Figure 6**). They found that the field runs along the length of the Pillars, a morphology consistent with the field having been dragged or reorientated by the pillar formation process. However, the DCF estimated field strength is non-negligible (170–320 μG), sufficient to support the Pillars against radial collapse. This suggests that the process of pillar formation may have compressed an initially dynamically negligible field to be dynamically important, though the magnetic field is still not strong enough to prevent the destruction of the Pillars by the ionizing cluster.

Large scale *Planck* polarization observations of photo-ionized regions have also been used to learn more about the magnetic field properties in the host molecular cloud, and the characteristics of the compressed gas. Planck Collaboration Int. XXXIV (2016) used *Planck* polarization data for the Rosette Nebula in the Monoceros molecular cloud with Faraday rotation measurements to construct an analytic model of the magnetic field, where the magnetic field is inclined 45° to the line of sight with $|\vec{B}| = 6.5$–9 μG in the molecular cloud.

4.6. Polarization Observations of Infrared Dark Clouds

Infrared Dark Clouds (IRDCs) are high column density, often filamentary, molecular clouds usually seen in silhouette against the bright IR emission of the Galactic plane, and may represent precursors of high mass star forming regions (Rathborne et al., 2006). Since IRDCs are typically > 1 kpc

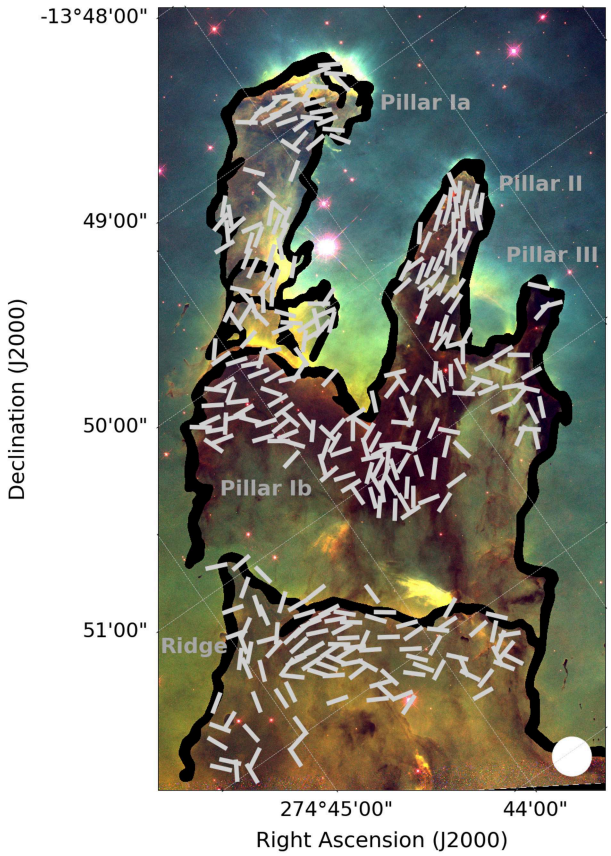

FIGURE 6 | JCMT/POL-2 850μm magnetic field vectors in the Pillars of Creation in M16 (polarization vectors rotated by 90°) overlaid on Hubble Space Telescope imaging—Figure 1 from Pattle et al. (2018) © AAS, reproduced with permission; HST imaging from Hester et al. (1996), Hubble Legacy Archive.

distant, they are typically studied with higher resolution ground-based polarimeters. Many IRDCs have been observed by JCMT/SCUPOL (Matthews et al., 2009), and CSO/Hertz (Dotson et al., 2010), however only a handful have been analyzed in any detail.

Pillai et al. (2015) analyzed JCMT/SCUPOL and CSO/Hertz observations of the IRDCs G11.11 − 0.12 and G0.253 + 0.016 (Matthews et al., 2009), finding that in G11.11−0.12 the magnetic field runs perpendicular to the main filament, while the field in a lower-density filament merging with the main filament is parallel to its length. In both IRDCs they infer that the energy in the magnetic field is at least as strong as energy of the turbulent motions of the gas ($\mathcal{M}_A \leq 1$), and comparable to that of self-gravity.

More recently Liu et al. (2018) observed the filamentary IRDC G035.39-00.33 with JCMT/POL-2, where the filament width was barely resolved with POL-2's ∼14″ FWHM beam. Over most of the IRDC they found that the magnetic field is perpendicular to the main filament, with a DCF inferred magnetic field strength of ∼50 μG. However toward the massive collapsing starless clump candidate "c8," they infer a pinched magnetic field geometry implying that the field lines may be being dragged in by the infalling gas motions. Future observations with higher resolution JCMT/POL-2 450 μm polarimetry, IRAM/NIKA-2, or the upcoming LMT/TolTEC polarimeter (FWHM ∼ 5″) may soon be able to resolve in detail the interaction between magnetic fields and gravity within nearby IRDCs.

5. MAGNETIC FIELDS IN Bok GLOBULES

Bok globules (Bok and Reilly, 1947), isolated clumps of molecular gas containing a few tens of solar masses within a diameter of a few tenths of a parsec (e.g., Launhardt et al., 2010), are a relatively simple environment in which the magnetic field geometry of starless and protostellar cores can be studied. As Bok globules are isolated objects (e.g., Alves et al., 2001), all emission associated with the globule is likely to come from the globule itself, although issues of grain misalignment at high densities remain (e.g., Jones et al., 2015). Bok globules may be starless or may harbor one or more protostars (e.g., Launhardt et al., 2010). Submillimeter polarimetric observations to date have focussed on globules harboring protostars.

Most submillimeter polarimetric observations of Bok globules to date have been performed at 850μm using SCUPOL, with which Vallée et al. (2000) observed CB 003, CB 034E, CB 054, CB 068, and CB 230, while Henning et al. (2001) observed CB 26, CB 54, and DC 253-1.6. CB 068 was marginally detected with the CSO/Hertz polarimeter (Dotson et al., 2010). Magnetic fields in Bok globules are generally found to be approximately linear in projection across the globule. Similarly, Ward-Thompson et al. (2009) observed the magnetic field across the Bok globule CB3 with JCMT/SCUPOL, finding the magnetic field to be linear in projection, and offset ∼ 40° to the core's minor axis—a likely projection effect (Basu, 2000; see also section 7).

Bok globules are an excellent environment for testing models of grain alignment, being isolated, fairly spherical, and generally having simple internal density structures and magnetic field geometries (e.g., Brauer et al., 2016). Depolarization at high column densities is typically observed in Bok globules (e.g., Vallée et al., 2000). However, at least some Bok globules show high polarization fractions at high densities, specifically CB 068, with $p \sim 10\%$ (Vallée et al., 2000). Vallée et al. (2003) argue that CB 068 (which hosts a young protostar) has an ordered field (∼150 μG), and low turbulence, making it a good environment for grain alignment to persist to high densities.

Wolf et al. (2003) estimated field strengths of $\sim 10^2$ μG for the Bok globules B335, CB 230, and CB 244, all of which have embedded protostars. They find the magnetic field to be aligned with the major axis of B335 and CB 230, and compare these to the less evolved CB 26 and CB 54 (cf. Henning et al., 2001), in which the field is weakly aligned with the outflow axis. Wolf et al. (2003) propose that the magnetic field in such systems evolves from being aligned parallel with the outflow direction to being aligned parallel to the disc midplane.

6. MAGNETIC FIELDS WITHIN FILAMENTS

There is strong evidence for a bimodality in the orientation of magnetic fields with respect to filaments in molecular clouds (see section 4.2). Filaments are preferentially found to run either

perpendicular or parallel to the local magnetic field direction in the surrounding, lower-density, medium. However, the behavior of magnetic fields within filaments is less well-characterized. In this section we summarize single-dish observations of magnetic fields within dense filaments, and in the immediate surroundings of filaments.

6.1. Magnetized Accretion Onto Filaments

André et al. (2014) proposed that filaments gain mass through magnetized accretion (see also Nakamura and Li, 2008; Palmeirim et al., 2013). In this paradigm, the sub-filaments, or striations, seen running perpendicular to self-gravitating filaments, and parallel to the magnetic field in the low density material surrounding these filaments, are accretion streams (Palmeirim et al., 2013). Star formation begins when the filament exceeds its maximum line mass for gravitational stability (Ostriker, 1964; see discussion below) and fragments.

Detections of magnetic fields running perpendicular to filaments on small scales have largely been made using optical or near-infrared extinction polarimetry (Sugitani et al., 2011; Palmeirim et al., 2013; Matthews et al., 2014; Panopoulou et al., 2016). Some submillimeter detections exist: Matthews et al. (2014) present BLAST-Pol observations marginally resolving the Lupus I filament, finding the magnetic field to run perpendicular to the filament direction, matching optical polarimetry results. Similarly, Cox et al. (2016) compare Planck 353 GHz observations of Musca to optical polarimetry and Herschel submillimeter imaging, finding the magnetic field in the low-density material to run perpendicular to the filament, and parallel to striations, as shown in **Figure 7**.

While Palmeirim et al. (2013) demonstrate large-scale red-shifted and blue-shifted CO emission preferentially located on opposite sides of the L1495 filament (using FCRAO data), the kinematics of such striations and sub-filaments—the theorized accretion streams—have not yet been observed in detail.

6.2. Magnetic Fields Within Nearby Filaments

The potential importance of magnetic fields within filaments was noted by Chandrasekhar and Fermi (1953). Magnetic fields may regulate the fragmentation and gravitational collapse of filaments (e.g., Fiege and Pudritz, 2000). However, the internal magnetic field geometry of filaments remains unclear. In order to conserve magnetic flux, field lines must either wrap around filaments (e.g., Nakamura et al., 1993; Fiege and Pudritz, 2000) or pass through them (e.g., Tomisaka, 2014; Burge et al., 2016).

Magnetic fields which wrap around filaments are referred to as "helical," loosely defined as a field with some form of toroidal and poloidal components. Such fields could be created through shear motion on an initially poloidal (axial) field (e.g., Fiege and Pudritz, 2000). Toroidal and poloidal fields play different roles in filament dynamics: poloidal fields provide support against collapse and fragmentation of filaments, while toroidal fields provide a confining tension (Fiege and Pudritz, 2000). Helical field geometries generally predict a decrease in polarization fraction toward the filament axis, an effect potentially degenerate with depolarization due to grain misalignment at high densities (e.g., Matthews et al., 2001b).

Magnetic fields which pass through a filament (generally referred to as "perpendicular") are expected to result in collapse of an initially cylindrical filament into a flattened, ribbon-like structure which may have an hourglass magnetic field across its cross-section (Tomisaka, 2014; Burge et al., 2016). In projection, the field lines will run along the length of a filament, with alternating minima and maxima in polarization fraction predicted across the filament's width (Tomisaka, 2015). Such a polarization structure has not yet been definitively observed, but provides a useful discriminant between the perpendicular and helical field models.

Observed filament radial density profiles may provide indirect evidence for the magnetic field geometry, and potentially a means of breaking projection effect and grain misalignment degeneracies. In unmagnetized filaments, density is predicted to fall as r^{-4} in the filament wings (Ostriker, 1964). For purely poloidal fields, density is predicted to fall off faster than r^{-4}, while for generically helical fields, the predicted index is shallower, varying from $r^{-1.8}$ to r^{-2} (Fiege and Pudritz, 2000). In models of perpendicular fields, the predicted index varies with model, but is shallower than the unmagnetized value (Tomisaka, 2014). However, all of these models are of non-accreting filaments, which is unlikely to be the case in practice. An understanding of the effect of accretion on observed filament density profiles would be necessary in order to use such profiles as a discriminant between magnetic field geometries.

Gravitationally unstable filaments are expected to fragment and collapse (Stodólkiewicz, 1963; Ostriker, 1964). Fiege and Pudritz (2000) presented a modification of the Ostriker (1964) critical line mass, taking into account magnetic support:

$$\left(\frac{M}{L}\right)_{crit,mag} = \left(\frac{M}{L}\right)_{crit} \left(1 - \frac{\mathcal{M}}{|\mathcal{W}|}\right)^{-1}, \qquad (21)$$

where M is the mass of a filament of length L, $(M/L)_{crit} = 2c_s^2/G$, the Ostriker (1964) critical line mass (c_s is sound speed, sometimes replaced with the full velocity dispersion), $\mathcal{M}$ is the magnetic energy per unit length, and $\mathcal{W}$ is the gravitational energy per unit length. $\mathcal{W} = -(M/L)^2 G$ for a generic uniform filament. Tomisaka (2014) also presents comparable magnetic critical line mass relations. In extremely massive filaments, the magnetic field may be distorted by flux-frozen gas motions caused by gravitational collapse of material along the filament (see discussion of OMC 1 below).

6.2.1. Planck Results

While Planck observations do not have sufficient resolution to observe fields within filaments in detail, Planck Collaboration et al. (2016) discuss their observations of the large-scale magnetic field morphology in three nearby filaments (Musca, L1506, B211), subtracting background emission by polynomial fitting. In these cases polarized emission from the filament can be separated from the "background" emission from the large-scale, low-density molecular cloud. The polarization angle in the filaments is found to be coherent, and offset from the background value

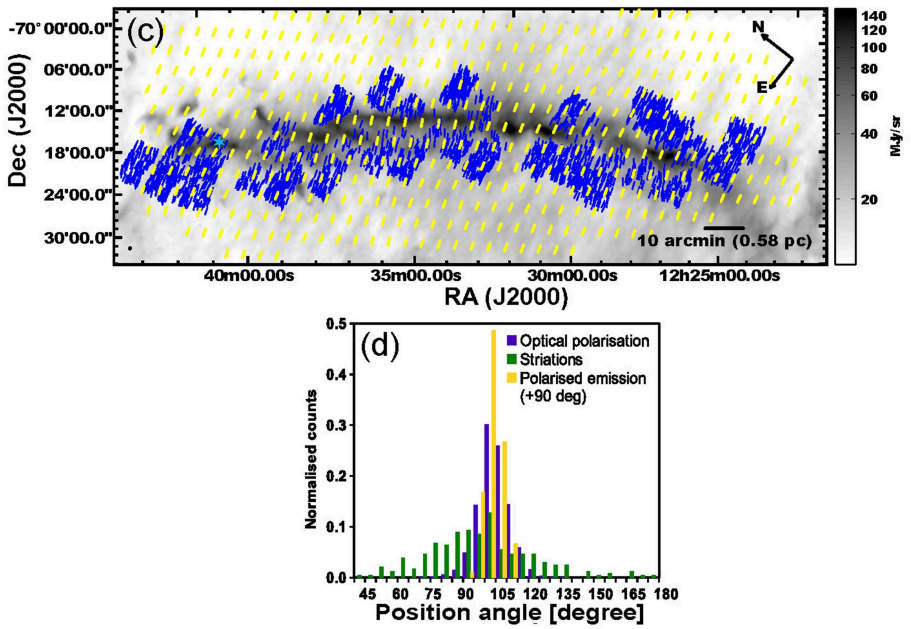

FIGURE 7 | The magnetic environment of the Musca filament; Figures 4c,d from Cox et al. (2016), reproduced with permission © ESO. **(Upper)** Image: Herschel SPIRE 250μm emission. Yellow vectors: Planck 353 GHz polarization vectors, rotated to trace the magnetic field direction. Blue vectors: starlight polarization vectors, tracing magnetic field direction. **(Lower)** Histograms of optical polarization, rotated emission polarization, and striation position angles, showing magnetic field direction and striation direction to be strongly peaked perpendicular to the direction of the filament.

by 12° (Musca), 54° (L1506), and 6° (B211; not significant), consistent with various models (e.g., Fiege and Pudritz, 2000; Tomisaka, 2014).

6.2.2. Filaments in Orion A and B

6.2.2.1. Orion A OMC-1

The high-mass OMC-1 region within the nearby Orion A "integral filament" has been observed many times in polarized emission (Rao et al., 1998; Schleuning, 1998; Vallée and Bastien, 1999; Coppin et al., 2000; Houde et al., 2004; Hildebrand et al., 2009; Ward-Thompson et al., 2017). The mean magnetic field direction in OMC-1 differs significantly from that in the rest of the integral filament (Houde et al., 2004). While the average magnetic field direction in OMC-1 is approximately perpendicular to the direction of the filament (Ward-Thompson et al., 2017), the field shows significant ordered deviations from cylindrical symmetry, particularly in a large-scale "hourglass" feature (Rao et al., 1998; Schleuning, 1998) centered on the gravitational interaction between the Orion BN/KL and South clumps (shown in **Figure 8**). This field morphology is posited to result from motion of these two massive clumps along the filament under gravity (Schleuning, 1998; Pattle et al., 2017). The field is highly ordered and strong, with DCF-method-measured strengths varying from 0.76 mG (Houde et al., 2009) to 6.6 ± 4.7 mG (Pattle et al., 2017). The observed distortion of the field suggests that OMC-1 is not magnetically dominated, although energetics analysis suggests that the magnetic field may have been compressed to become dynamically significant (Pattle et al., 2017). The three-dimensional magnetic field geometry of the region is not clear; Schleuning (1998) propose a model in which the magnetic field passes directly through the filament at an angle, but large-scale helical geometries for the integral filament have also been proposed (e.g., Poidevin et al., 2011; Schleicher and Stutz, 2018).

Monsch et al. (2018) observed a narrow, low-mass filament in the OMC-1 region in NH_3, and found that the magnetic field as observed with JCMT/POL-2 (Pattle et al., 2017; Ward-Thompson et al., 2017) runs parallel to filament. The filament has a very steep density profile, $r^{-5.1}$, inconsistent with predictions for toroidal fields but potentially consistent with an axial or perpendicular field. Both field and filament appear to extend radially from Orion BN/KL (the center of the OMC-1 region). It is thus a candidate for a "sub-filament," channeling material onto the central massive filament, in the André et al. (2014) model.

6.2.2.2. Orion A OMC-3

OMC-3 is considerably less massive than OMC-1, and so the dynamics of the region are less gravity-dominated (e.g., Salji et al., 2015). Matthews et al. (2001b) observed several independent vectors over the width of the filament with JCMT/SCUPOL, finding that the magnetic field geometry is consistent with a toroidal field wrapping the filament along most of its length. These observations are shown in **Figure 9**. Houde et al. (2004) (CSO/Hertz, 350μm) observed similar magnetic field geometries in OMC-3, but instead interpreted the magnetic field as perpendicular to the local filament direction. They also found that the average polarization direction remains approximately constant relative to a fixed position on the sky along the OMC-3

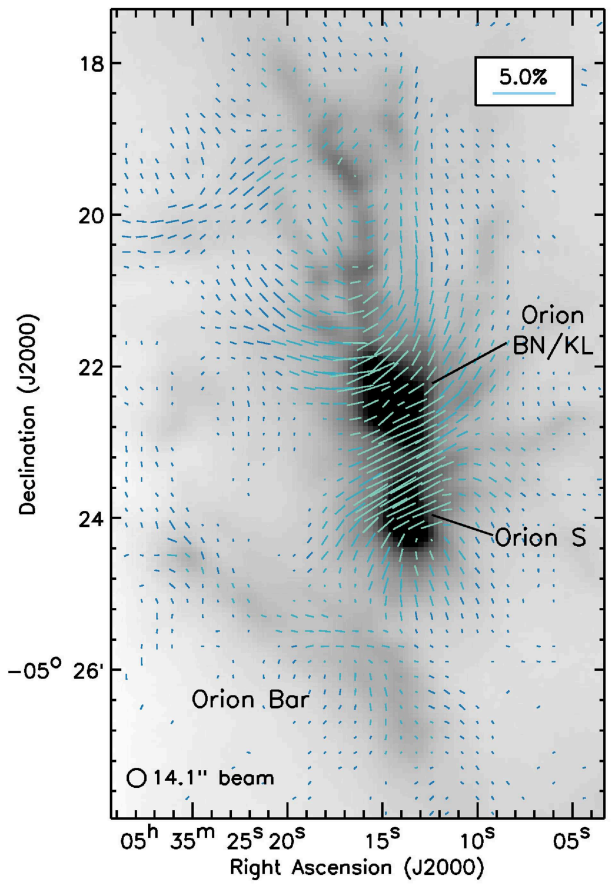

FIGURE 8 | The magnetic field morphology in OMC 1; Figure 1 from Pattle et al. (2017) © AAS. Reproduced with permission. Figure shows JCMT/POL-2 850 μm polarization vectors, rotated to trace magnetic field direction, overlaid on a SCUBA-2 850 μm emission image. Note "hourglass" magnetic field morphology, centered on the interaction between the Orion BN/KL and S clumps.

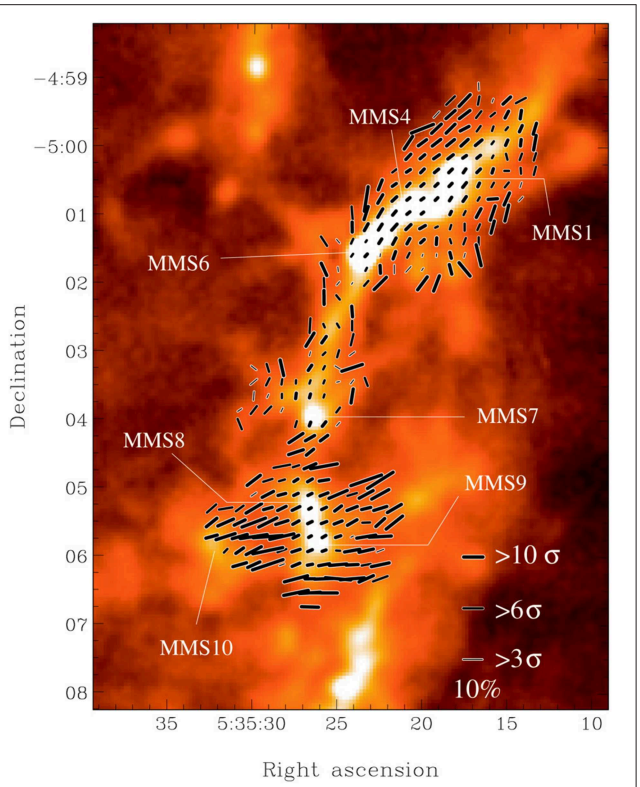

FIGURE 9 | The 850 μm polarization geometry in OMC 3; Figure 2 from Matthews et al. (2001b) © AAS. Reproduced with permission. JCMT/SCUPOL 850 μm polarization vectors (note: not rotated), overlaid on SCUBA 850 μm intensity map. Note significant change in polarization direction along the length of the filament.

filament, rather than changing direction as the filament does, suggesting that the magnetic field is relatively unaffected by gravitational effects in the filament.

Matthews et al. (2001b) discuss the significant depolarization seen toward the filament axis at 850μm, which could be due to decreasing grain alignment. However, they measure $\log p \propto -0.65 \log I$, which they note suggests grains are quite well-aligned at high densities, and that the observed depolarization is also consistent with predictions for a helical field. Matthews et al. (2001b) found no difference in behavior between regions of the filament with cores and those without, although the cores themselves are not well-resolved. Interferometric follow-up (Matthews et al., 2005) suggests that the field in the embedded cores is broadly aligned with the field in the larger filament.

Observations of OMC-3 provide a case study in the care which must be taken in the interpretation of polarized emission from objects that contain resolvable structure at many densities, in order to determine which structures the observed polarized emission is tracing. This is an issue on all size scales discussed in this work, but is particularly relevant to observations of filaments, in which the magnetic field properties may be expected to differ between the low-density envelope, the dense filament, and any embedded cores into which the dense filament has fragmented.

Figure 10 (Li et al., in prep.) shows CSO/SHARP 350 μm (unpublished data) and JCMT/SCUPOL 850μm observations of the OMC 3 region. Polarized intensity is shown in grayscale, with contours of total intensity overlaid. The JCMT/SCUPOL polarized intensity data show clear peaks associated with peaks in total intensity, whereas the shorter-wavelength CSO/SHARP data show no such correlation, with significant polarized intensity, but no clear peaks in emission. This suggests that the longer-wavelength JCMT/SCUPOL data are tracing the denser parts of the filament, while the CSO/SHARP data are tracing the filament envelope.

For optically thin emission, polarization observations not tracing the densest structure is likely to be due to grain misalignment at high densities (e.g., Jones et al., 2015), and a reasonable test of the densities traced by polarized emission is whether polarized intensity is correlated with total intensity. Where such a correlation exists, polarized emission can be expected to trace the full column of material. **Figure 10** can thus be interpreted as showing that in the dense parts of the filament, the larger, colder dust grains (which emit more of their light

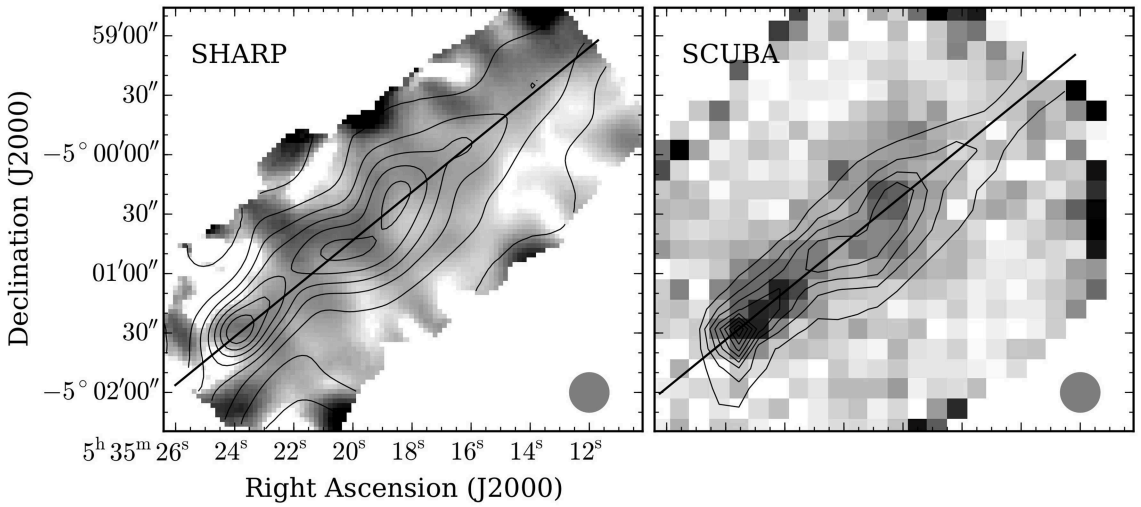

FIGURE 10 | CSO/SHARP 350 μm **(Left)** and JCMT/SCUPOL 850 μm **(Right)** observations of OMC 3 (Li et al., in prep.). Grayscale shows polarized intensity. Contours show total intensity, starting from 20% of peak intensity, and increasing in increments of 10%.

at longer wavelengths; e.g., Ossenkopf and Henning, 1994) are better aligned with the magnetic field than the smaller, warmer grains. In the RAT paradigm of grain alignment, the extinction of short-wavelength photons would prevent the alignment of small grains at high densities (e.g., Andersson et al., 2015). Thus the 350 μm data traces the magnetic field in the envelope surrounding the filament, while the 850 μm data traces the dense material of the filament itself. This may not be the case in all filaments, as the densities traced at a given wavelength will depend on grain properties, temperature and interstellar radiation field (ISRF). An additional caveat is that the difference in the chop throws of the SHARC-II and SCUBA cameras on detectable size scales has not been fully explored (see Fissel et al. (2016) for a discussion of the effect of background subtraction on polarization observations). Although this source provides an illustrative example only, consideration of such correlations is likely to be of general use.

6.2.2.3. Orion A OMC-2

Houde et al. (2004), using CSO/Hertz, found that the magnetic field in the north of OMC-2 agrees with that in OMC-3, but changes abruptly in the south of the region. Houde et al. (2004) tentatively associate this change with outflow activity in the vicinity of the source OMC-2 FIR 3. However, Poidevin et al. (2010), observing with JCMT/SCUPOL, did not find a correlation between outflow direction and magnetic field direction. Poidevin et al. (2010) found that OMC-2 is more weakly polarized than OMC-3, with a steeper decrease of p with I, a less well-ordered magnetic field, and higher levels of turbulence. Poidevin et al. (2010) argue that while magnetism dominates over turbulence in OMC-3, this is not clearly the case in OMC-2.

6.2.2.4. Orion A OMC-4

Houde et al. (2004) observed a small number of vectors in the OMC-4 region, finding a field orientation not clearly related either to that of the larger integral filament or to the geometry of the OMC-4 region itself.

OMC 1–4 are all contiguous parts of the integral filament (e.g., Bally, 2008). The magnetic field apparently having a different geometry and dynamic importance in different parts of the filament—with OMC-1 gravitationally-dominated, OMC-2 turbulence-dominated, and OMC-3 magnetically-dominated—suggests that the behavior of magnetic fields within filaments, and the evolution of the filaments themselves, depends strongly on local as well as large-scale environment.

6.2.2.5. Orion B

Matthews et al. (2002) observed the NGC 2071 and LBS 23N cores (discussed in section 7) and the NGC 2024 filament in Orion B at 850μm using JCMT/SCUPOL. NGC 2024 shows an ordered polarization geometry, consistent with a toroidal field threading the filament. They alternatively model the field toward NGC 2024 as resulting from the sweeping up of dense, magnetized gas by a foreground HII region (see also section 4.5), with the filament itself unmagnetized, but conclude through qualitative comparison with models that a helical field geometry within the filament is more consistent with observations. BIMA follow-up of NGC2024 shows that the small-scale field in the embedded cores generally matches that of the filament (Lai et al., 2002), supporting this interpretation.

6.3. Future Directions

In order to further our understanding of the magnetic field geometry within filaments, it is necessary to break the degeneracy between depolarization due to geometrical effects and that due to grain (mis)alignment at high densities. This requires observations with sufficient sensitivity and resolution to observe good radial profiles of polarization fraction and polarized intensity across filaments, as well as detailed predictions of polarization fraction as a function of radius for the various

proposed field geometries. Multi-wavelength observations can be used to investigate dust properties and the depth into filaments traced by magnetic fields, thus allowing some quantification of the reliability of polarization fraction as a tracer of field geometry.

7. POLARIZATION OBSERVATIONS OF STARLESS AND PROTOSTELLAR CORES

We here define starless cores to be small-scale overdensities within larger molecular clouds which, if gravitationally bound, will form an individual star or system of stars (Benson and Myers, 1989). Prestellar cores are the gravitationally bound subset of starless cores (Ward-Thompson et al., 1994). Protostellar cores are defined as envelope-dominated sources containing one to a few hydrostatic objects (i.e., Class 0 and I sources; Lada, 1987; Andre et al., 1993).

Detections of starless and protostellar cores in polarized light have until recently been piecemeal, and strongly limited by surface brightness. It is now becoming possible to systematically survey nearby star-forming regions to map magnetic fields in starless and protostellar cores. Total-power instruments remain the best tools for detecting starless cores, while protostellar cores are now more commonly observed with interferometers.

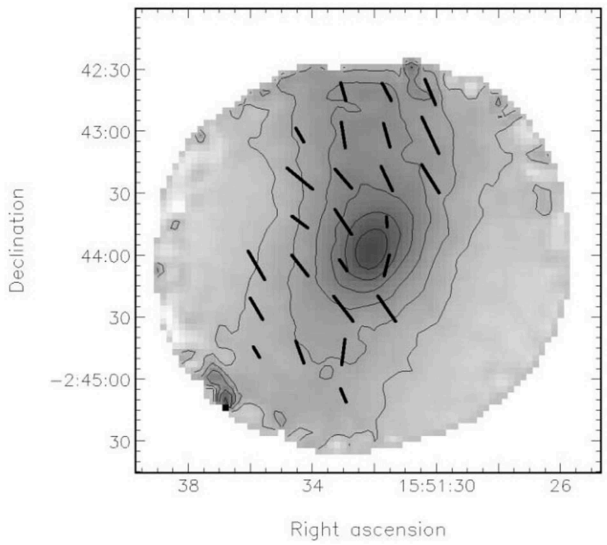

FIGURE 11 | JCMT/SCUPOL 850 μm magnetic field vectors (polarization vectors rotated by 90°), overlaid on 850 μm total intensity emission, in the starless core L183. Figure 1 from Crutcher et al. (2004) © AAS. Reproduced with permission. Note the ordered field structure across the core, and the lack of an hourglass-like field morphology. (Co-ordinates are B1950.0).

7.1. Starless Cores

The number of instruments with both the sensitivity and resolution required to detect polarized emission from starless cores remains very limited. Starless cores are extended objects with simple internal geometries, typically well-modeled by Bonnor-Ebert (Ebert, 1955; Bonnor, 1956) or Plummer-like (Plummer, 1911) distributions (e.g., Alves et al., 2001; Whitworth and Ward-Thompson, 2001), making observations with a total power component essential, as interferometers typically resolve out starless cores entirely.

Due to their small size and low surface brightness, imaging of individual starless and prestellar cores is largely restricted to the most local star-forming regions. The first detection of polarized submillimeter emission from three dense starless cores was reported by Ward-Thompson et al. (2000), who observed L1544 (140 pc; Elias, 1978), L183 (180 pc; Ward-Thompson et al., 2000) and L43 (150 pc; Ward-Thompson et al., 2000) at 850μm using JCMT/SCUPOL. Crutcher et al. (2004) used the DCF method to estimate magnetic field strengths for the same sources, finding $B_{pos} = 140\,\mu$G, 80 μG and 160 μG in L1544, L183, and L43, respectively, and that the three cores were, after correction for geometrical bias, approximately magnetically critical.

Kirk et al. (2006) observed two less-dense starless cores, L1498 and L1517B (both 140 pc), with JCMT/SCUPOL, estimating plane-of-sky field strengths of $10 \pm 7\,\mu$G and $30 \pm 10\,\mu$G respectively, again using the DCF method. The former value is comparable to a line-of-sight Zeeman measurement of the same region ($48 \pm 31\,\mu$G; Levin et al., 2001). In these cores, thermal support was found to dominate over non-thermal and magnetic support, with the cores being magnetically supercritical (unable to be supported by their internal magnetic fields alone).

Magnetic fields detected in isolated starless cores are typically relatively smooth and well-ordered, with detectable polarization across the cores. An example of such a field, in the starless core L183, is shown in **Figure 11**. Ward-Thompson et al. (2000) found that magnetic fields over the central core regions are typically aligned at $\sim 30°$ to the projected minor axis of the cores, a result ascribed to projection effects by Basu (2000). Notably, despite their ordered field morphologies, and despite being candidates for gravitational instability (e.g., Kirk et al., 2006), none of these cores show the classical "hourglass" magnetic field characteristic of ambipolar-diffusion-driven collapse. The precise role of the magnetic field in the evolution of these isolated cores is not clear. However, the magnetic field does not appear to be dynamically negligible, particularly in the denser set of cores.

The full set of observations made with JCMT/SCUPOL are cataloged by Matthews et al. (2009). This includes the five starless cores described above and L1287, observed by Curran and Chrysostomou (2007), listed as starless by Matthews et al. (2009), but with an associated energetic outflow (Curran and Chrysostomou, 2007). The JCMT/SCUPOL archive also contains observations of several nearby star-forming regions within which individual cores can be resolved, particularly the L1688 region in Ophiuchus: Oph A (Tamura, 1999), Oph B2 (Matthews et al., 2001a), and Oph C (Matthews et al., 2009).

Alves et al. (2014) observed the starless core Pipe-109 with APEX/PolKa, finding a highly-ordered magnetic field with significant depolarization at high column densities (note also Alves et al., 2015).

Observations made using CSO/Hertz are cataloged by Dotson et al. (2010). This catalog contains no isolated starless cores, but

includes the Oph A clump, containing a number of embedded starless cores.

A number of regions containing starless cores have been observed by the JCMT/POL-2 polarimeter, with significantly better sensitivity than was possible with its predecessor, SCUPOL. The Oph A and B clumps have been observed by Kwon et al. (2018) and Soam et al. (2018), respectively, as part of the BISTRO survey (Ward-Thompson et al., 2017). The $\sim$ 1800 AU linear resolution of these observations permits insight into the magnetic field morphology in the many starless and protostellar cores within the clumps (cf. Motte et al., 1998; Pattle et al., 2015). Kwon et al. (2018) measure field strengths varying from $0.2 - 5$ mG across Oph A, suggesting that the magnetic field is unlikely to be dynamically negligible anywhere in the region, but may vary significantly within it. Soam et al. (2018), observing the Oph B1 and B2 clumps, infer a typical magnetic field strength in Oph B2 of $630 \pm 410\,\mu$G, again suggesting that the magnetic fields in the cores in the region will not be negligible.

Discussion of these observations of well-resolved clumps has largely focussed on the properties of the clumps themselves, rather than individual embedded cores, in part due to limitations in sensitivity, but also due to uncertainties as to whether polarized emission from clumps and filaments traces the dense, star-forming gas or the larger- (clump/filament-)scale material (see discussion in section 6). Oph A has recently been observed in the far-infrared with the SOFIA/HAWC+ polarimeter (Harper et al., 2018; Santos et al., in prep.). These observations are shown alongside the JCMT/POL-2 polarization map of the region in **Figure 12**. Forthcoming polarization spectra across the 1–1,000 μm wavelength regime will provide additional insight into grain physics in regions such as Oph A, as discussed in section 2.

7.2. The Search for High-Mass Prestellar Cores

The debate over the existence of high-mass prestellar cores (with masses several times their Jeans mass, collapsing to form a massive star; e.g., Tan et al., 2014) continues. If such objects exist, they are likely to require significant internal magnetic support (e.g., Pillai et al., 2015). Pillai et al. (2015) analyse JCMT/SCUPOL observations of G11.11-0.12, positing that the source is a magnetically supported high-mass starless core. Due to the distance of most high-mass star-forming regions, most detections of high-mass star-forming "cores" are interferometric, for example, polarimetric observations of high-mass cores in DR21 (Ching et al., 2017), and in W51 (Tang et al., 2013) taken using the SMA. Single-dish data provide context for these observations, by mapping the larger-scale magnetic field in the surrounding material (e.g., Dotson et al., 2000; Chrysostomou et al., 2002; Vallée and Fiege, 2006).

7.3. Protostellar Cores

Protostellar cores differ from starless cores in that they have an internal heating source, and potentially an internal source of ionizing photons. These cores are thus generally warmer and brighter than their starless counterparts, and may be expected to contain dust grains better aligned with their internal magnetic fields (Jones et al., 2016).

Thanks to the presence of embedded sources and complex internal gas and dust structures (discs, accretion flows, etc.), protostellar cores make excellent targets for interferometric polarimetry. Much of the focus of polarimetric studies of protostellar cores has shifted to interferometric measurement—such as imaging of hourglass magnetic fields in NGC 1333A using the SMA (Girart et al., 2006), large-scale surveys such as TADPOL with CARMA (Hull et al., 2014), and high-resolution imaging of complex magnetic field geometries around protostars with ALMA (Hull et al., 2017). We summarize single-dish observations of protostellar sources to date here.

Models of magnetic fields in protostellar environments generally predict a symmetric field about the outflow axis of the system, with net polarization aligned either along the direction of the outflow, or with the plane of the disc (e.g., Greaves et al., 1997). Early observations of the magnetic fields in the envelopes of young protostars were largely made using the Aberdeen/QMW polarimeter on the UKT14 camera on the JCMT (Minchin et al., 1995; Tamura et al., 1995; Holland et al., 1996; Greaves et al., 1997). Tamura et al. (1995) and Minchin et al. (1995) found magnetic fields perpendicular to the major axes of protostellar envelopes and aligned with large-scale molecular outflows, whereas Holland et al. (1996) found that in the prototypical Class 0 source VLA 1623, the magnetic field is perpendicular to the outflow, and so suggested that the outflow cannot be magnetically collimated on large scales. Greaves et al. (1997) found that for Class 0 sources with outflows aligned in or near the plane of the sky, the magnetic field is typically perpendicular to the outflow, whereas for outflows aligned close to the line of sight, the magnetic field is parallel to the outflow direction, a bimodality in behavior common to a number of models of the magnetic field structure of protostellar envelopes. Greaves et al. (1997) also found polarization fraction to be anticorrelated with outflow opening angle and with ratio of bolometric luminosity to 1.3 mm luminosity (both proxies for age), leading them to suggest that magnetic fields are more ordered in younger protostellar sources.

JCMT/SCUPOL observed a larger set of protostars and clumps containing embedded protostars, most of which were first published by Matthews et al. (2009). A number of protostellar sources have been observed using CSO/SHARP: NGC 1333 IRAS 4 (Attard et al., 2009), the Class 0 protostars B335, L1527, and IC348-SMM2 (Davidson et al., 2011), DG Tau (T Tauri) (Krejny et al., 2011), and the Class 0 protostar L1157-mm (Stephens et al., 2013). Of these Attard et al. (2009) and Stephens et al. (2013) found the magnetic field to be broadly aligned with outflow direction, while Davidson et al. (2011) found magnetic field vectors consistent with a pinched magnetic field geometry in the protostellar discs of B335 and IC348-MM2 (indicative of magnetized disc formation), while in L1527 they propose that the outflow is sufficiently energetic to have disordered the magnetic field. Chapman et al. (2013) stacked observations of seven protostellar cores observed with CSO/SHARP, and found a positive correlation between the magnetic field direction and the symmetry axis of the (stacked) core, as well as between the field and outflow directions. Chapman et al. (2013) also present some

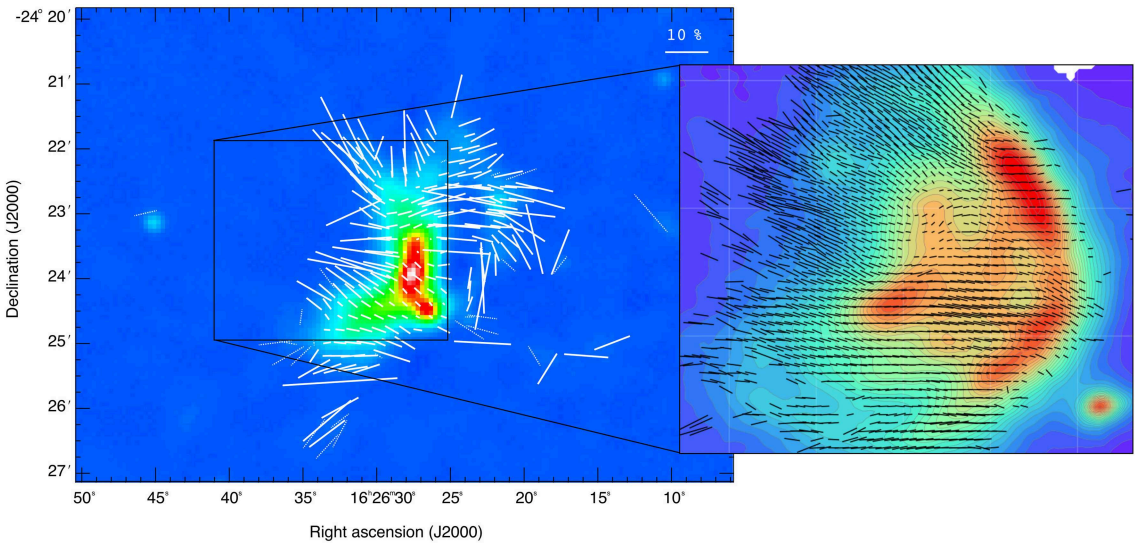

FIGURE 12 | The magnetic field structure of the Oph A region, containing a number of starless and protostellar cores. Magnetic field vectors (polarization vectors rotated by 90°) shown were observed with JCMT/POL-2 (left, 850 μm; Kwon et al., 2018 © AAS, reproduced with permission) and SOFIA/HAWC+ (right, 214μm; Harper et al., 2018; Santos et al. in prep.; reproduced with permission of the HAWC+ team).

evidence for a pinch in the stacked magnetic field, consistent with magnetically-dominated evolution.

Single-dish polarimetric observations of clumps containing protostellar cores include observations of the Oph A region, discussed above. Other observations include the Orion B NGC 2071 and LBS 23N clumps (Matthews et al., 2002). NGC 2071 is a massive core forming multiple protostars, showing a uniform magnetic field geometry oriented perpendicular to the most powerful outflow in the region, with a DCF-inferred field strength of 56 μG. LBS 23N, however, shows a more disordered field geometry and significant depolarization toward its various starless and protostellar cores. Matthews and Wilson (2002b) observed the lower-mass Barnard 1 clump in Perseus, which again contains both protostellar and starless cores. An ordered polarization pattern is seen across the clump, with significant depolarization toward the dense cores. These observations of clumps containing starless and protostellar cores do not show significant differences in polarization fraction or $\log p - \log I$ index between starless and protostellar cores, on scales observed by the JCMT.

7.4. Comparison With Simulations

Few direct comparisons have been made between observations and simulations of magnetic fields in starless cores, in part due to the paucity of observations. Most comparison between models and observations has been to numerical and (semi-)analytic models of ambipolar-diffusion-driven core collapse (e.g., Mouschovias, 1976a,b; Ciolek and Mouschovias, 1994; Basu, 2000; Ciolek and Basu, 2000).

MHD modeling of star-forming cores began with Machida et al. (2004) and subsequent papers, which focussed on cores harboring protostars. Subsequent work includes, e.g., Dib et al. (2007) (clumps/cores), Price and Bate (2007) (protostellar environments), Boss and Keiser (2013) (protostellar environments and discs). These simulations have generally focussed on the time evolution of core collapse rather than on producing synthetic observations. Mocz et al. (2017) produce volume-weighted magnetic field maps for collapsing cores in a turbulent medium which, while presented at resolutions observable by interferometric instruments, could be smoothed to be comparable to maps of cores produced by single-dish instrumentation.

Radiative transfer modeling allows forward modeling of the magnetic fields observed in star-forming cores, using tools such as DustPol (Padovani et al., 2012) and POLARIS (Reissl et al., 2016) to produce magnetic field maps for model cores, to be compared to observations. Alternatively, modeling of observed field geometries can be treated as a highly degenerate inversion problem. POLCAT (Franzmann and Fiege, 2017) produces simulated polarization maps based on models of three-dimensional cores threaded by magnetic fields, in order to eliminate core and field geometries not consistent with the magnetic field observed in projection.

7.5. Depolarization

As discussed in section 3.6, the alignment of grains with magnetic fields is, in the absence of a source of energetic photons, expected to get progressively worse at increasing A_V. In the extreme case of a deeply embedded starless/prestellar core, it is not clear whether dust grains are coupled to the magnetic field (Jones et al., 2015).

Polarization holes—decreased polarization fraction at increased total intensity (typically a tracer of density in cold cores)—are seen in observations of starless cores (Ward-Thompson et al., 2000; Alves et al., 2014), of cores with very young hydrostatic sources (Kwon et al., 2018, observing the core SM1, which may contain an extremely young Class 0 source;

Friesen et al., 2014), and in single-dish observations of sources with embedded protostars (Wolf et al., 2003; Jones et al., 2016).

Jones et al. (2016) present CSO/SHARP total power data alongside CARMA interferometric imaging of an IRDC with an embedded massive protostar. The total power data, tracing larger size scales in the IRDC, show a steeper negative slope in the $\log p$-$\log I$ relation than the interferometric data tracing the material around the embedded source. This is interpreted as evidence that although dust grains in the IRDC are in general not aligned with the magnetic field at high densities, photon flux from the young protostar is driving grain alignment in its vicinity.

The extent to which polarization holes results from grain misalignment, or from complex field morphologies on scales smaller than the beam, is not clear. The facts that starless cores and protostellar cores show similar behaviors on large scales (e.g., Matthews and Wilson, 2002b), that $\log p$-$\log I$ indices vary within and between clouds (Matthews and Wilson, 2002a; Matthews et al., 2002), and that ordered fields are consistently seen in starless cores despite depolarization (e.g., Kirk et al., 2006), suggest that better modeling of 3D magnetic field geometries is required in order to determine the depth into starless cores to which single-dish polarization observations can trace. Such modeling is becoming possible through application of tools such as POLARIS, as described above (e.g., Valdivia et al., 2017).

7.6. Future Directions and the Potential of Large Surveys

There are many open questions in the field of polarimetry of starless and protostellar cores, not least as to the circumstances in which it can be said with confidence that the magnetic field in the densest, gravitationally unstable, parts of cores has been observed. The new generation of polarimetric surveys will allow us to begin addressing these questions in a systematic manner, by allowing comparison of meaningful numbers of starless, protostellar, embedded and isolated sources. Wide-area surveys also allow the possibility of stacking polarization fraction and polarized intensity images to improve signal-to-noise and so to determine something of the magnetic field properties in low-surface-brightness starless cores.

8. SUMMARY

In this chapter we have discussed submillimeter and far-infrared single dish continuum emission polarimetric observations of magnetic fields in star-forming regions. We discussed strategies for measuring polarized dust emission, and reviewed past, present and upcoming polarimeters.

We then summarized the most widely-used methods for estimating the strength and dynamic importance of magnetic fields in molecular clouds, as well as the means by which the depth into clouds to which polarization observations trace can be assessed. We compared the various implementations of the (Davis-)Chandrasekhar-Fermi (DCF) method of estimating magnetic field strength. Compilation of DCF measurements shows that the DCF method typically produces magnetic field strength values comparable to those measured directly from Zeeman splitting of spectral lines, for a given density. There is considerable variation in DCF results, with differences in results between different DCF implementations typically comparable to or greater than measurement uncertainty. We note the importance of testing DCF and other experimental methods against synthetic observations in order to determine their validity and accuracy.

Our ability to study magnetic fields on molecular cloud scales has been revolutionized by all-sky observations from the *Planck* satellite, as well as cloud-scale maps from BLASTPol and SPARO. These observations indicate that the energetic importance of magnetic fields on > 1 pc scales are typically equal to or larger than that of turbulent gas motions, and that magnetic fields appear to play an important role in the formation of dense cloud substructures. Observations of more clouds at higher resolution are needed to better constrain the role played by magnetic fields in all stages of molecular cloud formation and evolution.

Observations of Bok globules typically show ordered, linear, magnetic fields with field strengths $\sim 10^2$ μG. Most Bok globules show significant depolarization at high densities. In Bok globules harboring outflow-driving sources, the magnetic field may in some cases be aligned with the outflow direction. Being by definition isolated objects, generally with simple geometries, Bok globules are a useful environment in which to study magnetic fields.

As magnetic fields tend to be perpendicular to self-gravitating filaments in the low-density environment surrounding the filaments, some models predict that material is accreted onto such filaments along these magnetic field lines—a theory with some observational support in nearby filaments such as Taurus and Musca. However, the three-dimensional magnetic field geometry within such star-forming filaments is not well-characterized. Magnetic fields are expected to either wrap helically around filaments or to pass directly through them. In order to distinguish between these alternatives, and to break degeneracies between three-dimensional geometry and grain misalignment, well-resolved observations across filaments are required, ideally at more than one wavelength. Care needs to be taken to ensure that polarization observations trace the dense material of filaments, rather than the low-density envelope. The role of magnetic fields within filaments is likely to vary significantly with environment: for example, the well-studied integral filament in Orion A shows gravitationally-dominated, turbulence-dominated and magnetically-dominated behavior at various points along its length.

Observations of magnetic fields within starless cores remain strongly limited by surface brightness. Where detectable, magnetic fields in isolated starless cores are typically relatively smooth and well-ordered, with polarization detected across the cores, although depolarization toward high densities is seen. While observations of magnetic fields in starless cores do not clearly show the "hourglass" morphology predicted for magnetically-dominated, ambipolar-diffusion-driven star

formation, the ordered polarization patterns seen suggest that magnetic fields are of some dynamic importance in these objects. The depth into starless cores to which grains are aligned with the magnetic field remains uncertain. Magnetic fields in protostellar cores are more easily detectable, and generally seen to be ordered and, on the scales observable with single-dish instrumentation, aligned either parallel or perpendicular to outflow direction.

There remain many unanswered questions about the three-dimensional geometry, strength, dynamic importance, and physical role of magnetic fields in star-forming regions. The current and forthcoming generation of submillimeter polarimeters will expand significantly our measurements of magnetic fields; this, coupled with detailed comparison to models, should allow these questions to be addressed.

AUTHOR CONTRIBUTIONS

KP led the writing of sections 1, 3, 5, 6, and 7. LF led the writing of sections 2 and 4. Both authors contributed equally to section 8. Both authors read, commented on, contributed to and edited each others' sections.

FUNDING

KP acknowledges support from the Ministry of Science and Technology, Taiwan (Grant No. 106-2119-M-007-021-MY3). LF is a Jansky Fellow of the National Radio Astronomy Observatory (NRAO). NRAO is a facility of the National Science Foundation (NSF, operated under cooperative agreement by Associated Universities, Inc.).

REFERENCES

Adam, R., Adane, A., Ade, P. A. R., André, P., Andrianasolo, A., Aussel, H., et al. (2018). The NIKA2 large-field-of-view millimetre continuum camera for the 30 m IRAM telescope. *Astron. Astrophys*. 609:A115. doi: 10.1051/0004-6361/201731503

Alves, F. O., Frau, P., Girart, J. M., Franco, G. A. P., Santos, F. P., and Wiesemeyer, H. (2014). On the radiation driven alignment of dust grains: detection of the polarization hole in a starless core. *Astron. Astrophys.* 569:L1. doi: 10.1051/0004-6361/201424678

Alves, F. O., Frau, P., Girart, J. M., Franco, G. A. P., Santos, F. P., and Wiesemeyer, H. (2015). On the radiation driven alignment of dust grains: detection of the polarization hole in a starless core (Corrigendum). *Astron. Astrophys.* 574:C4. doi: 10.1051/0004-6361/201424678e

Alves, J. F., Lada, C. J., and Lada, E. A. (2001). Internal structure of a cold dark molecular cloud inferred from the extinction of background starlight. *Nature* 409, 159–161. doi: 10.1038/35051509

Andersson, B.-G., Lazarian, A., and Vaillancourt, J. E. (2015). Interstellar dust grain alignment. *Annu. Rev. Astron. Astrophys.* 53, 501–539. doi: 10.1146/annurev-astro-082214-122414

André, P., Di Francesco, J., Ward-Thompson, D., Inutsuka, S.-I., Pudritz, R. E., and Pineda, J. E. (2014). "From filamentary networks to dense cores in molecular clouds: toward a new paradigm for star formation," in *Protostars and Planets VI*, eds B. Klessen and D. Henning (Tucson: University of Arizona Press), 27–51.

Andre, P., Ward-Thompson, D., and Barsony, M. (1993). Submillimeter continuum observations of Rho Ophiuchi A - The candidate protostar VLA 1623 and prestellar clumps. *Astrophys. J.* 406, 122–141. doi: 10.1086/172425

Attard, M., Houde, M., Novak, G., Li, H.-B., Vaillancourt, J. E., Dowell, C. D., et al. (2009). Magnetic fields and infall motions in NGC 1333 IRAS 4. *Astrophys. J.* 702, 1584–1592. doi: 10.1088/0004-637X/702/2/1584

Austermann, J. E., Beall, J. A., Bryan, S. A., Dober, B., Gao, J., Hilton, G., et al. (2018). Millimeter-wave polarimeters using kinetic inductance detectors for TolTEC and beyond. *J. Low Temp. Phys.* 193, 120–127. doi: 10.1007/s10909-018-1949-5

Bally, J. (2008). "Overview of the Orion complex," in *Handbook of Star Forming Regions, Volume I*, ASP Monograph Series. ed B. Reipurth (San Francisco, CA: Astronomical Society of the Pacific Monograph Publications), 459.

Barvainis, R., Clemens, D. P., and Leach, R. (1988). Polarimetry at 1.3 MM using MILLIPOL - Methods and preliminary results for Orion. *Astron. J.* 95, 510–515. doi: 10.1086/114650

Bastien, P., Bissonnette, E., Simon, A., Coudé, S., Ade, P., Savini, G., et al. (2011). "POL-2: the SCUBA-2 polarimeter," in *Astronomical Polarimetry 2008: Science from Small to Large Telescopes*, volume 449 of *Astronomical Society of the Pacific Conference Series*, eds P. Bastien, N. Manset, D. P. Clemens, and N. St-Louis (San Francisco, CA: Astronomical Society of the Pacific Conference Series), 68.

Bastien, P., Jenness, T., and Molnar, J. (2005). "A polarimeter for SCUBA-2," in *Astronomical Polarimetry: Current Status and Future Directions*, volume 343 of *Astronomical Society of the Pacific Conference Series*, eds A. Adamson, C. Aspin, C. Davis, and T. Fujiyoshi (San Francisco, CA: Astronomical Society of the Pacific Conference Series), 69.

Basu, S. (2000). Magnetic fields and the triaxiality of molecular cloud cores. *Astrophys. J. Lett.* 540, L103–L106. doi: 10.1086/312885

Benson, P. J., and Myers, P. C. (1989). A survey for dense cores in dark clouds. *Astrophys. J. Suppl.* 71, 89–108. doi: 10.1086/191365

Bok, B. J., and Reilly, E. F. (1947). Small dark nebulae. *Astrophys. J.* 105:255. doi: 10.1086/144901

Bonnor, W. B. (1956). Boyle's Law and gravitational instability. *Month. Notices RAS* 116:351. doi: 10.1093/mnras/116.3.351

Boss, A. P., and Keiser, S. A. (2013). Collapse and fragmentation of magnetic molecular cloud cores with the Enzo AMR MHD Code. I. Uniform density spheres. *Astrophys. J.* 764:136. doi: 10.1088/0004-637X/764/2/136

Brauer, R., Wolf, S., and Reissl, S. (2016). On the origins of polarization holes in Bok globules. *Astron. Astrophys.* 588:A129. doi: 10.1051/0004-6361/201527546

Bryan, S., Austermann, J., Ferrusca, D., Mauskopf, P., McMahon, J., Montana, A., et al. (2018). Optical design of the TolTEC millimeter-wave camera. *ArXiv e-prints*. doi: 10.1117/12.2314130

Burge, C. A., Van Loo, S., Falle, S. A. E. G., and Hartquist, T. W. (2016). Ambipolar diffusion regulated collapse of filaments threaded by perpendicular magnetic fields. *Astron. Astrophys.* 596:A28. doi: 10.1051/0004-6361/201629039

Cashman, L. R., and Clemens, D. P. (2014). The magnetic field of cloud 3 in L204. *Astrophys. J.* 793:126. doi: 10.1088/0004-637X/793/2/126

Chandrasekhar, S., and Fermi, E. (1953). Magnetic fields in spiral arms. *Astrophys. J.* 118:113. doi: 10.1086/145731

Chapman, N. L., Davidson, J. A., Goldsmith, P. F., Houde, M., Kwon, W., Li, Z.-Y., et al. (2013). Alignment between flattened protostellar infall envelopes and ambient magnetic fields. *Astrophys. J.* 770:151. doi: 10.1088/0004-637X/770/2/151

Chapman, N. L., Goldsmith, P. F., Pineda, J. L., Clemens, D. P., Li, D., and Krčo, M. (2011). The magnetic field in Taurus probed by infrared polarization. *Astrophys. J.* 741:21. doi: 10.1088/0004-637X/741/1/21

Chen, C.-Y., King, P. K., and Li, Z.-Y. (2016). "Change of magnetic field-gas alignment at the gravity-driven Alfvénic transition in molecular clouds: implications for dust polarization observations. *Astrophys. J.* 829:84. doi: 10.3847/0004-637X/829/2/84

Ching, T.-C., Lai, S.-P., Zhang, Q., Girart, J. M., Qiu, K., and Liu, H. B. (2017). Magnetic fields in the massive dense cores of the DR21 filament: weakly magnetized cores in a strongly magnetized filament. *Astrophys. J.* 838:121. doi: 10.3847/1538-4357/aa65cc

Cho, J., and Yoo, H. (2016). A technique for constraining the driving scale of turbulence and a modified chandrasekhar-fermi method. *Astrophys. J.* 821:21. doi: 10.3847/0004-637X/821/1/21

Chrysostomou, A., Aitken, D. K., Jenness, T., Davis, C. J., Hough, J. H., Curran, R., et al. (2002). The magnetic field structure in W51A. *Astron. Astrophys.* 385, 1014–1021. doi: 10.1051/0004-6361:20020154

Ciolek, G. E., and Basu, S. (2000). Consistency of ambipolar diffusion models with infall in the L1544 protostellar core. *Astrophys. J.* 529, 925–931. doi: 10.1086/308293

Ciolek, G. E., and Mouschovias, T. C. (1994). Ambipolar diffusion, interstellar dust, and the formation of cloud cores and protostars. 3: typical axisymmetric solutions. *Astrophys. J.* 425, 142–160. doi: 10.1086/173971

Clemens, D. P., Leach, R. W., Barvainis, R., and Kane, B. D. (1990). Millipol, a millimeter/submillimeter wavelength polarimeter - Instrument, operation, and calibration. *Publ. ASP* 102, 1064–1076. doi: 10.1086/132735

Coppin, K. E. K., Greaves, J. S., Jenness, T., and Holland, W. S. (2000). Structure, star formation and magnetic fields in the OMC1 region. *Astron. Astrophys.* 356, 1031–1038. Available online at: http://aa.springer.de/bibs/0356003/2301031/small.htm

Cox, N. L. J., Arzoumanian, D., André, P., Rygl, K. L. J., Prusti, T., Men'shchikov, A., et al. (2016). Filamentary structure and magnetic field orientation in Musca. *Astron. Astrophys.* 590:A110. doi: 10.1051/0004-6361/201527068

Crutcher, R. M. (2012). Magnetic fields in molecular clouds. *Annu. Rev. Astron. Astrophys.* 50, 29–63. doi: 10.1146/annurev-astro-081811-125514

Crutcher, R. M., Nutter, D. J., Ward-Thompson, D., and Kirk, J. M. (2004). SCUBA polarization measurements of the magnetic field strengths in the L183, L1544, and L43 prestellar cores. *Astrophys. J.* 600, 279–285. doi: 10.1086/379705

Crutcher, R. M., Troland, T. H., Lazareff, B., and Kazes, I. (1996). CN zeeman observations of molecular cloud cores. *Astrophys. J.* 456:217. doi: 10.1086/176642

Crutcher, R. M., Wandelt, B., Heiles, C., Falgarone, E., and Troland, T. H. (2010). Magnetic fields in interstellar clouds from Zeeman observations: inference of total field strengths by Bayesian analysis. *Astrophys. J.* 725, 466–479. doi: 10.1088/0004-637X/725/1/466

Cudlip, W., Furniss, I., King, K. J., and Jennings, R. E. (1982). Far infrared polarimetry of W51A and M42. *Month. Notices RAS* 200, 1169–1173. doi: 10.1093/mnras/200.4.1169

Curran, R. L., and Chrysostomou, A. (2007). Magnetic fields in massive star-forming regions. *Month. Notices RAS* 382, 699–716. doi: 10.1111/j.1365-2966.2007.12399.x

Curran, R. L., Chrysostomou, A., Collett, J. L., Jenness, T., and Aitken, D. K. (2004). First polarimetry results of two candidate high-mass protostellar objects. *Astron. Astrophys.* 421, 195–202. doi: 10.1051/0004-6361:20034481

Davidson, J. A., Novak, G., Matthews, T. G., Matthews, B., Goldsmith, P. F., Chapman, N., et al. (2011). Magnetic field structure around low-mass Class 0 protostars: B335, L1527, and IC348-SMM2. *Astrophys. J.* 732:97. doi: 10.1088/0004-637X/732/2/97

Davis, C. J., Chrysostomou, A., Matthews, H. E., Jenness, T., and Ray, T. P. (2000). Submillimeter polarimetry of the protostellar outflow sources in Serpens with the Submillimeter Common-User Bolometer Array. *Astrophys. J. Lett.* 530, L115–L118. doi: 10.1086/312476

Davis, L. (1951). The strength of interstellar magnetic fields. *Phys. Rev.* 81, 890–891. doi: 10.1103/PhysRev.81.890.2

Davis, L. Jr., and Greenstein, J. L. (1951). The polarization of starlight by aligned dust grains. *Astrophys. J.* 114:206. doi: 10.1086/145464

Dib, S., Kim, J., Vázquez-Semadeni, E., Burkert, A., and Shadmehri, M. (2007). The virial balance of clumps and cores in molecular clouds. *Astrophys. J.* 661, 262–284. doi: 10.1086/513708

Dolginov, A. Z., and Mitrofanov, I. G. (1976). Orientation of cosmic dust grains. *Astrophys. Space Sci.* 43, 291–317. doi: 10.1007/BF00640010

Dotson, J. L., Davidson, J., Dowell, C. D., Schleuning, D. A., and Hildebrand, R. H. (2000). Far-infrared polarimetry of galactic clouds from the Kuiper Airborne Observatory. *Astrophys. J. Suppl.* 128, 335–370. doi: 10.1086/313384

Dotson, J. L., Novak, G., Renbarger, T., Pernic, D., and Sundwall, J. L. (1998). "SPARO: the submillimeter polarimeter for Antarctic remote observing," in *Advanced Technology MMW, Radio, and Terahertz Telescopes*, volume 3357 of *Proc. SPIE*, ed T. G. Phillips (Bellingham: SPIE (The International Society for Optics and Photonics)), 543–547.

Dotson, J. L., Vaillancourt, J. E., Kirby, L., Dowell, C. D., Hildebrand, R. H., and Davidson, J. A. (2010). 350 μm polarimetry from the Caltech Submillimeter Observatory. *Astrophys. J. Suppl.* 186, 406–426. doi: 10.1088/0067-0049/186/2/406

Dowell, C. D., HAWC+ Instrument Team, and HAWC+ Science Team (2018). "First Results on Interstellar Magnetic fields from the HAWC+ Instrument for SOFIA," *Americal Astronomical Society (AAS) Meeting Abstracts* Vol. 232, 103.05. Available online at: http://adsabs.harvard.edu/abs/2018AAS...23210305D

Dowell, C. D., Hildebrand, R. H., Schleuning, D. A., Vaillancourt, J. E., Dotson, J. L., Novak, G., et al. (1998). Submillimeter array polarimetry with Hertz. *Astrophys. J.* 504, 588–598. doi: 10.1086/306069

Dragovan, M. (1986). Submillimeter polarization in the Orion Nebula. *Astrophys. J.* 308, 270–280. doi: 10.1086/164498

Draine, B. T., and Weingartner, J. C. (1996). Radiative torques on interstellar grains. I. Superthermal spin-up. *Astrophys. J.* 470:551. doi: 10.1086/177887

Ebert, R. (1955). Über die Verdichtung von H I-Gebieten. Mit 5 Textabbildungen. *Zeitschrift Astrophysik* 37:217.

Elias, J. H. (1978). An infrared study of the Ophiuchus dark cloud. *Astrophys. J.* 224:453. doi: 10.1086/156393

Falceta-Gonçalves, D., Lazarian, A., and Kowal, G. (2008). Studies of regular and random magnetic fields in the ISM: statistics of polarization vectors and the Chandrasekhar-Fermi technique. *Astrophys. J.* 679, 537–551. doi: 10.1086/587479

Fiege, J. D., and Pudritz, R. E. (2000). Helical fields and filamentary molecular clouds - I. *Month. Notices RAS* 311, 85–104. doi: 10.1046/j.1365-8711.2000.03066.x

Fissel, L. M., Ade, P. A. R., Angilè, F. E., Ashton, P., Benton, S. J., Chen, C.-Y., et al. (2018). Relative alignment between the magnetic field and molecular gas structure in the Vela C giant molecular cloud using low and high density tracers. *ArXiv e-prints*. doi: 10.1088/0004-637X/797/1/27

Fissel, L. M., Ade, P. A. R., Angilè, F. E., Ashton, P., Benton, S. J., Devlin, M. J., et al. (2016). Balloon-borne submillimeter polarimetry of the Vela C molecular cloud: systematic dependence of polarization fraction on column density and local polarization-angle dispersion. *Astrophys. J.* 824:134. doi: 10.3847/0004-637X/824/2/134

Flett, A. M., and Murray, A. G. (1991). First results from a submillimetre polarimeter on the James Clerk Maxwell Telescope. *Month. Notices RAS* 249, 4P–6P. doi: 10.1093/mnras/249.1.4P

Foënard, G., Mangilli, A., Aumont, J., Hughes, A., Mot, B., Bernard, J., et al. (2018). PILOT balloon-borne experiment in-flight performance. *ArXiv e-prints*. Available online at: https://arxiv.org/abs/1804.05645

Franzmann, E. L., and Fiege, J. D. (2017). PolCat: modelling submillimetre polarization of molecular cloud cores using successive parametrized coordinate transformations. *Month. Notices RAS* 466, 4592–4613.

Friberg, P., Bastien, P., Berry, D., Savini, G., Graves, S. F., and Pattle, K. (2016). "POL-2: a polarimeter for the James-Clerk-Maxwell telescope," in *Millimeter, Submillimeter, and Far-Infrared Detectors and Instrumentation for Astronomy VIII*, volume 9914 of *Proc. SPIE*, ed H. Zmuidzidas (Bellingham: SPIE (The International Society for Optics and Photonics)), 991403.

Friesen, R. K., Di Francesco, J., Bourke, T. L., Caselli, P., Jørgensen, J. K., Pineda, J. E., et al. (2014). Revealing H_2D^+ depletion and compact structure in starless and protostellar cores with ALMA. *Astrophys. J.* 797:27.

Galitzki, N., Ade, P. A. R., Angilè, F. E., Ashton, P., Beall, J. A., Becker, D., et al. (2014a) The next generation BLAST experiment. *J. Astron. Instrument.* 3:1440001. doi: 10.1142/S2251171714400017

Galitzki, N., Ade, P. A. R., Angilè, F. E., Benton, S. J., Devlin, M. J., Dober, B., et al. (2014b). "The balloon-borne large aperture submillimeter telescope for polarimetry-BLASTPol: performance and results from the 2012 Antarctic flight," in *Ground-based and Airborne Telescopes V, volume 9145 of Proc. SPIE*, eds L. M. Stepp, R. Gilmozzi, and H. J. Hall (Bellingham: SPIE (The International Society for Optics and Photonics)), 91450R.

Gaspar Venancio, L. M., Doyle, D., Isaak, K., Onaka, T., Kaneda, H., Nakagawa, T., et al. (2017). "The SPICA telescope: design evolution and expected performance," in *Society of Photo-Optical Instrumentation Engineers (SPIE) Conference Series*, volume 10565 of *Society of Photo-Optical Instrumentation Engineers (SPIE) Conference Series* (Bellingham), 1056555.

Girart, J. M., Rao, R., and Marrone, D. P. (2006). Magnetic fields in the formation of sun-like stars. *Science* 313, 812–814. doi: 10.1126/science.1129093

Goldsmith, P. F., Heyer, M., Narayanan, G., Snell, R., Li, D., and Brunt, C. (2008). Large-scale structure of the molecular gas in Taurus revealed by

high linear dynamic range spectral line mapping. *Astrophys. J.* 680, 428–445. doi: 10.1086/587166

González-Casanova, D. F., and Lazarian, A. (2017). Velocity gradients as a tracer for magnetic fields. *Astrophys. J.* 835:41. doi: 10.3847/1538-4357/835/1/41

Greaves, J. S., Holland, W. S., Jenness, T., Chrysostomou, A., Berry, D. S., Murray, A. G., et al. (2003). A submillimetre imaging polarimeter at the James Clerk Maxwell Telescope. *Month. Notices RAS* 340, 353–361. doi: 10.1046/j.1365-8711.2003.06230.x

Greaves, J. S., Holland, W. S., and Ward-Thompson, D. (1997). Submillimeter polarimetry of class 0 protostars: constraints on magnetized outflow models. *Astrophys. J.* 480, 255–261. doi: 10.1086/303970

Güsten, R., Nyman, L. Å., Schilke, P., Menten, K., Cesarsky, C., and Booth, R. (2006). The Atacama Pathfinder EXperiment (APEX) - a new submillimeter facility for southern skies -. *Astron. Astrophys.* 454, L13–L16. doi: 10.1051/0004-6361:20065420

Harper, D. A., Runyan, M. C., Dowell, C. D., Wirth, C. J., Amato, M., Ames, T., et al. (2018). HAWC+, the far-infrared camera and polarimeter for SOFIA. *J. Astron. Instrum.* 7, 1840008–1025. doi: 10.1142/S2251171718400081

Heiles, C. (1996). The local direction and curvature of the galactic magnetic field derived from starlight polarization. *Astrophys. J.* 462:316. doi: 10.1086/177153

Heiles, C., and Robishaw, T. (2009). "Zeeman splitting in the diffuse interstellar medium-The Milky Way and beyond," in *Cosmic Magnetic Fields: From Planets, to Stars and Galaxies*, volume 259 of *IAU Symposium*, eds K. G. Strassmeier, A. G. Kosovichev, and J. E. Beckman (Cambridge, UK), 579–590.

Heitsch, F., Zweibel, E. G., Mac Low, M.-M., Li, P., and Norman, M. L. (2001). Magnetic field diagnostics based on far-infrared polarimetry: tests using numerical simulations. *Astrophys. J.* 561, 800–814. doi: 10.1086/323489

Henning, T., Wolf, S., Launhardt, R., and Waters, R. (2001). Measurements of the magnetic field geometry and strength in Bok globules. *Astrophys. J.* 561, 871–879. doi: 10.1086/323362

Hester, J. J., Scowen, P. A., Sankrit, R., Lauer, T. R., Ajhar, E. A., Baum, W. A., et al. (1996). Hubble space telescope WFPC2 imaging of M16: photoevaporation and emerging young stellar objects. *Astron. J.* 111:2349. doi: 10.1086/117968

Hildebrand, R. H., Davidson, J. A., Dotson, J. L., Dowell, C. D., Novak, G., and Vaillancourt, J. E. (2000). A primer on far-infrared polarimetry. *Publ. ASP* 112, 1215–1235. doi: 10.1086/316613

Hildebrand, R. H., Dragovan, M., and Novak, G. (1984). Detection of submillimeter polarization in the Orion nebula. *Astrophys. J. Lett.* 284, L51–L54. doi: 10.1086/184351

Hildebrand, R. H., Kirby, L., Dotson, J. L., Houde, M., and Vaillancourt, J. E. (2009). Dispersion of magnetic fields in molecular clouds. I. *Astrophys. J.* 696, 567–573. doi: 10.1088/0004-637X/696/1/567

Holland, W. S., Greaves, J. S., Ward-Thompson, D., and Andre, P. (1996). The magnetic field structure around protostars. Submillimetre polarimetry of VLA 1623 and S 106-IR/FIR. *Astron. Astrophys.* 309, 267–274.

Houde, M., Dowell, C. D., Hildebrand, R. H., Dotson, J. L., Vaillancourt, J. E., Phillips, T. G., et al. (2004). Tracing the magnetic field in Orion A. *Astrophys. J.* 604, 717–740. doi: 10.1086/382067

Houde, M., Vaillancourt, J. E., Hildebrand, R. H., Chitsazzadeh, S., and Kirby, L. (2009). Dispersion of magnetic fields in molecular clouds. II. *Astrophys. J.* 706, 1504–1516. doi: 10.1088/0004-637X/706/2/1504

Hull, C. L. H., Girart, J. M., Tychoniec, Ł., Rao, R., Cortés, P. C., Pokhrel, R., et al. (2017). ALMA observations of dust polarization and molecular line emission from the Class 0 protostellar source Serpens SMM1. *Astrophys. J.* 847:92. doi: 10.3847/1538-4357/aa7fe9

Hull, C. L. H., Plambeck, R. L., Kwon, W., Bower, G. C., Carpenter, J. M., Crutcher, R. M., et al. (2014). TADPOL: A 1.3 mm survey of dust polarization in star-forming cores and regions. *Astrophys. J. Suppl.* 213:13. doi: 10.1088/0067-0049/213/1/13

Hull, C. L. H., and Zhang, Q. (2019). Interferometric observations of magnetic fields in forming stars. *Front. Astron. Space Sci.* 6:3. doi: 10.3389/fspas.2019.00003

Jones, T. J., Bagley, M., Krejny, M., Andersson, B.-G., and Bastien, P. (2015). Grain alignment in starless cores. *Astron. J.* 149:31. doi: 10.1088/0004-6256/149/1/31

Jones, T. J., Gordon, M., Shenoy, D., Gehrz, R. D., Vaillancourt, J. E., and Krejny, M. (2016). SOFIA mid-infrared imaging and CSO submillimeter polarimetry observations of G034.43+00.24 MM1. *Astron. J.* 151:156. doi: 10.3847/0004-6256/151/6/156

Jow, D. L., Hill, R., Scott, D., Soler, J. D., Martin, P. G., Devlin, M. J., et al. (2018). An application of an optimal statistic for characterizing relative orientations. *Mon. Not. R. Astron. Soc.* 474, 1018–1027. doi: 10.1093/mnras/stx2736

Kirk, J. M., Ward-Thompson, D., and Crutcher, R. M. (2006). SCUBA polarization observations of the magnetic fields in the pre-stellar cores L1498 and L1517B. *Month. Notices RAS* 369, 1445–1450. doi: 10.1111/j.1365-2966.2006.10392.x

Klassen, M., Pudritz, R. E., and Kirk, H. (2017). Filamentary flow and magnetic geometry in evolving cluster-forming molecular cloud clumps. *Month. Notices RAS* 465, 2254–2276. doi: 10.1093/mnras/stw2889

Koch, P. M., Tang, Y.-W., and Ho, P. T. P. (2012a). Magnetic field strength maps for molecular clouds: a new method based on a polarization-intensity gradient relation. *Astrophys. J.* 747:79. doi: 10.1088/0004-637X/747/1/79

Koch, P. M., Tang, Y.-W., and Ho, P. T. P. (2012b). Quantifying the significance of the magnetic field from large-scale cloud to collapsing core: self-similarity, mass-to-flux ratio, and star formation efficiency. *Astrophys. J.* 747:80. doi: 10.1088/0004-637X/747/1/80

Koch, P. M., Tang, Y.-W., and Ho, P. T. P. (2013). Interpreting the role of the magnetic field from dust polarization maps. *Astrophys. J.* 775:77. doi: 10.1088/0004-637X/775/1/77

Krejny, M., Li, H., Matthews, T., Novak, G., Shinnaga, H., Vaillancourt, J., et al. (2011). "Submillimeter spectropolarimetry as a probe for grain growth in DG Tau," in *Astronomical Polarimetry 2008: Science from Small to Large Telescopes*, volume 449 of *Astronomical Society of the Pacific Conference Series*, eds P. Bastien, N. Manset, D. P. Clemens, and N. St-Louis (San Francisco, CA), 338.

Kusune, T., Sugitani, K., Nakamura, F., Watanabe, M., Tamura, M., Kwon, J., et al. (2016). Magnetic field of the Vela C molecular cloud. *Astrophys. J. Lett.* 830:L23. doi: 10.3847/2041-8205/830/2/L23

Kwon, J., Doi, Y., Tamura, M., Matsumura, M., Pattle, K., Berry, D., et al. (2018). A first look at BISTRO observations of the ρ Oph-A core. *Astrophys. J.* 859:4. doi: 10.3847/1538-4357/aabd82

Lada, C. J. (1987). "Star formation - From OB associations to protostars," in *Star Forming Regions, volume 115 of IAU Symposium*, eds M. Peimbert and J. Jugaku (Dordrecht), 1–17.

Lai, S.-P., Crutcher, R. M., Girart, J. M., and Rao, R. (2002). Interferometric mapping of magnetic fields in star-forming regions. II. NGC 2024 FIR 5. *Astrophys. J.* 566, 925–930. doi: 10.1086/338336

Lamarre, J.-M., Puget, J.-L., Ade, P. A. R., Bouchet, F., Guyot, G., Lange, A. E., et al. (2010). Planck pre-launch status: the HFI instrument, from specification to actual performance. *Astron. Astrophys.* 520:A9. doi: 10.1051/0004-6361/200912975

Launhardt, R., Nutter, D., Ward-Thompson, D., Bourke, T. L., Henning, T., Khanzadyan, T., et al. (2010). Looking into the hearts of Bok globules: millimeter and submillimeter continuum images of isolated star-forming cores. *Astrophys. J. Suppl.* 188, 139–177. doi: 10.1088/0067-0049/188/1/139

Lazarian, A., and Hoang, T. (2007). Radiative torques: analytical model and basic properties. *Month. Notices RAS* 378, 910–946. doi: 10.1111/j.1365-2966.2007.11817.x

Levin, S. M., Langer, W. D., Velusamy, T., Kuiper, T. B. H., and Crutcher, R. M. (2001). Measuring the magnetic field strength in L1498 with Zeeman-splitting observations of CCS. *Astrophys. J.* 555, 850–854. doi: 10.1086/321518

Li, H., Dowell, C. D., Kirby, L., Novak, G., and Vaillancourt, J. E. (2008). Design and initial performance of SHARP, a polarimeter for the SHARC-II camera at the Caltech Submillimeter Observatory. *Appl. Opt.* 47, 422–430. doi: 10.1364/AO.47.000422

Li, H., Griffin, G. S., Krejny, M., Novak, G., Loewenstein, R. F., Newcomb, M. G., et al. (2006). Results of SPARO 2003: mapping magnetic fields in giant molecular clouds. *Astrophys. J.* 648, 340–354. doi: 10.1086/505858

Li, H.-B., Dowell, C. D., Goodman, A., Hildebrand, R., and Novak, G. (2009). Anchoring magnetic field in turbulent molecular clouds. *Astrophys. J.* 704, 891–897. doi: 10.1088/0004-637X/704/2/891

Li, H.-B., and Henning, T. (2011). The alignment of molecular cloud magnetic fields with the spiral arms in M33. *Nature* 479, 499–501. doi: 10.1038/nature10551

Li, P. S., McKee, C. F., and Klein, R. I. (2015). Magnetized interstellar molecular clouds - I. Comparison between simulations and Zeeman observations. *Month. Notices RAS* 452, 2500–2527. doi: 10.1093/mnras/stv1437

Liu, T., Li, P. S., Juvela, M., Kim, K.-T., Evans, II, N. J., Di Francesco, J., et al. (2018). A holistic perspective on the dynamics of G035.39-00.33: the interplay between gas and magnetic fields. *Astrophys. J.* 859:151. doi: 10.3847/1538-4357/aac025

Machida, M. N., Tomisaka, K., and Matsumoto, T. (2004). First MHD simulation of collapse and fragmentation of magnetized molecular cloud cores. *Month. Notices RAS* 348, L1–L5. doi: 10.1111/j.1365-2966.2004.07402.x

Marsden, G., Ade, P. A. R., Bock, J. J., Chapin, E. L., Devlin, M. J., Dicker, S. R., et al. (2009). BLAST: resolving the cosmic submillimeter background. *Astrophys. J.* 707, 1729–1739. doi: 10.1088/0004-637X/707/2/1729

Matthews, B. C., Fiege, J. D., and Moriarty-Schieven, G. (2002). Magnetic fields in star-forming molecular clouds. III. Submillimeter polarimetry of intermediate-mass cores and filaments in Orion B. *Astrophys. J.* 569, 304–321. doi: 10.1086/339318

Matthews, B. C., Lai, S.-P., Crutcher, R. M., and Wilson, C. D. (2005). Multiscale magnetic fields in star-forming regions: interferometric polarimetry of the MMS 6 core of OMC-3. *Astrophys. J.* 626, 959–965. doi: 10.1086/430127

Matthews, B. C., McPhee, C. A., Fissel, L. M., and Curran, R. L. (2009). The legacy of SCUPOL: 850 μm imaging polarimetry from 1997 to 2005. *Astrophys. J. Suppl.* 182, 143–204. doi: 10.1088/0067-0049/182/1/143

Matthews, B. C., and Wilson, C. D. (2002a). Magnetic fields in star-forming molecular clouds. IV. Polarimetry of the filamentary NGC 2068 cloud in Orion B. *Astrophys. J.* 571, 356–365. doi: 10.1086/339915

Matthews, B. C., and Wilson, C. D. (2002b). Magnetic fields in star-forming molecular clouds. V. Submillimeter polarization of the Barnard 1 dark cloud. *Astrophys. J.* 574, 822–833. doi: 10.1086/341111

Matthews, B. C., Wilson, C. D., and Fiege, J. D. (2001a). "Magnetic fields in star-forming clouds: how can FIRST contribute?," in *The Promise of the Herschel Space Observatory*, volume 460 of *ESA Special Publication*, eds G. L. Pilbratt, J. Cernicharo, A. M. Heras, T. Prusti, and R. Harris (Noordwijk: ESA Publications), 463.

Matthews, B. C., Wilson, C. D., and Fiege, J. D. (2001b). Magnetic fields in star-forming molecular clouds. II. The depolarization effect in the OMC-3 filament of Orion A. *Astrophys. J.* 562, 400–423. doi: 10.1086/323375

Matthews, T. G., Ade, P. A. R., Angilè, F. E., Benton, S. J., Chapin, E. L., Chapman, N. L., et al. (2014). Lupus I observations from the 2010 flight of the balloon-borne large aperture submillimeter telescope for polarimetry. *Astrophys. J.* 784:116. doi: 10.1088/0004-637X/784/2/116

Mauskopf, P. D. (2018). Transition edge sensors and kinetic inductance detectors in astronomical instruments. *Publ. ASP* 130:082001.

Minchin, N. R., Sandell, G., and Murray, A. G. (1995). Submm polarimetric observations of NGC 1333 IRAS 4A and 4B: tracing the circumstellar magnetic field. *Astron. Astrophys.* 293, L61–L64.

Mocz, P., Burkhart, B., Hernquist, L., McKee, C. F., and Springel, V. (2017). Moving-mesh Simulations of Star-forming Cores in Magneto-gravo-turbulence. *Astrophys. J.* 838:40. doi: 10.3847/1538-4357/aa6475

Monsch, K., Pineda, J. E., Liu, H. B., Zucker, C., How-Huan Chen, H., Pattle, K., et al. (2018). Dense gas kinematics and a narrow filament in the Orion A OMC1 region using NH_3. *Astrophys. J.* 861:77. doi: 10.3847/1538-4357/aac8da

Motte, F., André, P., and Neri, R. (1998). The initial conditions of star formation in the rho Ophiuchi main cloud: wide-field millimeter continuum mapping. *Astron. Astrophys.* 336, 150–172.

Mouschovias, T. C. (1976a). Nonhomologous contraction and equilibria of self-gravitating, magnetic interstellar clouds embedded in an intercloud medium: star formation. I Formulation of the problem and method of solution. *Astrophys. J.* 206, 753–767. doi: 10.1086/154436

Mouschovias, T. C. (1976b). Nonhomologous contraction and equilibria of self-gravitating, magnetic interstellar clouds embedded in an intercloud medium: star formation. II - Results. *Astrophys. J.* 207, 141–158. doi: 10.1086/154478

Murray, A. G., Nartallo, R., Haynes, C. V., Gannaway, F., and Ade, P. A. R. (1997). "An imaging polarimeter for SCUBA," in *The Far Infrared and Submillimetre Universe.*, volume 401 of *ESA Special Publication*, ed A. Wilson (Noordwijk: ESA Publications), 405.

Myers, P. C., and Goodman, A. A. (1991). On the dispersion in direction of interstellar polarization. *Astrophys. J.* 373, 509–524. doi: 10.1086/170070

Nakamura, F., Hanawa, T., and Nakano, T. (1993). Fragmentation of filamentary molecular clouds with longitudinal and helical magnetic fields. *Publ. Astron. Soc. Japan* 45, 551–566.

Nakamura, F., and Li, Z.-Y. (2008). Magnetically regulated star formation in three dimensions: the case of the Taurus molecular cloud complex. *Astrophys. J.* 687, 354–375. doi: 10.1086/591641

Novak, G., Dotson, J. L., and Li, H. (2009). Dispersion of observed position angles of submillimeter polarization in molecular clouds. *Astrophys. J.* 695, 1362–1369. doi: 10.1088/0004-637X/695/2/1362

Novak, G., Gonatas, D. P., Hildebrand, R. H., and Platt, S. R. (1989). A 100-micron polarimeter for the Kuiper Airborne Observatory. *Publ. ASP* 101, 215–224. doi: 10.1086/132425

Ossenkopf, V., and Henning, T. (1994). Dust opacities for protostellar cores. *Astron. Astrophys.* 291, 943–959.

Ostriker, E. C., Stone, J. M., and Gammie, C. F. (2001). Density, velocity, and magnetic field structure in turbulent molecular cloud models. *Astrophys. J.* 546, 980–1005. doi: 10.1086/318290

Ostriker, J. (1964). The equilibrium of polytropic and isothermal cylinders. *Astrophys. J.* 140:1056. doi: 10.1086/148005

Otal, L. E. (2014). *The Optical System and the Astronomical Potential of A-MKID, a New Camera Using Microwave Kinetic Inductance Detector Technolog*. PhD thesis, University of Bonn.

Padoan, P., Goodman, A., Draine, B. T., Juvela, M., Nordlund, Å., and Rögnvaldsson, Ö. E. (2001). Theoretical models of polarized dust emission from protostellar cores. *Astrophys. J.* 559, 1005–1018. doi: 10.1086/322504

Padovani, M., Brinch, C., Girart, J. M., Jørgensen, J. K., Frau, P., Hennebelle, P., et al. (2012). Adaptable radiative transfer innovations for submillimetre telescopes (ARTIST). Dust polarisation module (DustPol). *Astron. Astrophys.* 543:A16. doi: 10.1051/0004-6361/201219028

Palmeirim, P., André, P., Kirk, J., Ward-Thompson, D., Arzoumanian, D., Könyves, V., et al. (2013). Herschel view of the Taurus B211/3 filament and striations: evidence of filamentary growth? *Astron. Astrophys.* 550:A38. doi: 10.1051/0004-6361/201220500

Panopoulou, G. V., Psaradaki, I., and Tassis, K. (2016). The magnetic field and dust filaments in the Polaris Flare. *Month. Notices RAS* 462, 1517–1529. doi: 10.1093/mnras/stw1678

Pattle, K., Ward-Thompson, D., Berry, D., Hatchell, J., Chen, H.-R., Pon, A., et al. (2017). The JCMT BISTRO survey: the magnetic field strength in the Orion A filament. *Astrophys. J.* 846:122. doi: 10.3847/1538-4357/aa80e5

Pattle, K., Ward-Thompson, D., Hasegawa, T., Bastien, P., Kwon, W., Lai, S.-P., et al. (2018). First observations of the magnetic field inside the Pillars of Creation: results from the BISTRO survey. *Astrophys. J. Lett.* 860:L6. doi: 10.3847/2041-8213/aac771

Pattle, K., Ward-Thompson, D., Kirk, J. M., White, G. J., Drabek-Maunder, E., Buckle, J., et al. (2015). The JCMT Gould Belt Survey: first results from the SCUBA-2 observations of the Ophiuchus molecular cloud and a virial analysis of its prestellar core population. *Month. Notices RAS* 450, 1094–1122. doi: 10.1093/mnras/stv376

Pillai, T., Kauffmann, J., Tan, J. C., Goldsmith, P. F., Carey, S. J., and Menten, K. M. (2015). Magnetic fields in high-mass infrared dark clouds. *Astrophys. J.* 799:74. doi: 10.1088/0004-637X/799/1/74

Pillai, T., Kauffmann, J., Wiesemeyer, H., and Menten, K. M. (2016). CN Zeeman and dust polarization in a high-mass cold clump. *Astron. Astrophys.* 591:A19. doi: 10.1051/0004-6361/201527803

Planck Collaboration Int. XIX (2015). Planck intermediate results. XIX. An overview of the polarized thermal emission from Galactic dust. *Astron. Astrophys.* 576:A104. doi: 10.1051/0004-6361/201424082

Planck Collaboration Int. XX (2015). Planck intermediate results. XX. Comparison of polarized thermal emission from Galactic dust with simulations of MHD turbulence. *Astron. Astrophys.* 576:A105. doi: 10.1051/0004-6361/201424086

Planck Collaboration Int. XXXIV (2016). Planck intermediate results. XXXIV. The magnetic field structure in the Rosette Nebula. *Astron. Astrophys. A&A* 586:A137. doi: 10.1051/0004-6361/201525616

Planck Collaboration Int. XXXV (2016). Planck intermediate results. XXXV. Probing the role of the magnetic field in the formation of structure in molecular clouds. *Astron. Astrophys. A&A* 586:A138. doi: 10.1051/0004-6361/201525896

Planck Collaboration VIII (2016). *Planck* 2015 results. VIII. High frequency instrument data processing: calibration and maps. *Astron. Astrophys. A&A* 594:A8. doi: 10.1051/0004-6361/201525820

Planck Collaboration, Ade, P. A. R., Aghanim, N., Alves, M. I. R., Arnaud, M., Arzoumanian, D., et al. (2016). Planck intermediate results. XXXIII. Signature of the magnetic field geometry of interstellar filaments in dust polarization maps. *Astron. Astrophys.* 586:A136. doi: 10.1051/0004-6361/201425305

Planck Collaboration, Aghanim, N., Akrami, Y., Alves, M. I. R., Ashdown, M., Aumont, J., et al. (2018). Planck 2018 results. XII. Galactic astrophysics using polarized dust emission. *ArXiv e-prints*.

Platt, S. R., Hildebrand, R. H., Pernic, R. J., Davidson, J. A., and Novak, G. (1991). 100-micron array polarimetry from the Kuiper Airborne Observatory - Instrumentation, techniques, and first results. *Publ. ASP* 103, 1193–1210.

Plummer, H. C. (1911). On the problem of distribution in globular star clusters. *Month. Notices RAS* 71, 460–470.

Poidevin, F., Bastien, P., and Jones, T. J. (2011). Multi-scale analysis of magnetic fields in filamentary molecular clouds in Orion A. *Astrophys. J.* 741:112. doi: 10.1088/0004-637X/741/2/112

Poidevin, F., Bastien, P., and Matthews, B. C. (2010). Magnetic field structures and turbulent components in the star-forming molecular clouds OMC-2 and OMC-3. *Astrophys. J.* 716, 893–906. doi: 10.1088/0004-637X/716/2/893

Poidevin, F., Falceta-Gonçalves, D., Kowal, G., de Gouveia Dal Pino, E., and Mário Magalhães, A. (2013). Magnetic field components analysis of the SCUPOL 850 μm polarization data catalog. *Astrophys. J.* 777:112. doi: 10.1088/0004-637X/777/2/112

Price, D. J., and Bate, M. R. (2007). The impact of magnetic fields on single and binary star formation. *Month. Notices RAS* 377, 77–90. doi: 10.1111/j.1365-2966.2007.11621.x

Rao, R., Crutcher, R. M., Plambeck, R. L., and Wright, M. C. H. (1998). High-resolution millimeter-wave mapping of linearly polarized dust emission: magnetic field structure in Orion. *Astrophys. J. Lett.* 502, L75–L78. doi: 10.1086/311485

Rathborne, J. M., Jackson, J. M., and Simon, R. (2006). Infrared dark clouds: precursors to star clusters. *Astrophys. J.* 641, 389–405. doi: 10.1086/500423

Reissl, S., Wolf, S., and Brauer, R. (2016). Radiative transfer with POLARIS. I. Analysis of magnetic fields through synthetic dust continuum polarization measurements. *Astron. Astrophys.* 593:A87. doi: 10.1051/0004-6361/201424930

Renbarger, T., Chuss, D. T., Dotson, J. L., Griffin, G. S., Hanna, J. L., Loewenstein, R. F., et al. (2004). Early results from SPARO: instrument characterization and polarimetry of NGC 6334. *Publ. ASP* 116, 415–424. doi: 10.1086/383623

Roelfsema, P. R., Shibai, H., Armus, L., Arrazola, D., Audard, M., Audley, M. D., et al. (2018). SPICA - a large cryogenic infrared space telescope unveiling the obscured Universe. *ArXiv e-prints*. doi: 10.1017/pasa.2018.15

Salji, C. J., Richer, J. S., Buckle, J. V., di Francesco, J., Hatchell, J., Hogerheijde, M., et al. (2015). The JCMT Gould Belt Survey: properties of star-forming filaments in Orion A North. *Month. Notices RAS* 449, 1782–1796. doi: 10.1093/mnras/stv369

Schleicher, D. R. G., and Stutz, A. (2018). Magnetic tension and instabilities in the Orion A integral-shaped filament. *Month. Notices RAS* 475, 121–127. doi: 10.1093/mnras/stx2975

Schleuning, D. A. (1998). Far-infrared and submillimeter polarization of OMC-1: evidence for magnetically regulated star formation. *Astrophys. J.* 493, 811–825. doi: 10.1086/305139

Schleuning, D. A., Dowell, C. D., Hildebrand, R. H., Platt, S. R., and Novak, G. (1997). HERTZ, a submillimeter polarimeter. *Publ. ASP* 109, 307–318. doi: 10.1086/133892

Seifried, D., Walch, S., Reissl, S., and Ibáñez-Mejía, J. C. (2019). SILCC-Zoom: polarisation and depolarisation in molecular clouds. *MNRAS*. 482, 2697–2716. doi: 10.1093/mnras/sty2831

Siringo, G., Kovács, A., Kreysa, E., Schuller, F., Weiss, A., Guesten, R., et al. (2012). "First results of the polarimeter for the Large APEX Bolometer Camera (LABOCA)," in *Millimeter, Submillimeter, and Far-Infrared Detectors and Instrumentation for Astronomy VI, volume 8452 of* Proc. SPIE, eds W. S. Holland and J. Zmuidzinas (Bellingham: SPIE (The International Society for Optics and Photonics)), 845206.

Soam, A., Pattle, K., Ward-Thompson, D., Lee, C. W., Sadavoy, S., Koch, P. M., et al. (2018). Magnetic fields towards Ophiuchus-B derived from SCUBA-2 polarization measurements. *ArXiv e-prints*. doi: 10.3847/1538-4357/aac4a6

Soler, J. D., Ade, P. A. R., Angilè, F. E., Ashton, P., Benton, S. J., Devlin, M. J., et al. (2017). The relation between the column density structures and the magnetic field orientation in the Vela C molecular complex. *Astron. Astrophys.* 603:A64. doi: 10.1051/0004-6361/201730608

Soler, J. D., Bracco, A., and Pon, A. (2018). The magnetic environment of the Orion-Eridanus superbubble as revealed by Planck. *Astron. Astrophys.* 609:L3. doi: 10.1051/0004-6361/201732203

Soler, J. D., and Hennebelle, P. (2017). What are we learning from the relative orientation between density structures and the magnetic field in molecular clouds? *Astron. Astrophys.* 607:A2. doi: 10.1051/0004-6361/201731049

Soler, J. D., Hennebelle, P., Martin, P. G., Miville-Deschênes, M.-A., Netterfield, C. B., and Fissel, L. M. (2013). An imprint of molecular cloud magnetization in the morphology of the dust polarized emission. *Astrophys. J.* 774:128. doi: 10.1088/0004-637X/774/2/128

Staguhn, J., Amatucci, E., Armus, L., Bradley, D., Carter, R., Chuss, D., et al. (2018). Origins space telescope: the far infrared imager and polarimeter FIP. *Proc. SPIE* 10698, 10698 – 10698 – 6. doi: 10.1117/12.2312626

Stephens, I. W., Looney, L. W., Kwon, W., Hull, C. L. H., Plambeck, R. L., Crutcher, R. M., et al. (2013). The magnetic field morphology of the class 0 protostar L1157-mm. *Astrophys. J. Lett.* 769:L15. doi: 10.1088/2041-8205/769/1/L15

Stodólkiewicz, J. S. (1963). On the gravitational instability of some magneto-hydrodynamical systems of astrophysical interest. Part III. *Acta Astron.* 13, 30–54.

Sugitani, K., Nakamura, F., Watanabe, M., Tamura, M., Nishiyama, S., Nagayama, T., et al. (2011). Near-infrared-imaging Polarimetry Toward Serpens South: revealing the Importance of the Magnetic Field. *Astrophys. J.* 734:63. doi: 10.1088/0004-637X/734/1/63

Sutin, B., Alvarez, M., Battaglia, N., Bock, J., Bonato, M., Borrill, J., et al. (2018). PICO - the probe of inflation and cosmic origins. *ArXiv e-prints*. doi: 10.1117/12.2311326

Tamura, M. (1999). "Submillimeter polarimetry of star forming regions: from cloud cores to circumstellar disks," in *Star Formation 1999*, ed T. Nakamoto (Nobeyama: Nobeyama Radio Observatory), 212–216.

Tamura, M., Hough, J. H., and Hayashi, S. S. (1995). 1 millimeter polarimetry of young stellar objects: low-mass protostars and T Tauri stars. *Astrophys. J.* 448:346. doi: 10.1086/175965

Tan, J. C., Beltrán, M. T., Caselli, P., Fontani, F., Fuente, A., Krumholz, M. R., et al. (2014). "Massive star formation," in *Protostars and Planets VI*, eds H. Beuther, R. Klessen, C. Dullemond, and T. Henning (Tucson: University of Arizona Press), 149–172. doi: 10.2458/azu_uapress_9780816531240-ch007

Tang, Y.-W., Ho, P. T. P., Koch, P. M., Guilloteau, S., and Dutrey, A. (2013). Dust continuum and polarization from envelope to cores in star formation: a case study in the W51 north region. *Astrophys. J.* 763:135. doi: 10.1088/0004-637X/763/2/135

Tassis, K., Dowell, C. D., Hildebrand, R. H., Kirby, L., and Vaillancourt, J. E. (2009). Statistical assessment of shapes and magnetic field orientations in molecular clouds through polarization observations. *Month. Notices RAS* 399, 1681–1693. doi: 10.1111/j.1365-2966.2009.15420.x

Tomisaka, K. (2014). Magnetohydrostatic equilibrium structure and mass of filamentary isothermal cloud threaded by lateral magnetic field. *Astrophys. J.* 785:24. doi: 10.1088/0004-637X/785/1/24

Tomisaka, K. (2015). Polarization structure of filamentary clouds. *Astrophys. J.* 807:47. doi: 10.1088/0004-637X/807/1/47

Valdivia, V., Maury, A., Hennebelle, P., Galametz, M., and Reissl, S. (2017). "Towards realistic predictions of mm/sub-mm polarized dust emission," in *Submm/mm/cm QUESO Workshop 2017 (QUESO2017)* (Garching), 30.

Vallée, J. P., and Bastien, P. (1999). Magnetism in interstellar nurseries at 760 microns. *Astrophys. J.* 526, 819–832. doi: 10.1086/308010

Vallée, J. P., Bastien, P., and Greaves, J. S. (2000). Highly polarized thermal dust emission in the Bok globule CB 068. *Astrophys. J.* 542, 352–358. doi: 10.1086/309531

Vallée, J. P., and Fiege, J. D. (2006). A cool filament crossing the warm protostar DR 21(OH): geometry, kinematics, magnetic vectors, and pressure balance. *Astrophys. J.* 636, 332–347. doi: 10.1086/497957

Vallée, J. P., and Fiege, J. D. (2007). OMC-1: a cool arching filament in a hot gaseous cavity: geometry, kinematics, magnetic vectors, and pressure balance. *Astron. J.* 133, 1012–1026. doi: 10.1086/511004

Vallée, J. P., Greaves, J. S., and Fiege, J. D. (2003). Magnetic structure of a dark Bok globule. *Astrophys. J.* 588, 910–917. doi: 10.1086/374309

Wang, J.-W., Lai, S.-P., Eswaraiah, C., Pattle, K., Di Francesco, J., Johnstone, D., et al. (2018). JCMT BISTRO survey: magnetic fields within the hub-filament structure in IC 5146. *arXiv e-prints*.

Ward-Thompson, D., Kirk, J. M., Crutcher, R. M., Greaves, J. S., Holland, W. S., and André, P. (2000). First observations of the magnetic field geometry in prestellar cores. *Astrophys. J. Lett.* 537, L135–L138. doi: 10.1086/312764

Ward-Thompson, D., Pattle, K., Bastien, P., Furuya, R. S., Kwon, W., Lai, S.-P., et al. (2017). First results from BISTRO – a SCUBA-2 polarimeter survey of the Gould Belt. *Astrophys. J.* 842:66. doi: 10.3847/1538-4357/aa70a0

Ward-Thompson, D., Scott, P. F., Hills, R. E., and Andre, P. (1994). A submillimetre continuum survey of pre protostellar cores. *Month. Notices RAS* 268:276. doi: 10.1093/mnras/268.1.276

Ward-Thompson, D., Sen, A. K., Kirk, J. M., and Nutter, D. (2009). Optical and submillimetre observations of Bok globules - tracing the magnetic field from low to high density. *Month. Notices RAS* 398, 394–400. doi: 10.1111/j.1365-2966.2009.15159.x

Wareing, C. J., Pittard, J. M., Falle, S. A. E. G., and Van Loo, S. (2016). Magnetohydrodynamical simulation of the formation of clumps and filaments in quiescent diffuse medium by thermal instability. *Month. Notices RAS* 459, 1803–1818. doi: 10.1093/mnras/stw581

Whittet, D. C. B., Hough, J. H., Lazarian, A., and Hoang, T. (2008). The efficiency of grain alignment in dense interstellar clouds: a reassessment of constraints from near-infrared polarization. *Astrophys. J.* 674, 304–315. doi: 10.1086/525040

Whitworth, A. P., and Ward-Thompson, D. (2001). An empirical model for protostellar collapse. *Astrophys. J.* 547, 317–322. doi: 10.1086/318373

Wiesemeyer, H., Hezareh, T., Kreysa, E., Weiss, A., Güsten, R., Menten, K. M., et al. (2014). Submillimeter polarimetry with PolKa, a reflection-type modulator for the APEX telescope. *Publ. ASP* 126:1027.

Wolf, S., Launhardt, R., and Henning, T. (2003). Magnetic field evolution in Bok globules. *Astrophys. J.* 592, 233–244. doi: 10.1086/375622

Wu, B., Tan, J. C., Nakamura, F., Van Loo, S., Christie, D., and Collins, D. (2017). GMC collisions as triggers of star formation. II. 3D turbulent, magnetized simulations. *Astrophys. J.* 835:137. doi: 10.3847/1538-4357/835/2/137

Young, K., Alvarez, M., Battaglia, N., Bock, J., Borrill, J., Chuss, D., et al. (2018). Optical design of PICO, a concept for a space mission to probe inflation and cosmic origins. *ArXiv e-prints*. doi: 10.1117/12.2309421

Yuen, K. H., and Lazarian, A. (2017). Tracing interstellar magnetic field using velocity gradient technique: application to atomic hydrogen data. *Astrophys. J. Lett.* 837:L24. doi: 10.3847/2041-8213/aa6255

Zweibel, E. G. (1990). Magnetic field-line tangling and polarization measurements in clumpy molecular gas. *Astrophys. J.* 362, 545–550. doi: 10.1086/169291

Conflict of Interest Statement: The authors declare that the research was conducted in the absence of any commercial or financial relationships that could be construed as a potential conflict of interest.

The reviewer TG declared a past co-authorship with one of the authors KP to the handling editor.

frontiers in Astronomy and Space Sciences

REVIEW
published: 05 March 2019
doi: 10.3389/fspas.2019.00003

Interferometric Observations of Magnetic Fields in Forming Stars

Charles L. H. Hull[1,2]* *and Qizhou Zhang*[3]

[1] National Astronomical Observatory of Japan, Santiago, Chile, [2] Joint ALMA Observatory, Santiago, Chile, [3] Harvard-Smithsonian Center for Astrophysics, Cambridge, MA, United States

The magnetic field is a key ingredient in the recipe of star formation. However, the importance of the magnetic field in the early stages of the formation of low- and high-mass stars is still far from certain. Over the past two decades, the millimeter and submillimeter interferometers BIMA, OVRO, CARMA, SMA, and most recently ALMA have made major strides in unveiling the role of the magnetic field in star formation at progressively smaller spatial scales; ALMA observations have recently achieved spatial resolutions of up to ∼100 and ∼1,000 au in nearby low- and high-mass star-forming regions, respectively. From the kiloparsec scale of molecular clouds down to the inner few hundred au immediately surrounding forming stars, the polarization at millimeter and submillimeter wavelengths is dominated by polarized thermal dust emission, where the dust grains are aligned relative to the magnetic field. Interferometric studies have focused on this dust polarization and occasionally on the polarization of spectral-line emission. We review the current state of the field of magnetized star formation, from the first BIMA results through the latest ALMA observations, in the context of several questions that continue to motivate the studies of high- and low-mass star formation. By aggregating and analyzing the results from individual studies, we come to several conclusions: (1) Magnetic fields and outflows from low-mass protostellar cores are randomly aligned, suggesting that the magnetic field at ∼1,000 au scales is not the dominant factor in setting the angular momentum of embedded disks and outflows. (2) Recent measurements of the thermal and dynamic properties in high-mass star-forming regions reveal small virial parameters, challenging the assumption of equilibrium star formation. However, we estimate that a magnetic field strength of a fraction of a mG to several mG in these objects could bring the dense gas close to a state of equilibrium. Finally, (3) We find that the small number of sources with hourglass-shaped magnetic field morphologies at 0.01–0.1 pc scales cannot be explained purely by projection effects, suggesting that while it does occur occasionally, magnetically dominated core collapse is not the predominant mode of low- or high-mass star formation.

Keywords: astronomy, low-mass star formation, high-mass star formation, polarization, magnetic fields, dust, interferometry, millimeter-wave observations

OPEN ACCESS

Edited by:
Ray S. Furuya,
Tokushima University, Japan

Reviewed by:
Keping Qiu,
Nanjing University, China
Aveek Sarkar,
Physical Research Laboratory, India

***Correspondence:**
Charles L. H. Hull
chat.hull@nao.ac.jp

Specialty section:
This article was submitted to Stellar and Solar Physics, a section of the journal Frontiers in Astronomy and Space Sciences

Received: *29 August 2018*
Accepted: *23 January 2019*
Published: *05 March 2019*

Citation:
Hull CLH and Zhang Q (2019) Interferometric Observations of Magnetic Fields in Forming Stars. Front. Astron. Space Sci. 6:3. doi: 10.3389/fspas.2019.00003

1. INTRODUCTION

Magnetic fields are known to play a critical role in many aspects of both low- and high-mass star formation. Even weakly ionized star-forming material is coupled to the ambient magnetic field, and thus the field can regulate (or prevent) the collapse and fragmentation of star-forming clouds (Hennebelle and Inutsuka, 2019; Krumholz and Federrath, 2019; Teyssier and Commerçon, 2019[1], in this volume), can influence the formation of protoplanetary disks (Wurster and Li, 2018, in this volume), and can launch bipolar outflows and jets from young protostars (Pudritz and Ray, 2019[2], in this volume). Mapping the morphology of magnetic fields in low- and high-mass star-forming regions is therefore critical to better understand how magnetic fields affect the star-formation process at early times, and how the role of the field changes relative to other dynamical effects (e.g., turbulence, rotation, thermal and radiation pressure, and gravitational collapse) as a function of spatial scale, source environment, and source mass. Over more than 50 years, studies of magnetic fields in low- and high-mass star-forming regions have been performed across a wide range of spatial scales, from the >100 pc scale of molecular clouds, to the 1 pc scale of clumps, to the 0.1 pc scale of dense cores, and finally to the 1,000–100 au scale of protostellar envelopes surrounding forming protostellar systems[3].

In this review we introduce the typical tracers of the magnetic field in star-forming regions, as well as the methods used to analyze the observations. We then discuss the state of the field of magnetized star formation, focusing primarily on the last three decades of high-resolution polarization studies by millimeter and submillimeter [hereafter combined into "(sub)millimeter"] interferometers including the Berkeley-Illinois-Maryland Association (BIMA) millimeter array, the Combined Array for Research in Millimeter-wave Astronomy (CARMA), the Submillimeter Array (SMA), and the Atacama Large Millimeter/submillimeter Array (ALMA)[4].

1.1. Magnetic Field Tracers (Plane-of-Sky Component)

1.1.1. Polarized Dust Emission

Polarized thermal emission from dust grains is the main tracer of the magnetic field in star-forming regions observed at high resolution and at (sub)millimeter wavelengths. Under most circumstances, oblong interstellar medium (ISM) dust grains with sizes $\ll 100\,\mu$m are aligned with their long axes perpendicular to magnetic field lines (e.g., Hildebrand, 1988). The currently accepted way to achieve this alignment is via the "radiative torque" (RAT) mechanism, where an anisotropic radiation field (e.g., the external UV field in the ISM, or the radiation from a deeply embedded protostar) causes grains to become aligned relative to the magnetic field (Lazarian, 2007; Hoang and Lazarian, 2009; Andersson et al., 2015)[5]. Thus, at the physical scales of star-forming clouds, cores, and envelopes (i.e., scales $\gtrsim 100$ au), magnetically aligned dust grains emit thermal radiation that is polarized perpendicular to the magnetic field. Observations of dust polarization, which comprise the vast majority of the single-dish and interferometric polarization observations to date, are discussed at length throughout this article.

1.1.2. Polarized Molecular-Line Emission

Polarization of molecular-line emission is another tracer of the magnetic field in star-forming regions. Molecular and atomic lines are sensitive to magnetic fields, which cause their spectral levels to split into magnetic sub-levels. For some molecules, linear polarization can arise when an anisotropy in the radiation and/or velocity field yields a population of magnetic sub-levels that are not in local thermodynamic equilibrium (LTE); this is known as the Goldreich-Kylafis (G-K) effect. Polarization from the G-K effect is most easily detected where the spectral line emission has an optical depth $\tau \approx 1$, when the ratio of the collision rate to the radiative transition rate (i.e., the spontaneous emission rate) is ~ 1, and where the gradient in the radiation and/or velocity field is large. The effect is strongest in the lowest rotational transitions of simple molecules such as CO, CS, HCN, SiO, or HCO^+. Spectral-line polarization from the G-K effect can be parallel or perpendicular to the magnetic field. Due to the different optical depths of the parallel and perpendicularly polarized components in different locations on the sky, polarization from the G-K effect ultimately traces the plane-of-sky magnetic field orientation with an ambiguity of 90° (Goldreich and Kylafis, 1981, 1982; Kylafis, 1983; Deguchi and Watson, 1984; Lis et al., 1988).

The first detections of the G-K effect were by Glenn et al. (1997), who presented National Radio Astronomy Observatory (NRAO) 12 m telescope observations of the evolved star IRC +10216, and by Greaves et al. (1999), who observed the galactic center and the high-mass star-forming clouds S140 and DR 21 using the James Clerk Maxwell Telescope (JCMT). In addition to these first observations, others have detected the G-K effect in molecular outflows from low-mass protostellar sources (e.g., Girart et al., 1999; Lai et al., 2002; Cortes et al., 2006; Lee et al., 2014, 2018a; Ching et al., 2016) as well as in high-mass protostellar sources (e.g., Lai et al., 2003; Cortes et al., 2005, 2008; Cortes and Crutcher, 2006). The G-K effect is a powerful way to trace the magnetic field in regions where the brightness of the

[1]Teyssier, R., and Commerçon, B. (2019). Numerical methods for simulating star formation. *Front. Astron. Space Sci.* under review.

[2]Pudritz, R. E., and Ray, T. P. (2019). The role of magnetic fields in protostellar outflows and star formation. *Front. Astron. Space Sci.* under review.

[3] In this review we follow the nomenclature used in Zhang et al. (2009) and Motte et al. (2018), who refer to a *cloud* as a structure 10–100 pc in size; a molecular *clump* as a structure 1 pc in size that forms massive stars along with a population of lower mass stars; and a *dense core* as a structure 0.01–0.1 pc in size that forms one or a group of stars. Following the nomenclature of, e.g., Hull et al. (2014), a protostellar *envelope* is a $\sim$1,000 au ($\sim$0.005 pc) structure comprising the densest part of the dense core, inside of which one or a few protostars form.

[4]Note that while we aim to provide an exhaustive review of the literature surrounding millimeter-wave interferometric observations of low- and high-mass stars, we mention only a few theoretical and single-dish polarization studies in order to support our narrative. We do not discuss other types of millimeter-wave polarization observations, i.e., toward the galactic center, quasars, or evolved stars.

[5]RATs that align grains with respect to the magnetic field B are sometimes known as "B-RATs," in contrast to other radiative torque mechanisms such as the "k-RATs" mentioned in section 5, where RATs align grains with respect to the radiation direction.

thermal dust emission is too low to detect polarization at the few-percent level, either because the source is too distant or because the column density of dust is too low (e.g., in an outflow cavity where the gas and dust have been driven away).

One way to resolve the 90° ambiguity in G-K observations is via radiative transfer modeling. This was done in Cortes et al. (2005), who expanded on the original G-K models (which assumed that gradients in the CO optical depth were responsible for the necessary anisotropy in the radiation field) by including bright, central sources as additional causes of anisotropy. They used these models to successfully reproduce the 90° difference in polarization angles seen toward the high-mass star-forming region DR 21(OH) in their 3 mm BIMA observations of CO ($J = 1 \rightarrow 0$) versus earlier 1.3 mm observations of CO ($J = 2 \rightarrow 1$) by Lai et al. (2003). While the modeling in Cortes et al. (2005) was successful, in general it is difficult to know the structure of the radiation field, especially in high-mass star-forming regions. Other methods exist to resolve the ambiguity, such as comparing polarization from both dust and spectral lines in the same region. This was done in DR 21(OH) by Lai et al. (2003) and Ching et al. (2016); however, it is not clear how strong the correlation should be between the polarization angles from the two types of emission, as the dust emission traces much denser material than the CO.

Looking to the future, in low-mass sources with well behaved outflows, or in protoplanetary disks, the radiation and velocity fields may be simple enough to allow us to more confidently break the ambiguity in polarization orientation. Given the high quality of ALMA data toward these types of sources and the fact that ALMA's sensitivity will allow us to probe polarization in multiple transitions of many different molecules, spectral-line polarization studies have a bright future.

Finally, one must exercise caution when interpreting polarized spectral-line observations, as linearly polarized spectral-line emission can be converted into circularly polarized emission via anisotropic resonant scattering. Several studies have detected non-Zeeman circularly polarized emission, including Houde et al. (2013) in Orion KL and Hezareh et al. (2013) in the supernova remnant SNR IC 443. These observations were from the polarimeters at the Caltech Submillimeter Observatory (CSO) and the Institut de Radioastronomie Millimétrique (IRAM) 30 m telescope, respectively (see Chamma et al., 2018 for more results from the SMA). The model described in those publications shows that resonant scattering can cause a rotation in the polarization position angle in maps of linear spectral-line polarization. Hezareh et al. (2013) used the detected Stokes V signal toward SNR IC 443 to correct the map of linear spectral-line polarization. After doing so, the polarization was well aligned with dust polarization observations using the PolKA polarimeter at the Atacama Pathfinder Experiment (APEX) telescope. The authors note that this effect is proportional to the square of the magnitude of the plane-of-sky magnetic field, which opens up the possibility of detecting the magnetic field via circular polarization observations of Zeeman-insensitive spectral lines.

1.1.3. The Velocity-Gradient Technique

Another method for probing the plane-of-sky magnetic field in star-forming regions is the "velocity-gradient technique" (VGT), which estimates the magnetic field orientation using the velocity gradients present in spectral-line observations. In turbulent regions that are not gravitationally bound, González-Casanova and Lazarian (2017) and Yuen and Lazarian (2017) showed that the magnetic field is expected to be oriented perpendicular to velocity gradients. The authors also extended their study to shocked and gravitationally bound regions (Yuen and Lazarian, under review), and argued that the VGT provides an even better view of the plane-of-sky magnetic field morphology in the interstellar medium (particularly in diffuse regions with a low column density of dust) than both the *Planck* polarization data (e.g., Planck Collaboration et al., 2015b) and observations of neutral HI "fibers," which also trace the interstellar magnetic field (Clark et al., 2014, 2015).

1.2. Magnetic Field Tracers (Line-of-Sight Component): The Zeeman Effect

The Zeeman effect is another important tracer of the magnetic field that has been observed primarily with single-dish radio telescopes to infer the line-of-sight magnetic field strength[6] in molecular clouds (Troland and Heiles, 1986; Crutcher et al., 1993; Crutcher, 1999). When threaded by a magnetic field, atomic hydrogen and molecules with a strong magnetic dipole moment will have the degeneracy in magnetic sub-levels lifted for states with non-zero angular momentum. This will split the radio frequency transitions into a number of linearly and elliptically polarized components separated slightly in frequency. Measuring this Zeeman splitting is the only way to directly measure a component of the magnetic field strength. However, we will not focus more on the thermal Zeeman effect in this review, as there are no reported observations with a (sub)millimeter-wavelength interferometer. For reviews of single-dish observations of magnetic fields in molecular clouds via the Zeeman effect, see Crutcher (2012) and Crutcher and Kemball (2019[7], in this volume).

1.3. Analysis Methods

1.3.1. Indirect Estimates of Magnetic Field Strength

The polarization arising from magnetically aligned dust grains and from the G-K effect yields the plane-of-sky magnetic field morphology. However, these observations do not contain information about the magnetic field strength. Since knowing the field strength is critical to our understanding of the importance of magnetic fields, a variety of indirect methods have thus been developed to estimate the field strength from these types of observations.

The most longstanding of these methods is the Davis-Chandrasekhar-Fermi (DCF) method (Davis, 1951; Chandrasekhar and Fermi, 1953), which uses the fact that turbulent motions should cause an observable scatter in what

[6]Note that under certain conditions one can derive the total magnetic field strength from the Zeeman effect (Heiles et al., 1993; Heiles and Crutcher, 2005). This has been seen several times toward galactic OH masers (Hutawarakorn et al., 2002; Fish and Reid, 2006; Caswell et al., 2014). However, in typical Zeeman observations of star-forming molecular clouds, the Zeeman signal is only strong enough to yield the strength of the magnetic field along the line of sight.

[7]Crutcher, R. M. and Kemball, A. J. (2019). Zeeman effect observations of regions of star formation. *Front. Astron. Space Sci.* under review.

would otherwise be a well ordered mean magnetic field. The original, simplest form of the DCF formula yields an estimate of the plane-of-sky magnetic field strength

$$B_{\rm POS} = \frac{\sqrt{4\pi\rho}}{\delta\phi}\delta V \ , \quad (1)$$

where ρ is the gas density, δV is the one-dimensional velocity dispersion, and $\delta\phi$ is the dispersion in polarization position angles. δV and $\delta\phi$ are both assumed to be caused by turbulent motions in the region being studied. The derivation of this expression also assumes that there is a mean magnetic field in the region, that the turbulence is incompressible and isotropic, and that the turbulent components of the kinetic and magnetic energies are in equipartition. Note that the DCF method also assumes that the dispersion is "small," i.e., that the turbulent magnetic energy is small compared with the mean-field magnetic energy in the system.

The DCF method was originally developed to estimate magnetic field strengths in the diffuse ISM, where perturbations in the magnetic field can be assumed to be caused by turbulent motions in the magnetized medium. Comparisons with MHD simulations of giant molecular clouds (GMCs) by Ostriker et al. (2001) found that at these scales, the original DCF method typically overestimates the magnetic field strength by a factor of ~ 2 because line-of-sight field tangling is not taken into account. Further simulations by Heitsch et al. (2001) also found that the true field strength is overestimated unless finite telescope resolution and self-gravity within the GMC are accounted for.

At the smaller scales of the individual star-forming clumps and cores that are probed by interferometers, gravity is almost always the dominant dynamical factor, and thus the structure of the background field must be removed before calculating the dispersion in polarization position angles. In two ideal cases with very clean examples of hourglass-shaped magnetic fields, Girart et al. (2006) and Qiu et al. (2014) removed the background hourglass field by subtracting a set of parabolic field lines from the data, after which they calculated the magnetic field dispersion relative to the background structure. In complicated cases, however, a more general method is necessary to remove arbitrary background field structure. This has been achieved by employing a second-order structure function of the polarization angle that allows the separation of the turbulent and mean magnetic-field components, with the underlying assumption that the mean-field component has an intrinsically larger spatial scale than the turbulent component (Falceta-Gonçalves et al., 2008; Hildebrand et al., 2009; Houde et al., 2009, 2011; Chitsazzadeh et al., 2012). Further refinements of these studies have also taken into account interferometric filtering effects (Houde et al., 2016).

Falceta-Gonçalves et al. (2008) used the structure-function approach to test the validity of the DCF technique using their MHD simulations. In addition to analyzing the effect of different telescope resolutions (their conclusion: lower-resolution observations tend to overestimate the field strength), they also derived a generalized form of the DCF equation, which allows for the separation of the turbulent and mean magnetic field components, and yielded magnetic-field estimates that were accurate to within $\sim$20%. More recently, Juárez et al. (2017) performed SMA observations of a magnetized high-mass star-forming region and used the structure-function method to compare the data with synthetic observations of gravity-dominated MHD simulations. They found the magnetic field strength estimates from both the observations and simulations to be in good agreement.

Koch et al. (2012) proposed another method of indirectly measuring the magnetic field strength that is also based on an ideal MHD framework. They argue that a position-dependent magnetic field strength in a polarization map can be calculated using the angle between the magnetic field and the gradient of the total-intensity emission, and a second angle between the local gravity direction and the gradient of the total-intensity emission. This is based on the assumption that the intensity gradient is a proxy for the direction of motion in the MHD force equation. For example, in a centrally concentrated, gravitationally bound core, the infalling motion will be along the intensity gradient (across the iso-intensity contours). This method requires observations of the magnetic-field morphology (i.e., via observations of thermal dust polarization or the G–K effect) in order to produce a spatial distribution of the magnetic field strength. However, unlike the DCF method, this method does not require spectral-line observations in the analysis. Estimations of magnetic field strengths using this method have been found to be consistent with previous estimations from the DCF method (see e.g., section 3.1).

1.3.2. The Mass-to-Flux Ratio

Merely measuring the magnetic field strength does not allow us to determine immediately the importance of the magnetic field in a given star-forming region. Therefore, in magnetic field studies it is common to compare the magnetic energy density with that of other dynamical quantities such as gravity, turbulence, and outflow feedback (see, e.g., Hull et al. 2017b for a comparison of magnetic energy with gravitational and outflow energy densities in the intermediate-mass Class 0 protostellar core Serpens SMM1).

Historically, there has been a strong focus on the comparison of gravity (which causes inward motion) and the magnetic field (whose tension provides resistance against infall across the field lines). The common quantity quoted as a metric for the importance of the magnetic field with respect to gravity is the "mass-to-flux ratio" M/Φ, where M is the mass of the object of interest and Φ is the flux of the magnetic field threading the object. As discussed in Crutcher (2004, and references therein), the maximum mass that can be supported by a given magnetic flux is given by $M_{\rm crit} = \Phi/2\pi\sqrt{G}$. However, it is more useful to discuss the dynamical status of an object by measuring the ratio λ of the observed mass-to-flux ratio to the critical mass-to-flux ratio:

$$\lambda = \frac{(M/\Phi)_{\rm obs}}{(M/\Phi)_{\rm crit}} \ . \quad (2)$$

Clouds that are supported by the magnetic field and are not collapsing are deemed "subcritical" ($\lambda < 1$), whereas those where gravity has overcome the resistance of the magnetic field are

referred to as "supercritical" ($\lambda > 1$). Crutcher (2012) analyzed data across a wide range of spatial scales that trace more than five orders of magnitude in densities, and found that when the hydrogen column density $N_H > 10^{21}\,\mathrm{cm}^{-2}$, all star-forming objects are supercritical (i.e., are collapsing). This value is less than the typical column densities of low-mass ($N_H \sim 10^{22} - 10^{23}\,\mathrm{cm}^{-2}$; e.g., Girart et al. 2006; Hull et al. 2017b) and high-mass ($N_H \sim 10^{23} - 10^{24}\,\mathrm{cm}^{-2}$; e.g., Girart et al. 2009) protostellar cores, and thus the types of objects we review in this article are all supercritical. This is reasonable, as most of them have already formed stars, as revealed by the presence of bipolar outflows. Furthermore, due to the sensitivity limits of CARMA and the SMA, most of the sources in previous interferometric surveys of polarization (Hull et al., 2014; Zhang et al., 2014) were chosen based on their strong millimeter flux, which correlates with the presence of embedded star formation.

1.4. Core-Mass Estimates From Dust Emission

In order to convert the observed millimeter-wave flux density S_ν contained within a given spatial area into a corresponding gas mass $M_{\rm gas}$, we can use the following relation:

$$M_{\rm gas} = \frac{S_\nu d^2}{\kappa_\nu B_\nu\,(T_d)}\ , \tag{3}$$

where d is the distance to the source, κ_ν is the opacity of the dust (Ossenkopf and Henning, 1994), and $B_\nu\,(T_d)$ is the Planck function at the frequency of the observations. T_d is the temperature of the dust, which is usually $\sim$20–50 K in a low-mass protostellar core (Girart et al., 2006), and as high as (or greater than) 100 K in a high-mass core (Girart et al., 2009). Once the dust mass is calculated, a gas-to-dust mass ratio of 100 is usually assumed in order to calculate the total (gas + dust) mass of the protostellar core. Note that such an estimate does not include the mass of the central star(s), which must be obtained by other means, e.g., via direct detection of a Keplerian disk around the source (e.g., Tobin et al., 2012; Ohashi et al., 2014) or via determination of the source's bolometric luminosity.

1.5. Motivating Questions in Low- and High-Mass Star Formation

The primary goal of observing the magnetic field at any spatial scale is to determine the importance (or lack thereof) of the magnetic field in the star-formation process. The steady progress toward this goal over the last two decades began with single-dish submillimeter polarization surveys probing $\gtrsim 20''$ scales using the Viper 2 m telescope at the South Pole (SPARO polarimeter, e.g., Dotson et al., 1998; Renbarger et al., 2004; Li et al., 2006), the JCMT (850 μm SCUBA polarimeter, e.g., Matthews et al. 2009), and the CSO (350 μm SHARP Li et al. 2008 and Hertz Dotson et al. 2010 polarimeters). A resurgence of single-dish studies has been brought about by results from the PolKa polarimeter at the APEX telescope (Siringo et al., 2004, 2012; Hezareh et al., 2013; Alves et al., 2014; Wiesemeyer et al., 2014), the BISTRO survey with the upgraded POL-2 polarimeter at the JCMT (e.g., Pattle et al., 2017, 2018; Ward-Thompson et al., 2017; Kwon J. et al., 2018; Soam et al., 2018), results from the polarimeter on the Balloon-borne Large Aperture Submillimeter Telescope (BLAST; Roy et al., 2011; Fissel et al., 2016; Gandilo et al., 2016), observations from the HAWC+ polarimeter (Vaillancourt et al., 2007) on the Stratospheric Observatory for Infrared Astronomy (SOFIA; e.g., Chuss et al., 2018; Gordon et al., 2018; Lopez-Rodriguez et al., 2018), and the galactic polarization maps from the *Planck* satellite (e.g., Planck Collaboration et al., 2015a,b,c, 2016a,b,c). These new studies will pave the way for future work with even more sensitive instruments such at the next-generation BLAST instrument (BLAST-TNG; Galitzki et al. 2014), the NIKA2 polarimeter at the IRAM 30 m telescope (Ritacco et al., 2017), and the TolTEC polarimeter at the Large Millimeter Telescope (LMT). For reviews on multi-scale/multi-wavelength studies and single-dish observations of magnetic fields, respectively, see Li and Law (2019)[8] and Pattle and Fissel (2019)[9], both in this volume.

There are a number of questions applicable to both low- and high-mass star formation that have been investigated using (sub)millimeter polarimetric observations. These include the (direct or indirect) measurements of the absolute magnetic field strength in star-forming material at different spatial scales, as well as the estimation of the dynamical importance of the magnetic field with respect to gravity (i.e., the mass-to-flux ratio; see section 1.3.2). Observations of magnetic fields across multiple spatial scales toward both low-mass (Li et al., 2009; Hull et al., 2014) and high-mass (Zhang et al., 2014; Li et al., 2015) protostellar sources have also been used to constrain the dynamical importance of the magnetic field based on the morphological consistency (or lack thereof) of the field as a function of scale. Generally, however, these observations have only compared two or three of the relevant spatial scales (i.e., 100 pc cloud scales, 1 pc clump scales, 0.1 pc dense-core scales, 1,000 au protostellar envelope scales, and 100 au disk scales). A full characterization of the magnetic field from galactic (*Planck*) scales down to scales approaching the 100 au size of protoplanetary disks has yet to be accomplished, but will be possible in the near future when upcoming polarization surveys of the full populations of protostars in entire molecular clouds are completed.

In the low-mass regime, single-dish observations probe the magnetic field in star-forming clouds at large scales, revealing the magnetic field from the scale of entire molecular clouds (*Planck*, BLAST) to the canonical, $\sim$0.1 pc dense core, where one or a few protostars will form (JCMT, CSO). One of the main benefits of single-dish studies is their ability to recover a larger range of spatial scales than interferometers, thus enabling an accurate characterization of the magnetic field in ambient cloud material. However, higher resolution is needed in order to probe the environments of individual stars; this is where results from the BIMA, CARMA, SMA, and ALMA interferometers dominate the discussion, allowing us to characterize the magnetic field from

[8]Li, H.-B., and Law, C. Y. (2019). Observing the impacts of magnetic fields on molecular clouds. *Front. Astron. Space Sci.* under review.

[9]Pattle, K., and Fissel, L. M. (2019). Submillimeter and far-infrared polarimetric observations of magnetic fields in star-forming regions. *Front. Astron. Space Sci.* under review.

scales of several × 1,000 au down to the scales of a few × 10 au accessible to ALMA[10]. The main questions that have been tackled over the last two decades using data from these interferometers include: **(1)** What is the importance of the magnetic field in regulating the collapse of star-forming cores? (section 2.1); **(2)** What is the relationship of bipolar outflows with the magnetic field? (section 2.2); and **(3)** What is the role of the magnetic field in the launching and collimation of bipolar outflows in low-mass protostars? (section 2.3).

Moving to the high-mass regime: high-mass stars ($M_* > 8\,M_\odot$) form predominantly in clustered environments where a population of stars are born with a range of stellar masses (Lada and Lada, 2003). These high-mass stellar populations form in dense cores that are embedded in parsec-scale, massive molecular clumps. This review will focus on several questions raised in recent studies of these high-mass sources, including **(4)** What is the dynamical role of magnetic fields in dense cores? (section 3.1); **(5)** What is the role of the magnetic field in the formation of disks and the launching of protostellar outflows in high-mass protostars? (section 3.2); **(6)** Do magnetic fields play a significant role in the fragmentation of molecular clumps and the formation of dense cores? (section 3.3); and **(7)** Does high-mass star formation proceed in virial equilibrium? (section 3.4).

The dense clustering nature of high-mass star formation implies considerable fragmentation within these massive molecular clumps, which distinguishes high-mass star formation from the more isolated process of low-mass star formation. High-mass regions also tend to have much more intense radiation environments, hosting HII regions whose radiative feedback and ionization can impact the ambient magnetic field. Another clear difference arises from the fact that the best-studied low-mass stars are forming at distances ∼10 × closer than typical high-mass star forming regions, allowing us to study the formation of individual low-mass protostellar systems and their associated outflows, jets, and disks in much greater detail than is possible in high-mass systems. Ultimately, however, studies of both low- and high-mass star formation use the same observing techniques and confront many of the same questions. In this review we focus on those questions that have been of the most interest to both communities in recent years.

2. MAGNETIC FIELDS IN LOW-MASS STAR FORMATION

The revolution of high-resolution, interferometric observations of polarization began with BIMA and the Owens Valley Radio Observatory (OVRO). These two sets of antennas were later combined into CARMA (Bock et al., 2006). Early observations with BIMA and OVRO[11] covered a wide range of topics, including polarization observations of dust, SiO, CO, and SiO masers toward iconic regions in Orion (Rao et al., 1998; Plambeck et al., 2003; Girart et al., 2004; Matthews et al., 2005) as well as observations of individual protostars (Girart et al., 1999; Cortes et al., 2006; Kwon et al., 2006). These first observations, combined with the extensive follow-up from CARMA, the SMA, ALMA form the body of work motivating this review. Below we put this work in the context of a narrative addressing several of the major open questions in the field of magnetized low-mass[12] star formation.

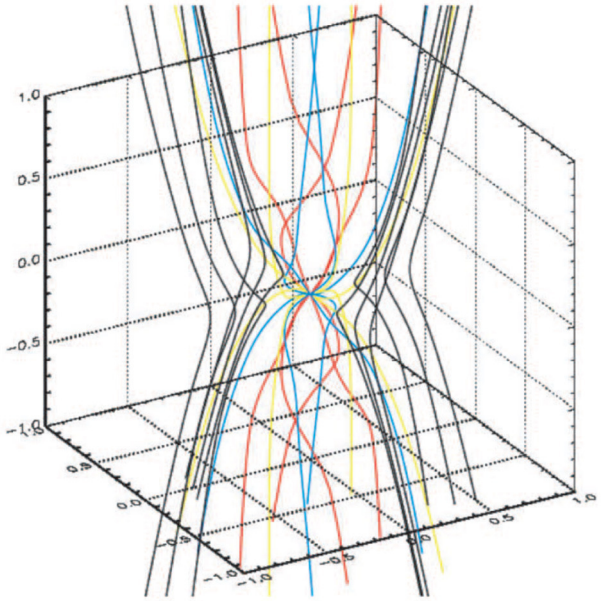

FIGURE 1 | A model from Allen et al. (2003) showing an hourglass-shaped magnetic field configuration in a collapsing, magnetized star-forming core. Reproduced with permission from the American Astronomical Society (AAS).

2.1. The Role of the Magnetic Field in Protostellar Collapse

In models of magnetically regulated protostellar collapse (e.g., Mouschovias, 1976a,b, 1991; Mouschovias and Ciolek, 1999), a strong, well ordered magnetic field provides outward pressure support of the infalling material. This is because the field is coupled (or "frozen") to the small fraction of charged particles in the weakly ionized gas. However, in non-turbulent models, the non-ideal MHD effect of ambipolar diffusion (Mestel and Spitzer, 1956) enables the neutral material (which comprises the bulk of the star-forming core) to slip slowly past the magnetic field lines,

[10]At the high resolutions achievable by ALMA, several studies have revealed polarization in well resolved maps of protoplanetary disks; however, it appears that in many cases the polarized emission is from dust scattering and not from magnetically aligned dust grains (see section 5).

[11]The two polarization results from OVRO are observations toward NGC 1333-IRAS 4A and IRAS 16293 (Akeson et al., 1996; Akeson and Carlstrom, 1997); however, OVRO was known to have issues with polarization calibration, which is the most likely explanation for the inconsistency of those results with later observations of the same sources (Girart et al., 1999, 2006, 2008; Rao et al., 2009).

[12]We do not treat the topic of intermediate-mass star formation separately in this review. As many of the characteristics of the early stages of intermediate- and low-mass star formation are thought to be similar (Beltrán, 2015), we include references to several intermediate-mass objects and regions in this section. Many of these intermediate-mass sources are in Orion (e.g., Takahashi et al., 2006, 2019; Hull et al., 2014), but there are also objects in other regions, such as Serpens SMM1 in the Serpens Main molecular cloud (van Kempen et al., 2016; Hull et al., 2017b).

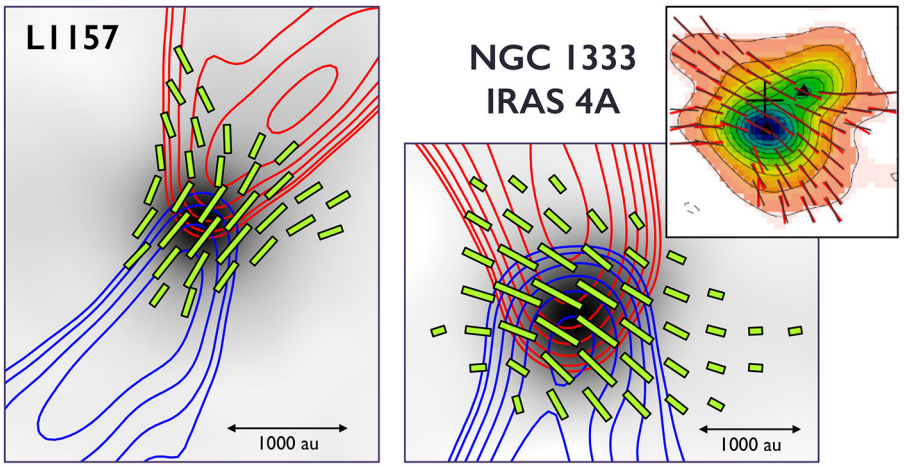

FIGURE 2 | Observations of hourglass-shaped magnetic field configurations (line segments). The rightmost, overlapping panels are NGC 1333-IRAS 4A, observed by the SMA in Girart et al. (2006, top), and again by CARMA in Hull et al. (2014, bottom/background). The SMA and CARMA observations are zoomed to the same spatial scale. The left-hand panel is the isolated Class 0 protostar L1157 (adapted from Hull et al., 2014; see also Stephens et al., 2013). Figures reproduced with permission from *Science* magazine and the AAS.

thus removing magnetic flux and eventually allowing collapse to proceed once the mass-to-flux ratio exceeds the critical value.

One of the predicted signposts of highly magnetized star formation is that at high enough densities ($\gtrsim 10^4\,\mathrm{cm}^{-3}$), the collapse of strongly magnetized gas should pinch the magnetic field into an "hourglass" shape with a symmetry axis perpendicular to the major axis of a flattened, $\sim$1000 au "pseudodisk" (Galli and Shu, 1993a,b). The hourglass is expected to persist down to scales <1,000 au (Fiedler and Mouschovias, 1993; Galli and Shu, 1993b; Allen et al., 2003; Gonçalves et al., 2008; Frau et al., 2011; Kataoka et al., 2012; Mocz et al., 2017); see **Figure 1**. And indeed, the predicted hourglass has now been seen in a number of interferometric observations of low-mass protostellar cores (Girart et al., 1999, 2006, 2008; Rao et al., 2009; Stephens et al., 2013; Hull et al., 2014; Maury et al., 2018; Sadavoy et al., 2018a; Kwon W. et al., under review, see **Figure 2**), suggesting that some protostellar cores do form in strongly magnetized regions. For a discussion of constraining strong-field star formation via observations of hourglass-shaped magnetic fields, see section 4.

A second signpost of strong-field star formation is the consistency of the magnetic field orientation across multiple spatial scales. If the field is strong relative to other dynamical effects, observations at small scales should reveal a magnetic field whose original orientation is preserved from the parsec scale of the cloud in which the source is embedded. To date, multi-scale studies of the magnetic field in low- and high-mass star-forming regions have compared two or three scales: i.e., $\sim$kpc galactic scales to $\sim$0.1 pc dense-core scales in Stephens et al. (2011); 100 pc cloud scales to 0.1 pc dense-core scales in Li et al. (2009, 2015); 1 pc clump scales to 0.1 pc dense-core scales in Zhang et al. (2014), continuing down to $\sim$0.01 pc scales in Girart et al. (2013) and Ching et al. (2017); 0.1 pc dense core scales to 1,000 au protostellar envelope scales in Hull et al. (2014) and Davidson et al. (2014); and 0.1 pc to 1,000 au to 100 au scales in Hull et al. (2017a,b).

In the low-mass regime, Li et al. (2009) found striking consistency between the magnetic field orientation in the Orion molecular cloud derived from background starlight polarization at $\sim$100 pc scales versus polarized thermal dust emission at $\sim$0.1 pc scales. Hull et al. (2014) took this one step further, finding consistency in the field orientation in just a few of the low-mass protostars in their sample from scales of $\sim$0.1 pc to $\sim$1,000 au. The sample of sources from Hull et al. (2014) that maintained consistency in the magnetic field orientation down to scales of $\sim$1,000 au tended to be those sources with a higher polarization fraction, which implies that the magnetic fields in those sources are more ordered, and thus may be more dynamically important.

Among those sources with consistent large-to-small scales magnetic fields are several with known hourglass morphologies, including OMC3 MMS6 (Hull et al., 2014), NGC 1333-IRAS 4A (Girart et al., 2006), L1157 (Stephens et al., 2013), and L1448 IRS 2 (Kwon W. et al., under review). The magnetic field strengths have been estimated toward the latter three objects, an are all relatively high, on the order of $\gtrsim$1 mG, which is similar to values obtained in high-mass regions (see section 3.1). However, while the values are high [5 mG in IRAS 4A (Girart et al., 2006); 1.3–3.5 mG in L1157 (Stephens et al., 2013); and 750 μG in L1448 IRS 2 (Kwon W. et al., under review)], the mass-to-flux ratios calculated for the two most magnetized sources (IRAS 4A and L1157) are both slightly greater than the critical value (1.7 and 1.1 for IRAS 4A and L1157, respectively), which is reasonable, considering that the objects have already collapsed to form protostars.

Follow-up studies with ALMA of individual sources from previous surveys (e.g., Hull et al., 2014) have suggested that consistency in the magnetic field orientation across spatial scales may be the exception rather than the rule at scales smaller than $\sim$0.1 pc. Indeed, detailed multi-scale follow-up studies by Hull et al. (2017a,b) of Ser-emb 8 and Serpens SMM1, two Class 0 protostellar sources in the Serpens Main molecular cloud, found

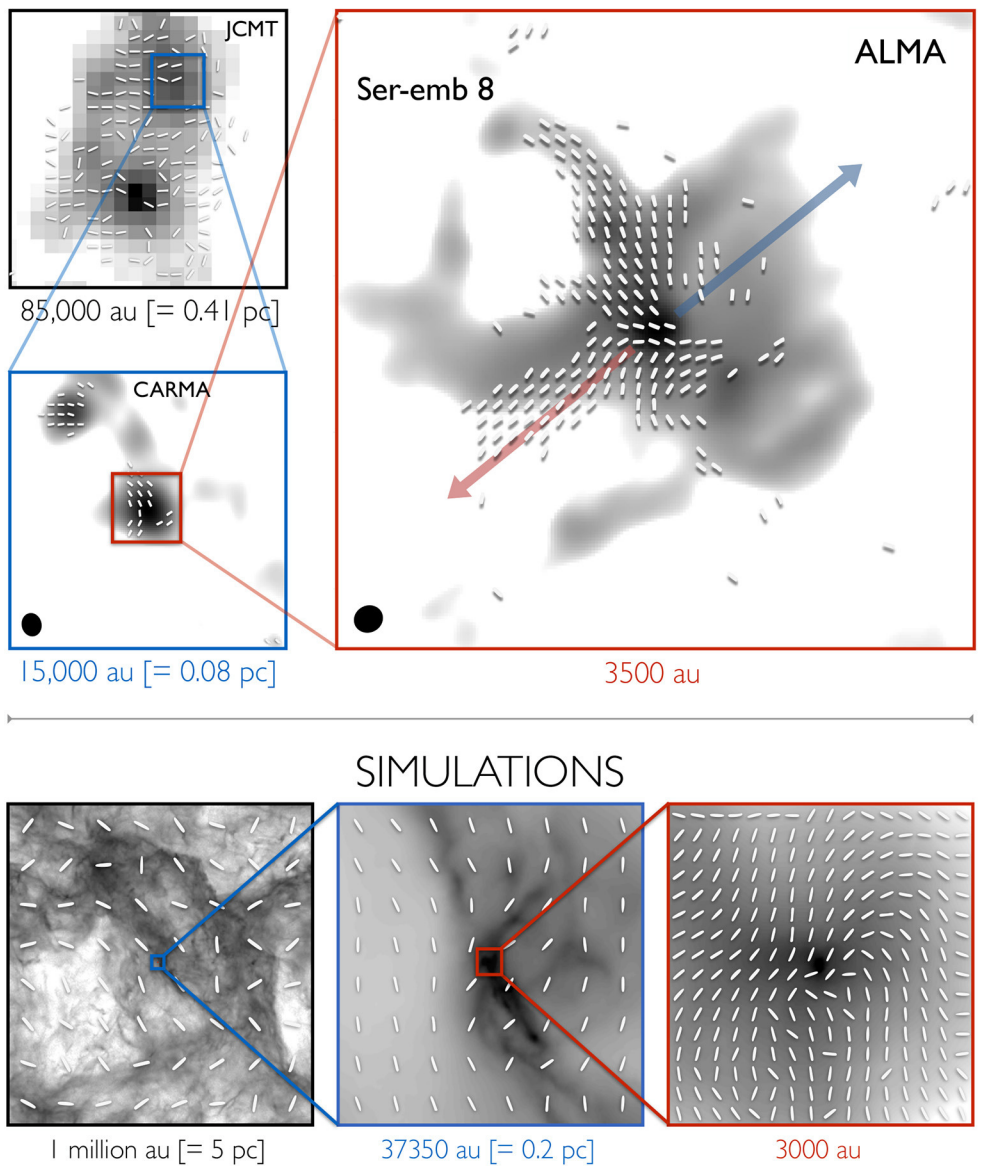

FIGURE 3 | (Top) Multi-scale observations of the magnetic field (line segments) toward the low-mass Class 0 protostar Ser-emb 8. Grayscale is total-intensity (Stokes *I*) thermal dust emission. Observations are from the JCMT at 850 μm (top-left; Matthews et al., 2009), CARMA at 1.3 mm (bottom-left; Hull et al., 2014), and ALMA at 870 μm (right). The red and blue arrows indicate the red- and blueshifted lobes of the bipolar outflow from Ser-emb 8 traced in CO ($J = 2 \rightarrow 1$). The data show the inconsistency of the magnetic field across spatial scales, and are consistent with moving-mesh AREPO MHD simulations **(Bottom)** whose initial conditions include a magnetic field that is weak compared with turbulence at large (5 pc) scales. Adapted from Hull et al. (2017a). Reproduced with permission from the AAS.

significant deviations in the magnetic field morphology across spatial scales ranging from $\sim$ 0.1 pc down to $\sim$ 100 au.

In the case of Serpens SMM1, it appears that the deviations at the $\sim$ 100 au scales probed by ALMA are due to shaping of the magnetic field by the bipolar outflow. This is in spite of the fact that the magnetic field strength is estimated to be quite high, $\sim$ 5.7 mG (Hull et al., 2017b). The fact that dynamics are shaping the magnetic field morphology in this source is not surprising, however, as the magnetic is comparable to the kinetic energy in the outflow. This is in contrast to sources like NGC 1333-IRAS 4A, where estimates by Girart et al. (2006) show that the magnetic energy is clearly dominant over turbulent motions in the source.

In the case of Ser-emb 8, the outflow does not have a clear effect on the magnetic field, and yet the field morphology is still not consistent across scales. A comparison of the Ser-emb 8 data with moving-mesh AREPO gravoturbulent MHD simulations (Mocz et al., 2017) suggests that Ser-emb 8 may have formed in an environment where dynamical effects such as turbulence and infall dominate the magnetic field, in contrast to the strong-field examples described above; see **Figure 3**. These results are

qualitatively consistent with other simulations studying star formation in weakly magnetized turbulent environments (e.g., Seifried et al., 2015; Offner and Chaban, 2017), suggesting that the importance of the magnetic field at the smallest scales of star formation lies along a continuum, from the bright, highly polarized examples of strong-field star formation to the more complex examples of star formation in regions dominated by dynamical processes. Large, high-resolution polarization surveys by ALMA will reveal the distribution of low-mass protostars across this continuum of magnetic importance, and will allow us to compare with results from high-mass regions such as those by Zhang et al. (2014), who found that the magnetic field is dynamically important at the larger spatial scales probed by their observations (see section 3.3).

2.2. Misalignment of Outflows and Magnetic Fields

For more than a decade, one of the primary ways that astronomers have tested the importance of the magnetic field in star-forming regions has been via comparisons of the orientations of bipolar outflows/jets and the ambient magnetic field. This is because if a protostellar core is very strongly magnetized, the magnetic field has the ability to align all of the relevant axes: the axis of the (well ordered and poloidal) magnetic field, the symmetry axis of the pseudodisk, the rotational axis of the protostellar disk, and the axis of the outflow and/or jet emanating from the central source. This happens because of the "magnetic braking" phenomenon (Allen et al., 2003), where a strong magnetic field removes angular momentum from the central source and causes the angular momentum (and thus disk/outflow) and magnetic axes to align (e.g., Machida et al., 2006).

This same magnetic braking phenomenon can potentially lead to what has come to be known as the "magnetic braking catastrophe," where a strong magnetic field aligned with the core rotation axis can suppress the formation of a Keplerian disk in MHD simulations (e.g., Galli et al., 2006; Mellon and Li, 2008; Li et al., 2011). This may lead to the formation of sources like L1157 (Stephens et al., 2013) and B335 (Maury et al., 2018), which have outflows aligned with the magnetic field, and which have as-of-yet undetectably small disks ($\lesssim$10 au). However, since it is known that large Keplerian disks form around many protostellar sources, a variety of methods have been proposed to overcome this problem, including the introduction of an initial misalignment between the rotation axis and the magnetic field, which enhances disk formation (e.g., Hennebelle and Ciardi, 2009; Joos et al., 2012; Krumholz et al., 2013; Li et al., 2013), and the consideration of non-ideal MHD effects such as ambipolar diffusion (Dapp et al., 2012; Masson et al., 2016; Tsukamoto et al., 2018), Ohmic dissipation (Dapp et al., 2012; Tomida et al., 2015; Tsukamoto et al., 2018), the Hall effect (Tsukamoto et al., 2015, 2017; Wurster et al., 2018), and magnetic reconnection (Santos-Lima et al., 2012; Li et al., 2014).

Observationally, if very strong magnetic fields were the norm, then the rotational axes of protostellar disks, and the jets and outflows that emanate from them, should all be parallel with the ambient magnetic field. A study of seven low-mass protostellar cores by Chapman et al. (2013) found a correlation between outflows and magnetic fields at $\sim$0.1 pc scales. However, the majority of the studies of this type have come to the opposite conclusion. For example, Ménard and Duchêne (2004) found that the optical jets from classical T Tauri stars in the Taurus-Auriga molecular cloud are randomly oriented with respect to the parsec-scale magnetic field observed via background-starlight polarization observations. Targon et al. (2011) obtained a similar result for 28 regions spread over the Galaxy, finding no strong correlations between protostellar jets and the ambient magnetic field. On the $\sim$0.1 pc scales of high-mass star-forming cores, Curran and Chrysostomou (2007) and Zhang et al. (2014) used thermal dust polarization observations by the JCMT and the SMA, respectively, to determine that outflows and inferred magnetic fields are randomly aligned. Finally, Hull et al. (2013, 2014) used the 1.3 mm polarization system at CARMA (Hull and Plambeck, 2015) to observe dust polarization toward a sample of low- and high-mass sources, and found that the outflows and $\sim$1,000 au-scale magnetic fields in the low-mass sources were randomly aligned. In **Figure 4**, we compile all of the outflow-versus-magnetic-field angles derivable to date from interferometric observations of low-mass protostellar cores (Girart et al., 1999, 2006, 2008; Rao et al., 2009; Hull et al., 2013, 2014, 2017a,b; Stephens et al., 2013; Cox et al., 2018; Galametz et al., 2018; Harris et al., 2018; Maury et al., 2018; Sadavoy et al., 2018a; Kwon W. et al., under review), and come to the same conclusion: while a few sources have well-aligned outflows and magnetic fields (e.g., those on the very bottom-left of the plot in **Figure 4** that are climbing the 0–20° curve, several of

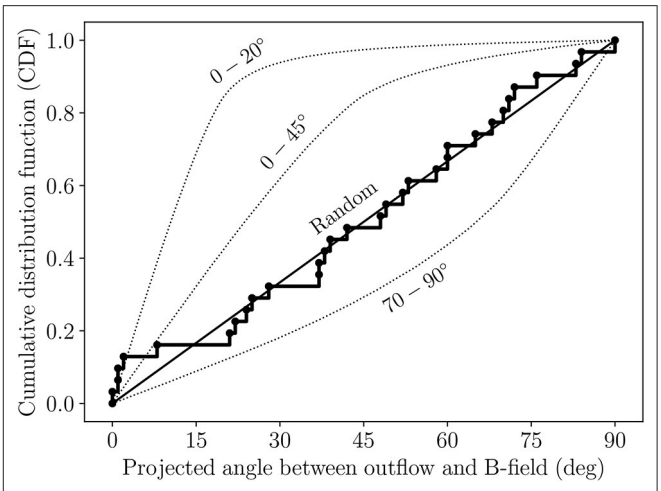

FIGURE 4 | The thick, stepped curve shows the cumulative distribution function (CDF) of the (projected) angles between the bipolar outflows and the mean magnetic-field orientations in the full sample of low-mass protostellar cores observed to date in full polarization with BIMA, the SMA, CARMA, and ALMA. The dotted curves are the CDFs from Monte Carlo simulations where the magnetic fields and outflows are oriented within 20, 45, and 70–90° of one another, respectively. The straight line is the CDF for random orientation. The plot shows that outflows appear to be randomly aligned with magnetic fields in the sample of low-mass sources whose magnetic fields have been observed with $\sim$500–1,000 au resolution.

which have hourglass-shaped field morphologies; see section 4), overall protostellar outflows and magnetic fields measured at 1,000 au-scales are randomly aligned.

The finding from several studies that magnetic fields and outflows are randomly oriented suggests that most protostars form out of material with a magnetic field that is too weak to maintain a consistent orientation all the way down to the 0.1–10 au scales where outflows are launched. Rather, it seems likely that dynamical effects such as turbulence and infall are more important than the magnetic field when it comes to dictating the ultimate angular-momentum direction at the small ($<$ 1,000 au) scales relevant for the formation of protostellar disks and outflows/jets. This claim is corroborated by the analysis by Lee J. W. Y. et al. (2017) of the synthetic observations (produced using the `Dustpol` radiative transfer software; Padovani et al., 2012) of two MHD simulations with different initial mass-to-flux ratios (Offner and Chaban, 2017). They concluded that while the protostar that formed in the strong-field case exhibited a correlation between the outflow and the magnetic field, the weaker-field case showed a random orientation. This is most likely because asymmetric accretion from the turbulent envelope stochastically reoriented the disk/outflow during the earliest (Class 0) formation stage, ultimately decoupling the source from the natal magnetic field (see, e.g., simulations by Chen and Ostriker, 2018).

Two non-magnetic studies focused on the alignment of protostellar outflows with respect to the natal filamentary structure in which the sources formed, and on the relative alignment of the outflows from wide ($\sim$1,000 au) and tight ($<$ 250 au) binary/multiple systems. Both studies used data from the MASSES survey at the SMA (Lee et al., 2015; Stephens et al., 2018). Regarding outflows versus filaments, Stephens et al. (2017a) studied the relative orientation of 57 protostellar outflows in the Perseus molecular cloud (derived from the SMA MASSES data) with the local filamentary structure (derived from *Herschel* observations), and found that the orientations are consistent with a random distribution. Their results held regardless of protostellar age, multiplicity, or the opacity of the dense core, suggesting that the angular momentum of the protostellar cores and outflow-launching disks are independent of the large-scale structure out of which the protostars are forming. Regarding the orientation of outflows from multiple systems, Lee et al. (2016) used SMA MASSES observations to determine that the outflows from proto-multiple systems in the Perseus molecular cloud are randomly aligned. Offner et al. (2016) followed up with MHD simulations that are consistent with the SMA observations, arguing that multiple systems with randomly oriented angular momenta are likely to have formed from turbulent fragmentation.

The turbulent fragmentation scenario is consistent with recent ALMA observations of multiple systems with misaligned protoplanetary disks (Jensen and Akeson, 2014; Lee J.-E. et al., 2017). However, observations by Tobin et al. (2016a) have found evidence for an alternative theory of multiple formation: disk fragmentation (Kratter et al., 2010). The VLA Nascent Disk and Multiplicity Survey of Perseus Protostars (VANDAM) by Tobin et al. (2016b) found a bimodality in the multiplicity of systems; they argued that the wide multiples are the result of turbulent fragmentation, whereas the tight multiples are the result of disk fragmentation. This latter conclusion was strengthened in a follow-up study by Tobin et al. (2018), who observed a sample of tight binaries from the VANDAM survey with ALMA in both continuum and spectral lines.

Recent work by Galametz et al. (2018) focused on the role of the magnetic field in the formation of multiple systems using an SMA survey of magnetic fields in protostellar cores. They found tantalizing evidence that a large misalignment between the outflow and the magnetic field is found preferentially in protostars with higher rotational energies. This $\sim$90° misalignment observed in some objects could thus be due to the winding of the magnetic field lines in the equatorial plane by strong rotation. Furthermore, they found hints that many of those same sources (i.e., those with approximately perpendicular outflows and magnetic fields) are wide multiple sources and/or have large disks, whereas the sources with well aligned magnetic fields and outflows tend to be single objects with small (or undetected) disks at the $\sim$500–1,500 au resolution of their observations. The trend of large disks being associated with sources that have misaligned magnetic fields and outflows was also tentatively seen in an analysis of Karl G. Jansky Very Large Array (VLA) observations of Class 0 and I protostars by Segura-Cox et al. (2018). These results suggest that the morphology and dynamical importance of magnetic fields at the scale of the protostellar envelope may significantly impact the outcome of protostellar collapse as well as the formation of disks and multiple systems. Large ALMA surveys in polarization toward binary/multiple systems will shed light on the impact of the magnetic field on multiple formation via both turbulent and disk fragmentation.

2.3. The Importance of the Magnetic Field in Launching Jets and Outflows

Magnetic fields play a critical role in launching and collimating both bipolar outflows and jets from young forming stars (Frank et al., 2014). Several theories exist to explain how outflows and jets are generated, including the "disk wind" theory where an outflow is launched from the magnetized, rotating surface of a disk (Konigl and Pudritz, 2000), and the "X-wind" theory where jets are launched close to the central protostar itself (Shu et al., 2000). Both of these theories require a magnetic field to function, and that magnetic field is expected to have both poloidal (i.e., along the outflow) and toroidal (perpendicular to the outflow) components due to the combination of infall, outflow, and rotational motions present near a forming star. Characterizing the magnetic field in outflows and jets can thus allow us to investigate the origin of outflows in the context of these different theories.

Historically, observations of dust polarization have been used mainly to study the magnetic field morphology in the optically thin dense cores of dust and gas surrounding embedded protostars. With the sensitivity and resolution of ALMA, it is now possible to detect polarized dust emission along the edges of outflow cavities (Hull et al., 2017b; Maury et al., 2018). However,

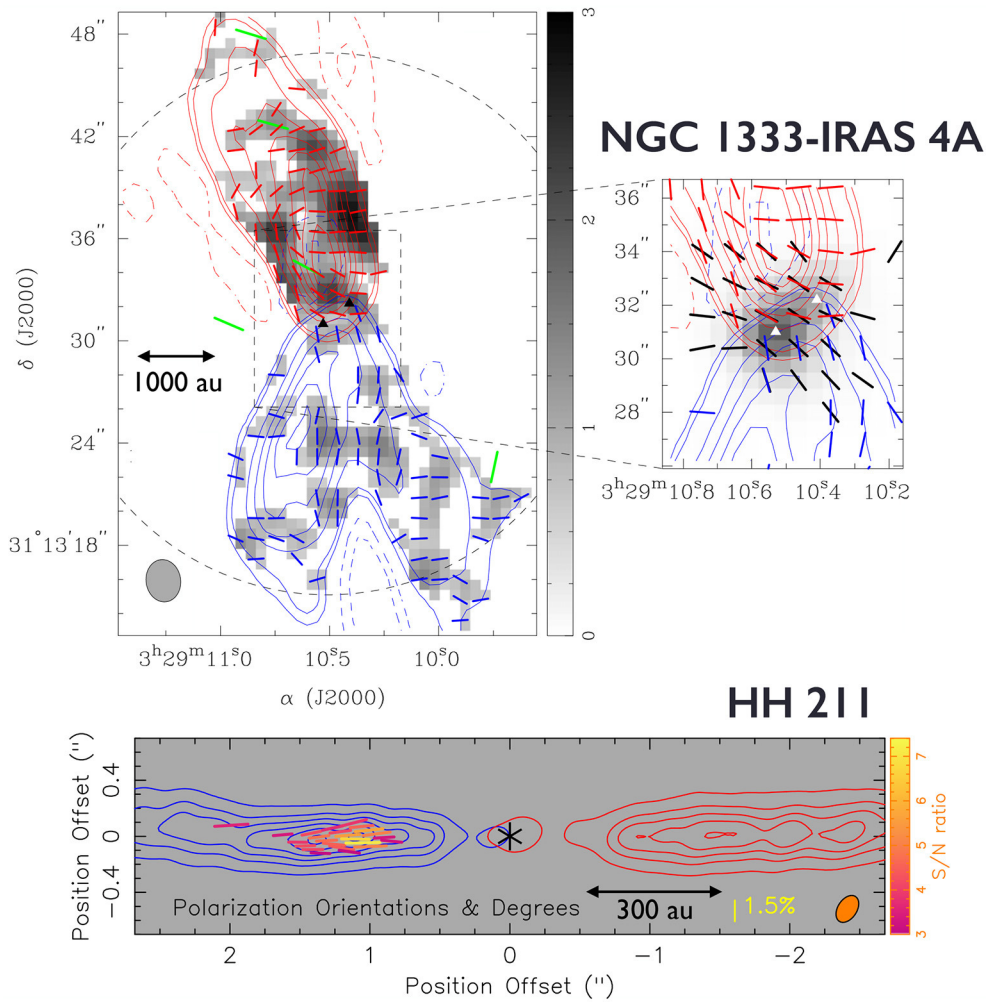

FIGURE 5 | Observations of spectral-line polarization from the G-K effect toward bipolar outflows from low-mass protostellar sources. **(Top left)** SMA observations of polarization of the CO ($J = 3 \rightarrow 2$) line (red and blue line segments) toward NGC 1333-IRAS 4A, adapted from Ching et al. (2016). The grayscale shows the CO ($J = 3 \rightarrow 2$) polarized intensity in units of Jy beam^{-1} km s^{-1}. The authors also compare with CO ($J = 2 \rightarrow 1$) BIMA polarization results from Girart et al. (1999), plotted in green. **(Top right)** Comparison of the SMA CO polarization data with the 870 μm dust polarization map (the black line segments have been rotated by 90° to reflect the inferred magnetic field direction). **(Bottom)** SMA observations of polarization in the SiO ($J = 8 \rightarrow 7$) line, adapted from Lee et al. (2018a). The colors of the line segments indicate different levels of significance in the polarized intensity; the lengths of the segments are scaled to the polarization fraction. The top panel was reproduced with permission from the AAS. The bottom panel was reproduced, with modifications, in accordance with the Creative Commons Attribution 4.0 International License (creativecommons.org/licenses/by/4.0).

there is not enough dust in the cavity itself (where the outflow has evacuated most of the material) to allow for a detection of the polarized emission. Therefore, in order to probe the magnetic field in the outflowing material, one must turn to observations of spectral-line polarization (see section 1.1.2).

While several studies have focused on SiO maser polarization (e.g., Plambeck et al., 2003), the majority of spectral-line polarization studies toward low-mass forming stars have targeted thermal CO and SiO emission polarized due to the G-K effect. Pioneering CO ($J = 2 \rightarrow 1$) polarization observations were performed with BIMA by Girart et al. (1999, 2004), Cortes et al. (2006), and Kwon et al. (2006). So far there has been one detection of SiO ($J = 8 \rightarrow 7$) polarization toward the low-mass protostar HH 211, tentatively detected by Lee et al. (2014) using the SMA, and recently confirmed by ALMA observations reported in Lee et al. (2018a): see the bottom panel of **Figure 5**.

The BIMA observations of CO ($J = 2 \rightarrow 1$) polarization toward the iconic Class 0 protostar NGC 1333-IRAS 4A by Girart et al. (1999) were the first interferometric detection of the G-K effect. Toward the central core, these observations are consistent with the magnetic field inferred from polarized dust emission. The observations by Girart et al. were followed up with the SMA by Ching et al. (2016) in the higher-energy transition CO ($J = 3 \rightarrow 2$). Ching et al. found good consistency between their observations and those by Girart et al. in the inner regions of the outflow where the polarization detections overlap. These

SMA observations, shown in **Figure 5** (top panel), allowed the authors to come to a number of conclusions. First was the fact that the data are consistent with a magnetic field in IRAS 4A that is poloidal at the base of the outflows (there are two outflows, each launched by a member of the embedded binary) and toroidally wrapped up further out in the outflow cavity. This observation, combined with the coexistence of a low-velocity outflow and a high-velocity jet in the source, led the authors to conclude that the outflows in IRAS 4A are most likely driven by MHD winds from the surface of a rotating disk.

3. MAGNETIC FIELDS IN HIGH-MASS STAR FORMATION

3.1. Magnetic Field Measurements at Core Scales

The first pioneering high-resolution observations of linearly polarized continuum and spectral-line emission toward high-mass star-forming regions were made with the BIMA interferometer. Rao et al. (1998) reported the first interferometric polarization observations of a high-mass star-forming region, toward Orion KL. They detected linear polarization at both 3.3 and 1.3 mm in the BIMA data at a resolution of 1,000–3,000 au, revealing abrupt changes in the magnetic field orientations among the continuum emission peaks. This chaotic distribution is in contrast to the uniform magnetic field topology in the lower resolution polarization maps revealed by single dish telescopes (e.g., Schleuning, 1998; Houde et al., 2004; Pattle et al., 2017; Ward-Thompson et al., 2017).

Shortly after the Orion KL study, Lai et al. (2001) reported polarization observations of W51 e1 and e2 in the 1.3 mm continuum emission using BIMA. Later, Tang et al. (2009b) and Koch et al. (2018) published results toward the same source using the SMA and ALMA, respectively. W51 is a cloud complex that harbors massive star formation at various evolutionary stages (Ginsburg et al., 2015; Saral et al., 2017). W51 east hosts an active star-forming molecular clump with as many as 10 compact radio continuum sources over the 0.2 pc projected area of sources e1 and e2 (Ginsburg et al., 2016). Zhang and Ho (1997) reported inverse P-Cygni profile in the e2 core in the NH_3 $(J,K) = (1,1)$, (2,2), and (3,3) spectral lines, consistent with infall motions of the dense gas. Lai et al. (2001) detected linear polarization in the continuum emission in the e2 and e8 cores at a resolution of 14,000 au using BIMA and found that the inferred plane-of-sky components of the magnetic fields are mostly uniform, with an average position angle of 113° in the e2 and 105° in the e8 core. Using the DCF method, the authors estimated a magnetic field strength of 0.8 and 1.3 mG in the e2 and e8 cores, respectively.

More sensitive observations of continuum emission at 870 μm toward W51 using the SMA revealed a non-uniform magnetic field morphology at a higher resolution of 3,300 au (Tang et al., 2009b). Tang et al. explored the possible reasons for the different distributions between the BIMA and the SMA images, finding that interferometric spatial filtering is the most likely cause. This spatial filtering by interferometers can be an advantage, as it allows us to probe magnetic fields at different spatial scales, thus revealing the dynamical role of the magnetic field across the many spatial scales relevant to the star-formation process.

Figure 6 shows the magnetic field maps obtained by the SMA and later by ALMA at various spatial resolutions toward W51 e2 and e8. The figure shows a pinched, hourglass morphology in the e2 core at a resolution of 3,300 au (the top-middle panel), and significantly more substructures at a resolution of 1,500 au (top-right panel). Koch et al. (2018) speculate that the additional substructure in the magnetic field is the result of gravitational collapse at high densities that pulls and/or bends the field lines.

One of the key questions in the fields of magnetized low- and high-mass star formation is whether the magnetic field is dynamically important relative to turbulence and gravity. Koch et al. (2010) applied the two-point correlation function technique (Hildebrand et al., 2009) and found a ratio of turbulent to magnetic energy ranging from 0.7 to 1.27 at scales ranging from $\sim$15,000 au down to $\sim$500 au. Koch et al. (2012) proposed a polarization-intensity-gradient technique that can be used to derive a distribution of magnetic field strength in a given source (see section 1.3.1). Applying the technique to the polarization map of W51 e2, Koch et al. (2012) found a field strength of 7.7 mG. This value is in agreement with the estimate by Tang et al. (2009b), who derived the field strength from the SMA polarization observations. However, it is higher than that found by Lai et al. (2001), who used lower-resolution BIMA polarization observations probing larger spatial scales. The different values reported by Lai et al. (2001) and Koch et al. (2012) can be explained by the fact that the magnetic field strength increases toward smaller spatial scales where the gas density is higher.

Besides W51, another region of massive star formation whose magnetic field has been well studied is DR 21(OH) and its neighboring regions along the DR 21 filament (Lai et al., 2003; Cortes et al., 2005; Girart et al., 2013; Hull et al., 2014; Houde et al., 2016; Ching et al., 2017, 2018). DR 21(OH) was first imaged in linear polarization using BIMA in the CO ($J = 2 \rightarrow 1$) transition and 1.3 mm continuum emission (Lai et al., 2003). These results were followed up in the CO ($J = 1 \rightarrow 0$) transition and 3.4 mm continuum emission using BIMA (Cortes et al., 2005); in the CO ($J = 3 \rightarrow 2$) transition and 870 μm continuum emission using the SMA (Girart et al., 2013; Zhang et al., 2014); and in the CO ($J = 2 \rightarrow 1$) transition and 1.3 mm continuum emission with CARMA (Hull et al., 2014; Houde et al., 2016). Strong polarization was detected in both 1.3 mm and 870 μm continuum emission. The field strength derived using the two-point correlation function is 2.1 mG, yielding a mass-to-flux ratio of 6 $\times$ the critical value (Girart et al., 2013). The field strength is consistent with the value reported by Lai et al. (2003) using the DCF method. Ching et al. (2017) imaged five additional regions along the DR 21 filament using the SMA. The magnetic fields in all six cores display large dispersions, in contrast to the ordered magnetic field obtained with the JCMT at lower angular resolution (Vallée and Fiege, 2006; Matthews et al., 2009). The field strength derived from the DCF method ranges from 0.4 to 1.7 mG among the five cores, with mass-to-flux ratios from 1 to 4.3 $\times$ the critical value.

As was the case in many low-mass star formation studies (see section 2.1), significant effort has been devoted to the search

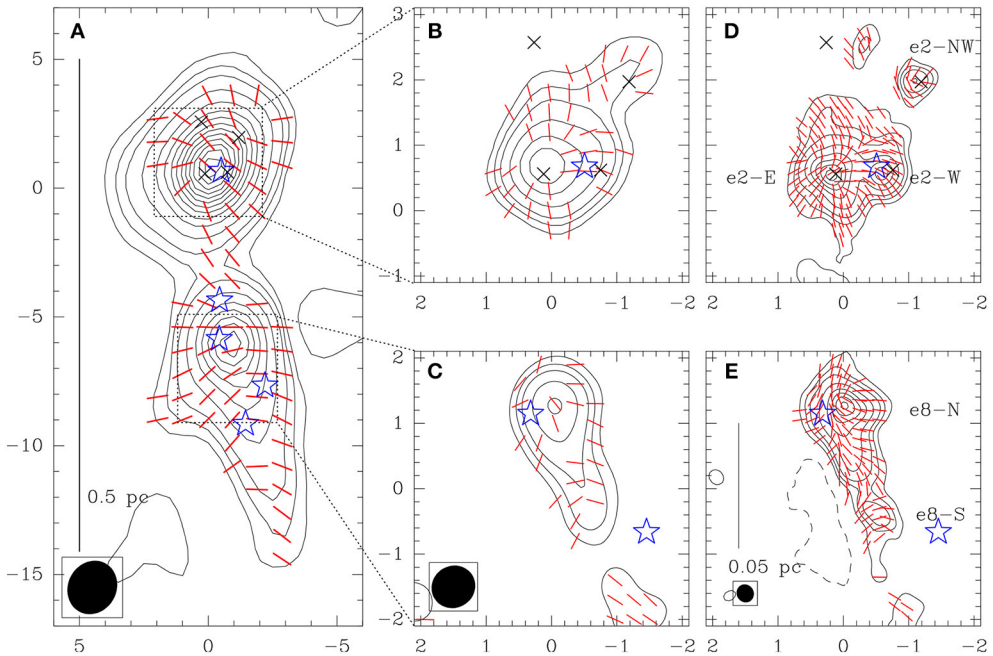

FIGURE 6 | Magnetic fields (red line segments) in W51 e2 and e8 obtained from the SMA and ALMA that exhibit more substructure at higher angular resolution. **(A)** SMA observations at 870 μm probing large scales at a resolution of 2″ (∼ 10,000 au). **(B,C)** SMA observations with a resolution of 0.″7 (∼ 3,500 au) at 870 μm. **(D,E)** ALMA observations at 1.3 mm with a resolution of 0.″26 (∼ 1,330 au). Contours are Stokes *I* dust continuum intensity at levels of 3, 6, 10, 20, 35, 50, 65, 80, 95... times 75 mJy beam^{-1} in **(A)**, 60 mJy beam^{-1} in **(B,C)**, and 6 mJy beam^{-1} in **(D,E)**. × symbols in **(A,B,D)** mark the known continuum sources W51 e2-E, e2-W, e2-NW, and e2-N. Star symbols indicate known ultra-compact HII (UCHII) regions. Synthesized beams are shown as ellipses at the lower-left corner of **(A,C,E)**. Adapted from Koch et al. (2018). Reproduced with permission from the AAS.

for pinched, hourglass-shaped magnetic field morphologies in massive dense cores. So far, the best examples of hourglass-shaped magnetic fields in massive dense cores are G31.41+0.31 and G240.31+0.07 (Girart et al., 2009; Qiu et al., 2014). G31.41+0.31 is a 500 $M_\odot$ hot molecular core with a luminosity of 3×10^5 $L_\odot$. Observed at resolutions as high as 2,400 au, the dense core does not appear to fragment in the dust continuum emission. However, sensitive observations with the VLA at 1.3 and 0.7 cm wavelength revealed two compact continuum objects with a projected separation of 1,300 au (Cesaroni et al., 2010). The dense core exhibits infall motions as well as rotation over a scale of 14,000 au. Magnetic fields inferred from the 870 μm continuum emission reveal a distribution that is pinched along the major axis of the flattened core (Girart et al., 2009). No molecular outflows have been definitively identified in this region. Observations in the CO ($J = 2 \rightarrow 1$) transition found a velocity gradient along the major axis of the flattened core (Cesaroni et al., 2011); however, it is not clear if the gradient represents an outflow, or if it is due to core rotation. The strength of the plane-of-sky component of the magnetic field is 9.7 mG, implying a turbulence-to-magnetic-energy ratio of 0.35. The rotational velocity within the core inferred from spectral-line observations of high-density tracers indicates significant magnetic braking. G31.41+0.31 is a case where the magnetic field dominates the turbulence and the dynamics in the system.

Similar to G31.41+0.31, G240.31+0.07 is a massive star-forming region with an hourglass magnetic field morphology (Qiu et al., 2014). As shown in **Figure 7**, the dust continuum emission reveals a flattened structure extended along the northeast–southwest direction that has fragmented into three cores, each harboring at least one massive young star. A wide-angle, bipolar outflow is seen in the CO emission (Qiu et al., 2009), with the outflow axis parallel to the minor axis of the flattened dense core. Polarization observations at 870 μm reveal a magnetic field topology pinched along the major axis of the core. The magnetic field strength estimated from the DCF method is 1.2 mG, with a mass-to-flux ratio of 1.2 × the critical value, and a turbulent-to-magnetic-energy ratio of 0.4. G240.31+0.07 is another clear example of a massive star-forming core in which the magnetic field dominates the turbulence and the dynamics in the system.

So far, the overwhelming majority of publications on interferometric observations of magnetic fields are studies of individual objects. The improvement in sensitivity with the advent of the CARMA and SMA polarimeters led to surveys of small—but significantly larger—samples of objects. See section 2.1 for a discussion of the TADPOL survey of predominantly low-mass sources by Hull et al. (2014). On the high-mass end, Zhang et al. (2014) reported polarization detections in 14 massive star-forming clumps from a survey of 21 star forming regions. This effort significantly increased the number of clumps with magnetic fields detections and consequently enabled statistical analyses of the ensemble behavior of magnetic fields in massive star-forming regions. To date, there are approximately 24 unique high-mass

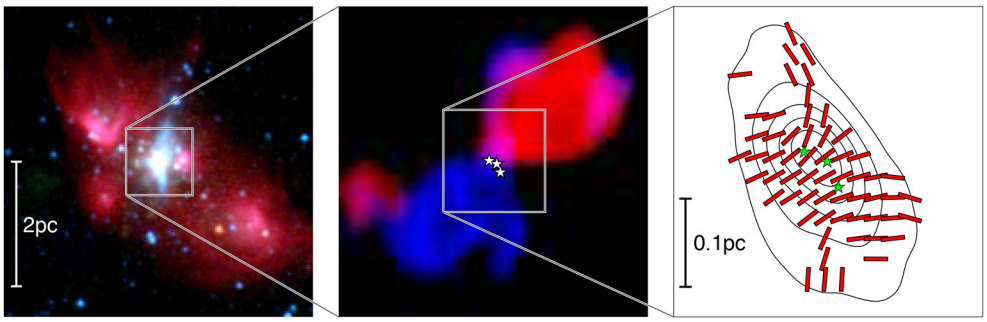

FIGURE 7 | Magnetic field (red line segments in the right panel) in the high-mass star formation region G240.31+0.07 inferred from dust continuum polarization at 870 μm with the SMA (Qiu et al., 2014; Zhang et al., 2014). The left panel presents an overview of the region in a three-color composite of *Spitzer* IRAC images in the 3.6 μm (green), 4.5 μm (blue), and 8.0 μm (red) bands; the middle panel shows a wide-angle bipolar molecular outflow in the CO ($J = 2 \rightarrow 1$) line (Qiu et al., 2009). The star symbols indicate the known continuum peaks. Reproduced with permission from the AAS.

star forming clumps that have been observed in polarization with interferometers. They are Orion KL, NGC 2071, W3, W3(OH), DR 21(OH), DR 21 filament, G192, G30.79, NGC 6334 I/In/IV/V, W51 e and N, IRAS 18306, IRAS 18089, W43, NGC 7538, G5.89, NGC 2264C1, G34.4, G35.2N, G31.41+0.31, and G240.31+0.07 (Rao et al., 1998; Lai et al., 2001, 2003; Cortes and Crutcher, 2006; Cortes et al., 2006, 2008, 2016; Girart et al., 2009, 2013; Tang et al., 2009a,b, 2010; Beuther et al., 2010; Chen et al., 2012; Liu et al., 2013; Qiu et al., 2013, 2014; Frau et al., 2014; Hull et al., 2014; Sridharan et al., 2014; Wright et al., 2014; Zhang et al., 2014; Li et al., 2015; Houde et al., 2016; Ching et al., 2017; Juárez et al., 2017; Koch et al., 2018) Magnetic fields toward these sources display diverse topologies. In sections 3.2, 3.3, 3.4, and 4 we discuss findings and interesting trends from the statistical analysis of this sample. While the analysis represents a significant advance in the study of the role of the magnetic field in high-mass star formation, the limitations and biases in the sample used in the analysis cannot be overlooked. One of the most significant limitations is that non-detections are not included in the statistics. The advent of ALMA will increase the size of the sample drastically, enabling significantly more robust analysis within the next decade.

3.2. Outflow—Core Magnetic Field Connection

Linear polarization from CO rotational transitions (i.e., from the G-K effect) probes magnetic fields in molecular gas with densities from 10^2 to 10^3 cm^{-3}. This can be an effective tool for tracing magnetic fields in protostellar outflows. In the context of high-mass star formation, Lai et al. (2003) reported the first detection of linear polarization in the CO ($J = 2 \rightarrow 1$) transition in DR 21(OH). The inferred magnetic field orientation is in the east–west direction, aligned with the major axis of the CO outflows. Subsequent polarimetric observations in the CO ($J = 1 \rightarrow 0$) transition by Cortes et al. (2005) found linear polarization perpendicular to that of the CO ($J = 2 \rightarrow 1$) transition. While this disagreement may be reconciled by anisotropy in the CO optical depth and external radiation field (see section 1.1.2), it highlights the difficulty of interpreting spectral-line polarization from the G-K effect. Finally, Beuther et al. (2010) reported detections of spectral-line polarization in the CO ($J = 3 \rightarrow 2$) transition in IRAS 18089-1732. Using the DCF method, they derived a magnetic field strength of 28 μG. A similar field strength of 10 μG is reported in DR 21(OH) by Cortes et al. (2005).

Despite the early success in detecting spectral-line polarization primarily in DR 21(OH), very few protostellar sources have shown detectable spectral-line linear polarization since those early results. In the survey of 14 high-mass protostellar clumps by Zhang et al. (2014), only DR 21(OH) had detectable polarization in the CO ($J = 3 \rightarrow 2$) transition (Girart et al., 2013). The limited sensitivity of the SMA may be a contributing factor to these non-detections. Furthermore, the CO emission is typically spatially extended, which presents an additional challenge when imaging linear polarization, since Stokes Q and U can be either positive or negative, and a lack of short-spacing information in sparsely sampled interferometric data can produce negative emission that may be confused with the polarization signal in Stokes Q and U. Both factors are mitigated by ALMA, which provides significant improvements in sensitivity and imaging fidelity over BIMA, CARMA, and the SMA.

Probing magnetic fields in accretion disks around high-mass protostars is challenging in two regards. First, extremely high angular resolution observations are required to achieve the $\sim$100 au linear scales of a disk at a typical source distance of several kpc. Second, at the typical high densities and optical depths in these disks, the polarized emission may be contaminated (and sometimes dominated) by self-scattering of large dust grains (see section 5). For example, Girart et al. (2018) observed polarized emission from the disk associated with the radio jet HH 80-81. These deep ALMA observations in the 1.14 mm continuum emission spatially resolved a flattened disk with a radius of 291 au. The disk is partially optically thick and its polarized emission appears to be dominated by self-scattering of large dust grains.

In the absence of magnetic field information in protostellar outflows and disks, the comparison of magnetic fields in cores with outflow axes offers an alternative to assess the importance of magnetic fields in the formation of disks and outflows in high-mass systems. As discussed in section 2.1, when collapsing to form stars, strongly magnetized cores are expected to form a disk and outflow system with the major axis of the outflow parallel to the magnetic field. Zhang et al. (2014) compared outflow axes with the plane-of-the-sky component of magnetic fields in cores from which the outflows originate. They found a slight preference around 0° and 90° in angles between the magnetic field and the outflow axis. However, due to the small sample size, the data are consistent with a random orientation of magnetic fields and outflows. This lack of correlation, if confirmed by more statistically significant samples, suggests that angular momentum in accretion disks is not dictated by the orientation of the magnetic field in the cores. The dynamical importance of the magnetic field thus appears to weaken relative to gravity and angular momentum from the core to the disk scales.

3.3. Fragmentation and Cluster Formation

The clustering nature of massive stars implies that there must be considerable fragmentation in parsec-scale molecular clumps in order to produce a cluster of stars. Gravity, turbulence, magnetic fields, and stellar feedback all influence fragmentation and the outcome of cluster formation. The dynamical role of the magnetic field during the fragmentation of molecular clumps can be assessed if the magnetic field strength is measured directly. As mentioned in section 1.2, this can be achieved by observing circular polarization from the Zeeman effect. While observations of the Zeeman effect have been carried in HI and OH line emission using the VLA (Crutcher, 2012; Crutcher and Kemball, 2019[7]), these observations probe a low-density medium that may not be directly involved in gravitational collapse. There are no reported interferometric observations of the Zeeman effect in dense molecular gas, although ALMA is likely to reshape this field once precise measurements of circular polarization become available to the user community. Future interferometric observations of the Zeeman effect (measuring the line-of-sight magnetic field), when combined with linear dust and spectral-line polarization observations (measuring the plane-of-sky field), will allow much more robust estimates of the total magnetic field strengths in star-forming regions.

A powerful indirect method that can be used to assess the dynamical role of magnetic fields in protocluster formation is the analysis of the distribution of magnetic fields within cluster-forming molecular clumps. Numerical simulations of turbulent, magnetized molecular clouds offer clues about magnetic field topologies in strong and weak field regimes. When the magnetic field is strong relative to turbulence, the field is less disturbed and appears to be ordered (e.g., Ostriker et al., 2001).

Observationally, such a study becomes meaningful only when a statistically significant sample is involved. Zhang et al. (2014) compared dust polarization in dense cores probed by the SMA with the polarization in the parental molecular clumps observed by single-dish telescopes in a sample of 14 high-mass star forming regions; the results show a bimodal distribution in polarization angles. As shown in **Figure 8**, magnetic fields on dense-core scales are not randomly distributed, but are either parallel or perpendicular to the field orientations in their parental clumps. A later study of a larger sample of 50 primarily high-mass sources by Koch et al. (2014) compared the magnetic field orientation with the gradient of the total dust emission and came to the same conclusion. These findings indicate that the magnetic fields are dynamically important in cluster-forming clumps, and that the field is strong enough on the clump scale to channel the material along the field lines into dense cores during the gravitational collapse. While Hull et al. (2014) found hints of consistency in the magnetic field orientation from ∼0.1 pc to ∼1,000 au scales in a few low-mass sources (see section 2.1), the results at the ∼1–0.1 pc scales from Koch et al. (2014) and Zhang et al. (2014) are much more significant, suggesting that the magnetic field may be more dynamically important at parsec scales.

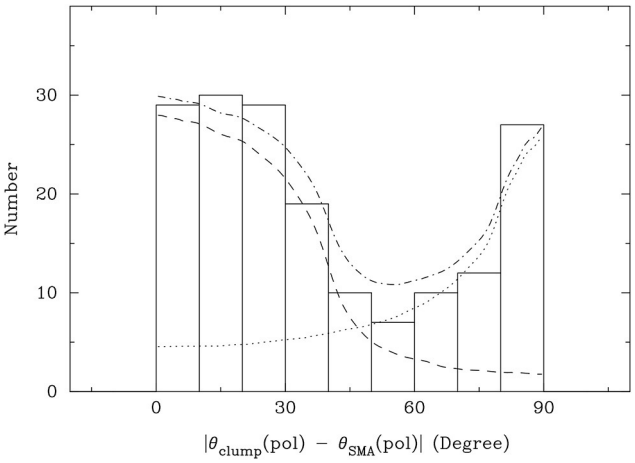

FIGURE 8 | The distribution of polarization angles in dense cores with respect to polarization angles of their parental clumps. The dashed line represents the probability distribution of the plane-of-the-sky-projected orientations of pairs of vectors with 0 – 40° opening angles randomly oriented in space. The dotted line represents the probability distribution where the vectors are preferentially perpendicular, with 80 – 90° opening angles. The dashed-dotted line represents the contributions from the two distributions. Adapted from Zhang et al. (2014). Figures reproduced with permission from the AAS.

3.4. Virial Equilibrium in Massive Cores and Cluster Formation

An essential component of the classical view of star formation is that dense cores should be in a state of an approximate virial equilibrium (Larson, 1981; Shu et al., 1987; McKee and Tan, 2003). However, there is increasing evidence from recent observations that cores forming high-mass protostars may not be in virial equilibrium. Pillai et al. (2011) carried out a stability analysis in two infrared dark clouds (IRDCs) and found that the virial parameter $\alpha_{\rm vir}$, defined as the ratio between the virial mass $M_{\rm Virial}$ and the gas mass $M_{\rm gas}$, is typically between 0.1 to 0.3. These results are corroborated by Kauffmann et al. (2013), who compiled a large sample of massive clumps from surveys and found that a significant fraction of them have

virial parameters $\ll 2$, where 2 is the value expected from a pressure confined, self-gravitating Bonnor-Ebert sphere. More recently, Traficante et al. (2018) pointed out that the virial mass can be underestimated because the spectral line emission of a tracer molecule preferentially probes sections of a cloud with gas densities above the critical density of the line transition. This effect may result in an underestimate of the observed line width, and hence lead to a small virial parameter. However, since the effective excitation density of a line transition is typically lower than the critical density due to radiative trapping of photons when the optical depth is non-negligible, this effect may not be as significant. For example, many of the virial analyses in the literature use the NH_3 and N_2H^+ lines, which often exhibit consistent line widths despite having critical densities that differ by more than a factor of 5.

These small virial parameters appear to challenge the picture of star formation in which gas evolves in a state of equilibrium. However, the virial analyses discussed above do not include contributions from magnetic fields, which may provide significant support in dense cores. Frau et al. (2014) carried out continuum polarization measurements of NGC 7538 with the SMA and found a magnetic field strength of 2.3–2.6 mG in the region. Frau et al. also performed a detailed energetics comparison of the gravitational potential energy, turbulent support, thermal pressure, and magnetic support. Among the 13 dense cores analyzed, the magnetic support amounts to 0.2 to 2.4 × the combined effect from turbulent and thermal pressure. More than half (eight out of 14) of the cores have magnetic support comparable to the turbulent and thermal support. In addition, the virial parameters including the magnetic support vary from 0.1 in the central region where star formation takes place to 8 in cores that are influenced significantly by molecular outflows.

The studies of NGC 7538 by Frau et al. (2014) and Wright et al. (2014) demonstrate that magnetic fields can indeed be a significant contributor to the support of dense cores. Such an analysis should be extended to high-mass star-forming regions at earlier evolutionary stages when stellar feedback has not significantly altered the initial physical conditions. To that end, Pillai et al. (2011) Zhang et al. (2015) Ohashi et al. (2016), Sanhueza et al. (2017), and Lu et al. (2018) performed virial analyses in high-mass star forming regions prior to the development of strong HII regions. The interferometric observations allowed the identification of structures < 0.1 pc in size within massive clumps. **Figure 9** presents a comparison of the virial mass and the gas mass for structures identified in 12 high-mass star forming regions (Pillai et al., 2011; Zhang et al., 2015; Ohashi et al., 2016; Lu et al., 2018). The virial mass is computed as

$$M_{\rm Virial} = \frac{3kR\sigma_v^2}{G} \ , \qquad (4)$$

where σ_v is the line-of-sight velocity dispersion due to both non-thermal and thermal broadening, R is the radius, and G the gravitational constant. $k = \frac{5-2a}{3-a}$ is a correction factor related to the density profile $\rho \propto r^{-a}$. We assume a constant density in the structure, i.e., $a = 0$, which leads to the maximum value

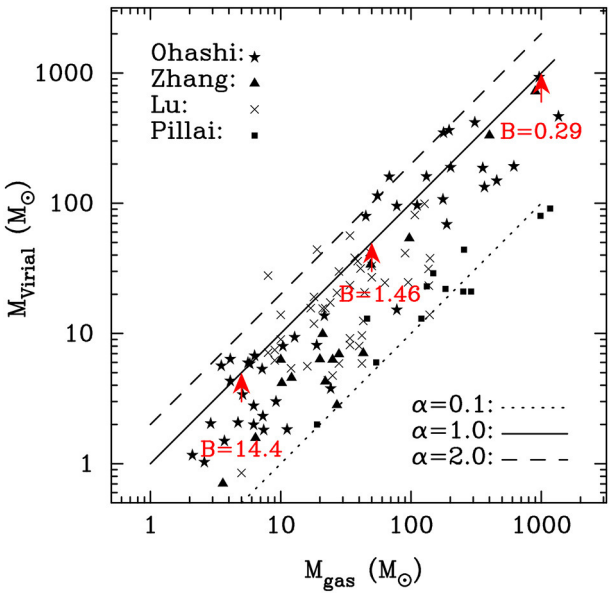

FIGURE 9 | Virial mass $M_{\rm Virial}$ vs. gas mass $M_{\rm gas}$ for clumps and cores in 12 high-mass star forming regions. The data were taken from Pillai et al. (2011), Zhang et al. (2015), Ohashi et al. (2016) and Lu et al. (2018). The virial mass includes contributions from thermal and non-thermal line widths. The gas mass was derived from dust continuum emission. The dashed, solid, and dotted lines denote virial parameters $\alpha_{\rm vir} = M_{\rm Virial}/M_{\rm gas}$ of 2, 1, and 0.1, respectively. The majority of the data points have $\alpha_{\rm vir} < 1$, indicating that clumps and cores are far from virial equilibrium when contributions from magnetic fields are not included. The red arrows indicate the strength of the magnetic field (in mG) that are required to increase $\alpha_{\rm vir}$ from 0.5 to 1.0 (see section 3.4).

in the correction factor ($k = 5/3$) and thus the maximum virial mass. The gas mass is derived from the dust continuum emission (see section 1.4). **Figure 9** reveals that the dense gas structures in these high-mass star forming regions have virial parameters < 2. Furthermore, a large fraction of the dense gas structures have virial parameters $\ll 2$. Since there are no direct measurements of magnetic fields for this sample, we compute the magnetic field required to increase the virial parameter from 0.5 to 1.0. The magnetic virial mass (Hennebelle and Chabrier, 2008) is computed as

$$M_{\rm Mag} = \frac{5R\sigma_A^2}{6G} \ , \qquad (5)$$

where $\sigma_A = \frac{B}{\sqrt{4\pi\rho}}$ is the Alfvénic velocity corresponding to a magnetic field strength B and density ρ. We compute the magnetic field strengths when $M_{\rm Mag} = M_{\rm Virial} = 0.5M_{\rm gas}$. Assuming a representative gas mass $M_{\rm gas}$ and radius R for the clumps ($M_{\rm gas} = 1{,}000\,{\rm M}_\odot$, $R = 0.5$ pc), cores ($M_{\rm gas} = 50\,{\rm M}_\odot$, $R = 0.05$ pc), and condensations ($M_{\rm gas} = 5\,{\rm M}_\odot$, $R = 0.005$ pc), we find required magnetic field strengths of 0.29, 1.46, and 14.4 mG, respectively. Under these conditions, the virial parameters would be 0.5 without the contribution of magnetic fields, and would increase to 1 after the inclusion of magnetic fields. The required field strengths are in broad agreement with typical literature values of magnetic fields that were derived using

the DCF method based on polarization observations of massive star-forming regions.

Recent measurements of the thermodynamic properties in high-mass star-forming regions reveal small virial parameters that appear to challenge the assumption of equilibrium star formation. However, a lack of magnetic field measurements in these same regions leaves open the possibility of virialized star formation, since the field strength of a fraction of a mG to several mG could bring the dense gas close to a state of equilibrium. With the advent of ALMA, we expect significant progress to be made on this vital question in high-mass star formation as more observations of both spectral lines and polarization are carried out over the coming years.

4. CONSTRAINING STRONG-FIELD STAR FORMATION WITH STATISTICS OF HOURGLASS-SHAPED MAGNETIC FIELDS

There are approximately 32 unique interferometric observations of low-mass (Class 0, 0/I, or I) star-forming cores exhibiting significant polarization detections that are not obviously dominated by dust scattering. They are L1448 IRS 2, L1448N(B), L1448C, NGC 1333-IRAS 2A, SVS 13A, SVS 13B, NGC 1333-IRAS 4A, Per-emb-21, NGC 1333-IRAS 7, NGC 1333-IRAS 4B, IRAS 03282+3035, IRAS 03292+3039, B1-c, B1-b, HH 211 mm, HH797, L1551 NE, NGC 2024 FIR 5, OMC3-MMS5, OMC3-MMS6, OMC2-FIR3, OMC2-FIR4, VLA 1623, IRAS 16293A, IRAS 16293B, Ser-emb 8, Ser-emb 8 (N), Serpens SMM1-a, Serpens SMM1-b, B335, L1157, and CB 230 (Girart et al., 1999, 2006; Lai et al., 2002; Rao et al., 2009; Alves et al., 2011; Hull et al., 2013, 2014, 2017a,b; Stephens et al., 2013; Segura-Cox et al., 2015; Cox et al., 2018; Galametz et al., 2018; Harris et al., 2018; Maury et al., 2018; Sadavoy et al., 2018a,b; Kwon W. et al., under review).

Among them, NGC 1333-IRAS 4A, IRAS 16293A, L1157, NGC 2024 FIR 5, OMC3 MMS 6, L1448 IRS 2, B335, VLA 1623, and B1-c (9/32 $\approx$ 28%) exhibit hourglass morphologies, consistent with magnetically dominant star formation (Girart et al., 1999, 2006; Lai et al., 2002; Rao et al., 2009; Alves et al., 2011; Stephens et al., 2013; Hull et al., 2014; Cox et al., 2018; Galametz et al., 2018; Maury et al., 2018; Sadavoy et al., 2018a; Kwon W. et al., under review).

On the high-mass side, there are 24 unique high-mass star forming clumps observed in polarization with interferometers. They are Orion KL, NGC 2071, W3, W3(OH), DR 21(OH), DR 21 filament, G192, G30.79, NGC 6334 I/In/IV/V, W51 e and N, IRAS 18306, IRAS 18089, W43, NGC 7538, G5.89, NGC 2264C1, G34.43+0.24, G35.2N, G31.41+0.31, and G240.31+0.07 (Rao et al., 1998; Lai et al., 2001, 2003; Cortes and Crutcher, 2006; Cortes et al., 2006, 2008, 2016; Girart et al., 2009, 2013; Tang et al., 2009a,b, 2010; Beuther et al., 2010; Chen et al., 2012; Liu et al., 2013; Qiu et al., 2013, 2014; Frau et al., 2014; Hull et al., 2014; Sridharan et al., 2014; Wright et al., 2014; Zhang et al., 2014; Li et al., 2015; Houde et al., 2016; Ching et al., 2017; Juárez et al., 2017; Koch et al., 2018).

Of these, G31.41+0.31, G240.31+0.07, NGC 6334 I and In, and W51 e2 (5/24 $\approx$ 21%) exhibit hourglass magnetic field configurations (Girart et al., 2009; Tang et al., 2009a; Qiu et al., 2014; Li et al., 2015).

A pinched/hourglass-shaped magnetic field configuration can yield a range of magnetic-field morphologies when projected in the plane of the sky (Frau et al., 2011). When the main axis of the system is aligned with the line of sight, the plane-of-sky component of the field is oriented radially outward. This scenario was proposed by Girart et al. (2013) to explain the magnetic field topology in DR 21(OH). Among the low- and high-mass objects with robust detections of polarization (and thus inferred magnetic fields), 28% of the low-mass sources and 21% of the high-mass sources exhibit hourglass configurations. Assuming that the sample is randomly oriented in three dimensions, the probability than an hourglass axis will be oriented within 30° of the line of sight is $\sim$13% (Frau et al., 2011 show that an angle closer to the line of sight than $\sim$30° yields a mostly radial pattern). Therefore, the majority of the objects ($\sim$87%) should display an hourglass shape if the variations in magnetic field morphologies were solely due to projection effects.

The fact that only a small fraction of the objects exhibit hourglass morphologies suggests that the scenario of magnetically dominant core collapse is not the predominant mode of low- or high-mass star formation. However, we should note that when taking into account the projection effect, the fraction of the detected hourglass reaches 28/87% $\approx$1/3 for low-mass and 21/87% $\approx$1/4 for high-mass sources. Such fractions are not negligible, and are even more significant considering the various environmental and dynamical differences between sources, as well as the observational limitations that may hinder the detection of an hourglass—in particular the sensitivity and dynamic range limitations of the pre-ALMA interferometers.

Of the sources observed by ALMA that clearly lack hourglass magnetic field morphologies, only one so far (Ser-emb 8 in Hull et al., 2017a; see **Figure 3**) shows a truly chaotic morphology, presumably having been influenced by turbulence and infall. However, the few ALMA polarization observations published to date have shown more examples of magnetic fields that seem to have been shaped by bipolar outflows. These observations are challenging to interpret, as magnetic fields aligned with the walls of an outflow cavity can look quite similar to an hourglass when observed with low resolution. Thus, future studies will need to carefully consider how to determine which "hourglasses" are preserved from the natal collapse phase, such as in NGC 1333-IRAS 4A, where at $\sim$1,000 au scales the hourglass appears to be unperturbed by the two outflows emanating at different angles from the embedded binary (Girart et al., 2006); vs. which are caused by outflow/jet feedback, such as in Serpens SMM1 (Hull et al., 2017b) and B335 (Maury et al., 2018).

We further caution that the above values are lower limits that are limited by telescope resolution: i.e., in the high-mass case, we consider each source as unique, despite the fact that each clump is likely to have more than one protostellar object. This is even true in the low-mass case: for example, SMA observations were able to distinguish the magnetic fields in SVS 13A and B, whereas CARMA observations were not; and ALMA observations were able to map the magnetic fields in Serpens SMM1-a and b separately, whereas CARMA and SMA observations were not.

Finally, and perhaps most important, the number of objects observed with interferometers remains small: observations by ALMA are likely to increase the sample size significantly in the near future, enabling studies that will establish far better statistical constraints.

5. POLARIZATION FROM DUST SCATTERING

While polarized emission from dust scattering is independent of the magnetic field, we briefly mention it here because this young, quickly growing subfield emerged from studies that were attempting to make resolved maps of the magnetic field in protoplanetary disks, which is one of the longstanding goals of disk- and star-formation studies. Rao et al. (2014) reported a tentative detection of a toroidally wrapped magnetic field in the Class 0 protostar IRAS 16293B at $\sim$75 au resolution using the SMA. However, on the whole, pre-ALMA full polarization observations of disks did not have the sensitivity or the resolution necessary to make well resolved maps of low-level ($\lesssim$1%) polarized dust emission (Hughes et al., 2009, 2013).

Around the same time that ALMA started producing polarization results, several theoretical studies suggested that polarized (sub)millimeter-wave emission from protoplanetary disks could be caused by the self-scattering of emission from (sub)millimeter-sized dust grains (Kataoka et al., 2015, 2016a; Pohl et al., 2016; Yang et al., 2016a,b), consistent with previous work by Cho and Lazarian (2007). Kataoka et al. (2016a) and Yang et al. (2016b) explained the 1.3 mm CARMA polarization observations by Stephens et al. (2014) of the Class I/II source HL Tau in the context of this self-scattering mechanism. Self-scattering can also explain the polarization pattern observed in the Class II protoplanetary disk IM Lup in 870 μm ALMA observations by Hull et al. (2018b), and similar observations of HD 163296 by Dent et al. (2019).

The situation became even more complex when Tazaki et al. (2017) proposed yet another mechanism that can cause polarization in disks: dust grains whose minor axes are aligned with the gradient in the dust emission (this work is rooted in the radiative torque model by Lazarian, 2007). This mechanism, which is sometimes referred to as "*k*-RATs" (i.e., where *k* is the orientation of the gradient in the dust emission; see also Footnote 5), is different from self-scattering by dust grains. However, similar to self-scattering, it is independent of any magnetic field that might be in the disk. Polarization from *k*-RATs, which has a morphology that is azimuthal, is broadly consistent with 3 mm ALMA observations of polarization in the HL Tau disk (Kataoka et al., 2017), although Yang et al. (2019) found that their *k*-RAT model did not reproduce the data when examined in detail. The transition from possible *k*-RAT alignment at long (3 mm) wavelengths to scattering at short (870 μm) wavelengths was shown clearly by Stephens et al. (2017b), who reported high-resolution ALMA polarization results at 870 μm and 1.3 mm, complementing the 3 mm observations reported by Kataoka et al. (2017). The intermediate-wavelength 1.3 mm data exhibit a morphology consistent with roughly equal contributions of self-scattering and *k*-RATs.

Other recent results have interpretations that are not as clear. These include observations of the edge-on HH 111 and HH 212 disks (Lee et al., 2018b), the high-mass protostellar disk Cepheus A HW2 (Fernández-López et al., 2016), and the transition disk HD 142527 (Kataoka et al., 2016b; Ohashi et al., 2018); the polarized emission from these objects may be caused by either scattering or magnetically aligned grains (*B*-RATs). Observations of the low-mass disks CW Tau and DG Tau (Bacciotti et al., 2018) and the massive GGD27 MM1 disk (Girart et al., 2018) associated with the iconic HH 80-81 radio jet show polarization that may be caused by dust self-scattering and/or *k*-RATs. Polarization observations of a number of embedded Class 0 protostars by Segura-Cox et al. (2015), Cox et al. (2018), Harris et al. (2018), Sadavoy et al. (2018a,b), and Takahashi et al. (2019) sometimes show signs of scattering in the inner regions of sources and magnetic alignment in the outer regions. Finally, Alves et al. (2018) reported $\sim$30 au-resolution observations of the Class I binary source BHB07-11, which exhibits consistent polarization patterns at 3 mm, 1.3 mm, and 850 μm. They argue that the polarized emission most likely arises from magnetically aligned dust grains.

We emphasize that studies of (sub)millimeter polarization from disks are in their infancy. More observations and more mature, detailed models are necessary before we will be able to determine whether there is, in fact, any contribution from magnetic fields in the polarized emission from disks around young forming stars.

6. SUMMARY

The steady improvement in telescope sensitivity at the (sub)millimeter-wave bands where dust continuum emission is strong has led to a revolution in interferometric observations of linear polarization over the past two decades. In recent years, both CARMA and the SMA conducted surveys of magnetic fields in samples of >10 star-forming cores/clumps. These studies have proven insightful in revealing the statistical behavior of magnetic fields in star formation. However, while individual case studies continue to be fruitful, large, less biased surveys that target statistically significant samples of sources are the only way to further constrain the dynamical role of magnetic fields in the star formation process.

Studies of low-mass star formation have found that while there are a few cases where the magnetic field seems to regulate the collapse of star-forming material across the scales from clouds/clumps to cores to envelopes, there are also many cases where the multi-scale magnetic field morphology shows no consistency. Furthermore, the resolution and sensitivity of ALMA have yielded new observations that show evidence of shaping of the magnetic field by bipolar outflows at the $\sim$100 au scale in some (but not all) sources. A few recent observations of spectral-line polarization by the SMA and ALMA have shed light on the importance of magnetic fields in the launching of outflows. More observations of this type

with ALMA will enhance this subfield significantly in the coming years.

Studies of high-mass star formation found that magnetic fields are not the dominant force within the parsec scale of molecular clumps. However, fields appear to be dynamically important in the fragmentation of clumps into 0.1 pc-scale cores. Furthermore, molecular gas with densities $>10^4$ cm^{-3} in high-mass star formation appears to be far from virial equilibrium if magnetic fields do not contribute significantly to the dynamical process. This significant departure from the state of virialization appears to challenge the basic assumption of equilibrium star formation. Direct measurements of magnetic fields will shed more insight on this important issue.

In both the low- and high-mass regimes, comparisons of outflow vs. magnetic field orientations have yielded random alignment. The outflow is a probe of the angular momentum at the smallest scales in the source, and thus the limited data currently available point to a scenario where angular momentum is far more important than the magnetic field at the small ($<$ 1,000 au) scales of individual forming protostars.

The role of magnetic fields in the formation of high- and low-mass disks is less clear due to a small number of observations, and the issue of scattering by dust. Near-future studies targeting the Zeeman and G-K effects may finally be able to access information about the magnetic field in disks (e.g., Brauer et al., 2017). Furthermore, high resolution studies at longer wavelengths in regions that are optically thick (and thus dominated by scattering) in the ALMA data will be made possible by future telescopes such as the Next Generation Very Large Array (ngVLA; Carilli et al., 2015). The ngVLA will be a powerful tool for studying magnetized star formation (Isella et al., 2015; Hull et al., 2018a), as it will offer dramatic improvements in the sensitivity, resolution, and image fidelity over the current VLA, which has enabled just a few studies of polarization in the very brightest low- and high-mass star-forming sources (Carrasco-González et al., 2010; Cox et al., 2015); (Liu et al., 2016, 2018).

Despite major advances in recent years, the studies presented in this review—in particular the survey studies—are biased toward objects with detectable polarization. Nearly all low- and high-mass star forming objects have embedded protostars (and sometimes HII regions, in the case of high-mass sources). A crucial, under-explored area of star formation involves studying the initial conditions of the magnetic field before feedback (e.g., infall, outflows, and radiation) has altered its morphology. However, this has rarely been achieved due to a lack of sensitivity. In the coming years, large, multi-scale, multi-telescope surveys of magnetic fields in star-forming clouds covering the full range of evolutionary stages will allow us to break new ground in our studies of magnetized star formation.

AUTHOR CONTRIBUTIONS

CH led the writing of the sections about low-mass star formation and scattering. QZ led the section about high-mass star formation. Both authors wrote the abstract, introduction, hourglass-statistics section, and summary.

FUNDING

CH acknowledges the support of both the NAOJ Fellowship as well as JSPS KAKENHI grant 18K13586. QZ acknowledges the support of the the Smithsonian Institute SSA grant, Are Magnetic Fields Dynamically Important in Massive Star Formation?

ACKNOWLEDGMENTS

CH and QZ acknowledge the two referees for their careful reading of the manuscript and for the insightful comments, which led to a more clear and thorough presentation of this review. CH acknowledges Paulo Cortés, Martin Houde, and Josep Miquel Girart for the useful discussion. The BIMA array was operated by the Berkeley-Illinois-Maryland Association with support from the National Science Foundation. Support for CARMA construction was derived from the states of California, Illinois, and Maryland, the James S. McDonnell Foundation, the Gordon and Betty Moore Foundation, the Kenneth T. and Eileen L. Norris Foundation, the University of Chicago, the Associates of the California Institute of Technology, and the National Science Foundation. The Submillimeter Array is a joint project between the Smithsonian Astrophysical Observatory and the Academia Sinica Institute of Astronomy and Astrophysics, and is funded by the Smithsonian Institution and the Academia Sinica. ALMA is a partnership of ESO (representing its member states), NSF (USA) and NINS (Japan), together with NRC (Canada), NSC and ASIAA (Taiwan), and KASI (Republic of Korea), in cooperation with the Republic of Chile. The Joint ALMA Observatory is operated by ESO, AUI/NRAO, and NAOJ. The National Radio Astronomy Observatory is a facility of the National Science Foundation operated under cooperative agreement by Associated Universities, Inc.

Facilities: ALMA, APEX, BIMA, BLAST, BLAST-TNG, CARMA, CSO, IRAM 30 m, JCMT, LMT, NRAO 12 m, SMA, SOFIA, Viper, VLA.

Software: APLpy, an open-source plotting package for Python hosted at `aplpy.github.com` (Robitaille and Bressert, 2012). Common Astronomy Software Applications (CASA, McMullin et al., 2007). Astropy (Astropy Collaboration et al., 2018).

REFERENCES

Akeson, R. L., and Carlstrom, J. E. (1997). Magnetic field structure in protostellar envelopes. *Astrophys. J.* 491, 254–266. doi: 10.1086/304949

Akeson, R. L., Carlstrom, J. E., Phillips, J. A., and Woody, D. P. (1996). Millimeter interferometric polarization imaging of the young stellar object NGC 1333/IRAS 4A. *Astrophys. J.* 456:L45. doi: 10.1086/309856

Allen, A., Li, Z.-Y., and Shu, F. H. (2003). Collapse of magnetized singular isothermal toroids. II. Rotation and magnetic braking. *Astrophys. J.* 599, 363–379. doi: 10.1086/379243

Alves, F. O., Frau, P., Girart, J. M., Franco, G. A. P., Santos, F. P., and Wiesemeyer, H. (2014). On the radiation driven alignment of dust grains: detection of the polarization hole in a starless core. *Astron. Astrophys.* 569:L1. doi: 10.1051/0004-6361/201424678

Alves, F. O., Girart, J. M., Lai, S.-P., Rao, R., and Zhang, Q. (2011). The magnetic field in the NGC 2024 FIR 5 dense core. *Astrophys. J.* 726:63. doi: 10.1088/0004-637X/726/2/63

Alves, F. O., Girart, J. M., Padovani, M., Galli, D., Franco, G. A. P., Caselli, P., et al. (2018). Magnetic field in a circumbinary disk around a Class I YSO. *Astron. Astrophys.* 616:A56.

Andersson, B.-G., Lazarian, A., and Vaillancourt, J. E. (2015). Interstellar dust grain alignment. *Annu. Rev. Astron. Astrophys.* 53, 501–539. doi: 10.1146/annurev-astro-082214-122414

Astropy Collaboration, Price-Whelan, A. M., Sipőcz, B. M., Günther, H. M., Lim, P. L., Crawford, S. M., et al. (2018). The astropy project: building an open-science project and status of the v2.0 Core Package. *Astron. J.* 156:123. doi: 10.3847/1538-3881/aabc4f

Bacciotti, F., Girart, J. M., Padovani, M., Podio, L., Paladino, R., Testi, L., et al. (2018). ALMA observations of polarized emission toward the CW Tau and DG Tau protoplanetary disks: constraints on dust grain growth and settling. *ApJ*. 865:L12. doi: 10.3847/2041-8213/aadf87

Beltrán, M. T. (2015). Observational perspective of the youngest phases of intermediate-mass stars. *Astrophys. Space Sci.* 355, 283–290. doi: 10.1007/s10509-014-2151-0

Beuther, H., Vlemmings, W. H. T., Rao, R., and van der Tak, F. F. S. (2010). Magnetic field structure in a high-mass outflow/disk system. *Astrophys. J. Lett.* 724, L113–L117. doi: 10.1088/2041-8205/724/1/L113

Bock, D., Bolatto, A. D., Hawkins, D. W., Kemball, A. J., Lamb, J. W., Plambeck, R. L., et al. (2006). "First results from CARMA: the combined array for research in millimeter-wave astronomy," in *Society of Photo-Optical Instrumentation Engineers (SPIE) Conference Series, Vol. 6267*. 13.

Brauer, R., Wolf, S., and Flock, M. (2017). Magnetic fields in circumstellar disks. The potential of Zeeman observations. *Astron. Astrophys.* 607:A104. doi: 10.1051/0004-6361/201731140

Carilli, C. L., McKinnon, M., Ott, J., Beasley, A., Isella, A., Murphy, E., et al. (2015). Next generation very large Array Memo No. 5: science working groups – project overview. *arXiv [Preprints]. arXiv: 1510.06438*.

Carrasco-González, C., Rodríguez, L. F., Anglada, G., Martí, J., Torrelles, J. M., and Osorio, M. (2010). A magnetized jet from a massive protostar. *Science* 330:1209. doi: 10.1126/science.1195589

Caswell, J. L., Green, J. A., and Phillips, C. J. (2014). Parkes full polarization spectra of OH masers - II. Galactic longitudes 240deg to 350deg. *Month. Not. R. Astron. Soc.* 439, 1680–1739. doi: 10.1093/mnras/stu046

Cesaroni, R., Beltrán, M. T., Zhang, Q., Beuther, H., and Fallscheer, C. (2011). Dissecting a hot molecular core: the case of G31.41+0.31. *Astron. Astrophys.* 533:A73. doi: 10.1051/0004-6361/201117206

Cesaroni, R., Hofner, P., Araya, E., and Kurtz, S. (2010). The structure of hot molecular cores over 1000 AU. *Astron. Astrophys.* 509:A50. doi: 10.1051/0004-6361/200912877

Chamma, M. A., Houde, M., Girart, J. M., and Rao, R. (2018). Non-Zeeman circular polarization of molecular spectral lines in the ISM. *Month. Not. R. Astron. Soc.* 480, 3123–3131. doi: 10.1093/mnras/sty2068

Chandrasekhar, S., and Fermi, E. (1953). Magnetic fields in spiral arms. *Astrophys. J.* 118:113. doi: 10.1086/145731

Chapman, N. L., Davidson, J. A., Goldsmith, P. F., Houde, M., Kwon, W., Li, Z.-Y., et al. (2013). Alignment between flattened protostellar infall envelopes and ambient magnetic fields. *Astrophys. J.* 770:151. doi: 10.1088/0004-637X/770/2/151

Chen, C.-Y., and Ostriker, E. C. (2018). Geometry, kinematics, and magnetization of simulated prestellar cores. *Astrophys. J.* 865:34. doi: 10.3847/1538-4357/aad905

Chen, H.-R., Rao, R., Wilner, D. J., and Liu, S.-Y. (2012). The magnetized environment of the W3(H_2O) protostars. *Astrophys. J. Lett.* 751:L13. doi: 10.1088/2041-8205/751/1/L13

Ching, T.-C., Lai, S.-P., Zhang, Q., Girart, J. M., Qiu, K., and Liu, H. B. (2017). Magnetic fields in the massive dense cores of the DR21 filament: weakly magnetized cores in a strongly magnetized filament. *Astrophys. J.* 838:121. doi: 10.3847/1538-4357/aa65cc

Ching, T.-C., Lai, S.-P., Zhang, Q., Girart, J. M., Qiu, K., and Liu, H. B. (2018). Interactions between gas dynamics and magnetic fields in the massive dense cores of the DR21 filament. *Astrophys. J.* 865:110. doi: 10.3847/1538-4357/aad9fc

Ching, T.-C., Lai, S.-P., Zhang, Q., Yang, L., Girart, J. M., and Rao, R. (2016). Helical magnetic fields in the NGC 1333 IRAS 4A protostellar outflows. *Astrophys. J.* 819:159. doi: 10.3847/0004-637X/819/2/159

Chitsazzadeh, S., Houde, M., Hildebrand, R. H., and Vaillancourt, J. (2012). Characterization of turbulence from submillimeter dust emission. *Astrophys. J.* 749:45. doi: 10.1088/0004-637X/749/1/45

Cho, J., and Lazarian, A. (2007). Grain alignment and polarized emission from magnetized T tauri disks. *Astrophys. J.* 669, 1085–1097. doi: 10.1086/521805

Chuss, D. T., Andersson, B.-G, Bally, J., Dotson, J. L., Dowell, C. D., Guerra, J. A. et al. (2018). HAWC+/SOFIA multiwavelength polarimetric observations of OMC-1. *arXiv:1810.08233*.

Clark, S. E., Hill, J. C., Peek, J. E., Putman, M. E., and Babler, B. L. (2015). Neutral hydrogen structures trace dust polarization angle: implications for cosmic microwave background foregrounds. *Phys. Rev. Lett.* 115:241302. doi: 10.1103/PhysRevLett.115.241302

Clark, S. E., Peek, J. E. G., and Putman, M. E. (2014). Magnetically aligned H I fibers and the rolling hough transform. *Astrophys. J.* 789:82. doi: 10.1088/0004-637X/789/1/82

Cortes, P., and Crutcher, R. M. (2006). Interferometric mapping of magnetic fields: G30.79 FIR 10. *Astrophys. J.* 639, 965–968. doi: 10.1086/498971

Cortes, P. C., Crutcher, R. M., and Matthews, B. C. (2006). Interferometric mapping of magnetic fields: NGC 2071IR. *Astrophys. J.* 650, 246–251. doi: 10.1086/507460

Cortes, P. C., Crutcher, R. M., Shepherd, D. S., and Bronfman, L. (2008). Interferometric mapping of magnetic fields: the massive star-Forming region G34.4+0.23 MM. *Astrophys. J.* 676, 464–471. doi: 10.1086/524355

Cortes, P. C., Crutcher, R. M., and Watson, W. D. (2005). Line polarization of molecular lines at radio frequencies: the case of DR 21(OH). *Astrophys. J.* 628, 780–788. doi: 10.1086/430815

Cortes, P. C., Girart, J. M., Hull, C. L. H., Sridharan, T. K., Louvet, F., Plambeck, R., et al. (2016). Interferometric mapping of magnetic fields: the ALMA view of the massive star-forming clump W43-MM1. *Astrophys. J. Lett.* 825:L15. doi: 10.3847/2041-8205/825/1/L15

Cox, E. G., Harris, R. J., Looney, L. W., Li, Z.-Y., Yang, H., Tobin, J. J., et al. (2018). ALMA's polarized view of 10 protostars in the perseus molecular cloud. *Astrophys. J.* 855:92. doi: 10.3847/1538-4357/aaacd2

Cox, E. G., Harris, R. J., Looney, L. W., Segura-Cox, D. M., Tobin, J., Li, Z.-Y., et al. (2015). High-resolution 8 mm and 1 cm polarization of IRAS 4A from the VLA Nascent Disk and Multiplicity (VANDAM) Survey. *Astrophys. J. Lett.* 814:L28. doi: 10.1088/2041-8205/814/2/L28

Crutcher, R. M. (1999). Magnetic fields in molecular clouds: observations confront theory. *Astrophys. J.* 520, 706–713. doi: 10.1086/307483

Crutcher, R. M. (2004). What drives star formation? *Astrophys. Space Sci.* 292, 225–237. doi: 10.1023/B:ASTR.0000045021.42255.95

Crutcher, R. M. (2012). Magnetic fields in molecular clouds. *Annu. Rev. Astron. Astrophys.* 50, 29–63. doi: 10.1146/annurev-astro-081811-125514

Crutcher, R. M., Troland, T. H., Goodman, A. A., Heiles, C., Kazes, I., and Myers, P. C. (1993). OH Zeeman observations of dark clouds. *Astrophys. J.* 407, 175–184. doi: 10.1086/172503

Curran, R. L., and Chrysostomou, A. (2007). Magnetic fields in massive star-forming regions. *Month. Not. R. Astron. Soc.* 382, 699–716. doi: 10.1111/j.1365-2966.2007.12399.x

Dapp, W. B., Basu, S., and Kunz, M. W. (2012). Bridging the gap: disk formation in the Class 0 phase with ambipolar diffusion and Ohmic dissipation. *Astron. Astrophys.* 541:A35. doi: 10.1051/0004-6361/201117876

Davidson, J. A., Li, Z.-Y., Hull, C. L. H., Plambeck, R. L., Kwon, W., Crutcher, R. M., et al. (2014). Testing magnetic field models for the class 0 protostar L1527. *Astrophys. J.* 797:74. doi: 10.1088/0004-637X/797/2/74

Davis, L. (1951). The strength of interstellar magnetic fields. *Phys. Rev.* 81, 890–891. doi: 10.1103/PhysRev.81.890.2

Deguchi, S., and Watson, W. D. (1984). Linear polarization of molecular lines at radio frequencies. *Astrophys. J.* 285, 126–133. doi: 10.1086/162483

Dent, W. R. F., Pinte, C., Cortes, P. C., Ménard, F., Hales, A., Fomalont, E., et al. (2019). Submillimetre dust polarisation and opacity in the HD163296 protoplanetary ring system. *Month. Not. R. Astron. Soc.* 482, L29–L33. doi: 10.1093/mnrasl/sly181

Dotson, J. L., Novak, G., Renbarger, T., Pernic, D., and Sundwall, J. L. (1998). "SPARO: the submillimeter polarimeter for Antarctic remote observing," in *Advanced Technology MMW, Radio, and Terahertz Telescopes, Vol. 3357*, ed T. G. Phillips, 543–547. doi: 10.1117/12.317388

Dotson, J. L., Vaillancourt, J. E., Kirby, L., Dowell, C. D., Hildebrand, R. H., and Davidson, J. A. (2010). 350 μm polarimetry from the caltech submillimeter observatory. *Astrophys. J. Suppl. Ser.* 186, 406–426. doi: 10.1088/0067-0049/186/2/406

Falceta-Gonçalves, D., Lazarian, A., and Kowal, G. (2008). Studies of regular and random magnetic fields in the ISM: statistics of polarization vectors and the chandrasekhar-fermi technique. *Astrophys. J.* 679, 537-551. doi: 10.1086/587479

Fernández-López, M., Stephens, I. W., Girart, J. M., Looney, L., Curiel, S., Segura-Cox, D., et al. (2016). 1.3 mm polarized emission in the circumstellar disk of a massive protostar. *Astrophys. J.* 832:200. doi: 10.3847/0004-637X/832/2/200

Fiedler, R. A., and Mouschovias, T. C. (1993). Ambipolar diffusion and star formation: formation and contraction of axisymmetric cloud cores. II. Results. *Astrophys. J.* 415:680. doi: 10.1086/173193

Fish, V. L., and Reid, M. J. (2006). Full-polarization observations of OH masers in massive star-forming regions. II. Maser properties and the interpretation of polarization. *Astrophys. J. Suppl. Ser.* 164, 99–123. doi: 10.1086/502650

Fissel, L. M., Ade, P. A. R., Angilè, F. E., Ashton, P., Benton, S. J., Devlin, M. J., et al. (2016). Balloon-borne submillimeter polarimetry of the vela C molecular cloud: systematic dependence of polarization fraction on column density and local polarization-angle dispersion. *Astrophys. J.* 824:134. doi: 10.3847/0004-637X/824/2/134

Frank, A., Ray, T. P., Cabrit, S., Hartigan, P., Arce, H. G., Bacciotti, F., et al. (2014). "Jets and outflows from star to cloud: observations confront theory," in *Protostars and Planets VI*, eds H. Beuther, R. S. Klessen, C. P. Dullemond, and T. Henning (Tucson, AZ: University of Arizona Press), 451–474. doi: 10.2458/azu_uapress_9780816531240-ch020

Frau, P., Galli, D., and Girart, J. M. (2011). Comparing star formation models with interferometric observations of the protostar NGC 1333 IRAS 4A. I. Magnetohydrodynamic collapse models. *Astron. Astrophys.* 535:A44. doi: 10.1051/0004-6361/201117813

Frau, P., Girart, J. M., Zhang, Q., and Rao, R. (2014). Shaping a high-mass star-forming cluster through stellar feedback. The case of the NGC 7538 IRS 1-3 complex. *Astron. Astrophys.* 567:A116. doi: 10.1051/0004-6361/201423917

Galametz, M., Maury, A., Girart, J. M., Rao, R., Zhang, Q., Gaudel, M., et al. (2018). SMA observations of the polarized dust emission in solar-type Class 0 protostars: the magnetic field properties at envelope scales. *Astron. Astrophys.* 616:A139. doi: 10.1051/0004-6361/201833004

Galitzki, N., Ade, P. A. R., Angilè, F. E., Ashton, P., Beall, J. A., Becker, D., et al. (2014). The next generation BLAST experiment. *J. Astron. Instrum.* 3:1440001. doi: 10.1142/S2251171714400017

Galli, D., Lizano, S., Shu, F. H., and Allen, A. (2006). Gravitational collapse of magnetized clouds. I. Ideal magnetohydrodynamic accretion flow. *Astrophys. J.* 647, 374–381. doi: 10.1086/505257

Galli, D., and Shu, F. H. (1993a). Collapse of magnetized molecular cloud cores. I. Semianalytical solution. *Astrophys. J.* 417:220. doi: 10.1086/173305

Galli, D., and Shu, F. H. (1993b). Collapse of magnetized molecular cloud cores. II. Numerical results. *Astrophys. J.* 417:243. doi: 10.1086/173306

Gandilo, N. N., Ade, P. A. R., Angilè, F. E., Ashton, P., Benton, S. J., Devlin, M. J., et al. (2016). Submillimeter polarization spectrum in the vela C molecular cloud. *Astrophys. J.* 824:84. doi: 10.3847/0004-637X/824/2/84

Ginsburg, A., Bally, J., Battersby, C., Youngblood, A., Darling, J., Rosolowsky, E., et al. (2015). The dense gas mass fraction in the W51 cloud and its protoclusters. *Astron. Astrophys.* 573:A106. doi: 10.1051/0004-6361/201424979

Ginsburg, A., Goss, W. M., Goddi, C., Galván-Madrid, R., Dale, J. E., Bally, J., et al. (2016). Toward gas exhaustion in the W51 high-mass protoclusters. *Astron. Astrophys.* 595:A27. doi: 10.1051/0004-6361/201628318

Girart, J. M., Beltrán, M. T., Zhang, Q., Rao, R., and Estalella, R. (2009). Magnetic fields in the formation of massive stars. *Science* 324:1408. doi: 10.1126/science.1171807

Girart, J. M., Crutcher, R. M., and Rao, R. (1999). Detection of polarized CO emission from the molecular outflow in NGC 1333 IRAS 4A. *Astrophys. J. Lett.* 525, L109–L112. doi: 10.1086/312345

Girart, J. M., Fernandez-Lopez, M., Li, Z.-Y., Yang, H., Estalella, R., Anglada, G., et al. (2018). Resolving the polarized dust emission of the disk around the massive star powering the HH80-81 radio jet. *Astrophys. J. Lett.* 856:L27. doi: 10.3847/2041-8213/aab76b

Girart, J. M., Frau, P., Zhang, Q., Koch, P. M., Qiu, K., Tang, Y.-W., et al. (2013). DR 21(OH): a highly fragmented, magnetized, turbulent dense core. *Astrophys. J.* 772:69. doi: 10.1088/0004-637X/772/1/69

Girart, J. M., Greaves, J. S., Crutcher, R. M., and Lai, S.-P. (2004). BIMA and JCMT spectropolarimetric observations of the CO J = 2 - 1 line towards Orion KL/IRc2. *Astrophys. Space Sci.* 292, 119–125. doi: 10.1023/B:ASTR.0000045007.35868.17

Girart, J. M., Rao, R., and Marrone, D. P. (2006). Magnetic fields in the formation of sun-like stars. *Science* 313, 812–814. doi: 10.1126/science.1129093

Girart, J. M., Rao, R., and Marrone, D. P. (2008). SMA observations of the magnetic fields around a low-mass protostellar system. *Astrophys. Space Sci.* 313, 87–90. doi: 10.1007/s10509-007-9592-7

Glenn, J., Walker, C. K., Bieging, J. H., and Jewell, P. R. (1997). Millimeter-wave spectropolarimetry of evolved stars: evidence for polarized molecular line emission. *Astrophys. J. Lett.* 487, L89–L92. doi: 10.1086/310863

Goldreich, P., and Kylafis, N. D. (1981). On mapping the magnetic field direction in molecular clouds by polarization measurements. *Astrophys. J. Lett.* 243, L75–L78. doi: 10.1086/183446

Goldreich, P., and Kylafis, N. D. (1982). Linear polarization of radio frequency lines in molecular clouds and circumstellar envelopes. *Astrophys. J.* 253, 606–621. doi: 10.1086/159663

Gonçalves, J., Galli, D., and Girart, J. M. (2008). Modeling the magnetic field in the protostellar source NGC 1333 IRAS 4A. *Astron. Astrophys.* 490, L39–L42. doi: 10.1051/0004-6361:200810861

González-Casanova, D. F., and Lazarian, A. (2017). Velocity gradients as a tracer for magnetic fields. *Astrophys. J.* 835:41. doi: 10.3847/1538-4357/835/1/41

Gordon, M. S., Lopez-Rodriguez, E., Andersson, B.-G., Clarke, M., Coude, S., Moullet, A., et al. (2018). SOFIA community science I: HAWC+ Polarimetry of 30 Doradus. *eprint arXiv:1811.03100.*

Greaves, J. S., Holland, W. S., Friberg, P., and Dent, W. R. F. (1999). Polarized CO emission from molecular clouds. *Astrophys. J. Lett.* 512, L139–L142. doi: 10.1086/311888

Harris, R. J., Cox, E. G., Looney, L. W., Li, Z.-Y., Yang, H., Fernández-López, M., et al. (2018). ALMA observations of polarized 872 μm dust emission from the protostellar systems VLA 1623 and L1527. *Astrophys. J.* 861:91. doi: 10.3847/1538-4357/aac6ec

Heiles, C., and Crutcher, R. (2005). "Magnetic fields in diffuse HI and molecular clouds," in *Cosmic Magnetic Fields, Vol. 664 of Lecture Notes in Physics*, eds R. Wielebinski and R. Beck (Berlin: Springer Verlag), 137. doi: 10.1007/11369875_7

Heiles, C., Goodman, A. A., McKee, C. F., and Zweibel, E. G. (1993). "Magnetic fields in star-forming regions - Observations," in *Protostars and Planets III*, eds E. H. Levy and J. I. Lunine, 279–326.

Heitsch, F., Zweibel, E. G., Mac Low, M.-M., Li, P., and Norman, M. L. (2001). Magnetic field diagnostics based on far-infrared polarimetry: tests using numerical simulations. *Astrophys. J.* 561, 800–814. doi: 10.1086/323489

Hennebelle, P., and Chabrier, G. (2008). Analytical theory for the initial mass function: CO clumps and prestellar cores. *Astrophys. J.* 684, 395–410. doi: 10.1086/589916

Hennebelle, P., and Ciardi, A. (2009). Disk formation during collapse of magnetized protostellar cores. *Astron. Astrophys.* 506, L29–L32. doi: 10.1051/0004-6361/200913008

Hennebelle, P., and Inutsuka, S.-I. (2019). The role of magnetic field in molecular cloud formation and evolution. *Front. Astron. Space Sci. arXiv [Preprint]. arXiv:1902.00798.*

Hezareh, T., Wiesemeyer, H., Houde, M., Gusdorf, A., and Siringo, G. (2013). Non-Zeeman circular polarization of CO rotational lines in SNR IC 443. *Astron. Astrophys.* 558:A45. doi: 10.1051/0004-6361/201321900

Hildebrand, R. H. (1988). Magnetic fields and stardust. *Q. J. R. Astron. Soc.* 29, 327–351.

Hildebrand, R. H., Kirby, L., Dotson, J. L., Houde, M., and Vaillancourt, J. E. (2009). Dispersion of magnetic fields in molecular clouds. I. *Astrophys. J.* 696, 567–573. doi: 10.1088/0004-637X/696/1/567

Hoang, T., and Lazarian, A. (2009). Grain alignment induced by radiative torques: effects of internal relaxation of energy and complex radiation field. *Astrophys. J.* 697, 1316–1333. doi: 10.1088/0004-637X/697/2/1316

Houde, M., Dowell, C. D., Hildebrand, R. H., Dotson, J. L., Vaillancourt, J. E., Phillips, T. G., et al. (2004). Tracing the Magnetic Field in Orion A. *Astrophys. J.* 604, 717–740. doi: 10.1086/382067

Houde, M., Hezareh, T., Jones, S., and Rajabi, F. (2013). Non-zeeman circular polarization of molecular rotational spectral lines. *Astrophys. J.* 764:24. doi: 10.1088/0004-637X/764/1/24

Houde, M., Hull, C. L. H., Plambeck, R. L., Vaillancourt, J. E., and Hildebrand, R. H. (2016). Dispersion of magnetic fields in molecular clouds. IV. analysis of interferometry data. *Astrophys. J.* 820:38. doi: 10.3847/0004-637X/820/1/38

Houde, M., Rao, R., Vaillancourt, J. E., and Hildebrand, R. H. (2011). Dispersion of magnetic fields in molecular clouds. III. *Astrophys. J.* 733:109. doi: 10.1088/0004-637X/733/2/109

Houde, M., Vaillancourt, J. E., Hildebrand, R. H., Chitsazzadeh, S., and Kirby, L. (2009). Dispersion of magnetic fields in molecular clouds. II. *Astrophys. J.* 706, 1504–1516. doi: 10.1088/0004-637X/706/2/1504

Hughes, A. M., Hull, C. L. H., Wilner, D. J., and Plambeck, R. L. (2013). Interferometric upper limits on millimeter polarization of the disks around DG Tau, GM Aur, and MWC 480. *Astron. J.* 145:115. doi: 10.1088/0004-6256/145/4/115

Hughes, A. M., Wilner, D. J., Cho, J., Marrone, D. P., Lazarian, A., Andrews, S. M., et al. (2009). Stringent limits on the polarized submillimeter emission from protoplanetary disks. *Astrophys. J.* 704, 1204–1217. doi: 10.1088/0004-637X/704/2/1204

Hull, C. L. H., Carrasco-González, C., Williams, P. K. G., Girart, J. M., Robishaw, T., Galván-Madrid, R., et al. (2018a). "Magnetic fields in forming stars with the ngVLA," in *Science with a Next Generation Very Large Array, ASP Conference Series, Vol. 517, ASP Monograph 7*, ed E. Murphy. 357.

Hull, C. L. H., Girart, J. M., Tychoniec, Ł., Rao, R., Cortés, P. C., Pokhrel, R., et al. (2017b). ALMA observations of dust polarization and molecular line emission from the class 0 protostellar source serpens SMM1. *Astrophys. J.* 847:92. doi: 10.3847/1538-4357/aa7fe9

Hull, C. L. H., Mocz, P., Burkhart, B., Goodman, A. A., Girart, J. M., Cortés, P. C., et al. (2017a). Unveiling the role of the magnetic field at the smallest scales of star formation. *Astrophys. J. Lett.* 842:L9. doi: 10.3847/2041-8213/aa71b7

Hull, C. L. H., and Plambeck, R. L. (2015). The 1.3 mm full-stokes polarization system at CARMA. *J. Astron. Instrum.* 4:1550005. doi: 10.1142/S2251171715500051

Hull, C. L. H., Plambeck, R. L., Bolatto, A. D., Bower, G. C., Carpenter, J. M., Crutcher, R. M., et al. (2013). Misalignment of Magnetic Fields and Outflows in Protostellar Cores. *Astrophys. J.* 768:159. doi: 10.1088/0004-637X/768/2/159

Hull, C. L. H., Plambeck, R. L., Kwon, W., Bower, G. C., Carpenter, J. M., Crutcher, R. M., et al. (2014). TADPOL: A 1.3 mm survey of dust polarization in star-forming cores and regions. *Astrophys. J. Suppl. Ser.* 213:13. doi: 10.1088/0067-0049/213/1/13

Hull, C. L. H., Yang, H., Li, Z.-Y., Kataoka, A., Stephens, I. W., Andrews, S., et al. (2018b). ALMA observations of polarization from dust scattering in the IM Lup protoplanetary disk. *Astrophys. J.* 860:82. doi: 10.3847/1538-4357/aabfeb

Hutawarakorn, B., Cohen, R. J., and Brebner, G. C. (2002). OH masers and magnetic fields in the bipolar outflow source W75N. *Month. Not. R. Astron. Soc.* 330, 349–364. doi: 10.1046/j.1365-8711.2002.05068.x

Isella, A., Hull, C. L. H., Moullet, A., Galván-Madrid, R., Johnstone, D., Ricci, L., et al. (2015). Next generation very large Array Memo No. 6, Science Working Group 1: the cradle of life. *arXiv [Preprints]. arXiv:1510.06444.*

Jensen, E. L. N., and Akeson, R. (2014). Misaligned protoplanetary disks in a young binary star system. *Nature* 511, 567–569. doi: 10.1038/nature13521

Joos, M., Hennebelle, P., and Ciardi, A. (2012). Protostellar disk formation and transport of angular momentum during magnetized core collapse. *Astron. Astrophys.* 543:A128. doi: 10.1051/0004-6361/201118730

Juárez, C., Girart, J. M., Zamora-Avilés, M., Tang, Y.-W., Koch, P. M., Liu, H. B., et al. (2017). Magnetized converging flows toward the hot core in the intermediate/high-mass star-forming region NGC 6334 V. *Astrophys. J.* 844:44. doi: 10.3847/1538-4357/aa78a6

Kataoka, A., Machida, M. N., and Tomisaka, K. (2012). Exploring magnetic field structure in star-forming cores with polarization of thermal dust emission. *Astrophys. J.* 761:40. doi: 10.1088/0004-637X/761/1/40

Kataoka, A., Muto, T., Momose, M., Tsukagoshi, T., and Dullemond, C. P. (2016a). Grain size constraints on HL tau with polarization signature. *Astrophys. J.* 820:54. doi: 10.3847/0004-637X/820/1/54

Kataoka, A., Muto, T., Momose, M., Tsukagoshi, T., Fukagawa, M., Shibai, H., et al. (2015). Millimeter-wave polarization of protoplanetary disks due to dust scattering. *Astrophys. J.* 809:78. doi: 10.1088/0004-637X/809/1/78

Kataoka, A., Tsukagoshi, T., Momose, M., Nagai, H., Muto, T., Dullemond, C. P., et al. (2016b). Submillimeter polarization observation of the protoplanetary disk around HD 142527. *Astrophys. J. Lett.* 831:L12. doi: 10.3847/2041-8205/831/2/L12

Kataoka, A., Tsukagoshi, T., Pohl, A., Muto, T., Nagai, H., Stephens, I. W., et al. (2017). The evidence of radio polarization induced by the radiative grain alignment and self-scattering of dust grains in a protoplanetary disk. *Astrophys. J. Lett.* 844:L5. doi: 10.3847/2041-8213/aa7e33

Kauffmann, J., Pillai, T., and Goldsmith, P. F. (2013). Low virial parameters in molecular clouds: implications for high-mass star formation and magnetic fields. *Astrophys. J.* 779:185. doi: 10.1088/0004-637X/779/2/185

Koch, P. M., Tang, Y., and Ho, P. T. P. (2010). Magnetic field properties in high-mass star formation from large to small scales: a statistical analysis from polarization data. *Astrophys. J.* 721, 815–827. doi: 10.1088/0004-637X/721/1/815

Koch, P. M., Tang, Y.-W., and Ho, P. T. P. (2012). Magnetic field strength maps for molecular clouds: a new method based on a polarization-intensity gradient relation. *Astrophys. J.* 747:79. doi: 10.1088/0004-637X/747/1/79

Koch, P. M., Tang, Y.-W., Ho, P. T. P., Yen, H.-W., Su, Y.-N., and Takakuwa, S. (2018). Polarization properties and magnetic field structures in the high-mass star-forming region W51 observed with ALMA. *Astrophys. J.* 855:39. doi: 10.3847/1538-4357/aaa4c1

Koch, P. M., Tang, Y.-W., Ho, P. T. P., Zhang, Q., Girart, J. M., Chen, H.-R. V., et al. (2014). The importance of the magnetic field from an SMA-CSO-combined sample of star-forming regions. *Astrophys. J.* 797:99. doi: 10.1088/0004-637X/797/2/99

Konigl, A., and Pudritz, R. E. (2000). "Disk winds and the accretion-outflow connection," in *Protostars Planets IV*, eds V. Mannings, A. P. BOSS, and S. S. Russell (Tucson: The University of Arizona Press), 759.

Kratter, K. M., Matzner, C. D., Krumholz, M. R., and Klein, R. I. (2010). On the role of disks in the formation of stellar systems: a numerical parameter study of rapid accretion. *Astrophys. J.* 708, 1585–1597. doi: 10.1088/0004-637X/708/2/1585

Krumholz, M. R., Crutcher, R. M., and Hull, C. L. H. (2013). Protostellar disk formation enabled by weak, misaligned magnetic fields. *Astrophys. J. Lett.* 767, L11–L15. doi: 10.1088/2041-8205/767/1/L11

Krumholz, M. R., and Federrath, C. (2019). The role of magnetic fields in setting the star formation rate and the initial mass function. *Front. Astron. Space Sci.* 6:7. doi: 10.3389/fspas.2019.00007

Kwon, J., Doi, Y., Tamura, M., Matsumura, M., Pattle, K., Berry, D., et al. (2018). A first look at BISTRO observations of the ρ Oph-A core. *Astrophys. J.* 859:4. doi: 10.3847/1538-4357/aabd82

Kwon, W., Looney, L. W., Crutcher, R. M., and Kirk, J. M. (2006). Two bipolar outflows and magnetic fields in the multiple protostar system L1448 IRS 3. *Astrophys. J.* 653, 1358–1368. doi: 10.1086/508920

Kylafis, N. D. (1983). Polarization of interstellar radio-frequency lines and magnetic field direction. *Astrophys. J.* 267, 137–150. doi: 10.1086/160851

Lada, C. J., and Lada, E. A. (2003). Embedded clusters in molecular clouds. *Annu. Rev. Astron. Astrophys.* 41, 57–115. doi: 10.1146/annurev.astro.41.011802.094844

Lai, S.-P., Crutcher, R. M., Girart, J. M., and Rao, R. (2001). Interferometric mapping of magnetic fields in star-forming regions. I. W51 e1/e2 Molecular Cores. *Astrophys. J.* 561, 864–870. doi: 10.1086/323372

Lai, S.-P., Crutcher, R. M., Girart, J. M., and Rao, R. (2002). Interferometric mapping of magnetic fields in star-forming regions. II. NGC 2024 FIR 5. *Astrophys. J.* 566, 925–930. doi: 10.1086/338336

Lai, S.-P., Girart, J. M., and Crutcher, R. M. (2003). Interferometric mapping of magnetic fields in star-forming regions. III. Dust and CO Polarization in DR 21(OH). *Astrophys. J.* 598, 392–399. doi: 10.1086/378769

Larson, R. B. (1981). Turbulence and star formation in molecular clouds. *Month. Not. R. Astron. Soc.* 194, 809–826. doi: 10.1093/mnras/194.4.809

Lazarian, A. (2007). Tracing magnetic fields with aligned grains. *J. Quant. Spec. Radiat. Transf.* 106, 225–256. doi: 10.1016/j.jqsrt.2007.01.038

Lee, C.-F., Hwang, H.-C., Ching, T.-C., Hirano, N., Lai, S.-P., Rao, R., et al. (2018a). Unveiling a magnetized jet from a low-mass protostar. *Nat. Commun.* 9:4636. doi: 10.1038/s41467-018-07143-8

Lee, C.-F., Li, Z.-Y., Ching, T.-C., Lai, S.-P., and Yang, H. (2018b). ALMA dust polarization observations of two young edge-on protostellar disks. *Astrophys. J.* 854:56. doi: 10.3847/1538-4357/aaa769

Lee, C.-F., Rao, R., Ching, T.-C., Lai, S.-P., Hirano, N., Ho, P. T. P., et al. (2014). Magnetic field structure in the flattened envelope and jet in the young protostellar system HH 211. *Astrophys. J. Lett.* 797:L9. doi: 10.1088/2041-8205/797/1/L9

Lee, J.-E., Lee, S., Dunham, M. M., Tatematsu, K., Choi, M., Bergin, E. A., et al. (2017). Formation of wide binaries by turbulent fragmentation. *Nat. Astron.* 1:0172. doi: 10.1038/s41550-017-0172

Lee, J. W. Y., Hull, C. L. H., and Offner, S. S. R. (2017). Synthetic observations of magnetic fields in protostellar cores. *Astrophys. J.* 834:201. doi: 10.3847/1538-4357/834/2/201

Lee, K. I., Dunham, M. M., Myers, P. C., Arce, H. G., Bourke, T. L., Goodman, A. A., et al. (2016). Misalignment of outflow axes in the proto-multiple systems in perseus. *Astrophys. J. Lett.* 820:L2. doi: 10.3847/2041-8205/820/1/L2

Lee, K. I., Dunham, M. M., Myers, P. C., Tobin, J. J., Kristensen, L. E., Pineda, J. E., et al. (2015). Mass assembly of stellar systems and their evolution with the SMA (MASSES). Multiplicity and the physical environment in L1448N. *Astrophys. J.* 814:114. doi: 10.1088/0004-637X/814/2/114

Li, H., Dowell, C. D., Kirby, L., Novak, G., and Vaillancourt, J. E. (2008). Design and initial performance of SHARP, a polarimeter for the SHARC-II camera at the Caltech Submillimeter Observatory. *Appl. Opt.* 47, 422–430. doi: 10.1364/AO.47.000422

Li, H., Griffin, G. S., Krejny, M., Novak, G., Loewenstein, R. F., Newcomb, M. G., et al. (2006). Results of SPARO 2003: mapping magnetic fields in giant molecular clouds. *Astrophys. J.* 648, 340–354. doi: 10.1086/505858

Li, H.-b., Dowell, C. D., Goodman, A., Hildebrand, R., and Novak, G. (2009). Anchoring magnetic field in turbulent molecular clouds. *Astrophys. J.* 704, 891–897. doi: 10.1088/0004-637X/704/2/891

Li, H. B., Yuen, K. H., Otto, F., Leung, P. K., Sridharan, T. K., Zhang, Q., et al. (2015). Self-similar fragmentation regulated by magnetic fields in a region forming massive stars. *Nature* 520, 518–521. doi: 10.1038/nature14291

Li, Z.-Y., Krasnopolsky, R., and Shang, H. (2011). Non-ideal MHD effects and magnetic braking catastrophe in protostellar disk formation. *Astrophys. J.* 738:180. doi: 10.1088/0004-637X/738/2/180

Li, Z.-Y., Krasnopolsky, R., and Shang, H. (2013). Does magnetic-field-rotation misalignment solve the magnetic braking catastrophe in protostellar disk formation? *Astrophys. J.* 774:82. doi: 10.1088/0004-637X/774/1/82

Li, Z.-Y., Krasnopolsky, R., Shang, H., and Zhao, B. (2014). On the role of pseudodisk warping and reconnection in protostellar disk formation in turbulent magnetized cores. *Astrophys. J.* 793:130. doi: 10.1088/0004-637X/793/2/130

Lis, D. C., Goldsmith, P. F., Dickman, R. L., Predmore, C. R., Omont, A., and Cernicharo, J. (1988). Linear polarization of millimeter-wave emission lines in clouds without large velocity gradients. *Astrophys. J.* 328, 304–314. doi: 10.1086/166293

Liu, H. B., Hasegawa, Y., Ching, T.-C., Lai, S.-P., Hirano, N., and Rao, R. (2018). Detection of 40-48 GHz dust continuum linear polarization towards the Class 0 young stellar object IRAS 16293-2422. *Astron. Astrophys.* 617:A3. doi: 10.1051/0004-6361/201832699

Liu, H. B., Lai, S.-P., Hasegawa, Y., Hirano, N., Rao, R., Li, I.-H., et al. (2016). Detection of linearly polarized 6.9 mm continuum emission from the class 0 young stellar object NGC 1333 IRAS4A. *Astrophys. J.* 821:41. doi: 10.3847/0004-637X/821/1/41

Liu, H. B., Qiu, K., Zhang, Q., Girart, J. M., and Ho, P. T. P. (2013). Gas kinematics and the dragged magnetic field in the high-mass molecular outflow source G192.16-3.84: an SMA View. *Astrophys. J.* 771:71. doi: 10.1088/0004-637X/771/1/71

Lopez-Rodriguez, E., Antonucci, R., Chary, R.-R., and Kishimoto, M. (2018). The highly polarized dusty emission core of cygnus A. *Astrophys. J. Lett.* 861:L23. doi: 10.3847/2041-8213/aacff5

Lu, X., Zhang, Q., Liu, H. B., Sanhueza, P., Tatematsu, K., Feng, S., et al. (2018). Filamentary fragmentation and accretion in high-mass star-forming molecular clouds. *Astrophys. J.* 855:9. doi: 10.3847/1538-4357/aaad11

Machida, M. N., Matsumoto, T., Hanawa, T., and Tomisaka, K. (2006). Evolution of rotating molecular cloud core with oblique magnetic field. *Astrophys. J.* 645, 1227–1245. doi: 10.1086/504423

Masson, J., Chabrier, G., Hennebelle, P., Vaytet, N., and Commerçon, B. (2016). Ambipolar diffusion in low-mass star formation. I. General comparison with the ideal magnetohydrodynamic case. *Astron. Astrophys.* 587:A32. doi: 10.1051/0004-6361/201526371

Matthews, B. C., Lai, S.-P., Crutcher, R. M., and Wilson, C. D. (2005). Multiscale magnetic fields in star-forming regions: interferometric polarimetry of the MMS 6 core of OMC-3. *Astrophys. J.* 626, 959–965. doi: 10.1086/430127

Matthews, B. C., McPhee, C. A., Fissel, L. M., and Curran, R. L. (2009). The legacy of SCUPOL: 850 μm imaging polarimetry from 1997 to 2005. *Astrophys. J. Suppl. Ser.* 182, 143–204. doi: 10.1088/0067-0049/182/1/143

Maury, A. J., Girart, J. M., Zhang, Q., Hennebelle, P., Keto, E., Rao, R., et al. (2018). Magnetically regulated collapse in the B335 protostar? I. ALMA observations of the polarized dust emission. *Month. Not. R. Astron. Soc.* 477, 2760–2765. doi: 10.1093/mnras/sty574

McKee, C. F., and Tan, J. C. (2003). The formation of massive stars from turbulent cores. *Astrophys. J.* 585, 850–871. doi: 10.1086/346149

McMullin, J. P., Waters, B., Schiebel, D., Young, W., and Golap, K. (2007). "CASA architecture and applications," In *Astronomical Data Analysis Software and Systems XVI, Vol. 376 of Astronomical Society of the Pacific Conference Series, Vol. 376*, eds R. A. Shaw, F. Hill, and D. J. Bell (Arizona), 127.

Mellon, R. R., and Li, Z.-Y. (2008). Magnetic braking and protostellar disk formation: the ideal MHD limit. *Astrophys. J.* 681, 1356–1376. doi: 10.1086/587542

Ménard, F., and Duchêne, G. (2004). On the alignment of Classical T Tauri stars with the magnetic field in the Taurus-Auriga molecular cloud. *Astron. Astrophys.* 425, 973–980. doi: 10.1051/0004-6361:20041338

Mestel, L., and Spitzer, L., Jr. (1956). Star formation in magnetic dust clouds. *Month. Not. R. Astron. Soc.* 116:503. doi: 10.1093/mnras/116.5.503

Mocz, P., Burkhart, B., Hernquist, L., McKee, C. F., and Springel, V. (2017). Moving-mesh simulations of star-forming cores in magneto-gravo-turbulence. *Astrophys. J.* 838:40. doi: 10.3847/1538-4357/aa6475

Motte, F., Bontemps, S., and Louvet, F. (2018). High-mass star and massive cluster formation in the milky way. 56, 41–82. doi: 10.1146/annurev-astro-091916-055235

Mouschovias, T. C. (1976a). Nonhomologous contraction and equilibria of self-gravitating, magnetic interstellar clouds embedded in an intercloud medium: star formation. I Formulation of the problem and method of solution. *Astrophys. J.* 206, 753–767. doi: 10.1086/154436

Mouschovias, T. C. (1976b). Nonhomologous contraction and equilibria of self-gravitating, magnetic interstellar clouds embedded in an intercloud medium: star formation. II - Results. *Astrophys. J.* 207, 141–158. doi: 10.1086/154478

Mouschovias, T. C. (1991). Magnetic braking, ambipolar diffusion, cloud cores, and star formation - Natural length scales and protostellar masses. *Astrophys. J.* 373, 169–186. doi: 10.1086/170035

Mouschovias, T. C., and Ciolek, G. E. (1999). "Magnetic fields and star formation: a theory reaching adulthood," in *NATO Advanced Science Institutes (ASI) Series C*, eds C. J. Lada and N. D. Kylafis, 305.

Offner, S. S. R. and Chaban, J. (2017). Impact of protostellar outflows on turbulence and star formation efficiency in magnetized dense cores. *Astrophys. J.* 847:104. doi: 10.3847/1538-4357/aa8996

Offner, S. S. R., Dunham, M. M., Lee, K. I., Arce, H. G., and Fielding, D. B. (2016). The turbulent origin of outflow and spin misalignment in multiple star systems. *Astrophys. J. Lett.* 827:L11. doi: 10.3847/2041-8205/827/1/L11

Ohashi, N., Saigo, K., Aso, Y., Aikawa, Y., Koyamatsu, S., Machida, M. N., et al. (2014). Formation of a keplerian disk in the infalling envelope around L1527 IRS: transformation from infalling motions to kepler motions. *Astrophys. J.* 796:131. doi: 10.1088/0004-637X/796/2/131

Ohashi, S., Kataoka, A., Nagai, H., Momose, M., Muto, T., Hanawa, T., et al. (2018). Two different grain size distributions within the protoplanetary disk around HD 142527 revealed by ALMA polarization observation. *Astrophys. J.* 864:81. doi: 10.3847/1538-4357/aad632

Ohashi, S., Sanhueza, P., Chen, H.-R. V., Zhang, Q., Busquet, G., Nakamura, F., et al. (2016). Dense core properties in the infrared dark cloud G14.225-0.506 revealed by ALMA. *Astrophys. J.* 833:209. doi: 10.3847/1538-4357/833/2/209

Ossenkopf, V., and Henning, T. (1994). Dust opacities for protostellar cores. *Astron. Astrophys.* 291, 943–959.

Ostriker, E. C., Stone, J. M., and Gammie, C. F. (2001). Density, velocity, and magnetic field structure in turbulent molecular cloud models. *Astrophys. J.* 546, 980–1005. doi: 10.1086/318290

Padovani, M., Brinch, C., Girart, J. M., Jørgensen, J. K., Frau, P., Hennebelle, P., et al. (2012). Adaptable radiative transfer innovations for submillimetre telescopes (ARTIST). Dust polarisation module (DustPol). *Astron. Astrophys.* 543:A16. doi: 10.1051/0004-6361/201219028

Pattle, K., Ward-Thompson, D., Berry, D., Hatchell, J., Chen, H.-R., Pon, A., et al. (2017). The JCMT BISTRO survey: the magnetic field strength in the Orion A filament. *Astrophys. J.* 846:122. doi: 10.3847/1538-4357/aa80e5

Pattle, K., Ward-Thompson, D., Hasegawa, T., Bastien, P., Kwon, W., Lai, S.-P., et al. (2018). First observations of the magnetic field inside the Pillars of Creation: results from the BISTRO survey. *Astrophys. J. Lett.* 860:L6. doi: 10.3847/2041-8213/aac771

Pillai, T., Kauffmann, J., Wyrowski, F., Hatchell, J., Gibb, A. G., and Thompson, M. A. (2011). Probing the initial conditions of high-mass star formation. II. Fragmentation, stability, and chemistry towards high-mass star-forming regions G29.96-0.02 and G35.20-1.74. *Astron. Astrophys.* 530:A118. doi: 10.1051/0004-6361/201015899

Plambeck, R. L., Wright, M. C. H., and Rao, R. (2003). Magnetic field morphology of Orion IRc2 from 86 GHz SiO maser polarization images. *Astrophys. J.* 594, 911–918. doi: 10.1086/377097

Planck Collaboration, Adam, R., Ade, P. A. R., Aghanim, N., Alves, M. I. R., and et al. (2016a). Planck intermediate results. XXXII. The relative orientation between the magnetic field and structures traced by interstellar dust. *Astron. Astrophys.* 586:A135. doi: 10.1051/0004-6361/201425044

Planck Collaboration, Ade, P. A. R., Aghanim, N., Alina, D., Alves, M. I. R., and et al. (2015b). Planck intermediate results. XIX. An overview of the polarized thermal emission from Galactic dust. *Astron. Astrophys.* 576:A104. doi: 10.1051/0004-6361/201424082

Planck Collaboration, Ade, P. A. R., Aghanim, N., Alina, D., Alves, M. I. R., Aniano, G., et al. (2015a). Planck intermediate results. XX. Comparison of polarized thermal emission from Galactic dust with simulations of MHD turbulence. *Astron. Astrophys.* 576:A105. doi: 10.1051/0004-6361/201424086

Planck Collaboration, Ade, P. A. R., Aghanim, N., Alina, D., Aniano, G., Armitage-Caplan, C., et al. (2015c). Planck intermediate results. XXI. Comparison of polarized thermal emission from Galactic dust at 353 GHz with interstellar polarization in the visible. *Astron. Astrophys.* 576:A106. doi: 10.1051/0004-6361/201424087

Planck Collaboration, Ade, P. A. R., Aghanim, N., Alves, M. I. R., Arnaud, M., Arzoumanian, D., et al. (2016b). Planck intermediate results. XXXIII. Signature of the magnetic field geometry of interstellar filaments in dust polarization maps. *Astron. Astrophys.* 586:A136. doi: 10.1051/0004-6361/201425305

Planck Collaboration, Ade, P. A. R., Aghanim, N., Alves, M. I. R., Arnaud, M., Arzoumanian, D., et al. (2016c). Planck intermediate results. XXXV. Probing the role of the magnetic field in the formation of structure in molecular clouds. *Astron. Astrophys.* 586:A138. doi: 10.1051/0004-6361/201525896

Pohl, A., Kataoka, A., Pinilla, P., Dullemond, C. P., Henning, T., and Birnstiel, T. (2016). Investigating dust trapping in transition disks with millimeter-wave polarization. *Astron. Astrophys.* 593:A12. doi: 10.1051/0004-6361/201628637

Qiu, K., Zhang, Q., Menten, K. M., Liu, H. B., and Tang, Y.-W. (2013). From poloidal to toroidal: detection of a well-ordered magnetic field in the high-mass protocluster G35.2-0.74 N. *Astrophys. J.* 779:182. doi: 10.1088/0004-637X/779/2/182

Qiu, K., Zhang, Q., Menten, K. M., Liu, H. B., Tang, Y.-W., and Girart, J. M. (2014). Submillimeter array observations of magnetic fields in G240.31+0.07: an hourglass in a massive cluster-forming core. *Astrophys. J. Lett.* 794:L18. doi: 10.1088/2041-8205/794/1/L18

Qiu, K., Zhang, Q., Wu, J., and Chen, H.-R. (2009). Submillimeter array observations of the molecular outflow in high-mass star-forming region G240.31+0.07. *Astrophys. J.* 696, 66–74. doi: 10.1088/0004-637X/696/1/66

Rao, R., Crutcher, R. M., Plambeck, R. L., and Wright, M. C. H. (1998). High-resolution millimeter-wave mapping of linearly polarized dust emission: magnetic field structure in Orion. *Astrophys. J. Lett.* 502:L75. doi: 10.1086/311485

Rao, R., Girart, J. M., Lai, S.-P., and Marrone, D. P. (2014). Detection of a magnetized disk around a very young protostar. *Astrophys. J. Lett.* 780:L6. doi: 10.1088/2041-8205/780/1/L6

Rao, R., Girart, J. M., Marrone, D. P., Lai, S.-P., and Schnee, S. (2009). IRAS 16293: a "Magnetic" tale of two cores. *Astrophys. J.* 707, 921–935. doi: 10.1088/0004-637X/707/2/921

Renbarger, T., Chuss, D. T., Dotson, J. L., Griffin, G. S., Hanna, J. L., Loewenstein, R. F., et al. (2004). Early results from SPARO: instrument characterization and polarimetry of NGC 6334. *Publ. ASP* 116, 415–424. doi: 10.1086/383623

Ritacco, A., Ponthieu, N., Catalano, A., Adam, R., Ade, P., André, P., et al. (2017). Polarimetry at millimeter wavelengths with the NIKA camera: calibration and performance. *Astron. Astrophys.* 599:A34. doi: 10.1051/0004-6361/201629666

Robitaille, T., and Bressert, E. (2012). APLpy: astronomical plotting library in python. *Astrophysics Source Code Library.*

Roy, A., Ade, P. A. R., Bock, J. J., Chapin, E. L., Devlin, M. J., Dicker, S. R., et al. (2011). The balloon-borne large aperture submillimeter telescope (BLAST) 2005: a 10 deg^2 survey of star formation in cygnus X. *Astrophys. J.* 727:114. doi: 10.1088/0004-637X/727/2/114

Sadavoy, S. I., Myers, P. C., Stephens, I. W., Tobin, J., Commercon, B., Henning, T., et al. (2018a). Dust polarization toward embedded protostars in ophiuchus with ALMA. I. VLA 1623. *Astrophys. J.* 859:165. doi: 10.3847/1538-4357/aac21a

Sadavoy, S. I., Myers, P. C., Stephens, I. W., Tobin, J., Kwon, W., Segura-Cox, D., et al. (2018b). Dust polarization toward embedded protostars in ophiuchus with ALMA. II. IRAS 16293-2422. *Astrophys. J.* 869:115. doi: 10.3847/1538-4357/aaef81

Sanhueza, P., Jackson, J. M., Zhang, Q., Guzmán, A. E., Lu, X., Stephens, I. W., et al. (2017). A massive prestellar clump hosting no high-mass cores. *Astrophys. J.* 841:97. doi: 10.3847/1538-4357/aa6ff8

Santos-Lima, R., de Gouveia Dal Pino, E. M., and Lazarian, A. (2012). The role of turbulent magnetic reconnection in the formation of rotationally supported protostellar disks. *Astrophys. J.* 747:21. doi: 10.1088/0004-637X/747/1/21

Saral, G., Hora, J. L., Audard, M., Koenig, X. P., Martínez-Galarza, J. R., Motte, F., et al. (2017). Young stellar objects in the massive star-forming regions W51 and W43. *Astrophys. J.* 839:108. doi: 10.3847/1538-4357/aa6575

Schleuning, D. A. (1998). Far-infrared and submillimeter polarization of OMC-1: evidence for magnetically regulated star formation. *Astrophys. J.* 493:811. doi: 10.1086/305139

Segura-Cox, D. M., Looney, L. W., Stephens, I. W., Fernández-López, M., Kwon, W., Tobin, J. J., et al. (2015). The magnetic field in the class 0 protostellar disk of L1527. *Astrophys. J. Lett.* 798:L2. doi: 10.1088/2041-8205/798/1/L2

Segura-Cox, D. M., Looney, L. W., Tobin, J. J., Li, Z.-Y., Harris, R. J., Sadavoy, S., et al. (2018). The VLA nascent disk and multiplicity survey of perseus protostars (VANDAM). V. 18 Candidate Disks around Class 0 and I Protostars in the Perseus Molecular Cloud. *Astrophys. J.* 866:161. doi: 10.3847/1538-4357/aaddf3

Seifried, D., Banerjee, R., Pudritz, R. E., and Klessen, R. S. (2015). Accretion and magnetic field morphology around Class 0 stage protostellar discs. *Month. Not. R. Astron. Soc.* 446, 2776–2788. doi: 10.1093/mnras/stu2282

Shu, F. H., Adams, F. C., and Lizano, S. (1987). Star formation in molecular clouds - Observation and theory. *Annu. Rev. Astron. Astrophys.* 25, 23–81. doi: 10.1146/annurev.aa.25.090187.000323

Shu, F. H., Najita, J. R., Shang, H., and Li, Z.-Y. (2000). X-winds theory and observations. *Protostars and Planets IV*, eds V. Mannings, A. P. Boss, and S. S. Russell (Tucson: University of Arizona Pres), 789–814.

Siringo, G., Kovács, A., Kreysa, E., Schuller, F., Weiss, A., Guesten, R., et al. (2012). "First results of the polarimeter for the Large APEX Bolometer Camera (LABOCA)," in *Millimeter, Submillimeter, and Far-Infrared Detectors and Instrumentation for Astronomy VI*, 845206. doi: 10.1117/12.925697

Siringo, G., Kreysa, E., Reichertz, L. A., and Menten, K. M. (2004). A new polarimeter for (sub)millimeter bolometer arrays. *Astron. Astrophys.* 422, 751–760. doi: 10.1051/0004-6361:20035832

Soam, A., Pattle, K., Ward-Thompson, D., Lee, C. W., Sadavoy, S., Koch, P. M., et al. (2018). Magnetic fields towards Ophiuchus-B derived from SCUBA-2 polarization measurements. *Astrophys. J.* 861:65. doi: 10.3847/1538-4357/aac4a6

Sridharan, T. K., Rao, R., Qiu, K., Cortes, P., Li, H., Pillai, T., et al. (2014). Hot Core, outflows, and magnetic fields in W43-MM1 (G30.79 FIR 10). *Astrophys. J. Lett.* 783:L31. doi: 10.1088/2041-8205/783/2/L31

Stephens, I. W., Dunham, M. M., Myers, P. C., Pokhrel, R., Bourke, T. L., Vorobyov, E. I., et al. (2018). Mass assembly of stellar systems and their evolution with the SMA - 1.3 mm subcompact data release. *Astrophys. J. Suppl.* 237:22. doi: 10.3847/1538-4365/aacda9

Stephens, I. W., Dunham, M. M., Myers, P. C., Pokhrel, R., Sadavoy, S. I., Vorobyov, E. I., et al. (2017a). Alignment between protostellar outflows and filamentary structure. *Astrophys. J.* 846:16. doi: 10.3847/1538-4357/aa8262

Stephens, I. W., Looney, L. W., Dowell, C. D., Vaillancourt, J. E., and Tassis, K. (2011). The galactic magnetic field's effect in star-forming regions. *Astrophys. J.* 728:99. doi: 10.1088/0004-637X/728/2/99

Stephens, I. W., Looney, L. W., Kwon, W., Fernández-López, M., Hughes, A. M., Mundy, L. G., et al. (2014). Spatially resolved magnetic field structure in the disk of a T Tauri star. *Nature* 514, 597–599. doi: 10.1038/nature 13850

Stephens, I. W., Looney, L. W., Kwon, W., Hull, C. L. H., Plambeck, R. L., Crutcher, R. M., et al. (2013). The magnetic field morphology of the class 0 protostar L1157-mm. *Astrophys. J. Lett.* 769:L15. doi: 10.1088/2041-8205/769/1/L15

Stephens, I. W., Yang, H., Li, Z.-Y., Looney, L. W., Kataoka, A., Kwon, W., et al. (2017b). ALMA reveals transition of polarization pattern with wavelength in HL Tau's disk. *Astrophys. J.* 851:55. doi: 10.3847/1538-4357/aa998b

Takahashi, S., Machida, M. N., Tomisaka, K., Ho, P. T. P., Fomalont, E. B., Nakanishi, K. et al. (2019). ALMA high angular resolution polarization study: an extremely young class 0 source, OMC-3/MMS 6. *Astrophys. J.* 872:70. doi: 10.3847/1538-4357/aaf6ed

Takahashi, S., Saito, M., Takakuwa, S., and Kawabe, R. (2006). Millimeter- and submillimeter-wave observations of the OMC-2/3 region. I. Dispersing and rotating core around the intermediate-mass protostar MMS 7. *Astrophys. J.* 651, 933–944. doi: 10.1086/507482

Tang, Y.-W., Ho, P. T. P., Girart, J. M., Rao, R., Koch, P., and Lai, S.-P. (2009a). Evolution of magnetic fields in high mass star formation: submillimeter array dust polarization image of the ultracompact H II region G5.89-0.39. *Astrophys. J.* 695, 1399–1412. doi: 10.1088/0004-637X/695/2/1399

Tang, Y.-W., Ho, P. T. P., Koch, P. M., Girart, J. M., Lai, S.-P., and Rao, R. (2009b). Evolution of magnetic fields in high-mass star formation: linking field geometry and collapse for the W51 e2/e8 Cores. *Astrophys. J.* 700, 251–261. doi: 10.1088/0004-637X/700/1/251

Tang, Y.-W., Ho, P. T. P., Koch, P. M., and Rao, R. (2010). High-angular resolution dust polarization measurements: shaped B-field lines in the massive star-forming region Orion BN/KL. *Astrophys. J.* 717, 1262–1273. doi: 10.1088/0004-637X/717/2/1262

Targon, C. G., Rodrigues, C. V., Cerqueira, A. H., and Hickel, G. R. (2011). Correlating the interstellar magnetic field with protostellar jets and its sources. *Astrophys. J.* 743:54. doi: 10.1088/0004-637X/743/1/54

Tazaki, R., Lazarian, A., and Nomura, H. (2017). Radiative grain alignment in protoplanetary disks: implications for polarimetric observations. *Astrophys. J.* 839:56. doi: 10.3847/1538-4357/839/1/56

Tobin, J. J., Hartmann, L., Chiang, H.-F., Wilner, D. J., Looney, L. W., Loinard, L., et al. (2012). A Õ.2-solar-mass protostar with a Keplerian disk in the very young L1527 IRS system. *Nature* 492, 83–85. doi: 10.1038/nature 11610

Tobin, J. J., Kratter, K. M., Persson, M. V., Looney, L. W., Dunham, M. M., Segura-Cox, D., et al. (2016a). A triple protostar system formed via fragmentation of a gravitationally unstable disk. *Nature* 538, 483–486. doi: 10.1038/nature 20094

Tobin, J. J., Looney, L. W., Li, Z.-Y., Chandler, C. J., Dunham, M. M., Segura-Cox, D., et al. (2016b). The VLA nascent disk and multiplicity survey of perseus protostars (VANDAM). II. Multiplicity of protostars in the perseus molecular cloud. *Astrophys. J.* 818:73. doi: 10.3847/0004-637X/818/1/73

Tobin, J. J., Looney, L. W., Li, Z.-Y., Sadavoy, S. I., Dunham, M. M., Segura-Cox, D., et al. (2018). The VLA/ALMA Nascent Disk and Multiplicity (VANDAM) survey of perseus protostars. VI. Characterizing the formation mechanism for close multiple systems. 867:43. doi: 10.3847/1538-4357/aae1f7

Tomida, K., Okuzumi, S., and Machida, M. N. (2015). Radiation magnetohydrodynamic simulations of protostellar collapse: nonideal magnetohydrodynamic effects and early formation of circumstellar disks. *Astrophys. J.* 801:117. doi: 10.1088/0004-637X/801/2/117

Traficante, A., Lee, Y.-N., Hennebelle, P., Molinari, S., Kauffmann, J., and Pillai, T. (2018). A possible observational bias in the estimation of the virial parameter in virialized clumps. *Astron. Astrophys.* 619:L7. doi: 10.1051/0004-6361/201833513

Troland, T. H., and Heiles, C. (1986). Interstellar magnetic field strengths and gas densities Observational and theoretical perspectives. *Astrophys. J.* 301, 339–345. doi: 10.1086/163904

Tsukamoto, Y., Iwasaki, K., Okuzumi, S., Machida, M. N., and Inutsuka, S. (2015). Bimodality of circumstellar disk evolution induced by the hall current. *Astrophys. J. Lett.* 810:L26. doi: 10.1088/2041-8205/810/2/L26

Tsukamoto, Y., Okuzumi, S., Iwasaki, K., Machida, M. N., and Inutsuka, S. (2018). Does misalignment between magnetic field and angular momentum enhance or suppress circumstellar disk formation? *Astrophys. J.* 868:22. doi: 10.3847/1538-4357/aae4dc

Tsukamoto, Y., Okuzumi, S., Iwasaki, K., Machida, M. N., and Inutsuka, S.-i. (2017). The impact of the Hall effect during cloud core collapse: Implications for circumstellar disk evolution. *Publ. ASJ* 69:95. doi: 10.1093/pasj/psx113

Vaillancourt, J. E., Chuss, D. T., Crutcher, R. M., Dotson, J. L., Dowell, C. D., Harper, D. A., et al. (2007). "Far-infrared polarimetry from the Stratospheric Observatory for Infrared Astronomy," in *Infrared Spaceborne Remote Sensing and Instrumentation XV*, 66780D. doi: 10.1117/12.730922

Vallée, J. P., and Fiege, J. D. (2006). A cool filament crossing the warm protostar DR 21(OH): geometry, kinematics, magnetic vectors, and pressure balance. *Astrophys. J.* 636, 332–347. doi: 10.1086/497957

van Kempen, T. A., Hogerheijde, M. R., van Dishoeck, E. F., Kristensen, L. E., Belloche, A., Klaassen, P. D., et al. (2016). Outflow forces in intermediate-mass star formation. *Astron. Astrophys.* 587:A17. doi: 10.1051/0004-6361/201424725

Ward-Thompson, D., Pattle, K., Bastien, P., Furuya, R. S., Kwon, W., Lai, S.-P., et al. (2017). First results from BISTRO: a SCUBA-2 polarimeter survey of the gould belt. *Astrophys. J.* 842:66. doi: 10.3847/1538-4357/aa70a0

Wiesemeyer, H., Hezareh, T., Kreysa, E., Weiss, A., Güsten, R., Menten, K. M., et al. (2014). Submillimeter polarimetry with PolKa, a reflection-type modulator for the APEX telescope. *Publ. ASP* 126:1027. doi: 10.1086/679002

Wright, M. C. H., Hull, C. L. H., Pillai, T., Zhao, J.-H., and Sandell, G. (2014). NGC 7538 IRS 1: interaction of a polarized dust spiral and a molecular outflow. *Astrophys. J.* 796:112. doi: 10.1088/0004-637X/796/2/112

Wurster, J., Bate, M. R., and Price, D. J. (2018). Hall effect-driven formation of gravitationally unstable discs in magnetized molecular cloud cores. *Month. Not. R. Astron. Soc.* 480, 4434–4442. doi: 10.1093/mnras/sty2212

Wurster, J., and Li, Z.-Y. (2018). The role of magnetic fields in the formation of protostellar discs. *Front. Astron. Space Sci.* 5:39. doi: 10.3389/fspas.2018.00039

Yang, H., Li, Z.-Y., Looney, L., and Stephens, I. (2016a). Inclination-induced polarization of scattered millimetre radiation from protoplanetary discs: the case of HL Tau. *Month. Not. R. Astron. Soc.* 456, 2794–2805. doi: 10.1093/mnras/stv2633

Yang, H., Li, Z.-Y., Looney, L. W., Cox, E. G., Tobin, J., Stephens, I. W., et al. (2016b). Disc polarization from both emission and scattering of magnetically aligned grains: the case of NGC 1333 IRAS 4A1. *Month. Not. R. Astron. Soc.* 460, 4109–4121. doi: 10.1093/mnras/stw1253

Yang, H., Li, Z.-Y., Stephens, I. W., Kataoka, A., and Looney, L. (2019). Does HL Tau disk polarization in ALMA band 3 come from radiatively aligned grains? 483, 2371–2381. doi: 10.1093/mnras/sty3263

Yuen, K. H., and Lazarian, A. (2017). Tracing interstellar magnetic field using velocity gradient technique: application to atomic hydrogen data. *Astrophys. J. Lett.* 837:L24. doi: 10.3847/2041-8213/aa6255

Zhang, Q., and Ho, P. T. P. (1997). Dynamical collapse in W51 massive cores: NH_3 observations. *Astrophys. J.* 488, 241–257. doi: 10.1086/304667

Zhang, Q., Qiu, K., Girart, J. M., Liu, H. B., Tang, Y.-W., Koch, P. M., et al. (2014). Magnetic fields and massive star formation. *Astrophys. J.* 792:116. doi: 10.1088/0004-637X/792/2/116

Zhang, Q., Wang, K., Lu, X., and Jiménez-Serra, I. (2015). Fragmentation of molecular clumps and formation of a protocluster. *Astrophys. J.* 804:141. doi: 10.1088/0004-637X/804/2/141

Zhang, Q., Wang, Y., Pillai, T., and Rathborne, J. (2009). Fragmentation at the earliest phase of massive star formation. *Astrophys. J.* 696, 268–273. doi: 10.1088/0004-637X/696/1/268

Conflict of Interest Statement: The authors declare that the research was conducted in the absence of any commercial or financial relationships that could be construed as a potential conflict of interest.

The reviewer KQ declared a past co-authorship with one of the authors QZ to the handling editor.

frontiers in Astronomy and Space Sciences

REVIEW
published: 20 February 2019
doi: 10.3389/fspas.2019.00007

The Role of Magnetic Fields in Setting the Star Formation Rate and the Initial Mass Function

Mark R. Krumholz [1,2]* *and Christoph Federrath* [1,2]

[1] *Research School of Astronomy and Astrophysics, Australian National University, Canberra, ACT, Australia,* [2] *Centre of Excellence for Astronomy in Three Dimensions (ASTRO-3D), Canberra, ACT, Australia*

Star-forming gas clouds are strongly magnetized, and their ionization fractions are high enough to place them close to the regime of ideal magnetohydrodyamics on all but the smallest size scales. In this review we discuss the effects of magnetic fields on the star formation rate (SFR) in these clouds, and on the mass spectrum of the fragments that are the outcome of the star formation process, the stellar initial mass function (IMF). Current numerical results suggest that magnetic fields by themselves are minor players in setting either the SFR or the IMF, changing star formation rates and median stellar masses only by factors of $\sim 2-3$ compared to non-magnetized flows. However, the indirect effects of magnetic fields, via their interaction with star formation feedback in the form of jets, photoionization, radiative heating, and supernovae, could have significantly larger effects. We explore evidence for this possibility in current simulations, and suggest avenues for future exploration, both in simulations and observations.

Keywords: galaxies: star formation, ISM: clouds, ISM: kinematics and dynamics, ISM: magnetic fields, magnetohydrodynamics (MHD), stars: formation, turbulence

OPEN ACCESS

Edited by:
Yusuke Tsukamoto, Kagoshima University, Japan

Reviewed by:
Sami Marcel Dib, University of Copenhagen, Denmark
Stella Offner, University of Texas at Austin, United States

***Correspondence:**
Mark R. Krumholz
mark.krumholz@anu.edu.au

Specialty section:
This article was submitted to Stellar and Solar Physics, a section of the journal Frontiers in Astronomy and Space Sciences

Received: *03 September 2018*
Accepted: *29 January 2019*
Published: *20 February 2019*

Citation:
Krumholz MR and Federrath C (2019) The Role of Magnetic Fields in Setting the Star Formation Rate and the Initial Mass Function. Front. Astron. Space Sci. 6:7. doi: 10.3389/fspas.2019.00007

1. INTRODUCTION

Star-forming molecular clouds are threaded by magnetic fields that are likely inherited from the galactic-scale interstellar medium out of which they condensed (see the review by Hennebelle and Inutsuka in this volume). These fields certainly influence cloud morphology and evolution. However, it remains an open question to what extent magnetic fields set the main quantitative outcomes of the star formation process: the rate at which molecular clouds convert their gaseous mass into stars, and the distribution of the masses of the resultant stars. The goal of this review is to summarize current observational and theoretical evidence that points toward a quantitative answer to these questions.

1.1. Basic Physical Considerations

Any attempt to understand the role of magnetic fields in regulating the collapse and fragmentation of molecular clouds must begin from some basic physical considerations. The virial theorem provides a useful tool with which to describe the relative importance of magnetic forces in comparison to the forces of gravity, turbulent ram pressure, and thermal pressure. For a fixed control volume V containing fluid of density ρ and velocity $\mathbf{v}$, with magnetic field $\mathbf{B}$ and gravitational potential ϕ, this is (McKee and Zweibel, 1992)

$$\frac{1}{2}\ddot{I} = 2\left(\mathcal{T}-\mathcal{T}_0\right) + \left(\mathcal{B}-\mathcal{B}_0\right) + \mathcal{W} - \frac{1}{2}\frac{d}{dt}\int_{\partial V}\left(\rho \mathbf{v} r^2\right)\cdot d\mathbf{S}, \quad (1)$$

where $\ddot{I}$ is the second derivative of the moment of inertia of the mass inside V, $\mathcal{T} = (1/2)\int(3P+\rho v^2)\,dV$ is the total translational thermal plus kinetic energy, $\mathcal{B} = (1/8\pi)\int B^2\,dV$ is the total magnetic energy (with $B \equiv |\mathbf{B}|$), $\mathcal{W} = -\int \rho \mathbf{r}\cdot\nabla\phi\,dV$ is the gravitational potential energy, and $\mathcal{T}_0$ and $\mathcal{B}_0$ represent the fluid and magnetic stresses, respectively, across the surface of V. The right hand side of this equation expresses how the various forces together cause the material inside the volume to accelerate inward or outward. The final term, involving a time-derivative of the mass flux across the surface ∂V of volume V, represents the change in inertia within the control volume not due to forces, but instead due to bulk flows of mass across the boundary.

Taking ratios of the force terms on the right-hand side of the virial theorem to form dimensionless ratios yields numbers that express their relative importance. Taking the ratio of the magnetic term to the two parts of the kinetic term yields

$$\frac{\mathcal{B}}{(3/2)\int P\,dV} \sim \frac{B^2/8\pi}{P} \sim \beta^{-1} \quad (2)$$

and

$$\frac{\mathcal{B}}{(1/2)\int \rho v^2\,dV} \sim \frac{B^2/8\pi}{\rho v^2} \sim \left(\frac{v_A}{v}\right)^2 \sim \mathcal{M}_A^{-2}, \quad (3)$$

where

$$v_{\rm A} = \frac{B}{\sqrt{4\pi\rho}} \quad (4)$$

is the Alfvén speed. The quantities β and $\mathcal{M}_{\rm A}$ are the plasma β and Alfvén Mach number, respectively, and it is immediately clear that they describe the importance of magnetic forces in comparison to thermal and turbulent pressure. If $\beta \ll 1$, magnetic pressure greatly exceeds thermal pressure, and if $\mathcal{M}_A \ll 1$, magnetic pressure greatly exceeds turbulent pressure.

Similarly, taking the ratio of the magnetic and gravitational terms, and assuming that the volume's self-gravity dominates over any external field so that its gravitational energy may be expressed as $\mathcal{W} \sim -GM^2/R$, we have

$$\frac{\mathcal{B}}{\mathcal{W}} \sim \frac{B^2R^3/8\pi}{GM^2/R}, \quad (5)$$

where M is the mass within the volume and $R \sim V^{1/3}$ is its characteristic size. For ideal magnetohydrodynamics (MHD), the magnetic flux through the volume is fixed if there is no mass flux through its surface, and thus it is convenient to re-express this ratio in terms of the magnetic flux $\Phi_B \sim BR^2$, so that

$$\frac{\mathcal{B}}{\mathcal{W}} \sim \frac{\Phi_B^2}{GM^2} \sim \left(\frac{M_\Phi}{M}\right)^2 \sim \mu_\Phi^{-2}, \quad (6)$$

where

$$M_\Phi \equiv \frac{1}{2\pi}\frac{\Phi_B}{\sqrt{G}} \quad (7)$$

is the magnetic critical mass (Mouschovias and Spitzer, 1976), defined as the maximum mass that can be supported against collapse by a specified magnetic flux, and $\mu_\Phi = M/M_\Phi$ is the mass measured in units of M_Φ. Clouds with $\mu_\Phi < 1$ are called magnetically subcritical, while those with $\mu_\Phi > 1$ are called magnetically supercritical. Note that the exact coefficient in M_Φ depends weakly on the configuration of the mass; the value $1/2\pi$ we have adopted in Equation (7) is for an infinite thin sheet (Nakano and Nakamura, 1978), but other plausible configurations give results that differ from this by only $\sim 10\%$ (Tomisaka et al., 1988).

Before moving on, we offer two cautions. First, the dimensionless ratios $\mathcal{M}_A$, β, and μ_Φ that we have defined in order to characterize the importance of magnetic terms in the virial theorem do not include the surface fluid stress term $\mathcal{T}_0$, surface magnetic stress $\mathcal{B}_0$, and bulk flow term $(1/2)(d/dt)\int_V(\rho \mathbf{v} r^2)\cdot d\mathbf{S}$. Simulations show that these can make order unity contributions to the right hand side of Equation (1) (Dib et al., 2007), and the main reason we have omitted them is purely pragmatic: they are generally much more difficult to determine from observations than the volumetric terms. Nonetheless, we should keep in mind that conclusions about the relative importance of magnetic forces relative to others might be altered if we could properly include the hard-to-measure surface terms.

The second caution is that we have implicitly assumed that μ_Φ is a constant, which is true only if the flux is conserved. This holds for ideal MHD, but non-ideal effects must become important at some point in the star formation process, as evidenced by the fact that the magnetic fields of young stars are far weaker than would be expected if all of the magnetic flux that threads a typical $\sim 1\ M_\odot$ interstellar cloud were trapped in the star into which it collapses (e.g., Paleologou and Mouschovias, 1983). Current simulations suggest that most loss of magnetic flux occurs on the scales of individual protostellar disks or smaller (e.g., Tomida et al., 2015; Tsukamoto et al., 2015; Nolan et al., 2017; Vaytet et al., 2018; Wurster et al., 2018; Zhao et al., 2018; see Li et al., 2014 for a review of earlier work), a scale that is mostly too small to be important for the SFR or the IMF. The non-ideal mechanism that operates on the largest scales is ion-neutral drift, also known as ambipolar diffusion, which allows a redistribution of magnetic flux in weakly-ionized plasma due to imperfect coupling between ions and neutrals. The importance of this mechanism can be characterized by the ambipolar diffusion Reynolds number $R_{\rm AD}$ (Zweibel and Brandenburg, 1997; Li et al., 2006, 2008), a quantity comparable to the classical fluid Reynolds number: the latter measures the ratio of the size scale of a turbulent flow to the size scale on which viscous dissipation occurs, while the former measures the ratio the flow size scale to the scale on which ions and neutrals are able to separate from one another. Observed dense molecular clumps have $R_{\rm AD} \approx 20$ (McKee et al., 2010), which places them close to but not strongly in the regime of ideal MHD (corresponding to $R_{\rm AD} \to \infty$). For this reason we will

assume ideal MHD throughout most of this review, and briefly introduce non-ideal effects when they are particularly relevant.

1.2. Historical and Observational Background

Theories of how magnetic fields regulate the star formation rate (SFR) and the stellar initial mass function (IMF) can be classified is in terms of the assumptions they make, either implicitly or explicitly, about the values of the dimensionless ratios defined in section 1.1. There is little doubt that $\beta < 1$, since molecular clouds are very cold and have low thermal pressures, but there is much more uncertainty about the values of $\mathcal{M}_A$ and μ_Φ. The dominant model of star formation prior to ca. 2,000 implicitly assumed that molecular clouds also had both $\mathcal{M}_A < 1$ and $\mu_\Phi < 1$ (e.g., Shu et al., 1987; Mouschovias and Ciolek, 1999), i.e., their magnetic fields were strong enough that the pressure they provided was both stronger than the turbulent ram pressure and sufficient to prevent gravitational collapse. A model in which most molecular gas is subcritical leads to a picture of star formation in which the dominant physical processes are the non-ideal MHD mechanisms responsible for violation of flux-freezing, which allows μ_Φ to increase until it is greater than unity (i.e., the cloud becomes supercritical) and collapse can proceed. This would imply that the rate of star formation is controlled by the rate at which mass is able to cross from $\mu_\Phi < 1$ to $\mu_\Phi > 1$ by non-ideal MHD effects (e.g., Tassis and Mouschovias, 2004; Shu et al., 2007), and that the IMF is determined by the mass distribution of the resulting supercritical structures (e.g. Shu et al., 2004; Kunz and Mouschovias, 2009).

However, painstaking observational work in the past two decades, summarized in the review by Crutcher (2012), has called these assumptions into question. In particular, observations of Zeeman splitting provide a direct measurement of line-of-sight magnetic field strengths in molecular clouds, and Zeeman surveys have failed to detect a significant population of molecular clouds with $\mu_\Phi < 1$, in contrast to atomic clouds, which mostly have $\mu_\Phi < 1$). For molecular gas they instead suggest a distribution of μ_Φ values whereby μ_Φ^{-1} is nearly flat from 0 to 1, i.e., clouds are uniformly distributed from nearly non-magnetized ($\mu_\Phi^{-1} = 0$) to lying on the boundary of super- and subcritical ($\mu_\Phi^{-1} = 1$). This would imply that the median molecular cloud has $\mu_\Phi \approx 2$, and is therefore supercritical. There are a few possible caveats to this conclusion. First, as noted above, a measurement of μ_Φ only characterizes the importance of the volumetric magnetic field, not any potential contribution from magnetic stresses at cloud surfaces. Second, since the Zeeman effect only allows one to measure the line of sight magnetic field, inferences of the μ_Φ distribution depend on statistical analysis of measurements along multiple sight lines under the assumption that magnetic field orientations along these sight lines are randomly distributed; if there are magnetic alignments over sufficiently large scales, this assumption might fail, in which case the statistical power of the conclusion would be reduced. Nonetheless, we regard these possibilities as unlikely, and so for most of this review we will adopt the view that observations favor $\mu_\Phi > 1$.

The value of $\mathcal{M}_\mathrm{A}$ is less certain. Observations of polarized thermal emission or polarized optical absorption by dust gains permit detection of the plane of the sky orientation of magnetic fields. These suggest that fields are relatively well-ordered (e.g., Heyer and Brunt, 2012; Li H.-B. et al., 2015; Pattle et al., 2017; Soam et al., 2018, though in some cases alignment appears to break down at very small scales—Soam et al., 2015; Ching et al., 2017; Hull et al., 2017b), and that they align well with structures in the gas column density (e.g., Planck Collaboration et al., 2016); simulations suggest that such features will be present only in flows with $\mathcal{M}_A \lesssim 1$ (e.g., Li et al., 2013; Li P. S. et al., 2015; Federrath, 2016a; Tritsis and Tassis, 2016, 2018; Mocz et al., 2017; Tritsis et al., 2018). On the other hand, Padoan and Nordlund (1999) and Padoan et al. (2004) compare a wide range of statistics on the density, velocity, and magnetic field structure in molecular clouds to simulations with both $\mathcal{M}_\mathrm{A} \approx 1$ and $\mathcal{M}_\mathrm{A} \gg 1$, and conclude that only the latter are consistent with the observations. If $\mathcal{M}_\mathrm{A} \lesssim 1$, this would require that clouds be threaded by well-ordered fields with a significant net flux that dominate the total magnetic energy budget, while if $\mathcal{M}_\mathrm{A} \gtrsim 1$ the fields could be ordered, but they could also have a small net flux and be dominated by a disordered component (Mac Low, 1999; Brunt et al., 2010), such as that produced by a turbulent dynamo.

Regardless of whether $\mathcal{M}_\mathrm{A} \approx 1$ or $\mathcal{M}_\mathrm{A} \gg 1$, the observation that $\mu_\Phi > 1$ has led theoretical focus in the past few years to shift to models in which molecular clouds are assumed to be "born" supercritical (e.g., Padoan and Nordlund, 1999; Mac Low and Klessen, 2004; Krumholz and McKee, 2005), rather than having to transition to this state via some slow, non-ideal MHD process. In such a picture, the primary regulator of both the SFR and the IMF is usually assumed to be some combination of turbulence (strongly magnetized if $\mathcal{M}_\mathrm{A} \lesssim 1$, weakly magnetized otherwise) and stellar feedback; see Krumholz (2014) for a recent review. In this context, magnetic fields are doubtless important for shaping the morphology of the ISM, particularly as regards to the filaments ubiquitously observed in both real molecular clouds and simulations. For example, magnetic fields clearly seem to play some role in determining the orientations of filaments (e.g., Planck Collaboration et al., 2016), and may be responsible for setting their widths as well (e.g., Seifried and Walch, 2015; Federrath, 2016b; Federrath et al., 2016). The relative orientations of magnetic fields and filaments appears to carry important information about whether flows in molecular clouds are predominantly solenoidal/shearing or compressive (Soler and Hennebelle, 2017). However, it is not clear that these morphological factors are linked to the quantitative "outputs" of the star formation process, the SFR and IMF. Answering this question in the context of a cloud where $\mu_\Phi > 1$ is the focus of the remainder of this review.

2. MAGNETIC FIELDS AND THE STAR FORMATION RATE

In this section we examine the question of how magnetic fields affect the rate of star formation in molecular clouds. We begin in section 2.1 with a brief review of the state of observations

of the star formation rate, and in section 2.2 we discuss recent theoretical and numerical work on the role that magnetic fields might play in explaining these observations. In section 2.3 we highlight an important and but poorly explored frontier: the interaction between magnetic fields and stellar feedback.

2.1. Observational Constraints on the Star Formation Rate

Star formation is a remarkably slow and inefficient process across nearly all size and mass scales. In nearby galaxies, the observed molecular gas depletion time (defined as the time required to convert all molecular gas to stars at the current star formation rate) at scales of $\gtrsim$ 100 pc is $\sim$ 1 Gyr (e.g., Bigiel et al., 2008; Blanc et al., 2009; Schruba et al., 2011; Rahman et al., 2012; Leroy et al., 2013, 2017). In comparison, the gas in molecular clouds has densities $n \gtrsim 30$ cm^{-3}, corresponding to free-fall times of at most $t_{\rm ff} = \sqrt{3\pi/32G\mu_{\rm H} n} \lesssim 10$ Myr; here $\mu_{\rm H} = 2.34 \times 10^{-24}$ is the mean mass per H nucleus for standard interstellar medium (ISM) composition. This implies that the star formation rate is a factor of $\gtrsim$ 100 smaller than what would be expected for clouds collapsing to stars in free-fall.

Formally, we can parameterize the efficiency of star formation in terms of the quantity $\epsilon_{\rm ff}$, defined such that a gas cloud of mass M, volume V, and free-fall time $t_{\rm ff}$ (evaluated at its mean density, $\rho = M/V$), and star formation rate $\dot{M}_*$ has

$$\epsilon_{\rm ff} = \frac{\dot{M}_*}{M/t_{\rm ff}}. \tag{8}$$

Intuitively $\epsilon_{\rm ff}$ represents the ratio of the observed star formation rate in a region to the maximal rate that would be expected if gas were to collapse in free-fall with nothing to inhibit it. Normalizing to $t_{\rm ff}$ is critical when one wishes to compare samples across a wide range of size and density scales, since denser objects invariably have higher star formation rates per unit mass simply as a result of their shorter dynamical times. If one does not remove the dependence on dynamical time by measuring $\epsilon_{\rm ff}$, rather than, for example, the specific star formation rate $\dot{M}_*/M$, then anything that correlates with density will appear to correlate with star formation activity.

2.1.1. Counts of Young Stellar Objects

The observations discussed above imply that, measured at kpc scales, $\epsilon_{\rm ff} \lesssim 0.01$. However, it is possible to constrain $\epsilon_{\rm ff}$ more precisely, and on smaller scales, with a variety of techniques. The most direct method is simply to count young stellar objects (YSO) within resolved nearby molecular clouds. If one knows the mean duration of the observed YSO phase (e.g., if the observed YSOs are selected based on the presence of 24 μm excess, which several lines of evidence suggest persists for $\approx$ 2 Myr—Evans et al., 2009), then the mass of YSOs in that phase provides an estimate of the star formation rate. Combining this with a measurement of a mass and an estimate of the volume density (uncertain since the line of sight depth of a cloud cannot usually be measured directly), yields an observational estimate of $\epsilon_{\rm ff}$. In the past decade a number of studies have been published using this methodology (Krumholz et al., 2012a; Federrath, 2013b; Lada et al., 2013; Evans et al., 2014; Krumholz, 2014; Salim et al., 2015; Heyer et al., 2016; Ochsendorf et al., 2017), and all published studies are consistent with an estimate $\epsilon_{\rm ff} \approx 0.01$, with roughly a factor of 3 scatter and a factor of 3 systematic uncertainty, mainly coming from uncertainties in the gas density and the duration of the observed YSO phase[1].

There is at present no evidence for systematic variation of $\epsilon_{\rm ff}$, as opposed to systematic variation in the overall or specific star formation rate, with properties of the magnetic field. To date the only published study searching for magnetic effects on the star formation rate from observation is that of Li et al. (2017), who analyze the cloud samples of Heiderman et al. (2010) and Lada et al. (2010). They define the orientation of a cloud on the sky as the direction in which the observed extinction map has the largest autocorrelation, and find that the star formation rate per unit mass is systematically higher in clouds where the large-scale magnetic field and cloud orientation vectors are closer to parallel. However, Krumholz et al. (2012a) analyzed the same samples and found that $\epsilon_{\rm ff}$ is nearly the same in all of the clouds they contain. Consequently, the most natural interpretation of the Li et al. (2017) study is not that magnetic fields have an important effect on the star formation rate, but instead that denser clouds are more likely to have magnetic fields oriented along rather than orthogonal to their long axis, and that the apparent correlation between star formation and magnetic fields is simply a result of both correlating with density. In order to demonstrate that magnetic fields (or any other cloud property) is changing the nature of the star formation process, one would need to show not merely that the star formation rate as a whole changes with that property, but that the star formation rate per dynamical time (i.e., $\epsilon_{\rm ff}$) does. There is some evidence for such variations in $\epsilon_{\rm ff}$ as a function of Mach number (e.g., Federrath, 2013b; Salim et al., 2015; Sharda et al., 2018), but there have been no comparable observational efforts to search for variations in $\epsilon_{\rm ff}$ as a function of magnetic properties.

2.1.2. Alternative Methods

While YSO counting is the most direct and unambiguous method of estimating $\epsilon_{\rm ff}$, one can only use it in relatively nearby clouds due to the need to resolve individual YSOs[2]. More distant targets require different methods. Three in common use are pixel

[1]Note that Ochsendorf et al. (2017) measure $\epsilon_{\rm ff}$ in molecular clouds in the Large Magellanic Cloud using two separate methods: counts of massive ($M \gtrsim 8\ M_\odot$) YSOs, and a cloud matching technique as described below. Our statement here applies to their YSO counting method, which gives a distribution of $\epsilon_{\rm ff}$ with a median of $\log \epsilon_{\rm ff} = -1.7$ and a 16th–84th percentile range from $\log \epsilon_{\rm ff} = -2.03$ to -1.25, consistent with both the median and the spread of the other YSO counting studies within the systematic uncertainty. By contrast their cloud matching method gives a median $\log \epsilon_{\rm ff} = -1.3$ with a 16th–84th percentile range $\log \epsilon_{\rm ff} = 1.74$ to -0.69, as we discuss below. The numerical median and percentile ranges we quote are compiled by Krumholz et al. (2018b), who derive them from Table 6 of Ochsendorf et al. (2017).

[2]As noted above, it is possible to extend the YSO counting method to the Magellanic Clouds, but at the price of substantially reduced sensitivity and increased uncertainty, because at such large distances observations can at present detect only very massive YSOs, $M \gtrsim 8\ M_\odot$ (Ochsendorf et al., 2016, 2017), which must then be extrapolated to estimate the mass of the unseen population of lower mass stars. Both this extrapolation and timescales of massive YSO evolution (needed to complete the estimate of $\epsilon_{\rm ff}$) are substantially uncertain.

statistics, the HCN to IR ratio, and cloud matching. The method of pixel statistics is to map the distributions of molecular gas and star formation in an external galaxy at high spatial resolution—typically tens of pc for the gas. The molecular gas map provides both the gas surface density and the velocity dispersion; the latter, together with an estimate of the stellar surface density, allows one to estimate the midplane volume density from hydrostatic equilibrium. Thus in each pixel one has available mass, free-fall time, and star formation rate, yielding an estimate of $\epsilon_{\rm ff}$. Studies using this method thus far yield $\epsilon_{\rm ff}$ with a dispersion comparable to that produced by YSO counting, but with a factor of $\sim$ 2 − 3 lower mean (Leroy et al., 2017; Utomo et al., 2018); given the systematic uncertainties in the methods, this is consistent with the distributions of $\epsilon_{\rm ff}$ being the same[3]. The HCN method exploits the fact that, because it is subthermally-excited at low density, HCN traces ISM at densities $\gtrsim 10^4$ cm^{-3} (Shirley, 2015; Onus et al., 2018), and thus one can estimate the local gas density producing HCN emission even if the emitting region is unresolved[4]. If one also uses a radiative transfer calculation to estimate the HCN emitting mass and correlates this with a tracer of the star formation rate (most commonly infrared luminosity), this provides all the ingredients necessary—mass, star formation rate, and free-fall time—to constrain $\epsilon_{\rm ff}$. As with pixel statistics and YSO counting, the result of this procedure is generally that $\epsilon_{\rm ff} \approx 0.01$ with a factor of $\sim$ 3 dispersion and a comparable systematic uncertainty (e.g., Wu et al., 2010; Usero et al., 2015; Stephens et al., 2016; Gallagher et al., 2018; Onus et al., 2018).

In the cloud matching technique, one constructs catalogs of molecular clouds and star-forming regions, and matches them up based on criteria of separation in position and velocity space. For each pair of matched clouds and star-forming regions, one infers the star formation rate of the star-forming region from its luminosity in IR or radio, and the mass and free-fall time of the cloud from its molecular line emission, yielding an estimate of $\epsilon_{\rm ff}$. In contrast to all other methods, for which the distribution of $\epsilon_{\rm ff}$ values inferred generally has a dispersion of only $\lesssim 0.5$ dex, cloud matching yields much larger dispersions of $\gtrsim 0.8$ dex, with some surveys producing a tail of clouds with $\epsilon_{\rm ff} \approx 1$ (Lee et al., 2016; Vutisalchavakul et al., 2016; Ochsendorf et al., 2017). In some of these studies the mean value of $\epsilon_{\rm ff}$ is also substantially higher than the value of $\epsilon_{\rm ff} \approx 0.01$ found by other methods. The difference in results cannot simply be a result of the cloud matching surveys targeting different regions or types of molecular cloud than the other studies, in part because cloud matching studies of the same region are often inconsistent with one another—Lee et al. (2016) and Vutisalchavakul et al. (2016) both studied the inner Milky Way, but obtained median values of $\epsilon_{\rm ff}$ that differ by ≈ 0.8 dex.

Instead, the source of the discrepancy between the different cloud matching studies, and between cloud matching and other methods, appears to be in the process of constructing the cloud and star-forming region catalogs and matching them to one another. Both molecular gas emission and star formation tracer maps are continuous or nearly so, particularly toward molecule-rich regions such as the inner Milky Way. The process of breaking these continuous maps up into discrete "clouds" and "star-forming complexes" necessarily involves choices about how to perform the decomposition, and because the "clouds" and "complexes" are not co-spatial, these choices must be made independently for each map, and then one must decide how to associate the "clouds" in one map with the "complexes" in the other. Depending on how one makes these choices, a wide range of outcomes are possible. The difference between the results of Lee et al. (2016) and Vutisalchavakul et al. (2016) arise primarily from the fact that Vutisalchavakul et al. use substantially more restrictive criteria for matching clouds with H II regions, and decline to estimate $\epsilon_{\rm ff}$ values for H II regions for which they cannot confidently identify a parent cloud. Lee et al. are much less restrictive in their matching. This problem is unique to cloud matching, because in all the other techniques (YSO counting, pixel statistics, and HCN) the star-forming tracer and the molecular gas are co-spatial, so however one chooses to break up maps of one, it is possible to use the same decomposition for the other.

Given this review of the observational literature, our tentative summary is that observations require that $\epsilon_{\rm ff} \approx 0.01$ appears to be ubiquitous across spatial scales, from kpc-sized swathes of galaxies to individual molecular clouds and clumps $\approx$ 1 pc in size, at densities up to $\sim 10^4$ cm^{-3}. This leads us to the central question for section 2: to what extent can magnetic fields in supercritical molecular clouds help explain this observation?

2.2. Magnetic Regulation of the SFR in Supercritical Clouds

In a cloud that is magnetically supercritical, magnetic fields alone cannot significantly inhibit collapse. To see this, one need merely examine the magnetic and gravitational terms in the virial theorem (Equation 1). For a cloud of mass M and radius R threaded by a uniform magnetic field B, the gravitational and magnetic terms in the virial theorem can be expressed as $\mathcal{W} \sim GM^2/R$ and $\mathcal{B} \sim GM_\Phi^2/R$, respectively; recall that M_Φ is the maximum mass that can be supported by the magnetic field. The key point to notice is that both these terms scale with radius as $1/R$, so that even if $|\mathcal{W}|$ is only slightly larger than $\mathcal{B}$ when a cloud is at some starting characteristic size R_0, the mismatch between these two terms will grow as the cloud contracts, such that, by the time the cloud has been reduced to a size $\sim R_0/2$, $|\mathcal{W}|$ will be larger than $\mathcal{B}$ by a factor of 2, and the collapse will accelerate only a factor of 2 slower than if the magnetic field were absent entirely. The point to take from this thought exercise is that, due to the $1/R$ scalings of the gravitational and magnetic terms in the virial theorem, even a magnetic field that nearly strong enough to

[3]Of course we cannot definitively rule out the possibility that there is in fact a systematic difference between the Milky Way and the LMC (the only two systems for which YSO counting is available) and the slightly more distant galaxies surveyed by Leroy et al. (2017) and Utomo et al. (2018). However, systematics due to the differences in method seem the more likely explanation.

[4]Kauffmann et al. (2017) argue that the density traced by HCN can be a factor of a few smaller if molecular clouds host a significant free electron population, which would help excite the HCN at lower densities. It is unclear at present to what extent Kauffmann et al.'s result, which is derived based on high-resolution observations of a single nearby source, can be extrapolated to the much larger scales on which HCN is generally used as a diagnostic of $\epsilon_{\rm ff}$.

render a cloud subcritical at the start of its life will only slightly delay collapse[5]. To the extent that ion-neutral drift is important, it only strengthens this conclusion, since this mechanism tends to decrease the magnetic flux and thus M_Φ in the densest regions. For this reason, we focus on the role of magnetized turbulence in regulating star formation rates, rather than on magnetic fields by themselves.

2.2.1. Star Formation Rates From Magnetized and Non-magnetized Turbulence

What do simulations tell us about the star formation rate of magnetized vs. unmagnetized turbulence? Here we focus on this question in the context of pure turbulence, deferring the question of the interaction of magnetic fields with stellar feedback to section 2.3. We show an example result from numerical simulations in **Figure 1**. As the figure shows, the presence of a dynamically significant magnetic field generally reduces the density contrast in turbulence, and leads to a pattern of star formation that is more distributed. The overall star formation rate decreases, or equivalently the time required to convert a fixed fraction of the gas to stars increases, as the magnetic field strength increases. A number of authors have conducted parameter studies of the star formation rate in supersonic turbulence as a function of magnetic field strength and other parameters (Price and Bate, 2009; Dib et al., 2010a; Padoan and Nordlund, 2011; Federrath and Klessen, 2012; Padoan et al., 2012). The primary finding from these studies is that, compared to a non-magnetized flow of equal Mach number and virial ratio (ratio of kinetic to gravitational potential energy), a magnetic field strong enough to render the gas trans-Alfvénic ($\mathcal{M}_{\rm A} \approx 1$) but still leave it supercritical ($\mu_\Phi < 1$) results in a star formation rate that is a factor of $\approx 2-3$ lower. This finding holds over a range of sonic Mach numbers $\mathcal{M} \approx 5-50$ and cloud virial ratios $\alpha_{\rm vir} \approx 1-5$. These findings indicate that magnetic fields by themselves cannot explain the low value of $\epsilon_{\rm ff}$, but that they can contribute non-negligibly toward an explanation.

The mechanism by which magnetic fields reduce the star formation rate is not entirely clear. Modern theories that attempt to explain the low value of $\epsilon_{\rm ff}$ as a consequence of turbulence generally contain a few basic ingredients (e.g., Krumholz and McKee, 2005; Hennebelle and Chabrier, 2011, 2013; Padoan and Nordlund, 2011; Federrath and Klessen, 2012; Hopkins, 2012, 2013; Padoan et al., 2012; Burkhart, 2018; Burkhart and Mocz, 2018). The first of these is that turbulence, possibly coupled with self-gravity, will impose a certain probability distribution function (PDF) on the gas density. In the simplest models this PDF is taken to be log normal, since numerous numerical and analytic studies show that isothermal, non-self-gravitating turbulence generates a PDF of this form. However, some models also add a time-dependent evolution of the high-density tail into a power law shape, since simulations of turbulence with self-gravity show that such tails tend to grow over time (e.g., Klessen, 2000; Dib and Burkert, 2005; Collins et al., 2011, 2012; Kritsuk et al., 2011; Federrath and Klessen, 2013; Girichidis et al., 2014; Burkhart et al., 2017; Scannapieco and Safarzadeh, 2018). The second is that the presence of turbulent motions imposes a critical density at which molecular clouds transition from gravitationally unbound and inert to bound and star-forming. Depending on the model, this density may be uniform everywhere, or it may depend on the particular length or size scale. Third, mass within a molecular cloud that exceeds the density threshold for stability is assumed to collapse into stars and be replaced with fresh, lower density material on some timescale. Again, depending on the model this timescale can be the local free-fall time in the high-density gas, the mean-density free-fall time of the entire cloud, or anything in between.

Models based on this paradigm of turbulent regulation appear to be able to reproduce a broad range of observables. For example, Padoan et al. (2017) simulate a large section of a galaxy in which molecular cloud turbulence is driven by supernovae; they study the distribution of $\epsilon_{\rm ff}$ values within individual molecular clouds, and find a median value of about 0.025, with a spread of ≈ 0.5 dex, fully consistent with the observed distribution. Similarly, Semenov et al. (2016) use a turbulence-regulated star formation prescription as a subgrid model in a galaxy-scale simulation, and show that the result agrees well with galactic-scale measurements of the correlation between star formation and gas surface densities.

In the context of these models, magnetic fields play a few potentially important roles, which in general tend to lower the star formation rate compared to a similar non-magnetized case. First, the presence of a magnetic field narrows the density PDF compared to what would prevail in a non-magnetic flow, because magnetic fields provide an additional support against shock compression that renders it more difficult to drive gas to high densities. This narrowing will lead to less mass exceeding the threshold density for the onset of collapse. This effect has been studied by a number of authors (e.g., Cho and Lazarian, 2003; Kowal et al., 2007; Burkhart et al., 2009; Molina et al., 2012; Mocz et al., 2017), but its magnitude is still not entirely certain, because it depends crucially on the scaling of magnetic field strength with density. The density jump across an isothermal shock of sonic Mach number $\mathcal{M}$ with pre-shock ratio of thermal to magnetic pressure β_0 will depend on how the pre- and post-shock magnetic fields compare, which is determined by the relative orientation between the field and the shock plane. This distribution of relative orientations is most conveniently expressed in terms of the magnetic field-density scaling.

For a constant magnetic field on both sides of the shock, expected if the typical shock is orthogonal to the local magnetic field, the density jump is $\rho_1/\rho_0 \propto \mathcal{M}^2$ independent of β_0, while for $B \propto \rho^{1/2}$, for example, $\rho_1/\rho_0 \propto \mathcal{M}^2\beta_0/(\beta_0+1)$; more detailed expressions for other scalings may be found in Molina et al. (2012) and Mocz and Burkhart (2018). In

[5]Our claim that $\mathcal{B}$ will become increasingly unimportant compared to $\mathcal{W}$ as a cloud collapses might fail if the collapse drives a significant dynamo. In this case the dynamo would cause an increase in the magnetic energy $\mathcal{B}$ without a concomitant increase in the net magnetic flux, so that our assumption that $\mathcal{B} \propto M_\Phi^2$ would fail (Birnboim et al., 2018). However, even if this does occur, since the dynamo is ultimately powered by the collapse, it is energetically limited to $\mathcal{B} < f|\mathcal{W}|$ for some $f < 1$. Thus our claim that a magnetic field can only delay collapse in a supercritical cloud by a factor of order unity continues to hold.

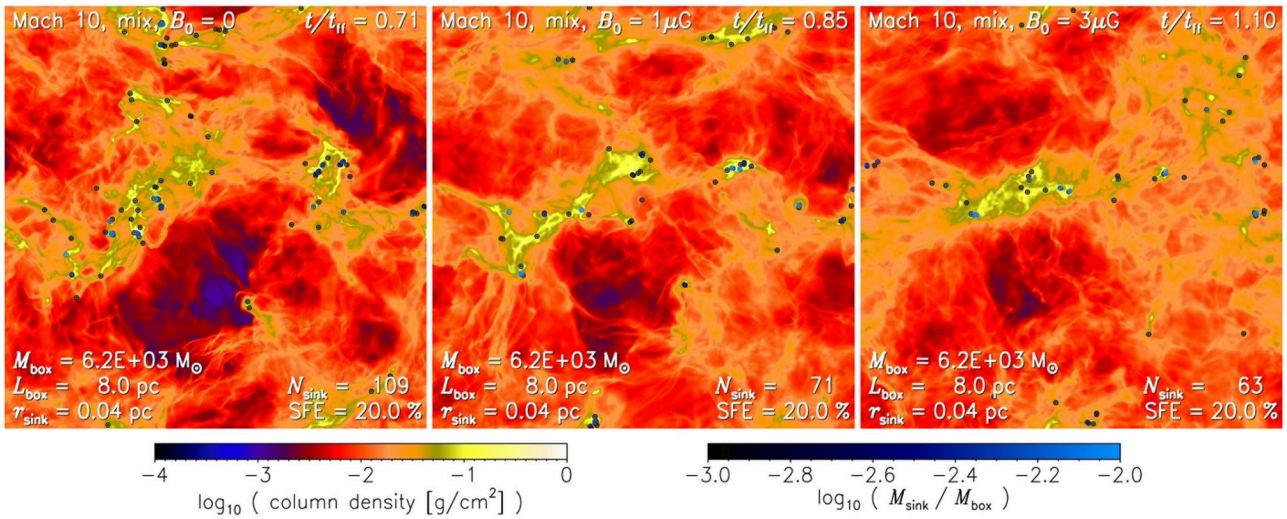

FIGURE 1 | Density projections in three simulations of self-gravitating MHD turbulence from Federrath and Klessen (2012). Each simulation takes place in a periodic box 8 pc on a side, initially containing 6,200 $M_\odot$ of isothermal gas with sound speed $c_S = 0.2$ km s^{-1}, driven with a mix of solenoidal and compressive turbulent modes at a sonic Mach number $\mathcal{M} = 10$. The three simulations were initialized with uniform magnetic fields with field strength $B = 0$, 1 μG, and 3 μG (left to right); once the turbulence reaches steady state, the corresponding Alfvén Mach numbers are $\mathcal{M}_A = \infty$, 13, and 2.7. Points show the locations of sink particles, with color indicating mass. All three simulations have been run to the point where 20% of the initial gas mass has converted to stars, but they have taken different lengths of time to reach this point.

the regime of super-Alfvénic turbulence ($\mathcal{M}_A \gg 1$) and in the absence of self-gravity, the turbulence is isotropic and both analytic arguments and simulations predict the latter scaling, $B \propto \rho^{1/2}$ (e.g., Collins et al., 2011, 2012). This leads to a prediction that the variance of the logarithmic density distribution depends on mean Mach number and plasma β as (Molina et al., 2012)

$$\sigma^2_{\ln \rho} = \ln\left(1 + b^2\mathcal{M}^2\frac{\beta}{\beta+1}\right), \quad (9)$$

where b is a constant of order unity that depends on the turbulent driving pattern (Federrath et al., 2008; Konstandin et al., 2012; Federrath and Banerjee, 2015). When $\beta \ll 1$, as is the case for observed molecular clouds,[6] this yields a significantly lower dispersion of densities than for a non-magnetized flow, $\beta = \infty$.

However, this relation breaks down in the trans- or sub-Alfvénic regime that we have argued above is likely more realistic. For such flows, the magnetic field appears to suppress the density variance less than what would be predicted by Equation (9). This may be because the anisotropy of sub-Alfvénic turbulence means that one can no longer assume a single, simple density-magnetic field scaling. For example, if strong magnetic fields confine turbulent motions to flow primarily along rather than across field lines, then most shocks will be predominantly orthogonal to the field, in which case the pre- and post-shock fields will be nearly identical, and magnetic forces will not provide any resistance to compression. It is also unclear if the scaling between B and ρ might be different for strongly self-gravitating flows. Li P. S. et al. (2015) find in simulations of the formation of an infrared dark cloud that volume-averaged density and magnetic field strengths are related by $\langle B\rangle \propto \langle\rho\rangle^{0.65}$, but it is unclear if the same powerlaw relationship applies point-wise, rather than averaged over volumes. In their self-gravitating simulations, Mocz et al. (2017) find scalings that vary from $B \propto \rho^{2/3}$ for initially-weak fields ($\mathcal{M}_A \gg 1$) to $B \propto \rho^{1/2}$ for initially-strong fields, with a smooth transition as a function of $\mathcal{M}_A$. In order to fully understand how magnetic fields modify the density PDF, more studies of this type, across a wider range of parameter space, will be needed to extend the Molina et al. (2012) scaling. In addition, there is a need for more extensive studies including the effects of ion-neutral drift. Only a few studies of this type have been published (Li et al., 2008; Downes, 2012; Meyer et al., 2014; Burkhart et al., 2015; Ntormousi et al., 2016), and they suggest that ion-neutral drift at the levels expected for molecular clumps with the observed value $R_{AD} \sim 20$ should partially offset the tendency of magnetic fields to narrow the density PDF, increasing the width back toward that produced in the non-magnetized limit. However, there has yet to be a comprehensive survey of parameter space.

A second way that magnetic fields can alter the star formation rate is by providing additional support against collapse, and thereby increasing the density threshold at which self-gravity becomes dominant. Consider a uniform spherical region of radius R, density ρ, 1D velocity dispersion σ, and magnetic field B; for this region, the condition for the right-hand side of the

[6]For 10 K gas that is 75% H_2 and 25% He by mass, typical properties in a molecular cloud, $\beta = 0.21 n_3/B_1^2$, where n_3 is the number density of H nuclei in units of 10^3 cm^{-3} and B_1 is the magnetic field strength in units of 10 μG. Crutcher (2012) finds typical field strengths $B_1 \approx 1$ at $n_3 \approx 1$, corresponding to $\beta \sim 0.1$, and $B_1 \approx 500$ at $n_3 \approx 1,000$, corresponding to $\beta \sim 10^{-3}$.

virial theorem (Equation 1) to be negative and thus indicative of collapse is, neglecting the surface terms

$$\rho > \frac{3}{4\pi GR^2}\left(c_s^2 + \sigma^2 + \frac{v_A^2}{2}\right) = \frac{3}{4\pi GR^2}\left[\left(1+\beta^{-1}\right)c_s^2 + \sigma^2\right]. \quad (10)$$

Thus a non-zero magnetic field, implying $v_A > 0$, makes it more difficult for a small-scale structure to collapse. A number of authors have suggested modified collapse criteria incorporating effects similar in functional form to Equation 10 (Hennebelle and Chabrier, 2008, 2009; Padoan and Nordlund, 2011; Federrath and Klessen, 2012; Hopkins, 2012, 2013). However, we caution that none of these modifications (nor, indeed, their original unmagnetized versions) properly account for the surface terms in the virial theorem, which can be non-negligible (Dib et al., 2007).

As with the density PDF, the importance of this effect depends on the small-scale magnetic field and its correlation with density: if $B \propto \rho^{1/2}$, as expected for super-Alfvénic, non-self-gravitating flows, this would imply $v_A \approx$ constant, in which case magnetic effects would impose a very important modification on the collapse criterion, because in observed molecular clouds $v_A/c_s \gtrsim 10$, so a magnetic field would have the effect of raising the effective sound speed of the gas by a factor of a few to ten. However, this may be an overestimate of the true effect, because the $B \propto \rho^{1/2}$ scaling follows only on scales where the turbulence is super-Alfvénic. Dense regions in turbulent media have smaller velocity dispersions, both because they tend to be physically small, and because density and velocity are anti-correlated (e.g., Offner et al., 2009a), and thus at scales dense enough to be candidates for collapse the $B \propto \rho^{1/2}$ scaling might break down because the field is anisotropic. Hopkins (2013) suggest an alternate collapse criterion that attempts to take this effect into account, but thus far it has not been tested in simulations.

Given the uncertainty on the scaling of magnetic field with density, it is not entirely clear which of the two mechanisms we have discussed—narrowing of the density PDF or increasing the threshold for collapse—is dominant in explaining how magnetic fields lower the star formation rate, or if both contribute comparably. Although they have not been explored extensively, for completeness we mention two other possible mechanisms that seem worth of investigation. First, one crucial ingredient of turbulence regulation models is the velocity power spectrum, which determines the scaling between σ and R in Equation (10) and analogous collapse conditions. There is limited evidence from some MHD simulations that the presence of a strong magnetic field might alter the velocity power spectrum (e.g., Lemaster and Stone, 2009; Collins et al., 2012), but the issue has received only limited exploration, and all published analytic models to date assume the same velocity power spectrum for magnetized and non-magnetized flows. Thus the potential impact of a velocity power spectrum that depends explicitly on magnetic field strength has not been explored. A second potential effect of magnetic fields is in models that include a powerlaw tail in the density PDF. The rate at which such tails develop, and the density at which they join onto the log normal part of the PDF, are at least potentially sensitive to the magnetic field strength. At present, however, no published models have examined this possibility. However, we emphasize that, while the *mechanism* by which magnetic fields reduce the star formation rate in a turbulent medium relative to the non-magnetized case is uncertain, the numerical experiments leave little doubt that the *amount* of reduction is roughly a factor of two to three, at least in the ideal MHD limit.

2.2.2. Effects on Maintenance of Turbulence

In addition to directly reducing the rate of star formation via their effects on the gas density structure and boundedness, magnetic fields may also affect the star formation rate in turbulent flows in two other ways. The first, via their effect on the rate at which turbulence decays, we discuss here, while the second, through their interaction with feedback, we defer to section 2.3.

One of the fundamental challenges in understanding the low observed value of $\epsilon_{\rm ff}$ via turbulence is that supersonic turbulence decays on a time scale comparable to the turbulent flow crossing time, which, in a system with virial ratio near unity, is comparable to the free-fall time (e.g., Tan et al., 2006). By itself, the presence of a magnetic field does not appear to change this basic result (e.g., Mac Low et al., 1998; Stone et al., 1998; Mac Low, 1999; Ostriker et al., 1999; Heitsch et al., 2001); at best strongly magnetized thin sheets can retain a small amount of excess kinetic energy in the form of incompressible motions in the sheet (Kim and Basu, 2013). However, there is one possible exception to this statement worth noting: while magnetic fields do not alter the decay rate of turbulence driven by external forcing, for example by star formation feedback, it is possible that they do alter the decay rate of turbulence that is driven by the self-gravitational compression of the gas itself (Birnboim et al., 2018). This effect is driven mainly because compression in a strongly magnetized gas causes the flow to become highly anisotropic, and anisotropy reduces the decay rate of supersonic turbulence because the decay rate becomes of order the crossing time in the most elongated, slowest direction (Cho and Lazarian, 2003; Hansen et al., 2011). We illustrate this effect in **Figure 2**. Consequently, while a compressing hydrodynamic fluid will remain turbulent only as long as the compression timescale is comparable to or smaller than the crossing timescale (Robertson and Goldreich, 2012), for a magnetized compressing fluid this requirement is considerably relaxed.

This effect has yet to be embedded in the context of an analytic or semi-analytic model, and simulations of collapsing magnetized clouds have generally included other physical mechanisms, particularly star formation feedback or thermal instability, that would make it hard to isolate the importance of this effect. Nonetheless, it seems possible that the increased efficiency of turbulent driving in a magnetized compressing medium relative to a non-compressing one may be important for explaining the ubiquity of turbulent motions observed in molecular clouds and the low value of $\epsilon_{\rm ff}$ that they appear to produce.

2.3. Magnetic Fields and Feedback

Perhaps the most important possible effect of magnetic fields on star formation rates is via their interaction with feedback. A full review of feedback mechanisms is beyond the scope of this paper, and we refer readers to Krumholz et al. (2014). Here we focus on

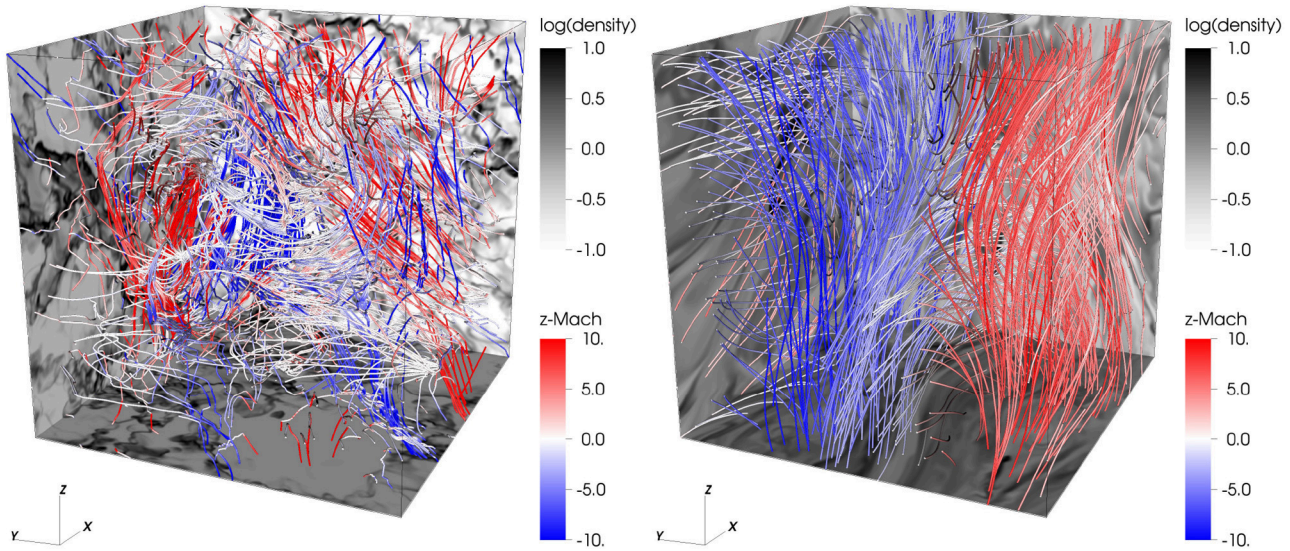

FIGURE 2 | Results from two simulations of compressing isothermal turbulence, without **(left)** and with **(right)** a magnetic field, from Birnboim et al. (2018). In both panels, lines show flow streamlines, with the *z*-velocity along the streamline color-coded by Mach number. Grayscale on the box edges indicates the logarithm of gas density, in units where the mean density in the computational domain is unity. The total velocity dispersions in the two simulations shown are comparable, but the simulation including a magnetic field has a much lower dissipation rate because the field has organized the flow into a highly-anisotropic state.

the interaction of feedback mechanisms with magnetic fields, and the impact of this interaction on star formation rates.

2.3.1. Protostellar Outflows

As mass falls onto forming stars, its angular momentum causes it to form disks, and matter orbiting in disks creates helical magnetic fields that launch some fraction of the accreting material into a fast-moving outflow (Bally, 2016, and references therein). Magnetic fields (and possibly also non-ideal MHD effects—e.g., Tomida et al., 2015; Tsukamoto et al., 2015; Nolan et al., 2017; Zhao et al., 2018) are clearly required for launching outflows in the first place. However, they also play a crucial role in regulating their interaction with the surrounding environment. Protostellar outflows are highly-collimated: Matzner and McKee (1999) show that, far from their launch point, all hydromagnetic winds approach a common momentum distribution

$$\frac{dp}{d\mu} \propto \frac{1}{\ln\left(2/\theta_0\right)\left(1+\theta_0^2-\mu^2\right)}, \tag{11}$$

where $\mu = \cos\theta$, θ is the angle relative to the central axis of the outflow, and $dp/d\mu$ is the differential momentum carried by the wind within a range of angles μ to $\mu + d\mu$. The parameter θ_0 specifies the intrinsic breadth of the outflow, and is typically small, implying a high degree of collimation: Matzner and McKee (1999) estimate $\theta_0 \approx 0.01$, which corresponds to 50% of the total outflow momentum being injected into 1% of the solid angle centered on the outflow axis.

Due to this high degree of collimation, for purely hydrodynamic flows (even if we neglect the fact that without magnetic fields no outflows would form at all), the effects of outflows should be very limited. Since pressure forces are generally negligible in molecular clouds, there is no efficient mechanism to redistribute the narrowly-focused outflow momentum. Consequently, one excepts that outflows will simply punch small holes into their parent clouds. Magnetic fields, on the other hand, couple gas across larger distances, and thus do provide a mechanism by which the momentum injected by an outflow can be shared with a larger quantity of gas. This should have the effect of making outflow feedback far more effective in the presence of magnetic fields. This effect is demonstrated clearly in the simulations of Offner and Liu (2018) in the context of exploring the effects of line-driven winds (as opposed to hydromagnetic winds) from intermediate mass stars on molecular clouds. They find that hydromagnetic waves that are launched from the working surfaces where winds impact molecular cloud material efficiently transfer energy and momentum over large distances, leading to significant turbulent motions far from the impact site.

Simulations bear out this conclusion. On the scales of individual cores with masses $\sim M_\odot$, Offner and Arce (2014) and Offner and Chaban (2017) find that, for fixed outflow properties and initial conditions, a decrease in the mass to magnetic critical mass ratio from $\mu_\Phi = \infty$ to $\mu_\Phi = 1.5$ (corresponding to an increase from zero magnetic field to near-critical) is associated with a reduction in the fraction of mass accreted onto the final star from ≈ 50 to $\approx 15\%$. Note, however, that this conclusion depends on the outflow properties being independent of the large-scale field, as is the case in Offner and Chaban (2017)'s simulations because the outflow launching region is not resolved, and thus the outflows are inserted by hand. In simulations with self-consistently launched outflows, Machida and Hosokawa (2013) find the opposite dependence, because stronger fields produce more magnetic braking, which

in turn makes the outflows weaker. However, it is unclear how realistic this conclusion is, since Machida and Hosokawa's simulations use laminar initial conditions with well-ordered fields, and simulations with turbulent initial conditions and fields find that these greatly reduce the effectiveness of magnetic braking (Santos-Lima et al., 2012; Seifried et al., 2012, 2013).

A similar dependence on magnetic fields is apparent in simulations of the formation of star clusters from gas clumps with masses of $\sim 100 - 1,000\ M_\odot$. For low-mass clusters, Hansen et al. (2012) found that outflows reduced the overall rate of star formation by a factor of ~ 2 in simulations that did not include magnetic fields, while for much more massive and dense clusters, Krumholz et al. (2012b) found an even smaller reduction in $\epsilon_{\rm ff}$, by a factor of ≈ 1.2. Murray et al. (2018) obtain a similarly-small effect. By contrast, simulations that include both outflows and magnetic fields find much stronger effects. Nakamura and Li (2007) and Wang et al. (2010) find that the combination of outflows plus magnetic fields yields a reduction in $\epsilon_{\rm ff}$ from ≈ 1 to ≈ 0.1 in clouds that are slightly magnetically supercritical. Moreover, the combination is sufficient to prevent the cloud from going into overall collapse, because outflow momentum coupled to the magnetic fields maintains the turbulent velocity dispersion, keeping the clouds near virial balance. Federrath (2015) find that magnetic fields plus outflows together produce $\epsilon_{\rm ff} \approx 0.04$, which, given the systematic uncertainties discussed in section 2.1, is within the range of the observations.

In simulations including both radiative heating from young stars and outflows, Myers et al. (2014) find that the combination of these two effects in the absence of magnetic fields yields $\epsilon_{\rm ff} = 0.17$, while adding magnetic fields at a level corresponding to $\mu_\Phi = 2$ reduces this to 0.07. Cunningham et al. (2018) obtain a similarly-large difference between runs with and without magnetic fields, which we illustrate in **Figure 3**. Most recently, Li et al. (2018) have obtained $\epsilon_{\rm ff} \approx 0.03 - 0.07$ (depending on exactly how they measure it) in a simulation that self-consistently follow the formation and evolution of a cloud with radiative and outflow feedback.

In summary, magnetic fields appear to have a multiplicative effect on outflow feedback, producing a significantly greater reduction in $\epsilon_{\rm ff}$ than do either magnetic fields without outflows, or outflows without magnetic fields. Modern simulations that include both effects are now able to reproduce values toward the high end of the observed $\epsilon_{\rm ff}$ distribution. The remaining discrepancy may be due to other physical effects still missing in the simulations, or due to systematic errors at the factor of ≈ 3 level affecting the observed $\epsilon_{\rm ff}$. There are systematic uncertainties on the values of $\epsilon_{\rm ff}$ from simulations as well, though these are likely somewhat smaller. For example, when measuring $\epsilon_{\rm ff}$ from a simulation, one must choose a Lagrangian region (e.g., all the mass above some density $\rho_{\rm min}$) or an Eulerian region (e.g., all the mass inside a simulation box) over which it is to be measured, and differences in how this region is chosen can lead to variations in the inferred $\epsilon_{\rm ff}$ value at the factor of ≈ 2 level. Similarly, multiple simulations carried out with the same physical setup by different random realizations of turbulence show $\approx 50\%$ variations in $\epsilon_{\rm ff}$ (Federrath and Klessen, 2012), though this issue has not been explored extensively in simulations including feedback due to their high computational cost.

2.3.2. Photoionization

While all forming stars likely produce outflows, only the most massive produce substantial ionizing luminosities. When such stars are present, however, they are probably the dominant sources of feedback at the scales of molecular clouds. Ionizing radiation heats the gas it encounters to temperatures $\approx 10^4$ K, such that the sound speed is ≈ 10 km s^{-1}, well above the escape speed in most molecular clouds. Consequently, the ionized gas rapidly escapes from the cloud, directly removing mass and exerting back-forces on the remaining neutral material that can potentially drive turbulence or eject even more mass. The development of an H II region is the observable manifestation of this phenomenon, and both analytic models (e.g., Matzner, 2002; Krumholz et al., 2006) and numerical simulations (e.g., Grudić et al., 2018; Kim et al., 2018) suggest that H II region formation is important for regulating star formation rates in molecular clouds.

What role do magnetic fields play in these processes? Krumholz et al. (2007b) provide a basic analytic outline, which they show roughly predicts the behavior of simulations. The ionized gas sound speed c_i is much larger than the Alfvén speed v_A in typical Galactic molecular clouds, so as an H II region begins expanding, the pressure of newly ionized gas is much larger than the magnetic pressure, and magnetic fields have little effect on the dynamics. As the ionized gas expands, however, its density drops, while the forces this gas exerts on neighboring neutral material cause it to compress, raising the magnetic field strength. Thus as H II regions evolve, the ionized gas pressure falls and the magnetic pressure and tension in the neighboring neutral material rise, until the forces become comparable. This occurs once the H II region reaches a characteristic size

$$r_m \equiv \left(\frac{c_i}{v_A}\right)^{4/3} \left(\frac{3Q}{4\pi\alpha_B f_e n_{\rm H,0}^2}\right)^{1/3} \approx 1.6\, Q_{49}^{1/3} B_2^{-4/3} T_4^{0.94}\ {\rm pc} \tag{12}$$

where $c_i \approx 10$ km s^{-1} is the ionized gas sound speed, v_A and $n_{\rm H,0}$ are the Alfvén speed and number density of H nuclei in the undisturbed neutral medium into which the H II region is expanding, Q is the ionizing luminosity measured in photons per unit time, α_B is the case B recombination coefficient, and f_e is the mean number of free electrons per hydrogen atom in the ionized region. In the numerical evaluation we have adopted $f_e = 1.1$ (i.e., assumed He is singly-ionized), and defined $Q_{49} = Q/10^{49}$ s^{-1}, $B_2 = B/100\ \mu$G, $T_4 = T/10^4$ K, with T the temperature in the H II region; we evaluate α_B using the powerlaw approximation given by Draine (2011). We have chosen the numerical scalings so that all parameters are typically of order unity for an early O star and the magnetic field strengths typically observed toward regions of massive star formation (Crutcher, 2012).

Since the magnetic characteristic radius r_m is smaller than the size of typical molecular clouds, magnetic forces will generally become non-negligible at some point during the evolution of a typical H II region. There is significant evidence for this from studies of H II region morphology. Simulations predict that significant magnetic forces cause H II regions to become

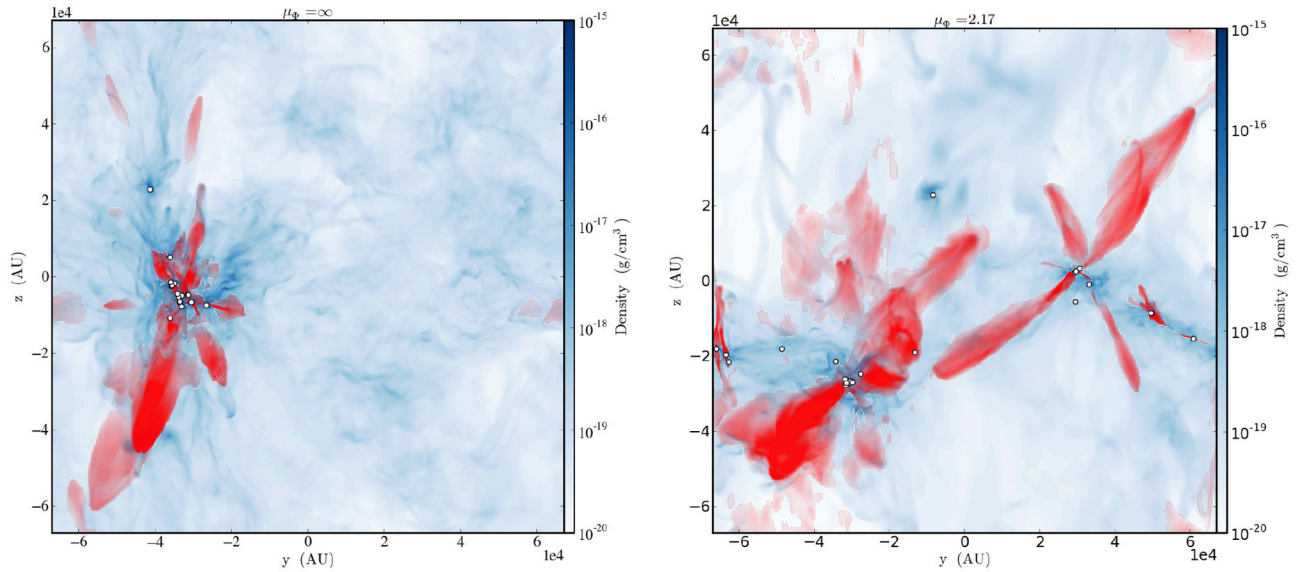

FIGURE 3 | Results from simulations of star cluster formation including outflows and radiative heating by Cunningham et al. (2018), comparing a case without magnetic fields (**left**, mass to magnetic critical mass ratio $\mu_\Phi = \infty$) to an otherwise-identical simulation with a strong magnetic field (**right**, mass to magnetic critical mass ratio $\mu_\Phi = 2.17$). Blue color shows volume-weighted mean density projected along each line of sight. Red color indicates the presence of gas moving with velocity greater than twice the RMS speed in the simulation domain, with the opacity becoming complete at fives times the RMS speed; thus the red color mostly traces outflows or gas entrained by them. White circles indicate the positions of protostars. Note how the simulation without magnetic fields has most of the mass collapsed into a single dense clump, with outflows poking small holes but not ejecting much mass. The strongly magnetized run has a more distributed morphology, and outflows are more effective at preventing the build-up of dense structures.

elongated along the direction of the large-scale field, while the field is distorted into a ring-like morphology tracing the dense shell that forms the H II region's boundary (Krumholz et al., 2007b; Arthur et al., 2011; Mackey and Lim, 2011; Wise and Abel, 2011). These features are in fact observed (Pellegrini et al., 2007; Tang et al., 2009). For example, Pavel and Clemens (2012) combine radio recombination line surveys for H II regions with near-IR polarimetry and find that young H II regions have their long axes preferentially aligned with the mean magnetic field of the galactic disk around them. Chen et al. (2017) measure the orientation of the magnetic field in the molecular gas ring N4, which traces the edges of an H II region, using near-IR polarimetry of background stars. They find that, exactly as the simulations predict, the magnetic field orientation on the plane of the sky is preferentially tangential to the ring, with 16/21 of the field orientation vectors lying within 30° of this direction, and 10/21 lying within 10°.

It is less clear, however, whether magnetic effects are quantitatively important when it comes to determining the star formation rate. Gendelev and Krumholz (2012) find that the compressed magnetic field associated with a magnetized H II region stores a significant energy reservoir, which at least has the potential to drive motions and convert a greater fraction of the injected energy to turbulence than would be the case for a non-magnetized region. While the latter effect has yet to be demonstrated in simulations of H II regions, the analogous process has been demonstrated for wind feedback by Offner and Liu (2018). Geen et al. (2015, 2017) find that magnetic fields help confine H II regions and prevent gas and ionizing photons from escaping; we reproduce two snapshots from their simulations in **Figure 4**. However, this effect changes the total H II region energy and momentum budget relatively little, suggesting that the impact on star formation (which is not included in their simulations) might also be relatively small. To date there have been far fewer systematic studies of the interaction of photoionization feedback with magnetic fields than for outflow feedback, and thus the range of possible effects is much less certain.

2.3.3. Supernovae, Winds, and Interface Mixing

Supernovae (SNe) represent another form of feedback with which it is possible for magnetic fields to interact. While photoionization is the dominant form of feedback on the scales of molecular clouds, SNe are more important at galactic scales, and in the past few years a number of authors have argued that either the large-scale rate of star formation in galaxies, the velocity dispersion of the ISM on large scales, or both, are ultimately dictated by the amount of radial momentum injected into the ISM when a SN explosion occurs (e.g., Dib et al., 2006; Joung and Mac Low, 2006; Hopkins et al., 2011; Ostriker and Shetty, 2011; Shetty and Ostriker, 2012; Faucher-Giguère et al., 2013; Krumholz et al., 2018a). For a single SN, many authors have found that this radial momentum budget is $\approx 3 \times 10^5\, M_\odot$ km s^{-1} per SN (e.g., Iffrig and Hennebelle, 2015; Kim and Ostriker, 2015; Martizzi et al., 2015; Walch and Naab, 2015), and theoretical models for the ISM often adopt this value.

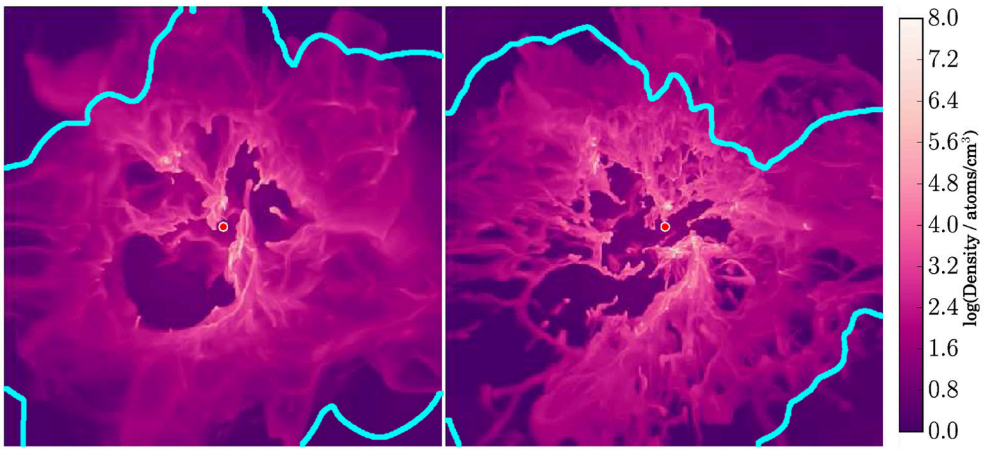

FIGURE 4 | Snapshots of two simulations by Geen et al. (2015), one with a magnetic field **(left)** and one without **(right)**. The region shown is a cube 27 pc on a side, with a single ionizing source with a luminosity $Q = 10^{48}$ ionizing photons s^{-1} located at the origin, indicated by the red circle. The slices show the state 2 Myr after the ionizing source turns on. Color shows the maximum density projected along each line of sight, as indicated by the color bar. The cyan contour marks the region where, somewhere along the line of sight, the ionization fraction exceeds 10%. Notice how the presence of the magnetic field has prevented the H II region from blowing out.

Since the Alfvén speed in galactic disks is far less than the expansion speeds of SN remnants (SNRs), at least until very late in their evolution, magnetic forces are generally unimportant for SNRs on large scales; this makes them fundamentally different than H II regions, where magnetic forces become important early on. However, magnetic fields may nevertheless play an important role on small scales. The dynamics of a SNR, particularly one driven by multiple SNe occurring over time, are ultimately controlled by the rate of radiative energy loss from the SN-heated gas that acts as a piston to drive the expansion of the surrounding cold ISM; the longer it takes the hot gas to radiate away its energy, the more energy is available to accelerate the cold ISM[7]. This energy loss, in turn, has the potential to be completely dominated by the interface layer between the hot and cold fluids, and thus the rate of energy loss depends critically upon the rate of mixing across the contact discontinuity separating hot and cold gas (McKee et al., 1984; Tenorio-Tagle et al., 1990, 1991; Strickland and Stevens, 1998). Differing assumptions about the rate of mixing lead to order of magnitude or larger variations in the predicted X-ray luminosities of hot bubbles (e.g., Dunne et al., 2003; Rosen et al., 2014), with corresponding variations in the amount of momentum that an expanding hot bubble can deliver before radiative cooling saps its energy (Keller et al., 2014, 2015; Fierlinger et al., 2016; Gentry et al., 2017).

This is not a small effect: for example, Gentry et al. (2017) survey a large parameter space of supernova number, metallicity, and ISM density using 1D simulations, and find that, if there is negligible mixing across the interface, a SNR driven by a cluster of 10 SNe will on average inject $\approx$ 10 times as much radial momentum *per SN* (i.e., about 3×10^6 $M_\odot$ km s^{-1} per SN instead of 3×10^5) as a SNR driven by a single star. Sharma et al. (2014) and Yadav et al. (2017) find similarly-large enhancements from clustering in their 3D simulations of a smaller parameter space. Averaging of the star cluster mass function, Gentry et al. (2017) find a net increase in momentum yield per SN of a factor of $\approx$ 4 compared to the commonly-adopted value. On the other hand, if there is efficient mixing, then clustering of SNe does not substantially change the momentum budget. Depending on the large-scale ISM model adopted, this factor of $\approx$ 4 variation in the SN momentum budget implies either a factor of $\approx$ 4 variation in the star formation rate, the ISM velocity dispersion, or some combination of the two. Consequently, any mechanism that alters the rate of mixing across contact discontinuities between hot and cold gas has the potential to alter the effects of SN feedback on the structure and star formation rate of the ISM at this level.

Magnetic fields potentially play an important role in this problem because they suppress mixing across contact discontinuities, and thus tend to push toward higher momentum yields from SNRs. This suppression takes two forms: first, magnetic fields prevent electrons from free-streaming across field lines, which tend to be parallel to the contact discontinuity as a result of sweeping-up of pre-existing fields by the expanding hot bubble; this greatly reduces the rate of thermal conduction (e.g., Vikhlinin et al., 2001; Markevitch and Vikhlinin, 2007). Second, by providing a surface tension-like force, magnetic fields parallel to an interface strongly suppress physical mixing between two fluids by suppressing instabilities such as Rayleigh-Taylor and Kelvin-Helmholtz that would otherwise mix fluids (e.g., Stone and Gardiner, 2007a,b; McCourt et al., 2015; Banda-Barragán et al., 2016, 2018). Offner and Arce (2015) find that this effect can be partially offset by magnetic kink instabilities, but the net amount of mixing across the interface is still reduced by the presence of a field. In direct simulations

[7]The arguments about SNRs that we make here apply equally well to bubbles of hot gas produced by the radiatively-driven winds of massive stars. We focus on SNRs because they are likely more important for regulating star formation rates, but the underlying physical issues are much the same for wind bubbles.

of SNR expansion, Gentry et al. (2019) find that, at fixed resolution, simulations including magnetic fields lead to SNRs having noticeably larger terminal radial momenta than purely hydrodynamic simulations.

However, the magnitude of this effect remains very poorly-understood due to the extremely challenging numerics of the problem. To obtain a result for the terminal momentum of a SNR one must of course simulate its full expansion, which will easily reach size scales of a few hundred pc if there are multiple SNe. However, one must simultaneously resolve the edge of the SNR well enough that numerical mixing does not dominate the transport rate across the contact discontinuity. The characteristic thickness of the interface, set by balancing the rate of conductive heat flux from hot to cold against the rate of radiative loss, is the Field length (Field, 1965; Koyama and Inutsuka, 2004),

$$\lambda_{\rm F} = \sqrt{\frac{\kappa_c T}{n_{\rm H}^2 \Lambda}}, \tag{13}$$

where κ_c is the conduction coefficient, T is the temperature, n is the number density of H nuclei, and Λ is the cooling function (i.e., the energy radiated per unit volume per unit time is $n_{\rm H}^2\Lambda$). The conductivity, assuming the unsaturated limit and a gas of fully ionized H and He in the usual interstellar ratio, is (Cowie and McKee, 1977)

$$\kappa_c \approx \frac{1.84\times10^{10} T_6^{5/2}}{29.9 + \ln(T_6 n_0^{-1/2})} \ {\rm erg\ s^{-1}\ K^{-1}\ cm^{-1}}, \tag{14}$$

while in the temperature range $\sim 10^4 - 10^6$ K that characterizes the interface, the cooling rate for Solar metallicity gas is (Draine, 2011)

$$\Lambda \approx 1.3\times10^{-22} T_6^{-0.7} \ {\rm erg\ cm^3\ s^{-1}}, \tag{15}$$

where $T_6 = T/10^6$ K and $n_0 = n_{\rm H}/1\ {\rm cm}^{-3}$. For $n_{\rm H} = 0.1\ {\rm cm}^{-3}$ and $T = 10^5$ K, typical interface values, we have $\lambda_{\rm F} \approx 0.05$ pc, implying that effective resolutions of $> 1,000^3$ would be required to capture the interface and the SNR as a whole in the same simulation.

Not surprisingly, numerical simulations have struggled to reach this goal. Without magnetic fields, Fierlinger et al. (2016) are able to obtain convergence in their 1D Eulerian simulations only if they impose a subgrid diffusion model that corresponds to assuming efficient turbulent mixing across the contact discontinuity. Gentry et al. (2017) do obtain convergence in their 1D simulations of SNR evolution with multiple SNe without such a model, but only using a pseudo-Lagrangian method to minimize numerical mixing across the hot-cold interface, and upon reaching a resolution $\Delta x \approx 0.03$ pc; they are unable to obtain convergence with Eulerian methods. In 3D hydrodynamic simulations, Yadav et al. (2017) and Gentry et al. (2019) find that SNR energies and momenta are still not converged at resolutions of a few tenths of a pc, the highest they could simulate. In contrast, Kim et al. (2017) do report convergence in their 3D simulations at a factor of several lower resolution, 1.5 pc, which they attribute to the fact that they simulate a non-uniform background into which the SNR expands, and that this makes convergence easier to obtain. Gentry et al. (2019), on the other hand, suggest that the convergence might instead be an artifact of mixing being dominated by the advection of the contact discontinuity across the grid, which might not converge as the resolution increases, since the front would mix less per cell but would have to cross a larger number of cells per unit time. In summary, we are still some distance from determining the true momentum of SNRs even in the hydrodynamic case. It seems unlikely we will be able to measure the difference between this case and the magnetized one until we make progress on issues of convergence.

2.3.4. Cosmic Ray Feedback

The final form of feedback that we discuss is cosmic rays (CRs). A full review of CR physics is well beyond the scope of this review, and we refer readers to Zweibel (2013) for a comprehensive treatment; here we only summarize the most important features. CRs are a population of non-thermal particles created when charged particles bounce back and forth across magnetized shocks; each passage through the shock increases the particle energy, allowing the shock to act like a particle accelerator. Magnetic fields are required to create CRs, but they are also critical for providing a mechanism by which CRs can couple to gas dynamics: CRs scatter off Alfvén waves or other inhomogeneities in magnetic fields, transferring momentum in the process. Thus CR feedback is fundamentally a magnetic process.

One critical question for CR feedback is the size scale on which it is effective. While any magnetized shock in a sufficiently-ionized plasma can accelerate CRs, the bulk of the CR energy budget on galactic scales comes from SN shocks, which convert $\sim$ 10% of their initial kinetic energy into CRs. This population is injected on the scales of SN remnants, which are much larger than individual molecular clouds, and the population further spreads out in height as it diffuses through the galactic magnetic field. Thus while the pressure provided by CRs at the midplane of the Milky Way or similar galaxies is comparable to the magnetic or turbulent ram pressures, the scale height of the CRs is much larger than that of the star-forming molecular gas (Boulares and Cox, 1990). For this reason, most recent work on CR feedback has focused on their possible role as drivers of galactic winds (e.g., Uhlig et al., 2012; Girichidis et al., 2018, among many others) or sources of heating in galaxy winds or halos (e.g., Wiener et al., 2013; Ruszkowski et al., 2017), in which role they would affect star formation only indirectly, but modulating the fuel supply for it. It is unclear if CRs can affect the SFR for gas already in a galaxy. Socrates et al. (2008) suggest that CR feedback prevents galactic SFRs per unit area from exceeding some maximum value. While observations do suggest that there is in fact an upper limit to galaxy areal SFRs, CRs are far from the only possible explanation for it (e.g., Crocker et al., 2018), and the Socrates et al. calculation

is not precise enough to allow quantitative comparison to the observations.

On the smaller scales of individual molecular clouds, for CR feedback to be dynamically significant there must be some mechanism for producing a CR pressure gradient[8]. One potential mechanism for producing a gradient is absorption of low-energy, non-relativistic CRs by molecular gas. Clouds with column densities $\gtrsim 10^{23}$ cm^{-2} dissipate CRs with the streaming instability, ultimately converting much of the CR energy to turbulent motions (Schlickeiser et al., 2016); to date there has been no exploration of whether this could be a significant source of turbulence in molecular clouds, that *a priori* it seems unlikely on energetic grounds, since the energy density of CRs at a galactic midplane is comparable to the mean kinetic energy density, while the kinetic energy density associated with turbulence in a molecular cloud is $\sim$ 2 orders of magnitude larger. One can make a similar point about another possible source of inhomogeneity, CRs generated by protostellar jets (Padovani et al., 2015): while these may be important sources of ionization, even if one assumes efficient CR acceleration such that $\approx$ 10% of the energy in jets is ultimately transferred to CRs, this is not enough to be dynamically significant compared to the binding energy of an entire molecular cloud. CRs accelerated in shocks from the winds of massive stars are a more promising potential origin for a locally-inhomogeneous CR population, since the associated energy budget is considerably larger. CRs created in such shocks are likely sub-dominant but non-negligible on galactic scales (Seo et al., 2018), but there is significant observational evidence that the CR population these generate is localized around massive star clusters (see the review by Bykov, 2014), and thus could potentially provide a dynamically-significant outward pressure that would lower SFRs. This possibility has yet to receive significant theoretical or observational attention.

3. THE ROLE OF MAGNETIC FIELDS FOR THE INITIAL MASS FUNCTION

3.1. Basics of the IMF and Observational Evidence

Extensive general reviews of the IMF—in particular the observational challenges involved in measuring the IMF—are provided by Offner et al. (2014) and Hopkins (2018). Here we concentrate on the effects of magnetic fields on the IMF. The IMF is the distribution of stellar masses at birth. We know from observational surveys that most stars have masses of about half the mass of our Sun ($M_\odot$). Stars with smaller masses are rarer. Stars more massive than the Sun also become rarer with increasing mass. The high-mass tail of the IMF is indeed a steeply decreasing power-law function with the number of stars $N(M) \propto M^{-1.35}$ (Salpeter, 1955; Miller and Scalo, 1979; de Marchi and Paresce, 2001; Kroupa, 2001; Chabrier, 2003, 2005; Parravano et al., 2011, 2018; Da Rio et al., 2012; Weisz et al., 2015a).

Figure 5 shows a compilation of various analytic fits to the observed IMF. There is clearly substantial disagreement on the low-mass end ($M \lesssim 1\,M_\odot$) with the turnover mass (or characteristic mass) varying between $\sim$ 0.1 and $\sim$ $0.4\,M_\odot$ depending on the parameterization. This disagreement is a result of the challenges in observing low-mass stars, taking into account multiplicity, and converting from a luminosity function to a mass function (Offner et al., 2014; Hopkins, 2018). For the high-mass tail ($M \gtrsim 1\,M_\odot$), however, there seems to be generally good agreement.

Efforts to search for systematic variation in the IMF have yielded mixed and often contradictory results. In the Milky Way, Weidner et al. (2013), Dib (2014), and Dib et al. (2017) argue that there is statistically-significant evidence for variation in both the low-mass and high-mass parts of the IMF from one star cluster to another. However, as pointed out by Krumholz (2014), the quoted uncertainties in these studies frequently ignore the two largest systematic uncertainties: errors in stellar masses derived from pre-main sequence tracks, and in errors in the masses and other properties of star clusters that are simply drawn from the literature, and rather than derived using homogeneous and uniform cluster definitions or analysis methods. Searches for IMF variation using homogeneous samples in external galaxies have for the most part found no statistically-significant variation at least at the high-mass end of the IMF that is accessible beyond the Milky Way (e.g., Andrews et al., 2013, 2014; Weisz et al., 2015b). The main exceptions are in the most massive star clusters, where Schneider et al. (2018, in 30 Doradus) and Hosek et al. (2019, in the Arches Cluster) have reported statistically-significant excesses of massive stars compared to the average IMF of the Galactic field. There is also more indirect evidence for bottom-heavy IMFs in massive elliptical galaxies (see the review by Hopkins, 2018). Given the highly uncertain status of observational searches for IMF variation, and the fact that at this point there is no reason to think any variations that might exist are linked to magnetic fields, we will not discuss this topic further.

Understanding the power-law tail in the IMF and the turnover at around 0.1–$0.4\,M_\odot$ are two of the most challenging open problems in astrophysics. The IMF has far-reaching consequences and applications, including the calibration of extra-galactic star formation relations used to understand galaxy formation and evolution (Green et al., 2010). The IMF is needed to interpret the colors, brightness and star formation activity of all galaxies in our Universe and it is the central ingredient for understanding galaxy formation and evolution, because the feedback from young stars is what powers the life cycle of galaxies.

Many physical processes may play a role in setting the characteristic mass and shape of the IMF, including gravity, turbulence, magnetic fields, and feedback, as proposed in theoretical models and seen in numerical simulations. However, we are not aware of any direct observational test of these theoretical predictions, especially when it comes to the role of magnetic fields for the IMF. Given the lack of observational constraints, we thus need to resort to theoretical models and

[8] An important distinction to draw here is between CRs providing a dynamically important pressure, and being important in other ways. CRs are certainly critical to the ionization state, temperature, and chemistry of molecular gas, even if they are not dynamically important.

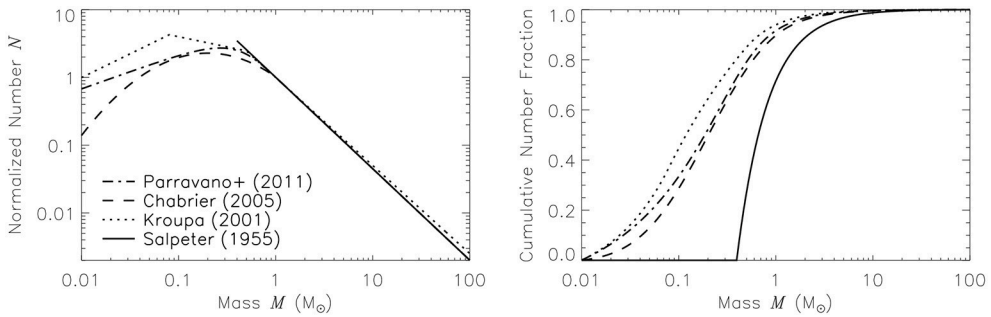

FIGURE 5 | Analytic fits to the observed IMF **(left)** and the cumulative mass function of stars **(right)**. Different lines show different parameterizations by Salpeter (1955) (solid), Kroupa (2001) (dotted), Chabrier (2005) (dashed), and Parravano et al. (2011) (dash-dotted). In this representation of the IMF, the number of stars is normalized such that $N = 1$ for $M = 1\,M_\odot$. While the high-mass tail ($M \gtrsim 1\,M_\odot$) seems fairly universal, the low-mass end ($M \lesssim 1\,M_\odot$) is much less well-constrained, with substantial variations in the number of low-mass stars and in the characteristic mass of the IMF.

numerical simulations to advance our understanding of the physical mechanisms that control the IMF.

3.2. Theoretical Models of the IMF

3.2.1. Magnetic Jeans Mass

Analytic work on the effects of magnetic fields for the IMF are scarce. The earliest and simplest approaches to incorporating magnetic fields into theories of the IMF simply assumed that fields would convert the geometry from spherical to filamentary, and then proceeded to calculate a Jeans length or mass in the resulting geometry, neglecting any further magnetic effects (e.g., Inutsuka, 2001; Larson, 2005). A slightly more sophisticated approach is to invoke a magnetic version of the Jeans length,

$$\lambda_{\rm J,mag} = \left[\frac{\pi c_{\rm s}^2 \left(1+\beta^{-1}\right)}{G\rho}\right]^{1/2} = \lambda_{\rm J}\left(1+\beta^{-1}\right)^{1/2}, \qquad (16)$$

which leads to the magnetic Jeans mass

$$M_{\rm J,mag} = \rho\frac{4\pi}{3}\left(\frac{\lambda_{\rm J,mag}}{2}\right)^3 = M_{\rm J}\left(1+\beta^{-1}\right)^{3/2}, \qquad (17)$$

where $\lambda_{\rm J}$ and $M_{\rm J}$ are the standard (purely thermal) Jeans length and mass, respectively. All we have done here is to replace the thermal pressure with the sum of thermal and magnetic pressure, giving rise to the $(1 + \beta^{-1})$ correction factors (Federrath and Klessen, 2012; Hopkins, 2013), introducing the plasma β in the relations. This simple concept shows that adding magnetic pressure raises the Jeans mass. If the Jeans mass plays a role in setting the characteristic mass of stars (Offner et al., 2014), then Equation 16 would suggest that adding magnetic pressure leads to more massive stars (or less fragmentation). For example, taking a typical value of $\beta = 0.3$ for molecular clouds leads to an increase compared to the purely thermal Jeans mass by a factor of ~ 9. We caution that this calculation is solely based on adding the magnetic pressure contribution to the Jeans mass, but ignores any potential effects of magnetic tension. These limitations have been discussed in Molina et al. (2012), Federrath and Klessen (2012), and Federrath and Banerjee (2015).

3.2.2. MHD Turbulence-Regulated IMF Theories

The structure and dynamics of molecular clouds and dense cores are largely determined by MHD turbulence (Elmegreen and Scalo, 2004; Mac Low and Klessen, 2004; McKee and Ostriker, 2007), and this MHD turbulence may not only control the rate of star formation, but also the mass of young stars. In the relevant context of magnetic fields, Padoan and Nordlund (2002) presented a theory of the IMF for which the density PDF and the turbulence power spectrum are the main ingredients, complemented by the MHD shock jump conditions. Assuming that the density contrast in an MHD shock is proportional to the Alfvén Mach number, i.e., $\rho'/\rho \propto \mathcal{M}_{\rm A}$ and the post-shock thickness $\ell'/\ell \propto \mathcal{M}_{\rm A}^{-1}$, combined with the velocity dispersion – size relation, $v \propto \ell^p$ with $p \sim 0.4$–0.5 from observations (Larson, 1981; Solomon et al., 1987; Ossenkopf and Mac Low, 2002; Heyer and Brunt, 2004; Roman-Duval et al., 2011) and numerical simulations (Kritsuk et al., 2007; Schmidt et al., 2009; Federrath et al., 2010; Federrath, 2013a), they derive a model for the high-mass tail of the IMF,

$$N(M) \propto M^{-3/(3-2p)}, \qquad (18)$$

which, for $p = 0.4$–0.5, gives high-mass slopes of -1.4 to -1.5 for the IMF, very close to the observed Salpeter (1955) slope. This slope is also consistent with the distribution of clump masses obtained in MHD turbulence simulations by Padoan et al. (2007), though the simulations did not include gravity.

A significant problem with the theoretical model by Padoan and Nordlund (2002) is that it needs a linear scaling of post-shock density and post-shock thickness with Mach number, as assumed above. However, MHD turbulence simulations with realistic values of the magnetic field show that the density contrast in shocks is not reduced by as much in the presence of magnetic fields as assumed in Padoan and Nordlund (2002). In fact, the more appropriate and effective scalings of post-shock density and thickness may be $\rho'/\rho \propto \mathcal{M}^2$ and $\ell'/\ell \propto \mathcal{M}^{-2}$, in which case the same derivation leads to

$$N(M) \propto M^{-3/(3-4p)}, \qquad (19)$$

for the high-mass tail, significantly too steep, i.e., with slopes of −2.1 to −3.0, much steeper than the observed Salpeter slope.

Hennebelle and Chabrier (2008, 2009, 2013) present a similar class of turbulence-regulated models of the IMF, based on the Press and Schechter (1974) formalism, that yields IMF predictions in good general agreement with the observed IMF. **Figure 6** shows the effect of adding magnetic fields in their model. Here we show predictions for the core mass function (CMF), i.e., a distribution that Hennebelle and Chabrier (2013) take to be shifted to three times higher masses compared to the IMF. We will comment further on the shift between the CMF and IMF in section 3.3.1, which might be the result of magnetic-field driven outflow feedback.

We see in **Figure 6** that the effect of the magnetic field (dashed and dotted lines for different magnetic field normalizations and scalings, bracketing the observed ranges) is relatively weak, when compared to the predictions without magnetic fields (solid lines). The magnetic field generally increases the characteristic mass of the IMF, consistent with the qualitative trend predicted simply by considering the magnetic Jeans mass (c.f.section 3.2.1), but by much less than the factor of ~ 9 based on Equation (17).

Looking in more detail at **Figure 6**, we see that a stronger dependence of B on the gas density (dash-dotted line) produce a stronger shift toward larger masses and stronger magnetic field normalizations (dashed line) yield a shallower slope in the high-mass tail. Both effects are the result of increased magnetic support, i.e., the addition of magnetic pressure to thermal pressure. These direct predictions by the Hennebelle and Chabrier (2013) theory of how the IMF would respond to different magnetic field strengths and field scalings with density have so far not been tested with numerical simulations.

In contrast, the role of magnetic fields in the analogous Hopkins (2013) model is that they are degenerate with other parameters, i.e., any change in the IMF induced by magnetic fields could be reproduced by a change in Mach number, turbulence driving parameter or adiabatic index γ. Thus, in these models, magnetic fields do not have distinct effects that could be isolated from variations in other parameters.

3.3. Numerical Simulations of the IMF

Numerical simulations find that the overall effect of magnetic fields is to reduce the fragmentation of the gas. This is seen in both molecular cloud simulations (Price and Bate, 2008; Dib et al., 2010a; Padoan and Nordlund, 2011; Federrath and Klessen, 2012; Federrath, 2015) and protostellar disk simulations (Price and Bate, 2007; Hennebelle and Teyssier, 2008; Bürzle et al., 2011; Hennebelle et al., 2011; Peters et al., 2011; Seifried et al., 2011). The physical reason for this is a combination of magnetic pressure and tension forces, the former with the effect of reducing compression, thereby increasing the effective Jeans mass (c.f. section 3.2.1), and the latter acting to keep together coherent filaments, gas streams, and shocks by magnetic tension. These effects tend to produce less fragmented, more massive dense cores when magnetic fields are included. If this direct effect of magnetic fields on the gas were the only relevant effect, we would expect magnetic fields to increase the characteristic mass of stars compared to the purely hydrodynamical case.

However, the situation is slightly more complicated, because magnetic fields are the main reason for mechanical feedback in the form of jets and outflows launched from the accretion disk around young stars (Pudritz et al., 2007; Frank et al., 2014). This jet/outflow feedback is also the reason why simple considerations based on magnetic Jeans mass (c.f. section 3.2.1), and the more sophisticated models presented in section 3.2.2, may ultimately fail when it comes to the effect of magnetic fields. These models do not include feedback—at least not its non-linear effect, which

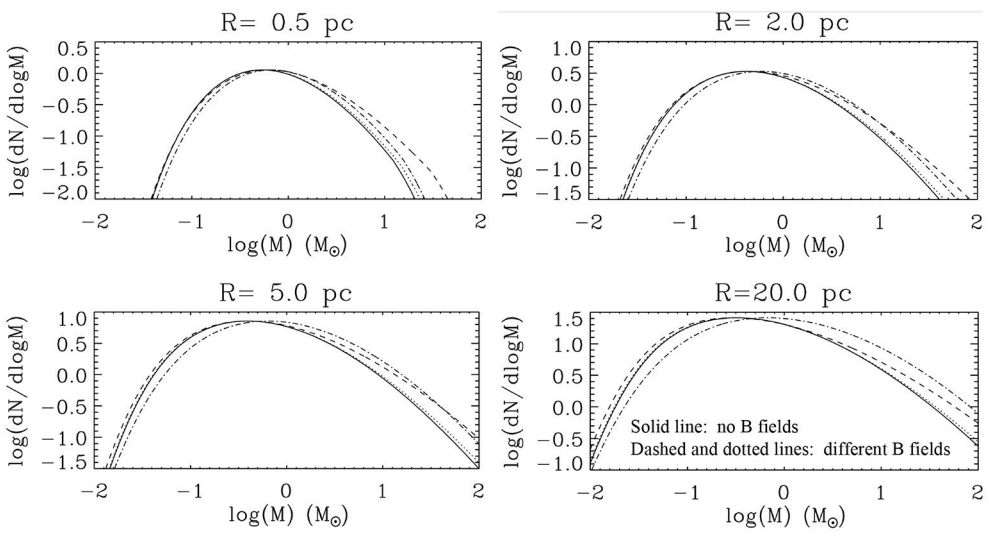

FIGURE 6 | Analytic predictions of the core mass function with and without magnetic fields for different cloud radii, $R = 0.5$–20 pc. The solid line is for the case without magnetic fields. The dotted line is for $B = 10\,\mu\mathrm{G}\,[n/(1,000\,\mathrm{cm}^{-3})]^{0.1}$, the dashed line for $B = 30\,\mu\mathrm{G}\,[n/(1,000\,\mathrm{cm}^{-3})]^{0.1}$, and the dash-dotted line for $B = 10\,\mu\mathrm{G}\,[n/(1,000\,\mathrm{cm}^{-3})]^{0.3}$, where n is the molecular hydrogen number density. Figure adopted from Hennebelle and Chabrier (2013).

can ultimately only be properly accounted for and quantified in fully three-dimensional, MHD calculations. Jet/outflow feedback may be particularly important because it is the first to kick in (before radiation feedback, winds, and supernovae) and is not only important for high-mass stars, but applies to all young stars (Krumholz, 2014). Radiation feedback may also play an important role in determining the IMF, and we discuss the interplay between it and magnetic fields in section 3.3.2.

3.3.1. Mechanical Feedback by Magnetically-Driven Jets and Outflows

3.3.1.1. The core-to-star efficiency

In the first part of this review we have seen that magnetically-driven outflows can reduce the SFR by factors of 2–3 and set the core-to-star efficiency to about 1/2. We therefore expect a significant impact also on the characteristic stellar mass and the IMF. Previous simulations have quantified this effect. For example, Hansen et al. (2012) found a reduction of the average stellar mass when outflow feedback was included in their simulations. Similarly, Federrath et al. (2014b) observed additional fragmentation with outflow feedback. This is shown in **Figure 7**, where we plot the number of sink particles formed in simulations with outflow feedback divided by the number of sink particles formed in runs without magnetically-driven outflows. **Figure 7** shows that $N_\star^{\rm with\ outflows}/N_\star^{\rm no\ outflows} \sim 1.5$ after one freefall time. This is the result of outflow-induced fragmentation; the outflows perturb and tear filamentary accretion flows, breaking them up into multiple new accretion streams. Similar behavior has been observed in earlier simulations by Li et al. (2010), Wang et al. (2010), and (Hansen et al., 2012).

Magnetically-driven outflow feedback has two important effects on the stellar mass. First, it reduces the accretion rate and limits the final star mass by removing gas from the feeding core, leading to a core-to-star efficiency of ~ 0.5. Second, it promotes fragmentation of the core, because the outflows tear up coherent accretion streams and perturb the core, such that more stars can form. This combined effect of magnetic outflows on the average stellar mass is shown in the bottom panel of **Figure 7**, which plots the ratio of the average stellar mass with and without outflow feedback, $\langle M_\star^{\rm with\ outflows}\rangle/\langle M_\star^{\rm no\ outflows}\rangle$. Comparing simulations with and without outflows, the mean stellar mass is the same at early times, immediately after the first collapsed objects form. However, stars grow more quickly in the simulations without outflows, so that after one free-fall time the mean stellar mass is a factor of ~ 3 smaller in simulations that include outflows. This factor of ~ 3 reduction in the final stellar mass is consistent with the results of other simulations (Li et al., 2010; Hansen et al., 2012b; Myers et al., 2014; Offner and Chaban, 2017; Cunningham et al., 2018). This suggests that magnetically-driven outflows may play a crucial role in controlling the observed shift of the core mass function to the IMF by a similar factor, 0.3–0.4 (Alves et al., 2007; Nutter and Ward-Thompson, 2007; Enoch et al., 2008; Myers, 2008; André et al., 2010; Könyves et al., 2010; Frank et al., 2014; Offner et al., 2014). However, we warn that the claim that the core mass function can be mapped directly to the IMF, and that the observed core mass function is universal and has a robustly-detected turnover like the IMF, have both been subject to considerable dispute in the literature (Dib et al., 2010b; Krumholz, 2014; Bertelli Motta et al., 2016; Guszejnov et al., 2016, 2018; Liptai et al., 2017; Liu et al., 2018); even if there is a link, the observed shift from the CMF to the IMF is not always ≈ 3 (e.g., Benedettini et al., 2018; Zhang G.-Y. et al., 2018).

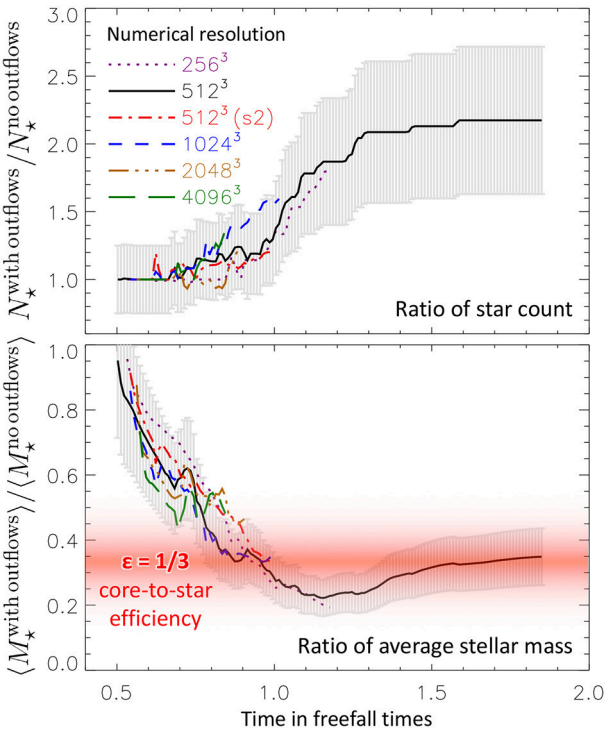

FIGURE 7 | Time evolution of the ratio of the number of sink particles formed in simulations with and without magneto-centrifugal outflows, $N_\star^{\rm with\ outflows}/N_\star^{\rm no\ outflows}$ **(top)**, and ratio of the average sink particle mass $\langle M_\star^{\rm with\ outflows}\rangle/\langle M_\star^{\rm no\ outflows}\rangle$ **(bottom)**. Different lines show different numerical resolutions, demonstrating convergence. After a freefall time, outflow feedback has increased the number of sink particles formed by a factor of ~ 1.5. The average sink particle mass is reduced by a factor of ~ 3 with outflow feedback. Figure adopted from Federrath et al. (2014b).

3.3.1.2. The role of magnetic field geometry

Most previous simulations of magnetically-driven jet launching started from a uniform magnetic field aligned with the rotation axis of the core that forms the disk. However, in reality we expect a significant un-ordered, turbulent component to be present. That turbulent field component may either be inherited from the parent molecular cloud or be generated by small-scale dynamo processes (Brandenburg and Subramanian, 2005; Schekochihin et al., 2007; Sur et al., 2010; Federrath et al., 2011a,b, 2014a; Schober et al., 2012, 2015; Schleicher et al., 2013; Federrath, 2016a).

Figure 8 shows the results of recent simulations by Gerrard et al. (under review), which the authors started with different magnetic field configurations in the core. They compare three simulations: one with a uniform field aligned with the rotation axis (left-hand panel), a second one that has a turbulent, tangled component in addition to the uniform field component,

such that both have the same contribution to the total field strength (middle panel), and a third simulation that starts with a completely turbulent magnetic field without any ordered guide-field component (right-hand panel). The initial conditions and physics included in the three simulations are otherwise identical, and the total rms field strength is 100 μG in all three cases.

We see in **Figure 8** that the uniform-field simulation produces a fast collimated jet aligned with the rotation axis of the disk. There is also a less-collimated wide-angle outflow component, but it does not carry much mass, compared to the case where both a uniform and turbulent magnetic field component is present (middle panel). This model is the most realistic and contains a fast collimated jet component and a wide-angle, low-speed outflow component previously seen in more idealized simulation setups (Banerjee and Pudritz, 2006; Machida et al., 2008; Federrath et al., 2014b; Kuruwita et al., 2017), and consistent with recent ALMA observations in Serpens South (Hodapp and Chini, 2018). Both components may carry away a significant amount of mass. This is why in this model the protostar has the lowest accretion rate of all three cases, with a protostar mass of 0.15 $M_\odot$ after 1,200 year, compared to 0.20 $M_\odot$ in the uniform-field case, at the same time after the protostar was formed.

A most striking result is the complete absence of an outflow in the fully turbulent field case. This demonstrates that an ordered magnetic field component aligned with the rotation axis of the disk is required to launch a magneto-centrifugally driven outflow, as described in the Blandford and Payne (1982) mechanism of wind launching.

Overall, the accretion histories of the three simulations vary by up to 100%—for example, about 500 year after protostar formation, the first protostar that forms in the fully turbulent field case has only reached 0.05 $M_\odot$, while the protostar in both the uniform-field and partially-turbulent field cases has a mass of about 0.10 $M_\odot$, i.e., significantly more massive, because the absence of addition magnetic-field pressure from the turbulent field component, which reduces the accretion rate onto the star. In summary, the magnetic field structure has significant impact on the jet launching and final mass of the protostar.

3.3.2. Radiation Feedback and Magnetic Fields

A number of authors have suggested the key physical process responsible for setting the location of the peak of the IMF is radiation feedback (Krumholz et al., 2007a; Bate, 2009; Krumholz, 2011; Guszejnov et al., 2016). The central argument behind this hypothesis is that isothermal MHD turbulence is a scale-free process, and thus is incapable of producing a mass function with a characteristic scale such as the IMF. Consistent with this claim, simulations have shown that isothermal turbulence without feedback tends to produce fragmentation to arbitrarily small mass scales, leading to a mass function that is a pure power law, or that has a peak dependent on the resolution of the simulation, rather than a function with a distinct peak such as the observed IMF (Bertelli Motta et al., 2016; Federrath et al., 2017; Liptai et al., 2017; Guszejnov et al., 2018; however, see Haugbølle et al., 2018 for a contrasting view). On the other hand, radiative heating of a collapsing cloud by the protostars forming within it, whose luminosity is primarily powered by accretion, naturally does produce a characteristic mass scale that appears consistent with the observed IMF peak. Simulations that include radiation feedback generally yield IMFs that converge with resolution and are in reasonable agreement with observations (Bate, 2009, 2012, 2014; Offner et al., 2009b; Krumholz et al., 2011, 2012b; Myers et al., 2014; Federrath et al., 2017; Cunningham et al., 2018; Li et al., 2018).

In the context of such models, what is the role of magnetic fields? Simulations offer limited guidance, because most published work on the IMF including radiative transfer has either omitted magnetic fields entirely (Bate, 2009, 2012, 2014; Offner et al., 2009b; Krumholz et al., 2011, 2012b) or included it in all runs carried out (Li et al., 2018). The only published works on the IMF that perform a controlled experiment by including radiation feedback and repeating a calculation both including and omitting magnetic fields are those of Price and Bate (2009), Myers et al. (2014), and Cunningham et al. (2018), and only the latter two of these also include outflows[9]. The general result of these studies is that, with the exception of their role in driving outflows, magnetic fields have only marginal effects on the final IMF. Krumholz et al. (2016) investigate why this should be by carrying out a detailed analysis of the simulations of Myers et al. (2014); they show that, on the small scales ($\sim$ few $\times$ 10^3 AU) where protostellar cores fragment, thermal pressure support (enhanced by radiative heating) is generally stronger than magnetic support, even in simulations that are only marginally magnetically supercritical on large scales. The fundamental reason is that the processes that lead to the production of protostars involve gathering mass along field lines and possibly also turbulent reconnection (Lazarian and Vishniac, 1999; Santos-Lima et al., 2012), so that the dense regions near protostars that might or might not fragment, thereby determining stars' characteristic masses, have μ_Φ values much larger than the average of the larger-scale cloud in which they are embedded.

We conclude this section by turning to the question of whether magnetic fields might play a larger role in shaping either the very low mass or very high mass parts of the IMF. On the massive end, the main distinguishing feature is that radiation feedback of massive stars is much more intense than that of low-mass stars, because for stars larger than $\sim$ 5 $M_\odot$ Kelvin-Helmholtz contraction (supplemented by the onset of nuclear burning in stars larger than a few tens of $M_\odot$) produces a luminosity that rises sharply with mass. Simulations of the formation of such stars beginning from massive protostellar cores show that magnetic fields tend to aid in the growth of such stars via four mechanisms (Commerçon et al., 2010, 2011; Myers et al., 2013). First, they suppress fragmentation directly by providing magnetic support. Second, by providing a means of angular momentum transport, magnetic fields tend to make the disks of massive stars smaller, keeping the mass closer to the central star where it is warmer and less prone to fragment. Third, the enhanced angular momentum transport increases the

[9] In the non-magnetized simulations the outflows are launched artificially via a sub-grid model, but this is also true in the magnetized simulations, since they do not have the resolution to follow outflow launching self-consistently while also running for long enough to allow meaningful statistical study of the IMF.

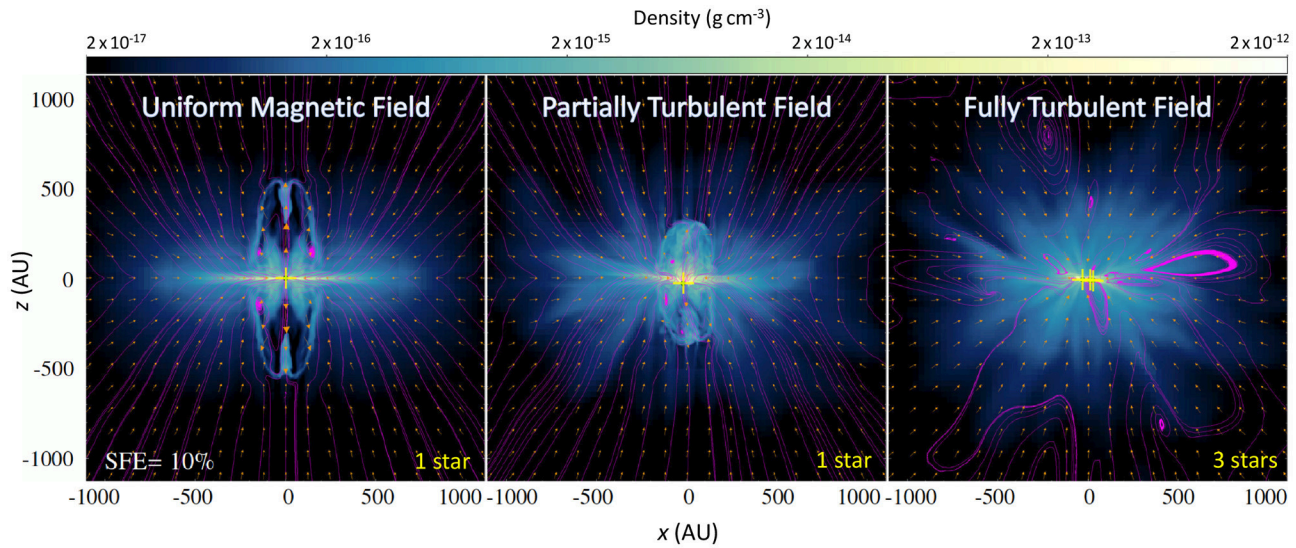

FIGURE 8 | Protostellar disc and jet formation simulations with different magnetic field geometries. The **(left)** panel shows the standard approach of using an initially uniform magnetic field aligned with the rotation axis of the core and disc. The **(middle)** panel adds a turbulent component to the uniform field component, such that both have the same rms. The **(right)** panel show the same simulation, but with a completely turbulent magnetic field (no guide-field component present). Outflows are strongest in the uniform-field case, with a fast collimated jet component launched from the inner parts of the disk. Partially turbulent magnetic fields still generate an outflow, but weaker and less collimated. In the absence of a uniform field component, however, jets are completely suppressed, but fragmentation of the disk is induced, i.e., three stars form in the fully turbulent case, compared to only a single star in the other two simulations. Figure adopted from Gerrard et al. (under review).

accretion rate onto the central star, making it more massive and thus more luminous. Fourth and finally, by creating protostellar outflows, magnetic fields provide a "vent" that stops radiation from building up to the points where radiation pressure begins to inhibit accretion (Krumholz et al., 2005; Cunningham et al., 2011; Peters et al., 2011; Kuiper et al., 2015, 2016). While these effects have all been demonstrated in idealized simulations starting from initial massive cores, it is unclear whether they are significant for production of the IMF overall.

Radiation and magnetic fields interact in a different way for very low mass stars and brown dwarfs. The majority of such objects likely form by direct fragmentation in much the same manner as stars near the peak of the IMF (e.g., see the review by Chabrier et al., 2014). However, formation via gravitational instability in the disk of a Solar-mass star represents a second possible formation channel, one for which we have direct observational evidence in at least some instances (Tobin et al., 2016). Magnetic fields (and non-ideal MHD effects) play a potentially-important role in modulating this channel, because they shape the properties of disks. In the extreme case of a protostellar core whose rotation axis is aligned with an initially-uniform magnetic field, and neglecting non-ideal effects, efficient magnetic braking prevents the formation of disks entirely (e.g., Mellon and Li, 2008; Hennebelle and Ciardi, 2009), and thus necessarily prevents the formation of brown dwarfs or other low mass objects via disk instability. In reality magnetic fields certainly do not suppress disk formation entirely; Keplerian disks are observed even around the youngest protostars (e.g., Tobin et al., 2012). There are numerous candidate explanations for why disks persist, including misalignment of the rotation axis and the magnetic field (Joos et al., 2012; Krumholz et al., 2013; Tsukamoto et al., 2018), suppressed magnetic braking due to turbulence (Seifried et al., 2012, 2013), and various non-ideal effects (Santos-Lima et al., 2012; Tsukamoto et al., 2015, 2018). Nonetheless, magnetic fields may reduce disk sizes compared to the purely hydrodynamic case, and smaller disks are in general more stable against self-gravity, because the matter is confined to regions where there is more stabilization by both shear and radiative heating from the central star (e.g., Kratter et al., 2010a). Thus magnetic fields likely reduce the incidence of disk fragmentation (Bürzle et al., 2011) and thereby suppress the disk formation channel for brown dwarfs and low mass stars. The amount of suppression is not yet known, since in the simulations carried out to date disk properties depend strongly on the assumed initial conditions. Moreover, even if magnetic fields do suppress disk fragmentation, it is not clear if this matters much for the overall IMF. Radiative heating by the central star renders disk fragmentation rare for stars near the peak of the IMF even in purely hydrodynamic simulations (e.g., Bate, 2009b, 2012; Offner et al., 2009b, 2010; Kratter et al., 2010b). Thus magnetic fields may simply further reduce a channel of brown dwarf formation that is already sub-dominant thanks to radiation feedback.

3.4. Prospects and Future Work on the IMF

We conclude that magnetic fields and feedback in the form of jets/outflows and radiation are important ingredients for understanding the IMF. Concerning magnetic fields in particular, there are two competing effects. On one hand, the magnetic field tends to directly reduce the fragmentation of cores and disks due to magnetic pressure and tension, therefore changing the physical conditions of the core and disk, even before stellar

feedback starts. The importance of this effect in simulations appears to depend on whether the simulations also include other mechanisms that suppress fragmentation, particularly radiation. In simulations including radiation, increasing the strength of magnetic fields from zero up to a level where the star-forming cloud is only barely supercritical increases the median stellar mass by a factor of $\approx 1.5-2$. On the other hand, magnetic fields also drive powerful jets and outflows, which limit the stellar mass and induce fragmentation. This effect produces an effective core-to-star efficiency of about 1/3. This effective core-to-star efficiency is the result of two effects. First, each individual core loses about 1/2 of its mass in the individual outflow of that core. Second, the outflows induce additional fragmentation of the filaments that feed the cores, thereby reducing the average star mass further by another factor of $\sim 2/3$. Because this feedback effect is comparable in magnitude but opposite in direction to the effects of magnetic fragmentation suppression, the net effect of both processes is to alter the location of the IMF peak at the factor of ≈ 2 level, smaller than one might expect based on consideration of either process alone.

Not only the magnitude of the magnetic field, but also its structure (ordered vs. turbulent) plays a critical role in controlling the strength of the outflows and in determining the resulting mass distribution of stars. Recent observational studies, for example with ALMA, are now beginning to reveal the complex magnetic field structures inside cores and disks, and in the outflows (Hull et al., 2017a; Cox et al., 2018; Zhang Y. et al., 2018), often showing turbulence and significant deviations from the classic hourglass shape. More observational constraints on the magnetic field geometry are needed to inform theoretical models and simulations.

In addition to the challenges in understanding the IMF at present day, we need to work even harder to understand what the mass function of primordial stars might have been. Observations so far can only provide indirect constraints on the mass of the first stars in the Universe. Simulations of the formation of the first stars indicate that the disks in which they form can fragment even under the conditions of primordial chemistry and cooling (Clark et al., 2011; Greif et al., 2011; Susa et al., 2014; Hirano et al., 2015). However, an important limitation of these studies is that they neither include magnetic fields nor jet/outflow feedback, both of which may play a crucial role also in primordial star formation (Federrath, 2018; Klessen, 2019).

4. SUMMARY AND PROSPECTS

Our view of the importance of magnetic fields in the process of star formation—and particularly in determining the two most important outputs of that process, the overall star formation rate (SFR) and the initial mass function (IMF) of stars—has changed dramatically over the last 15 years. Prior to that time, most theoretical models of star formation assigned magnetic support a key role in setting both the the SFR and the IMF. With the discovery that magnetic fields in star-forming regions are not as strong as once believed, so that most star-forming regions are magnetically supercritical, this view has shifted. In a supercritical region, magnetic fields cannot directly inhibit collapse by a substantial amount, and so magnetic fields alone cannot provide an explanation for the surprisingly-low rate of star formation that we observe on all scales, from individual clouds near the Sun to entire galaxies. Nor can they by themselves regulate the fragmentation of collapsing gas and thereby provide an explanation for the apparently universal or near-universal mass scale of stars.

While magnetic fields are no longer the star of the show, modern theoretical models and simulations tuned to match observed field strengths indicate that they still play a non-negligible supporting role. By providing resistance to turbulent compression and pressure that opposes gravity, magnetic fields directly reduce the ability of turbulence to gather gas into gravitationally-unstable clumps. This lowers the star formation rate by a factor of $2-3$ compared to the outcome in non-magnetized flows, and increases the median mass of those clumps that do become unstable and go on to form stars by a similar factor. The strength of this effect can be measured in simulations, but is not completely understood analytically, as it depends critically on how magnetic field strengths vary with density in a medium where the turbulence is supersonic and trans-Alfvénic. While we have a reasonable model for this correlation in super-Alfvénic flows, our model breaks down in the trans-Aflvénic regime that is more likely to characterize star formation. Progress toward a quantitative analytic understanding of how magnetic fields reduce the star formation rate and raise the mean mass of star-forming regions will require an extension of our understanding of the magnetic field-density correlation to this regime.

Magnetic fields also play a critical indirect role by providing the means for forming stars to launch jets and outflows. On small scales, outflows lower the mean stellar mass by a factor of ≈ 3, through a combination of ejecting gas that would otherwise accrete onto stars and by encouraging fragmentation. This nearly counters the effects of magnetic support in shifting the IMF to higher values, so that the combined effects of magnetic suppression of fragmentation and outflows is to change the mean stellar mass by only a factor of ≈ 2 compared to the outcome in a non-magnetized flow. On larger scales, outflows help stir turbulent motions in clouds and directly eject mass from collapsing regions, thereby lowering the rate of star formation by an additional factor of several compared to magnetized clouds without outflows, and by an order of magnitude or more compared to the case of purely hydrodynamic turbulence. Magnetic fields may also slow the rate of turbulent decay in collapsing clouds outright, although this prospect has thus far been demonstrated only in idealized compressing box simulations.

While the interplay of magnetic fields and outflows is now reasonably well if not fully understood, the interaction of magnetic fields with other forms of stellar feedback has been explored far less extensively. If there is any possibility for magnetic fields to return to a starring role in models of star formation, it lies in these unexplored frontiers. We highlight one particularly interesting prospect for further investigation, which is that magnetic fields might fundamentally change the way that

hot gas interacts with the cold ISM, by reducing the rate of material and thermal exchange across hot-cold gas interfaces. This could potentially make supernovae feedback much more effective than currently suspected, which in turn would have major implications for the star formation rate and, on larger scales, for the properties of galactic winds. However, this is just one example—the interaction of magnetic fields with other types of feedback is equally-poorly known, and the possibility remains that magnetic effects will again prove crucial to models of star formation.

AUTHOR CONTRIBUTIONS

All authors listed have made a substantial, direct and intellectual contribution to the work, and approved it for publication.

FUNDING

MK and CF acknowledge support from the Australian Research Council's *Discovery Projects* and *Future Fellowship* funding schemes, awards DP150104329 (CF), DP160100695 (MK), DP170100603 (CF), FT180100375 (MK) and FT180100495 (CF), and the Australia-Germany Joint Research Cooperation Scheme (UA-DAAD; both MK and CF).

ACKNOWLEDGMENTS

MK and CF both acknowledge the assistance of resources and services from the National Computational Infrastructure (NCI), which is supported by the Australian Government. We further acknowledge high-performance computing resources provided by the Leibniz Rechenzentrum and the Gauss Centre for Supercomputing (grants pr32lo, pr48pi and GCS Large-scale project 10391; CF), the Partnership for Advanced Computing in Europe (PRACE grant pr89mu; CF), and Australian National Computational Infrastructure grants jh2 (MK) and ek9 (CF) in the framework of the National Computational Merit Allocation Scheme and the ANU Allocation Scheme. We thank A. Tristis, B. Gerrard, and two referees for helpful comments.

REFERENCES

Alves, J., Lombardi, M., and Lada, C. J. (2007). The mass function of dense molecular cores and the origin of the IMF. *Astron. Astrophys.* 462, L17–L21. doi: 10.1051/0004-6361:20066389

André, P., Men'shchikov, A., Bontemps, S., Könyves, V., Motte, F., Schneider, N., et al. (2010). From filamentary clouds to prestellar cores to the stellar IMF: initial highlights from the Herschel Gould Belt Survey. *Astron. Astrophys.* 518:L102. doi: 10.1051/0004-6361/201014666

Andrews, J. E., Calzetti, D., Chandar, R., Elmegreen, B. G., Kennicutt, R. C., Kim, H., et al. (2014). Big fish in small ponds: massive stars in the low-mass clusters of M83. *Astrophys. J.* 793:4. doi: 10.1088/0004-637X/793/1/4

Andrews, J. E., Calzetti, D., Chandar, R., Lee, J. C., Elmegreen, B. G., Kennicutt, R. C., et al. (2013). An initial mass function study of the dwarf starburst galaxy NGC 4214. *Astrophys. J.* 767:51. doi: 10.1088/0004-637X/767/1/51

Arthur, S. J., Henney, W. J., Mellema, G., de Colle, F., and Vázquez-Semadeni, E. (2011). Radiation-magnetohydrodynamic simulations of H II regions and their associated PDRs in turbulent molecular clouds. *Month. Notices R. Astron. Soc.* 414, 1747–1768. doi: 10.1111/j.1365-2966.2011.18507.x

Bally, J. (2016). Protostellar outflows. *Annu. Rev. Astron. Astrophys.* 54, 491–528. doi: 10.1146/annurev-astro-081915-023341

Banda-Barragán, W. E., Federrath, C., Crocker, R. M., and Bicknell, G. V. (2018). Filament formation in wind-cloud interactions- II. Clouds with turbulent density, velocity, and magnetic fields. *Month. Notices R. Astron. Soc.* 473, 3454–3489. doi: 10.1093/mnras/stx2541

Banda-Barragán, W. E., Parkin, E. R., Federrath, C., Crocker, R. M., and Bicknell, G. V. (2016). Filament formation in wind-cloud interactions - I. Spherical clouds in uniform magnetic fields. *Month. Notices R. Astron. Soc.* 455, 1309–1333. doi: 10.1093/mnras/stv2405

Banerjee, R., and Pudritz, R. E. (2006). Outflows and jets from collapsing magnetized cloud cores. *Astrophys. J.* 641, 949–960. doi: 10.1086/500496

Bate, M. R. (2009). The importance of radiative feedback for the stellar initial mass function. *Month. Notices R. Astron. Soc.* 392, 1363–1380. doi: 10.1111/j.1365-2966.2008.14165.x

Bate, M. R. (2009b). The importance of radiative feedback for the stellar initial mass function. *Month. Notices R. Astron. Soc.* 392, 1363–1380.

Bate, M. R. (2012). Stellar, brown dwarf and multiple star properties from a radiation hydrodynamical simulation of star cluster formation. *Month. Notices R. Astron. Soc.* 419, 3115–3146. doi: 10.1111/j.1365-2966.2011.19955.x

Bate, M. R. (2014). The statistical properties of stars and their dependence on metallicity: the effects of opacity. *Month. Notices R. Astron. Soc.* 442, 285–313. doi: 10.1093/mnras/stu795

Benedettini, M., Pezzuto, S., Schisano, E., André, P., Könyves, V., Men'shchikov, A., et al. (2018). A catalogue of dense cores and young stellar objects in the Lupus complex based on Herschel. Gould Belt Survey observations. *Astron. Astrophys.* 619:A52. doi: 10.1051/0004-6361/201833364

Bertelli Motta, C., Clark, P. C., Glover, S. C. O., Klessen, R. S., and Pasquali, A. (2016). The IMF as a function of supersonic turbulence. *Month. Notices R. Astron. Soc.* 462, 4171–4182. doi: 10.1093/mnras/stw1921

Bigiel, F., Leroy, A., Walter, F., Brinks, E., de Blok, W. J. G., Madore, B., et al. (2008). The star formation law in nearby galaxies on sub-kpc scales. *Astron. J.* 136, 2846–2871. doi: 10.1088/0004-6256/136/6/2846

Birnboim, Y., Federrath, C., and Krumholz, M. (2018). Compression of turbulent magnetized gas in giant molecular clouds. *Month. Notices R. Astron. Soc.* 473, 2144–2159. doi: 10.1093/mnras/stx2426

Blanc, G. A., Heiderman, A., Gebhardt, K., Evans, N. J., and Adams, J. (2009). The spatially resolved star formation law from integral field spectroscopy: VIRUS-P observations of NGC 5194. *Astrophys. J.* 704, 842–862. doi: 10.1088/0004-637X/704/1/842

Blandford, R. D., and Payne, D. G. (1982). Hydromagnetic flows from accretion discs and the production of radio jets. *Month. Notices R. Astron. Soc.* 199, 883–903. doi: 10.1093/mnras/199.4.883

Boulares, A., and Cox, D. P. (1990). Galactic hydrostatic equilibrium with magnetic tension and cosmic-ray diffusion. *Astrophys. J.* 365, 544–558. doi: 10.1086/169509

Brandenburg, A., and Subramanian, K. (2005). Astrophysical magnetic fields and nonlinear dynamo theory. *Phys. Rep.* 417, 1–209. doi: 10.1016/j.physrep.2005.06.005

Brunt, C. M., Federrath, C., and Price, D. J. (2010). A method for reconstructing the variance of a 3D physical field from 2D observations: application to turbulence in the interstellar medium. *Month. Notices R. Astron. Soc.* 403, 1507–1515. doi: 10.1111/j.1365-2966.2009.16215.x

Burkhart, B. (2018). The star formation rate in the gravoturbulent interstellar medium. *Astrophys. J.* 863:118. doi: 10.3847/1538-4357/aad002

Burkhart, B., Falceta-Gonçalves, D., Kowal, G., and Lazarian, A. (2009). Density studies of MHD interstellar turbulence: statistical moments, correlations and bispectrum. *Astrophys. J.* 693, 250–266. doi: 10.1088/0004-637X/693/1/250

Burkhart, B., Lazarian, A., Balsara, D., Meyer, C., and Cho, J. (2015). Alfvénic turbulence beyond the ambipolar diffusion scale. *Astrophys. J.* 805:118. doi: 10.1088/0004-637X/805/2/118

Burkhart, B., and Mocz, P. (2018). The dense gas fraction and the critical density required for star formation. *Astrophys. J.*. arXiv:1805.11104.

Burkhart, B., Stalpes, K., and Collins, D. C. (2017). The Razor's edge of collapse: the transition point from lognormal to power-law distributions in molecular clouds. *Astrophys. J. Lett.* 834:L1. doi: 10.3847/2041-8213/834/1/L1

Bürzle, F., Clark, P. C., Stasyszyn, F., Greif, T., Dolag, K., Klessen, R. S., et al. (2011). Protostellar collapse and fragmentation using an MHD GADGET. *Month. Notices R. Astron. Soc.* 412, 171–186. doi: 10.1111/j.1365-2966.2010.17896.x

Bykov, A. M. (2014). Nonthermal particles and photons in starburst regions and superbubbles. *Astron. Astrophys. Rev.* 22:77. doi: 10.1007/s00159-014-0077-8

Chabrier, G. (2003). Galactic stellar and substellar initial mass function. *Publ. ASP* 115, 763–795. doi: 10.1086/376392

Chabrier, G. (2005). "The initial mass function: from Salpeter 1955 to 2005," in *The Initial Mass Function 50 Years Later, Vol. 327 of Astrophysics and Space Science Library*, eds E. Corbelli, F. Palla, and H. Zinnecker (Dordrecht: Springer), 41.

Chabrier, G., Johansen, A., Janson, M., and Rafikov, R. (2014). "Giant planet and brown dwarf formation," in *Protostars and Planets VI*, eds H. Beuther, R. S. Klessen, C. P. Dullemond, and T. Henning (Tucson, AZ: University of Arizona Press), 619.

Chen, Z., Jiang, Z., Tamura, M., Kwon, J., and Roman-Lopes, A. (2017). A curved magnetic field in the ring-like shell of bubble N4. *Astrophys. J.* 838:80. doi: 10.3847/1538-4357/aa65d3

Ching, T.-C., Lai, S.-P., Zhang, Q., Girart, J. M., Qiu, K., and Liu, H. B. (2017). Magnetic fields in the massive dense cores of the DR21 filament: weakly magnetized cores in a strongly magnetized filament. *Astrophys. J.* 838:121. doi: 10.3847/1538-4357/aa65cc

Cho, J., and Lazarian, A. (2003). Compressible magnetohydrodynamic turbulence: mode coupling, scaling relations, anisotropy, viscosity-damped regime and astrophysical implications. *Month. Notices R. Astron. Soc.* 345, 325–339. doi: 10.1046/j.1365-8711.2003.06941.x

Clark, P. C., Glover, S. C. O., Smith, R. J., Greif, T. H., Klessen, R. S., and Bromm, V. (2011). The formation and fragmentation of disks around primordial protostars. *Science* 331, 1040–1042. doi: 10.1126/science.1198027

Collins, D. C., Kritsuk, A. G., Padoan, P., Li, H., Xu, H., Ustyugov, S. D., et al. (2012). The two states of star-forming clouds. *Astrophys. J.* 750:13. doi: 10.1088/0004-637X/750/1/13

Collins, D. C., Padoan, P., Norman, M. L., and Xu, H. (2011). Mass and magnetic distributions in self-gravitating super-Alfvénic turbulence with adaptive mesh refinement. *Astrophys. J.* 731:59. doi: 10.1088/0004-637X/731/1/59

Commerçon, B., Hennebelle, P., Audit, E., Chabrier, G., and Teyssier, R. (2010). Protostellar collapse: radiative and magnetic feedbacks on small-scale fragmentation. *Astron. Astrophys.* 510:L3. doi: 10.1051/0004-6361/200913597

Commerçon, B., Hennebelle, P., and Henning, T. (2011). Collapse of massive magnetized dense cores using radiation magnetohydrodynamics: early fragmentation inhibition. *Astrophys. J. Lett.* 742:L9. doi: 10.1088/2041-8205/742/1/L9

Cowie, L. L., and McKee, C. F. (1977). The evaporation of spherical clouds in a hot gas. I - Classical and saturated mass loss rates. *Astrophys. J.* 211, 135–146. doi: 10.1086/154911

Cox, E. G., Harris, R. J., Looney, L. W., Li, Z.-Y., Yang, H., Tobin, J. J., et al. (2018). ALMA's polarized view of 10 protostars in the perseus molecular cloud. *Astrophys. J.* 855:92. doi: 10.3847/1538-4357/aaacd2

Crocker, R. M., Krumholz, M. R., Thompson, T. A., and Clutterbuck, J. (2018). The maximum flux of star-forming galaxies. *Month. Notices R. Astron. Soc.* 478, 81–94. doi: 10.1093/mnras/sty989

Crutcher, R. M. (2012). Magnetic fields in molecular clouds. *Annu. Rev. Astron. Astrophys.* 50, 29–63. doi: 10.1146/annurev-astro-081811-125514

Cunningham, A. J., Klein, R. I., Krumholz, M. R., and McKee, C. F. (2011). Radiation-hydrodynamic simulations of massive star formation with protostellar outflows. *Astrophys. J.* 740:107. doi: 10.1088/0004-637X/740/2/107

Cunningham, A. J., Krumholz, M. R., McKee, C. F., and Klein, R. I. (2018). The effects of magnetic fields and protostellar feedback on low-mass cluster formation. *Month. Notices R. Astron. Soc.* 476, 771–792. doi: 10.1093/mnras/sty154

Da Rio, N., Robberto, M., Hillenbrand, L. A., Henning, T., and Stassun, K. G. (2012). The initial mass function of the orion nebula cluster across the H-burning limit. *Astrophys. J.* 748:14. doi: 10.1088/0004-637X/748/1/14

de Marchi, G., and Paresce, F. (2001). "The mass function of galactic clusters and its evolution with time," in *Astronomische Gesellschaft Meeting Abstracts, Vol. 18 of Astronomische Gesellschaft Meeting Abstracts*, ed E. R. Schielicke, S0551D. Available online at: http://adsabs.harvard.edu/abs/2001AGM....18S0551D

Dib, S. (2014). Testing the universality of the IMF with Bayesian statistics: young clusters. *Month. Notices R. Astron. Soc.* 444, 1957–1981. doi: 10.1093/mnras/stu1521

Dib, S., Bell, E., and Burkert, A. (2006). The supernova rate-velocity dispersion relation in the interstellar medium. *Astrophys. J.* 638, 797–810. doi: 10.1086/498857

Dib, S., and Burkert, A. (2005). On the origin of the H I holes in the interstellar medium of dwarf irregular galaxies. *Astrophys. J.* 630, 238–249. doi: 10.1086/431785

Dib, S., Hennebelle, P., Pineda, J. E., Csengeri, T., Bontemps, S., Audit, E., et al. (2010a). The angular momentum of magnetized molecular cloud cores: a two-dimensional-three-dimensional comparison. *Astrophys. J.* 723, 425–439. doi: 10.1088/0004-637X/723/1/425

Dib, S., Kim, J., Vázquez-Semadeni, E., Burkert, A., and Shadmehri, M. (2007). The virial balance of clumps and cores in molecular clouds. *Astrophys. J.* 661, 262–284. doi: 10.1086/513708

Dib, S., Schmeja, S., and Hony, S. (2017). Massive stars reveal variations of the stellar initial mass function in the Milky Way stellar clusters. *Month. Notices R. Astron. Soc.* 464, 1738–1752. doi: 10.1093/mnras/stw2465

Dib, S., Shadmehri, M., Padoan, P., Maheswar, G., Ojha, D. K., and Khajenabi, F. (2010b). The IMF of stellar clusters: effects of accretion and feedback. *Month. Notices R. Astron. Soc.* 405, 401–420. doi: 10.1111/j.1365-2966.2010.16451.x

Downes, T. P. (2012). Driven multifluid magnetohydrodynamic molecular cloud turbulence. *Month. Notices R. Astron. Soc.* 425, 2277–2286. doi: 10.1111/j.1365-2966.2012.21577.x

Draine, B. T. (2011). *Physics of the Interstellar and Intergalactic Medium*. Princeton, NJ: Princeton University Press.

Dunne, B. C., Chu, Y.-H., Chen, C. H. R., Lowry, J. D., Townsley, L., Gruendl, R. A., et al. (2003). Diffuse X-Ray emission from the quiescent superbubble M17, the omega nebula. *Astrophys. J.* 590, 306–313. doi: 10.1086/375010

Elmegreen, B. G., and Scalo, J. (2004). Interstellar turbulence I: observations and processes. *Annu. Rev. Astron. Astrophys.* 42, 211–273. doi: 10.1146/annurev.astro.41.011802.094859

Enoch, M. L., Evans, N. J. II, Sargent, A. I., Glenn, J., Rosolowsky, E., and Myers, P. (2008). The mass distribution and lifetime of prestellar cores in perseus, serpens, and ophiuchus. *Astrophys. J.* 684, 1240–1259. doi: 10.1086/589963

Evans, N. J. II, Dunham, M. M., Jørgensen, J. K., Enoch, M. L., Merín, B., van Dishoeck, E. F., et al. (2009). The spitzer c2d legacy results: star-formation rates and efficiencies; evolution and lifetimes. *Astrophys. J. Suppl.* 181, 321–350. doi: 10.1088/0067-0049/181/2/321

Evans, N. J. II, Heiderman, A., and Vutisalchavakul, N. (2014). Star formation relations in nearby molecular clouds. *Astrophys. J.* 782:114. doi: 10.1088/0004-637X/782/2/114

Faucher-Giguère, C.-A., Quataert, E., and Hopkins, P. F. (2013). Feedback-regulated star formation in molecular clouds and galactic discs. *Month. Notices R. Astron. Soc.* 433, 1970–1990. doi: 10.1093/mnras/stt866

Federrath, C. (2013a). On the universality of supersonic turbulence. *Month. Notices R. Astron. Soc.* 436, 1245–1257. doi: 10.1093/mnras/stt1644

Federrath, C. (2013b). The origin of physical variations in the star formation law. *Month. Notices R. Astron. Soc.* 436, 3167–3172. doi: 10.1093/mnras/stt1799

Federrath, C. (2015). Inefficient star formation through turbulence, magnetic fields and feedback. *Month. Notices R. Astron. Soc.* 450, 4035–4042. doi: 10.1093/mnras/stv941

Federrath, C. (2016a). Magnetic field amplification in turbulent astrophysical plasmas. *J. Plasma Phys.* 82:535820601. doi: 10.1017/S0022377816001069

Federrath, C. (2016b). On the universality of interstellar filaments: theory meets simulations and observations. *Month. Notices R. Astron. Soc.* 457, 375–388. doi: 10.1093/mnras/stv2880

Federrath, C. (2018). The turbulent formation of stars. *Phys. Today* 71, 38–42. doi: 10.1063/PT.3.3947

Federrath, C., and Banerjee, S. (2015). The density structure and star formation rate of non-isothermal polytropic turbulence. *Month. Notices R. Astron. Soc.* 448, 3297–3313. doi: 10.1093/mnras/stv180

Federrath, C., Chabrier, G., Schober, J., Banerjee, R., Klessen, R. S., and Schleicher, D. R. G. (2011a). Mach number dependence of turbulent magnetic field amplification: solenoidal versus compressive flows. *Phys. Rev. Lett.* 107:114504. doi: 10.1103/PhysRevLett.107.114504

Federrath, C., and Klessen, R. S. (2012). The star formation rate of turbulent magnetized clouds: comparing theory, simulations, and observations. *Astrophys. J.* 761:156. doi: 10.1088/0004-637X/761/2/156

Federrath, C., and Klessen, R. S. (2013). On the star formation efficiency of turbulent magnetized clouds. *Astrophys. J.* 763:51. doi: 10.1088/0004-637X/763/1/51

Federrath, C., Klessen, R. S., and Schmidt, W. (2008). The density probability distribution in compressible isothermal turbulence: solenoidal versus compressive forcing. *Astrophys. J. Lett.* 688, L79–L82. doi: 10.1086/595280

Federrath, C., Krumholz, M., and Hopkins, P. F. (2017). Converging on the initial mass function of stars. *J. Phys. Conf. Ser.* 837:012007. doi: 10.1088/1742-6596/837/1/012007

Federrath, C., Rathborne, J. M., Longmore, S. N., Kruijssen, J. M. D., Bally, J., Contreras, Y., et al. (2016). The link between turbulence, magnetic fields, filaments, and star formation in the central molecular zone cloud G0.253+0.016. *Astrophys. J.* 832:143. doi: 10.3847/0004-637X/832/2/143

Federrath, C., Roman-Duval, J., Klessen, R. S., Schmidt, W., and Mac Low, M. (2010). Comparing the statistics of interstellar turbulence in simulations and observations. Solenoidal versus compressive turbulence forcing. *Astron. Astrophys.* 512:A81. doi: 10.1051/0004-6361/200912437

Federrath, C., Schober, J., Bovino, S., and Schleicher, D. R. G. (2014a). The turbulent dynamo in highly compressible supersonic plasmas. *Astrophys. J. Lett.* 797:L19. doi: 10.1088/2041-8205/797/2/L19

Federrath, C., Schrön, M., Banerjee, R., and Klessen, R. S. (2014b). Modeling jet and outflow feedback during star cluster formation. *Astrophys. J.* 790:128. doi: 10.1088/0004-637X/790/2/128

Federrath, C., Sur, S., Schleicher, D. R. G., Banerjee, R., and Klessen, R. S. (2011b). A new jeans resolution criterion for (M)HD simulations of self-gravitating gas: application to magnetic field amplification by gravity-driven turbulence. *Astrophys. J.* 731:62. doi: 10.1088/0004-637X/731/1/62

Field, G. B. (1965). Thermal instability. *Astrophys. J.* 142:531. doi: 10.1086/148317

Fierlinger, K. M., Burkert, A., Ntormousi, E., Fierlinger, P., Schartmann, M., Ballone, A., et al. (2016). Stellar feedback efficiencies: supernovae versus stellar winds. *Month. Notices R. Astron. Soc.* 456, 710–730. doi: 10.1093/mnras/stv2699

Frank, A., Ray, T. P., Cabrit, S., Hartigan, P., Arce, H. G., Bacciotti, F., et al. (2014). "Jets and outflows from star to cloud: observations confront theory," in *Protostars and Planets VI*, eds H. Beuther, R. S.Klessen, C. P. Dullemond and T. Henning (Tucson, AZ: University of Arizona Press), 451–474.

Gallagher, M. J., Leroy, A. K., Bigiel, F., Cormier, D., Jiménez-Donaire, M. J., Ostriker, E., et al. (2018). Dense gas, dynamical equilibrium pressure, and star formation in nearby star-forming galaxies. *Astrophys. J.* 858:90. doi: 10.3847/1538-4357/aabad8

Geen, S., Hennebelle, P., Tremblin, P., and Rosdahl, J. (2015). Photoionization feedback in a self-gravitating, magnetized, turbulent cloud. *Month. Notices R. Astron. Soc.* 454, 4484–4502. doi: 10.1093/mnras/stv2272

Geen, S., Soler, J. D., and Hennebelle, P. (2017). Interpreting the star formation efficiency of nearby molecular clouds with ionizing radiation. *Month. Notices R. Astron. Soc.* 471, 4844–4855. doi: 10.1093/mnras/stx1765

Gendelev, L., and Krumholz, M. R. (2012). Evolution of blister-type H II regions in a magnetized medium. *Astrophys. J.* 745:158. doi: 10.1088/0004-637X/745/2/158

Gentry, E. S., Krumholz, M. R., Dekel, A., and Madau, P. (2017). Enhanced momentum feedback from clustered supernovae. *Month. Notices R. Astron. Soc.* 465, 2471–2488. doi: 10.1093/mnras/stw2746

Gentry, E. S., Krumholz, M. R., Madau, P., and Lupi, A. (2019). The momentum budget of clustered supernova feedback in a 3D, magnetised medium. *Month. Notices R. Astron. Soc.* arXiv:1802.06860.

Girichidis, P., Konstandin, L., Whitworth, A. P., and Klessen, R. S. (2014). On the evolution of the density probability density function in strongly self-gravitating systems. *Astrophys. J.* 781:91. doi: 10.1088/0004-637X/781/2/91

Girichidis, P., Naab, T., Hanasz, M., and Walch, S. (2018). Cooler and smoother - the impact of cosmic rays on the phase structure of galactic outflows. *Month. Notices R. Astron. Soc.* 479, 3042–3067. doi: 10.1093/mnras/sty1653

Green, A. W., Glazebrook, K., McGregor, P. J., Abraham, R. G., Poole, G. B., Damjanov, I., et al. (2010). High star formation rates as the origin of turbulence in early and modern disk galaxies. *Nature* 467, 684–686. doi: 10.1038/nature09452

Greif, T. H., Springel, V., White, S. D. M., Glover, S. C. O., Clark, P. C., Smith, R. J., et al. (2011). Simulations on a moving mesh: the clustered formation of population III protostars. *Astrophys. J.* 737:75. doi: 10.1088/0004-637X/737/2/75

Grudić, M. Y., Hopkins, P. F., Faucher-Giguère, C.-A., Quataert, E., Murray, N., and Kereš, D. (2018). When feedback fails: the scaling and saturation of star formation efficiency. *Month. Notices R. Astron. Soc.* 475, 3511–3528. doi: 10.1093/mnras/sty035

Guszejnov, D., Hopkins, P. F., Grudić, M. Y., Krumholz, M. R., and Federrath, C. (2018). Isothermal fragmentation: is there a low-mass cut-off? *Month. Notices R. Astron. Soc. arXiv:1804.08574*. doi: 10.1093/mnras/sty1847

Guszejnov, D., Krumholz, M. R., and Hopkins, P. F. (2016). The necessity of feedback physics in setting the peak of the initial mass function. *Month. Notices R. Astron. Soc.* 458, 673–680. doi: 10.1093/mnras/stw315

Hansen, C. E., Klein, R. I., McKee, C. F., and Fisher, R. T. (2012). Feedback effects on low-mass star formation. *Astrophys. J.* 747:22. doi: 10.1088/0004-637X/747/1/22

Hansen, C. E., Klein, R. I., McKee, C. F., and Fisher, R. T. (2012b).Feedback Effects on Low-mass Star Formation.*Astrophys. J.* 747:22.

Hansen, C. E., McKee, C. F., and Klein, R. I. (2011). Anisotropy lengthens the decay time of turbulence in molecular clouds. *Astrophys. J.* 738:88. doi: 10.1088/0004-637X/738/1/88

Haugbølle, T., Padoan, P., and Nordlund, Å. (2018). The stellar IMF from isothermal MHD turbulence. *Astrophys. J.* 854:35. doi: 10.3847/1538-4357/aaa432

Heiderman, A., Evans, N. J. II, Allen, L. E., Huard, T., and Heyer, M. (2010). The star formation rate and gas surface density relation in the milky way: implications for extragalactic studies. *Astrophys. J.* 723, 1019–1037. doi: 10.1088/0004-637X/723/2/1019

Heitsch, F., Mac Low, M.-M., and Klessen, R. S. (2001). Gravitational collapse in turbulent molecular clouds. II. Magnetohydrodynamical turbulence. *Astrophys. J.* 547, 280–291. doi: 10.1086/318335

Hennebelle, P., and Chabrier, G. (2008). Analytical theory for the initial mass function: CO clumps and prestellar cores. *Astrophys. J.* 684, 395–410. doi: 10.1086/589916

Hennebelle, P., and Chabrier, G. (2009). Analytical theory for the initial mass function. II. properties of the flow. *Astrophys. J.* 702, 1428–1442. doi: 10.1088/0004-637X/702/2/1428

Hennebelle, P., and Chabrier, G. (2011). Analytical star formation rate from gravoturbulent fragmentation. *Astrophys. J. Lett.* 743:L29. doi: 10.1088/2041-8205/743/2/L29

Hennebelle, P., and Chabrier, G. (2013). Analytical theory for the initial mass function. III. Time dependence and star formation rate. *Astrophys. J.* 770:150. doi: 10.1088/0004-637X/770/2/150

Hennebelle, P., and Ciardi, A. (2009). Disk formation during collapse of magnetized protostellar cores. *Astron. Astrophys.* 506, L29–L32. doi: 10.1051/0004-6361/200913008

Hennebelle, P., Commerçon, B., Joos, M., Klessen, R. S., Krumholz, M., Tan, J. C., et al. (2011). Collapse, outflows and fragmentation of massive, turbulent and magnetized prestellar barotropic cores. *Astron. Astrophys.* 528:A72. doi: 10.1051/0004-6361/201016052

Hennebelle, P., and Teyssier, R. (2008). Magnetic processes in a collapsing dense core. II. Fragmentation. Is there a fragmentation crisis? *Astron. Astrophys.* 477, 25–34. doi: 10.1051/0004-6361:20078310

Heyer, M., Gutermuth, R., Urquhart, J. S., Csengeri, T., Wienen, M., Leurini, S., et al. (2016). The rate and latency of star formation in dense, massive clumps in the Milky Way. *Astron. Astrophys.* 588:A29. doi: 10.1051/0004-6361/201527681

Heyer, M. H. and Brunt, C. M. (2004). The universality of turbulence in galactic molecular clouds. *Astrophys. J. Lett.* 615, L45–L48. doi: 10.1086/425978

Heyer, M. H., and Brunt, C. M. (2012). Trans-Alfvénic motions in the Taurus molecular cloud. *Month. Notices R. Astron. Soc.* 420, 1562–1569. doi: 10.1111/j.1365-2966.2011.20142.x

Hirano, S., Hosokawa, T., Yoshida, N., Omukai, K., and Yorke, H. W. (2015). Primordial star formation under the influence of far ultraviolet radiation: 1540 cosmological haloes and the stellar mass distribution. *Month. Notices R. Astron. Soc.* 448, 568–587. doi: 10.1093/mnras/stv044

Hodapp, K. W., and Chini, R. (2018). Variability and jet activity in the YSO MHO˜3252˜Y3 in serpens south. *ArXiv e-prints*. doi: 10.3847/1538-4357/aad636

Hopkins, A. M. (2018). The dawes review 8: measuring the stellar initial mass function. *ArXiv e-prints*. doi: 10.1017/pasa.2018.29

Hopkins, P. F. (2012). An excursion-set model for the structure of giant molecular clouds and the interstellar medium. *Month. Notices R. Astron. Soc.* 423, 2016–2036. doi: 10.1111/j.1365-2966.2012.20730.x

Hopkins, P. F. (2013). A general theory of turbulent fragmentation. *Month. Notices R. Astron. Soc.* 430, 1653–1693. doi: 10.1093/mnras/sts704

Hopkins, P. F., Quataert, E., and Murray, N. (2011). Self-regulated star formation in galaxies via momentum input from massive stars. *Month. Notices R. Astron. Soc.* 417, 950–973. doi: 10.1111/j.1365-2966.2011.19306.x

Hosek, M. W. Jr, Lu, J. R., Anderson, J., Najarro, F., Ghez, A. M., Morris, M. R., et al. (2019). The unusual initial mass function of the arches cluster. *Astrophys. J.*. 870:44. doi: 10.3847/1538-4357/aaef90

Hull, C. L. H., Girart, J. M., Tychoniec, Ł., Rao, R., Cortés, P. C., Pokhrel, R., et al. (2017a). ALMA observations of dust polarization and molecular line emission from the class 0 protostellar source serpens SMM1. *Astrophys. J.* 847:92. doi: 10.3847/1538-4357/aa7fe9

Hull, C. L. H., Mocz, P., Burkhart, B., Goodman, A. A., Girart, J. M., Cortés, P. C., et al. (2017b). Unveiling the role of the magnetic field at the smallest scales of star formation. *Astrophys. J. Lett.* 842:L9. doi: 10.3847/2041-8213/aa71b7

Iffrig, O., and Hennebelle, P. (2015). Mutual influence of supernovae and molecular clouds. *Astron. Astrophys.* 576:A95. doi: 10.1051/0004-6361/201424556

Inutsuka, S.-I. (2001). The mass function of molecular cloud cores. *Astrophys. J. Lett.* 559, L149–L152. doi: 10.1086/323786

Joos, M., Hennebelle, P., and Ciardi, A. (2012). Protostellar disk formation and transport of angular momentum during magnetized core collapse. *Astron. Astrophys.* 543:A128. doi: 10.1051/0004-6361/201118730

Joung, M. K. R., and Mac Low, M.-M. (2006). Turbulent structure of a stratified supernova-driven interstellar medium. *Astrophys. J.* 653, 1266–1279. doi: 10.1086/508795

Kauffmann, J., Goldsmith, P. F., Melnick, G., Tolls, V., Guzman, A., and Menten, K. M. (2017). Molecular line emission as a tool for galaxy observations (LEGO). I. HCN as a tracer of moderate gas densities in molecular clouds and galaxies. *Astron. Astrophys.* 605:L5. doi: 10.1051/0004-6361/201731123

Keller, B. W., Wadsley, J., Benincasa, S. M., and Couchman, H. M. P. (2014). A superbubble feedback model for galaxy simulations. *Month. Notices R. Astron. Soc.* 442, 3013–3025. doi: 10.1093/mnras/stu1058

Keller, B. W., Wadsley, J., and Couchman, H. M. P. (2015). Cosmological galaxy evolution with superbubble feedback - I. Realistic galaxies with moderate feedback. *Month. Notices R. Astron. Soc.* 453, 3499–3509. doi: 10.1093/mnras/stv1789

Kim, C.-G., and Basu, S. (2013). Long-term evolution of decaying magnetohydrodynamic turbulence in the multiphase interstellar medium. *Astrophys. J.* 778:88. doi: 10.1088/0004-637X/778/2/88

Kim, C.-G., and Ostriker, E. C. (2015). Momentum injection by supernovae in the interstellar medium. *Astrophys. J.* 802:99. doi: 10.1088/0004-637X/802/2/99

Kim, C.-G., Ostriker, E. C., and Raileanu, R. (2017). Superbubbles in the multiphase ISM and the loading of galactic winds. *Astrophys. J.* 834:25. doi: 10.3847/1538-4357/834/1/25

Kim, J.-G., Kim, W.-T., and Ostriker, E. C. (2018). Modeling UV radiation feedback from massive stars. II. Dispersal of star-forming giant molecular clouds by photoionization and radiation pressure. *Astrophys. J.* 859:68. doi: 10.3847/1538-4357/aabe27

Klessen, R. S. (2000). One-point probability distribution functions of supersonic turbulent flows in self-gravitating Media. *Astrophys. J.* 535, 869–886. doi: 10.1086/308854

Klessen, R. S. (2019). "Formation of the first stars," in *Formation of the First Black Holes*, eds M. A. Latif and D. R. G. Schleicher (Singapore: World Scientific Publishing), 67–98. doi: 10.1142/10652

Konstandin, L., Girichidis, P., Federrath, C., and Klessen, R. S. (2012). A new density variance-mach number relation for subsonic and supersonic isothermal turbulence. *Astrophys. J.* 761:149. doi: 10.1088/0004-637X/761/2/149

Könyves, V., André, P., Men'shchikov, A., Schneider, N., Arzoumanian, D., Bontemps, S., et al. (2010). The Aquila prestellar core population revealed by Herschel. *Astron. Astrophys.* 518:L106. doi: 10.1051/0004-6361/201014689

Kowal, G., Lazarian, A., and Beresnyak, A. (2007). Density fluctuations in MHD turbulence: spectra, intermittency, and topology. *Astrophys. J.* 658, 423–445. doi: 10.1086/511515

Koyama, H., and Inutsuka, S.-i. (2004). The field condition: a new constraint on spatial resolution in simulations of the nonlinear development of thermal instability. *Astrophys. J. Lett.* 602, L25–L28. doi: 10.1086/382478

Kratter, K. M., Matzner, C. D., Krumholz, M. R., and Klein, R. I. (2010a). On the role of disks in the formation of stellar systems: a numerical parameter study of rapid accretion. *Astrophys. J.* 708, 1585–1597. doi: 10.1088/0004-637X/708/2/1585

Kratter, K. M., Murray-Clay, R. A., and Youdin, A. N. (2010b). The runts of the litter: why planets formed through gravitational instability can only be failed binary stars. *Astrophys. J.* 710, 1375–1386. doi: 10.1088/0004-637X/710/2/1375

Kritsuk, A. G., Norman, M. L., Padoan, P., and Wagner, R. (2007). The statistics of supersonic isothermal turbulence. *Astrophys. J.* 665, 416–431. doi: 10.1086/519443

Kritsuk, A. G., Norman, M. L., and Wagner, R. (2011). On the density distribution in star-forming interstellar clouds. *Astrophys. J. Lett.* 727:L20. doi: 10.1088/2041-8205/727/1/L20

Kroupa, P. (2001). On the variation of the initial mass function. *Month. Notices R. Astron. Soc.* 322, 231–246. doi: 10.1046/j.1365-8711.2001.04022.x

Krumholz, M. R. (2011). On the origin of stellar masses. *Astrophys. J.* 743:110. doi: 10.1088/0004-637X/743/2/110

Krumholz, M. R. (2014). The big problems in star formation: the star formation rate, stellar clustering, and the initial mass function. *Phys. Rep.* 539, 49–134. doi: 10.1016/j.physrep.2014.02.001

Krumholz, M. R., Bate, M. R., Arce, H. G., Dale, J. E., Gutermuth, R., Klein, R. I., et al. (2014). Star cluster formation and feedback. *Protostars Planets VI*, 243–266. doi: 10.2458/azu_uapress_9780816531240-ch011

Krumholz, M. R., Burkhart, B., Forbes, J. C., and Crocker, R. M. (2018a). A unified model for galactic discs: star formation, turbulence driving, and mass transport. *Month. Notices R. Astron. Soc.* 477, 2716–2740. doi: 10.1093/mnras/sty852

Krumholz, M. R., Crutcher, R. M., and Hull, C. L. H. (2013). Protostellar disk formation enabled by weak, misaligned magnetic fields. *Astrophys. J. Lett.* 767:L11. doi: 10.1088/2041-8205/767/1/L1

Krumholz, M. R., Dekel, A., and McKee, C. F. (2012a). A universal, local star formation law in galactic clouds, nearby galaxies, high-redshift disks, and starbursts. *Astrophys. J.* 745:69. doi: 10.1088/0004-637X/745/1/69

Krumholz, M. R., Klein, R. I., and McKee, C. F. (2007a). Radiation-hydrodynamic simulations of collapse and fragmentation in massive protostellar cores. *Astrophys. J.* 656, 959–979. doi: 10.1086/510664

Krumholz, M. R., Klein, R. I., and McKee, C. F. (2011). Radiation-hydrodynamic simulations of the formation of orion-like star clusters. I. Implications for the origin of the initial mass function. *Astrophys. J.* 740:74. doi: 10.1088/0004-637X/740/2/74

Krumholz, M. R., Klein, R. I., and McKee, C. F. (2012b). Radiation-hydrodynamic simulations of the formation of orion-like star clusters. II. The initial mass function from winds, turbulence, and radiation. *Astrophys. J.* 754:71. doi: 10.1088/0004-637X/754/1/71

Krumholz, M. R., Matzner, C. D., and McKee, C. F. (2006). The global evolution of giant molecular clouds. I. Model formulation and quasi-equilibrium behavior. *Astrophys. J.* 653, 361–382. doi: 10.1086/508679

Krumholz, M. R., and McKee, C. F. (2005). A general theory of turbulence-regulated star formation, from spirals to ultraluminous infrared galaxies. *Astrophys. J.* 630, 250–268. doi: 10.1086/431734

Krumholz, M. R., McKee, C. F., and Bland-Hawthorn, J. (2018b). Star clusters across cosmic time. *Annu. Rev. Astron. Astrophys.* arXiv:1812.01615.

Krumholz, M. R., McKee, C. F., and Klein, R. I. (2005). How protostellar outflows help massive stars form. *Astrophys. J. Lett.* 618, L33–L36. doi: 10.1086/427555

Krumholz, M. R., Myers, A. T., Klein, R. I., and McKee, C. F. (2016). What physics determines the peak of the IMF? Insights from the structure of cores in radiation-magnetohydrodynamic simulations. *Month. Notices R. Astron. Soc.* 460, 3272–3283. doi: 10.1093/mnras/stw1236

Krumholz, M. R., Stone, J. M., and Gardiner, T. A. (2007b). Magnetohydrodynamic evolution of H II regions in molecular clouds: simulation methodology, tests, and uniform media. *Astrophys. J.* 671, 518–535. doi: 10.1086/522665

Kuiper, R., Turner, N. J., and Yorke, H. W. (2016). Protostellar outflows and radiative feedback from massive stars. II. Feedback, star-formation efficiency, and outflow broadening. *Astrophys. J.* 832:40. doi: 10.3847/0004-637X/832/1/40

Kuiper, R., Yorke, H. W., and Turner, N. J. (2015). Protostellar outflows and radiative feedback from massive stars. *Astrophys. J.* 800:86. doi: 10.1088/0004-637X/800/2/86

Kunz, M. W., and Mouschovias, T. C. (2009). The initial core mass function due to ambipolar diffusion in molecular clouds. *Month. Notices R. Astron. Soc.* 399, L94–L98. doi: 10.1111/j.1745-3933.2009.00731.x

Kuruwita, R. L., Federrath, C., and Ireland, M. (2017). Binary star formation and the outflows from their discs. *Month. Notices R. Astron. Soc.* 470, 1626–1641. doi: 10.1093/mnras/stx1299

Lada, C. J., Lombardi, M., and Alves, J. F. (2010). On the star formation rates in molecular clouds. *Astrophys. J.* 724, 687–693. doi: 10.1088/0004-637X/724/1/687

Lada, C. J., Lombardi, M., Roman-Zuniga, C., Forbrich, J., and Alves, J. F. (2013). Schmidt's conjecture and star formation in molecular clouds. *Astrophys. J.* 778:133. doi: 10.1088/0004-637X/778/2/133

Larson, R. B. (1981). Turbulence and star formation in molecular clouds. *Month. Notices R. Astron. Soc.* 194, 809–826. doi: 10.1093/mnras/194.4.809

Larson, R. B. (2005). Thermal physics, cloud geometry and the stellar initial mass function. *Month. Notices R. Astron. Soc.* 359, 211–222. doi: 10.1111/j.1365-2966.2005.08881.x

Lazarian, A., and Vishniac, E. T. (1999). Reconnection in a weakly stochastic field. *Astrophys. J.* 517, 700–718.

Lee, E. J., Miville-Deschênes, M.-A., and Murray, N. W. (2016). Observational evidence of dynamic star formation rate in milky way giant molecular clouds. *Astrophys. J.* 833:229. doi: 10.3847/1538-4357/833/2/229

Lemaster, M. N., and Stone, J. M. (2009). Dissipation and heating in supersonic hydrodynamic and MHD turbulence. *Astrophys. J.* 691, 1092–1108. doi: 10.1088/0004-637X/691/2/1092

Leroy, A. K., Schinnerer, E., Hughes, A., Kruijssen, J. M. D., Meidt, S., Schruba, A., et al. (2017). Cloud-scale ISM structure and star formation in M51. *Astrophys. J.* 846:71. doi: 10.3847/1538-4357/aa7fef

Leroy, A. K., Walter, F., Sandstrom, K., Schruba, A., Munoz-Mateos, J.-C., Bigiel, F., et al. (2013). Molecular gas and star formation in nearby disk galaxies. *Astron. J.* 146:19. doi: 10.1088/0004-6256/146/2/19

Li, H., Griffin, G. S., Krejny, M., Novak, G., Loewenstein, R. F., Newcomb, M. G., et al. (2006). Results of SPARO 2003: mapping magnetic fields in giant molecular clouds. *Astrophys. J.* 648, 340–354. doi: 10.1086/505858

Li, H.-B., Fang, M., Henning, T., and Kainulainen, J. (2013). The link between magnetic fields and filamentary clouds: bimodal cloud orientations in the Gould Belt. *Month. Notices R. Astron. Soc.* 436, 3707–3719. doi: 10.1093/mnras/stt1849

Li, H.-B., Jiang, H., Fan, X., Gu, Q., and Zhang, Y. (2017). The link between magnetic field orientations and star formation rates. *Nat. Astron.* 1:0158. doi: 10.1038/s41550-017-0158

Li, H.-B., Yuen, K. H., Otto, F., Leung, P. K., Sridharan, T. K., Zhang, Q., et al. (2015). Self-similar fragmentation regulated by magnetic fields in a region forming massive stars. *Nature* 520, 518–521. doi: 10.1038/nature 14291

Li, P. S., Klein, R. I., and McKee, C. F. (2018). Formation of stellar clusters in magnetized, filamentary infrared dark clouds. *Month. Notices R. Astron. Soc.* 473, 4220–4241. doi: 10.1093/mnras/stx2611

Li, P. S., McKee, C. F., and Klein, R. I. (2015). Magnetized interstellar molecular clouds - I. Comparison between simulations and Zeeman observations. *Month. Notices R. Astron. Soc.* 452, 2500–2527. doi: 10.1093/mnras/stv1437

Li, P. S., McKee, C. F., Klein, R. I., and Fisher, R. T. (2008). Sub-Alfvénic nonideal MHD turbulence simulations with ambipolar diffusion. I. Turbulence statistics. *Astrophys. J.* 684, 380–394. doi: 10.1086/589874

Li, Z., Wang, P., Abel, T., and Nakamura, F. (2010). Lowering the characteristic mass of cluster stars by magnetic fields and outflow feedback. *Astrophys. J. Lett.* 720, L26–L30. doi: 10.1088/2041-8205/720/1/L26

Li, Z.-Y., Banerjee, R., Pudritz, R. E., Jørgensen, J. K., Shang, H., Krasnopolsky, R., and Maury, A. (2014). "The earliest stages of star and planet formation: core collapse, and the formation of disks and outflows," in *Protostars Planets VI*, eds H. Beuther, R. S. Klessen, C. P. Dullemond, and T. Henning (Tucson, AZ: University of Arizona Press), 173–194. doi: 10.2458/azu_uapress_9780816531240-ch008

Liptai, D., Price, D. J., Wurster, J., and Bate, M. R. (2017). Does turbulence determine the initial mass function? *Month. Notices R. Astron. Soc.* 465, 105–110. doi: 10.1093/mnras/stw2770

Liu, M., Tan, J. C., Cheng, Y., and Kong, S. (2018). The core mass function across galactic environments. II. Infrared dark cloud clumps. *Astrophys. J.* 862:105. doi: 10.3847/1538-4357/aacb7c

Mac Low, M., Klessen, R. S., Burkert, A., and Smith, M. D. (1998). Kinetic energy decay rates of supersonic and super-Alfvénic turbulence in star-forming clouds. *Phys. Rev. Lett.* 80, 2754–2757. doi: 10.1103/PhysRevLett.80.2754

Mac Low, M.-M. (1999). The energy dissipation rate of supersonic, magnetohydrodynamic turbulence in molecular clouds. *Astrophys. J.* 524, 169–178. doi: 10.1086/307784

Mac Low, M.-M., and Klessen, R. S. (2004). Control of star formation by supersonic turbulence. *Rev. Modern Phys.* 76, 125–194. doi: 10.1103/RevModPhys.76.125

Machida, M. N., and Hosokawa, T. (2013). Evolution of protostellar outflow around low-mass protostar. *Month. Notices R. Astron. Soc.* 431, 1719–1744. doi: 10.1093/mnras/stt291

Machida, M. N., Matsumoto, T., and Inutsuka, S. (2008). Magnetohydrodynamics of population III star formation. *Astrophys. J.* 685, 690–704. doi: 10.1086/591074

Mackey, J., and Lim, A. J. (2011). Effects of magnetic fields on photoionized pillars and globules. *Month. Notices R. Astron. Soc.* 412, 2079–2094. doi: 10.1111/j.1365-2966.2010.18043.x

Markevitch, M., and Vikhlinin, A. (2007). Shocks and cold fronts in galaxy clusters. *Phys. Rep.* 443, 1–53. doi: 10.1016/j.physrep.2007.01.001

Martizzi, D., Faucher-Giguère, C.-A., and Quataert, E. (2015). Supernova feedback in an inhomogeneous interstellar medium. *Month. Notices R. Astron. Soc.* 450, 504–522. doi: 10.1093/mnras/stv562

Matzner, C. D. (2002). On the role of massive stars in the support and destruction of giant molecular clouds. *Astrophys. J.* 566, 302–314. doi: 10.1086/338030

Matzner, C. D., and McKee, C. F. (1999). Bipolar molecular outflows driven by hydromagnetic protostellar winds. *Astrophys. J. Lett.* 526, L109–L112. doi: 10.1086/312376

McCourt, M., O'Leary, R. M., Madigan, A.-M., and Quataert, E. (2015). Magnetized gas clouds can survive acceleration by a hot wind. *Month. Notices R. Astron. Soc.* 449, 2–7. doi: 10.1093/mnras/stv355

McKee, C. F., Li, P. S., and Klein, R. I. (2010). Sub-Alfvénic non-ideal MHD turbulence simulations with ambipolar diffusion. II. Comparison with observation, clump properties, and scaling to physical units. *Astrophys. J.* 720, 1612–1634. doi: 10.1088/0004-637X/720/2/1612

McKee, C. F., and Ostriker, E. C. (2007). Theory of star formation. *Annu. Rev. Astron. Astrophys.* 45, 565–687. doi: 10.1146/annurev.astro.45.051806.110602

McKee, C. F., van Buren, D., and Lazareff, B. (1984). Photoionized stellar wind bubbles in a cloudy medium. *Astrophys. J. Lett.* 278, L115–L118. doi: 10.1086/184237

McKee, C. F., and Zweibel, E. G. (1992). On the virial theorem for turbulent molecular clouds. *Astrophys. J.* 399, 551–562. doi: 10.1086/171946

Mellon, R. R., and Li, Z.-Y. (2008). Magnetic braking and protostellar disk formation: the ideal MHD limit. *Astrophys. J.* 681, 1356–1376. doi: 10.1086/587542

Meyer, C. D., Balsara, D. S., Burkhart, B., and Lazarian, A. (2014). Observational diagnostics for two-fluid turbulence in molecular clouds as suggested by simulations. *Month. Notices R. Astron. Soc.* 439, 2197–2210. doi: 10.1093/mnras/stt1893

Miller, G. E., and Scalo, J. M. (1979). The initial mass function and stellar birthrate in the solar neighborhood. *Astrophys. J. Suppl.* 41, 513–547. doi: 10.1086/190629

Mocz, P., and Burkhart, B. (2018). Star formation from dense shocked regions in supersonic isothermal magneto-turbulence. *Month. Notices R. Astron. Soc.* arXiv:1805.11105. doi: 10.1093/mnras/sty1976

Mocz, P., Burkhart, B., Hernquist, L., McKee, C. F., and Springel, V. (2017). Moving-mesh simulations of star-forming cores in magneto-gravo-turbulence. *Astrophys. J.* 838:40. doi: 10.3847/1538-4357/aa6475

Molina, F. Z., Glover, S. C. O., Federrath, C., and Klessen, R. S. (2012). The density variance-Mach number relation in supersonic turbulence - I. Isothermal, magnetized gas. *Month. Notices R. Astron. Soc.* 423, 2680–2689. doi: 10.1111/j.1365-2966.2012.21075.x

Mouschovias, T. C., and Ciolek, G. E. (1999). "Magnetic fields and star formation: a theory reaching adulthood," in *NATO Advanced Science Institutes (ASI) Series C* (Dordrecht: Kluwer Academic Publishers), 305.

Mouschovias, T. C. and Spitzer, L. Jr. (1976). Note on the collapse of magnetic interstellar clouds. *Astrophys. J.* 210:326.

Murray, D., Goyal, S., and Chang, P. (2018). The effects of protostellar jet feedback on turbulent collapse. *Month. Notices R. Astron. Soc.* 475, 1023–1035. doi: 10.1093/mnras/stx3153

Myers, A. T., Klein, R. I., Krumholz, M. R., and McKee, C. F. (2014). Star cluster formation in turbulent, magnetized dense clumps with radiative and outflow feedback. *Month. Notices R. Astron. Soc.* 439, 3420–3438. doi: 10.1093/mnras/stu190

Myers, A. T., McKee, C. F., Cunningham, A. J., Klein, R. I., and Krumholz, M. R. (2013). The fragmentation of magnetized, massive star-forming cores with radiative feedback. *Astrophys. J.* 766:97. doi: 10.1088/0004-637X/766/2/97

Myers, P. C. (2008). Protostar mass due to infall and dispersal. *Astrophys. J.* 687, 340–353. doi: 10.1086/591664

Nakamura, F., and Li, Z.-Y. (2007). Protostellar turbulence driven by collimated outflows. *Astrophys. J.* 662, 395–412. doi: 10.1086/517515

Nakano, T., and Nakamura, T. (1978). Gravitational instability of magnetized gaseous disks 6. *Publ. ASJ* 30, 671–680.

Nolan, C. A., Salmeron, R., Federrath, C., Bicknell, G. V., and Sutherland, R. S. (2017). Centrifugally driven winds from protostellar accretion discs - I. Formulation and initial results. *Month. Notices R. Astron. Soc.* 471, 1488–1505. doi: 10.1093/mnras/stx1642

Ntormousi, E., Hennebelle, P., André, P., and Masson, J. (2016). The effect of ambipolar diffusion on low-density molecular ISM filaments. *Astron. Astrophys.* 589:A24. doi: 10.1051/0004-6361/201527400

Nutter, D., and Ward-Thompson, D. (2007). A SCUBA survey of Orion - the low-mass end of the core mass function. *Month. Notices R. Astron. Soc.* 374, 1413–1420. doi: 10.1111/j.1365-2966.2006.11246.x

Ochsendorf, B. B., Meixner, M., Chastenet, J., Tielens, A. G. G. M., and Roman-Duval, J. (2016). The location, clustering, and propagation of massive star formation in giant molecular clouds. *Astrophys. J.* 832:43. doi: 10.3847/0004-637X/832/1/43

Ochsendorf, B. B., Meixner, M., Roman-Duval, J., Rahman, M., and Evans, II, N. J. (2017). What sets the massive star formation rates and efficiencies of giant molecular clouds? *Astrophys. J.* 841:109. doi: 10.3847/1538-4357/aa704a

Offner, S. S. R., and Arce, H. G. (2014). Investigations of protostellar outflow launching and gas entrainment: hydrodynamic simulations and molecular emission. *Astrophys. J.* 784:61. doi: 10.1088/0004-637X/784/1/61

Offner, S. S. R., and Arce, H. G. (2015). Impact of winds from intermediate-mass stars on molecular cloud structure and turbulence. *Astrophys. J.* 811:146. doi: 10.1088/0004-637X/811/2/146

Offner, S. S. R., and Chaban, J. (2017). Impact of protostellar outflows on turbulence and star formation efficiency in magnetized dense cores. *Astrophys. J.* 847:104. doi: 10.3847/1538-4357/aa8996

Offner, S. S. R., Clark, P. C., Hennebelle, P., Bastian, N., Bate, M. R., Hopkins, P. F., Moraux, E., and Whitworth, A. P. (2014). "The origin and universality of the stellar initial mass function," in *Protostars and Planets VI*, eds H. Beuther, R. S. Klessen, C. P. Dullemond, and T. Henning (Tucson, AZ: University of Arizona Press), 53–75.

Offner, S. S. R., Hansen, C. E., and Krumholz, M. R. (2009a). Stellar kinematics of young clusters in turbulent hydrodynamic simulations. *Astrophys. J. Lett.* 704, L124–L128. doi: 10.1088/0004-637X/704/2/L124

Offner, S. S. R., Klein, R. I., McKee, C. F., and Krumholz, M. R. (2009b). The effects of radiative transfer on low-mass star formation. *Astrophys. J.* 703, 131–149. doi: 10.1088/0004-637X/703/1/131

Offner, S. S. R., Kratter, K. M., Matzner, C. D., Krumholz, M. R., and Klein, R. I. (2010). The formation of low-mass binary star systems via turbulent fragmentation. *Astrophys. J.* 725, 1485–1494. doi: 10.1088/0004-637X/725/2/1485

Offner, S. S. R., and Liu, Y. (2018). Turbulent action at a distance due to stellar feedback in magnetized clouds. *Nat. Astron.* 2, 896–900. doi: 10.1038/s41550-018-0566-1

Onus, A., Krumholz, M. R., and Federrath, C. (2018). Numerical calibration of the HCN−Star formation correlation. *Month. Notices R. Astron. Soc. arXiv:1801.09952.* doi: 10.1093/mnras/sty1662

Ossenkopf, V., and Mac Low, M.-M. (2002). Turbulent velocity structure in molecular clouds. *Astron. Astrophys.* 390, 307–326. doi: 10.1051/0004-6361:20020629

Ostriker, E. C., Gammie, C. F., and Stone, J. M. (1999). Kinetic and structural evolution of self-gravitating, magnetized clouds: 2.5-dimensional simulations of decaying turbulence. *Astrophys. J.* 513, 259–274. doi: 10.1086/306842

Ostriker, E. C., and Shetty, R. (2011). Maximally star-forming galactic disks. I. Starburst regulation via feedback-driven turbulence. *Astrophys. J.* 731, 41. doi: 10.1088/0004-637X/731/1/41

Padoan, P., Haugbølle, T., and Nordlund, Å. (2012). A simple law of star formation. *Astrophys. J. Lett.* 759:L27. doi: 10.1088/2041-8205/759/2/L27

Padoan, P., Haugbølle, T., Nordlund, Å., and Frimann, S. (2017). Supernova driving. IV. The star-formation rate of molecular clouds. *Astrophys. J.* 840:48. doi: 10.3847/1538-4357/aa6afa

Padoan, P., Jimenez, R., Juvela, M., and Nordlund, Å. (2004). The average magnetic field strength in molecular clouds: new evidence of super-alfvénic turbulence. *Astrophys. J. Lett.* 604, L49–L52. doi: 10.1086/383308

Padoan, P., and Nordlund, Å. (1999). A super-alfvénic model of dark clouds. *Astrophys. J.* 526, 279–294. doi: 10.1086/307956

Padoan, P., and Nordlund, Å. (2002). The stellar initial mass function from turbulent fragmentation. *Astrophys. J.* 576, 870–879. doi: 10.1086/341790

Padoan, P., and Nordlund, Å. (2011). The star formation rate of supersonic magnetohydrodynamic turbulence. *Astrophys. J.* 730:40. doi: 10.1088/0004-637X/730/1/40

Padoan, P., Nordlund, Å., Kritsuk, A. G., Norman, M. L., and Li, P. S. (2007). Two regimes of turbulent fragmentation and the stellar initial mass function from primordial to present-day star formation. *Astrophys. J.* 661, 972–981. doi: 10.1086/516623

Padovani, M., Hennebelle, P., Marcowith, A., and Ferrière, K. (2015). Cosmic-ray acceleration in young protostars. *Astron. Astrophys.* 582:L13. doi: 10.1051/0004-6361/201526874

Paleologou, E. V. and Mouschovias, T. C. (1983). The magnetic flux problem and ambipolar diffusion during star formation - One-dimensional collapse. I - Formulation of the problem and method of solution. *Astrophys. J.* 275, 838–857. doi: 10.1086/161578

Parravano, A., Hollenbach, D., and McKee, C. F. (2018). The high mass slope of the IMF. *Month. Notices R. Astron. Soc.* doi: 10.1093/mnras/sty1944

Parravano, A., McKee, C. F., and Hollenbach, D. J. (2011). An initial mass function for individual stars in galactic disks. I. Constraining the shape of the initial mass function. *Astrophys. J.* 726:27. doi: 10.1088/0004-637X/726/1/27

Pattle, K., Ward-Thompson, D., Berry, D., Hatchell, J., Chen, H.-R., Pon, A., et al. (2017). The JCMT BISTRO survey: the magnetic field strength in the orion a filament. *Astrophys. J.* 846:122. doi: 10.3847/1538-4357/aa80e5

Pavel, M. D., and Clemens, D. P. (2012). H II region driven galactic bubbles and their relationship to the galactic magnetic field. *Astrophys. J.* 760:150. doi: 10.1088/0004-637X/760/2/150

Pellegrini, E. W., Baldwin, J. A., Brogan, C. L., Hanson, M. M., Abel, N. P., Ferland, G. J., et al. (2007). A Magnetically supported photodissociation region in M17. *Astrophys. J.* 658, 1119–1135. doi: 10.1086/511258

Peters, T., Banerjee, R., Klessen, R. S., and Mac Low, M. (2011). The interplay of magnetic fields, fragmentation, and ionization feedback in high-mass star formation. *Astrophys. J.* 729:72. doi: 10.1088/0004-637X/729/1/72

Planck Collaboration, Ade, P. A. R., Aghanim, N., Alves, M. I. R., Arnaud, M., Arzoumanian, D., et al. (2016). Planck intermediate results. XXXV. Probing the role of the magnetic field in the formation of structure in molecular clouds. *Astron. Astrophys.* 586:A138. doi: 10.1051/0004-6361/201525896

Press, W. H., and Schechter, P. (1974). Formation of galaxies and clusters of galaxies by self-similar gravitational condensation. *Astrophys. J.* 187, 425–438. doi: 10.1086/152650

Price, D. J., and Bate, M. R. (2007). The impact of magnetic fields on single and binary star formation. *Month. Notices R. Astron. Soc.* 377, 77–90. doi: 10.1111/j.1365-2966.2007.11621.x

Price, D. J., and Bate, M. R. (2008). The effect of magnetic fields on star cluster formation. *Month. Notices R. Astron. Soc.* 385, 1820–1834. doi: 10.1111/j.1365-2966.2008.12976.x

Price, D. J., and Bate, M. R. (2009). Inefficient star formation: the combined effects of magnetic fields and radiative feedback. *Month. Notices R. Astron. Soc.* 398, 33–46. doi: 10.1111/j.1365-2966.2009.14969.x

Pudritz, R. E., Ouyed, R., Fendt, C., and Brandenburg, A. (2007). "Disk winds, jets, and outflows: theoretical and computational foundations," in *Protostars and Planets V*, eds B. Reipurth, D. Jewitt, and K. Keil (Tucson, AZ: University of Arizona Press), 277–294.

Rahman, N., Bolatto, A. D., Xue, R., Wong, T., Leroy, A. K., Walter, F., et al. (2012). CARMA Survey Toward Infrared-bright Nearby Galaxies (STING). II. Molecular gas star formation law and depletion time across the blue sequence. *Astrophys. J.* 745:183. doi: 10.1088/0004-637X/745/2/183

Robertson, B., and Goldreich, P. (2012). Adiabatic heating of contracting turbulent fluids. *Astrophys. J. Lett.* 750:L31. doi: 10.1088/2041-8205/750/2/L31

Roman-Duval, J., Federrath, C., Brunt, C., Heyer, M., Jackson, J., and Klessen, R. S. (2011). The turbulence spectrum of molecular clouds in the galactic ring survey: a density-dependent principal component analysis calibration. *Astrophys. J.* 740:120. doi: 10.1088/0004-637X/740/2/120

Rosen, A. L., Lopez, L. A., Krumholz, M. R., and Ramirez-Ruiz, E. (2014). Gone with the wind: where is the missing stellar wind energy from massive star clusters? *Month. Notices R. Astron. Soc.* 442, 2701–2716. doi: 10.1093/mnras/stu1037

Ruszkowski, M., Yang, H.-Y. K., and Zweibel, E. (2017). Global simulations of galactic winds including cosmic-ray streaming. *Astrophys. J.* 834:208. doi: 10.3847/1538-4357/834/2/208

Salim, D. M., Federrath, C., and Kewley, L. J. (2015). A universal, turbulence-regulated star formation law: from milky way clouds to high-redshift disk and starburst galaxies. *Astrophys. J. Lett.* 806:L36. doi: 10.1088/0004-637X/747/1/21

Salpeter, E. E. (1955). The luminosity function and stellar evolution. *Astrophys. J.* 121:161.

Santos-Lima, R., de Gouveia Dal Pino, E. M., and Lazarian, A. (2012). The role of turbulent magnetic reconnection in the formation of rotationally supported protostellar disks. *Astrophys. J.* 747:21. doi: 10.1088/2041-8205/806/2/L36

Scannapieco, E., and Safarzadeh, M. (2018). Modeling star formation as a Markov process in a supersonic gravoturbulent medium. *Astrophys. J. Lett.* 865:L14. doi: 10.3847/2041-8213/aae1f9

Schekochihin, A. A., Iskakov, A. B., Cowley, S. C., McWilliams, J. C., Proctor, M. R. E., and Yousef, T. A. (2007). Fluctuation dynamo and turbulent induction at low magnetic Prandtl numbers. *New J. Phys.* 9:300. doi: 10.1088/1367-2630/9/8/300

Schleicher, D. R. G., Schober, J., Federrath, C., Bovino, S., and Schmidt, W. (2013). The small-scale dynamo: breaking universality at high Mach numbers. *New J. Phys.* 15:023017. doi: 10.1088/1367-2630/15/2/023017

Schlickeiser, R., Caglar, M., and Lazarian, A. (2016). Cosmic rays and MHD turbulence generation in interstellar giant molecular clouds. *Astrophys. J.* 824:89. doi: 10.3847/0004-637X/824/2/89

Schmidt, W., Federrath, C., Hupp, M., Kern, S., and Niemeyer, J. C. (2009). Numerical simulations of compressively driven interstellar turbulence: I. Isothermal gas. *Astron. Astrophys.* 494:127. doi: 10.1051/0004-6361:200809967

Schneider, F. R. N., Sana, H., Evans, C. J., Bestenlehner, J. M., Castro, N., Fossati, L., et al. (2018). An excess of massive stars in the local 30 Doradus starburst. *Science* 359, 69–71. doi: 10.1126/science.aan0106

Schober, J., Schleicher, D., Federrath, C., Klessen, R., and Banerjee, R. (2012). Magnetic field amplification by small-scale dynamo action: Dependence on turbulence models and Reynolds and Prandtl numbers. *PhRvE* 85:026303. doi: 10.1103/PhysRevE.85.026303

Schober, J., Schleicher, D. R. G., Federrath, C., Bovino, S., and Klessen, R. S. (2015). Saturation of the turbulent dynamo. *Phys. Rev. E* 92:023010. doi: 10.1103/PhysRevE.92.023010

Schruba, A., Leroy, A. K., Walter, F., Bigiel, F., Brinks, E., de Blok, W. J. G., et al. (2011). A molecular star formation law in the atomic-gas-dominated regime in nearby galaxies. *Astron. J.* 142:37. doi: 10.1088/0004-6256/142/2/37

Seifried, D., Banerjee, R., Klessen, R. S., Duffin, D., and Pudritz, R. E. (2011). Magnetic fields during the early stages of massive star formation - I. Accretion and disc evolution. *Month. Notices R. Astron. Soc.* 417, 1054–1073. doi: 10.1111/j.1365-2966.2011.19320.x

Seifried, D., Banerjee, R., Pudritz, R. E., and Klessen, R. S. (2012). Disc formation in turbulent massive cores: circumventing the magnetic braking catastrophe. *Month. Notices R. Astron. Soc.* 423, L40–L44. doi: 10.1111/j.1745-3933.2012.01253.x

Seifried, D., Banerjee, R., Pudritz, R. E., and Klessen, R. S. (2013). Turbulence-induced disc formation in strongly magnetized cloud cores. *Month. Notices R. Astron. Soc.* 432, 3320–3331. doi: 10.1093/mnras/stt682

Seifried, D., and Walch, S. (2015). The impact of turbulence and magnetic field orientation on star-forming filaments. *Month. Notices R. Astron. Soc.* 452, 2410–2422. doi: 10.1093/mnras/stv1458

Semenov, V. A., Kravtsov, A. V., and Gnedin, N. Y. (2016). Nonuniversal star formation efficiency in turbulent ISM. *Astrophys. J.* 826:200. doi: 10.3847/0004-637X/826/2/200

Seo, J., Kang, H., and Ryu, D. (2018). The contribution of stellar winds to cosmic ray production. *J. Korean Astron. Soc.* 51, 37–48. doi: 10.5303/JKAS.2018.51.2.37

Sharda, P., Federrath, C., da Cunha, E., Swinbank, A. M., and Dye, S. (2018). Testing star formation laws in a starburst galaxy at redshift 3 resolved with ALMA. *Month. Notices R. Astron. Soc.* 477, 4380–4390. doi: 10.1093/mnras/sty886

Sharma, P., Roy, A., Nath, B. B., and Shchekinov, Y. (2014). In a hot bubble: why does superbubble feedback work, but isolated supernovae do not? *Month. Notices R. Astron. Soc.* 443, 3463–3476. doi: 10.1093/mnras/stu1307

Shetty, R., and Ostriker, E. C. (2012). Maximally star-forming galactic disks. II. Vertically resolved hydrodynamic simulations of starburst regulation. *Astrophys. J.* 754:2. doi: 10.1088/0004-637X/754/1/2

Shirley, Y. L. (2015). The critical density and the effective excitation density of commonly observed molecular dense gas tracers. *Publ. ASP* 127:299. doi: 10.1086/680342

Shu, F. H., Adams, F. C., and Lizano, S. (1987). Star formation in molecular clouds - Observation and theory. *Annu. Rev. Astron. Astrophys.* 25, 23–81. doi: 10.1146/annurev.aa.25.090187.000323

Shu, F. H., Allen, R. J., Lizano, S., and Galli, D. (2007). Formation of OB associations in galaxies. *Astrophys. J. Lett.* 662, L75–L77. doi: 10.1086/519375

Shu, F. H., Li, Z.-Y., and Allen, A. (2004). Does magnetic levitation or suspension define the masses of forming stars? *Astrophys. J.* 601, 930–951. doi: 10.1086/380602

Soam, A., Maheswar, G., Lee, C. W., Dib, S., Bhatt, H. C., Tamura, M., et al. (2015). Magnetic field structure around cores with very low luminosity objects. *Astron. Astrophys.* 573:A34. doi: 10.1051/0004-6361/201322536

Soam, A., Pattle, K., Ward-Thompson, D., Lee, C. W., Sadavoy, S., Koch, P. M., et al. (2018). Magnetic fields toward ophiuchus-B derived from SCUBA-2 polarization measurements. *Astrophys. J.* 861:65. doi: 10.3847/1538-4357/aac4a6

Socrates, A., Davis, S. W., and Ramirez-Ruiz, E. (2008). The eddington limit in cosmic rays: an explanation for the observed faintness of starbursting galaxies. *Astrophys. J.* 687, 202–215. doi: 10.1086/590046

Soler, J. D., and Hennebelle, P. (2017). What are we learning from the relative orientation between density structures and the magnetic field in molecular clouds? *Astron. Astrophys.* 607:A2. doi: 10.1051/0004-6361/201731049

Solomon, P. M., Rivolo, A. R., Barrett, J., and Yahil, A. (1987). Mass, luminosity, and line width relations of Galactic molecular clouds. *Astrophys. J.* 319, 730–741. doi: 10.1086/165493

Stephens, I. W., Jackson, J. M., Whitaker, J. S., Contreras, Y., Guzmán, A. E., Sanhueza, P., et al. (2016). Linking dense gas from the milky way to external galaxies. *Astrophys. J.* 824:29. doi: 10.3847/0004-637X/824/1/29

Stone, J. M., and Gardiner, T. (2007a). Nonlinear evolution of the magnetohydrodynamic Rayleigh-Taylor instability. *Phys. Fluids* 19:094104. doi: 10.1063/1.2767666

Stone, J. M., and Gardiner, T. (2007b). The magnetic Rayleigh-Taylor instability in three dimensions. *Astrophys. J.* 671, 1726–1735. doi: 10.1086/523099

Stone, J. M., Ostriker, E. C., and Gammie, C. F. (1998). Dissipation in Compressible Magnetohydrodynamic Turbulence. *Astrophys. J. Lett.* 508, L99–L102. doi: 10.1086/311718

Strickland, D. K., and Stevens, I. R. (1998). Predicting X-ray emission from wind-blown bubbles - limitations of FITS to ROSAT spectra. *Month. Notices R. Astron. Soc.* 297, 747–759. doi: 10.1046/j.1365-8711.1998.01583.x

Sur, S., Schleicher, D. R. G., Banerjee, R., Federrath, C., and Klessen, R. S. (2010). The generation of strong magnetic fields during the formation of the first stars. *Astrophys. J. Lett.* 721, L134–L138. doi: 10.1088/0004-637X/792/1/32

Susa, H., Hasegawa, K., and Tominaga, N. (2014). The mass spectrum of the first stars. *Astrophys. J.* 792:32. doi: 10.1088/2041-8205/721/2/L134

Tan, J. C., Krumholz, M. R., and McKee, C. F. (2006). Equilibrium star cluster formation. *Astrophys. J. Lett.* 641, L121–L124. doi: 10.1086/504150

Tang, Y.-W., Ho, P. T. P., Girart, J. M., Rao, R., Koch, P., and Lai, S.-P. (2009). Evolution of magnetic fields in high mass star formation: submillimeter array dust polarization image of the ultracompact H II region G5.89-0.39. *Astrophys. J.* 695, 1399–1412. doi: 10.1088/0004-637X/695/2/1399

Tassis, K., and Mouschovias, T. C. (2004). Ambipolar-diffusion timescale, star formation timescale, and the ages of molecular clouds: is there a discrepancy? *Astrophys. J.* 616, 283–287. doi: 10.1086/424901

Tenorio-Tagle, G., Bodenheimer, P., Franco, J., and Rozyczka, M. (1990). On the evolution of supernova remnants. I - Explosions inside pre-existing wind-driven bubbles. *Month. Notices R. Astron. Soc.* 244, 563–576.

Tenorio-Tagle, G., Rozyczka, M., Franco, J., and Bodenheimer, P. (1991). On the evolution of supernova remnants. II - Two-dimensional calculations of explosions inside pre-existing wind-driven bubbles. *Month. Notices R. Astron. Soc.* 251, 318–329.

Tobin, J. J., Hartmann, L., Chiang, H.-F., Wilner, D. J., Looney, L. W., Loinard, L., et al. (2012). A ˜0.2-solar-mass protostar with a Keplerian disk in the very young L1527 IRS system. *Nature* 492, 83–85. doi: 10.1038/nature11610

Tobin, J. J., Kratter, K. M., Persson, M. V., Looney, L. W., Dunham, M. M., Segura-Cox, D., et al. (2016). A triple protostar system formed via fragmentation of a gravitationally unstable disk. *Nature* 538, 483–486. doi: 10.1038/nature20094

Tomida, K., Okuzumi, S., and Machida, M. N. (2015). Radiation magnetohydrodynamic simulations of protostellar collapse: nonideal magnetohydrodynamic effects and early formation of circumstellar disks. *Astrophys. J.* 801:117. doi: 10.1088/0004-637X/801/2/117

Tomisaka, K., Ikeuchi, S., and Nakamura, T. (1988). Equilibria and evolutions of magnetized, rotating, isothermal clouds. II - The extreme case: Nonrotating clouds. *Astrophys. J.* 335, 239–262. doi: 10.1086/166923

Tritsis, A., Federrath, C., Schneider, N., and Tassis, K. (2018). A new method for probing magnetic field strengths from striations in the interstellar medium. *Month. Notices R. Astron. Soc.* 481, 5275–5285. doi: 10.1093/mnras/sty2677

Tritsis, A., and Tassis, K. (2016). Striations in molecular clouds: streamers or MHD waves? *Month. Notices R. Astron. Soc.* 462, 3602–3615. doi: 10.1093/mnras/stw1881

Tritsis, A., and Tassis, K. (2018). Magnetic seismology of interstellar gas clouds: Unveiling a hidden dimension. *Science* 360, 635–638. doi: 10.1126/science.aao1185

Tsukamoto, Y., Iwasaki, K., Okuzumi, S., Machida, M. N., and Inutsuka, S. (2015). Effects of Ohmic and ambipolar diffusion on formation and evolution of first cores, protostars, and circumstellar discs. *Month. Notices R. Astron. Soc.* 452, 278–288. doi: 10.1093/mnras/stv1290

Tsukamoto, Y., Okuzumi, S., Iwasaki, K., Machida, M. N., and Inutsuka, S. (2018). Does misalignment between magnetic field and angular momentum enhance or suppress circumstellar disk formation? *Astrophys. J.* 868:22. doi: 10.3847/1538-4357/aae4dc

Uhlig, M., Pfrommer, C., Sharma, M., Nath, B. B., Enßlin, T. A., and Springel, V. (2012). Galactic winds driven by cosmic ray streaming. *Month. Notices R. Astron. Soc.* 423, 2374–2396. doi: 10.1111/j.1365-2966.2012.21045.x

Usero, A., Leroy, A. K., Walter, F., Schruba, A., García-Burillo, S., Sandstrom, K., et al. (2015). Variations in the star formation efficiency of the dense molecular gas across the disks of star-forming galaxies. *Astron. J.* 150:115. doi: 10.1088/0004-6256/150/4/115

Utomo, D., Sun, J., Leroy, A. K., Kruijssen, J. M. D., Schinnerer, E., Schruba, A., et al. (2018). Star formation efficiency per free-fall time in nearby galaxies. *Astrophys. J.* 861:L18. doi: 10.3847/2041-8213/aacf8f

Vaytet, N., Commerçon, B., Masson, J., González, M., and Chabrier, G. (2018). Protostellar birth with ambipolar and ohmic diffusion. *Astron. Astrophys.* 615:A5. doi: 10.1051/0004-6361/201732075

Vikhlinin, A., Markevitch, M., and Murray, S. S. (2001). Chandra estimate of the magnetic field strength near the cold front in A3667. *Astrophys. J. Lett.* 549, L47–L50. doi: 10.1086/319126

Vutisalchavakul, N., Evans, N. J. II, and Heyer, M. (2016). Star formation relations in the milky way. *Astrophys. J.* 831:73. doi: 10.3847/0004-637X/831/1/73

Walch, S., and Naab, T. (2015). The energy and momentum input of supernova explosions in structured and ionized molecular clouds. *Month. Notices R. Astron. Soc.* 451, 2757–2771. doi: 10.1093/mnras/stv1155

Wang, P., Li, Z., Abel, T., and Nakamura, F. (2010). Outflow feedback regulated massive star formation in parsec-scale cluster-forming clumps. *Astrophys. J.* 709, 27–41. doi: 10.1088/0004-637X/709/1/27

Weidner, C., Kroupa, P., and Pflamm-Altenburg, J. (2013). The m_{max}-M_{ecl} relation, the IMF and IGIMF: probabilistically sampled functions. *Month. Notices R. Astron. Soc.* 434, 84–101. doi: 10.1093/mnras/stt1002

Weisz, D. R., Johnson, L. C., Foreman-Mackey, D., Dolphin, A. E., Beerman, L. C., Williams, B. F., et al. (2015a). The high-mass stellar initial mass function in M31 clusters. *Astrophys. J.* 806:198.

Weisz, D. R., Johnson, L. C., Foreman-Mackey, D., Dolphin, A. E., Beerman, L. C., Williams, B. F., et al. (2015b). The high-mass stellar initial mass function in M31 clusters. *Astrophys. J.* 806:198. doi: 10.1088/0004-637X/806/2/198

Wiener, J., Zweibel, E. G., and Oh, S. P. (2013). Cosmic ray heating of the warm ionized medium. *Astrophys. J.* 767:87.

Wise, J. H., and Abel, T. (2011). ENZO+MORAY: radiation hydrodynamics adaptive mesh refinement simulations with adaptive ray tracing. *Month. Notices R. Astron. Soc.* 414, 3458–3491. doi: 10.1111/j.1365-2966.2011.18646.x

Wu, J., Evans, N. J. II, Shirley, Y. L., and Knez, C. (2010). The properties of massive, dense clumps: mapping surveys of HCN and CS. *Astrophys. J. Suppl.* 188, 313–357. doi: 10.1088/0067-0049/188/2/313

Wurster, J., Bate, M. R., and Price, D. J. (2018). The collapse of a molecular cloud core to stellar densities using radiation non-ideal magnetohydrodynamics. *Month. Notices R. Astron. Soc.* 475, 1859–1880. doi: 10.1093/mnras/stx3339

Yadav, N., Mukherjee, D., Sharma, P., and Nath, B. B. (2017). How multiple supernovae overlap to form superbubbles. *Month. Notices R. Astron. Soc.* 465, 1720–1740. doi: 10.1093/mnras/stw2522

Zhang, G.-Y., Xu, J.-L., Vasyunin, A. I., Semenov, D. A., Wang, J.-J., Dib, S., et al. (2018). Physical properties and chemical composition of the cores in the California molecular cloud. *Astron. Astrophys.* 620:A163. doi: 10.1051/0004-6361/201833622

Zhang, Y., Higuchi, A. E., Sakai, N., Oya, Y., Lopez-Sepulcre, A., Imai, M., et al. (2018). Rotation in the NGC 1333 IRAS 4C outflow. *Astrophys. J.. arXiv:1808.00346*. doi: 10.3847/1538-4357/aad7ba

Zhao, B., Caselli, P., Li, Z.-Y., and Krasnopolsky, R. (2018). Decoupling of magnetic fields in collapsing protostellar envelopes and disc formation and fragmentation. *Month. Notices R. Astron. Soc.* 473, 4868–4889. doi: 10.1093/mnras/stx2617

Zweibel, E. G. (2013). The microphysics and macrophysics of cosmic rays. *Phys. Plasmas* 20:055501. doi: 10.1063/1.4807033

Zweibel, E. G., and Brandenburg, A. (1997). Current sheet formation in the interstellar medium. *Astrophys. J.* 478:563.

Conflict of Interest Statement: The authors declare that the research was conducted in the absence of any commercial or financial relationships that could be construed as a potential conflict of interest.

frontiers in Astronomy and Space Sciences

REVIEW
published: 28 March 2019
doi: 10.3389/fspas.2019.00005

The Role of Magnetic Field in Molecular Cloud Formation and Evolution

Patrick Hennebelle[1,2]* *and Shu-ichiro Inutsuka*[3]

[1] Laboratoire AIM, Paris-Saclay, CEA/IRFU/SAp, CNRS, Université Paris Diderot, Gif-sur-Yvette, France, [2] LERMA (UMR CNRS 8112), Ecole Normale Supérieure, Paris, France, [3] Department of Physics, Nagoya University, Nagoya, Japan

We review the role that magnetic field may have on the formation and evolution of molecular clouds. After a brief presentation and main assumptions leading to ideal MHD equations, their most important correction, namely the ion-neutral drift is described. The nature of the multi-phase interstellar medium (ISM) and the thermal processes that allows this gas to become denser are presented. Then we discuss our current knowledge of compressible magnetized turbulence, thought to play a fundamental role in the ISM. We also describe what is known regarding the correlation between the magnetic and the density fields. Then the influence that magnetic field may have on the interstellar filaments and the molecular clouds is discussed, notably the role it may have on the pre-stellar dense cores as well as regarding the formation of stellar clusters. Finally we briefly review its possible effects on the formation of molecular clouds themselves. We argue that given the magnetic intensities that have been measured, it is likely that magnetic field is (i) responsible of reducing the star formation rate in dense molecular cloud gas by a factor of a few, (ii) strongly shaping the interstellar gas by generating a lot of filaments and reducing the numbers of clumps, cores and stars, although its exact influence remains to be better understood. Moreover at small scales, magnetic braking is likely a dominant process that strongly modifies the outcome of the star formation process. Finally, we stress that by inducing the formation of more massive stars, magnetic field could possibly enhance the impact of stellar feedback.

Keywords: magnetic field, molecular clouds, star formation, gravity, turbulence, multi-phase, ionization, filaments

OPEN ACCESS

Edited by:
Christopher F. McKee, University of California, Berkeley, United States

Reviewed by:
Mark Reuben Krumholz, Australian National University, Australia
Eve Ostriker, Princeton University, United States

***Correspondence:**
Patrick Hennebelle
patrick.hennebelle@cea.fr

Specialty section:
This article was submitted to Stellar and Solar Physics, a section of the journal Frontiers in Astronomy and Space Sciences

Received: *02 October 2018*
Accepted: *28 January 2019*
Published: *28 March 2019*

Citation:
Hennebelle P and Inutsuka S (2019) The Role of Magnetic Field in Molecular Cloud Formation and Evolution. Front. Astron. Space Sci. 6:5. doi: 10.3389/fspas.2019.00005

1. INTRODUCTION

The interstellar cycle, which takes place within galaxies, is fundamental for our universe as it controls the formation of stars and therefore the evolution of galaxies. Yet given the broad range of spatial scales and the profusion of physical processes involved, our understanding is still very incomplete. Amongst other processes, namely gravity, compressible turbulence, radiation, cosmic rays and stellar feedback, magnetic field is also contributing significantly to the evolution of the interstellar medium (ISM) and more specifically to the formation of stars. As a matter of evidence, the magnetic energy in the ISM is comparable to the other energies as for example the kinematic one. Deciphering the various roles that magnetic field is playing is however not obvious, (i) because measuring it remains a challenge, (ii) because magnetic field is not a mere pressure and is highly non-isotropic in nature, (iii) because observations do not allow us to easily vary the parameters as it is possible to do in experiments. This however can be done in numerical simulations where the influence of a specific parameter, like the magnetic intensity, can be modified and studied.

This review is dedicated to the role magnetic field is playing in the formation and evolution of molecular clouds. Given the complex multi-scale nature of these latter, this represents a challenge as several physical processes and astrophysical objects have to be discussed, in particular because as stressed above, the magnetic field is strongly interacting with other phenomena, that need to be described for self-consistency.

The plan of the paper is as follows. In section 2, we describe the equations of the magneto-hydrodynamics (MHD) that are used to compute and predict the evolution of molecular clouds. We give some ideas of how these equations are inferred first in the ideal MHD framework, that is to say when the fluid and the magnetic field are perfectly coupled. Then we briefly discuss the most important correction that must be taken into account in molecular clouds, namely the ion-neutral drift or ambipolar diffusion. In section 3, the multi-phase nature of the ISM is discussed: how the gas cools and heats, the principle of thermal instability and its non-linear regime. The role that magnetic field may have in the transition from warm atomic gas into cold and dense gas is emphasized. In section 4, the nature of the turbulence in the ISM is presented. First some elements of the magnetized incompressible turbulence are given, stressing the ideas and problems that are still debated. Second the more realistic compressible and multi-phase magnetized turbulence is addressed, reporting the various numerical studies that have been performed. The influence that the ion-neutral drift may have on turbulence is discussed. Section 5 is specifically dedicated to the correlation between density and magnetic field including the magnetic intensity and the magnetic orientation. Section 6 is specifically dedicated to puzzling astrophysical objects, namely the filaments that, in a sense, constitute sub-structures of molecular clouds. The question of their formation, the physical origin of the possible characteristic width that has been recently inferred and their fragmentation in star forming cores are discussed. In section 7, the molecular clouds themselves are eventually addressed. We start by reviewing the role that ambipolar diffusion may have in the magnetically dominated clouds, particularly regarding the fundamental question of the low efficient formation of stars in galaxies. Then the properties of the prestellar cores which form in dedicated numerical simulations of these clouds are described stressing the effect that magnetic field may have. Finally the role that magnetic field may have in stellar clusters formation is presented. In section 8, we briefly review the works in which the impact of the magnetic field on molecular cloud formation has been addressed. Section 9 concludes the paper.

2. MHD EQUATIONS

For the sake of completeness and because readers may find it useful, a short derivation and discussion of the MHD equations is given. We start with the ideal MHD, which amongst other approximations assume the non-relativistic limit, that is to say the fluid velocities are much smaller than the speed of light c. We also discuss a correction to these set of equations in the presence of neutral particles since the ionization degree in the ISM is small.

2.1. Ideal MHD

The equations of ideal MHD assume that the fluids are perfect conductors. The Lorentz force, which is the force that the electromagnetic fields $\boldsymbol{E}$ and $\boldsymbol{B}$ exert on the fluid must be taken into account. The electromagnetic fields evolution is obviously described by the Maxwell equations. Written in CGS units, these equations are

$$\boldsymbol{\nabla}\cdot\boldsymbol{B} = 0, \tag{1}$$

$$\boldsymbol{\nabla}\cdot\boldsymbol{E} = 4\pi\rho_e, \tag{2}$$

$$c\boldsymbol{\nabla}\times\boldsymbol{E} = -\frac{\partial \boldsymbol{B}}{\partial t}, \tag{3}$$

$$c\boldsymbol{\nabla}\times\boldsymbol{B} = 4\pi\boldsymbol{j} + \frac{\partial \boldsymbol{E}}{\partial t}, \tag{4}$$

ρ_e and $\boldsymbol{j}$ are the fluid charge and current densities. The equation for charge conservation links these two quantities

$$\frac{\partial \rho_e}{\partial t} + \boldsymbol{\nabla}\cdot\boldsymbol{j} = 0\,. \tag{5}$$

While in a perfect conductor at rest, $\boldsymbol{E_R}$ vanishes, the situation is different when it moves. The rest fields $\boldsymbol{E_R}$ and $\boldsymbol{B_R}$ and the fields in the observer frame, $\boldsymbol{E}$ and $\boldsymbol{B}$ are related using the Lorentz transformation, as detailed by e.g., Landau and Lifshitz (1960), Shu (1992), and Spruit (2013). Considering the Lorentz force $\boldsymbol{F}$ and $\boldsymbol{F_R}$, we get:

$$\boldsymbol{F} = q(\boldsymbol{E} + \frac{\boldsymbol{v}}{c}\times\boldsymbol{B})\,, \tag{6}$$

$$\boldsymbol{F_R} = q\boldsymbol{E_R}\,. \tag{7}$$

Since the force does not depend on the reference frame: $\boldsymbol{F} = \boldsymbol{F_R}$ and therefore

$$\boldsymbol{E_R} = \boldsymbol{E} + \frac{\boldsymbol{v}}{c}\times\boldsymbol{B}\,, \tag{8}$$

$$\boldsymbol{B_R} = \boldsymbol{B}\,. \tag{9}$$

Since the perfect conductor assumption is made, $\boldsymbol{E_R} = \boldsymbol{0}$, and

$$\boldsymbol{E} = -\frac{\boldsymbol{v}}{c}\times\boldsymbol{B}\,. \tag{10}$$

Combining it with Equation (3) we obtain:

$$\frac{\partial \boldsymbol{B}}{\partial t} = \boldsymbol{\nabla}\times(\boldsymbol{v}\times\boldsymbol{B})\,. \tag{11}$$

The Lorentz force per unit volume, $\boldsymbol{f_L}$, can be expressed as

$$\boldsymbol{f_L} = \rho_e\boldsymbol{E} + \frac{1}{c}\boldsymbol{j}\times\boldsymbol{B}\,. \tag{12}$$

In the non-relativistic limit, the displacement current in Equation (4) can be neglected, leading to

$$\boldsymbol{\nabla}\times\boldsymbol{B} = \frac{4\pi}{c}\boldsymbol{j}\,. \tag{13}$$

Since local electroneutrality is assumed, we have $\rho_E = 0$ and

$$\boldsymbol{f_L} = \frac{(\boldsymbol{\nabla \times B}) \boldsymbol{\times B}}{4\pi}. \quad (14)$$

This leads to the standard form of the ideal MHD equations

$$\frac{\partial \rho}{\partial t} + \boldsymbol{\nabla}\cdot(\rho \boldsymbol{v}) = 0, \quad (15)$$

$$\rho\left[\frac{\partial \boldsymbol{v}}{\partial t} + (\boldsymbol{v}\cdot\boldsymbol{\nabla})\boldsymbol{v}\right] = -\boldsymbol{\nabla} P + \frac{(\boldsymbol{\nabla \times B}) \boldsymbol{\times B}}{4\pi}, \quad (16)$$

$$\rho\left[\frac{\partial \boldsymbol{e}}{\partial t} + (\boldsymbol{v}\cdot\boldsymbol{\nabla})\boldsymbol{e}\right] = -P(\boldsymbol{\nabla}\cdot\boldsymbol{v}) - \rho\mathcal{L}, \quad (17)$$

$$\frac{\partial \boldsymbol{B}}{\partial t} = \boldsymbol{\nabla \times}(\boldsymbol{v \times B}). \quad (18)$$

where $\mathcal{L}$ is the net loss function and describes the radiative heating and cooling of the gas. This must be complemented by an equation of state to close the system of equations. A perfect gas is a good assumption for the ISM, $P = (\gamma - 1)\rho\epsilon$, where γ is the adiabatic index of the gas.

It is useful to get a better insight and physical interpretation of the MHD equations to rewrite the Lorentz force as

$$\boldsymbol{f_L} = \frac{(\boldsymbol{\nabla \times B}) \boldsymbol{\times B}}{4\pi} = -\boldsymbol{\nabla}\left(\frac{B^2}{8\pi}\right) + \frac{(\boldsymbol{B}\cdot\boldsymbol{\nabla})\boldsymbol{B}}{4\pi} \quad (19)$$

The first term is called the magnetic pressure. The second is the magnetic tension (see the detailed discussion page 13 in the lecture by Spruit, 2013).

2.2. Non-ideal MHD: the Ion-Neutral Drift

In many situations, ideal MHD is not a sufficiently good assumption and additional effects need to be accounted for. In the context of molecular clouds the dominant correction is the so-called ambipolar diffusion. Since the neutrals are not charged they are not subject to the Lorentz force which applies only on the ions. However through collisions the neutrals and the ions exchange momentum and therefore the Lorentz force has an influence on the neutrals through the ions. If the number of ions is large, i.e., if the ionization is high, the number of collisions is expected to be large and ideal MHD remains a good approximation. However in molecular clouds the ionization is usually of the order of 10^{-7} and therefore the two fluid are not perfectly coupled. The ions drag the field lines and drift with respect to the neutrals implying that the latter can cross the field lines. The field is not frozen in the gas anymore. Because of the low ionization, it is thus possible to neglect the inertia of the ions and a reasonable assumption is that of the equilibrium between the Lorentz force and the drag force exerted on the ions. This leads to:

$$\frac{(\nabla \times \mathbf{B}) \times \mathbf{B}}{4\pi} = \gamma_{ad}\rho\rho_i(\mathbf{V}_i - \mathbf{V}), \quad (20)$$

where ρ_i and V_i are the ion density and velocity, respectively, $\gamma_{ad} \simeq 3.5\times10^{13}$ cm^3 g^{-1} s^{-1} is the drag coefficient (Mouschovias and Paleologou, 1981). Equation (20), gives the ion velocity as a function of the neutral velocity and the Lorentz force. Combining it with the induction equation one gets

$$\partial_t \mathbf{B} + \nabla\times(\mathbf{B}\times\mathbf{V}) = \nabla\times\left(\frac{1}{4\pi\gamma_{ad}\rho\rho_i}((\nabla\times\mathbf{B})\times\mathbf{B})\times\mathbf{B}\right). \quad (21)$$

The left-hand side is the induction equation of ideal MHD. The right-hand side describes the ion-neutral drift. It is not rigorously speaking a diffusion term although it entails second order spatial derivatives. From this equation a typical time scale for ambipolar diffusion can easily be inferred

$$\tau_{\rm ad} \simeq \frac{4\pi\gamma_{ad}\rho\rho_i L^2}{B^2}, \quad (22)$$

where L is the characteristic spatial scale of the problem, which could be the size of the prestellar cores or the filaments as described below. Ionization equilibrium leads to $\rho_i = C\sqrt{\rho}$, where $C = 3\times10^{-16}$ cm$^{-3/2}$ g$^{1/2}$.

As Equation (20) neglects the ion inertia, it is called the strong coupling limit (e.g., Shu, 1992; Mac Low et al., 1995; Masson et al., 2012). Ideally, it is necessary to consider two fluids the neutral and the ions coupled through the collisional term. The difficulty however with this approach is that the Alfvén speed associated to the ions is several orders of magnitude larger than the Alfvén speed associated to the neutrals. This makes numerical simulations very difficult to perform because the timesteps are then very small. For this reason an alternative approximation, called the heavy ion approximation has been developed (Li et al., 2006). It consists in artificially increasing the mass of the ions to lower their Alfvén speed while modifying the ion-neutral cross-section to maintain constant the friction coefficient.

Finally, let us mention that the ion-neutral friction leads to energy dissipation and therefore constitute a source of heating in Equation (17) which is equal to $\gamma_{ad}\rho\rho_i(\mathbf{V}_i - \mathbf{V})^2$.

3. THE FORMATION OF DENSE GAS IN THE ISM

Here we describe how the formation of dense gas out of diffuse atomic gas is achieved in the ISM. A brief description of the cooling and heating processes, essential to understand how the ISM becomes denser is given. We then describe the principle of thermal instability on the role magnetic field may have. Finally, a dynamical scenario for the formation of molecular clouds is sketched, stressing how magnetic field is acting.

3.1. Thermal Structure of ISM and Thermal Instability

In this section, our knowledge about thermal physics of ISM is presented. To calculate the equilibrium temperature of ISM as a function of gas density, one must equate heating and cooling function taking into account several physical processes. The detailed analysis for the thermal equilibrium state in the neutral atomic phase can be found, for example, in Wolfire et al. (2003) while Koyama and Inutsuka (2000) (see also e.g., Glover and Clark, 2012; Gong et al., 2017) extended their calculation for

unshielded gas up to gas densities $10^3\ \mathrm{cm}^{-3} < n < 10^6\ \mathrm{cm}^{-3}$ (see **Figure 1**). The main heating mechanisms are the photoelectric emission from small grains and PAHs, ionization by cosmic rays and soft X-rays, and the formation and photodissociation of H_2. The local FUV field is supposed to be on the order of Habing's value ($G_0 = 1.7$ and is adopted in **Figure 1**). The dominant cooling processes are the line emission from H, C, O, Si, and Fe, by rovibrational lines from H_2 and CO, as well as by atomic and molecular collisions with dust grains. The transition to the molecule-dominated phase depends on both gas density and column density as well as the radiation field (see Sternberg et al., 2014 for analysis and discussion of the relative importance of H_2 self-shielding and dust shielding). The chemistry and cooling in gas with a range of density, column, metallicity, and radiation fields is discussed e.g., in Glover and Clark (2012) and Gong et al. (2017). To describe these thermal processes a set of three time-dependent equations for ionization and recombination of hydrogen, and formation and dissociation of molecules should be solved. Self-shielding effects must also be taken into account to calculate the H_2 photodissociation. **Figure 1** portrays the resulting temperature, pressure, and the relevant chemical species as functions of number density for unshielded gas. At high column density, inside molecular clouds, the dominant molecular cooling process is due to the CO molecules (at densities above $10^5\ \mathrm{cm}^{-3}$ dust cooling becomes dominant) and the heating one comes from cosmic rays. A complete thermal balance description of the high density gas, which can be found for instance in Neufeld et al. (1995), is beyond the scope of the present review.

The basic property of thermal stability can be related to the slope of heat-loss function, $\mathcal{L} = \rho\Lambda - \Gamma$, where $\rho\Lambda$ is the cooling function per volume and Γ is the heating function. Field (1965) studied in details the stability conditions of a uniform medium subject to heating and cooling. In particular, he inferred the isobaric criterion which is given by

$$\left(\frac{\partial \mathcal{L}}{\partial T}\right)_{\mathrm{P}} < 0 \Leftrightarrow \left(\frac{\partial P}{\partial \rho}\right)_{\mathcal{L}} < 0. \tag{23}$$

Mathematically, it corresponds to $p < 1$ in the case $\Lambda \propto T^p$. Typically this unstable phase occurs for temperature between $\sim$ 100 and $\sim$ 5,000 K. **Figure 2** shows the growth rate of thermal instability as a function of the wavelength of the linear perturbation. The dashed curve corresponds to the case of the unperturbed state in equilibrium. The thermal conduction tends to make the system isothermal, and hence, it stabilizes the perturbations with sufficiently small wavelengths. The critical wavelength (the largest wavelength stabilized by thermal conduction) is called "Field length" named after the pioneer of this analysis:

$$\lambda_{\mathrm{c}} = 2\pi \left\{ \frac{\rho}{K} \left[\frac{\partial \mathcal{L}}{\partial T} \right]_{\mathrm{P}} \right\}^{-1/2} \sim \sqrt{\frac{KT}{\rho^2 \Lambda}} \equiv \lambda_{\mathrm{F}}, \tag{24}$$

where K denotes the coefficient of thermal conduction.

In the case where the spatially uniform perturbed state is not in thermal balance, the criterion for the instability is $p < 2$ for $\Lambda \propto T^p$, and hence, the range of the unstable temperature becomes wider (Schwarz et al., 1972). The dispersion relation for isobarically cooling medium is portrayed by the solid curve in **Figure 2** (Koyama and Inutsuka, 2000). The growth rate presents a peak at a wavelength that is about ten times larger than the

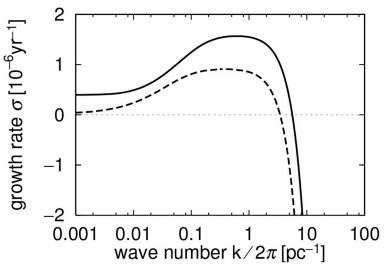

FIGURE 2 | The dispersion relation for condensation mode of thermal instability analyzed in Koyama and Inutsuka (2000). The dashed curve denotes the classical result for the case of thermal equilibrium unperturbed state. The solid curve denotes for the case of an isobarically contracting unperturbed state. Reproduced from Koyama and Inutsuka (2000) with permission of ApJ.

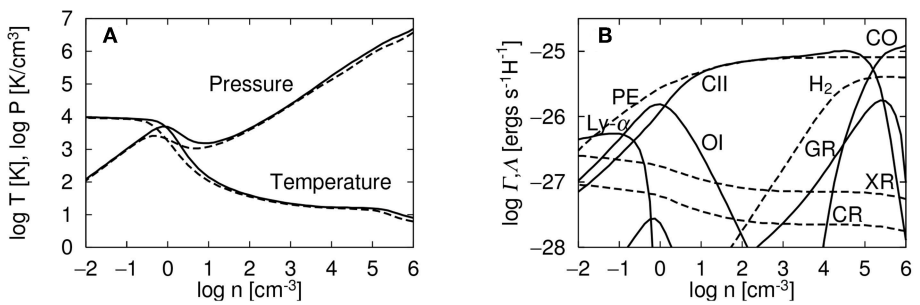

FIGURE 1 | A phase diagram of ISM and important heating and cooling processes shown in Koyama and Inutsuka (2000). **(A)** Equilibrium temperature and pressure with absorbing column density of $10^{19}\ \mathrm{cm}^{-2}$ (solid lines), $10^{20}\ \mathrm{cm}^{-2}$ (dashed lines). **(B)** Heating (dashed lines) and cooling rates (solid lines) for unshielded gas per hydrogen nucleus at equilibrium. Heating processes are, photoelectric effect from small grains and PAHs (PE), X-ray (XR), Cosmic-ray (CR), and H_2 formation/destruction. Cooling processes are CII fine-structure (CII), OI fine-structure (OI), Hydrogen Lyman-α (Ly-α), CO rotation/vibration line (CO), and atomic and molecular collisions with dust grains (GR). Reproduced from Koyama and Inutsuka (2000) with permission of ApJ.

Field length implying that thermal instability tends to produce structures larger than the Field length.

3.2. The Effect of Magnetic Field on Thermal Instability

The effect of magnetic field on the linear growth of thermal instability was studied in detail by Ames (1973). Obviously a sufficiently strong magnetic field suppresses the motion perpendicular to the magnetic field lines. This is because in slab geometry, the magnetic pressure is simply proportional to the density square (as magnetic field is proportional to density), therefore the increase of the magnetic pressure can compensate for the decrease of the thermal pressure. However the perturbations in the direction along the magnetic field are not suppressed and remain unstable, if the cooling function satisfies the instability criteria. The non-linear development of the thermal instability has been studied by various authors (Hennebelle and Pérault, 2000; Piontek and Ostriker, 2004; Inoue et al., 2007; van Loo et al., 2007; Inoue and Inutsuka, 2008, 2009; Choi and Stone, 2012) while the effects of non-ideal MHD on thermal instability have been studied by various papers. Inoue et al. (2007) have done one-dimensional two-fluid simulations where neutral and charged components are self-consistently described as two fluids. They found that regardless of the initial conditions used to set up the simulation, the magnetic field strength in dense regions ends up being a few μG.

3.3. Formation of Molecular Clouds

It is believed that most of the volume in the thin ($\sim 10^2$pc) disk of our Milky Way Galaxy is filled by warm neutral medium (WNM) and warm or hot ionized medium (e.g., Ferrière, 2001). In contrast, a significant fraction of gaseous mass resides in the cold dense medium that occupies only a small fraction of the spatial volume. Sufficiently dense ($> 10^3 \mathrm{cm}^{-3}$) gas tends to be in large ($>$ a few pc) clouds whose column density is sufficiently large to protect molecular hydrogen against external dissociating radiation. Giant molecular clouds are observed to be the sites of massive star formation. Once a massive ($> 10 M_\odot$) star is created in a molecular cloud, it radiates intense ultraviolet radiation inside the cloud that results in the creation of an expanding ionized region, i.e., HII region. The expanding HII regions are supposed not only to quench the further star formation, but also to destroy the parental molecular clouds (Dale and Bonnell, 2011; Walch et al., 2012; Dale et al., 2013; Geen et al., 2015, 2017; Gavagnin et al., 2017; Kim et al., 2018). Since we suppose that our Milky Way Galaxy is in a steady state over a timescale of Galactic rotation ($\sim 10^8$yr), molecular clouds are continuously created at a rate that compensate the destruction by massive stars.

How are the cold dense clouds created? According to the phase diagram of ISM shown in section 3.1, we can identify that the formation process of cold dense HI gas ($> 10\,\mathrm{cm}^{-3}$) from WNM should be a phase transition dynamics that increase the density abruptly (Hennebelle and Pérault, 1999; Koyama and Inutsuka, 2000). Several studies (Koyama and Inutsuka, 2002; Piontek and Ostriker, 2004; Audit and Hennebelle, 2005; Heitsch et al., 2006; Vázquez-Semadeni et al., 2006) have shown that this phase transition always results in the creation of long-lasting turbulent motions where cold HI clumps are embedded in WNM. The amplitude of turbulent velocities of cold HI gas tends to be a few km s^{-1}, a fraction of the sound speed of the WNM (10 km s^{-1}). Therefore, the resulting turbulence appears to be supersonic with respect to the sound speed of cold medium ($\sim$ 1km s^{-1}) but actually subsonic with respect to the WNM, which constitutes the inter clump medium. Therefore the turbulence of the atomic interstellar gas is a combination of subsonic and supersonic motions. Let us stress that the CNM tends to behave as a supersonic gas even so it is embedded into an environment with respect to which it is subsonic. This is because the CNM fragments collide supersonically.

Now a description of how molecular clouds are created is proposed. An important question is whether they can be created by a single compression event from WNM or whether they are more gradually created from cold dense HI clouds. Inoue and Inutsuka (2008), Inoue and Inutsuka (2009), Heitsch et al. (2009), and Körtgen and Banerjee (2015) have given a somewhat negative answer to the former question. Inoue and Inutsuka (2012) have given the positive answer to the latter question. More detailed analyses are done by Iwasaki et al. (2018). **Figure 3** shows typical results of the compression of magnetized multiphase HI clouds by shock waves. The relative angle (θ) between the shock wave propagation direction and the mean magnetic field is 3° (upper panel), 11° (middle panel), 36° (lower panel), respectively. The compression with a small angle results in the creation of substantial molecular gas. But if the relative angle is larger than a certain critical value, the propagation of shock wave only result in the magnetically supported HI clouds. Note that the value of this critical angle depends on the velocity of the incoming flow of the magnetic field and of the time since for long enough time, the post-shock layer will always be at least partially molecular. In practice, there is however a distribution of angles between the magnetic field and the incoming flow. Quantifying this distribution would therefore be important to constraint the scenario of molecular cloud formation. Detailed investigations from larger scale simulations (see section 8) have shown that there is a clear trend for magnetic and velocity fields to be preferentially aligned (e.g., Iffrig and Hennebelle, 2017), which would imply that aligned configurations are more frequent than expected.

4. THE NATURE OF MHD TURBULENCE IN THE DENSE ISM

Turbulence is ubiquitous in fluid dynamics and unsurprisingly, many observations suggest that molecular clouds are turbulent (e.g., Elmegreen and Scalo, 2004; Hennebelle and Falgarone, 2012). It is likely the case that together with gravity, turbulence is playing a significant role in the evolution of molecular clouds for example by creating strong density fluctuations, owing to its supersonic nature, that may serve as seed for the mass reservoir of future stars. More generally, interstellar turbulence is an agent that imposes order in the form of coherent structures and correlations between the various fields of the flows. Turbulence

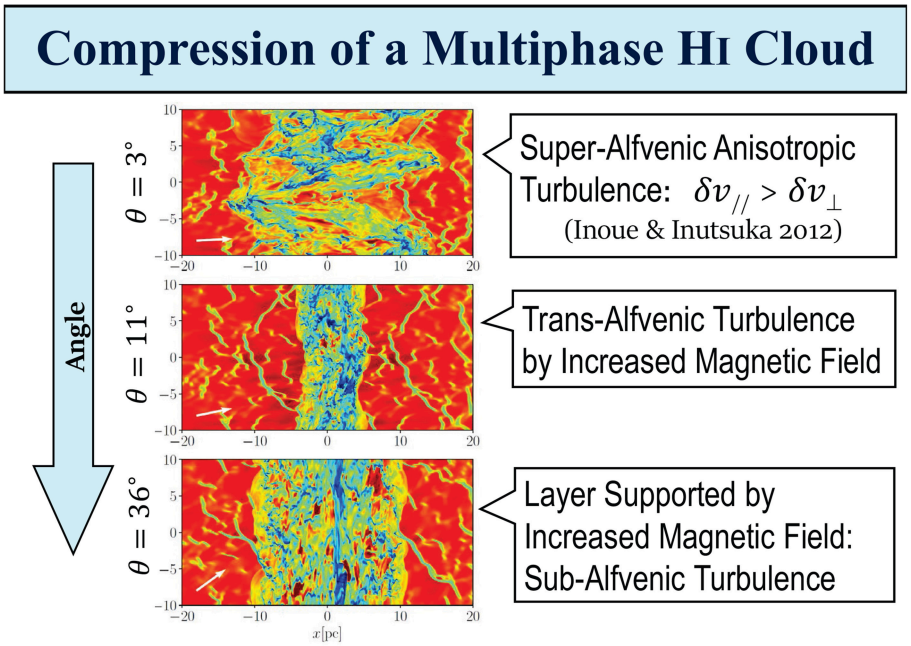

FIGURE 3 | The result of compression of multiphase HI clouds by shock waves (Iwasaki et al., 2018). The column density is shown (red stands for WNM while Blue-green represents CNM). The relative angle (θ) between the shock wave propagation direction and the mean magnetic field is 3° **(Upper panel)**, 11° **(Middle panel)**, and 36° **(Lower panel)**, respectively.

is likely responsible of many, if not almost all[1], of the observed motions. How magnetic field affects turbulence in molecular clouds is the main focus of this section.

4.1. Turbulence in *Ideal* MHD Framework

Before starting a description of the turbulence, an important issue should be stressed. *Ideal* MHD implies that fluid particles are attached to their field lines, that is to say they can flow along the field lines but cannot go across them. In a turbulent fluid, given the stochastic nature of the motions, such a situation would lead to a field that would be so tangled, that quickly motions would be prohibited. This implies that *Ideal* MHD cannot, strictly speaking, be correct for a turbulent fluid and that some reconnection, that is to say some changes of the field lines topology must be occurring. The physical origin of this reconnection is still debated but an appealing model has been proposed by Lazarian and Vishniac (1999). In this view the reconnection is driven by turbulence and is a multi-scale process, that is unrelated to the details of the microphysical processes (Lazarian et al., 2015). It is certainly the case, at least in numerical simulations of MHD turbulence, where the numerical diffusivity is often controlling the reconnection, that the MHD is far to be ideal. This process, in particular, induces an effective diffusion of the magnetic flux, that is therefore not fully frozen as one would expect if MHD was truly ideal.

[1]In principle gravity and stellar feedback are two other sources whose signature can sometimes be clearly recognized. In many circumstances however, it is likely difficult to clearly separate the different contributions as gravity and feedback trigger turbulent motions.

4.1.1. Incompressible Magnetized Turbulence

For pure hydrodynamics, i.e., in the absence of magnetic field, the Kolmogorov dimensional scaling relation, appears to provide a good description (Kolmogorov, 1941). However, MHD flows are more complicated and in spite of intensive efforts, even the energy powerspectrum of MHD turbulence is still debated. The first model to predict a powerspectrum has been done by Iroshnikov (1963) and Kraichnan (1965) who infer $v_l \propto l^{1/4}$ and $E(k) = k^2 P_v(k) \propto k^{-3/2}$. The power spectrum $E(k) \propto k^{-3/2}$ is therefore shallower than the Kolmogorov one. One of the fundamental assumptions of Iroshnikov (1963) and Kraichnan (1965) is that the eddies are isotropic. However, numerical and observational data suggest that in MHD turbulence the energy transfer occurs mainly in the field perpendicular direction (Biskamp, 2003).

An important step forward has been accomplished by Goldreich and Sridhar (1995). They proposed a theory in which anisotropy of the eddies is accounted for. As the energy cascade proceeds to smaller scales, turbulent eddies get more and more elongated in the direction of the magnetic field. They assume that the Alfvén time-scale and the non-linear cascade time-scale are comparable, $k_z V_a \simeq v k_\perp$, while the cascade time in the direction perpendicular to the field leads to $v_\perp \propto k_\perp^{-1/3}$. The wave vector along the z-axis is thus expressed as $k_z \propto k_\perp^{2/3}$. The energy transfer time is therefore different from the Iroshnikov-Kraichnan estimate, and identical to the one obtained by Kolmogorov. One gets $E(k_\perp) \propto k_\perp^{-5/3}$. This issue has been further studied (e.g., Cho et al., 2002; Boldyrev, 2005; Lee et al., 2010; Beresnyak, 2011; Mason et al., 2012; Wan et al., 2012) and

remains still debated. It is however clear from the numerous numerical simulations performed that the turbulence is very anisotropic (e.g., Grappin and Müller, 2010).

4.1.2. Compressible Magnetized Turbulence

Since molecular clouds are both magnetized and super-sonic (with typical Mach numbers on the order of 10), compressible magnetized turbulence has received considerable attention during the last two decades. Because of its simplicity many works have been assuming an isothermal equation of state. More recently 2-phase medium has also been considered.

One of the major question that has been under investigation when the importance of turbulence was established, was the origin of the turbulence in molecular clouds and more precisely how the observed turbulence could be maintained. Since turbulence is expected to decay in one crossing time, this would imply that either molecular clouds were young, either there was a source that was continuously rejuvenating the turbulent energy, either the turbulence was decaying slower than expected. Several works have been investigating the latter assumption (e.g., Mac Low et al., 1998; Ostriker et al., 2001; Birnboim et al., 2018). They conclude that while magnetic field introduces some delay compared to the hydrodynamical case, the decay still occurs too rapidly, that is to say in about one crossing time, to explain the high level of turbulence found in molecular clouds.

The second major reason to study turbulence is obviously to get a statistical description of the fluctuations arising in molecular clouds and this has been addressed in several studies (e.g., Mac Low et al., 1998; Padoan and Nordlund, 1999; Ostriker et al., 2001; Cho and Lazarian, 2003). In this respect, one of the most comprehensive set of simulations relevant for the MHD turbulence arising in the 2-phase interstellar medium has been performed by Kritsuk et al. (2017). Five runs are presented where the mean density (2 and 5 cm^{-3}), magnetic field ($\simeq$ 1, 3, and 10 μG) and root mean square velocity are varied. The total box size is 200 pc and a random forcing in the Fourier space is applied to sustain the turbulent motions. A cooling function relevant for the ISM is employed and it leads to the existence of WNM and CNM. **Figure 4** displays the energies as a function of time, the magnetic field PDF, the powerspectra of kinetic and magnetic energies as well as the longitudinal structure function for run A (mean density is 5 cm^{-3}, magnetic intensity of 10 μG and rms velocity about 16 km s^{-1}) of Kritsuk et al. (2017). As can be seen for this particular run the magnetic and kinetic energies are comparable. The PDF is broad and magnetic intensities larger than 100 μG are sometimes found. The energies present power spectra with exponent compatible with -3/2 although the inertial range is probably not extended enough to make this value well determined. Interestingly, we note that the structure function is stiffer in the CNM than in the WNM. Clearly this is because the former is highly supersonic while the latter is nearly transsonic. Let us also stress that the anisotropic nature of the MHD turbulence, which present elongated structures along the magnetic field as inferred in the incompressible case, is still present in the compressible case as shown for example by Vestuto et al. (2003) or Beresnyak et al. (2005).

Due to its very non-linear nature, the description presented in most works is essentially numerical however some recent theoretical progress have been accomplished for the understanding of how the cascade proceeds in a magnetized, compressible, self-gravitating and isothermal gas by Banerjee and Kritsuk (2017) and Banerjee and Kritsuk (2018) following the work of Galtier and Banerjee (2011). In this work a complete expression of the total energy transfer is obtained as mixed second-order structure functions (see Equation 33 of Banerjee and Kritsuk, 2018). The contributions of pure kinetic, magnetic, gravitational and thermodynamic terms are clearly identified and will allow future works to clarify their respective roles and importance.

4.1.3. How Magnetic Field Affects the Density PDF

The density PDF is a key quantity in the ISM, particularly for the star formation process. Several models aiming at providing explanations for the two most fundamental problems of star formation, namely the initial mass function of stars (Padoan et al., 1997; Hennebelle and Chabrier, 2008) and the star formation rate (Padoan and Nordlund, 2011; Hennebelle and Falgarone, 2012; Federrath and Banerjee, 2015) directly depend on the density PDF.

The density of cold and weakly self-gravitating molecular gas has been found to present a lognormal distribution. It is likely the result of random shocks induced by the compressible turbulence and the multiplicative nature of the density variable leading, to a Gaussian distribution of $\log \rho$. A useful calculation has been inferred by Hopkins (2013), who derived a log-Poisson distribution for the density, using intermittent models developed in the context of incompressible turbulence. The mathematical expression of the density distribution presents a free parameter that controls the degree of intermittency and the deviation from the lognormal distribution. Hopkins (2013) compared this expression with PDF from numerical simulations and obtain very good agreement. This is particularly interesting for the high Mach number runs in which important deviations from the lognormal behavior are observed. Another important aspect regarding the cold and non-self-gravitating gas is the cooling or more precisely the effective equation of state, that is to say the pressure vs. density relation. In most of the studies the isothermal assumption has been made. However powerlaws instead of lognormal have been inferred for polytropic flows. Federrath and Banerjee (2015) carried out a set of calculations for polytropic flows, i.e., following $P \propto \rho^{\Gamma}$ for $\Gamma = 0.7$, 1 and 5/3. They inferred modest differences between $\Gamma = 0.7$ and 1 that do not strongly deviate from lognormal distribution. On the other hand, significant deviations were obtained for $\Gamma = 5/3$ in particular the low density part of the PDF is better described by a powerlaw.

The effect of the magnetic field on the density PDF has also been studied in the isothermal case (e.g., Ostriker et al., 2001; Lemaster and Stone, 2008) and in two-phase flows (e.g., Hennebelle et al., 2008; Kritsuk et al., 2018). It has generally been found that magnetic field has a limited impact. This agrees with the conclusion that the gas which is not self-gravitating tends to flow along magnetic field lines. Molina et al. (2012) carried out isothermal simulations with various Mach numbers.

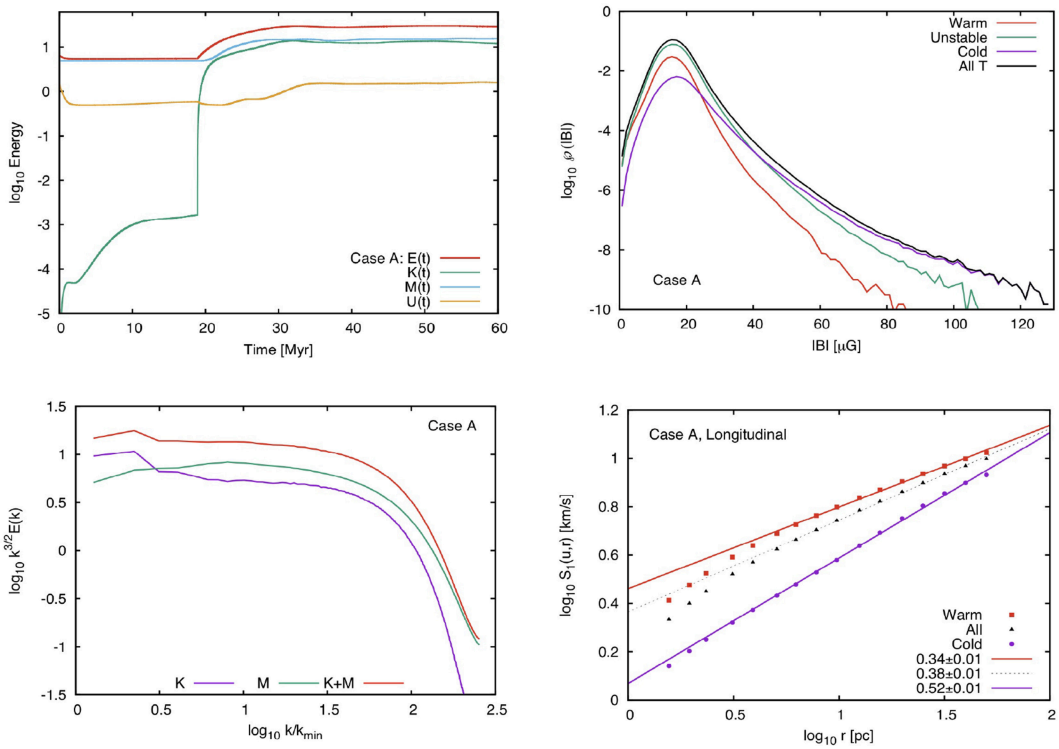

FIGURE 4 | Results of simulations of ISM magnetized turbulence performed by Kritsuk et al. (2017). **(Top-left panel)** Shows the total, kinetic, magnetic and internal energies as a function of time. **(Top-right panel)** Displays the magnetic field PDF in the warm, unstable and cold phases. **(Bottom-left panel)** Portrays the powerspectra of the kinetic, magnetic and total energies while **(bottom-right panel)** shows the structure functions of the velocity in the various phases of the ISM.

They inferred that in the transsonic and subsonic flows, the density PDF of magnetized and pure hydrodynamical cases are very similar. They report however significant differences for supersonic flows. An analytic expression which is an extension of the lognormal distribution has been proposed. From their **Figure 1**, it appears that the difference between hydrodynamical and magnetized runs are important only for the low density gas while the PDF at high densities are almost identical.

4.2. The Influence of the Ion-Neutral Drift on MHD Turbulence

As discussed in section 2.2 the ion-neutral friction is an important source of energy dissipation in the interstellar medium and particularly within molecular clouds. Likely enough this should have an impact on the development of turbulence and presumably modifies the fluctuations at small scales. Here we describe the various efforts that have been undertaken to investigate this aspect. We first describe the effects of the ion-neutral friction on MHD waves and then discuss the numerical simulations, which have been performed and the conclusions.

4.2.1. How Ion-Neutral Drift Affects Wave Propagation

The impact of ion-neutral friction on the propagation of MHD waves has been first investigated by Kulsrud and Pearce (1969) considering a fluid of ions and a fluid of neutrals (see e.g., Lequeux, 2005, for a more recent and complete discussion). Although they restrict the discussion to Alfvén waves only, the dispersion relation obtained is of the third order making a complete discussion a little tedious. They found that there are several wavelength domains to be considered.

In the long wavelength limit, the ions and the neutrals are well coupled because the dynamical time is short with respect to the ion-neutral friction time. In this limit the strong coupling approximation can be used and the dispersion relation is

$$\omega = i\frac{k^2 V_A^2}{2\gamma_{ad}\rho_i} \pm \sqrt{k^2 V_A^2 - \left(\frac{k^2 V_A^2}{2\gamma_{ad}\rho_i}\right)^2}, \qquad (25)$$

where k is the wavenumber and V_A is the Alfvén speed of the neutrals (i.e., $V_A = B/\sqrt{4\pi\rho}$). The waves propagate at the Alfvén speed of the neutrals. They dissipate in a time scale that is proportional to $k^2 \propto \lambda^{-2}$, where λ is the wavelength. If $k > 2\gamma_{ad}\rho_i/V_A$, the waves do not propagate any more. This is because the friction is too intense.

In the short wavelength limit (which is not described by Equation 25), the waves propagate at the Alfvén speed of the ions, which for typical molecular cloud conditions, is roughly thousand times the Alfvén speed of the neutral (because typical ionization is on the order of 10^{-7}). This is because in this limit the wave frequency is shorter than the ion-neutral friction time,

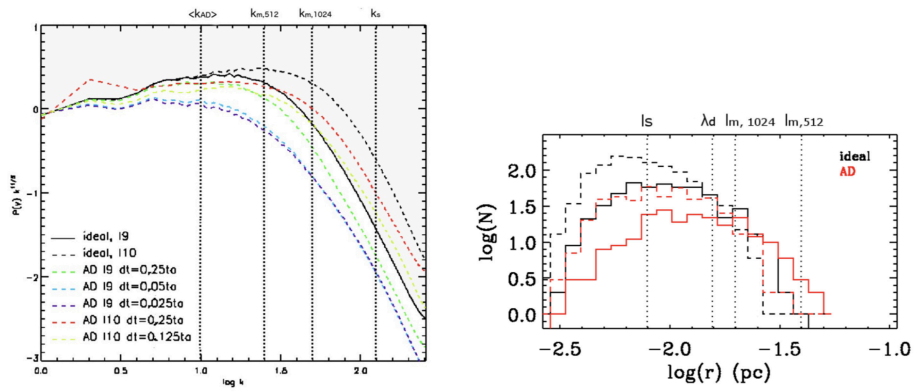

FIGURE 5 | (Left panel) Compensated velocity powerspectra for the decaying MHD simulations with ambipolar diffusion (from Ntormousi et al., 2016). The various runs include ideal MHD with 512^3 (l9) and 1024^3 (l10) resolution and a series of runs with ambipolar diffusion with the same two resolutions and various values of the minimum timesteps allowed. The powerspectra present major deviation from the ideal MHD runs at scales smaller than the ambipolar diffusion one. **(Right panel)** Distribution of filament width in MHD simulations with and without ambipolar diffusion. The solid lines are for a resolution of 512^3 while the dashed ones correspond to 1024^3. Reproduced from Ntormousi et al. (2016) with permission of A&A.

thus the neutrals cannot follow the ions. The dissipation time, in this regime is independent of λ.

Balsara (1996) has been performing a complete analysis by solving for all modes and also by solving for the strong coupling approximation. He concluded that the slow MHD modes are less affected by the dissipation induced by the ion-neutral friction, particularly when the propagation of the waves is along the field lines. He also found that in the long wavelength limit, the strong coupling approximation is very accurate and can be employed.

4.2.2. Turbulence With Ion-Neutral Drift

From these analytical results, it is clear that ion-neutral friction leads to wave damping and should therefore affect the turbulent cascade. To quantify the scale at which this may happen it is usual to infer the scale at which the Reynolds number, in which the viscosity is taken to be the ion-neutral friction, is about 1 (see section 6.2.3). This scales is called l_{ad} or l_{diss}, depending on the authors.

One of the first simulations, that have been performed, are the ones by Oishi and Mac Low (2006) using the strong coupling approximation. They conclude that contrary to the simple analytical estimate, the simulations do not reveal a clear sign of a specific smoothing or dissipative scale. Other simulations like the ones performed by Li et al. (2008), Downes and O'Sullivan (2011), and Ntormousi et al. (2016) found that ion-neutral friction affects the turbulent fluctuations at a scale below the ambipolar diffusion one leading to a smoother structure. Left-panel of **Figure 5** displays the velocity powerspectra of ideal MHD simulations at various resolution and of simulations that include the ion-neutral friction for the same numerical resolutions and for various minimum timesteps allowed (in these calculation an explicit scheme is employed and the smallest timesteps is enforced by raising the ionization if needed). Clearly the powerspectra with ion-neutral friction present sign of dissipation at a scale that is about l_{ad} although numerical convergence could not be obtained.

Burkhart et al. (2015) presented three calculations with various Alfvénic and sonic Mach numbers using the heavy ions approximation. They computed structure functions and compare the results with the prediction made by Goldreich and Sridhar (1995). They also performed mode decomposition as described by Cho and Lazarian (2003), that is to say identifying the Alfvén, fast and slow modes. Part of their results are displayed in **Figure 6**. While the super-Alfvénic simulation present structure functions compatible with the prediction of Goldreich and Sridhar (1995), even below the ambipolar diffusion scale, l_{ad}, the Alfvén waves component of the sub-Alfvénic simulation shows clear sign of decay below l_{ad}.

Clearly the nature of MHD turbulence in the presence of ion-neutral friction is not well understood and requires further investigation.

5. HOW MAGNETIC FIELD CORRELATES WITH THE DENSITY FIELD

A major question to understand the role of the magnetic field in molecular cloud evolution is how it correlates with the other fields and in particular with the density. Two aspects are particularly important, first how the mean magnetic intensity varies with the density and second how the magnetic field direction correlates with structures like filaments and more generally how the magnetic field direction correlates with density gradients.

5.1. The *B* vs. *N* Relation

Since the pioneering work of Troland and Heiles (1986), it is well established (Crutcher et al., 2010) that the mean magnetic intensity is independent of gas density, n, for values up to about 300 cm^{-3}. At higher densities, that is to say at least up to 10^{6-7} cm^{-3}, the mean magnetic intensity has been found to increase

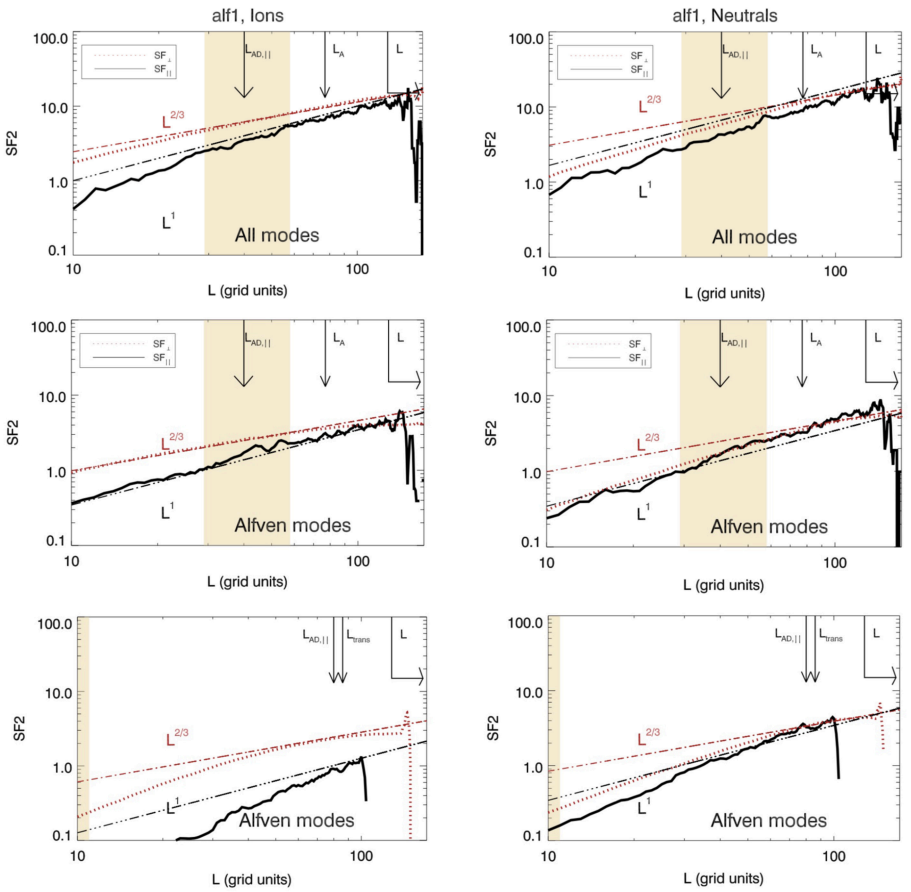

FIGURE 6 | Structure function in MHD turbulence with ion-neutral friction from Burkhart et al. (2015). **(Left panel)** Show the structure function for the ions while the **right panels** display the structure functions for the neutrals. The first and second rows are for a supersonic and super Alfvénic simulation while the third row is for a sub-Alfvénic one. For the second and third panel mode decomposition has been performed and only the Alfvén modes are shown. As can be seen from third row, they are strongly damped in the sub-Alfvévic case why they roughly follow the expected scaling from ideal MHD theory in the super-Alfvénic one. Reproduced from Burkhart et al. (2015) with permission of ApJ.

with n broadly like a powerlaw, that is to say $B \simeq n^{\kappa}$. The exact value of κ is still a matter of debate. Earlier works (Crutcher, 1999) obtained $\kappa = 1/2$ but more elaborated Bayesian analysis led to $\kappa \simeq 0.65$ (Crutcher et al., 2010). Understanding the physical origin of this behavior is important to unravel the star formation process in general. In particular, the mass to magnetic flux ratio, M/ϕ, can be estimated by combining the column density of the observed component along the line of sight and the observed magnetic intensity. This leads to the conclusion that the atomic and diffuse molecular gas is *subcritical*, that is to say dominated by the magnetic field, while dense regions, such as dense cores, are generally supercritical.

Before describing the results inferred from numerical simulations, it is worth to recall the different behaviors that can be expected. If the contraction occurs along the field lines, then the magnetic field is not amplified and $B \propto n^{\kappa}$ with $\kappa = 0$. If the motion is perpendicular to the field lines, then it is easy to show that n/B stays constant (combining the continuity and induction equations in one dimension) and thus $\kappa = 1$. Note that in this configuration the magnetic pressure is proportional to n^2 and therefore quickly halts any contraction. Qualitatively at least, these two cases represent, respectively, a situation in which the magnetic field is strong and weak with respect to the kinetic motions, i.e., sub and super-Alfvénic situations. In the sub-Alfvénic case, the magnetic field guides the flow and forces the contraction along the field lines while in the super-Alfvénic case, it is advected by the flow and the transverse component of the field is amplified.

If the contraction is spherical, for example driven by gravity, then the mass enclosed is simply $\propto \rho R^3$, R being the cloud radius, while the magnetic flux is $\propto BR^2$ thus leading to $B \propto n^{2/3}$. It is, however, likely that a contracting cloud does not remain spherical, especially if the magnetic field is not negligible. In this case, it is expected that an equilibrium along the field lines settles leading to $c_s^2 \simeq \phi$, where ϕ is the gravitational potential. The Poisson equation leads $\phi \propto nh^2$ where h is the thickness of the cloud along the field lines. Then, as the mass enclosed is now $\propto nR^2h$ while the magnetic flux is still $\propto BR^2$, we get $B \propto c_s n^{1/2}$.

Basu (2000) has compared the data provided by Crutcher (1999) with this expression and has obtained a good agreement, which improves if the velocity dispersion σ instead of c_s is used. Another even simpler interpretation of this relation is energy equipartition between magnetic and kinetic energy, $B^2/(4\pi) \propto n\sigma^2$.

Several theoretical studies have been investigating the B vs n relation. In particular various simulations of 3D ideal MHD turbulence tend to show that in realistic ISM conditions and without gravity (e.g., Padoan and Nordlund, 1999; Hennebelle et al., 2008; Banerjee et al., 2009), the magnetic intensity weakly depends on the density field. A weak correlation is found with typically $\kappa \simeq 0.1 - 0.2$. This has been interpreted in the context of the 2-phase ISM by Hennebelle and Pérault (2000) as a consequence of the magnetic tension, which tends to unbend the magnetic field lines and to align the magnetic and the velocity fields. This eventually facilitates the gas contraction. For polytropic flows, the lack of correlation is due to the various types of MHD waves having different scalings of the field strength with the density (Ostriker et al., 2001; Passot and Vázquez-Semadeni, 2003; Burkhart et al., 2009). Indeed while for fast waves, magnetic intensity and density are correlated, they are anti-correlated for slow waves and not correlated for Alfvén waves. Thus, in a turbulent transsonic flow, as is the multi-phase HI, the field strength is a consequence of the complete history of wave propagation. Note that in supersonic and superalfvénic simulations, more vigorous dependence of B on the density is inferred (Ostriker et al., 2001; Burkhart et al., 2009). The simulations which treat both self-gravity and turbulence find that at high density the magnetic intensity is $\propto n^{0.5}$ (Hennebelle et al., 2008; Banerjee et al., 2009), which accords well with the analytical predictions deduced above. More recently Li et al. (2015) performed high resolution adaptive mesh simulations for a weak and a strong initial magnetization and performed clump identification. They then investigated the relation between the mean magnetic field, $\bar{B}$ and the mean density, $\bar{n}$, within the clumps and inferred $\bar{B} \propto \bar{n}^{0.65}$ in good agreement with the Crutcher et al. (2010) result. This may seemingly suggest that at the scale of the clumps themselves, the contraction is nearly isotropic. This is in good agreement with the results reported by Mocz et al. (2017) where simulations with a broad range of Alfvénic Mach number, $\mathcal{M}_A$, have been presented. When $\mathcal{M}_A > 1$, the clumps follow $B \propto n^{2/3}$, while when $\mathcal{M}_A < 1$, $B \propto n^{1/2}$ is inferred.

5.2. The Orientation of Magnetic Field

The orientation, or more generally the topology, of the magnetic field is expected to play a significant role in the formation of structures. For example as discussed above strong toroidal fields can induce instabilities in filaments while poloidal ones tend to stabilize them (Fiege and Pudritz, 2000). Another example comes from the work of Nagai et al. (1998), where linear stability analysis of a magnetized self-gravitating layer has been performed (see also Van Loo et al., 2014). They show that the orientation of the most unstable mode tends to be correlated with the magnetic field direction. The result depends on the external pressure that determines the scale height, z_b at which the solution is truncated. If $z_b \gg l_0$, l_0 being the Jeans length, then the fastest growing mode is aligned with the magnetic field, resulting in filaments which are perpendicular to the field direction. The physical reason is that, since the width is large relative to the Jeans length, the layer is compressible and density fluctuations are easier to develop along the magnetic field. On the other hand when $z_b \ll l_0$, the fastest growing mode is perpendicular to the magnetic field and the filaments are aligned with it. This is because the layer is almost incompressible (since the scale height is smaller than the Jeans length), thus the instability develops through the bending of the layer. As perturbations whose wave vectors are perpendicular to the magnetic field do not bend the field lines, these perturbations develop more easily.

Observationally significant progresses have recently been accomplished regarding the magnetic field orientation. The polarization observations by the Planck satellite reveal that in the diffuse ISM, the elongated column density structures traced tend to be predominantly aligned with the magnetic field within the structures (Planck Collaboration et al., 2016). This statistics for the low column density gas are comparable to that found between low column density fibers traced by H_I emission and the magnetic field (Clark et al., 2014). The analysis of the Planck data toward nearby molecular clouds reveals that the relative orientation between the structures and the magnetic field depends on the column density, $N_{\rm H}$. It is mostly parallel at $\log(N_{\rm H}) \simeq 21.7\,{\rm cm}^{-2}$ and mostly perpendicular at $\log(N_{\rm H}) \geq 21.7\,{\rm cm}^{-2}$ (Planck Collaboration et al., 2016).

A detailed analysis of the angle, ϕ between the magnetic field and the density gradient,

$$\cos\phi = \frac{\nabla\rho \times \mathbf{B}}{|\nabla\rho|\,|\mathbf{B}|}, \tag{26}$$

in numerical simulations has been carried out by Soler et al. (2013) using the simulations presented in Dib et al. (2010). In these numerical experiments the gas is isothermal and the

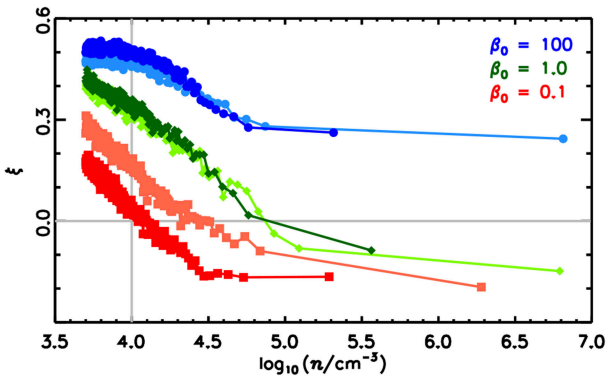

FIGURE 7 | Relative orientation parameter, ξ vs. gas density, $n \equiv \rho/\mu$ from Soler et al. (2013). The values of ξ correspond to the relative orientation between $\nabla\rho$ and B in density bins with $n > 500\,{\rm cm}^{-3}$. The values $\xi > 0$ correspond to $\nabla\rho$ mostly perpendicular to B and $\xi < 0$ correspond to $\nabla\rho$ mostly parallel to B. The gray horizontal line is $\xi = 0$. The darker colors represent the early snapshots and the lighter colors, the later snapshots. The gray vertical line, drawn for reference, corresponds to $n = 10^4\,{\rm cm}^{-3}$. Reproduced from Soler et al. (2013) with permission of A&A.

turbulence, seeded initially with an initial Mach number of about 10, is decaying. Through shocks and self-gravity dense clumps and filaments quickly form. Three values of magnetization, characterized by the initial β, equals to the thermal over magnetic pressure have been explored namely 100 (weakly magnetized), 1 and 0.1 (strongly magnetized). A value of $\xi > 0$ means that the dominant configuration is $\cos\phi \simeq 0$, that is to say the magnetic field and the density gradient tend to be perpendicular, which in turns implies that the magnetic field and density isocontour tend to be parallel. To quantify the alignment, in each density bin, the difference between the numbers of cells having, respectively $|\cos\phi| < 0.25$ and $|\cos\phi| > 0.75$ (see Soler et al., 2013) has been computed. **Figure 7** shows the dependence of ξ with the gas density for the three runs at two timesteps. For the low magnetization ($\beta = 100$), ξ remains positive for all density bins, with a clear trend for $\cos\phi$ to increase at large densities (i.e., ϕ goes to smaller values). For the more magnetized case, ξ becomes negative at high densities and the density value at which this happens drops with β. This in particular shows that at low densities the magnetic field tends to be aligned with the filaments while at high densities it is more perpendicular to them. While the physical origin of this last trend is simply that the gas is channeled by the magnetic field, when it is strong enough, along the field lines, the mechanism by which the alignment occurs at low density is less obvious. To better understand it, Soler and Hennebelle (2017) have obtained an exact equation for the evolution of ϕ. It is simply obtained by combining the Faraday and continuity equations,

$$\frac{d(\cos\phi)}{dt} = \frac{\partial_i(\partial_j v_j)}{(R_k R_k)^{1/2}}[-b_i + r_i\cos\phi] + \partial_i v_j[r_i r_j - b_i b_j]\cos\phi, \tag{27}$$

where

$$r_i \equiv \frac{R_i}{(R_k R_k)^{1/2}},\ R_i = \partial_i \rho, \tag{28}$$

$$b_i \equiv \frac{B_i}{(B_k B_k)^{1/2}}, \tag{29}$$

By numerically estimating the different terms in the right-hand side of Equation (27), Soler and Hennebelle (2017) showed that the mean value of the first term, which entails second spatial derivatives, quickly goes to zero. They therefore concluded that the second term is mainly responsible of the evolution of $\cos\phi$. As can be seen this second term vanishes either if B and $\nabla\rho$ are orthogonal, in which case $\cos\theta = 0$, or if they are parallel, in which case $r_i r_j - b_i b_j = 0$. This could suggest that $\cos\phi$ has two attractors, 0 and ± 1 although this obviously depend on the sign of the velocity derivatives. Numerical estimates using MHD simulations, show that indeed, on average, the mean value of $\cos\phi$ follows the sign of the velocity terms.

Therefore the aligned configurations ($\phi = 0$ or π) and perpendicular ones ($\phi = \pi/2$) are favored. They are simple consequences of the fluid equations (more precisely continuity and Faraday equations).

Recently Gómez et al. (2018) have investigated the detailed structure of the magnetic field inside a self-gravitating filament, which forms in a turbulent environment. Similarly to other studies, they found that the magnetic field is primarily perpendicular to the supercritical filaments. However, they note that due to the gravitational infall along the filament, the field lines are further bent resulting in a "U"-shaped magnetic field line geometry. An equilibrium eventually settles due to the diffusion processes, that equilibrate with the transport by the infall motions. **Figure 8** displays the magnetic field structure on top of the column density within the filament.

6. FILAMENTS

While the density PDF provides very important information on the ISM, it should be kept in mind that they miss an essential piece of information, i.e., the spatial correlations or the shape of the interstellar clouds. While it has been recognized that the ISM is remarkably filamentary for many years, recent studies carried out by Herschel led to quantitative statistical estimates of their properties (André et al., 2014).

The first question that has to be addressed is what is the origin of this ubiquitous filamentary structure? Second, Herschel studies have also revealed that the filaments have a possible characteristic width of about 0.1 pc, which is surprising and needs to be explained although it is worth stressing that this result has for now been obtained only in nearby molecular clouds. Finally, it seems that most star forming cores sit inside self-gravitating filaments (Polychroni et al., 2013; Könyves et al., 2015), seemingly suggesting that filaments may be one important step of the star formation process.

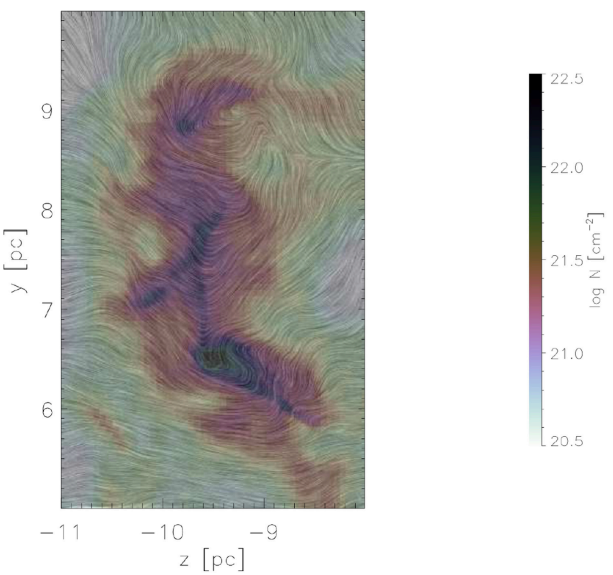

FIGURE 8 | Structure of the magnetic field within a self-gravitating filament (Gómez et al., 2018). The structure of the mass weighted magnetic field integrated along the line of sight is shown on top of the column density. The magnetic field, that is primarily perpendicular to the direction of the filament, is then further stretched by the collapsing motions along the filament, resulting in a "U"-shaped magnetic field line geometry.

6.1. Formation of Filaments

It is well known that gravity amplifies anisotropies and tends to promote the formation of filaments. In the context of molecular clouds this is particularly evident in studies like the ones performed by Nagai et al. (1998), Smith et al. (2014), Gómez and Vázquez-Semadeni (2014), Federrath (2015), Gong and Ostriker (2015), Chen and Ostriker (2015), and Camacho et al. (2016). This is simply because the gravitational force being the gradient of a scalar, it is stronger along the shortest axis of a clump. However, gravity can not explain all the observed filaments because many filaments are not self-gravitating. Indeed, the atomic gas (HI) is itself rather filamentary (Miville-Deschênes et al., 2003; McClure-Griffiths et al., 2006; Clark et al., 2014), but is far from being self-gravitating. It seems therefore that other processes could lead to filament formation. To investigate this issue Hennebelle (2013) performed MHD and hydrodynamical turbulent simulations of the ISM and computed the clump aspect ratio. These simulations include interstellar cooling and therefore present a 2-phase structure as described above. Gravity is not included. They have an initial velocity dispersion which corresponds to a Mach number of 10 and then decay. Hennebelle (2013) found that magnetic field makes the clumps more filamentary as seen from **Figure 9** that portray the column density in an hydrodynamical and an MHD run. This is indeed quantified by **Figure 10**, which shows the aspect ratio of the clumps that have been extracted from the simulations using a friend of friend algorithm. It reveals that on average the clumps in the MHD case have a smaller μ_2/μ_3, where μ_2 and μ_3 are the inertia matrix eigenvalues of the clumps. Hennebelle (2013) also found that the filament axis tends to be aligned with the strain, i.e., the direction along which the fluid particles are stretched by the velocity field. This suggests that indeed turbulence, and even more likely, MHD turbulence naturally produces elongated structures. This is in good agreement with the anisotropic nature of MHD turbulence which, as discussed in sections 4.1.1 and 4.1.2 produces structures elongated along the magnetic field.

Inoue and Inutsuka (2016) demonstrated that, in shock compressed layers of typical magnetized ISM, filamentary cold

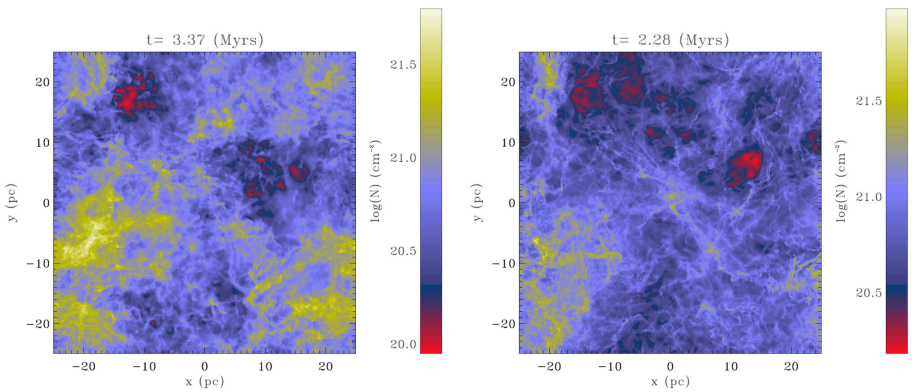

FIGURE 9 | Column density for one snapshot of a decaying turbulence experiment. Left hydrodynamical run, right MHD run (from Hennebelle, 2013). Initially the field is uniform and has an intensity of 5μG. The magnetized run presents a more filamentary structure that the hydrodynamical run as can seen through visual inspection and confirmed by detailed analysis (see **Figure 10**). Reproduced from Hennebelle (2013) with permission of A&A.

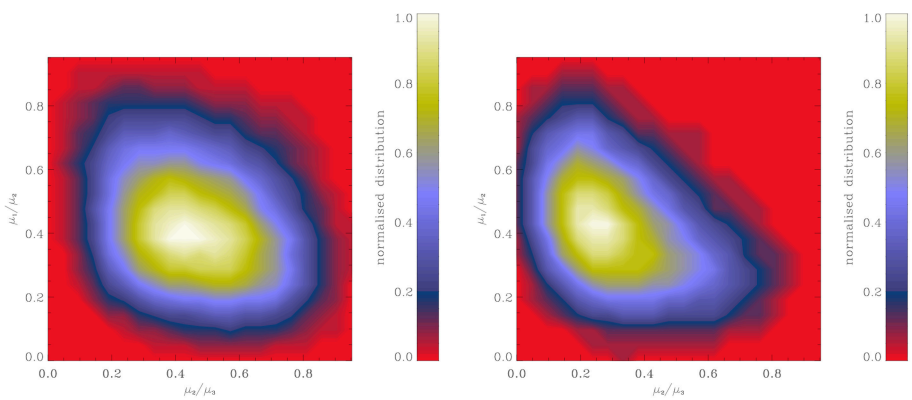

FIGURE 10 | Normalized bidimensional histogram displaying μ_1/μ_2 as a function of μ_2/μ_3 where μ_1, μ_2, and μ_3 are the inertia matrix eigenvalues, μ_1 being the smallest (from Hennebelle, 2013). **(Left panel)** Hydrodynamical simulation. **(Right panel)** MHD simulation. Clearly the MHD run present structures that on average tends to be more elongated (i.e., have a smaller μ_2/μ_3) than the hydrodynamical ones. Reproduced from Hennebelle (2013) with permission of A&A.

HI clouds are naturally created by thermal instability, and they also showed that stretched HI filaments that align with the local magnetic fields are due to the turbulent shear strain induced at the shock front. Prominent filaments are also found in magnetized shock-compressed dense layer (Inutsuka et al., 2015; Ntormousi et al., 2017), as illustrated in **Figure 11**, while again the unmagnetized runs produce much less elongated structures (Ntormousi et al., 2017), seemingly suggesting that the effect is generic and not sensitive to particular configurations. In the case of shock-compressed molecular layers denser than HI clouds, the massive filamentary clouds are perpendicular to the mean magnetic field lines. The mechanism to create such a prominent feature can be interpreted as the generic interaction of a shock wave and a magnetized medium with significant density inhomogeneity in pre-shock state (Inoue and Fukui, 2013; Inoue et al., 2018). This mechanism does not require self-gravity but the latter enhances the accretion of gas along the magnetic field lines onto the massive filament. Note that in some calculations (e.g., Inutsuka et al., 2015), substructures connected, and often perpendicular, to the main filaments are also observed. These structures are reminiscent of the *striations* that have been reported in molecular clouds (e.g., Heyer et al., 2016), where they appear as highly elongated along the magnetic field. Tritsis and Tassis (2016) have performed several numerical calculations to investigate their origin and concluded that they are most likely a consequence of non-linear MHD waves due to inhomogeneous density fields. Similar conclusion has been reached by Chen and Ostriker (2014) who presented a series of magnetized simulations and identified a network of small filaments aligned with the magnetic field in the simulations with the lowest β and estimate that this later must be < 0.2 to get prominent striations.

The role of the magnetic field in the formation of filaments is likely important because it makes the flow more coherent therefore allowing the existing filaments to survive longer. In a related way, the flows tend also to be more organized when they are magnetized. For example several studies have concluded that velocity and magnetic field are preferentially aligned (see for example Matthaeus et al., 2008; Banerjee et al., 2009; Iffrig and Hennebelle, 2017). This is also consistent with the recent finding that the magnetic field direction and the density gradients are clearly correlated (Koch et al., 2013, 2014; Soler et al., 2013; Planck Collaboration et al., 2016; Soler and Hennebelle, 2017) as discussed in section 5.2.

Let us reiterate that there is not necessarily a unique mechanism that leads to the formation of filaments. In particular it is clear that both magnetic field and self-gravity tend to produce highly elongated structures. While it seems difficult to invoke the latter in the formation of diffuse filaments, it very likely plays a determinant role in the formation of the most massive ones. This is particularly obvious in series of simulations presented by Federrath (2016) where filaments can form under the influence of gravity and MHD turbulence only.

6.2. A Characteristic Width?

Perhaps the most intriguing and recent aspect of filaments is the possible existence of a characteristic width, of about 0.1 pc, and even more surprising is the fact that this remains true

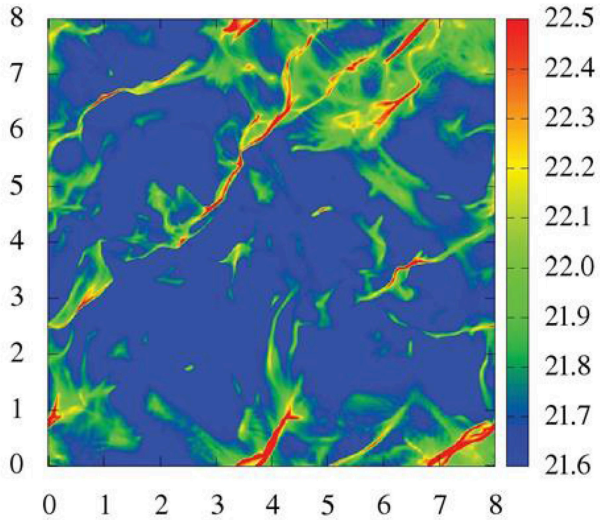

FIGURE 11 | Formation of supercritical filaments and striations (Inutsuka et al., 2015) in a shocked layer (seen face on). In this calculation the filaments are self-gravitating (and therefore named supercritical) and the striations are mainly perpendicular to the filaments. Reproduced from Inutsuka et al. (2015) with permission of A&A.

for filaments of column densities spanning almost 3 orders of magnitude (Arzoumanian et al., 2011; André et al., 2014; Koch and Rosolowsky, 2015). Indeed both gravity and turbulence tend to be scale free processes and usually produce powerlaws. For example the Jeans length varies by more than one order of magnitude in the above mentioned filament sample. This analysis on the width distribution in Herschel observation has triggered many subsequent papers on this issue. While Juvela et al. (2012), Alves de Oliveira et al. (2014), and Koch and Rosolowsky (2015) essentially confirmed the earlier findings, Panopoulou et al. (2017) pointed out the tension between the characteristic width and the spatial power spectra of the data that show no characteristic scale. This tension could be removed by the fact that the masses in the filaments with a characteristic width corresponds to a small fraction of the total mass in the whole molecular clouds and hence they provide small contribution in the spatial power spectra in observational emission maps. Hacar et al. (2018) showed the velocity coherent filamentary structures (so-called fibers) have a median widths that is a factor of three smaller than 0.1pc in the integral shape filament in Orion using ALMA observation of molecular emission from N_2H^+ (1-0). However, Clarke et al. (2018) cautioned about line-of-sight confusion in the analysis of velocity coherent structure according to their synthetic observations of simulated filaments. Note also that high-resolution ALMA observation has not yet been reported for dust continuum emission that has a dynamic range in emission much larger than in molecular line observation. These observations lead to the question of why we tend to observe a characteristic width of molecular filaments, at least, apparently with the spatial resolution typical in Herschel observation. Part of the answer may be the finite resolution as recently claimed by Panopoulou et al. (2017). This may account for some of the

observed filaments in particular the low column density ones that are not as prominent as the very dense ones.

Various explanations (André et al., 2014) have been put forward to account for this fact, three of them are described below.

6.2.1. Jeans Length and Self-Gravitational Equilibrium

It would appear logical that the width of supercritical filaments is directly related to the mean Jeans length within the filament. However, as stressed by (Arzoumanian et al., 2011), the Jeans length drops with density which is at odds from the nearly constant width that is inferred from observations. However Fischera and Martin (2012) argued that the characteristic size of the filaments is simply the result of mechanical equilibrium in the radial direction. Assuming that the filaments are pressure bounded, they find that the equilibrium of the isothermal gas, between thermal pressure and gravity leads to a diameter of about 0.1 pc with a weak dependence on the column density. While this explanation could be valid for nearly critical filaments and is indeed observed in numerical simulations (Smith et al., 2014), it cannot account for very supercritical filaments as thermal support is unable to resist gravity. The effects of magnetic field are also studied by Tomisaka (2014) and Auddy et al. (2016) where a bidimensional equilibrium is considered, with the filaments being rather ribbons due to the anisotropic Lorentz force. Again the finite width of the massive filament cannot be explained even with magnetic field, unless the strength of the field is exceptionally large.

6.2.2. The Sonic Length Argument

If filaments are produced in shocks, then their density, ρ_f, should be linked to the background density, ρ_0 by the Rankine-Hugoniot relation: $\rho_f = \rho_0 M^2$, where M is the Mach number, $M = v/c_s$. The velocity on the other hand is linked to the scale as $v(L) \simeq v_0 (L/1\mathrm{pc})^{\eta}$ which is simply the Larson relation discussed above and $v_0 \simeq 0.8$ km s^{-1} while $\eta \simeq 0.4 - 0.5$. As the size of the shocked layer is simply given by $L_f = L\rho_0/\rho_f$, we get $L_f = (c_s/v_0)^2 \times L(L/1\mathrm{pc})^{-2\eta}$. In particular assuming that $\eta = 0.5$, the shocked layer becomes independent of the fluctuation size and with $c_s \simeq 0.2$ km s^{-1}, we get $L_f \simeq 0.07$ pc which is close to the thickness inferred by Arzoumanian et al. (2011). This explanation has been generalized to the magnetic case by Federrath (2015), who argue that it reproduces the simulations well. Note, however, that this argument only explains the thickness of the sheet-like structure that is geometrically different from the filament. In addition, this explanation neglects the effect of self-gravity, and hence, cannot explain why the massive filaments are supported against excessive self-gravitational forces that are expected to trigger the radial collapse of the filaments.

The model considered by Auddy et al. (2016) is more elaborated as they considered a 2D equilibrium with magnetic field lines perpendicular to its surface. Along the field lines the structure, which is described as a ribbon, is really narrow and typically below 0.1 pc, while perpendicularly it is confined by the ram pressure and its length, close to 0.1 pc, is essentially the sonic length.

6.2.3. The Ion-Neutral Friction

A third class of explanations has invoked the ion-neutral friction that provides a source of dissipation, the ion-neutral drift presents a characteristic time namely $\rho_i \gamma$. From Equation (21) a magnetic Reynolds number (e.g., McKee et al., 2010; Hennebelle, 2013) can be inferred

$$R_{e,m} = \frac{V(l) l}{\nu}, \tag{30}$$

where $\nu = B^2/(4\pi\gamma_{ad}\rho\rho_i)$. Assuming that the energy flux, $\epsilon = \rho V(l)^3/l$, is constant through the scales, one gets

$$R_{e,m} = \frac{\epsilon^{1/3}\rho^{-1/3} l^{4/3}}{\nu}. \tag{31}$$

Estimating ϵ at the integral scale, L_0, we obtain

$$R_{e,m} = \left(\frac{\rho_0}{\rho}\right)^{1/3} \frac{V_0}{L_0^{1/3}} \frac{4\pi\gamma_{ad}\rho\rho_i}{B^2} l^{4/3}. \tag{32}$$

The smallest scale that can be reached in a turbulent cascade is typically obtained when the Reynolds number is equal to about 1. This leads for l_{diss}, the dissipation length, the following expression:

$$l_{diss} = \left(\frac{L_0^{1/3}}{\rho_0^{1/3} V_0}\right)^{3/4} \left(\frac{B^2}{4\pi\gamma_{ad}\rho^{2/3}\rho_i}\right)^{3/4}. \tag{33}$$

Typical values for the ISM are $V_0 = 2.5$ km s^{-1}, $\rho_0 = 100$ cm^{-3} and $L_0 = 10$ pc The magnetic intensity is about 5 μG in the diffuse gas and 10-20μG in the molecular gas for densities of a few 10^3 cm^{-3}. In the molecular gas the ionization is about $10^{-6} - 10^{-7}$ (Le Petit et al., 2006; Bergin and Tafalla, 2007) and the ion density ρ_i is given by $C\sqrt{\rho}$, where $C = 3\times10^{-16}$ cm$^{-3/2}$ g$^{1/2}$. For a density of 10^3 cm^{-3}, a magnetic intensity of 20μG, this leads to $l_{diss} \simeq 0.2$ pc. Obviously Equation (33) depends on physical parameters such as V_0 and B and therefore should present variations. It is worth realizing that the first term of the right-hand side is the energy flux to the power 1/4. The energy flux, at least in Kolmogorov theory, is expected to be constant through scales. The second term may also present weak variations since $\rho_i \propto \rho^{1/2}$, it is proportional to $(B^2\rho^{-7/6})^{3/4}$ while observations reveal that $B \propto \rho^{1/2}$ is not a bad approximation (Crutcher, 1999).

Hennebelle and André (2013) have developed a phenomenological model of a self-gravitating and accreting filament in which turbulent support insures the filament stability. The turbulence is maintained by the kinetic energy of accreting material, while the dissipation comes from the ion-neutral friction. A key prediction of this model is that the thickness of the filament is indeed about 0.1 pc and importantly does not depend on the density and column density of the filament. The reason stems from the fact that the ion-neutral drift operates on a timescale that is proportional to the ion density and that this latter is proportional to the neutral density in this regime. This dependence cancels out with the square-root of the gas density dependence of the freefall time.

However, so far this characteristic width has not been observed in numerical simulations. Ntormousi et al. (2016) have performed a detailed analysis of the filament width distribution (in simulations that do not include self-gravity) and found that while ion-neutral friction affects the density structure and reduces the numbers of small scale filaments, it does not produce a characteristic width near 0.1 pc as can be seen in **Figure 5**. This may be a consequence of the non-isotropic nature of this dissipation. In particular motions along the magnetic field lines are not dissipated by this mechanism.

To conclude, let us stress that while some of these explanations succeed to explain the observed width in some specific range of column density, none of the existing simulations performed so far have reproduced the characteristic width over 3 orders of magnitude in column density. Therefore, the origin of the apparent universal widths of the filamentary molecular clouds is still unclear. The problem could possibly be less severe because of the bias due to finite resolution (Panopoulou et al., 2017) which may lead to artificial structures. Let us stress however that the massive filaments are surrounded by an extended r^{-2} envelope which has not been considered in the bias analysis of Panopoulou et al. (2017), therefore these objects are clearly defined and apparently well resolved. Note that it is quite possible that the bias described by Panopoulou et al. (2017) may also be present in the analysis of some of the numerical simulations.

6.3. Fragmentation and Core Formation Within Filaments

It has since long been recognized that cores often form in dense filaments (e.g., Dutrey et al., 1991) and several studies have performed stability analysis of hydrodynamical (e.g., Inutsuka and Miyama, 1992) and magnetized filaments (e.g., Nakamura et al., 1993; Fiege and Pudritz, 2000; Hanawa and Tomisaka, 2015; Hanawa et al., 2017). As the fastest growing mode has been found to be about four times the filament diameter, Inutsuka and Miyama (1992) argued that the fragments are expected to be separated by nearly four times this value. Fiege and Pudritz (2000) investigated the stability of filament threated by an helical magnetic field and conclude that although significant toroidal field can reduce significantly the growth rate of gravitationally driven modes, they lead to the development of the sausage instability.

Recent Herschel results have rejuvenated interest in filament forming cores. In particular (Polychroni et al., 2013; Könyves et al., 2015) have established that in nearby molecular clouds about 70–80% of dense cores lie within filaments. This may indicate that filaments are playing a significant role in the star formation process although the mass distribution of cores lying inside and outside filaments may not be drastically different (see Figure 17 of Könyves et al., 2015).

In light of recent results by Herschel, several other studies aiming at understanding the fragmentation of filaments in cores have been carried out to investigate various aspects of the non-linear fragmentation of filaments into cores. Clarke et al. (2016) performed a series of numerical simulations to study the fragmentation of a filament that is accreting instead of being at equilibrium as assumed in previous studies. Due to the gravo-acoustic modes induced by accretion, the dispersion relation varies with the accretion rate. Gritschneder et al. (2017) carried out simulations to study the response of a critical filaments to bending modes. These modes, which tend to make the filament oscillates perpendicularly to its main axis, lead to fragmentation. The cores which form have a spacing that matches the wavelength of the sinusoidal perturbation of the bending modes. Therefore inferring filament properties from characteristic spacing should be considered with care. Clarke et al. (2017) performed simulations where turbulence is seeded in accreting filaments and show that this generates fibers that are similar to the ones observed in Taurus (Hacar et al., 2013). They speculate that these fibers may suppress radial collapse within super-critical filaments.

Given the importance of filaments, it seems important to clarify the outcome of the fragmentation of filamentary molecular clouds and to understand the resulting properties of star forming cores. One of the most important outcome is the mass distribution of dense core, or so-called "core mass function" (Könyves et al., 2015).

Chen and Ostriker (2014) and Chen and Ostriker (2015) proposed a model for anisotropic core formation. In this model, filaments first form by flow of material along the magnetic field in post-shock layers where the field is strong. After filaments have acquired enough material that quasi-spherical regions are supercritical, strongly self-gravitating cores condense out. The two-step process predicts a characteristic core size and mass (Equation 7 of Chen and Ostriker, 2015) and post-shock magnetic field that depends on the pre-shock density and inflow velocity but not on the pre-shock magnetic field strength. Numerical results are generally consistent with this (see Figures 10, 11 of Chen and Ostriker, 2015).

The first attempt to obtain the mass function of prestellar cores from a filament structure was done by Inutsuka (2001) in the case of the simple quasi-equilibrium filament, i.e., the filament supported by the thermal pressure and hence not radially collapsing. In particular, Inutsuka (2001) found that a line-mass spectrum $\delta^2 \propto k^n$ with $n \sim -1.5$ leads to a mass function of clumps whose power law exponent is close to -2.5, i.e., $dn/dM \propto M^{-2.5}$. Note that the mass function discussed in his paper corresponds to the mass function of the systems, i.e., groups of stars, that may include binary or multiple stars. Roy et al. (2015) have recently measured the power spectrum of density fluctuations along sub-critical filaments of the Gould Belt Survey. They infer that $\delta^2 \propto k^{-1.6}$. If confirmed in a larger ensemble of filaments, this could explain the origin of the core mass function and its apparent universality.

Lee et al. (2017) have recently proposed an analytical theory to predict both the core mass function (CMF) and the mass function of groups of cores of supercritical filaments. The theory, which generalizes the calculations performed by Inutsuka (2001) and Hennebelle and Chabrier (2008), considers magnetized filaments assumed to be radially supported by turbulent motions and takes into account thermal, turbulent and magnetic supports. It predicts the CMF, which is found to depend on the mass per unit lengths (MpL) and the magnetic intensity. In particular, it

is found that in the absence of magnetic field, filaments with high MpL fragment in too many small cores. In the presence of magnetic field with moderate intensities and for sufficiently high MpL, CMF compatible with observed ones are inferred.

7. THE ROLE OF MAGNETIC FIELD IN THE EVOLUTION OF MOLECULAR CLOUDS AND CLUSTERS

In this section we more specifically address the role of the magnetic field regarding the evolution of molecular clouds as a whole and their ability to form stars. We also discuss the properties of the star forming dense cores, which form in these clouds.

7.1. Subcritical Clouds

Historically, one of the important questions related to the star formation process in the universe is the rate at which a galaxy is forming stars. In particular it is known since the work of Zuckerman and Evans (1974) (see Kennicutt and Evans, 2012, for a more recent discussion) that the star formation rate, at least in the Milky Way, is about hundred times lower than one would expect if the dense gas would be entirely in freefall. The origin of this factor hundred has remained mysterious during many years and magnetic field has been invoked to solve the problem (e.g., Shu et al., 1987).

To assess the importance of the magnetic field, one can compute the ratio of the magnetic over gravitational energies. As an illustrative example one can envisage a uniform spherically symmetric cloud of mass M, volume V, radius R. It is threaded by a uniform magnetic field of intensity B. The magnetic flux, Φ, is given by $\pi R^2 B$. In ideal MHD, the field is frozen into the gas and Φ remains constant. In this case we have

$$\frac{E_{\rm mag}}{E_{\rm grav}} = \frac{B^2 V}{8\pi} \times \frac{2R}{5GM^2} \propto \frac{B^2 R^4}{M^2} \propto \left(\frac{\Phi}{M}\right)^2. \qquad (34)$$

Interestingly, E_{mag}/E_{grav} is constant and in particular does not depend on the cloud radius.

It is clear from Equation (34), that there is a critical value of the magnetic intensity for which the gravitational collapse is impeded even if the cloud was strongly compressed. Mouschovias and Spitzer (1976) have calculated accurately the critical value of the mass-to-flux ratio using the virial theorem and numerical calculations of the cloud bidimensional equilibrium. A cloud which has a mass-to-flux ratio smaller than this critical value cannot collapse and is called subcritical. It is called supercritical when the mass-to-flux is larger than the critical value. It is usual to define $\mu = (M/\Phi)/(M/\Phi)_{\rm crit}$. Large values of μ correspond to small magnetic fields and thus supercritical clouds.

Considering a magnetically supported dense core, also called subcritical core, the evolution is considerably slown down being almost quasi-static for most of the time. The neutrals slowly cross the field lines and the magnetic flux is gradually reduced up to the point where the core becomes critical and dynamical collapse proceeds. Estimating the time it takes is obviously the central question. To do so, clouds in virial equilibrium are considered, leading to $B^2/4\pi \simeq M\rho G/R$. The ratio of the ambipolar time, $\tau_{\rm ad}$ given by Equation 22, and the freefall time, $\tau_{\rm ff} \propto (G\rho)^{-1/2}$, (Shu et al., 1987) is then estimated to be

$$\frac{\tau_{\rm ad}}{\tau_{\rm ff}} \propto \frac{\gamma_{ad} C}{\sqrt{G}}, \qquad (35)$$

where it has been assumed that $\rho = C\sqrt{\rho_i}$. It is remarkable that in this expression there is no dependence in the physical parameters, such as the density, magnetic field and size. The exact value of $\tau_{\rm ad}/\tau_{\rm ff}$ depends on the assumed geometrical coefficients. It is typically on the order of 10 [Shu et al. (1987) estimated $\tau_{\rm ad}/\tau_{\rm dyn} = 8$].

Equation (35) shows that the ambipolar diffusion process can reduce the star formation rate by almost an order of magnitude if the field is strong enough to compensate gravity. This would bring the star formation rate much closer to the observed values (e.g., Shu et al., 1987). To better quantify this process, one dimensional simulations of subcritical clouds have been performed (e.g., Basu and Mouschovias, 1995). For very subcritical cores and values of μ of about 0.1, Basu and Mouschovias (1995) inferred a collapse time equal to 15 freefall times. With critical cores, $\mu \simeq 1$, the collapse takes roughly $\simeq$3 freefall times.

More recently, a series of simulations aiming at simulating subcritical and turbulent molecular clouds have been performed (Basu and Ciolek, 2004; Heitsch et al., 2004; Li and Nakamura, 2004; Nakamura and Li, 2008, 2011; van Loo et al., 2008; Vázquez-Semadeni et al., 2011; Bailey and Basu, 2014; Bailey et al., 2017). Typically it has been found that under the influence of ambipolar diffusion but also of turbulence, areas of high column densities and lower magnetization develop. These regions are typically supercritical and form gravitationally bound cores, that in turns form stars. This is portrayed in **Figure 12** where the column density in the direction of the initial magnetic field is shown as well as the isocontour of critical mass-to-flux ratio.

In all these calculations, it has been found that subcritical magnetic fields decrease very substantially, down to few percent, the star formation rate. For example **Figure 13** shows the mass of the dense gas and the mass within sink particles for a series of calculations including different magnetizations and with or without ambipolar diffusion. As can be seen the mass within sink particles (i.e., "stars") is almost 2 orders of magnitude smaller with an initial magnetic field of 4 μG than with a field of 2μG (one must keep in mind that these values correspond to the magnetization of the diffuse gas out of which the molecular cloud is assembled). It is also interesting to notice that in these calculations, the ambipolar diffusion makes only a modest difference. This indicates that a lot of magnetic flux is actually diffused through turbulence rather than ambipolar diffusion. Alternatively, this may also indicate that some gas is being accreted along the field lines, therefore reducing locally the mass-to-flux ratio.

Note that the interaction between turbulence and ambipolar diffusion can be complex. For example Li and Nakamura (2004) and Nakamura and Li (2008) found that stars may actually form

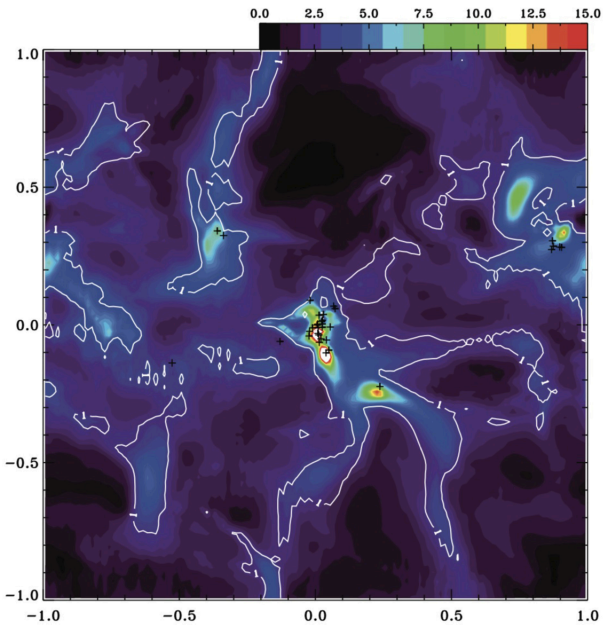

FIGURE 12 | Spatial distribution of column density and mass-to-flux ratio in an initially subcritical and turbulent molecular cloud (Nakamura and Li, 2008). Inside the contour the gas is supercritical and has collapsed at several places. Outside the contour it is still subcritical. Reproduced from Nakamura and Li (2008) with permission of ApJ.

more rapidly when the turbulence is higher because turbulence leads to a faster ambipolar diffusion by creating stronger shocks where the gradients of magnetic field are steep.

7.2. The Properties of Cores in Magnetized Molecular Clouds

We now turn to a discussion on the core properties that have been inferred from MHD simulations. As various rather different setups have been inferred we first start with a brief description of the numerical experiments, which have been performed. Here we restrict the discussion to studies that have explicitly discussed core statistics, i.e., self-gravitating structures formed within simulations that handle MHD and gravity. The cores are identified using a clump finding algorithm and then only the ones which are effectively self-gravitating are selected. Given that the typical size of dense cores is a fraction of 0.1 pc (e.g., Ward-Thompson et al., 2007), the spatial resolution achieved in these calculations is typically a fraction of 0.01 pc.

7.2.1. Numerical Setups of the Various Numerical Experiments

As several setups and initial conditions have been considered, we first give a quick overview of the different choices that have been made.

7.2.1.1. Prescribed molecular clouds

Many numerical experiments start with a uniform density cloud or a mildly peaked one (Basu and Ciolek, 2004; Li and Nakamura, 2004; Vázquez-Semadeni et al., 2005; Tilley and Pudritz, 2007; Nakamura and Li, 2008, 2011; Bailey and Basu, 2014; Bailey et al., 2017). The gas is assumed to be isothermal and self-gravity is treated. The initial field is usually uniform and various intensities ranging from 0 to significantly magnetized, are being assumed. Some velocity field with an amplitude corresponding to a Mach number up to 10, is usually prescribed. In these works either artificial driving of the turbulence is applied (Vázquez-Semadeni et al., 2005) either turbulence is free to decay. Nakamura and Li (2008) and Nakamura and Li (2011) include protostellar outflows, which drive turbulent motions. Ambipolar diffusion in the strong coupling limit is applied in some of these works.

7.2.1.2. Colliding flows

The colliding flow setup (e.g., Hennebelle et al., 2008; Banerjee et al., 2009; Vázquez-Semadeni et al., 2011; Clark et al., 2012; Valdivia et al., 2016) has also been used to study core formation (Chen and Ostriker, 2014, 2015). It consists in imposing two streams of gas with supersonic sound speed that create a dense shocked layer, which eventually gives rise to a layer of denser gas. The advantage of this setup is that the cloud is built and not imposed as it is the case for the previous setup. In particular, it is initially not self-gravitating. The other advantage is that the turbulence within the cloud is a consequence of the incoming flow. Chen and Ostriker (2014) and Chen and Ostriker (2015) vary the Mach number of the incoming flow and the magnetization. They treat ambipolar diffusion in the strong coupling approximation. In this scenario the transverse component of the magnetic field is amplified in the shock bounded layer as the colliding flow is super-Alfvénic.

7.2.1.3. Zooming-in from galactic box calculations

One of the restrictions of the two previous setups is that the initial conditions or boundary conditions have to be assumed. Moreover the statistics remain limited because, to unsure good resolution, the computational domain is typically few parsecs across. To circumvent these difficulties, Hennebelle (2018) has performed adaptive mesh refinement simulations of a kpc numerical domain. These simulations includes stratification, induced by the gravitational field due to stars and dark matter. They start with only WNM and have an initial magnetic field parallel to the equatorial plane of about $3\mu G$. In a first phase, supernova driving is applied. Once a self-consistent multi-phase and turbulent ISM is obtained, nine levels of adaptive mesh are employed to refine a region of 100×100 pc^2. This provides a final resolution of about 4×10^{-3} pc.

7.2.2. Core Properties

In the studies presented above, many core properties have been inferred. Here we restrict the discussion to 4 of them, comparing the results obtained in the different configurations explored. In spite of the relatively broad diversity of these latter, the results are in relatively good agreement.

7.2.2.1. Core mass spectrum

The mass spectrum of dense cores is likely to be important because they constitute the eventual mass reservoirs of stars. Moreover the core mass function (CMF) has been found to have a shape similar to the stellar initial mass function (IMF)

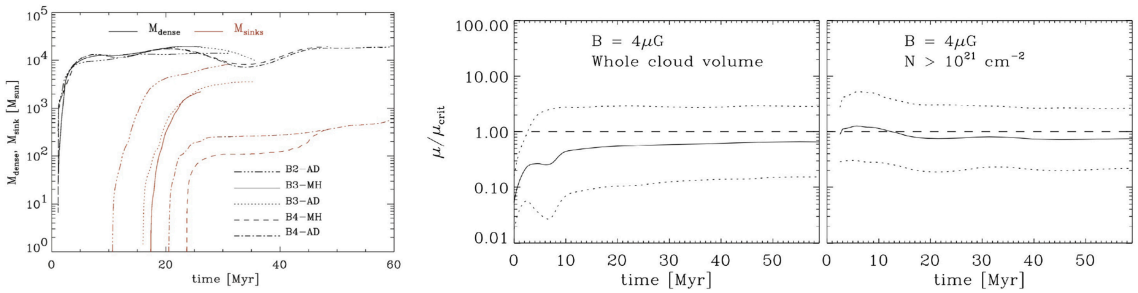

FIGURE 13 | Mass of dense gas and distribution of mass-to-flux ratio in a molecular clouds formed from colliding flows (Vázquez-Semadeni et al., 2011). Three initial magnetizations are being shown, namely 2, 3, and 4 μG and runs with and without ambipolar diffusion have been performed.

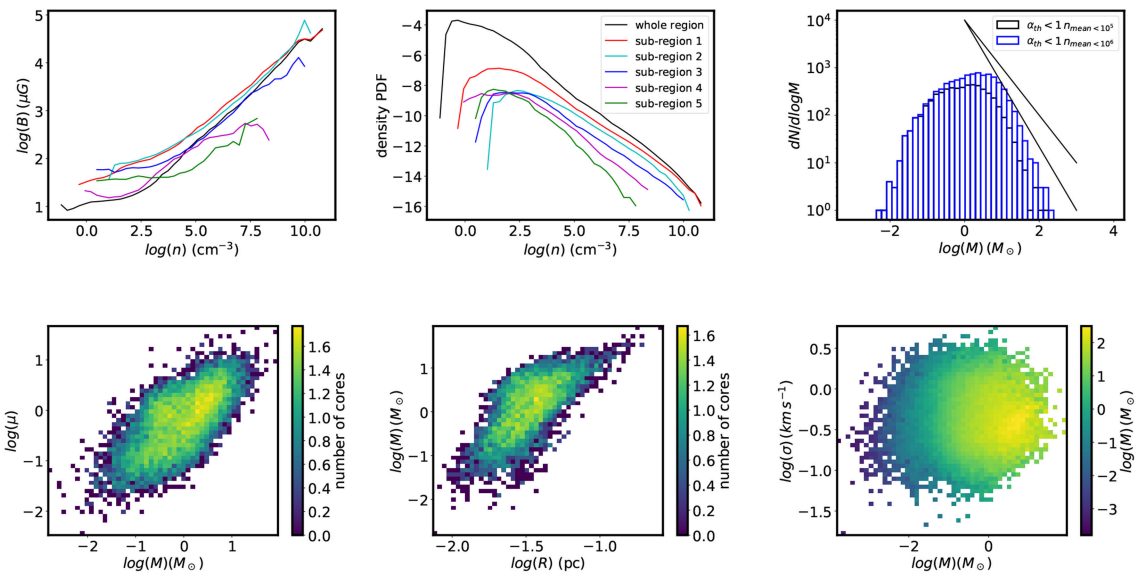

FIGURE 14 | Global flow properties and dense core statistics in a zooming-in calculation that goes from 1 kpc box size to 4 × 10^{-3} pc resolution (Hennebelle, 2018). Top-left panel: magnetic intensity vs. density in the whole refined region of the AMR simulation and in 5 star-forming subregions. Top-middle panel: same as top-left panel for the density distribution. Top-right: mass spectrum of dense cores (defined as thermally supercritical objects for 2 different thresholds of their mean density). Bottom-left panel: mass-to-flux ratio vs. mass for the thermally supercritical cores. Bottom-middle: mass-size relation of the thermally supercritical cores. Bottom-right: internal velocity dispersion relation vs. mass of all cores. Reproduced from Hennebelle (2018) with permission of A&A.

(Ward-Thompson et al., 2007; Offner et al., 2014), seemingly suggesting that the CMF may be at the origin of the IMF. Note that this possible link between the CMF and the IMF is still a matter of debate and numerous studies argue that the IMF is not linked to the CMF (see section 7.4.1 and Offner et al., 2014 for a recent review on this topic). The CMF has been computed by Tilley and Pudritz (2007), Nakamura and Li (2008), Nakamura and Li (2011), Chen and Ostriker (2014), and Hennebelle (2018). It has generally been found that the CMF *resembles* the observed ones (Könyves et al., 2015). In particular, it presents a peak and a powerlaw at large masses (see top-right panel of **Figure 14**) with a slope close to the observed one (Tilley and Pudritz, 2007; Nakamura and Li, 2011; Hennebelle, 2018). The slope is compatible with the idea that cores form under the combined influence of gravity and turbulent support (Hennebelle and Chabrier, 2008) while magnetic field does not appear to have a strong influence (e.g., Figure 11 of Nakamura and Li, 2011) in good agreement with theory (Hennebelle and Chabrier, 2013).

The question of the peak is far less clear. Observationally a peak around 0.5–1 $M_\odot$ has been inferred (Könyves et al., 2015), though higher resolution observations need to confirm its robustness. In the simulations the existence of the peak must also be handled with care. First of all, simulations that have no preferred scales like isothermal simulations with ideal MHD can be freely rescaled to any units. This means that the peak is a direct function of the initial conditions. Second of all numerical convergence must be carefully verified. For example Hennebelle (2018) performed runs at different resolutions and concluded that indeed the peak of the CMF varies with numerical resolution. Note that Gong and Ostriker (2015) on the contrary concluded that numerical convergence is reached in their colliding flow calculations. The most likely

reason of this discrepancy comes from the differences of the physical conditions studied and in particular the global gravitational stability of the simulated regions. Indeed gravity induces density PDF with high density powerlaw tails in which case the CMF may not present a peak at all (see discussion in Lee and Hennebelle, 2018a,b).

Once rescaled to the mean Jeans mass (e.g., Tilley and Pudritz, 2007; Chen and Ostriker, 2014, 2015), the dependence of the CMF on physical parameters has been found to be limited. In particular, Chen and Ostriker (2015) found a modest dependence of the CMF onto the magnetic intensity. This is at first surprising as magnetic field is part of the total support. To account for this weak dependence, they propose an anisotropic scenario in which contraction first start along the field lines before enough mass is accumulated to trigger contraction perpendicularly to the field lines.

A complementary information is provided by the mass-size relation (displayed in bottom-middle panel of **Figure 14**) which has been studied by Chen and Ostriker (2014), Chen and Ostriker (2015), and Hennebelle (2018). Typically a relation $M \propto R^{\alpha}$, with $\alpha \simeq 2$ has been inferred.

7.2.2.2. Magnetization

The magnetization of cores is a fundamental parameter to determine. Indeed magnetic field has been found to influence significantly the collapse of cores and in particular the formation of planet-forming disks through magnetic braking (Inutsuka, 2012; Li et al., 2014; Hennebelle et al., 2016).

Chen and Ostriker (2015) provide (Figure 12) the mass-to-flux as a function of the core mass. They found that most cores are supercritical with typical values for μ of about 2. A clear trend is seen for μ to increase with the core mass. The dependence of the μ distribution on the initial large scale magnetic field and the Mach number of the colliding flow is found to be relatively weak

Hennebelle (2018) has been measuring the mass-to-flux ratio in cores identified as thermally supercritical, that is to say cores that would collapse if only thermal support was present. The result is displayed in bottom-left panel of **Figure 14** where the mass-to-flux is displayed as a function of the core mass. The mass-to-flux is found to increase with the mass and is roughly proportional to it with $\mu \simeq 1$ for $M \simeq 1\,M_{\odot}$. However, a relatively broad distribution is inferred and for a given mass, the mass-to-flux distribution spans almost one order of magnitude. Note that many of these cores would actually not collapse (unless they accrete more mass along the field lines) as they are subcritical and therefore magnetically supported.

7.2.2.3. Velocity dispersion

The velocity dispersion in and around cores has received a lot of attention. Nakamura and Li (2008) and Nakamura and Li (2011) found that the velocity dispersion in cores present a large spread and goes from sonic (i.e., the velocity dispersion is close to the sound speed) to a Mach number larger than 5, with values up to 2–3 km s^{-1}. They found that there is no clear dependence of the velocity dispersion with the mass or the size. This is very similar with what is reported in Hennebelle (2018) and displayed in the bottom-right panel of **Figure 14**.

Nakamura and Li (2011) reported that the velocity dispersion is significantly reduced when the magnetization is high. Typically the cores formed in highly magnetized clouds tend to have trans-sonic to sub-sonic motions only.

7.2.2.4. Magnetic field orientation and core shape

The relationship between core shapes and the direction of the magnetic field has been analyzed by Chen and Ostriker (2018). They found that in colliding flow simulations cores are generally triaxial, and the magnetic field tends to be parallel to the shortest axis and perpendicular to the longest axis, with internal and external magnetic field direction correlated. This is a natural consequence of the formation of cores within filaments and the fact that magnetic field tends to be perpendicular to self-gravitating filaments as explained previously (e.g., Soler et al., 2013; Gómez et al., 2018). They also found that core angular momentum vectors are not aligned with the direction of the (internal or external) magnetic field. As explained below, this may be important in the context of protoplanetary disk formation.

7.3. The Influence of Magnetic Field on Low Mass Collapsing Cores

The collapse of low mass prestellar cores leads to the formation of small groups of stars, a process known as fragmentation, and to the formation of protoplanetary centrifugally supported disks. It is presently believed that magnetic field has a drastic influence on the outcome of collapsing cores.

7.3.1. The Magnetic Braking Process

A fundamental difference between hydrodynamical and magnetized prestellar cores comes from the evolution of angular momentum. In the absence of a substantial magnetic field, the latter is essentially conserved and becomes dominant drastically affecting the evolution of the core (e.g., Matsumoto and Hanawa, 2003). In a magnetized core, the situation is different. Because of magnetic tension, angular momentum can be exchanged between fluid particles. Typically this exchange occurs between a cloud and an intercloud medium and happens through torsional Alfvén waves, which propagate in the intercloud medium (Mouschovias and Paleologou, 1981; Shu et al., 1987; Joos et al., 2012). To estimate the characteristic time scale of magnetic braking let $\rho_{\rm icm}$ be the density of the intercloud medium. For simplicity, we consider that the magnetic field is parallel to the cloud rotation axis. The torsional Alfvén waves propagate at a speed, $V_a = B/\sqrt{4\pi\rho_{\rm icm}}$. The magnetic braking is important if a significant fraction of the cloud angular momentum has been delivered to the intercloud medium. This occurs when the waves have reached a distance $l \times \rho_{\rm icm} \simeq R \times \rho_0$. This leads to

$$\tau_{\rm br} \simeq \frac{R}{V_a}\frac{\rho_0}{\rho_{\rm icm}}. \tag{36}$$

Equation (36) is obtained assuming a very simple geometry. Other estimates in different geometries can be found in the references mentioned above. In particular, the braking depends on the angle between the magnetic field and the rotation axis, it also depends whether the field lines are uniform or fan out, in which case the braking time can be considerably reduced.

7.3.2. Disk Formation: A Magnetically Controlled Process?

In the aligned configuration, the braking time can become so short that the formation of the centrifugally supported disks can be even entirely prevented (e.g., Allen et al., 2003; Galli et al., 2006; Price and Bate, 2007; Hennebelle and Fromang, 2008; Li et al., 2014), a process known as catastrophic braking. More recent studies have revealed that the aligned configuration is however too simplified and that disks should form in magnetized clouds, although in general the disks are smaller and fragment less than in the hydrodynamical case. These studies fall in two categories. First, the magnetic braking is reduced because (i) the magnetic field and the rotation axis are non-aligned (Joos et al., 2012; Gray et al., 2018), (ii) the turbulent velocity field diffuses the magnetic field (Santos-Lima et al., 2012; Joos et al., 2013), (iii) the turbulent field makes the structure of the magnetic field less coherent (Seifried et al., 2013). Note that Gray et al. (2018) performed turbulent simulations in which the angular momentum is aligned with the magnetic field and show that disks do not form or are much smaller than in the same simulations for which there is no alignment. They concluded that misalignment may be the dominant effect. The second category of processes that limits catastrophic braking is non-ideal MHD. This has been studied by numerous groups (Inutsuka, 2012; Li et al., 2014; Hennebelle et al., 2016; Machida et al., 2016; Masson et al., 2016; Wurster et al., 2016; Zhao et al., 2018). These works found that small disks (i.e., disks significantly smaller than in the hydrodynamical case) form. Moreover, the turbulence and the magnetic configurations (i.e., misalignment) tend to be less important when non-ideal MHD processes are accounted for.

7.3.3. How Magnetic Field Changes the Fragmentation of Low Mass Cores

In typical conditions, that is to say with low rotation speed and relatively high thermal support, low mass cores generally fragment in several objects (Matsumoto and Hanawa, 2003). This fragmentation is due to the generation of the density fluctuations induced by turbulence or by gravity itself. Rotation considerably helps by maintaining important quantities of gas in equilibrium leading to the formation of massive, highly unstable disks. The issue of fragmentation is therefore strongly dependent of the initial conditions, namely the rotation and turbulence level as well as the presence of density perturbations initially. Several studies have been dedicated to the influence of magnetic field in this process (e.g., Machida et al., 2005, 2008; Hennebelle and Teyssier, 2008; Commerçon et al., 2010; Wurster et al., 2017). It has been found that when the density perturbations are low, typically 10% or so, the magnetic field is drastically reducing fragmentation, which happens only when the magnetic intensity is low. This is because when no strong density perturbations is initially present, the fragmentation occurs through rotation and the formation of massive, highly unstable disks. However, magnetic field gets efficiently wind up by the differential rotation which develops in the core inner part. As discussed above, angular momentum is then efficiently extracted and the disks are smaller. Another important effect, which further reduces rotationally induced fragmentation, is the magnetic pressure itself, particularly the one associated to the toroidal magnetic field. This pressure adds up to the thermal one and makes the disks more stable (Hennebelle and Teyssier, 2008). This stabilization seems to persist even when non-ideal MHD effects are accounted for (Wurster et al., 2017). On the other hand density perturbations of large amplitude, that is to say of about 50%, are sufficiently unstable to collapse individually even in the absence of rotation. In this case, magnetic field is unable to impede fragmentation (Hennebelle and Teyssier, 2008; Wurster et al., 2017).

7.4. Is Magnetic Field Playing a Role in the Formation of Clusters?

It is believed that stars do not form in isolation but rather in clusters (e.g., Longmore et al., 2014). Indeed, observationally stars do not form in the bulk of molecular clouds but instead in their denser parts. Large surveys have recently revealed ensemble of massive clumps in which stars are actively forming (Fall et al., 2010; Urquhart et al., 2014; Traficante et al., 2015). These clumps have masses up to several thousands of solar masses and are very good candidates for being stellar cluster progenitors. Given that these objects are relatively massive it is unlikely that magnetic field plays a major contribution on the formation and global equilibrium of these massive clumps. Numerical simulations are able to reproduce reasonably well the global properties of these massive clumps such as their mass-size relation, simply by invoking gravity and turbulence (Lee and Hennebelle, 2016a,b), starting with reasonable ISM magnetic intensities, magnetic energies a few times above the thermal ones but well below the kinetic and gravitational energies are obtained.

There are however several aspects that deserve particular attention and which are now examined. First of all, does magnetic field influences the small scale fragmentation, that is to say the formation of the stars themselves? Does magnetic field enhance stellar feedback? Does magnetic field increase the coupling between clusters and outflows and jets?

7.4.1. Does Magnetic Field Affect the Small Scale Fragmentation in Stellar Clusters?

One fundamental goal of cluster studies is to infer the mass function of stars that form and whether it can reproduce the IMF. Several studies have been investigating this issue using sink particles (e.g., Bate, 2012; Myers et al., 2013; Offner et al., 2014; Lee and Hennebelle, 2018a). As the present review focusses on the possible role of magnetic field, the discussion below is restricted to this aspect specifically.

7.4.1.1. MHD barotropic calculations

Before we describe the calculations that include radiative processes, we first consider the simpler barotropic case. Such simulations have been performed by Price and Bate (2008) and Hennebelle et al. (2011) (see also Peters et al., 2011, who even included photo-ionisation from the central star) who have simulated the collapse of several tens $M_\odot$ turbulent cores. The turbulent and gravitational energies were initially comparable and various magnetic intensities have been explored. It has been found that the fragmentation is reduced when the mass-to-flux

is smaller than $\simeq$5. The fragment number is reduced by roughly a factor of 2 for the strongest magnetization. It has been found that during the collapse, efficient magnetic diffusion occurs due to the turbulent velocity field, which explains why fragmentation is reduced by a factor 2 only.

Recently Lee and Hennebelle (2018c) studied the collapse of 1000 $M_\odot$ clumps with various magnetization. As sink particles, are being used, the initial mass function was studied. They concluded that while magnetic field reduces a bit the number of objects, it is of secondary importance to determine the shape of the IMF. This is in part due to the fact that the peak is determined at very small scale (100 AU or so) and at very high density where the magnetic intensity weakly depends on the large scale initial conditions and therefore tends to have the same value irrespectively of the initial value.

7.4.1.2. MHD radiative calculations

Collapse calculations of massive collapsing cores, in which both the magnetic field and the radiative transfer have been taken into account, have been carried out.

Price and Bate (2009), found that the magnetic field and the radiative feedback play complementary effects. Magnetic field supports the diffuse gas at large scale and radiative feedback, by heating the inner part of the core, reduces the fragmentation in many objects.

Simulations including magnetic field and radiative feedback, which follow the collapse up to AU scales, have been performed by Commerçon et al. (2011), Myers et al. (2013), Myers et al. (2014), and Cunningham et al. (2018). It has been found that in some circumstances, the combination of magnetic field and radiative feedback may be reducing fragmentation significantly. This is due to the fact that magnetic field induces efficient magnetic braking and reduces the amount of angular momentum in the cloud inner part. Consequently, the accretion is more focused in a magnetized core than in an hydrodynamical one. In this latter case strong angular momentum prevents the gas to fall in the cloud center. Thus the accretion luminosity, which is $\propto M\dot{M}/R$ is much higher since M and $\dot{M}$ are larger while R is smaller. The temperature in magnetized cores is therefore higher than in hydrodynamical ones and this reduces the fragmentation within the former.

7.4.2. Does Magnetic Field Enhance Stellar Feedback?

A possibly important consequence of the magnetic field could be related to this very last point. This is because stellar feedback critically depends on the stellar masses. This is the case for the HII radiation, the winds and of course the supernova explosions, which require the stellar mass to be larger than 8 $M_\odot$. For example numerous authors (Dale and Bonnell, 2011; Walch et al., 2012; Geen et al., 2015, 2017) found that in Milky Way type conditions, HII regions likely destroy molecular clouds quickly after they form stars, likely limiting the star formation efficiency of these objects.

Arthur et al. (2011) (see also Mackey and Lim, 2011; Gendelev and Krumholz, 2012) performed both unmagnetized and magnetized simulations of the expansion of an HII region in a molecular clumps and studied in details the resulting structure of the field. They found that the magnetic field does not change very significantly the expansion in itself but reduces the small scale fragmentation and radiation-driven pillars. The field in the neutral expanding shell is preferentially parallel to the shell while in the ionized gas inside the shell it is more perpendicular to it.

Since magnetic field tends to reduce fragmentation, it is likely that without magnetic field the stars would be on average less massive and therefore their HII radiation which is proportional to M^{2-3} (e.g., Vacca et al., 1996), would be significantly reduced. Since numerical simulations are not able yet to self-consistently predict the mass of the stars and follow the large scale evolution of the parent clouds subject to their feedback, it is however not possible to get a firm confirmation of this effect.

7.4.3. Does Magnetic Field Improve the Coupling With Jets?

The influence that jets may have on a proto stellar clusters has been investigated at pc scales (Li and Nakamura, 2006; Carroll et al., 2009; Cunningham et al., 2009; Wang et al., 2010; Federrath, 2015) and inside massive cores (e.g., Cunningham et al., 2011).

Li and Nakamura (2006) (see also Wang et al., 2010; Federrath, 2015) carried out calculations for a 10^3 $M_\odot$ clump. A stationary state has been obtained. Turbulence is sustained by outflows which counteract gravity, delaying the collapse significantly. Wang et al. (2010) and Federrath (2015) carried out simulations in which several physical processes are progressively included, namely initial turbulence, magnetic field and outflows. Each of them reduces the star formation rate by a factor of a few. When all of them are included the star formation rate is typically 10 times lower than when the protocluster is in freefall.

The question as to whether turbulence may be sustained by protostellar outflows has been investigated by Cunningham et al. (2009) and Carroll et al. (2009). They reached the conclusion that in a turbulent medium, even without a magnetic field, the outflows couple to the surrounding gas and trigger turbulence efficiently. They inferred an energy powerspectrum that is stiffer than the usual powerspectra found in large scale driven turbulence (e.g., Kritsuk et al., 2007; Hennebelle and Falgarone, 2012). Murray et al. (2018) have reached a somehow different conclusion as they find that the outflows have only a modest influence on the driving of turbulence.

Offner and Chaban (2017) and Offner and Liu (2018) have performed a series of low mass dense core collapse and studied the influence of outflows on the collapsing core and in particular, the efficiency of the driving of turbulence within the envelope of the core. They conclude that outflows can drive efficiently turbulence in the envelope and that the efficiency of the driving increases with magnetic intensity.

8. THE ROLE OF MAGNETIC FIELD IN ISM SELF-REGULATED MODELS

Important efforts have also been undertaken to self-consistently simulate the interstellar medium within galaxies. Because

modeling galaxies as a whole is very challenging in terms of scales, many models (e.g., de Avillez and Breitschwerdt, 2005; Joung and Mac Low, 2006; Gent et al., 2013; Kim et al., 2013) consider a computational box of about 1 kpc sometimes called galactic box. Since the typical supernova remnant radius is about 50 pc, this constitutes a good compromise between spatial resolution and molecular cloud statistics (though at the expense of solving the large galactic scales). The most recent models consider an external vertical gravitational field, which represents the gravity of stars and dark matter, follow the star formation (up to spatial scales of about 1–4 pc) and deliver stellar feedback (due to massive stars and essentially though not exclusively supernovae). This leads to a self-regulated ISM in which a turbulent cascade takes place. The energy is injected at the large and intermediate (around or above 100 pc) scales and decay at the small ones.

8.1. Star Formation Rate and Vertical Equilibrium

The importance of the spatial and temporal correlations between the supernova remnants and the star forming dense gas has been stressed by recent studies (Hennebelle and Iffrig, 2014; Gatto et al., 2015). When the supernovae are randomly placed, the feedback they provide is inefficient and does not reduce the star formation rate appreciably. On the other hand, when the supernova explosions correlate with the dense gas, star formation rates in better agreement with the observed values are inferred (Kim et al., 2013; Hennebelle and Iffrig, 2014). In these simulations, the thickness of the galactic disk is also compatible with the observed values while it is too thin in simulations where the supernovae are randomly placed. As recently stressed by Girichidis et al. (2016) cosmic rays may change this conclusion. Also these models produce a realistic multi-phase magnetized ISM with densities and temperature that are reminiscent of the WNM and CNM. When a magnetic field of a few μG is initially present in the simulations, the magnetic intensities stay compatible with the observed values. It has been found that magnetic field contributes to the galactic vertical equilibrium although its contribution is lower than the one of the turbulent dispersion and it has also been inferred that the star formation rate is somewhat reduced in the presence of a magnetic field by a factor that is on the order of 2 (Kim and Ostriker, 2015; Iffrig and Hennebelle, 2017; Girichidis et al., 2018). One important limit of these models is that the feedback is delivered immediately after the stars are formed, while supernovae arise 4-40 Myr after their progenitor formation. Given that the typical freefall time of a typical star forming cloud is only a few Myr. This is a significant effect that the most advanced models (Kim and Ostriker, 2017; Colling et al., 2018; Girichidis et al., 2018) are now taking into account. It should be stressed however that in order to treat the feedback injection properly star formation and evolution should be treated self-consistently. In practice, this would require to resolve spatial scales that are much smaller than what is currently possible for this type of modeling.

8.2. Turbulence and Clumps

Iffrig and Hennebelle (2017) have carried out a series of 1024^3 simulations which allow to infer the statistics of turbulence and the properties of structures. In spite of the stratification, the powerspectra are broadly compatible with earlier works (see e.g., Kritsuk et al., 2007) though the velocity powerspectrum is closer to the classical Kolmogorov exponent than the stiffer, almost Burgers like, values inferred in supersonic isothermal turbulence. This likely is a consequence of the magnetized, multi-phase structure since the velocity dispersion is not much larger than the sound speed and Alfvén speed of the WNM. The ratio of the energies of the compressible modes and solenoidal ones depends on the altitude. In the mid-plane, the compressible modes dominate while above a certain altitude, which varies with the magnetic intensity, the solenoidal ones dominate. The stronger the magnetic intensity, the lower is the altitude above which solenoidal modes dominate. This conclusion is different from the one of Padoan et al. (2016) who found that the solenoidal modes always dominate. The discrepancy is most certainly due to the absence of stratification in Padoan et al. (2016). The dense clouds have been extracted from the simulations of Iffrig and Hennebelle (2017) and Padoan et al. (2016) using simple clump finders. Their statistical properties such as the mass spectra, the mass-size and the internal velocity dispersion-size relations are all reminiscent of the observed cloud properties (e.g., Miville-Deschênes et al., 2017) though Iffrig and Hennebelle (2017) mentioned that the internal velocity dispersion are possibly smaller than within observed clouds. This may indicate the need for other energy injection sources such as the one due to the large galactic scale gravitational instabilities (Krumholz and Burkhart, 2016). The distribution of the mass-to-flux ratio, μ, of the clouds has also been inferred (see also Inoue and Inutsuka, 2012). It is broadly proportional to the square-root of the cloud mass, which has been interpreted as the mass being proportional to the volume while the flux is proportional to the surface. The value of μ also depends on the density threshold used to define the clouds. The lower the density threshold, the lower μ.

8.3. A Possible Link Between Magnetic Field and Clump Mass Function

To understand the overall star formation rates in the Galaxy we have to know, not only the star formation rate in an individual cloud, but also the mass distribution of molecular clouds, which determines the total number of stars created in the Galaxy. It is actually difficult to accurately determine the mass function of molecular clouds in our Galaxy because of the line-of-sight contamination and limited knowledge on the distances to the clouds. Thanks to the development of observations, the mass function of GMC can now be determined in nearby face-on galaxies such as M51 (Colombo et al., 2014). For example Colombo et al. (2014) reported that the exponent of the power-law slope of mass function varies depending on relative location to the spiral arm structure and the galactic center. Thus theoretical studies for the cloud properties may shed light on our understanding of the formation and destruction of molecular clouds. As mentioned in the previous sections, however, it is still difficult to perform direct numerical simulations of an ensemble of molecular clouds and study in details the small scale physics such as formation and destruction of molecular

clouds. Earlier attempts to propose analytical models can be found in Kwan (1979), Scoville and Hersh (1979), and Tomisaka (1986) that formulated the so-called coagulation equation for molecular clouds. In these investigation the growth of clouds are, however, supposed to be driven by the cloud-cloud collision and missed the importance of gas accretion onto molecular clouds. The recent theoretical finding of the long timescale of molecular cloud formation (Inoue and Inutsuka, 2009) and the importance of gradual growth process by accretion of dense HI gas (Inoue and Inutsuka, 2012) stress the crucial need for accretion contribution in the coagulation equation (Kobayashi et al., 2017, 2018).

In this section, we present an analytical model that suggests a link between the magnetic field and the clump mass function because of the impact of the former onto the cloud formation time. In section 3.3 we have shown that the existence of magnetic field may possibly significantly increase the formation timescale of molecular clouds. Let's propose an estimate of the actual value of the cloud formation timescale in our Galaxy. The radius of a supernova remnant (SNR) can be on the order of 100pc after the expansion over the typical age $\sim$ 1 Myr. We may assume that the creation rate of SNRs in our Galaxy is $10^{-2}\mathrm{yr}^{-1}$ Thus, the volume occupied by SNRs can be calculated as $100^3 \times 10^{-2}\mathrm{yr}^{-1} \times 1\mathrm{Myr} = 10^{10}\mathrm{pc}^3$. This value is roughly the same as the volume of Galactic thin disk ($10\mathrm{kpc}^2 \times 100\mathrm{pc}$) where molecular clouds reside. This means that ISM in Galactic thin disk is swept up by SNR once per 1 Myr (McKee and Ostriker, 1977). If we ignore the magnetic field, the molecular cloud can be simply created by a single, may be a few compressions of warm neutral medium by the propagation of a shock wave. As shown in Section 3.3, however, molecular clouds could be created after several compressions (up to 10) and thus, the actual timescale of cloud formation should be several Myr.

To infer the clump mass spectrum, we can adopt coarse graining of short-timescale ($\sim$ a few Myr) events of the growth and destruction of clouds, and describe the long timescale evolution by the continuity equation of molecular clouds in mass space (Kobayashi et al., 2017)

$$\frac{\partial N}{\partial t} + \frac{\partial}{\partial M}\left(N\frac{dM}{dt}\right) = -\frac{N}{T_\mathrm{d}} + \left(\frac{dN}{dt}\right)_\mathrm{coll}, \qquad (37)$$

where $N(dM/dt)$ denotes the flux of mass function in mass space, T_d is the cloud disruption timescale, dM/dt describes the growth rate of the molecular cloud, and the last term accounts for the growth due to cloud-cloud collision. If the contribution from cloud-cloud collisions is negligible (Kobayashi et al., 2017, 2018) and the mass growth can be approximated by $dM/dt = M/T_\mathrm{f}$ with the growth timescale T_f, a steady state solution of the above equation is $N(M) = M^{-\alpha}$, where $\alpha = 1 + T_\mathrm{f}/T_\mathrm{d}$ (Inutsuka et al., 2015). In a gas rich environment such as a spiral arm of a disk galaxy, we expect $T_* \sim T_\mathrm{f}$, and thus, $T_\mathrm{f} \lesssim T_\mathrm{d}$, which corresponds to $1 < \alpha \lesssim 2$. For example, $T_\mathrm{f} = 10\mathrm{Myr}$ corresponds to $\alpha \approx 1.7$, which agrees nicely with observations (Solomon et al., 1987; Kramer et al., 1998; Heyer et al., 2001; Roman-Duval et al., 2010). However, in a region with very limited amount of gaseous material, T_f is expected to be large and possibly even larger than $T_\mathrm{d} = T_* + 4\mathrm{Myr}$, which produces $\alpha > 2$. This may explain the observations in M33 (Gratier et al., 2012) and in M51 (Colombo et al., 2014). The more detailed description of the molecular cloud mass function can be found in Kobayashi et al. (2017, 2018) where the effect of cloud-cloud collisions is explicitly taken into account.

Note that the effects of magnetic field that slows down the cloud formation are taken into account in the above analysis as a large value of the cloud formation timescale ($T_\mathrm{f} > 1$ Myr). If we ignore the effect of magnetic field and simply choose the dynamical compression rate of ISM as the value of the cloud formation timescale T_f=1Myr, the powerlaw exponent of the mass function of molecular cloud would be too small ($\alpha \sim 1$), which is in stark contrast to the observed values. Therefore we may conclude that magnetic field is playing an important role in the mass distribution of molecular clouds in our Galaxy.

9. CONCLUSIONS

This review is dedicated to the role that magnetic field may have in the formation and evolution of molecular clouds. Significant progress has been accomplished in the last years in our understanding of the molecular cloud in particular and star formation process in general. We have a better, although still incomplete, knowledge of the structures, filaments, cores, clumps, clusters, formation mechanisms.

Most likely these gaseous structures are all the product of magnetized turbulence interacting with gravity. Given the values of the magnetic intensities that have been measured, numerical simulations seem to indicate that the number of objects that form at all scales, from clumps to stars, is likely reduced by a factor of a few due to the action of the magnetic field. Accordingly their masses tend to be also a few times larger than what it would be with pure hydrodynamics. The shapes of the clouds are also strongly affected by magnetic field, which tends to create filamentary structures as well as clouds that have flattened along the magnetic field lines that permeate them. More generally the whole dynamics of the ISM is significantly modified and cannot be accurately interpreted without taking magnetic fields into account.

While it is now almost certain that magnetic fields do not regulate the star formation process by reducing the star formation rate drastically, as proposed three decades ago, it is likely the case that magnetic fields contribute to reduce it by a factor of a few. Moreover since it has been found by various groups that magnetic field tends to reduce the fragmentation and to produce stars with larger mass, another possible consequence of magnetic field is to enhance stellar feedback and therefore to reduce the star formation rate and efficiency in molecular clouds. This latter aspect remains however to be confirmed as numerical simulations are not able now to cover the necessary range of scales. Finally we stress that magnetic field is likely to have drastic consequences on the formation of protoplanetary disks through magnetic braking by reducing and even possibly controlling their size.

AUTHOR CONTRIBUTIONS

PH and SI were both responsible for writing and editing the manuscript.

FUNDING

This work is supported by Grant-in-aids from the Ministry of Education, Culture, Sports, Science, and Technology (MEXT) of Japan (16H02160, 18H05436, 18H05437).

ACKNOWLEDGMENTS

We thank the two referees for constructive remarks and critical reading of the manuscript. We thank various contributions from Philippe André, Edouard Audit, Doris Arzoumanian, Gilles Chabrier, Benoit Commerçon, Edith Falgarone, Sébastien Fromang, Samuel Geen, Olivier Iffrig, Tsuyoshi Inoue, Kazunari Iwasaki, Hiroshi Koyama, Yueh-Ning Lee, Anaelle Maury, Evangelia Ntormousi, Juan-Diego Soler, Romain Teyssier, Valeska Valdivia.

REFERENCES

Allen, A., Li, Z.-Y., and Shu, F. H. (2003). Collapse of Magnetized Singular Isothermal Toroids. II. Rotation and Magnetic Braking. *Astrophys. J.* 599, 363–379. doi: 10.1086/379243

Alves de Oliveira, C., Schneider, N., Merín, B., Prusti, T., Ribas, Á., Cox, N. L. J., et al. (2014). Herschel view of the large-scale structure in the <ASTROBJ>Chamaeleon</ASTROBJ> dark clouds. *Astron. Astrophys.* 568:A98. doi: 10.1051/0004-6361/201423504

Ames, S. (1973). Magneto-gravitational and thermal instability in the galactic disk. *Astrophys. J.* 182, 387–404. doi: 10.1086/152147

André, P., Di Francesco, J., Ward-Thompson, D., Inutsuka, S.-I., Pudritz, R. E., and Pineda, J. E. (2014). "From filamentary networks to dense cores in molecular clouds: toward a new paradigm for star formation," in *Protostars Planets VI*, eds H. Beuther, R. S. Klessen, C. P. Dullemond, and T. Henning (Tucson, AZ: University of Arizona Press), 27–51.

Arthur, S. J., Henney, W. J., Mellema, G., de Colle, F., and Vázquez-Semadeni, E. (2011). Radiation-magnetohydrodynamic simulations of H II regions and their associated PDRs in turbulent molecular clouds. *Mont. Notices RAS* 414, 1747–1768. doi: 10.1111/j.1365-2966.2011.18507.x

Arzoumanian, D., André, P., Didelon, P., Könyves, V., Schneider, N., Men'shchikov, A., et al. (2011). Characterizing interstellar filaments with Herschel in IC 5146. *Astron. Astrophys.* 529:L6. doi: 10.1051/0004-6361/201116596

Auddy, S., Basu, S., and Kudoh, T. (2016). A magnetic ribbon model for star-forming filaments. *Astrophys. J.* 831:46. doi: 10.3847/0004-637X/831/1/46

Audit, E., and Hennebelle, P. (2005). Thermal condensation in a turbulent atomic hydrogen flow. *Astron. Astrophys.* 433, 1–13. doi: 10.1051/0004-6361:20041474

Bailey, N. D., and Basu, S. (2014). Non-ideal magnetohydrodynamic simulations of the two-stage fragmentation model for cluster formation. *Astrophys. J.* 780:40. doi: 10.1088/0004-637X/780/1/40

Bailey, N. D., Basu, S., and Caselli, P. (2017). Ionisation in turbulent magnetic molecular clouds. I. Effect on density and mass-to-flux ratio structures. *Astron. Astrophys.* 601:A18. doi: 10.1051/0004-6361/201628273

Balsara, D. S. (1996). Wave propagation in molecular clouds. *Astrophys. J.* 465:775. doi: 10.1086/177462

Banerjee, R., Vázquez-Semadeni, E., Hennebelle, P., and Klessen, R. S. (2009). Clump morphology and evolution in MHD simulations of molecular cloud formation. *Mont. Notices RAS* 398, 1082–1092. doi: 10.1111/j.1365-2966.2009.15115.x

Banerjee, S., and Kritsuk, A. G. (2017). Exact relations for energy transfer in self-gravitating isothermal turbulence. *Phys. Rev. E* 96:053116. doi: 10.1103/PhysRevE.96.053116

Banerjee, S., and Kritsuk, A. G. (2018). Energy transfer in compressible magnetohydrodynamic turbulence for isothermal self-gravitating fluids. *Phys. Rev. E* 97:023107. doi: 10.1103/PhysRevE.97.023107

Basu, S. (2000). Magnetic fields and the triaxiality of molecular cloud cores. *Astrophys. J. Lett.* 540, L103–L106. doi: 10.1086/312885

Basu, S., and Ciolek, G. E. (2004). Formation and collapse of nonaxisymmetric protostellar cores in planar magnetic molecular clouds. *Astrophys. J. Lett.* 607, L39–L42. doi: 10.1086/421464

Basu, S., and Mouschovias, T. C. (1995). Magnetic braking, ambipolar diffusion, and the formation of cloud cores and protostars. III. Effect of the initial mass-to-flux ratio. *Astrophys. J.* 453:271. doi: 10.1086/176387

Bate, M. R. (2012). Stellar, brown dwarf and multiple star properties from a radiation hydrodynamical simulation of star cluster formation. *Mont. Notices RAS* 419, 3115–3146. doi: 10.1111/j.1365-2966.2011.19955.x

Beresnyak, A. (2011). Spectral slope and kolmogorov constant of MHD turbulence. *Phys. Rev. Lett.* 106:075001. doi: 10.1103/PhysRevLett.106.075001

Beresnyak, A., Lazarian, A., and Cho, J. (2005). Density scaling and anisotropy in supersonic magnetohydrodynamic turbulence. *Astrophys. J. Lett.* 624, L93–L96. doi: 10.1086/430702

Bergin, E. A., and Tafalla, M. (2007). Cold dark clouds: the initial conditions for star formation. *Annu. Rev. Astron. Astrophys.* 45, 339–396. doi: 10.1146/annurev.astro.45.071206.100404

Birnboim, Y., Federrath, C., and Krumholz, M. (2018). Compression of turbulent magnetized gas in giant molecular clouds. *Mont. Notices RAS* 473, 2144–2159. doi: 10.1093/mnras/stx2426

Biskamp, D. (2003). *Magnetohydrodynamic Turbulence*. Cambridge, UK: Cambridge University Press.

Boldyrev, S. (2005). On the spectrum of magnetohydrodynamic turbulence. *Astrophys. J. Lett.* 626, L37–L40. doi: 10.1086/431649

Burkhart, B., Falceta-Gonçalves, D., Kowal, G., and Lazarian, A. (2009). Density studies of MHD interstellar turbulence: statistical moments, correlations and bispectrum. *Astrophys. J.* 693, 250–266. doi: 10.1088/0004-637X/693/1/250

Burkhart, B., Lazarian, A., Balsara, D., Meyer, C., and Cho, J. (2015). Alfvénic turbulence beyond the ambipolar diffusion scale. *Astrophys. J.* 805:118. doi: 10.1088/0004-637X/805/2/118

Camacho, V., Vázquez-Semadeni, E., Ballesteros-Paredes, J., Gómez, G. C., Fall, S. M., and Mata-Chávez, M. D. (2016). Energy budget of forming clumps in numerical simulations of collapsing clouds. *Astrophys. J.* 833:113. doi: 10.3847/1538-4357/833/1/113

Carroll, J. J., Frank, A., Blackman, E. G., Cunningham, A. J., and Quillen, A. C. (2009). Outflow-driven turbulence in molecular clouds. *Astrophys. J.* 695, 1376–1381. doi: 10.1088/0004-637X/695/2/1376

Chen, C.-Y., and Ostriker, E. C. (2014). Formation of magnetized prestellar cores with ambipolar diffusion and turbulence. *Astrophys. J.* 785:69. doi: 10.1088/0004-637X/785/1/69

Chen, C.-Y., and Ostriker, E. C. (2015). Anisotropic formation of magnetized cores in turbulent clouds. *Astrophys. J.* 810:126. doi: 10.1088/0004-637X/810/2/126

Chen, C.-Y., and Ostriker, E. C. (2018). Geometry, kinematics, and magnetization of simulated prestellar cores. *Astrophys. J.* 865:34. doi: 10.3847/1538-4357/aad905

Cho, J., and Lazarian, A. (2003). Compressible magnetohydrodynamic turbulence: mode coupling, scaling relations, anisotropy, viscosity-damped regime and astrophysical implications. *Mont. Notices RAS* 345, 325–339. doi: 10.1046/j.1365-8711.2003.06941.x

Cho, J., Lazarian, A., and Vishniac, E. T. (2002). Simulations of magnetohydrodynamic turbulence in a strongly magnetized medium. *Astrophys. J.* 564, 291–301. doi: 10.1086/324186

Choi, E., and Stone, J. M. (2012). The effect of anisotropic conduction on the thermal instability in the interstellar medium. *Astrophys. J.* 747:86. doi: 10.1088/0004-637X/747/2/86

Clark, P. C., Glover, S. C. O., Klessen, R. S., and Bonnell, I. A. (2012). How long does it take to form a molecular cloud? *Mont. Notices RAS* 424, 2599–2613. doi: 10.1111/j.1365-2966.2012.21259.x

Clark, S. E., Peek, J. E. G., and Putman, M. E. (2014). Magnetically aligned H I fibers and the rolling hough transform. *Astrophys. J.* 789:82. doi: 10.1088/0004-637X/789/1/82

Clarke, S. D., Whitworth, A. P., Duarte-Cabral, A., and Hubber, D. A. (2017). Filamentary fragmentation in a turbulent medium. *Mont. Notices RAS* 468, 2489–2505. doi: 10.1093/mnras/stx637

Clarke, S. D., Whitworth, A. P., and Hubber, D. A. (2016). Perturbation growth in accreting filaments. *Mont. Notices RAS* 458, 319–324. doi: 10.1093/mnras/stw407

Clarke, S. D., Whitworth, A. P., Spowage, R. L., Duarte-Cabral, A., Suri, S. T., Jaffa, S. E., et al. (2018). Synthetic $C^{18}O$ observations of fibrous filaments: the problems of mapping from PPV to PPP. *Mont. Notices RAS* 479, 1722–1746. doi: 10.1093/mnras/sty1675

Colling, C., Hennebelle, P., Geen, S., Iffrig, O., and Bournaud, F. (2018). Impact of galactic shear and stellar feedback on star formation. *Astron. Astrophys.* 620:A21. doi: 10.1051/0004-6361/201833161

Colombo, D., Hughes, A., Schinnerer, E., Meidt, S. E., Leroy, A. K., Pety, J., et al. (2014). The PdBI arcsecond whirlpool survey (PAWS): environmental dependence of giant molecular cloud properties in M51. *Astrophys. J.* 784:3. doi: 10.1088/0004-637X/784/1/3

Commerçon, B., Hennebelle, P., Audit, E., Chabrier, G., and Teyssier, R. (2010). Protostellar collapse: radiative and magnetic feedbacks on small-scale fragmentation. *Astron. Astrophys.* 510:L3. doi: 10.1051/0004-6361/200913597

Commerçon, B., Hennebelle, P., and Henning, T. (2011). Collapse of massive magnetized dense cores using radiation magnetohydrodynamics: early fragmentation inhibition. *Astrophys. J. Lett.* 742:L9. doi: 10.1088/2041-8205/742/1/L9

Crutcher, R. M. (1999). Magnetic fields in molecular clouds: observations confront theory. *Astrophys. J.* 520, 706–713. doi: 10.1086/307483

Crutcher, R. M., Wandelt, B., Heiles, C., Falgarone, E., and Troland, T. H. (2010). Magnetic fields in interstellar clouds from zeeman observations: inference of total field strengths by Bayesian analysis. *Astrophys. J.* 725, 466–479. doi: 10.1088/0004-637X/725/1/466

Cunningham, A. J., Frank, A., Carroll, J., Blackman, E. G., and Quillen, A. C. (2009). Protostellar outflow evolution in turbulent environments. *Astrophys. J.* 692, 816–826. doi: 10.1088/0004-637X/692/1/816

Cunningham, A. J., Klein, R. I., Krumholz, M. R., and McKee, C. F. (2011). Radiation-hydrodynamic simulations of massive star formation with protostellar outflows. *Astrophys. J.* 740:107. doi: 10.1088/0004-637X/740/2/107

Cunningham, A. J., Krumholz, M. R., McKee, C. F., and Klein, R. I. (2018). The effects of magnetic fields and protostellar feedback on low-mass cluster formation. *Mont. Notices RAS* 476, 771–792. doi: 10.1093/mnras/sty154

Dale, J. E., and Bonnell, I. (2011). Ionizing feedback from massive stars in massive clusters: fake bubbles and untriggered star formation. *Mont. Notices RAS* 414, 321–328. doi: 10.1111/j.1365-2966.2011.18392.x

Dale, J. E., Ercolano, B., and Bonnell, I. A. (2013). Ionizing feedback from massive stars in massive clusters - III. Disruption of partially unbound clouds. *Mont. Notices RAS* 430, 234–246. doi: 10.1093/mnras/sts592

de Avillez, M. A., and Breitschwerdt, D. (2005). Global dynamical evolution of the ISM in star forming galaxies. I. High resolution 3D simulations: effect of the magnetic field. *Astron. Astrophys.* 436, 585–600. doi: 10.1051/0004-6361:20042146

Dib, S., Hennebelle, P., Pineda, J. E., Csengeri, T., Bontemps, S., Audit, E., et al. (2010). The angular momentum of magnetized molecular cloud cores: a two-dimensional-three-dimensional comparison. *Astrophys. J.* 723, 425–439. doi: 10.1088/0004-637X/723/1/425

Downes, T. P., and O'Sullivan, S. (2011). Multifluid magnetohydrodynamic turbulent decay. *Astrophys. J.* 730:12. doi: 10.1088/0004-637X/730/1/12

Dutrey, A., Duvert, G., Castets, A., Langer, W. D., Bally, J., and Wilson, R. W. (1991). Periodically spaced fragmentation in Orion A. *Astron. Astrophys.* 247, L9–L12.

Elmegreen, B. G., and Scalo, J. (2004). Interstellar turbulence I: observations and processes. *Annu. Rev. Astron. Astrophys.* 42, 211–273. doi: 10.1146/annurev.astro.41.011802.094859

Fall, S. M., Krumholz, M. R., and Matzner, C. D. (2010). Stellar feedback in molecular clouds and its influence on the mass function of young star clusters. *Astrophys. J. Lett.* 710, L142–L146. doi: 10.1088/2041-8205/710/2/L142

Federrath, C. (2015). Inefficient star formation through turbulence, magnetic fields and feedback. *Mont. Notices RAS* 450, 4035–4042. doi: 10.1093/mnras/stv941

Federrath, C. (2016). On the universality of interstellar filaments: theory meets simulations and observations. *Mont. Notices RAS* 457, 375–388. doi: 10.1093/mnras/stv2880

Federrath, C., and Banerjee, S. (2015). The density structure and star formation rate of non-isothermal polytropic turbulence. *Mont. Notices RAS* 448, 3297–3313. doi: 10.1093/mnras/stv180

Ferrière, K. M. (2001). The interstellar environment of our galaxy. *Rev. Mod. Phys.* 73, 1031–1066. doi: 10.1103/RevModPhys.73.1031

Fiege, J. D., and Pudritz, R. E. (2000). Helical fields and filamentary molecular clouds - II. Axisymmetric stability and fragmentation. *Mont. Notices RAS* 311, 105–119. doi: 10.1046/j.1365-8711.2000.03067.x

Field, G. B. (1965). Thermal instability. *Astrophys. J.* 142:531. doi: 10.1086/148317

Fischera, J., and Martin, P. G. (2012). Physical properties of interstellar filaments. *Astron. Astrophys.* 42:A77. doi: 10.1051/0004-6361/201218961

Galli, D., Lizano, S., Shu, F. H., and Allen, A. (2006). Gravitational collapse of magnetized clouds. I. Ideal magnetohydrodynamic accretion flow. *Astrophys. J.* 647, 374–381. doi: 10.1086/505257

Galtier, S., and Banerjee, S. (2011). Exact relation for correlation functions in compressible isothermal turbulence. *Phys. Rev. Lett.* 107:134501. doi: 10.1103/PhysRevLett.107.134501

Gatto, A., Walch, S., Low, M.-M. M., Naab, T., Girichidis, P., Glover, S. C. O., et al. (2015). Modelling the supernova-driven ISM in different environments. *Mont. Notices RAS* 449, 1057–1075. doi: 10.1093/mnras/stv324

Gavagnin, E., Bleuler, A., Rosdahl, J., and Teyssier, R. (2017). Star cluster formation in a turbulent molecular cloud self-regulated by photoionization feedback. *Mont. Notices RAS* 472, 4155–4172. doi: 10.1093/mnras/stx2222

Geen, S., Hennebelle, P., Tremblin, P., and Rosdahl, J. (2015). Photoionization feedback in a self-gravitating, magnetized, turbulent cloud. *Mont. Notices RAS* 454, 4484–4502. doi: 10.1093/mnras/stv2272

Geen, S., Soler, J. D., and Hennebelle, P. (2017). Interpreting the star formation efficiency of nearby molecular clouds with ionizing radiation. *Mont. Notices RAS* 471, 4844–4855. doi: 10.1093/mnras/stx1765

Gendelev, L., and Krumholz, M. R. (2012). Evolution of blister-type H II regions in a magnetized medium. *Astrophys. J.* 745:158. doi: 10.1088/0004-637X/745/2/158

Gent, F. A., Shukurov, A., Fletcher, A., Sarson, G. R., and Mantere, M. J. (2013). The supernova-regulated ISM - I. The multiphase structure. *Mont. Notices RAS* 432, 1396–1423. doi: 10.1093/mnras/stt560

Girichidis, P., Naab, T., Walch, S., Hanasz, M., Mac Low, M.-M., Ostriker, J. P., et al. (2016). Launching cosmic-ray-driven outflows from the magnetized interstellar medium. *Astrophys. J. Lett.* 816:L19. doi: 10.3847/2041-8205/816/2/L19

Girichidis, P., Seifried, D., Naab, T., Peters, T., Walch, S., Wünsch, R., et al. (2018). The SILCC project - V. The impact of magnetic fields on the chemistry and the formation of molecular clouds. *Mont. Notices RAS* 480, 3511–3540. doi: 10.1093/mnras/sty2016

Glover, S. C. O., and Clark, P. C. (2012). Approximations for modelling CO chemistry in giant molecular clouds: a comparison of approaches. *Mont. Notices RAS* 421, 116–131. doi: 10.1111/j.1365-2966.2011.20260.x

Goldreich, P., and Sridhar, S. (1995). Toward a theory of interstellar turbulence. 2: strong alfvenic turbulence. *Astrophys. J.* 438, 763–775. doi: 10.1086/175121

Gómez, G. C., and Vázquez-Semadeni, E. (2014). Filaments in simulations of molecular cloud formation. *Astrophys. J.* 791:124. doi: 10.1088/0004-637X/791/2/124

Gómez, G. C., Vázquez-Semadeni, E., and Zamora-Avilés, M. (2018). The magnetic field structure in molecular cloud filaments. *Mont. Notices RAS* 480, 2939–2944. doi: 10.1093/mnras/sty2018

Gong, M., and Ostriker, E. C. (2015). Prestellar core formation, evolution, and accretion from gravitational fragmentation in turbulent converging flows. *Astrophys. J.* 806:31. doi: 10.1088/0004-637X/806/1/31

Gong, M., Ostriker, E. C., and Wolfire, M. G. (2017). A simple and accurate network for hydrogen and carbon chemistry in the interstellar medium. *Astrophys. J.* 843:38. doi: 10.3847/1538-4357/aa7561

Grappin, R., and Müller, W. C. (2010). Scaling and anisotropy in magnetohydrodynamic turbulence in a strong mean magnetic field. *Phys. Rev. E* 82:026406. doi: 10.1103/PhysRevE.82.026406

Gratier, P., Braine, J., Rodriguez-Fernandez, N. J., Schuster, K. F., Kramer, C., Corbelli, E., et al. (2012). Giant molecular clouds in the Local Group galaxy M 33. *Astron. Astrophys.* 542:A108. doi: 10.1051/0004-6361/201116612

Gray, W. J., McKee, C. F., and Klein, R. I. (2018). Effect of angular momentum alignment and strong magnetic fields on the formation of protostellar discs. *Mont. Notices RAS* 473, 2124–2143. doi: 10.1093/mnras/stx2406

Gritschneder, M., Heigl, S., and Burkert, A. (2017). Oscillating filaments. I. Oscillation and geometrical fragmentation. *Astrophys. J.* 834:202. doi: 10.3847/1538-4357/834/2/202

Hacar, A., Tafalla, M., Forbrich, J., Alves, J., Meingast, S., Grossschedl, J., et al. (2018). An ALMA study of the Orion Integral Filament. I. Evidence for narrow fibers in a massive cloud. *Astron. Astrophys.* 610:A77. doi: 10.1051/0004-6361/201731894

Hacar, A., Tafalla, M., Kauffmann, J., and Kovács, A. (2013). Cores, filaments, and bundles: hierarchical core formation in the L1495/B213 Taurus region. *Astron. Astrophys.* 554:A55. doi: 10.1051/0004-6361/201220090

Hanawa, T., Kudoh, T., and Tomisaka, K. (2017). Fragmentation of a filamentary cloud permeated by a perpendicular magnetic field. *Astrophys. J.* 848:2. doi: 10.3847/1538-4357/aa8b6d

Hanawa, T., and Tomisaka, K. (2015). Structure and stability of filamentary clouds supported by lateral magnetic field. *Astrophys. J.* 801:11. doi: 10.1088/0004-637X/801/1/11

Heitsch, F., Slyz, A. D., Devriendt, J. E. G., Hartmann, L. W., and Burkert, A. (2006). The birth of molecular clouds: formation of atomic precursors in colliding flows. *Astrophys. J.* 648, 1052–1065. doi: 10.1086/505931

Heitsch, F., Stone, J. M., and Hartmann, L. W. (2009). Effects of magnetic field strength and orientation on molecular cloud formation. *Astrophys. J.* 695, 248–258. doi: 10.1088/0004-637X/695/1/248

Heitsch, F., Zweibel, E. G., Slyz, A. D., and Devriendt, J. E. G. (2004). Turbulent ambipolar diffusion: numerical studies in two dimensions. *Astrophys. J.* 603, 165–179. doi: 10.1086/381428

Hennebelle, P. (2013). On the origin of non-self-gravitating filaments in the ISM. *Astron. Astrophys.* 556:A153. doi: 10.1051/0004-6361/201321292

Hennebelle, P. (2018). The FRIGG project: from intermediate galactic scales to self-gravitating cores. *Astron. Astrophys.* 611:A24. doi: 10.1051/0004-6361/201731071

Hennebelle, P., and André, P. (2013). Ion-neutral friction and accretion-driven turbulence in self-gravitating filaments. *Astron. Astrophys.* 560:A68. doi: 10.1051/0004-6361/201321761

Hennebelle, P., Banerjee, R., Vázquez-Semadeni, E., Klessen, R. S., and Audit, E. (2008). From the warm magnetized atomic medium to molecular clouds. *Astron. Astrophys.* 486, L43–L46. doi: 10.1051/0004-6361:200810165

Hennebelle, P., and Chabrier, G. (2008). Analytical theory for the initial mass function: CO clumps and prestellar cores. *Astrophys. J.* 684, 395–410. doi: 10.1086/589916

Hennebelle, P., and Chabrier, G. (2013). Analytical theory for the initial mass function. III. Time dependence and star formation rate. *Astrophys. J.* 770:150. doi: 10.1088/0004-637X/770/2/150

Hennebelle, P., Commerçon, B., Chabrier, G., and Marchand, P. (2016). Magnetically self-regulated formation of early protoplanetary disks. *Astrophys. J. Lett.* 830:L8. doi: 10.3847/2041-8205/830/1/L8

Hennebelle, P., Commerçon, B., Joos, M., Klessen, R. S., Krumholz, M., Tan, J. C., et al. (2011). Collapse, outflows and fragmentation of massive, turbulent and magnetized prestellar barotropic cores. *Astron. Astrophys.* 528:A72. doi: 10.1051/0004-6361/201016052

Hennebelle, P., and Falgarone, E. (2012). Turbulent molecular clouds. *Astron. Astrophys. Rev.* 20:55. doi: 10.1007/s00159-012-0055-y

Hennebelle, P., and Fromang, S. (2008). Magnetic processes in a collapsing dense core. I. Accretion and ejection. *Astron. Astrophys.* 477, 9–24. doi: 10.1051/0004-6361:20078309

Hennebelle, P., and Iffrig, O. (2014). Simulations of magnetized multiphase galactic disc regulated by supernovae explosions. *Astron. Astrophys.* 570:A81. doi: 10.1051/0004-6361/201423392

Hennebelle, P., and Pérault, M. (1999). Dynamical condensation in a thermally bistable flow. Application to interstellar cirrus. *Astron. Astrophys.* 351, 309–322.

Hennebelle, P., and Pérault, M. (2000). Dynamical condensation in a magnetized and thermally bistable flow. Application to interstellar cirrus. *Astron. Astrophys.* 359, 1124–1138.

Hennebelle, P., and Teyssier, R. (2008). Magnetic processes in a collapsing dense core. II. Fragmentation. Is there a fragmentation crisis? *Astron. Astrophys.* 477, 25–34. doi: 10.1051/0004-6361:20078310

Heyer, M., Goldsmith, P. F., Yıldız, U. A., Snell, R. L., Falgarone, E., and Pineda, J. L. (2016). Striations in the Taurus molecular cloud: Kelvin-Helmholtz instability or MHD waves? *Mont. Notices RAS* 461, 3918–3926. doi: 10.1093/mnras/stw1567

Heyer, M. H., Carpenter, J. M., and Snell, R. L. (2001). The equilibrium state of molecular regions in the outer galaxy. *Astrophys. J.* 551, 852–866. doi: 10.1086/320218

Hopkins, P. F. (2013). A model for (non-lognormal) density distributions in isothermal turbulence. *Mont. Notices RAS* 430, 1880–1891. doi: 10.1093/mnras/stt010

Iffrig, O., and Hennebelle, P. (2017). Structure distribution and turbulence in self-consistently supernova-driven ISM of multiphase magnetized galactic discs. *Astron. Astrophys.* 604:A70. doi: 10.1051/0004-6361/201630290

Inoue, T., and Fukui, Y. (2013). Formation of massive molecular cloud cores by cloud-cloud collision. *Astrophys. J. Lett.* 774:L31. doi: 10.1088/2041-8205/774/2/L31

Inoue, T., Hennebelle, P., Fukui, Y., Matsumoto, T., Iwasaki, K., and Inutsuka, S.-i. (2018). The formation of massive molecular filaments and massive stars triggered by a magnetohydrodynamic shock wave. *Publ. ASJ* 70:S53. doi: 10.1093/pasj/psx089

Inoue, T., and Inutsuka, S.-i. (2008). Two-fluid magnetohydrodynamic simulations of converging H I flows in the interstellar medium. I. Methodology and basic results. *Astrophys. J.* 687, 303–310. doi: 10.1086/590528

Inoue, T., and Inutsuka, S.-i. (2009). Two-fluid magnetohydrodynamics simulations of converging H I flows in the interstellar medium. II. Are molecular clouds generated directly from a warm neutral medium? *Astrophys. J.* 704, 161–169. doi: 10.1088/0004-637X/704/1/161

Inoue, T., and Inutsuka, S.-i. (2012). Formation of turbulent and magnetized molecular clouds via accretion flows of H I clouds. *Astrophys. J.* 759:35. doi: 10.1088/0004-637X/759/1/35

Inoue, T., and Inutsuka, S.-i. (2016). Formation of H I clouds in shock-compressed interstellar medium: physical origin of angular correlation Between filamentary structure and magnetic field. *Astrophys. J.* 833:10. doi: 10.3847/0004-637X/833/1/10

Inoue, T., Inutsuka, S.-i., and Koyama, H. (2007). The role of ambipolar diffusion in the formation process of moderately magnetized diffuse clouds. *Astrophys. J. Lett.* 658, L99–L102. doi: 10.1086/514816

Inutsuka, S.-I. (2001). The mass function of molecular cloud cores. *Astrophys. J. Lett.* 559, L149–L152. doi: 10.1086/323786

Inutsuka, S.-I. (2012). Present-day star formation: from molecular cloud cores to protostars and protoplanetary disks. *Prog. Theor. Exp. Phys.* 2012:01A307. doi: 10.1093/ptep/pts024

Inutsuka, S.-I., Inoue, T., Iwasaki, K., and Hosokawa, T. (2015). The formation and destruction of molecular clouds and galactic star formation. An origin for the cloud mass function and star formation efficiency. *Astron. Astrophys.* 580:A49. doi: 10.1051/0004-6361/201425584

Inutsuka, S.-I., and Miyama, S. M. (1992). Self-similar solutions and the stability of collapsing isothermal filaments. *Astrophys. J.* 388, 392–399. doi: 10.1086/171162

Iroshnikov, P. S. (1963). Turbulence of a conducting fluid in a strong magnetic field. *Astronomicheskii Zhurnal* 40:742.

Iwasaki, K., Tomida, K., Inoue, T., and Inutsuka, S.-i. (2018). The early stage of molecular cloud formation by compression of two-phase atomic gases. *arXiv*.

Joos, M., Hennebelle, P., and Ciardi, A. (2012). Protostellar disk formation and transport of angular momentum during magnetized core collapse. *Astron. Astrophys.* 543:A128. doi: 10.1051/0004-6361/201118730

Joos, M., Hennebelle, P., Ciardi, A., and Fromang, S. (2013). The influence of turbulence during magnetized core collapse and its consequences on low-mass star formation. *Astron. Astrophys.* 554:A17. doi: 10.1051/0004-6361/201220649

Joung, M. K. R., and Mac Low, M.-M. (2006). Turbulent structure of a stratified supernova-driven interstellar medium. *Astrophys. J.* 653, 1266–1279. doi: 10.1086/508795

Juvela, M., Malinen, J., and Lunttila, T. (2012). Profiles of interstellar cloud filaments. Observational effects in synthetic sub-millimetre observations. *Astron. Astrophys.* 544:A141. doi: 10.1051/0004-6361/201219558

Kennicutt, R. C., and Evans, N. J. (2012). Star formation in the milky way and nearby galaxies. *Annu. Rev. Astron. Astrophys.* 50, 531–608. doi: 10.1146/annurev-astro-081811-125610

Kim, C.-G., and Ostriker, E. C. (2015). Vertical equilibrium, energetics, and star formation rates in magnetized galactic disks regulated by momentum feedback from supernovae. *Astrophys. J.* 815:67. doi: 10.1088/0004-637X/815/1/67

Kim, C.-G., and Ostriker, E. C. (2017). Three-phase interstellar medium in galaxies resolving evolution with star formation and supernova feedback (TIGRESS): algorithms, fiducial model, and convergence. *Astrophys. J.* 846:133. doi: 10.3847/1538-4357/aa8599

Kim, C.-G., Ostriker, E. C., and Kim, W.-T. (2013). Three-dimensional hydrodynamic simulations of multiphase galactic disks with star formation Feedback. I. Regulation of star formation rates. *Astrophys. J.* 776:1. doi: 10.1088/0004-637X/776/1/1

Kim, J.-G., Kim, W.-T., and Ostriker, E. C. (2018). Modeling UV radiation feedback from massive stars. II. Dispersal of star-forming giant molecular clouds by photoionization and radiation pressure. *Astrophys. J.* 859:68. doi: 10.3847/1538-4357/aabe27

Kobayashi, M. I. N., Inutsuka, S.-I., Kobayashi, H., and Hasegawa, K. (2017). Evolutionary description of giant molecular cloud mass functions on galactic disks. *Astrophys. J.* 836:175. doi: 10.3847/1538-4357/836/2/175

Kobayashi, M. I. N., Kobayashi, H., Inutsuka, S.-I., and Fukui, Y. (2018). Star formation induced by cloud-cloud collisions and galactic giant molecular cloud evolution. *Publ. ASJ* 70:S59. doi: 10.1093/pasj/psy018

Koch, E. W., and Rosolowsky, E. W. (2015). Filament identification through mathematical morphology. *Mont. Notices RAS* 452, 3435–3450. doi: 10.1093/mnras/stv1521

Koch, P. M., Tang, Y.-W., and Ho, P. T. P. (2013). Interpreting the role of the magnetic field from dust polarization maps. *Astrophys. J.* 775:77. doi: 10.1088/0004-637X/775/1/77

Koch, P. M., Tang, Y.-W., Ho, P. T. P., Zhang, Q., Girart, J. M., Chen, H.-R. V., et al. (2014). The importance of the magnetic field from an SMA-CSO-combined sample of star-forming regions. *Astrophys. J.* 797:99. doi: 10.1088/0004-637X/797/2/99

Kolmogorov, A. (1941). The local structure of turbulence in incompressible viscous fluid for very large reynolds' numbers. *Akademiia Nauk SSSR Doklady* 30, 301–305.

Könyves, V., André, P., Men'shchikov, A., Palmeirim, P., Arzoumanian, D., Schneider, N., et al. (2015). A census of dense cores in the Aquila cloud complex: SPIRE/PACS observations from the Herschel Gould Belt survey. *Astron. Astrophys.* 584:A91. doi: 10.1051/0004-6361/201525861

Körtgen, B., and Banerjee, R. (2015). Impact of magnetic fields on molecular cloud formation and evolution. *Mont. Notices RAS* 451, 3340–3353. doi: 10.1093/mnras/stv1200

Koyama, H., and Inutsuka, S.-I. (2000). Molecular cloud formation in shock-compressed layers. *Astrophys. J.* 532, 980–993. doi: 10.1086/308594

Koyama, H., and Inutsuka, S.-i. (2002). An origin of supersonic motions in interstellar clouds. *Astrophys. J. Lett.* 564, L97–L100. doi: 10.1086/338978

Kraichnan, R. H. (1965). Inertial-range spectrum of hydromagnetic turbulence. *Phys. Fluids* 8, 1385–1387. doi: 10.1063/1.1761412

Kramer, C., Stutzki, J., Rohrig, R., and Corneliussen, U. (1998). Clump mass spectra of molecular clouds. *Astron. Astrophys.* 329, 249–264.

Kritsuk, A. G., Flauger, R., and Ustyugov, S. D. (2018). Dust-polarization maps for local interstellar turbulence. *Phys. Rev. Lett.* 121:021104. doi: 10.1103/PhysRevLett.121.021104

Kritsuk, A. G., Norman, M. L., Padoan, P., and Wagner, R. (2007). The statistics of supersonic isothermal turbulence. *Astrophys. J.* 665, 416–431. doi: 10.1086/519443

Kritsuk, A. G., Ustyugov, S. D., and Norman, M. L. (2017). The structure and statistics of interstellar turbulence. *N. J. Phys.* 19:065003. doi: 10.1088/1367-2630/aa7156

Krumholz, M. R., and Burkhart, B. (2016). Is turbulence in the interstellar medium driven by feedback or gravity? An observational test. *Mont. Notices RAS* 458, 1671–1677. doi: 10.1093/mnras/stw434

Kulsrud, R., and Pearce, W. P. (1969). The effect of wave-particle interactions on the propagation of cosmic rays. *Astrophys. J.* 156:445. doi: 10.1086/149981

Kwan, J. (1979). The mass spectrum of interstellar clouds. *Astrophys. J.* 229, 567–577. doi: 10.1086/156990

Landau, L. D., and Lifshitz, E. M. (1960). "Electrodynamics of Continuous Media," in *Course of Theoretical Physics* (Oxford: Pergamon Press).

Lazarian, A., Eyink, G. L., Vishniac, E. T., and Kowal, G. (2015). "Magnetic reconnection in astrophysical environments," in *Magnetic Fields in Diffuse Media, volume 407 of Astrophysics and Space Science Library*, Vol. 311, eds A. Lazarian, E. M. de Gouveia Dal Pino, and C. Melioli (Royal Society).

Lazarian, A., and Vishniac, E. T. (1999). Reconnection in a weakly stochastic field. *Astrophys. J.* 517, 700–718. doi: 10.1086/307233

Le Petit, F., Nehmé, C., Le Bourlot, J., and Roueff, E. (2006). A model for atomic and molecular interstellar gas: the meudon PDR code. *Astrophys. J. Suppl.* 164, 506–529. doi: 10.1086/503252

Lee, E., Brachet, M. E., Pouquet, A., Mininni, P. D., and Rosenberg, D. (2010). Lack of universality in decaying magnetohydrodynamic turbulence. *Phys. Rev. E* 81:016318. doi: 10.1103/PhysRevE.81.016318

Lee, Y.-N., and Hennebelle, P. (2016a). Formation of a protocluster: a virialized structure from gravoturbulent collapse. I. Simulation of cluster formation in a collapsing molecular cloud. *Astron. Astrophys.* 591:A30. doi: 10.1051/0004-6361/201527981

Lee, Y.-N., and Hennebelle, P. (2016b). Formation of a protocluster: a virialized structure from gravoturbulent collapse. II. A two-dimensional analytical model for a rotating and accreting system. *Astron. Astrophys.* 591:A31. doi: 10.1051/0004-6361/201527982

Lee, Y.-N., and Hennebelle, P. (2018a). Stellar mass spectrum within massive collapsing clumps. I. Influence of the initial conditions. *Astron. Astrophys.* 611:A88. doi: 10.1051/0004-6361/201731522

Lee, Y.-N., and Hennebelle, P. (2018b). Stellar mass spectrum within massive collapsing clumps. II. Thermodynamics and tidal forces of the first Larson core. A robust mechanism for the peak of the IMF. *Astron. Astrophys.* 611:A89. doi: 10.1051/0004-6361/201731523

Lee, Y.-N., and Hennebelle, P. (2018c). Stellar mass spectrum within massive collapsing clumps III. Effects of temperature and magnetic field. *arXiv*.

Lee, Y.-N., Hennebelle, P., and Chabrier, G. (2017). Analytical core mass function (CMF) from filaments: under which circumstances can filament fragmentation reproduce the CMF? *Astrophys. J.* 847:114. doi: 10.3847/1538-4357/aa898f

Lemaster, M. N., and Stone, J. M. (2008). Density probability distribution functions in supersonic hydrodynamic and MHD turbulence. *Astrophys. J. Lett.* 682:L97. doi: 10.1086/590929

Lequeux, J. (2005). "The Interstellar Medium," in *Translation from the French language edition of: Le Milieu Interstellaire 2003, Astronomy and Astrophysics Library* (Berlin: Springer; EDP Sciences).

Li, P. S., McKee, C. F., and Klein, R. I. (2006). The heavy-ion approximation for ambipolar diffusion calculations for weakly ionized plasmas. *Astrophys. J.* 653, 1280–1291. doi: 10.1086/508977

Li, P. S., McKee, C. F., and Klein, R. I. (2015). Magnetized interstellar molecular clouds - I. Comparison between simulations and Zeeman observations. *Mont. Notices RAS* 452, 2500–2527. doi: 10.1093/mnras/stv1437

Li, P. S., McKee, C. F., Klein, R. I., and Fisher, R. T. (2008). Sub-Alfvénic nonideal MHD turbulence simulations with ambipolar diffusion. I. Turbulence statistics. *Astrophys. J.* 684, 380–394. doi: 10.1086/589874

Li, Z.-Y., Banerjee, R., Pudritz, R. E., Jørgensen, J. K., Shang, H., Krasnopolsky, R., et al. (2014). "The earliest stages of star and planet formation: core collapse, and the formation of disks and outflows," in *Protostars and Planets VI*, eds H. Beuther, R. S. Klessen, C. P. Dullemond, and T. Henning (Tucson, AZ: University of Arizona Press), 173–194.

Li, Z.-Y., and Nakamura, F. (2004). Magnetically regulated star formation in turbulent clouds. *Astrophys. J. Lett.* 609, L83–L86. doi: 10.1086/422839

Li, Z.-Y., and Nakamura, F. (2006). Cluster formation in protostellar outflow-driven turbulence. *Astrophys. J. Lett.* 640, L187–L190. doi: 10.1086/503419

Longmore, S. N., Kruijssen, J. M. D., Bastian, N., Bally, J., Rathborne, J., Testi, L., et al. (2014). "The formation and early evolution of young massive clusters," in *Protostars and Planets VI*, eds H. Beuther, R. S. Klessen, C. P. Dullemond, and T. Henning (Tucson, AZ: University of Arizona Press), 291–314.

Mac Low, M.-M., Klessen, R. S., Burkert, A., and Smith, M. D. (1998). Kinetic energy decay rates of supersonic and Super-Alfvénic turbulence in star-forming clouds. *Phys. Rev. Lett.* 80, 2754–2757. doi: 10.1103/PhysRevLett.80.2754

Mac Low, M.-M., Norman, M. L., Konigl, A., and Wardle, M. (1995). Incorporation of ambipolar diffusion into the ZEUS magnetohydrodynamics code. *Astrophys. J.* 442, 726–735. doi: 10.1086/175477

Machida, M. N., Matsumoto, T., Hanawa, T., and Tomisaka, K. (2005). Collapse and fragmentation of rotating magnetized clouds - II. Binary formation and fragmentation of first cores. *Mont. Notices RAS* 362, 382–402. doi: 10.1111/j.1365-2966.2005.09327.x

Machida, M. N., Matsumoto, T., and Inutsuka, S.-I. (2016). Conditions for circumstellar disc formation - II. Effects of initial cloud stability and mass accretion rate. *Mont. Notices RAS* 463, 4246–4267. doi: 10.1093/mnras/stw2256

Machida, M. N., Tomisaka, K., Matsumoto, T., and Inutsuka, S.-I. (2008). Formation scenario for wide and close binary systems. *Astrophys. J.* 677, 327–347. doi: 10.1086/529133

Mackey, J., and Lim, A. J. (2011). Effects of magnetic fields on photoionized pillars and globules. *Mont. Notices RAS* 412, 2079–2094. doi: 10.1111/j.1365-2966.2010.18043.x

Mason, J., Perez, J. C., Boldyrev, S., and Cattaneo, F. (2012). Numerical simulations of strong incompressible magnetohydrodynamic turbulence. *Phys. Plasmas* 19:055902. doi: 10.1063/1.3694123

Masson, J., Chabrier, G., Hennebelle, P., Vaytet, N., and Commerçon, B. (2016). Ambipolar diffusion in low-mass star formation. I. General comparison with the ideal magnetohydrodynamic case. *Astron. Astrophys.* 587:A32. doi: 10.1051/0004-6361/201526371

Masson, J., Teyssier, R., Mulet-Marquis, C., Hennebelle, P., and Chabrier, G. (2012). Incorporating ambipolar and ohmic diffusion in the AMR MHD code RAMSES. *Astrophys. J. Suppl.* 201:24. doi: 10.1088/0067-0049/201/2/24

Matsumoto, T., and Hanawa, T. (2003). Fragmentation of a molecular cloud core versus fragmentation of the massive protoplanetary disk in the main accretion phase. *Astrophys. J.* 595, 913–934. doi: 10.1086/377367

Matthaeus, W. H., Pouquet, A., Mininni, P. D., Dmitruk, P., and Breech, B. (2008). Rapid alignment of velocity and magnetic field in magnetohydrodynamic turbulence. *Phys. Rev. Lett.* 100:085003. doi: 10.1103/PhysRevLett.100.085003

McClure-Griffiths, N. M., Dickey, J. M., Gaensler, B. M., Green, A. J., and Haverkorn, M. (2006). Magnetically dominated strands of cold hydrogen in the riegel-crutcher cloud. *Astrophys. J.* 652, 1339–1347. doi: 10.1086/508706

McKee, C. F., Li, P. S., and Klein, R. I. (2010). Sub-Alfvénic non-ideal MHD turbulence simulations with ambipolar diffusion. II. Comparison with observation, clump properties, and scaling to physical units. *Astrophys. J.* 720, 1612–1634. doi: 10.1088/0004-637X/720/2/1612

McKee, C. F., and Ostriker, J. P. (1977). A theory of the interstellar medium - Three components regulated by supernova explosions in an inhomogeneous substrate. *Astrophys. J.* 218, 148–169. doi: 10.1086/155667

Miville-Deschênes, M.-A., Joncas, G., Falgarone, E., and Boulanger, F. (2003). High resolution 21 cm mapping of the Ursa Major Galactic cirrus: power spectra of the high-latitude H I gas. *Astron. Astrophys.* 411, 109–121. doi: 10.1051/0004-6361:20031297

Miville-Deschênes, M.-A., Murray, N., and Lee, E. J. (2017). Physical properties of molecular clouds for the entire milky way disk. *Astrophys. J.* 834:57. doi: 10.3847/1538-4357/834/1/57

Mocz, P., Burkhart, B., Hernquist, L., McKee, C. F., and Springel, V. (2017). Moving-mesh simulations of star-forming cores in magneto-gravo-turbulence. *Astrophys. J.* 838:40. doi: 10.3847/1538-4357/aa6475

Molina, F. Z., Glover, S. C. O., Federrath, C., and Klessen, R. S. (2012). The density variance-Mach number relation in supersonic turbulence - I. Isothermal, magnetized gas. *Mont. Notices RAS* 423, 2680–2689. doi: 10.1111/j.1365-2966.2012.21075.x

Mouschovias, T. C., and Paleologou, E. V. (1981). Ambipolar diffusion in interstellar clouds - Time-dependent solutions in one spatial dimension. *Astrophys. J.* 246, 48–64. doi: 10.1086/158897

Mouschovias, T. C., and Spitzer, L, Jr. (1976). Note on the collapse of magnetic interstellar clouds. *Astrophys. J.* 210:326. doi: 10.1086/154835

Murray, D., Goyal, S., and Chang, P. (2018). The effects of protostellar jet feedback on turbulent collapse. *Mont. Notices RAS* 475, 1023–1035. doi: 10.1093/mnras/stx3153

Myers, A. T., Klein, R. I., Krumholz, M. R., and McKee, C. F. (2014). Star cluster formation in turbulent, magnetized dense clumps with radiative and outflow feedback. *Mont. Notices RAS* 439, 3420–3438. doi: 10.1093/mnras/stu190

Myers, A. T., McKee, C. F., Cunningham, A. J., Klein, R. I., and Krumholz, M. R. (2013). The fragmentation of magnetized, massive star-forming cores with radiative feedback. *Astrophys. J.* 766:97. doi: 10.1088/0004-637X/766/2/97

Nagai, T., Inutsuka, S.-I., and Miyama, S. M. (1998). An origin of filamentary structure in molecular clouds. *Astrophys. J.* 506, 306–322. doi: 10.1086/306249

Nakamura, F., Hanawa, T., and Nakano, T. (1993). Fragmentation of filamentary molecular clouds with longitudinal and helical magnetic fields. *Publ. ASJ* 45, 551–566.

Nakamura, F., and Li, Z.-Y. (2008). Magnetically regulated star formation in three dimensions: the case of the taurus molecular cloud complex. *Astrophys. J.* 687, 354–375. doi: 10.1086/591641

Nakamura, F., and Li, Z.-Y. (2011). Clustered star formation in magnetic clouds: properties of dense cores formed in outflow-driven turbulence. *Astrophys. J.* 740:36. doi: 10.1088/0004-637X/740/1/36

Neufeld, D. A., Lepp, S., and Melnick, G. J. (1995). Thermal balance in dense molecular clouds: radiative cooling rates and emission-line luminosities. *Astrophys. J. Suppl.* 100:132. doi: 10.1086/192211

Ntormousi, E., Dawson, J. R., Hennebelle, P., and Fierlinger, K. (2017). The role of magnetic fields in the structure and interaction of supershells. *Astron. Astrophys.* 599:A94. doi: 10.1051/0004-6361/201629268

Ntormousi, E., Hennebelle, P., André, P., and Masson, J. (2016). The effect of ambipolar diffusion on low-density molecular ISM filaments. *Astron. Astrophys.* 589:A24. doi: 10.1051/0004-6361/201527400

Offner, S. S. R., and Chaban, J. (2017). Impact of protostellar outflows on turbulence and star formation efficiency in magnetized dense cores. *Astrophys. J.* 847:104. doi: 10.3847/1538-4357/aa8996

Offner, S. S. R., Clark, P. C., Hennebelle, P., Bastian, N., Bate, M. R., Hopkins, P. F., et al. (2014). "The origin and universality of the stellar initial mass function," in *Protostars and Planets VI*, eds H. Beuther, R. S. Klessen, C. P. Dullemond, and T. Henning (Tucson, AZ: University of Arizona Press), 53–75.

Offner, S. S. R., and Liu, Y. (2018). Turbulent action at a distance due to stellar feedback in magnetized clouds. *Nat. Astron.* 2, 896–900. doi: 10.1038/s41550-018-0566-1

Oishi, J. S., and Mac Low, M.-M. (2006). The inability of ambipolar diffusion to set a characteristic mass scale in molecular clouds. *Astrophys. J.* 638, 281–285. doi: 10.1086/498818

Ostriker, E. C., Stone, J. M., and Gammie, C. F. (2001). Density, velocity, and magnetic field structure in turbulent molecular cloud models. *Astrophys. J.* 546, 980–1005. doi: 10.1086/318290

Padoan, P., and Nordlund, Å. (1999). A super-Alfvénic model of dark clouds. *Astrophys. J.* 526, 279–294. doi: 10.1086/307956

Padoan, P., and Nordlund, Å. (2011). The star formation rate of supersonic magnetohydrodynamic turbulence. *Astrophys. J.* 730:40. doi: 10.1088/0004-637X/730/1/40

Padoan, P., Nordlund, A., and Jones, B. J. T. (1997). The universality of the stellar initial mass function. *Mont. Notices RAS* 288, 145–152. doi: 10.1093/mnras/288.1.145

Padoan, P., Pan, L., Haugbølle, T., and Nordlund, Å. (2016). Supernova driving. I. The origin of molecular cloud turbulence. *Astrophys. J.* 822:11. doi: 10.3847/0004-637X/822/1/11

Panopoulou, G. V., Psaradaki, I., Skalidis, R., Tassis, K., and Andrews, J. J. (2017). A closer look at the 'characteristic' width of molecular cloud filaments. *Mont. Notices RAS* 466, 2529–2541. doi: 10.1093/mnras/stw3060

Passot, T., and Vázquez-Semadeni, E. (2003). The correlation between magnetic pressure and density in compressible MHD turbulence. *Astron. Astrophys.* 398, 845–855. doi: 10.1051/0004-6361:20021665

Peters, T., Banerjee, R., Klessen, R. S., and Mac Low, M.-M. (2011). The interplay of magnetic fields, fragmentation, and ionization feedback in high-mass star formation. *Astrophys. J.* 729:72. doi: 10.1088/0004-637X/729/1/72

Piontek, R. A., and Ostriker, E. C. (2004). Thermal and magnetorotational instability in the interstellar medium: two-dimensional numerical simulations. *Astrophys. J.* 601, 905–920. doi: 10.1086/380785

Planck Collaboration, Ade, P. A. R., Aghanim, N., Alves, M. I. R., Arnaud, M., Arzoumanian, D., et al. (2016). Planck intermediate results. XXXV. Probing the role of the magnetic field in the formation of structure in molecular clouds. *Astron. Astrophys.* 586:A138. doi: 10.1051/0004-6361/201525896

Polychroni, D., Schisano, E., Elia, D., Roy, A., Molinari, S., Martin, P., et al. (2013). Two mass distributions in the L 1641 molecular clouds: the herschel connection of dense cores and filaments in orion A. *Astrophys. J. Lett.* 777:L33. doi: 10.1088/2041-8205/777/2/L33

Price, D. J., and Bate, M. R. (2007). The impact of magnetic fields on single and binary star formation. *Mont. Notices RAS* 377, 77–90. doi: 10.1111/j.1365-2966.2007.11621.x

Price, D. J., and Bate, M. R. (2008). The effect of magnetic fields on star cluster formation. *Mont. Notices RAS* 385, 1820–1834. doi: 10.1111/j.1365-2966.2008.12976.x

Price, D. J., and Bate, M. R. (2009). Inefficient star formation: the combined effects of magnetic fields and radiative feedback. *Mont. Notices RAS* 398, 33–46. doi: 10.1111/j.1365-2966.2009.14969.x

Roman-Duval, J., Jackson, J. M., Heyer, M., Rathborne, J., and Simon, R. (2010). Physical properties and galactic distribution of molecular clouds identified in the galactic ring survey. *Astrophys. J.* 723, 492–507. doi: 10.1088/0004-637X/723/1/492

Roy, A., André, P., Arzoumanian, D., Peretto, N., Palmeirim, P., Könyves, V., et al. (2015). Possible link between the power spectrum of interstellar filaments and the origin of the prestellar core mass function. *Astron. Astrophys.* 584:A111. doi: 10.1051/0004-6361/201526431

Santos-Lima, R., de Gouveia Dal Pino, E. M., and Lazarian, A. (2012). The role of turbulent magnetic reconnection in the formation of rotationally supported protostellar disks. *Astrophys. J.* 747:21. doi: 10.1088/0004-637X/747/1/21

Schwarz, J., McCray, R., and Stein, R. F. (1972). Formation of clouds in a cooling interstellar medium. *Astrophys. J.* 175:673. doi: 10.1086/151588

Scoville, N. Z., and Hersh, K. (1979). Collisional growth of giant molecular clouds. *Astrophys. J.* 229, 578–582. doi: 10.1086/156991

Seifried, D., Banerjee, R., Pudritz, R. E., and Klessen, R. S. (2013). Turbulence-induced disc formation in strongly magnetized cloud cores. *Mont. Notices RAS* 432, 3320–3331. doi: 10.1093/mnras/stt682

Shu, F. H. (1992). *The Physics of Astrophysics. Volume II: Gas Dynamics.* Mill Valley, CA: University Science Books.

Shu, F. H., Adams, F. C., and Lizano, S. (1987). Star formation in molecular clouds - Observation and theory. *Annu. Rev. Astron. Astrophys.* 25, 23–81. doi: 10.1146/annurev.aa.25.090187.000323

Smith, R. J., Glover, S. C. O., and Klessen, R. S. (2014). On the nature of star-forming filaments - I. Filament morphologies. *Mont. Notices RAS* 445, 2900–2917. doi: 10.1093/mnras/stu1915

Soler, J. D., and Hennebelle, P. (2017). What are we learning from the relative orientation between density structures and the magnetic field in molecular clouds? *Astron. Astrophys.* 607:A2. doi: 10.1051/0004-6361/201731049

Soler, J. D., Hennebelle, P., Martin, P. G., Miville-Deschênes, M.-A., Netterfield, C. B., and Fissel, L. M. (2013). An imprint of molecular cloud magnetization in the morphology of the dust polarized emission. *Astrophys. J.* 774:128. doi: 10.1088/0004-637X/774/2/128

Solomon, P. M., Rivolo, A. R., Barrett, J., and Yahil, A. (1987). Mass, luminosity, and line width relations of Galactic molecular clouds. *Astrophys. J.* 319, 730–741. doi: 10.1086/165493

Spruit, H. C. (2013). Essential magnetohydrodynamics for astrophysics. *arXiv*.

Sternberg, A., Le Petit, F., Roueff, E., and Le Bourlot, J. (2014). H I-to-H_2 transitions and H I column densities in galaxy star-forming regions. *Astrophys. J.* 790:10. doi: 10.1088/0004-637X/790/1/10

Tilley, D. A., and Pudritz, R. E. (2007). The formation of star clusters - II. 3D simulations of magnetohydrodynamic turbulence in molecular clouds. *Mont. Notices RAS* 382, 73–94. doi: 10.1111/j.1365-2966.2007.12371.x

Tomisaka, K. (1986). Formation of giant molecular clouds by coagulation of small clouds and spiral structure. *Publ. ASJ* 38, 95–109.

Tomisaka, K. (2014). Magnetohydrostatic equilibrium structure and mass of filamentary isothermal cloud threaded by lateral magnetic field. *Astrophys. J.* 785:24. doi: 10.1088/0004-637X/785/1/24

Traficante, A., Fuller, G. A., Peretto, N., Pineda, J. E., and Molinari, S. (2015). The initial conditions of stellar protocluster formation - II. A catalogue of starless and protostellar clumps embedded in IRDCs in the Galactic longitude range $15^\circ \leq l \leq 55^\circ$. *Mont. Notices RAS* 451, 3089–3106. doi: 10.1093/mnras/stv1158

Tritsis, A., and Tassis, K. (2016). Striations in molecular clouds: streamers or MHD waves? *Mont. Notices RAS* 462, 3602–3615. doi: 10.1093/mnras/stw1881

Troland, T. H., and Heiles, C. (1986). Interstellar magnetic field strengths and gas densities Observational and theoretical perspectives. *Astrophys. J.* 301, 339–345. doi: 10.1086/163904

Urquhart, J. S., Moore, T. J. T., Csengeri, T., Wyrowski, F., Schuller, F., Hoare, M. G., et al. (2014). ATLASGAL - towards a complete sample of massive star forming clumps. *Mont. Notices RAS* 443, 1555–1586. doi: 10.1093/mnras/stu1207

Vacca, W. D., Garmany, C. D., and Shull, J. M. (1996). The Lyman-Continuum fluxes and stellar parameters of O and early B-type stars. *Astrophys. J.* 460:914. doi: 10.1086/177020

Valdivia, V., Hennebelle, P., Gérin, M., and Lesaffre, P. (2016). H_2 distribution during the formation of multiphase molecular clouds. *Astron. Astrophys.* 587:A76. doi: 10.1051/0004-6361/201527325

van Loo, S., Falle, S. A. E. G., Hartquist, T. W., and Barker, A. J. (2008). The effect of ambipolar resistivity on the formation of dense cores. *Astron. Astrophys.* 484, 275–280. doi: 10.1051/0004-6361:200809432

van Loo, S., Falle, S. A. E. G., Hartquist, T. W., and Moore, T. J. T. (2007). Shock-triggered formation of magnetically-dominated clouds. *Astron. Astrophys.* 471, 213–218. doi: 10.1051/0004-6361:20077430

Van Loo, S., Keto, E., and Zhang, Q. (2014). Core and filament formation in magnetized, self-gravitating isothermal layers. *Astrophys. J.* 789:37. doi: 10.1088/0004-637X/789/1/37

Vázquez-Semadeni, E., Banerjee, R., Gómez, G. C., Hennebelle, P., Duffin, D., and Klessen, R. S. (2011). Molecular cloud evolution - IV. Magnetic fields, ambipolar diffusion and the star formation efficiency. *Mont. Notices RAS* 414, 2511–2527. doi: 10.1111/j.1365-2966.2011.18569.x

Vázquez-Semadeni, E., Kim, J., Shadmehri, M., and Ballesteros-Paredes, J. (2005). The lifetimes and evolution of molecular cloud cores. *Astrophys. J.* 618, 344–359. doi: 10.1086/425951

Vázquez-Semadeni, E., Ryu, D., Passot, T., González, R. F., and Gazol, A. (2006). Molecular cloud evolution. I. molecular cloud and thin cold neutral medium sheet formation. *Astrophys. J.* 643, 245–259. doi: 10.1086/502710

Vestuto, J. G., Ostriker, E. C., and Stone, J. M. (2003). Spectral properties of compressible magnetohydrodynamic turbulence from numerical simulations. *Astrophys. J.* 590, 858–873. doi: 10.1086/375021

Walch, S. K., Whitworth, A. P., Bisbas, T., Wünsch, R., and Hubber, D. (2012). Dispersal of molecular clouds by ionizing radiation. *Mont. Notices RAS* 427, 625–636. doi: 10.1111/j.1365-2966.2012.21767.x

Wan, M., Osman, K. T., Matthaeus, W. H., and Oughton, S. (2012). Investigation of intermittency in magnetohydrodynamics and solar wind turbulence: scale-dependent kurtosis. *Astrophys. J.* 744:171. doi: 10.1088/0004-637X/744/2/171

Wang, P., Li, Z.-Y., Abel, T., and Nakamura, F. (2010). Outflow feedback regulated massive star formation in parsec-scale cluster-forming clumps. *Astrophys. J.* 709, 27–41. doi: 10.1088/0004-637X/709/1/27

Ward-Thompson, D., André, P., Crutcher, R., Johnstone, D., Onishi, T., and Wilson, C. (2007). "An observational perspective of low-mass dense cores II: evolution toward the initial mass function," in *Protostars and Planets V*, eds B. Reipurth, D. Jewitt, and K. Keil (Tucson: University of Arizona Press), 33–46.

Wolfire, M. G., McKee, C. F., Hollenbach, D., and Tielens, A. G. G. M. (2003). Neutral atomic phases of the interstellar medium in the galaxy. *Astrophys. J.* 587, 278–311. doi: 10.1086/368016

Wurster, J., Price, D. J., and Bate, M. R. (2016). Can non-ideal magnetohydrodynamics solve the magnetic braking catastrophe? *Mont. Notices RAS* 457, 1037–1061. doi: 10.1093/mnras/stw013

Wurster, J., Price, D. J., and Bate, M. R. (2017). The impact of non-ideal magnetohydrodynamics on binary star formation. *Mont. Notices RAS* 466, 1788–1804. doi: 10.1093/mnras/stw3181

Zhao, B., Caselli, P., Li, Z.-Y., and Krasnopolsky, R. (2018). Decoupling of magnetic fields in collapsing protostellar envelopes and disc formation and fragmentation. *Mont. Notices RAS* 473, 4868–4889. doi: 10.1093/mnras/stx2617

Zuckerman, B., and Evans, II, N. J. (1974). Models of massive molecular clouds. *Astrophys. J. Lett.* 192, L149–L152.

Conflict of Interest Statement: The authors declare that the research was conducted in the absence of any commercial or financial relationships that could be construed as a potential conflict of interest.

frontiers in Astronomy and Space Sciences

REVIEW
published: 13 December 2018
doi: 10.3389/fspas.2018.00039

The Role of Magnetic Fields in the Formation of Protostellar Discs

James Wurster[1]* *and Zhi-Yun Li*[2]

[1] School of Physics and Astronomy, University of Exeter, Exeter, United Kingdom, [2] Astronomy Department, University of Virginia, Charlottesville, VA, United States

The formation of a protostellar disc is a natural outcome during the star formation process. As gas in a molecular cloud core collapses under self-gravity, the angular momentum of the gas will slow its collapse on small scales and promote the formation of a protostellar disc. Although the angular momenta of dense star-forming cores remain to be fully characterized observationally, existing data indicates that typical cores have enough angular momenta to form relatively large, 100 au-scale, rotationally supported discs, as illustrated by hydrodynamic simulations. However, the molecular clouds are observed to be permeated by magnetic fields, which can in principle strongly affect the evolution of angular momentum during the core collapse through magnetic braking. Indeed, in the ideal magnetohydrodynamic (MHD) limit, magnetic braking has been shown to be so efficient as to remove essentially all of the angular momentum of the material close to the forming star such that disc formation is suppressed. This failure to produce discs in idealized cores is known as the magnetic braking catastrophe. The catastrophe must be averted in order for the all-important rotationally supported discs to appear, but when and how this happens remains debated. We review the resolutions proposed to date, with emphasis on misalignment, turbulence and especially non-ideal effects. Non-ideal MHD accounts for charged and neutral species, making it a natural extension to the ideal MHD approximation, since molecular clouds are only weakly ionized. The dissipative non-ideal effects diffuse the magnetic field to weaken it, and the dispersive term redirects the magnetic field to promote or hinder disc formation, dependent upon the magnetic geometry. When self-consistently applying non-ideal processes, rotationally supported discs of at least tens of au form, thus preventing the magnetic braking catastrophe. The non-ideal processes are sensitive to the magnetic field strength, cosmic ray ionization rate, and gas and dust grain properties, thus a complete understanding of the host molecular cloud is required. Therefore, the properties of the host molecular cloud—and especially its magnetic field—cannot be ignored when numerically modeling the formation and evolution of protostellar discs.

Keywords: magnetic fields, magnetohydrodynamics (MHD), non-ideal MHD, star formation, protostellar discs

OPEN ACCESS

Edited by:
Yusuke Tsukamoto,
Kagoshima University, Japan

Reviewed by:
Kengo Tomida,
Osaka University, Japan
Matthew Kunz,
Princeton University, United States

***Correspondence:**
James Wurster
j.wurster@exeter.ac.uk

Specialty section:
This article was submitted to Stellar and Solar Physics, a section of the journal Frontiers in Astronomy and Space Sciences

Received: *29 June 2018*
Accepted: *15 November 2018*
Published: *13 December 2018*

Citation:
Wurster J and Li Z-Y (2018) The Role of Magnetic Fields in the Formation of Protostellar Discs. Front. Astron. Space Sci. 5:39. doi: 10.3389/fspas.2018.00039

1. INTRODUCTION

The broad outline of low-mass star formation has been known since at least (Larson, 1969), although many specific details are still under investigation. In Larson's description, which is the foundation for all current low-mass star formation models, a piece of the interstellar cloud (a molecular cloud core in modern terminology) collapses under self-gravity. The collapse is initially isothermal,

since radiation is efficiently radiated away. However, as the density increases at the center of the core, it becomes optically thick to the radiation, which leads to an increase in thermal pressure support against self-gravity and the formation of the first hydrostatic or first Larson core. The first hydrostatic core continues to accrete material from the collapsing envelope, and its mass, density and temperature increase until the temperature rises above ∼2,000 K; this temperature triggers the dissociation of H_2, allowing the core to further collapse. This second collapse phase is rapid, and lasts until most of the H_2 has been dissociated, at which point the second hydrostatic or stellar core has formed. The temperature continues to rise until nuclear burning starts and the star is formed.

The formation of star-forming molecular cloud cores is not fully understood[1]. These cores are observed to be initially slowly rotating, with ratios of rotational energy to gravitational potential being $\beta \lesssim 0.15$ with typical values of $\beta \sim 0.02$ (Goodman et al., 1993). However, their angular velocities are typically one to two orders of magnitude smaller than inferred by conservation of angular momentum (for a review, see Goldsmith and Arquilla, 1985). Therefore, there must exist some mechanism that will shed the angular momentum to allow these slowly rotating cloud cores to form (e.g., Spitzer, 1968).

As the rotating cloud core collapses under self-gravity, in the absence of magnetic fields, the rotation slows the collapse such that the gas forms a large protostellar disc as early as during the first core stage, and certainly by the Class 0 phase, as indicated by observations (e.g., Tobin et al., 2012; Murillo et al., 2013; Codella et al., 2014; Lee et al., 2017) and found in numerical simulations (e.g., Boss, 1993; Yorke et al., 1993, 1995; Boss and Myhill, 1995; Bate et al., 2014; Tomida, 2014; Wurster et al., 2018c). Conservation laws and observations thus both suggest that protostellar discs are a natural byproduct of the star formation process.

Molecular clouds are observed to be strongly magnetized (e.g., Crutcher, 1999; Bourke et al., 2001; Heiles and Crutcher, 2005; Troland and Crutcher, 2008), and magnetic fields are efficient at transporting angular momentum away from a collapsing core (known as "magnetic braking"; e.g., Mestel and Spitzer, 1956; Mouschovias and Paleologou, 1979, 1980; Basu and Mouschovias, 1994, 1995; Mellon and Li, 2008). On the cloud scale, magnetic braking likely occurs early in the cloud's formation and is responsible (at least in part) for reducing the angular momentum to the observed values (e.g., Mouschovias, 1983). Near the center of the collapsing core, magnetic braking means that discs are less necessary to conserve angular momentum since it is transported away. This reduced angular momentum may delay the formation of the disc until during or after the stellar core phase, or may prevent it altogether. In idealized numerical simulations including ideal magnetohydrodynamics (MHD), protostellar discs either fail to form or are much smaller than the observed sizes. This is known as the magnetic braking catastrophe (Allen et al., 2003; Galli et al., 2006).

[1]The focus of this review is on disc formation, thus for the remainder of this paper, we will assume that a slowly rotating cloud core has successfully formed.

Magnetic fields support charged gas against gravitational collapse, thus a common characterization of the relative importance of the gravitational and magnetic forces is the normalized mass-to-flux ratio,

$$\mu \equiv \frac{M/\Phi_{\rm B}}{(M/\Phi_{\rm B})_{\rm crit}}, \tag{1}$$

where

$$\frac{M}{\Phi_{\rm B}} \equiv \frac{M}{\pi R^2 B}, \tag{2}$$

is the mass-to-flux ratio and

$$\left(\frac{M}{\Phi_{\rm B}}\right)_{\rm crit} = \frac{c_1}{3\pi}\sqrt{\frac{5}{G}}, \tag{3}$$

is the critical value where the gravitational and magnetic forces balance; in these equations, M is the total mass contained within a core of radius R, $\Phi_{\rm B}$ is the magnetic flux threading the surface of the spherical core assuming a uniform magnetic field of strength B, G is the gravitational constant and $c_1 \simeq 0.53$ is a dimensionless coefficient numerically determined by Mouschovias and Spitzer (1976). The critical value of $\mu = 1$ suggests that the gravitational and magnetic forces balance one another. For large super-critical values ($\mu \gtrsim 20$), the magnetic field is inconsequential for core collapse, and the evolution is similar to that of a purely hydrodynamic cloud (e.g., Bate et al., 2014). For sub-critical values ($\mu < 1$), the magnetic field will prevent the collapse of the cloud core altogether. Observations suggest $\mu \sim 2 - 10$ in molecular cloud cores (e.g., Crutcher, 1999; Bourke et al., 2001; Heiles and Crutcher, 2005), however, this value could be even smaller after correcting for projection effects (Li et al., 2013a).

Although widely used, the mass-to-flux ratio should be used with caution, since the equation and the critical value are dependent on the geometry. While the above equations assume spherical geometry, a mass-to-flux ratio for a thin sheet is given in Nakano and Nakamura (1978), and the ratio for an oblate spheroid is given in Mouschovias and Spitzer (1976).

We will begin the review by describing the observational motivations in section 2, followed by a description of ideal MHD in the introduction to section 3. Our focus will then shift to numerical models, where we demonstrate the magnetic braking catastrophe (section 3.1), followed by attempts to prevent it while still keeping the ideal MHD approximation (sections 3.2 and 3.3). We will then introduce non-ideal MHD (section 4), and show the recent success of those simulations in preventing the magnetic braking catastrophe. We will conclude in section 5.

2. OBSERVATIONAL MOTIVATIONS

The notion of a magnetized interstellar medium (ISM) dates back more than half a century, to at least the detection of polarized starlight (Hall, 1949; Hiltner, 1949) and its interpretation as coming from the absorption of the unpolarized starlight by magnetically aligned grains in the foreground medium (Davis and Greenstein, 1951; see Andersson et al., 2015 for a recent review). With the advent of observational capabilities,

the magnetic fields in the ISM in general, and star-forming molecular clouds in particular, are becoming increasingly better characterized. For example, the PLANCK all-sky survey of the dust polarization leaves little doubt that a rather ordered magnetic field component exists in all nearby clouds (Planck Collaboration et al., 2015), as reviewed by H. B. Li in this volume. Observations have also revealed the prevalence of the magnetic field on the smaller scales of individual cores of molecular clouds and protostellar envelopes, as reviewed by Pattle et al., Crutcher & Kemball, and Hull & Zhang, in this volume.

As an illustration, we show in **Figure 1** the dust polarization detected with the Atacama Large Millimeter/submillimeter Array (ALMA) around the Class 0 protostar B335 (Maury et al., 2018). The polarization orientations are rotated by 90° to trace the magnetic field directions in the plane of the sky. It is immediately clear that not only a magnetic field is present on large scale, but also it shows coherent structures. In particular, the (projected) field appears to be significantly pinched near the equator of the system, as defined by the bipolar molecular outflows. The pinch is direct evidence that the magnetic field is interacting with the envelope material, through a magnetic tension force. Whether such a magnetic force is strong enough to affect the dynamics of the core collapse and especially disc formation is the question that we seek to address in this article.

There is some indirect evidence that magnetic fields may play a role in disk (and binary) formation. For example, Maury et al. (2010) concluded that core collapse models with a relatively strong magnetic field are more consistent with their IRAM-PdBI observations of Class 0 protostellar systems than their hydrodynamic (non-magnetic) counterparts. In the particular case of B335, the specific angular momentum is observed to decrease rapidly toward the central protostar, with a rotationally supported disk (if present) smaller than $\sim$ 10 au (Yen et al., 2015). The decrease in specific angular momentum and small disk could result naturally from the braking by a magnetic field, which has now been mapped in detail with ALMA (Maury et al., 2018). In addition, there is some tentative evidence that protostellar sources with misaligned magnetic field and rotation axis (inferred from outflow direction) tend to have larger disks (e.g., Segura-Cox et al., 2016), which is consistent with magnetized disk formation simulations (e.g., Hennebelle and Ciardi, 2009; Joos et al., 2012; Krumholz et al., 2013; Li et al., 2013b).

Finding evidence for the magnetic field on the disc scale is more challenging. Spatially resolved dust polarization has been detected in discs around a number of young stellar objects, using the Submillimeter Array (SMA; e.g., Rao et al., 2014), the Combined Array for Research in Millimeter-wave Astronomy (CARMA; e.g., Stephens et al., 2014; Segura-Cox et al., 2015), the Very Large Array (VLA; e.g., Cox et al., 2015; Liu et al., 2016), and especially ALMA (e.g., Kataoka et al., 2017; Stephens et al., 2017; Alves et al., 2018; Bacciotti et al., 2018; Cox et al., 2018; Girart et al., 2018; Harris et al., 2018; Hull et al., 2018; Lee et al., 2018; Sadavoy et al., 2018; Dent et al., 2019). However, with the exception of BHB 07-11 (Alves et al., 2018) and possibly a few other cases, the majority of the sources do not show any evidence for dust grains aligned by the generally expected toroidal magnetic fields; their polarization patterns are better explained by dust scattering instead (Kataoka et al., 2015, 2016; Yang et al., 2016a,b, 2017). The reader is referred to Hull & Zhang's article in this volume for a more detailed discussion. In any case, whether and how the disc is connected to the protostellar envelope through a magnetic field remain to be determined observationally.

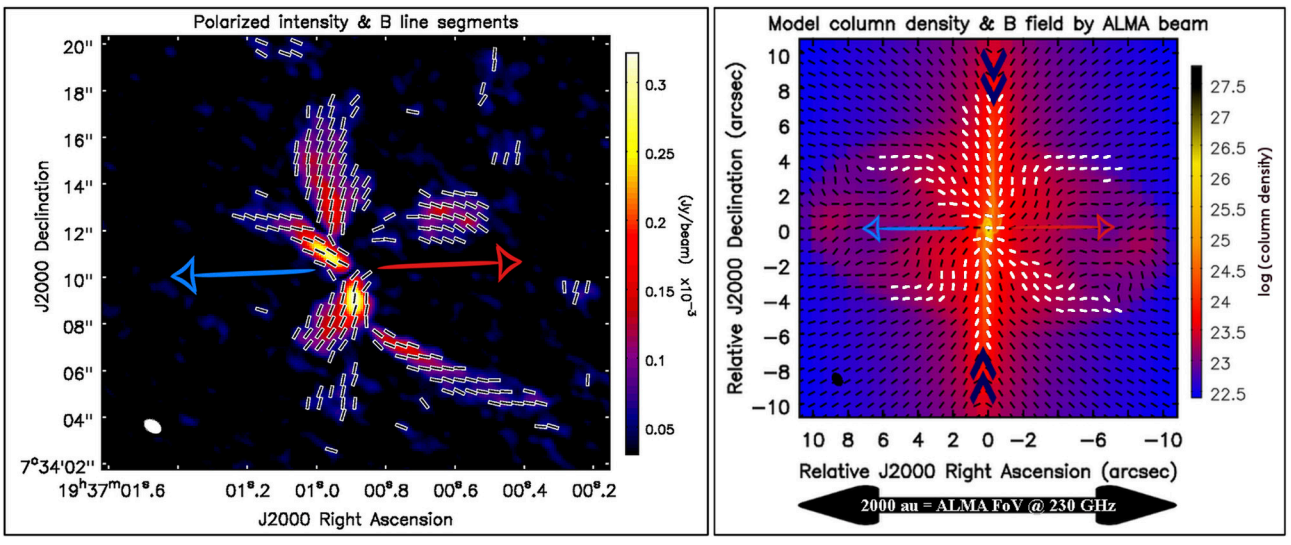

FIGURE 1 | An example of the magnetic field traced by dust polarization around an observation (left-hand panel) and a numerical model (right-hand panel) of the solar-type Class 0 protostar B335. The background image in the right-hand panel is the ALMA polarized dust continuum emission, and the superimposed lines infer the magnetic field orientations (i.e. the polarization angle rotated by 90°). This figure is inspired by Figures 1 and 3 of Maury et al. (2018), and was created by A. J. Maury for this publication.

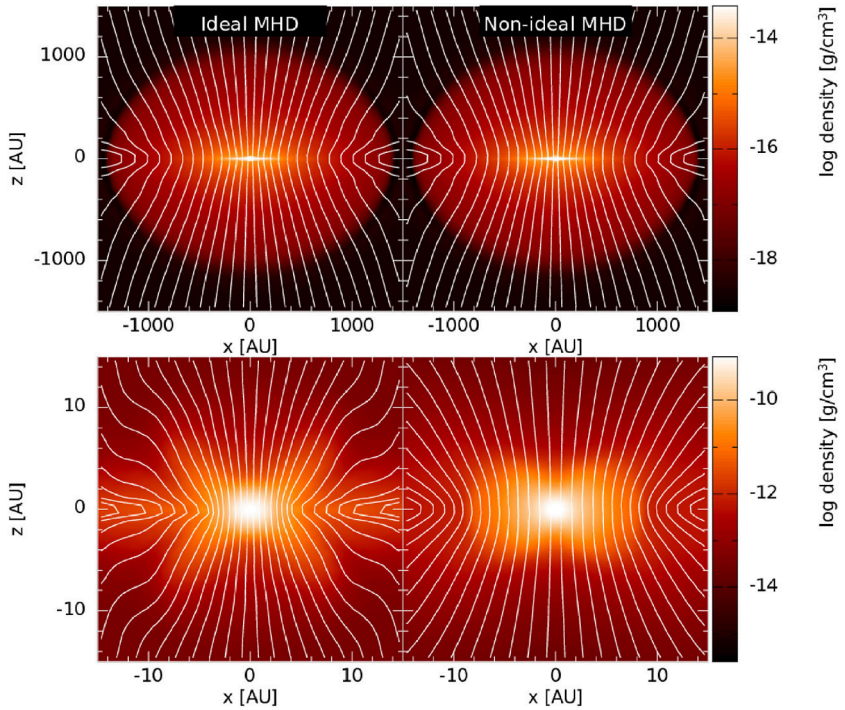

FIGURE 2 | The magnetic field lines superimposed on a density slice during the first hydrostatic core phase for ideal and non-ideal MHD simulations. The initial mass-to-flux ratio is five times the critical value (i.e., $\mu_0 = 5$). In ideal MHD, the magnetic field lines are dragged inwards as the cloud core collapses, creating the characteristic hour-glass shape. On the large scale, the non-ideal effects have minimal effect on the strength and structure of the magnetic field, whereas on the small scale, the neutral particles flow through the magnetic field lines to form the first hydrostatic core, while preventing the magnetic field lines from becoming pinched and preventing a strong magnetic field from building up in the core (bottom). These images are inspired by Figure 2 of Price and Bate (2007) and Figure 1 of Bate et al. (2014).

3. DISC FORMATION IN THE IDEAL MHD LIMIT

The simplest approximation when modeling magnetic fields is to use ideal MHD, where it is assumed that the gas is sufficiently ionized such that the magnetic field is well coupled to the bulk neutral gas. In this approximation, the induction equation is given by

$$\frac{\partial \boldsymbol{B}}{\partial t} = \nabla \times (\boldsymbol{v} \times \boldsymbol{B}) \,, \tag{4}$$

where $\boldsymbol{v}$ is the gas velocity and $\boldsymbol{B}$ is the magnetic field. Since the gas is tied to the magnetic field lines, the lines are dragged in as the gas collapses (assuming $\mu_0 > 1$), causing a characteristic hour-glass shape; see the left-hand column of **Figure 2** for numerical results, which nicely complement the observational results in **Figure 1**. This pinching effect becomes less prominent as the magnetic field becomes stronger, since the stronger field is harder to bend (see Figure 2 of Price and Bate, 2007). If the magnetic field were to be dragged all the way into the central stellar object, then the stellar field strength would be millions of gauss, which is much higher than the kilo-gauss field typically observed in young stars. This is a manifestation of the so-called "magnetic flux problem" in star formation (Babcock and Cowling, 1953; Mestel and Spitzer, 1956; Shu et al., 2006)[2].

In purely hydrodynamics simulations, large protostellar discs can form due to conservation of angular momentum. In the presence of magnetic fields, angular momentum can be efficiently transported away from the collapsing central region (e.g., Mestel and Spitzer, 1956; Mouschovias and Paleologou, 1979, 1980; Basu and Mouschovias, 1994, 1995; Mellon and Li, 2008), and not enough angular momentum remains for a rotationally supported disc to form. This is the magnetic braking catastrophe, as first demonstrated by Allen et al. (2003, see also the pioneering work by Tomisaka, 2000): Rotationally supported discs do not form in idealized numerical simulations in the presence of magnetic fields of realistic strengths. Analytical studies by Joos et al. (2012) estimated that $\mu \leq 10$ should be enough to suppress disc formation.

There have been many numerical simulations of disc formation under the assumption of ideal MHD. Most simulations are initialized with a rotating spherical cloud core which is threaded with a magnetic field that is parallel to the rotation axis (section 3.1). However, molecular clouds contain turbulent flows

[2]Given the focus of this review, the magnetic flux problem will not be addressed here; see Wurster et al. (2018d) for a recent discussion.

(e.g., Heyer and Brunt, 2004), which form large scale structures (e.g., Padoan and Nordlund, 2002; McKee and Ostriker, 2007; Ward-Thompson et al., 2010), and it is these chaotic structures that can collapse to form cores that ultimately collapse to form stars and protostellar discs. Thus, a more realistic scenario is that the magnetic fields are initially misaligned with the rotation axis (see section 3.2), or the velocity field initially contains a significant turbulent component (see section 3.3).

3.1. Idealized Initial Conditions

The simplest and most common initial condition for disc formation from a collapsing molecular cloud core is to thread a magnetic field parallel to the rotation axis of a spherical core that is in solid-body rotation; the initial magnetic field strength is characterized by the initial mass-to-flux ratio, μ_0, for the core as a whole. The early ideal MHD simulations were performed under the assumption of an isothermal or barotropic equation of state and were performed in two-dimensional (e.g., Allen et al., 2003; Mellon and Li, 2008) or three-dimensional (e.g., Machida et al., 2004; Price and Bate, 2007; Hennebelle and Fromang, 2008; Duffin and Pudritz, 2009; Machida et al., 2011; Zhao et al., 2011; Santos-Lima et al., 2012; Seifried et al., 2012). Later studies were radiative three-dimensional calculations that included simplified ideal magnetic fields calculations (e.g., Boss, 1997, 1999), or solved the complete MHD equations (e.g., Boss, 2002, 2005, 2007, 2009; Commerçon et al., 2010; Tomida et al., 2010, 2013; Bate et al., 2014). Subsequent studies included radiation and ideal magnetic fields as part of a parameter study (e.g., Tomida, 2014; Tomida et al., 2015; Tsukamoto et al., 2015b; Vaytet et al., 2018; Wurster et al., 2018a,c,d). When using moderate to strong magnetic fields, these studies all found efficient magnetic braking, and none of them formed a protostellar disc.

For a demonstration of the magnetic braking catastrophe, Bate et al. (2014) simulated four magnetized models and one hydrodynamical model. **Figure 3** shows the face-on and edge-on gas densities in a slice through the first hydrostatic core, and these figures are representative of ideal MHD models in the literature. With weak or no magnetic fields ($\mu_0 = 100$, Hydro), the first core is rotating quickly enough and is massive enough to become bar unstable and forms a gravitationally unstable disc that is dominated by spiral arms (e.g., Bate, 1998, 2010, 2011; Saigo and Tomisaka, 2006; Saigo et al., 2008; Machida et al., 2010).

As analytically predicted by Joos et al. (2012), there are no discs in the models with $\mu_0 \leq 10$, however, pseudo-discs do form; a pseudo-disc is an over-density of gas around a protostar that is not centrifugally supported, not in equilibrium, and is resulted from the anisotropy of the magnetic support against gravity (Galli and Shu, 1993; Li and Shu, 1996), although, throughout the literature, authors use this term to refer to a variety of disc-like structures. The pseudo-discs in Bate et al. (2014) do not increase in size, nor do they ever become Keplerian discs. This study clearly demonstrates the magnetic braking catastrophe, at least up to the formation of the first hydrostatic core.

When considering the long term evolution of the system, discs may yet form. In their ideal MHD simulations, Machida and Hosokawa (2013) find that discs form in their models by the end of the Class 0 phase, and increase in mass into the Class I phase. As the envelope is depleted, the magnetic braking becomes less efficient, which allows these discs to form as speculated earlier by Mellon and Li (2008, see also section 4.2.1); when their strongly magnetized models end in the Class I phase, the discs have masses ∼40 per cent of the mass of the protostar itself.

This leads to the open question of when protostellar discs form. If they form in later stages (e.g., Class I or II), then there may be no magnetic braking catastrophe in the numerical simulations; if they form early in the Class 0 phase, then the catastrophe persists, and one must go beyond the idealized initial conditions to form a discs if the magnetic field is strong and well-coupled to the gas. Future observations are required to determine when in the star formation process its protostellar disc forms.

3.2. Misaligned Magnetic Fields

There have been several studies investigating the impact of misaligned magnetic fields on the formation of discs (eg., Matsumoto and Tomisaka, 2004; Machida et al., 2006; Matsumoto et al., 2006; Hennebelle and Ciardi, 2009; Joos et al., 2012; Krumholz et al., 2013; Li et al., 2013b; Lewis et al., 2015; Lewis and Bate, 2017). Similar to the literature, we define the angle θ such that the angular momentum $\boldsymbol{J}$ and magnetic field $\boldsymbol{B}$ vectors are parallel and aligned when $\theta \equiv 0^\circ$. The components of the angular momentum that are parallel and perpendicular to the magnetic field are $\boldsymbol{J}_\parallel = |\boldsymbol{J} \cdot \boldsymbol{B}| / |\boldsymbol{B}|$ and $\boldsymbol{J}_\perp = |\boldsymbol{J} \times \boldsymbol{B}| / |\boldsymbol{B}|$, respectively.

Two-dimensional analytical models of collapsing cylinders by Mouschovias and Paleologou (1979) found that magnetic braking can reduce the angular momentum of a cloud by a few orders of magnitude if $\theta = 90^\circ$. All other parameters being the same, this indicates that systems with $\theta = 0^\circ$ are more likely to form discs than their $\theta = 90^\circ$ counterparts. However, this pioneering work did not include the gravitational collapse, which can modify the magnetic field configuration and affect the braking efficiency.

The results of Mouschovias and Paleologou (1979) were later confirmed by the three-dimensional models of Matsumoto and Tomisaka (2004). In these models, the perpendicular component of the angular momentum, $\boldsymbol{J}_\perp$, decreased faster than the parallel component, indicating that magnetic braking was more efficient for the perpendicular component. This component decreased rapidly and by a few orders of magnitude in their models with $\theta = 45$ and 90°; the component $\boldsymbol{J}_\parallel$ decreased only by a factor of a few in their models with $\theta = 0$ and 45° (see their Figure 4). These results broadly agree with the parameter study by Machida et al. (2006), who also find that magnetic braking acts primarily on the component perpendicular to the rotation axis. They conclude that discs form more easily when $\theta = 0^\circ$.

Several studies, however, reach the opposite conclusion: Discs form more easily when $\theta = 90^\circ$. Joos et al. (2012) find that massive discs form in all of their misaligned models, requiring as little as $\theta = 20^\circ$ to allow a massive disc to form. The exceptions are their models with the strongest magnetic field strength, $\mu_0 = 2$, in which discs never form, independent of θ. As the evolution progresses, the pseudo-discs continue to accrete, increasing both their mass and angular momentum; more massive discs form for larger θ, and faster rotating discs form for weaker magnetic fields (larger μ_0).

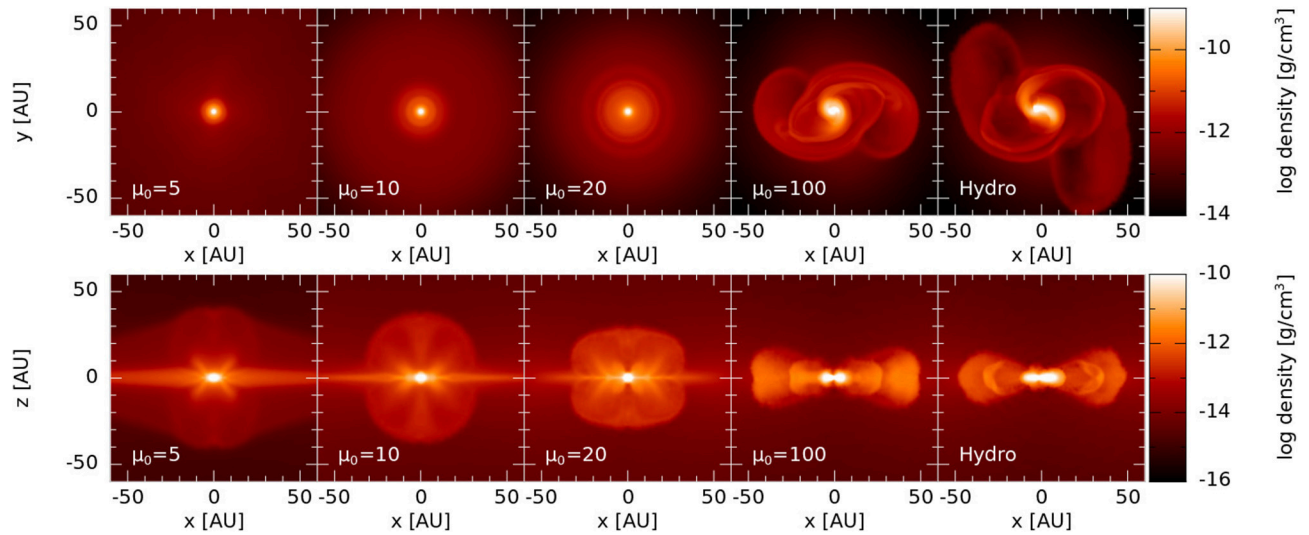

FIGURE 3 | The face-on (top row) and edge-on (bottom row) gas density in a slice through the centre of the first hydrostatic core for ideal MHD models of decreasing magnetic field strength (increasing μ_0; left to right) and a pure hydrodynamics model. Gravitationally unstable discs form for $\mu_0 > 20$, whereas only pseudo-discs only form in the remaining models. This is inspired by Figure 4 of Bate et al. (2014), and was created for this publication using the data from Bate et al. (2014).

Except in the case of very strong magnetic fields, Li et al. (2013b) find the initially misaligned magnetic field allows rotationally supported discs to form in the dense cores, even when no discs form in the aligned models. In their models, the magnetic field lines are wrapped into a snail-shaped curtain when $\theta = 90°$, and this configuration hinders outflows. With negligible outflows, the angular momentum remains near the protostar, allowing the formation of the disc.

In Lewis and Bate (2017), the pseudo-disc increases in size and forms larger arms as the misalignment increases since the gas can easily flow along the horizontal magnetic field component. For $\theta = 20$ and 45°, the pseudo-discs are warped such that the inner regions are perpendicular to the rotation-axis, while the outer regions are perpendicular to the magnetic field.

In summary, misalignment between the rotation axis and the magnetic field lines may promote or hinder the formation of rotationally supported discs. Machida et al. (2006) found that for slow rotators, magnetic braking aligns the rotation axis and the magnetic field (in agreement with Lewis and Bate, 2017 if comparing the outer parts of the discs), and for fast rotators, the magnetic field aligns through a dynamo action. This suggests that the effect of misalignment may, at least in part, be a result of the initial conditions. Thus, at the time of writing, the effect of misalignment on disc formation is inconclusive.

3.3. Turbulent Initial Conditions

There are several studies of disc formation in massive turbulent magnetized molecular clouds ($M > 100 M_\odot$; e.g., Santos-Lima et al., 2012, 2013; Seifried et al., 2012, 2013; Myers et al., 2013; Li et al., 2014; Fielding et al., 2015; Gray et al., 2018), as well a number of studies that begin from turbulent, low-mass cores ($M < 10 M_\odot$; e.g., Matsumoto and Hanawa, 2011; Joos et al., 2013; Li et al., 2014; Matsumoto et al., 2017; Lewis and Bate, 2018); for scales consistent with this review, we focus on the latter studies. These low-mass simulations reach contradicting results, with some studies suggesting increased turbulence promotes disc formation (Joos et al., 2013; Li et al., 2014), while others suggest it hinders discs formation (Matsumoto and Hanawa, 2011; Matsumoto et al., 2017; Lewis and Bate, 2018).

Figure 4 illustrates the effect of how increasing the Mach number, $\mathcal{M}$, of the turbulent velocity field imposed on a slowly rotating, pre-stellar cloud core hinders disc formation. As the Mach number is increased, the resulting pseudo-disc is smaller, and the rotating gas becomes less Keplerian. For $\mathcal{M} = 1$, the system is disrupted and no pseudo-disc forms. In the most turbulent model, the initial ratio of turbulent to rotational energy is $E_{\rm turb}/E_{\rm rot} = 26$, and Lewis and Bate (2018) argue that $E_{\rm turb}/E_{\rm rot} \lesssim 1$ is required for the formation of a pseudo-disc. By increasing the initial rotation such that $E_{\rm turb}/E_{\rm rot} = 1.6$, they form a disrupted pseudo-disc, while increasing it such that $E_{\rm turb}/E_{\rm rot} = 1.06$, they form a slowly rotating pseudo-disc.

On slightly larger spatial scales before the first hydrostatic core forms, Matsumoto and Hanawa (2011) find that models without turbulence produce axisymmetric oblate or prolate clouds (depending on initial mass). As the turbulence is increased, the clouds become more chaotic and disrupted. As the gravitational collapse continues, each model eventually forms a spherical first core surrounded by a disc-like envelope (with the exception of one model with weak magnetic fields and moderate turbulence).

Following the long-term evolution of their turbulent models, Matsumoto et al. (2017) formed a disc in each model, and the disc mass and radius increased with time. In agreement with non-turbulent studies, they consistently found larger discs in models with weaker magnetic fields. However, they also consistently found larger discs in models with weaker turbulence (all other parameters being held constant). Thus, they concluded, turbulence hindered disc formation.

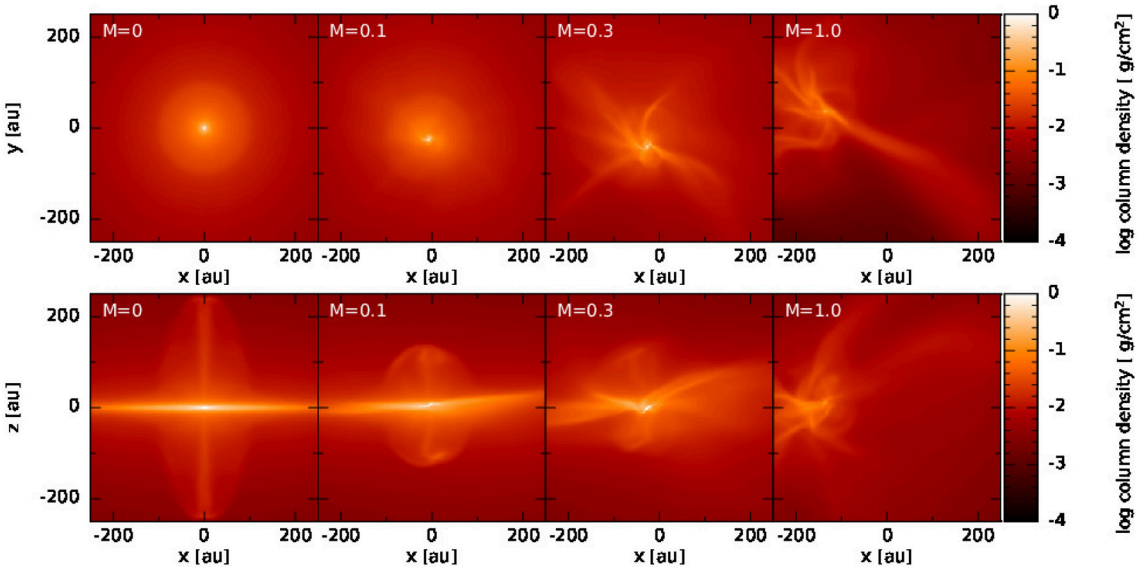

FIGURE 4 | The face-on **(Top row)** and edge-on **(Bottom row)** gas column density projections showing disc formation in models in a relatively strong ($\mu_0 = 5$) magnetic field with a turbulent velocity field imposed onto a solid-body rotation. The Mach number is shown in each panel. The figures are taken ∼500 yr after sink formation (i.e., when the maximum density has reached $\rho_{\rm max} = 10^{-10}$ g cm^{-3}). Increasing turbulence in these models hinders disc formation. These are inspired by Figure 7 of Lewis and Bate (2018), but are from lower resolution models.

In their strongest magnetic field model, the disc radii and masses were nearly indistinguishable between their two turbulent models ($\mathcal{M} = 0.5, 1$; see their Figures 5, 6), suggesting that at these magnetic field strengths, the strength of turbulence played a secondary role in the cloud's evolution.

Contrary to the above, **Figure 5** illustrates the effect of how increasing the Mach number, $\mathcal{M}$ promotes disc formation. In the models of Li et al. (2014), a disc-like structure begins to form at $\mathcal{M} = 0.5$, however, it is still partially disrupted. At larger Mach numbers, the disc becomes more prominent, and for $\mathcal{M} = 1$, has a Keplerian rotational profile. They conclude that the promotion of disc formation is a result of the warping of the pseudo-disc and the magnetic decoupling-triggered reconnection of the severely pinched field lines near the central object.

Joos et al. (2013) presented a suite of models, and found massive discs in all their simulations with weak magnetic fields, and very small discs in their strongly magnetized models; at both strong and weak magnetic field strength, the disc growth rate is approximately independent of the Mach number. For moderate magnetic field strengths, the disc growth rates are dependent on the Mach number such that a $\sim 0.6 M_\odot$ disc forms in the same length of time it takes to form a $\sim 0.4 M_\odot$ disc in a laminar model (the model has an initial mass of $5 M_\odot$). In these models, the turbulence diffuses the magnetic field out of the central region, generating an effective magnetic diffusivity prompted by magnetic reconnection, and hence weakening the magnetic field (see also Weiss, 1966; Santos-Lima et al., 2012). Turbulence also induces a misalignment between the rotation axis and the magnetic field (see also Seifried et al., 2012; Gray et al., 2018) of $20 - 60°$, which reduces the magnetic braking. The effect of these two mechanisms is to allow for larger discs to form.

In summary, turbulence can hinder or promote disc formation. Thus, as with the studies of initial magnetic field alignment, initial conditions will likely play an important role in determining the outcome.

4. NON-IDEAL MHD AND DISC FORMATION

It is well known that the dense, star-forming, cores of molecular clouds are lightly ionized (Bergin and Tafalla, 2007), with detailed models finding ionization fractions as low as $n_{\rm e}/n_{\rm H_2} = 10^{-14}$ (Nakano and Umebayashi, 1986; Umebayashi and Nakano, 1990; Nishi et al., 1991; Nakano et al., 2002). The low ionization level means that the magnetic field is no longer perfectly coupled to the bulk neutral material, rendering the ideal MHD approximation questionable. A proper treatment of the non-ideal MHD effects is required, including a detailed calculation of the abundances of the electrons, ions and charged dust grains.

There are several methods of numerically modeling multiple species. They can be modeled explicitly (e.g., Inoue et al., 2007; Inoue and Inutsuka, 2008, 2009), where each species has its own continuity and momentum equation. In this method, the species interact directly with each other through terms in the momentum and energy equations. Electrons are not explicitly treated because their mass is much less than those of other particles. The induction equation is as given in Equation 4, except that it only includes the velocity of the charged species.

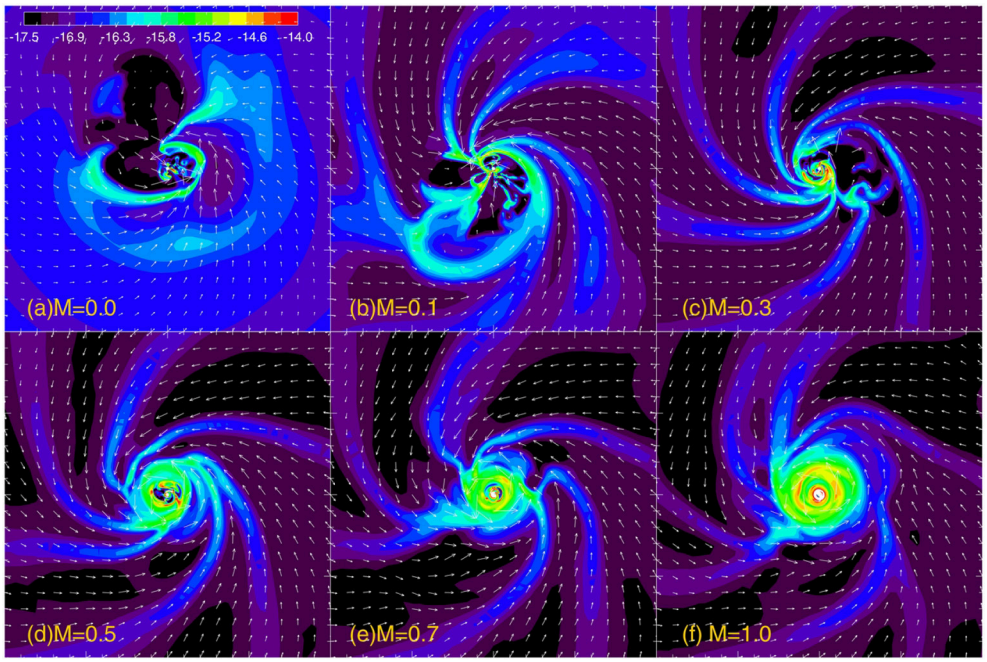

FIGURE 5 | The gas density (color) and velocity (vectors) in the mid-plane for models with increasing Mach number (printed in the bottom left-hand corner of each frame). Each frame is ∼1,400 au on each side. In this suite of simulations, increasing the Mach number promotes disc formation. This is Figure 2 of Li et al. (2014). ©AAS. Reproduced with permission.

Under the assumptions that mass density is dominated by the neutral mass density, and that collisions occur predominantly between charged species and neutrals, then the inertia and pressure of the charged species and collisions between charged species can be safely neglected (e.g., O'Sullivan and Downes, 2006; Rodgers-Lee et al., 2016). In this approximation, each species has its own continuity equation, but only the neutral species has a momentum equation; additional equations are included to govern the interactions (e.g., energy transfer) between the species. Other studies include dust grains, and include continuity equations for the neutral gas and total grain density but not the charged gas species (e.g., Ciolek and Mouschovias, 1993, 1994; Tassis and Mouschovias, 2005a,b, 2007a,b,c; Kunz and Mouschovias, 2009, 2010).

The continuity equation can be constructed to evolve total mass density rather than species mass density if the strong coupling approximation is invoked; in this approximation, the ion pressure and momentum are negligible compared to that of the neutrals, and the magnetic field and neutral flows evolve on a timescale that is long compared to the timescale of the charged particles (e.g., Wardle and Koenigl, 1993; Ciolek and Mouschovias, 1994; Mac Low et al., 1995; Wardle and Ng, 1999; Choi et al., 2009). In approximation, there is one continuity and one momentum equation. This method is typically used by those studying the formation of protostellar discs (e.g., Krasnopolsky et al., 2010; Tomida et al., 2015; Tsukamoto et al., 2015b,a; Masson et al., 2016; Wurster et al., 2016; Vaytet et al., 2018; Wurster et al., 2018c).

Except in the cases where the charged and neutral species interact directly through their own momentum equations, the induction equation is modified to account for the species of different charges, viz.,

$$\begin{aligned}\frac{\partial \boldsymbol{B}}{\partial t} &= \left.\frac{\partial \boldsymbol{B}}{\partial t}\right|_{\rm ideal} + \left.\frac{\partial \boldsymbol{B}}{\partial t}\right|_{\rm non\text{-}ideal} \\ &= \boldsymbol{\nabla} \times (\boldsymbol{v} \times \boldsymbol{B}) - \boldsymbol{\nabla} \times \\ &\left\{ \eta_{\rm O} (\boldsymbol{\nabla} \times \boldsymbol{B}) + \eta_{\rm H} (\boldsymbol{\nabla} \times \boldsymbol{B}) \times \hat{\boldsymbol{B}} - \eta_{\rm A} \left[(\boldsymbol{\nabla} \times \boldsymbol{B}) \times \hat{\boldsymbol{B}} \right] \times \hat{\boldsymbol{B}} \right\}, \end{aligned} \tag{5}$$

where all the micro-physics governing the species properties and interactions is contained within the coefficients, η. In the case of, e.g., O'Sullivan and Downes (2006) and Rodgers-Lee et al. (2016), the species densities are taken directly from the continuity equation, whereas sub-grid algorithms are required if not explicitly evolving the density of the charged species or if using the strong coupling approximation. The three coefficients represent the different regimes of interactions between the neutrals and the charged particles:

1. Ohmic resistivity, $\eta_{\rm O}$: ions, electrons and charged grains are completely decoupled from the magnetic field,
2. Hall effect (ion-electron drift), $\eta_{\rm H}$: massive particles (ions, charged grains) are decoupled from the magnetic field while electrons remain coupled (i.e., the electrons are frozen into the magnetic field, which drifts through the ions and charged grains), and

3. Ambipolar diffusion (ion-neutral drift), $\eta_{\rm A}$: both massive charged particles (ions, charged grains) and electrons are coupled to the magnetic field (i.e., the charged particles are frozen into the magnetic field, which drifts through the neutrals).

Ohmic resistivity and ambipolar diffusion are both diffusive terms, with the associated energy dissipation given by Wurster et al. (2014)

$$\frac{\partial u}{\partial t} = \left.\frac{\partial u}{\partial t}\right|_{\rm ideal} + \frac{\left|\boldsymbol{\nabla}\times\boldsymbol{B^2}\right|}{\rho}\eta_{\rm O} + \frac{1}{\rho}\left\{|\boldsymbol{\nabla}\times\boldsymbol{B}|^2 - \left[(\boldsymbol{\nabla}\times\boldsymbol{B})\cdot\hat{\boldsymbol{B}}\right]^2\right\}\eta_{\rm A}, \tag{6}$$

where u is the internal energy. Physically, these non-ideal processes allow the neutral and selected ionized particles to slip through the magnetic field, which typically leads to a redistribution of the magnetic field lines relative to the bulk neutral matter. In particular, a concentration of matter may not lead to as large an increase in the magnetic field strength as in the ideal MHD limit.

Ohmic resistivity is typically important at the highest densities, such as the inner midplane regions of the protostellar disc, while ambipolar diffusion typically dominates at relatively low densities, such as the molecular cloud core itself, and the upper and outer regions of the protostellar disc (e.g., Shu et al., 2006; Wardle, 2007; Machida et al., 2008; Wurster et al., 2018a). **Figure 2** shows the magnetic field lines on both the molecular cloud core and protostellar disc scales for ideal and non-ideal MHD. When using ideal MHD, the magnetic field lines are dragged into the center, causing an enhancement in the magnetic field strength, and creating the expected "hour-glass shaped" field lines. Since the neutral gas can slip through the magnetic field lines in the non-ideal MHD case, the field lines do not become as pinched, resulting in a weaker central magnetic field strength.

The Hall effect is dispersive rather than dissipative, and typically dominates at the intermediate densities between the two diffusive regimes, including in parts of the dense core and protostellar disc (e.g., Sano and Stone, 2002a,b; see Figure 3 of Li et al., 2011 for an illustrative example). Unlike the other terms, the Hall effect can change the magnetic geometry of the system without any dissipation. Specifically, it will generate a toroidal magnetic field from a poloidal magnetic field, where the resulting magnetic torques can induce a rotation in an otherwise non-rotating medium (for an example, see Figure 15 of Li et al., 2011; for a sketch of the processes, see Figure 1 of Tsukamoto et al., 2017). When the polarity of the initial poloidal magnetic field is reversed, the resulting toroidal magnetic field and rotation would also be in the opposite direction. This has implications if the system is already rotating, since the Hall effect will either transport angular momentum to or from the central region, thus will either increase or decrease the angular velocity of the local gas (Wardle, 2007; Braiding and Wardle, 2012a). Assuming $\eta_{\rm H} < 0$ (as is reasonable in protostellar discs; Tsukamoto et al., 2015a; Marchand et al., 2016; Wurster, 2016; Wurster et al., 2016), then the Hall effect will increase the angular momentum in the disc if the magnetic field vector and rotation axis are initially anti-aligned, and will decrease the angular momentum if the two vectors are aligned (e.g., Krasnopolsky et al., 2011; Li et al., 2011; Braiding and Wardle, 2012a,b; Tsukamoto et al., 2015a, 2017; Wurster et al., 2016, 2018a,c).

4.1. Calculating the Non-ideal MHD Coefficients

When using the modified induction equation as given in Equation 5, the dependencies of the non-ideal coefficients are $\eta \equiv \eta\left(\rho_{\rm gas}, T_{\rm gas}, B, n_j, m_j, eZ_j\right)$ for an arbitrary number of species, where n_j, m_j and eZ_j are the number density, mass and electric charge of species j, and only the charged species (i.e., $eZ_j \neq 0$) contribute to η; the equations can be found in Wardle and Ng (1999), Wardle (2007) and other papers, and thus will not be repeated here.

The species to be included in the calculation must be selected in advance, with the reaction rates between them determined experimentally or estimated theoretically (e.g., as presented in the UMIST Database; McElroy et al., 2013). The ionization sources must also be selected in advance, with the primary source for disc formation in typical molecular clouds being cosmic rays. The cosmic ray ionization rate is given by $\zeta_{\rm cr} \approx \zeta_{\rm cr,0}\exp\left(-\Sigma/\Sigma_{\rm cr}\right)$, where $\Sigma_{\rm cr}$ is the characteristic column density for the attenuation of cosmic rays and $\zeta_{\rm cr,0}$ is the unattenuated cosmic ray ionization rate. The latter has a canonical value of $\zeta_{\rm cr,0} = 10^{-17}$ s^{-1} for the Milky Way ISM (Spitzer and Tomasko, 1968; Umebayashi and Nakano, 1981). The cosmic ray ionization rate can vary from one region to another in the Galaxy (e.g., it is expected to be higher near a supernova remnant that can accelerate cosmic rays) and be modified by propagation effects, such as magnetic mirroring (e.g., Chandran, 2000; Padovani et al., 2009). As a cloud core collapses and a protostellar disc forms, the inner regions of the disc are shielded from cosmic rays (Padovani et al., 2014), thus other ionization sources become important, such as ionization by X-rays and energetic particles from young stellar objects, and ionization by radionuclide decay. Canonical X-rays are slightly less energetic and have a shorter attenuation depths than cosmic rays, thus will only affect the surface of the disc (e.g., Igea and Glassgold, 1999; Turner and Sano, 2008). The ionization from radionuclide decay, however, has rates ranging from $\zeta_{\rm r} \approx 10^{-23}$ to 10^{-18} s^{-1} depending on the ionization source (e.g., Kunz and Mouschovias, 2009; Umebayashi and Nakano, 2009) and can persist throughout the disc. Thus, ionization from radionuclide decay may be the dominant ionization source near the midplane of the disc.

Along with ions, molecular clouds include dust grains, which are important in coupling the magnetic field to the gas (Nishi et al., 1991). These are typically included in the numerical calculations of η assuming a single grain population with a fixed radius, fixed bulk density, and a fixed gas-to-dust ratio. However, the grain size greatly affects the strength of the non-ideal effects; for example, Wurster et al. (2018b) showed that smaller grains tend to yield larger non-ideal MHD coefficients (see their Figure 2). However, molecular clouds do not contain a single grain size; one commonly used size distribution is the MRN (Mathis et al., 1977) grain distribution, $\mathrm{d}n_{\rm g}(a)/\mathrm{d}a \propto n_{\rm H}a^{-3.5}$, where $n_{\rm H}$ is the number density of the hydrogen nucleus and $n_{\rm g}(a)$ is the number density of grains with a radius smaller than a (Draine and Lee,

1984). The non-ideal MHD coefficients are sensitive to the upper and lower limits of the distribution. In particular, removing the very small grains of ∼10 to a few 100 Å from the distribution would increase the ambipolar diffusivity by $\sim 1-2$ orders of magnitude at number densities below 10^{10} cm^{-3} (Zhao et al., 2016).

As the non-ideal coefficients increase in value (either by increasing local density, magnetic field strength, or decreasing ionization rate), the numerical timestep required for numerical stability decreases (e.g., Mac Low et al., 1995; Choi et al., 2009; Bai, 2014; Wurster et al., 2014, 2018b). The two-dimensional simulations of Kunz and Mouschovias (2009) and Dapp et al. (2012) include all the above discussed ionization mechanisms to allow for a very low ionization fraction, and end their calculations prior to the timestep becoming prohibitively small. However, this is not currently computationally possible for global three-dimensional simulations of disc formation and evolution. Thus, as a crude approximation, studies typically use $\zeta = \zeta_{\rm cr,0} = 10^{-17}$ s^{-1}.

There are several private algorithms (e.g., Nakano et al., 2002; Kunz and Mouschovias, 2009; Okuzumi, 2009; Dapp et al., 2012; Tsukamoto et al., 2015b; Zhao et al., 2016, 2018; Higuchi et al., 2018) and publicly available codes (e.g Marchand et al., 2016; Wurster, 2016) that solve chemical networks of varying complexity to calculate the number density of each species, which can then be used to self-consistently calculate the non-ideal MHD coefficients. These algorithms include ionization and reconnection amongst the included species (including dust), and ionization from cosmic rays. The results are expectedly dependent on the complexity of the networks and the input parameters, however, there is broad qualitative agreement among them. However, a direct comparison is difficult due to the parameter dependence, and even a single algorithm can produce widely varying results with small changes to its input parameters (e.g., the assumed dust grain properties).

4.2. Numerical Models

Ohmic resistivity was the first non-ideal effect to be included in analytical and numerical studies in attempts to prevent the magnetic braking catastrophe. This was followed by ambipolar diffusion, and finally the Hall effect. As discussed below, various studies reached various conclusions. However, recent three-dimensional radiation magnetohydrodynamical simulations (Tsukamoto et al., 2015a, 2017; Wurster et al., 2016, 2018c) have suggested that the Hall effect can prevent the magnetic braking catastrophe.

4.2.1. Ohmic Resistivity and Ambipolar Diffusion

A first attempt to solve the magnetic braking catastrophe was by Shu et al. (2006). They derived the equations governing the gravitational collapse of a molecular cloud core in the presence of a magnetic field, and included the effects of Ohmic diffusion. They noted that in order to reduce the magnetic field strength near the central stellar object to a value consistent with meteoritic evidence, $\eta_{\rm O} \approx 2\times10^{20}$ cm^2 s^{-1} is required, which is a few orders of magnitude larger than estimated from kinetic theory (Shu et al., 2006). A similar calculation by Krasnopolsky et al. (2010) was able to reduce the required value using different assumptions, but $\eta_{\rm O}$ remained uncomfortably high. Recent calculations of $\eta_{\rm O}$ using chemical networks of varying complexity have shown that this value can be reached in the center of the first hydrostatic core during the first core phase (e.g., Marchand et al., 2016; Wurster, 2016). However, this high value persists over a very small $\rho - T$ phase-space, and values much lower than this are expected in the protostellar disc and background medium.

Contradicting the results of Shu et al. (2006) and Krasnopolsky et al. (2010), the three-dimensional numerical studies of Inutsuka et al. (2010) and Machida et al. (2011) formed protostellar discs; the latter formed a disc of r $\gtrsim$ 100 au and their simulations used sink particles and the barotropic equation of state and were evolved until most of the envelope (i.e., the gas that was initially in the cloud core) had been accreted. As the envelope was accreted, the Alfvén waves became less efficient at transporting angular momentum from the gas near the protostar to the remaining envelope (simply because there was not much gas remaining in the envelope, as pointed out earlier in Mellon and Li, 2008). With less envelope and hence less magnetic braking, a ∼40 au protostellar disc formed by $\sim10^4$ yr which grew to ∼100 au by $\sim10^5$ yr. A similar study by Wurster et al. (2016) found ∼10 au discs formed after $\sim3\times10^4$ yr; this smaller disc was likely a result of a lower Ohmic resistivity and a larger sink particle. Even smaller Ohmic-enabled discs were found in the semi-analytic calculations of Dapp and Basu (2010) and Dapp et al. (2012).

Ohmic resistivity is expected to become important at the highest densities, especially late in the star formation process. However, by this stage, unless $\eta_{\rm O}$ was much higher than expected early on or the envelope was mostly depleted, the magnetic field could have already extracted enough angular momentum from the less dense regions to prevent discs from forming.

This possibility provides a strong motivation to study ambipolar diffusion, which was expected to be important in the early stages of star formation when the density of the molecular cloud core was still relatively low. This had long been included in cloud core formation models as a method to diffuse the magnetic field to initiate the quasi-static formation in an initially magnetically subcritical cloud and the later collapse of the cloud core (as first demonstrated by Mouschovias, 1976, 1977, 1979). On the smaller scales regarding protostar formation, it was hoped that this process could diffuse out enough of the magnetic field to permit a Keplerian disc to form. Analytical calculations by Hennebelle et al. (2016) predicted that an ∼18 au disc should form when accounting for ambipolar diffusion for parameters typical of molecular cloud cores (see their Equation 13); this is much smaller than the 100 au-scale discs that would typically form in the absence of a magnetic field (see also Equation 14 of Hennebelle et al., 2016).

Numerical simulations have not provided a consensus regarding the effect of ambipolar diffusion. Mellon and Li (2009) re-performed their ideal MHD study from Mellon and Li (2008) but included ambipolar diffusion. Using two-dimensional axisymmetric models, they concluded that ambipolar diffusion alone did not weaken the magnetic braking enough to allow the formation of a disc that is resolvable by their simulations. Their conclusion held even when using a cosmic ray ionization rate ten times lower than canonical (i.e., making the system

more neutral). However, their spherical-polar numerical domain included a 6.7 au hole at the center, thus discs below this radius could necessarily not form, and the artificial boundaries may have suppressed disc formation at radii even slightly larger than the boundary (for comment on effect of sink sizes, see Machida et al., 2014).

In the three-dimensional studies of Masson et al. (2016), Keplerian discs formed during the first hydrostatic core phase in their models that included ambipolar diffusion. Using a mass-to-flux ratio of 5 times critical and an initial rotation of $\beta_{\rm rot} = 0.02$ (the ratio of rotational energy to gravitational potential energy), a disc of ∼80 au formed; for similar initial conditions, small, disc-like structures formed at late times when using ideal MHD. By inclining the initial magnetic field (c.f. section 3.2) by $\theta = 40^\circ$ in the ideal MHD models, there was negligible effect on disc formation, leading them to conclude that ambipolar diffusion was more important than inclination in terms of disc formation. In their models with ambipolar diffusion, the discs formed more easily and were more massive in the non-aligned case.

Figure 6 shows the angular momentum in the first hydrostatic core (i.e., the gas that would collapse to form a rotationally supported disc if enough angular momentum is present) for three three-dimensional models by Tsukamoto et al. (2015b). After the first core has formed, there is least angular momentum in the ideal MHD model; there is approximately twice as much angular momentum when Ohmic resistivity is included, and approximately 5 times more when both Ohmic resistivity and ambipolar diffusion are included. In their model with Ohmic resistivity + ambipolar diffusion, a small ∼1 au disc formed. At a similar time in the model with Ohmic resistivity + ambipolar diffusion by Tomida et al. (2015), a centrifugally supported disc of radius ∼5 au formed, although it did not have a Keplerian profile; in their counterpart model that only included Ohmic resistivity, the centrifugally supported disc was ∼1 au.

Although the disc in Tomida et al. (2015) is only ∼5 au and remains approximately constant in size throughout their simulation, they expect it to grow with time as the envelope is depleted, as discussed above and in Tomida et al. (2013). By the end of the simulation (approximately 1 year after the formation of the stellar core), the disc is supported by the centrifugal force with substantial contribution from the gas pressure. At this time, the disc is rotating rapidly enough that it has triggered the gravito-rotational instability (e.g., Toomre, 1964; Bate, 1998; Saigo and Tomisaka, 2006; Saigo et al., 2008) and become non-axisymmetric.

In a followup study, Tomida et al. (2017) modeled the long term evolution using sink particles. In agreement with their previous work, the disc stays small at early times due to efficient magnetic braking. As the disc evolves, magnetic braking becomes less efficient both due to the magnetic field dissipating in the disc and the dissipation of the envelope. Eventually, the disc becomes unstable, forming an $m = 2$ perturbation (see also Hennebelle et al., 2016). The gravitational torques become more efficient at transporting angular momentum than the magnetic fields, thus control the future evolution of the disc. By the end of the Class I phase, the disc radius is in excess of 200 au.

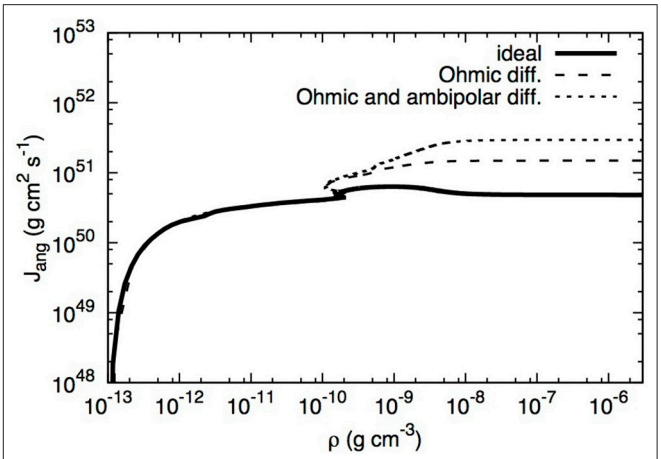

FIGURE 6 | The angular momentum in the first hydrostatic core for models using ideal MHD, Ohmic diffusion, and Ohmic and ambipolar diffusions. The Ohmic+ambipolar model has enough angular momentum to form a ∼1 au rotationally-supported disc, whereas discs do not form in the other two models. This figure is inspired by Figure 6 of Tsukamoto et al. (2015b), and was created by Y. Tsukamoto for this publication using the data published in Tsukamoto et al. (2015b).

Vaytet et al. (2018) modeled the collapse to the stellar core including Ohmic resistivity + ambipolar diffusion. During the first core phase, the gas is funneled into the core along two dense filaments that arise from an initial $m = 2$ perturbation. The disc-like structure in their ideal MHD model is "puffier" than their resistive counterpart, but neither model appears to form a disc. One month after the formation of the stellar core, they find a "second core disc" of radius $r \lesssim 0.1$ au that has a Keplerian velocity profile.

Zhao et al. (2016, 2018) stressed the importance of the grain size on the ambipolar diffusivity (see also Dapp et al., 2012). They explored a range of grain sizes, initial magnetic field strengths and rotation rates, and found that rotationally supported structures often form early around the stellar seed but disappear at later times. Such structures can persist and grow to sizes of 20–40 au even for a rather strong initial magnetic field corresponding to a dimensionless mass-to-flux ratio of $\mu_0 = 2.4$ when the very small grains are removed from an MRN size distribution. Whether such grains are indeed removed or not, through, e.g., grain coagulation, remain to be determined.

4.2.2. Complete Non-ideal MHD Description

Including the Hall effect in numerical models becomes computationally expensive due to the small timestep constraint (e.g., Sano and Stone, 2002a; Bai, 2014; Tsukamoto et al., 2015a; Wurster et al., 2016, 2018b), thus, at the time of writing, there are only a few global two-dimensional (Krasnopolsky et al., 2011; Li et al., 2011) and three-dimensional (Tsukamoto et al., 2015a, 2017; Wurster et al., 2016, 2018a,c,d) global disc-formation studies that include this process.

The first simulation to include the Hall effect in a global simulation was Krasnopolsky et al. (2011). This simulation was a two-dimensional axisymmetric Eulerian simulation that

included gravity of a pre-formed protostar but no self-gravity amongst the gas. The Hall coefficient, $\eta_{\rm H}$, was set as a constant positive value, which is the opposite sign as found by later studies (e.g., Tsukamoto et al., 2015a; Marchand et al., 2016; Wurster, 2016; Wurster et al., 2016). They formed rotationally supported discs in all models that included the Hall effect, except for their model with the weakest resistivity.

Figure 7 shows the rotational profiles for three models in the study by Krasnopolsky et al. (2011), where they varied the initial alignment of the rotation and magnetic field vectors. In the outer regions of their models, the Hall effect is too weak to have any significant effect on the evolution of the gas, thus the gas simply follows the initial velocity profile combined with the effect of gravity. In the inner region of all three models, the Hall effect spins up the gas to reach a Keplerian profile. In the aligned model (left panel), the Hall effect contributes to the initial rotation, whereas in the anti-aligned case (right panel), it detracts from it; in the anti-aligned case, the Hall velocity is strong enough to cancel out the initial rotational profile and form a counter-rotating disc with a Keplerian profile.

In their followup study, Li et al. (2011) self-consistently calculated the value for $\eta_{\rm H}$, which now necessarily varied in space and time; $\eta_{\rm H} < 0$, and the maximum of its absolute value was lower than the value used in their previous study. Given their parameter space, no model formed a rotationally supported disc. The Hall effect did spin up the material of the gas near the protostar, but it was not significant enough to reach Keplerian velocities.

Subsequent studies led by Tsukamoto and Wurster modeled the three-dimensional collapse of a molecular cloud core through to at least the end of the first core phase. The models typically included self-consistent calculations of the non-ideal MHD coefficients, included flux limited diffusion and excluded sink particles[3]. When using the canonical, unattenuated cosmic ray ionization rate of $\zeta_{\rm cr} = 10^{-17}{\rm s}^{-1}$, Tsukamoto et al. (2015a) and Wurster et al. (2018c) find that rotationally supported discs form if the magnetic field and rotation vectors are anti-aligned, whereas no disc forms if they are aligned. The top row in **Figure 8** shows the gas column density for ideal MHD, non-ideal MHD and hydrodynamic models in the midplane during the first hydrostatic core phase. In both studies (Tsukamoto et al., 2015a; Wurster et al., 2018c), the disc has a radius of $r \sim 25$ au, and becomes bar-unstable during the first core phase. For comparison, a purely hydrodynamics model formed a disc of ∼60 au, and this disc is formed even earlier during the first core phase due to the lack of magnetic support. Expectedly, the purely hydrodynamic disc has the largest angular momentum in the first core and/or disc (see **Figure 9**). However, the Hall effect in the anti-aligned non-ideal model decreases magnetic braking, permitting the angular momentum to remain in the gas near/in the first core, and hence permitting the disc to form. The angular momentum in the disc is approximately half that of the purely hydrodynamics model (Wurster et al., 2018c). By aligning the magnetic field and the rotation axis, the angular momentum again decreases by a factor of ∼12, to a value too low for a disc to form.

The models presented in **Figures 6**, **9** use slightly different initial conditions, however, both ideal MHD models have similar final angular momenta in their first cores, thus can be reasonably compared. By including Ohmic resistivity and ambipolar diffusion, the angular momentum in the first core increases to $L_{\rm fc} \sim 2.5 \times 10^{51}{\rm g\ cm^2\ s^{-1}}$ (dotted line in **Figure 6**), which is higher than when the three non-ideal terms are added in the aligned orientation (double-dot line in **Figure 9**). Therefore, some of the angular momentum gain caused by Ohmic resistivity and ambipolar diffusion is lost by including the Hall effect in an aligned orientation. As previously discussed, additional angular momentum is gained by the Hall effect in the anti-aligned case. Summarily, the order of angular momenta in the first core is $L_{\rm fc}$(ideal MHD) $<$ $L_{\rm fc}$(Ohmic+ambipolar+Hall; aligned) $<$ $L_{\rm fc}$(Ohmic+ambipolar) $<$ $L_{\rm fc}$(Ohmic+ambipolar+Hall; anti−aligned) $<$ $L_{\rm fc}$(Hydrodynamics).

Given that the anti-aligned non-ideal model formed a large disc while the aligned model did not, Tsukamoto et al. (2015a) proposed that there should be a bi-modality in the population of discs around stars—that is, approximately half of the Class 0 objects should have protostellar discs. However, this assumption was made assuming the magnetic field was either aligned or anti-aligned with the rotation axis. Since there is observational evidence that the magnetic field appears to be randomly orientated with respect to the rotation axis, at least on the 1000 au scale (Hull et al., 2013), Tsukamoto et al. (2017) modeled various angles between the rotation axis and the magnetic field. The angular momentum in the first core is shown in **Figure 10** for various initial orientations, and it differs by an order of magnitude between the two extreme angles: $\theta = 0$ and 180°. Changing the angle by 45° from either extreme value has a minimal effect on the angular momentum evolution, and even a change of 70° only changes the final angular momentum by a factor of a few. Thus, the models with $\theta \neq 90°$ have angular momenta evolutions that are similar to either $\theta = 0$ or 180°, suggesting that, even if the initial magnetic fields are randomly orientated with the rotation axis, the bi-modality in disc sizes should exist, with large discs forming for $\theta \gtrsim 100°$ and negligible discs forming for $\theta \lesssim 80°$.

The magnetic field strength and plasma β for an ideal model and two non-ideal MHD models are shown in bottom two rows of **Figure 8**. As expected, the magnetic field is dragged into the core of the ideal MHD model, thus its first hydrostatic core has a very strong field strength. However, in the non-ideal cases, the neutrals can slip through the magnetic field, thus a dense core forms, but its central magnetic field strength is weaker than in the ideal MHD model. Unlike the neutrals, the velocities of the charged particles decrease and they approach the core due to the non-ideal effects. This allows the charged particles, and the magnetic flux they drag in, to pileup in a torus around the core. This torus of charged particles expands outwards in radius as more charged particles pile up, further enhancing the magnetic field. This is a demonstration of a "magnetic wall," which is thoroughly discussed in the two-dimensional models of Tassis and Mouschovias (2005b) and first predicted to exist analytically

[3] Wurster et al. (2016) used 6.7 au sink particles together with a barotropic equation of state in their disc formation study using PHANTOM (Price et al., 2018).

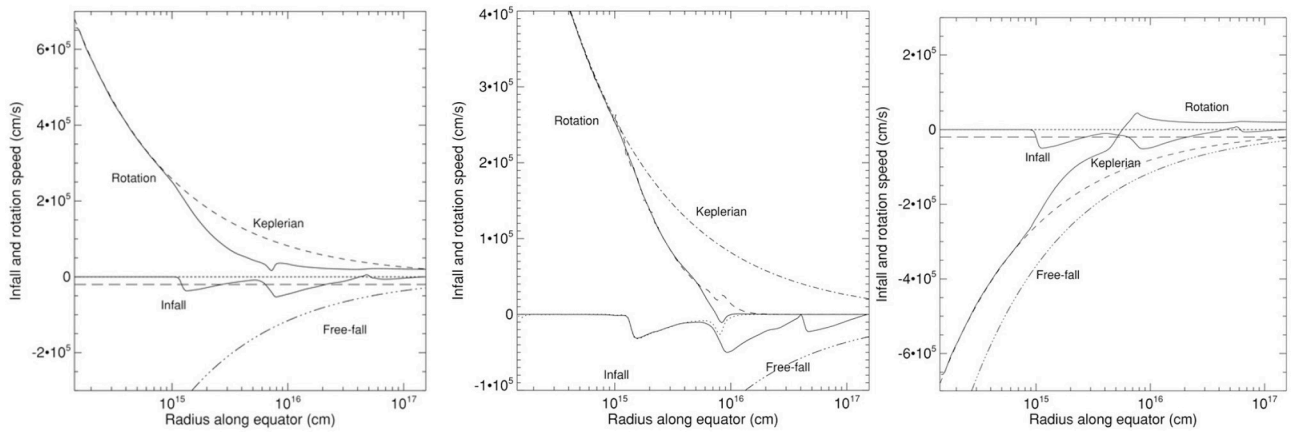

FIGURE 7 | Rotational profiles for aligned, no rotation and anti-aligned two-dimensional models. The initial rotation in the rotating models is $v_\phi = -2 \times 10^4$ cm s^{-1}. The gas in the outer regions is governed by the initial conditions, while Keplerian discs of $r \sim 10^{15}$ cm form in all three models. These are Figures 1b, 3b, and 2b of Krasnopolsky et al. (2011). ©AAS. Reproduced with permission.

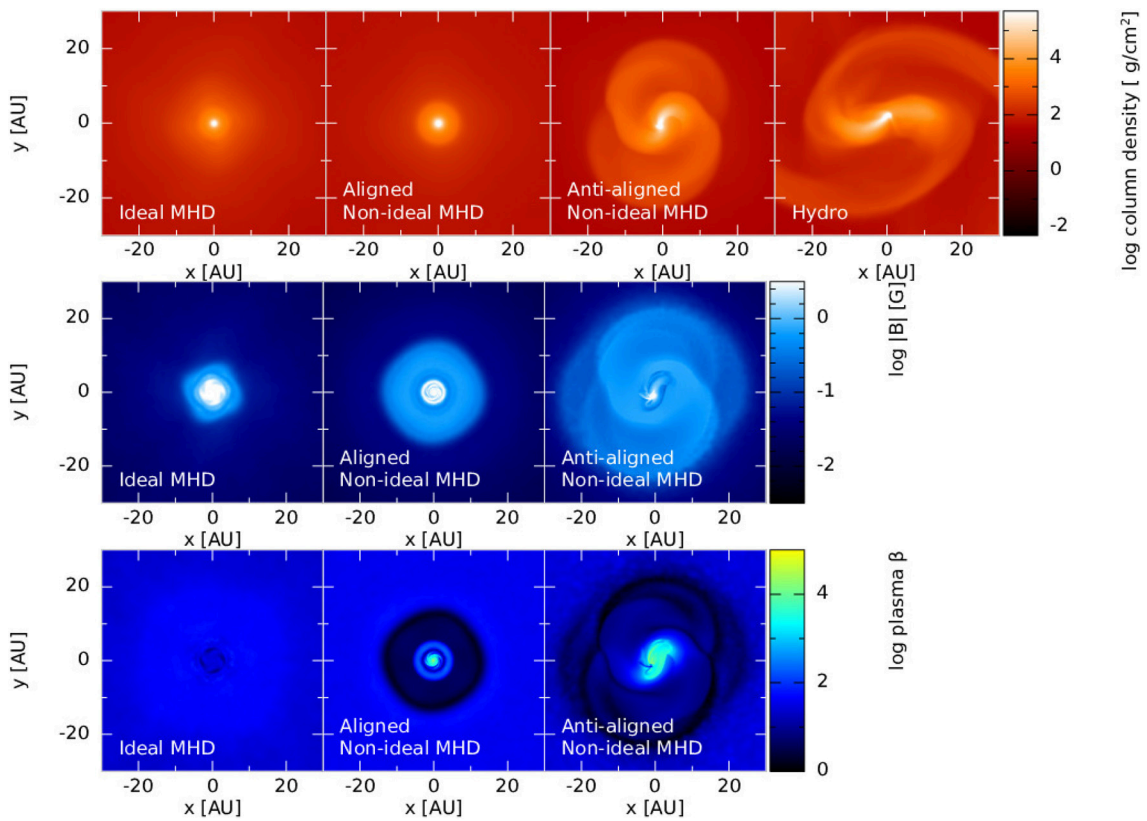

FIGURE 8 | The gas column density **(top)**, magnetic field strength **(middle)** and plasma β **(bottom)** in a slice through the mid-plane of an ideal MHD model, two non-ideal MHD models (Ohmic+ambipolar+Hall; $\zeta_{cr} = 10^{-17}$s^{-1}) with different initial orientations of the magnetic field, and purely hydrodynamics model (top row only). The snapshots are near the end of the first core phase. When the rotation and magnetic field vector are aligned, the non-ideal MHD model is similar to the ideal MHD model with no disc, but when the vectors are anti-aligned, a gravitationally unstable disc forms, similar to the hydrodynamics model. The maximum magnetic field strength is in the disc for the anti-aligned non-ideal model, while it is in the center of the first core for the remaining two models. The disc in the anti-aligned model is supported by gas pressure. The figure is adapted/inspired by Figures 1 and 8 of Wurster et al. (2018c) and Figure 1 of Tsukamoto et al. (2015a) and was created for this publication using the data from Wurster et al. (2018c).

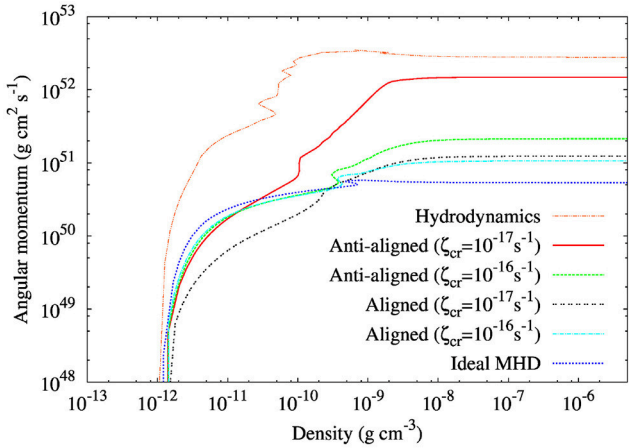

FIGURE 9 | The angular momentum in the first hydrostatic core which collapses to form a disc for models with various cosmic ray ionization rates, ζ_{cr}. Only the purely hydrodynamics and the anti-aligned ($\zeta_{cr} = 10^{-17}$s^{-1}) models form discs, both of which become bar-unstable. The angular momentum of the ideal MHD model differs slightly from that shown in **Figure 6** due to different initial conditions. This is adapted from Figure 2 of Wurster et al. (2018c), and was created for this publication using the data from Wurster et al. (2018c).

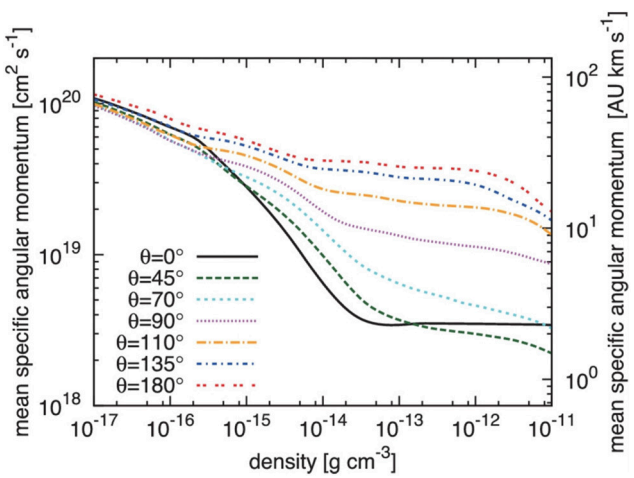

FIGURE 10 | The angular momentum in the first hydrostatic core which collapses to form a disc for non-ideal MHD models at various angles θ between the rotation axis and magnetic field vector; $\theta = 0°$ represents the aligned case. Except for the $\theta = 90°$ case, the angular momenta are grouped around $\theta = 0°$ and $\theta = 180°$, suggesting a bi-modality in disc sizes. This figure is Figure 6 of Tsukamoto et al. (2017), and is reproduced with permission.

by Li and McKee (1996). In the non-ideal MHD models shown above, the magnetic wall occurs at $r \sim 1$–3 au from the center of the core.

In the domain presented in **Figure 8**, plasma $\beta > 1$, indicating that gas pressure is greater than magnetic pressure everywhere. The disc in the anti-aligned model has plasma $\beta > 100$ due to the rotationally supported disc; in the disc, magnetic diffusion is efficient and the magnetic flux is removed from the region (Tsukamoto et al., 2015a). In the center of the aligned model, plasma β becomes high, but this region is small enough that disc formation is not possible. Finally, the strong magnetic field in the ideal simulations yields plasma $\beta < 100$ over the entire computational domain, again iterating the importance of magnetic fields in that model. Similar results with slightly lower values of plasma β are reached in Tsukamoto et al. (2015a, see their Figure 1), since their initial magnetic field strength is stronger than in the figures presented here.

These two studies discussed here, Tsukamoto et al. (2015a) and Wurster et al. (2018c), both modeled the gravitational collapse of a 1M$_\odot$ molecular cloud core, however many of the remaining initial parameters were different, including the initial rotation rate, radius, magnetic field strength, and microphysical properties that controlled the coefficients of the non-ideal MHD terms. Thus, gravitationally unstable discs forming around the time of the first core in anti-aligned models that include the Hall effect is a robust result.

Concurrent to the study of Tsukamoto et al. (2015a), Wurster et al. (2016) studied the evolution of the disc until ∼5,000 yr after the formation of the protostar; these simulations included sink particles and the barotropic equation of state. In their aligned models that include, respectively, only the Hall effect and all three non-ideal MHD terms, no discs formed. In their anti-aligned models, ∼38 and ∼15 au discs formed, respectively. The disc radius in the non-ideal model with the three terms remained approximately constant until the end of the simulation, while the model with only the Hall effect decreased slightly to ∼20 au by 5,000 yr. Neither disc formed a bar-mode instability, since this instability would be stabilized by the sink particle. The disc in the non-ideal model is smaller than the ∼25 au discs from the previous studies, but both sink particles and the barotropic equation of state have been shown to reduce the disc sizes compared to models that exclude sink particles and include radiation hydrodynamics (e.g., Tomida et al., 2013; Machida et al., 2014; Lewis and Bate, 2018; Wurster et al., 2018c).

Finally, the effect of the cosmic ray ionization rate was studied in Wurster et al. (2018a). When the ionization rate is increased by even a factor of ten compared to the canonical value for the interstellar medium, the angular momentum in the first core is low enough such that no discs form, independent of magnetic field orientation. This indicates the importance of the value of the cosmic ray ionization rate: if it is too high, then rotationally supported discs cannot form, despite the initial conditions. This may have implications for, e.g., starburst galaxies (e.g., Bisbas et al., 2015) or the Galactic Center (e.g., Oka et al., 2005) where the cosmic ray ionization rate is 10–100 times higher than the canonical value of $\zeta_{cr,0} = 10^{-17}$ s^{-1}.

5. CONCLUSION

Protostellar discs have been observed around young stars at all stages of evolution, and naturally form alongside their host star. The star forming environment has strong magnetic fields, low ionization fractions, and non-laminar velocity flows. The focus of this article is on how the magnetic field affects the formation

of disc in lightly ionized molecular cloud cores where non-ideal MHD effects are important.

Early numerical simulations of star formation that include strong magnetic fields under the ideal MHD approximation fail to form discs during the star forming process; this is known as the magnetic braking catastrophe. Given that discs are observed, this highlighted the need for including additional physical ingredients in the simulations. Several studies continued using the ideal MHD approximation, but made their initial conditions less idealized. By misaligning the magnetic field and rotation vectors, larger or smaller discs could form depending on the study, hence likely depending on the initial conditions. The misalignment can be naturally induced by a turbulent velocity field, which can speed up the removal of magnetic flux near the center and thus promote disc formation through enhanced magnetic reconnection; however, increasing turbulence has also been numerically observed to hinder disc formation. Given that reconnection in ideal MHD simulations is necessarily realized numerically, this process needs to be evaluated more carefully.

Molecular clouds are observed to be mostly neutral, and the interaction between neutral and charged particles gives rise to three non-ideal effects: Ohmic resistivity, ambipolar diffusion and the Hall effect. When ambipolar diffusion is included in numerical simulations, small discs of 1–5 au are expected to form over an extended period of time; even larger discs can form if very small grains are removed from the grain size distribution. When the Hall effect is included and the magnetic field vector is anti-aligned with the rotation axis, larger discs of 25 au or more form. However, these results may be subject to initial conditions and the choice of parameters such as dust grain properties or ionization rates.

In summary, considerable progress has been made in averting the magnetic braking catastrophe, through turbulence and related field-rotation misalignment in the ideal MHD limit, enhanced ambipolar diffusion, and especially the Hall effect in the case of anti-aligned magnetic field and rotation axis. Further progress is expected when these and other effects are taken into account together, especially in simulations that can run to the end of the protostellar accretion phase of star formation. These more comprehensive models will be guided by, and be used to interpret, the increasingly more detailed multi-scale observations of the gas kinematics and magnetic fields in the ALMA era.

AUTHOR CONTRIBUTIONS

JW and Z-YL were both responsible for writing and editing the manuscript.

ACKNOWLEDGMENTS

We would like to thank the referees for very thorough and insightful reports which have greatly contributed to the quality of this manuscript. JW acknowledges support from the European Research Council under the European Community's Seventh Framework Programme (FP7/2007- 2013 grant agreement no. 339248). Z-YL is supported in part by NASA NNX14AB38G, NASA 80NSSC18K1095 and NSF AST-1815784 and AST-1716259. The calculations for this review were performed on the DiRAC Complexity machine, jointly funded by STFC and the Large Facilities Capital Fund of BIS (STFC grants ST/K000373/1, ST/K0003259/1 and ST/M006948/1), and the University of Exeter Supercomputer, a DiRAC Facility jointly funded by STFC, the Large Facilities Capital Fund of BIS, and the University of Exeter, and the RIVANNA computer cluster at the University of Virginia.

REFERENCES

Allen, A., Li, Z.-Y., and Shu, F. H. (2003). Collapse of magnetized singular isothermal toroids. II. Rotation and magnetic braking. *Astrophys. J.* 599, 363–379. doi: 10.1086/379243

Alves, F. O., Girart, J. M., Padovani, M., Galli, D., Franco, G. A. P., Caselli, P., et al. (2018). Magnetic field in a young circumbinary disk. *Astron. Astrophys.* 616:A56. doi: 10.1051/0004-6361/201832935

Andersson, B.-G., Lazarian, A., and Vaillancourt, J. E. (2015). Interstellar dust grain alignment. *Annu. Rev. Astron. Astrophys.* 53, 501–539. doi: 10.1146/annurev-astro-082214-122414

Babcock, H. W., and Cowling, T. G. (1953). General magnetic fields in the Sun and stars (Report on progress of astronomy). *Month. Notices of the RAS* 113, 357–381. doi: 10.1093/mnras/113.3.357

Bacciotti, F., Girart, J. M., Padovani, M., Podio, L., Paladino, R., Testi, L., et al. (2018). ALMA observations of polarized emission toward the CW Tau and DG Tau protoplanetary disks: constraints on dust grain growth and settling. *Astrophys. J.* 865:L12. doi: 10.3847/2041-8213/aadf87

Bai, X.-N. (2014). Hall-effect-controlled gas dynamics in protoplanetary disks. I. Wind solutions at the inner disk. *Astrophys. J.* 791:137. doi: 10.1088/0004-637X/791/2/137

Basu, S., and Mouschovias, T. C. (1994). Magnetic braking, ambipolar diffusion, and the formation of cloud cores and protostars. 1: axisymmetric solutions. *Astrophys. J.* 432, 720–741. doi: 10.1086/174611

Basu, S., and Mouschovias, T. C. (1995). Magnetic braking, ambipolar diffusion, and the formation of cloud cores and protostars. III. Effect of the initial mass-to-flux ratio. *Astrophys. J.* 453:271. doi: 10.1086/176387

Bate, M. R. (1998). Collapse of a molecular cloud core to stellar densities: the first three-Dimensional calculations. *Astrophys. J.* 508, L95–L98. doi: 10.1086/311719

Bate, M. R. (2010). Collapse of a molecular cloud core to stellar densities: the radiative impact of stellar core formation on the circumstellar disc. *Month. Notices RAS* 404, L79–L83. doi: 10.1111/j.1745-3933.2010.00839.x

Bate, M. R. (2011). Collapse of a molecular cloud core to stellar densities: the formation and evolution of pre-stellar discs. *Month. Notices RAS* 417, 2036–2056. doi: 10.1111/j.1365-2966.2011.19386.x

Bate, M. R., Tricco, T. S., and Price, D. J. (2014). Collapse of a molecular cloud core to stellar densities: stellar-core and outflow formation in radiation magnetohydrodynamic simulations. *Month. Notices RAS* 437, 77–95. doi: 10.1093/mnras/stt1865

Bergin, E. A., and Tafalla, M. (2007). Cold dark clouds: the initial conditions for star formation. *Annu. Rev. Astron. Astrophys.* 45, 339–396. doi: 10.1146/annurev.astro.45.071206.100404

Bisbas, T. G., Papadopoulos, P. P., and Viti, S. (2015). Effective destruction of CO by Cosmic rays: implications for tracing H_2 gas in the universe. *Astrophys. J.* 803:37. doi: 10.1088/0004-637X/803/1/37

Boss, A. P. (1993). Collapse and fragmentation of molecular cloud cores. I - Moderately centrally condensed cores. *Astrophys. J.* 410, 157–167. doi: 10.1086/172734

Boss, A. P. (1997). Giant planet formation by gravitational instability. *Science* 276, 1836–1839. doi: 10.1126/science.276.5320.1836

Boss, A. P. (1999). Collapse and fragmentation of molecular cloud cores. VI. Slowly rotating magnetic clouds. *Astrophys. J.* 520, 744–750. doi: 10.1086/307479

Boss, A. P. (2002). Collapse and fragmentation of molecular cloud cores. VII. Magnetic fields and multiple protostar formation. *Astrophys. J.* 568, 743–753. doi: 10.1086/339040

Boss, A. P. (2005). Collapse and fragmentation of molecular cloud cores. VIII. Magnetically supported infinite sheets. *Astrophys. J.* 622, 393–403. doi: 10.1086/428113

Boss, A. P. (2007). Collapse and fragmentation of molecular cloud cores. IX. Magnetic braking of initially filamentary clouds. *Astrophys. J.* 658, 1136–1143. doi: 10.1086/512061

Boss, A. P. (2009). Collapse and fragmentation of molecular cloud cores. X. Magnetic braking of prolate and oblate cores. *Astrophys. J.* 697, 1940–1945. doi: 10.1088/0004-637X/697/2/1940

Boss, A. P., and Myhill, E. A. (1995). Collapse and fragmentation of molecular cloud cores. III. Initial differential rotation. *Astrophys. J.* 451:218. doi: 10.1086/176213

Bourke, T. L., Myers, P. C., Robinson, G., and Hyland, A. R. (2001). New OH zeeman measurements of magnetic field strengths in molecular clouds. *Astrophys. J.* 554, 916–932. doi: 10.1086/321405

Braiding, C. R., and Wardle, M. (2012a). The hall effect in star formation. *Month. Notices RAS* 422, 261–281. doi: 10.1111/j.1365-2966.2012.20601.x

Braiding, C. R., and Wardle, M. (2012b). The Hall effect in accretion flows. *Month. Notices RAS* 427, 3188–3195. doi: 10.1111/j.1365-2966.2012.22001.x

Chandran, B. D. G. (2000). Confinement and isotropization of galactic cosmic rays by molecular-cloud magnetic mirrors when turbulent scattering is weak. *Astrophys. J.* 529, 513–535. doi: 10.1086/308232

Choi, E., Kim, J., and Wiita, P. J. (2009). An explicit scheme for incorporating ambipolar diffusion in a magnetohydrodynamics code. *Astrophys. J.* 181, 413–420. doi: 10.1088/0067-0049/181/2/413

Ciolek, G. E., and Mouschovias, T. C. (1993). Ambipolar diffusion, interstellar dust, and the formation of cloud cores and protostars. I. Basic physics and formulation of the problem. *Astrophys. J.* 418:774. doi: 10.1086/173435

Ciolek, G. E., and Mouschovias, T. C. (1994). Ambipolar diffusion, interstellar dust, and the formation of cloud cores and protostars. 3: typical axisymmetric solutions. *Astrophys. J.* 425, 142–160. doi: 10.1086/173971

Codella, C., Cabrit, S., Gueth, F., Podio, L., Leurini, S., Bachiller, R., et al. (2014). The ALMA view of the protostellar system HH212. The wind, the cavity, and the disk. *Astron. Astrophys.* 568:L5. doi: 10.1051/0004-6361/201424103

Commerçon, B., Hennebelle, P., Audit, E., Chabrier, G., and Teyssier, R. (2010). Protostellar collapse: radiative and magnetic feedbacks on small-scale fragmentation. *Astron. Astrophys.* 510:L3. doi: 10.1051/0004-6361/200913597

Cox, E. G., Harris, R. J., Looney, L. W., Li, Z.-Y., Yang, H., Tobin, J. J., et al. (2018). ALMA's polarized view of 10 protostars in the perseus molecular cloud. *Astrophys. J.* 855:92. doi: 10.3847/1538-4357/aaacd2

Cox, E. G., Harris, R. J., Looney, L. W., Segura-Cox, D. M., Tobin, J., Li, Z.-Y., et al. (2015). High-resolution 8 mm and 1 cm polarization of IRAS 4A from the VLA nascent disk and multiplicity (VANDAM) survey. *Astrophys. J.* 814:L28. doi: 10.1088/2041-8205/814/2/L28

Crutcher, R. M. (1999). Magnetic fields in molecular clouds: observations confront theory. *Astrophys. J.* 520, 706–713. doi: 10.1086/307483

Dapp, W. B., and Basu, S. (2010). Averting the magnetic braking catastrophe on small scales: disk formation due to Ohmic dissipation. *Astron. Astrophys.* 521:L56. doi: 10.1051/0004-6361/201015700

Dapp, W. B., Basu, S., and Kunz, M. W. (2012). Bridging the gap: disk formation in the Class 0 phase with ambipolar diffusion and Ohmic dissipation. *Astron. Astrophys.* 541:A35. doi: 10.1051/0004-6361/201117876

Davis, L. Jr., and Greenstein, J. L. (1951). The polarization of starlight by aligned dust grains. *Astrophys. J.* 114:206. doi: 10.1086/145464

Dent, W. R. F., Pinte, C., Cortes, P. C., Ménard, F., Hales, A., Fomalont, E., et al. (2019). Submillimetre dust polarisation and opacity in the HD163296 protoplanetary ring system. *Month. Notices RAS.* 482, L29–L33. doi: 10.1093/mnrasl/sly181

Draine, B. T., and Lee, H. M. (1984). Optical properties of interstellar graphite and silicate grains. *Astrophys. J.* 285, 89–108. doi: 10.1086/162480

Duffin, D. F., and Pudritz, R. E. (2009). The early history of protostellar disks, outflows, and binary stars. *Astrophys. J.* 706, L46–L51. doi: 10.1088/0004-637X/706/1/L46

Fielding, D. B., McKee, C. F., Socrates, A., Cunningham, A. J., and Klein, R. I. (2015). The turbulent origin of spin-orbit misalignment in planetary systems. *Month. Notices RAS* 450, 3306–3318. doi: 10.1093/mnras/stv836

Galli, D., Lizano, S., Shu, F. H., and Allen, A. (2006). Gravitational collapse of magnetized clouds. I. Ideal magnetohydrodynamic accretion flow. *Astrophys. J.* 647, 374–381. doi: 10.1086/505257

Galli, D., and Shu, F. H. (1993). Collapse of magnetized molecular cloud cores. II. Numerical results. *Astrophys. J.* 417:243. doi: 10.1086/173306

Girart, J. M., Fernández-López, M., Li, Z.-Y., Yang, H., Estalella, R., Anglada, G., et al. (2018). Resolving the polarized dust emission of the disk around the massive star powering the HH 80-81 radio jet. *Astrophys. J.* 856:L27. doi: 10.3847/2041-8213/aab76b

Goldsmith, P. F., and Arquilla, R. (1985). "Rotation in dark clouds," in *Protostars and Planets II*, eds D. C. Black and M. S. Matthews (University of Arizona Press), 137–149.

Goodman, A. A., Benson, P. J., Fuller, G. A., and Myers, P. C. (1993). Dense cores in dark clouds. VIII - Velocity gradients. *Astrophys. J.* 406, 528–547. doi: 10.1086/172465

Gray, W. J., McKee, C. F., and Klein, R. I. (2018). Effect of angular momentum alignment and strong magnetic fields on the formation of protostellar discs. *Month. Notices RAS* 473, 2124–2143. doi: 10.1093/mnras/stx2406

Hall, J. S. (1949). Observations of the polarized light from stars. *Science* 109, 166–167. doi: 10.1126/science.109.2825.166

Harris, R. J., Cox, E. G., Looney, L. W., Li, Z.-Y., Yang, H., Fernández-López, M., et al. (2018). ALMA observations of polarized 872 μm dust emission from the protostellar systems VLA 1623 and L1527. *Astrophys. J.* 861:91. doi: 10.3847/1538-4357/aac6ec

Heiles, C., and Crutcher, R. (2005). "Magnetic fields in diffuse HI and molecular clouds," in *Cosmic Magnetic Fields*, volume 664 of *Lecture Notes in Physics*, eds R. Wielebinski and R. Beck (Berlin: Springer Verlag), 137.

Hennebelle, P., and Ciardi, A. (2009). Disk formation during collapse of magnetized protostellar cores. *Astron. Astrophys.* 506, L29–L32. doi: 10.1051/0004-6361/200913008

Hennebelle, P., Commerçon, B., Chabrier, G., and Marchand, P. (2016). Magnetically self-regulated formation of early protoplanetary disks. *Astrophys. J.* 830:L8. doi: 10.3847/2041-8205/830/1/L8

Hennebelle, P., and Fromang, S. (2008). Magnetic processes in a collapsing dense core. I. Accretion and ejection. *Astron. Astrophys.* 477, 9–24. doi: 10.1051/0004-6361:20078309

Heyer, M. H., and Brunt, C. M. (2004). The universality of turbulence in galactic molecular clouds. *Astrophys. J.* 615, L45–L48. doi: 10.1086/425978

Higuchi, K., Machida, M. N., and Susa, H. (2018). Evolution of magnetic fields in collapsing star-forming clouds under different environments. *Month. Notices RAS* 475, 3331–3347. doi: 10.1093/mnras/sty046

Hiltner, W. A. (1949). On the presence of polarization in the continuous radiation of stars. II. *Astrophys. J.* 109:471. doi: 10.1086/145151

Hull, C. L. H., Plambeck, R. L., Bolatto, A. D., Bower, G. C., Carpenter, J. M., Crutcher, R. M., et al. (2013). Misalignment of magnetic fields and outflows in protostellar cores. *Astrophys. J.* 768:159. doi: 10.1088/0004-637X/768/2/159

Hull, C. L. H., Yang, H., Li, Z.-Y., Kataoka, A., Stephens, I. W., Andrews, S., et al. (2018). ALMA observations of polarization from dust scattering in the IM lup protoplanetary disk. *Astrophys. J.* 860:82. doi: 10.3847/1538-4357/aabfeb

Igea, J., and Glassgold, A. E. (1999). X-ray ionization of the disks of young stellar objects. *Astrophys. J.* 518, 848–858. doi: 10.1086/307302

Inoue, T., and Inutsuka, S.-i. (2008). Two-fluid magnetohydrodynamic simulations of converging H I flows in the interstellar medium. I. Methodology and basic results. *Astrophys. J.* 687, 303–310. doi: 10.1086/590528

Inoue, T., and Inutsuka, S.-i. (2009). Two-fluid magnetohydrodynamics simulations of converging H I flows in the interstellar medium. II. Are molecular clouds generated directly from a warm neutral medium? *Astrophys. J.* 704, 161–169. doi: 10.1088/0004-637X/704/1/161

Inoue, T., Inutsuka, S.-I., and Koyama, H. (2007). The role of ambipolar diffusion in the formation process of moderately magnetized diffuse clouds. *Astrophys. J.* 658, L99–L102. doi: 10.1086/514816

Inutsuka, S.-i., Machida, M. N., and Matsumoto, T. (2010). Emergence of Protoplanetary Disks and Successive Formation of Gaseous

Planets by Gravitational Instability. *Astrophys. J. Lett.* 718, L58–L62. doi: 10.1088/2041-8205/718/2/L58

Joos, M., Hennebelle, P., and Ciardi, A. (2012). Protostellar disk formation and transport of angular momentum during magnetized core collapse. *Astron. Astrophys.* 543:A128. doi: 10.1051/0004-6361/201118730

Joos, M., Hennebelle, P., Ciardi, A., and Fromang, S. (2013). The influence of turbulence during magnetized core collapse and its consequences on low-mass star formation. *Astron. Astrophys.* 554:A17. doi: 10.1051/0004-6361/201220649

Kataoka, A., Muto, T., Momose, M., Tsukagoshi, T., Fukagawa, M., Shibai, H., et al. (2015). Millimeter-wave polarization of protoplanetary disks due to dust scattering. *Astrophys. J.* 809:78. doi: 10.1088/0004-637X/809/1/78

Kataoka, A., Tsukagoshi, T., Momose, M., Nagai, H., Muto, T., Dullemond, C. P., et al. (2016). Submillimeter polarization observation of the protoplanetary disk around HD 142527. *Astrophys. J.* 831:L12. doi: 10.3847/2041-8205/831/2/L12

Kataoka, A., Tsukagoshi, T., Pohl, A., Muto, T., Nagai, H., Stephens, I. W., et al. (2017). The evidence of radio polarization induced by the radiative grain alignment and self-scattering of dust grains in a protoplanetary disk. *Astrophys. J.* 844:L5. doi: 10.3847/2041-8213/aa7e33

Krasnopolsky, R., Li, Z.-Y., and Shang, H. (2010). Disk formation enabled by enhanced resistivity. *Astrophys. J.* 716, 1541–1550. doi: 10.1088/0004-637X/716/2/1541

Krasnopolsky, R., Li, Z.-Y., and Shang, H. (2011). Disk formation in magnetized clouds enabled by the Hall effect. *Astrophys. J.* 733:54. doi: 10.1088/0004-637X/733/1/54

Krumholz, M. R., Crutcher, R. M., and Hull, C. L. H. (2013). Protostellar disk formation enabled by weak, misaligned magnetic fields. *Astrophys. J.* 767:L11. doi: 10.1088/2041-8205/767/1/L11

Kunz, M. W., and Mouschovias, T. C. (2009). The nonisothermal stage of magnetic star formation. I. Formulation of the problem and method of solution. *Astrophys. J.* 693, 1895–1911. doi: 10.1088/0004-637X/693/2/1895

Kunz, M. W., and Mouschovias, T. C. (2010). The non-isothermal stage of magnetic star formation - II. Results. *Month. Notices RAS* 408, 322–341. doi: 10.1111/j.1365-2966.2010.17110.x

Larson, R. B. (1969). Numerical calculations of the dynamics of collapsing proto-star. *Month. Notices RAS* 145:271. doi: 10.1093/mnras/145.3.271

Lee, C.-F., Li, Z.-Y., Ching, T.-C., Lai, S.-P., and Yang, H. (2018). ALMA dust polarization observations of two young edge-on protostellar disks. *Astrophys. J.* 854:56. doi: 10.3847/1538-4357/aaa769

Lee, C.-F., Li, Z.-Y., Ho, P. T. P., Hirano, N., Zhang, Q., and Shang, H. (2017). First detection of equatorial dark dust lane in a protostellar disk at submillimeter wavelength. *Sci. Adv.* 3:e1602935. doi: 10.1126/sciadv.1602935

Lewis, B. T., and Bate, M. R. (2017). The dependence of protostar formation on the geometry and strength of the initial magnetic field. *Month. Notices RAS* 467, 3324–3337. doi: 10.1093/mnras/stx271

Lewis, B. T., and Bate, M. R. (2018). Shaken and stirred: the effects of turbulence and rotation on disc and outflow formation during the collapse of magnetised molecular cloud cores. *Month. Notices RAS.* 477, 4241–4256. doi: 10.1093/mnras/sty829

Lewis, B. T., Bate, M. R., and Price, D. J. (2015). Smoothed particle magnetohydrodynamic simulations of protostellar outflows with misaligned magnetic field and rotation axes. *Month. Notices RAS* 451, 288–299. doi: 10.1093/mnras/stv957

Li, H.-B., Fang, M., Henning, T., and Kainulainen, J. (2013a). The link between magnetic fields and filamentary clouds: bimodal cloud orientations in the Gould Belt. *Month. Notices RAS* 436, 3707–3719. doi: 10.1093/mnras/stt1849

Li, Z.-Y., Krasnopolsky, R., and Shang, H. (2011). Non-ideal MHD effects and magnetic braking catastrophe in protostellar disk formation. *Astrophys. J.* 738:180. doi: 10.1088/0004-637X/738/2/180

Li, Z.-Y., Krasnopolsky, R., and Shang, H. (2013b). Does magnetic-field-rotation misalignment solve the magnetic braking catastrophe in protostellar disk formation? *Astrophys. J.* 774:82. doi: 10.1088/0004-637X/774/1/82

Li, Z.-Y., Krasnopolsky, R., Shang, H., and Zhao, B. (2014). On the role of pseudodisk warping and reconnection in protostellar disk formation in turbulent magnetized cores. *Astrophys. J.* 793:130. doi: 10.1088/0004-637X/793/2/130

Li, Z.-Y., and McKee, C. F. (1996). Hydromagnetic accretion shocks around low-mass protostars. *Astrophys. J.* 464:373. doi: 10.1086/177329

Li, Z.-Y., and Shu, F. H. (1996). Magnetized singular isothermal toroids. *Astrophys. J.* 472:211. doi: 10.1086/178056

Liu, H. B., Lai, S.-P., Hasegawa, Y., Hirano, N., Rao, R., Li, I.-H., et al. (2016). Detection of linearly polarized 6.9 mm continuum emission from the class 0 young stellar object NGC 1333 IRAS4A. *Astrophys. J.* 821:41. doi: 10.3847/0004-637X/821/1/41

Mac Low, M.-M., Norman, M. L., Konigl, A., and Wardle, M. (1995). Incorporation of ambipolar diffusion into the ZEUS magnetohydrodynamics code. *Astrophys. J.* 442, 726–735. doi: 10.1086/175477

Machida, M. N., and Hosokawa, T. (2013). Evolution of protostellar outflow around low-mass protostar. *Month. Notices RAS* 431, 1719–1744. doi: 10.1093/mnras/stt291

Machida, M. N., Inutsuka, S.-i., and Matsumoto, T. (2008). High- and low-velocity magnetized outflows in the star formation process in a gravitationally collapsing cloud. *Astrophys. J.* 676, 1088–1108. doi: 10.1086/528364

Machida, M. N., Inutsuka, S.-I., and Matsumoto, T. (2010). Formation process of the circumstellar disk: long-term simulations in the main accretion phase of star formation. *Astrophys. J.* 724, 1006–1020. doi: 10.1088/0004-637X/724/2/1006

Machida, M. N., Inutsuka, S.-I., and Matsumoto, T. (2011). Effect of magnetic braking on circumstellar disk formation in a strongly magnetized cloud. *Publ. ASJ* 63:555. doi: 10.1093/pasj/63.3.555

Machida, M. N., Inutsuka, S.-I., and Matsumoto, T. (2014). Conditions for circumstellar disc formation: effects of initial cloud configuration and sink treatment. *Month. Notices RAS* 438, 2278–2306. doi: 10.1093/mnras/stt2343

Machida, M. N., Matsumoto, T., Hanawa, T., and Tomisaka, K. (2006). Evolution of rotating molecular cloud core with oblique magnetic field. *Astrophys. J.* 645, 1227–1245. doi: 10.1086/504423

Machida, M. N., Tomisaka, K., and Matsumoto, T. (2004). First MHD simulation of collapse and fragmentation of magnetized molecular cloud cores. *Month. Notices RAS* 348, L1–L5. doi: 10.1111/j.1365-2966.2004.07402.x

Marchand, P., Masson, J., Chabrier, G., Hennebelle, P., Commerçon, B., and Vaytet, N. (2016). Chemical solver to compute molecule and grain abundances and non-ideal MHD resistivities in prestellar core-collapse calculations. *Astron. Astrophys.* 592:A18. doi: 10.1051/0004-6361/201526780

Masson, J., Chabrier, G., Hennebelle, P., Vaytet, N., and Commerçon, B. (2016). Ambipolar diffusion in low-mass star formation. I. General comparison with the ideal magnetohydrodynamic case. *Astron. Astrophys.* 587:A32. doi: 10.1051/0004-6361/201526371

Mathis, J. S., Rumpl, W., and Nordsieck, K. H. (1977). The size distribution of interstellar grains. *Astrophys. J.* 217, 425–433. doi: 10.1086/155591

Matsumoto, T., and Hanawa, T. (2011). Protostellar collapse of magneto-turbulent cloud cores: shape during collapse and outflow formation. *Astrophys. J.* 728:47. doi: 10.1088/0004-637X/728/1/47

Matsumoto, T., Machida, M. N., and Inutsuka, S.-i. (2017). Circumstellar disks and outflows in turbulent molecular cloud cores: possible formation mechanism for misaligned systems. *Astrophys. J.* 839:69. doi: 10.3847/1538-4357/aa6a1c

Matsumoto, T., Nakazato, T., and Tomisaka, K. (2006). Alignment of Outflows with Magnetic Fields in Cloud Cores. *Astrophys. J.* 637, L105–L108. doi: 10.1086/500646

Matsumoto, T., and Tomisaka, K. (2004). Directions of outflows, disks, magnetic fields, and rotation of young stellar objects in collapsing molecular cloud cores. *Astrophys. J.* 616, 266–282. doi: 10.1086/424897

Maury, A. J., André, P., Hennebelle, P., Motte, F., Stamatellos, D., Bate, M., et al. (2010). Toward understanding the formation of multiple systems. A pilot IRAM-PdBI survey of Class 0 objects. *A&A* 512:A40. doi: 10.1051/0004-6361/200913492

Maury, A. J., Girart, J. M., Zhang, Q., Hennebelle, P., Keto, E., Rao, R., et al. (2018). Magnetically regulated collapse in the B335 protostar? I. ALMA observations of the polarized dust emission. *Month. Notices RAS* 477, 2760–2765. doi: 10.1093/mnras/sty574

McElroy, D., Walsh, C., Markwick, A. J., Cordiner, M. A., Smith, K., and Millar, T. J. (2013). The UMIST database for astrochemistry 2012. *Astron. Astrophys.* 550:A36. doi: 10.1051/0004-6361/201220465

McKee, C. F., and Ostriker, E. C. (2007). Theory of star formation. *Annu. Rev. Astron. Astrophys.* 45, 565–687. doi: 10.1146/annurev.astro.45.051806.110602

Mellon, R. R., and Li, Z.-Y. (2008). Magnetic braking and protostellar disk formation: the ideal MHD limit. *Astrophys. J.* 681, 1356–1376. doi: 10.1086/587542

Mellon, R. R., and Li, Z.-Y. (2009). Magnetic braking and protostellar disk formation: ambipolar diffusion. *Astrophys. J.* 698, 922–927. doi: 10.1088/0004-637X/698/1/922

Mestel, L., and Spitzer, Jr., L. (1956). Star formation in magnetic dust clouds. *Month. Notices RAS* 116:503. doi: 10.1093/mnras/116.5.503

Mouschovias, T. C. (1976). Nonhomologous contraction and equilibria of self-gravitating, magnetic interstellar clouds embedded in an intercloud medium: star formation. II - Results. *Astrophys. J.* 207, 141–158. doi: 10.1086/154478

Mouschovias, T. C. (1977). A connection between the rate of rotation of interstellar clouds, magnetic fields, ambipolar diffusion, and the periods of binary stars. *Astrophys. J.* 211, 147–151. doi: 10.1086/154912

Mouschovias, T. C. (1979). Ambipolar diffusion in interstellar clouds - A new solution. *Astrophys. J.* 228, 475–481. doi: 10.1086/156868

Mouschovias, T. C. (1983). "Magnetic braking and angular momenta of protostars," in *Solar and Stellar Magnetic Fields: Origins and Coronal Effects*, Volume 102 of *IAU Symposium*, ed J. O. Stenflo (Dordrecht), 479–484.

Mouschovias, T. C., and Paleologou, E. V. (1979). The angular momentum problem and magnetic braking - an exact time-dependent solution. *Astrophys. J.* 230, 204–222. doi: 10.1086/157077

Mouschovias, T. C., and Paleologou, E. V. (1980). Magnetic braking of an aligned rotator during star formation - an exact, time-dependent solution. *Astrophys. J.* 237, 877–899. doi: 10.1086/157936

Mouschovias, T. C., and Spitzer, Jr., L. (1976). Note on the collapse of magnetic interstellar clouds. *Astrophys. J.* 210:326. doi: 10.1086/154835

Murillo, N. M., Lai, S.-P., Bruderer, S., Harsono, D., and van Dishoeck, E. F. (2013). A Keplerian disk around a Class 0 source: ALMA observations of VLA1623A. *Astron. Astrophys.* 560:A103. doi: 10.1051/0004-6361/201322537

Myers, A. T., McKee, C. F., Cunningham, A. J., Klein, R. I., and Krumholz, M. R. (2013). The fragmentation of magnetized, massive star-forming cores with radiative feedback. *Astrophys. J.* 766:97. doi: 10.1088/0004-637X/766/2/97

Nakano, T. and Nakamura, T. (1978). Gravitational instability of magnetized gaseous disks 6. *Publ. ASJ* 30, 671–680.

Nakano, T., Nishi, R., and Umebayashi, T. (2002). Mechanism of magnetic flux loss in molecular clouds. *Astrophys. J.* 573, 199–214. doi: 10.1086/340587

Nakano, T., and Umebayashi, T. (1986). Dissipation of magnetic fields in very dense interstellar clouds. I - Formulation and conditions for efficient dissipation. *Month. Notices RAS* 218, 663–684. doi: 10.1093/mnras/218.4.663

Nishi, R., Nakano, T., and Umebayashi, T. (1991). Magnetic flux loss from interstellar clouds with various grain-size distributions. *Astrophys. J.* 368, 181–194. doi: 10.1086/169682

Oka, T., Geballe, T. R., Goto, M., Usuda, T., and McCall, B. J. (2005). Hot and diffuse clouds near the galactic center probed by metastable $H^+_3 1_1$,. *Astrophys. J.* 632, 882–893. doi: 10.1086/432679

Okuzumi, S. (2009). Electric charging of dust aggregates and its effect on dust coagulation in protoplanetary disks. *Astrophys. J.* 698, 1122–1135. doi: 10.1088/0004-637X/698/2/1122

O'Sullivan, S., and Downes, T. P. (2006). An explicit scheme for multifluid magnetohydrodynamics. *Month. Notices RAS* 366, 1329–1336. doi: 10.1111/j.1365-2966.2005.09898.x

Padoan, P., and Nordlund, Å. (2002). The stellar initial mass function from turbulent fragmentation. *Astrophys. J.* 576, 870–879. doi: 10.1086/341790

Padovani, M., Galli, D., and Glassgold, A. E. (2009). Cosmic-ray ionization of molecular clouds. *Astron. Astrophys.* 501, 619–631. doi: 10.1051/0004-6361/200911794

Padovani, M., Galli, D., Hennebelle, P., Commerçon, B., and Joos, M. (2014). The role of cosmic rays on magnetic field diffusion and the formation of protostellar discs. *Astron. Astrophys.* 571:A33. doi: 10.1051/0004-6361/201424035

Planck Collaboration, Ade, P. A. R., Aghanim, N., Alina, D., Alves, M. I. R., Armitage-Caplan, C., Arnaud, M., et al. (2015). Planck intermediate results. XIX. An overview of the polarized thermal emission from Galactic dust. *Astron. Astrophys.* 576:A104. doi: 10.1051/0004-6361/201424082

Price, D. J., and Bate, M. R. (2007). The impact of magnetic fields on single and binary star formation. *Month. Notices RAS* 377, 77–90. doi: 10.1111/j.1365-2966.2007.11621.x

Price, D. J., Wurster, J., Tricco, T. S., Nixon, C., Toupin, S., Pettitt, A., et al. (2018). Phantom: a smoothed particle hydrodynamics and magnetohydrodynamics code for astrophysics. *Publ. Astron. Soc. Aust.* 35:e031. doi: 10.1017/pasa.2018.25

Rao, R., Girart, J. M., Lai, S.-P., and Marrone, D. P. (2014). Detection of a Magnetized Disk around a Very Young Protostar. *Astrophys. J.* 780:L6. doi: 10.1088/2041-8205/780/1/L6

Rodgers-Lee, D., Ray, T. P., and Downes, T. P. (2016). Global multifluid simulations of the magnetorotational instability in radially stratified protoplanetary discs. *Month. Notices RAS* 463, 134–145. doi: 10.1093/mnras/stw1980

Sadavoy, S. I., Myers, P. C., Stephens, I. W., Tobin, J., Commerçon, B., Henning, T., et al. (2018). Dust Polarization toward Embedded Protostars in Ophiuchus with ALMA. I. VLA 1623. *Astrophys. J.* 859:165. doi: 10.3847/1538-4357/aac21a

Saigo, K., and Tomisaka, K. (2006). Evolution of first cores in rotating molecular cores. *Astrophys. J.* 645, 381–394. doi: 10.1086/504028

Saigo, K., Tomisaka, K., and Matsumoto, T. (2008). Evolution of first cores and formation of stellar cores in rotating molecular cloud cores. *Astrophys. J.* 674, 997–1014. doi: 10.1086/523888

Sano, T., and Stone, J. M. (2002a). The effect of the Hall term on the nonlinear evolution of the magnetorotational instability. I. Local axisymmetric simulations. *Astrophys. J.* 570, 314–328. doi: 10.1086/339504

Sano, T., and Stone, J. M. (2002b). The effect of the Hall term on the nonlinear evolution of the magnetorotational instability. II. Saturation level and critical magnetic reynolds number. *Astrophys. J.* 577, 534–553. doi: 10.1086/342172

Santos-Lima, R., de Gouveia Dal Pino, E. M., and Lazarian, A. (2012). The role of turbulent magnetic reconnection in the formation of rotationally supported protostellar disks. *Astrophys. J.* 747:21. doi: 10.1088/0004-637X/747/1/21

Santos-Lima, R., de Gouveia Dal Pino, E. M., and Lazarian, A. (2013). Disc formation in turbulent cloud cores: is magnetic flux loss necessary to stop the magnetic braking catastrophe or not? *Month. Notices RAS* 429, 3371–3378. doi: 10.1093/mnras/sts597

Segura-Cox, D. M., Harris, R. J., Tobin, J. J., Looney, L. W., Li, Z.-Y., Chandler, C., et al. (2016). The VLA nascent disk and multiplicity survey: first look at resolved candidate disks around class 0 and I protostars in the perseus molecular cloud. *Astrophys. J.* 817:L14. doi: 10.3847/2041-8205/817/2/L14

Segura-Cox, D. M., Looney, L. W., Stephens, I. W., Fernández-López, M., Kwon, W., Tobin, J. J., et al. (2015). The magnetic field in the class 0 protostellar disk of L1527. *Astrophys. J.* 798:L2. doi: 10.1088/2041-8205/798/1/L2

Seifried, D., Banerjee, R., Pudritz, R. E., and Klessen, R. S. (2012). Disc formation in turbulent massive cores: circumventing the magnetic braking catastrophe. *Month. Notices RAS* 423, L40–L44. doi: 10.1111/j.1745-3933.2012.01253.x

Seifried, D., Banerjee, R., Pudritz, R. E., and Klessen, R. S. (2013). Turbulence-induced disc formation in strongly magnetized cloud cores. *Month. Notices RAS* 432, 3320–3331. doi: 10.1093/mnras/stt682

Shu, F. H., Galli, D., Lizano, S., and Cai, M. (2006). Gravitational collapse of magnetized clouds. II. The role of ohmic dissipation. *Astrophys. J.* 647, 382–389. doi: 10.1086/505258

Spitzer, L. Jr. (1968). *Dynamics of Interstellar Matter and the Formation of Stars*. Chicago, IL: University of Chicago Press.

Spitzer, L. Jr., and Tomasko, M. G. (1968). Heating of H i regions by energetic particles. *Astrophys. J.* 152:971. doi: 10.1086/149610

Stephens, I. W., Looney, L. W., Kwon, W., Fernández-López, M., Hughes, A. M., Mundy, L. G., et al. (2014). Spatially resolved magnetic field structure in the disk of a T Tauri star. *Nature* 514, 597–599. doi: 10.1038/nature13850

Stephens, I. W., Yang, H., Li, Z.-Y., Looney, L. W., Kataoka, A., Kwon, W., et al. (2017). ALMA reveals transition of polarization pattern with wavelength in HL Tau's disk. *Astrophys. J.* 851:55. doi: 10.3847/1538-4357/aa998b

Tassis, K., and Mouschovias, T. C. (2005a). Magnetically controlled spasmodic accretion during star formation. I. Formulation of the problem and method of solution. *Astrophys. J.* 618, 769–782. doi: 10.1086/424479

Tassis, K., and Mouschovias, T. C. (2005b). Magnetically controlled spasmodic accretion during star formation. II. Results. *Astrophys. J.* 618, 783–794. doi: 10.1086/424480

Tassis, K., and Mouschovias, T. C. (2007a). Protostar formation in magnetic molecular clouds beyond ion detachment. I. Formulation of the problem and method of solution. *Astrophys. J.* 660, 370–387. doi: 10.1086/512760

Tassis, K., and Mouschovias, T. C. (2007b). Protostar formation in magnetic molecular clouds beyond ion detachment. II. Typical axisymmetric solution. *Astrophys. J.* 660, 388–401. doi: 10.1086/512761

Tassis, K., and Mouschovias, T. C. (2007c). Protostar formation in magnetic molecular clouds beyond ion detachment. III. A parameter study. *Astrophys. J.* 660, 402–417. doi: 10.1086/512762

Tobin, J. J., Hartmann, L., Chiang, H.-F., Wilner, D. J., Looney, L. W., Loinard, L., et al. (2012). A ˜0.2-solar-mass protostar with a Keplerian disk in the very young L1527 IRS system. *Nature* 492, 83–85. doi: 10.1038/nature11610

Tomida, K. (2014). Radiation magnetohydrodynamic simulations of protostellar collapse: low-metallicity environments. *Astrophys. J.* 786:98. doi: 10.1088/0004-637X/786/2/98

Tomida, K., Machida, M. N., Hosokawa, T., Sakurai, Y., and Lin, C. H. (2017). Grand-design spiral arms in a young forming circumstellar disk. *Astrophys. J.* 835:L11. doi: 10.3847/2041-8213/835/1/L11

Tomida, K., Okuzumi, S., and Machida, M. N. (2015). Radiation magnetohydrodynamic simulations of protostellar collapse: nonideal magnetohydrodynamic effects and early formation of circumstellar disks. *Astrophys. J.* 801:117. doi: 10.1088/0004-637X/801/2/117

Tomida, K., Tomisaka, K., Matsumoto, T., Hori, Y., Okuzumi, S., Machida, M. N., et al. (2013). Radiation magnetohydrodynamic simulations of protostellar collapse: protostellar core formation. *Astrophys. J.* 763:6. doi: 10.1088/0004-637X/763/1/6

Tomida, K., Tomisaka, K., Matsumoto, T., Ohsuga, K., Machida, M. N., and Saigo, K. (2010). Radiation magnetohydrodynamics simulation of protostellar collapse: two-component molecular outflow. *Astrophys. J.* 714, L58–L63. doi: 10.1088/2041-8205/714/1/L58

Tomisaka, K. (2000). The evolution of the angular momentum distribution during star formation. *Astrophys. J.* 528, L41–L44. doi: 10.1086/312417

Toomre, A. (1964). On the gravitational stability of a disk of stars. *Astrophys. J.* 139, 1217–1238. doi: 10.1086/147861

Troland, T. H., and Crutcher, R. M. (2008). Magnetic fields in dark cloud cores: arecibo OH zeeman observations. *Astrophys. J.* 680, 457–465. doi: 10.1086/587546

Tsukamoto, Y., Iwasaki, K., Okuzumi, S., Machida, M. N., and Inutsuka, S. (2015a). Bimodality of circumstellar disk evolution induced by the hall current. *Astrophys. J.* 810:L26. doi: 10.1088/2041-8205/810/2/L26

Tsukamoto, Y., Iwasaki, K., Okuzumi, S., Machida, M. N., and Inutsuka, S. (2015b). Effects of Ohmic and ambipolar diffusion on formation and evolution of first cores, protostars, and circumstellar discs. *Month. Notices RAS* 452, 278–288. doi: 10.1093/mnras/stv1290

Tsukamoto, Y., Okuzumi, S., Iwasaki, K., Machida, M. N., and Inutsuka, S.-i. (2017). The impact of the Hall effect during cloud core collapse: implications for circumstellar disk evolution. *Publ. ASJ* 69:95. doi: 10.1093/pasj/psx113

Turner, N. J., and Sano, T. (2008). Dead zone accretion flows in protostellar disks. *Astrophys. J.* 679:L131. doi: 10.1086/589540

Umebayashi, T., and Nakano, T. (1981). Fluxes of energetic particles and the ionization rate in very dense interstellar clouds. *Publ. ASJ* 33:617.

Umebayashi, T., and Nakano, T. (1990). Magnetic flux loss from interstellar clouds. *Month. Notices RAS* 243, 103–113. doi: 10.1093/mnras/243.1.103

Umebayashi, T., and Nakano, T. (2009). Effects of radionuclides on the ionization state of protoplanetary disks and dense cloud cores. *Astrophys. J.* 690, 69–81. doi: 10.1088/0004-637X/690/1/69

Vaytet, N., Commerçon, B., Masson, J., González, M., and Chabrier, G. (2018). Protostellar birth with ambipolar and ohmic diffusion. *Astron. Astrophys.* 615:A5. doi: 10.1051/0004-6361/201732075

Wardle, M. (2007). Magnetic fields in protoplanetary disks. *Astrophys. Space Sci.* 311, 35–45. doi: 10.1007/s10509-007-9575-8

Wardle, M., and Koenigl, A. (1993). The structure of protostellar accretion disks and the origin of bipolar flows. *Astrophys. J.* 410, 218–238. doi: 10.1086/172739

Wardle, M., and Ng, C. (1999). The conductivity of dense molecular gas. *Month. Notices RAS* 303, 239–246. doi: 10.1046/j.1365-8711.1999.02211.x

Ward-Thompson, D., Kirk, J. M., André, P., Saraceno, P., Didelon, P., Könyves, V., et al. (2010). A Herschel study of the properties of starless cores in the Polaris Flare dark cloud region using PACS and SPIRE. *Astron. Astrophys.* 518:L92. doi: 10.1051/0004-6361/201014618

Weiss, N. O. (1966). The expulsion of magnetic flux by eddies. *Proc. R. Soc. Lond. Ser. A* 293, 310–328. doi: 10.1098/rspa.1966.0173

Wurster, J. (2016). NICIL: a stand alone library to self-consistently calculate non-ideal magnetohydrodynamic coefficients in molecular cloud cores. *Publ. Astron. Soc. Aust.* 33:e041. doi: 10.1017/pasa.2016.34

Wurster, J., Bate, M. R., and Price, D. J. (2018a). The collapse of a molecular cloud core to stellar densities using radiation non-ideal magnetohydrodynamics. *Month. Notices RAS* 475, 1859–1880. doi: 10.1093/mnras/stx3339

Wurster, J., Bate, M. R., and Price, D. J. (2018b). The effect of extreme ionization rates during the initial collapse of a molecular cloud core. *Month. Notices RAS* 476, 2063–2074. doi: 10.1093/mnras/sty392

Wurster, J., Bate, M. R., and Price, D. J. (2018c). Hall effect-driven formation of gravitationally unstable discs in magnetized molecular cloud cores. *Month. Notices RAS* 480, 4434–4442. doi: 10.1093/mnras/sty2212

Wurster, J., Bate, M. R., and Price, D. J. (2018d). On the origin of magnetic fields in stars. *Month. Notices RAS* 481, 2450–2457. doi: 10.1093/mnras/sty2438

Wurster, J., Price, D. J., and Ayliffe, B. (2014). Ambipolar diffusion in smoothed particle magnetohydrodynamics. *Month. Notices RAS* 444, 1104–1112. doi: 10.1093/mnras/stu1524

Wurster, J., Price, D. J., and Bate, M. R. (2016). Can non-ideal magnetohydrodynamics solve the magnetic braking catastrophe? *Month. Notices RAS* 457, 1037–1061. doi: 10.1093/mnras/stw013

Yang, H., Li, Z.-Y., Looney, L., and Stephens, I. (2016a). Inclination-induced polarization of scattered millimetre radiation from protoplanetary discs: the case of HL Tau. *Month. Notices RAS* 456, 2794–2805. doi: 10.1093/mnras/stv2633

Yang, H., Li, Z.-Y., Looney, L. W., Cox, E. G., Tobin, J., Stephens, I. W., et al. (2016b). Disc polarization from both emission and scattering of magnetically aligned grains: the case of NGC 1333 IRAS 4A1. *Month. Notices RAS* 460, 4109–4121. doi: 10.1093/mnras/stw1253

Yang, H., Li, Z.-Y., Looney, L. W., Girart, J. M., and Stephens, I. W. (2017). Scattering-produced (sub)millimetre polarization in inclined discs: optical depth effects, near-far side asymmetry and dust settling. *Month. Notices RAS* 472, 373–388. doi: 10.1093/mnras/stx1951

Yen, H.-W., Koch, P. M., Takakuwa, S., Ho, P. T. P., Ohashi, N., and Tang, Y.-W. (2015). Observations of infalling and rotational motions on a 1000 AU scale around 17 class 0 and 0/I protostars: hints of disk growth and magnetic braking? *Astrophys. J.* 799:193. doi: 10.1088/0004-637X/799/2/193

Yorke, H. W., Bodenheimer, P., and Laughlin, G. (1993). The formation of protostellar disks. I - 1 M(solar). *Astrophys. J.* 411, 274–284. doi: 10.1086/172827

Yorke, H. W., Bodenheimer, P., and Laughlin, G. (1995). The formation of protostellar disks. 2: disks around intermediate-mass stars. *Astrophys. J.* 443, 199–208. doi: 10.1086/175514

Zhao, B., Caselli, P., and Li, Z.-Y. (2018). Effect of grain size on differential desorption of volatile species and on non-ideal MHD diffusivity. *Month. Notices RAS* 478, 2723–2736. doi: 10.1093/mnras/sty1165

Zhao, B., Caselli, P., Li, Z.-Y., Krasnopolsky, R., Shang, H., and Nakamura, F. (2016). Protostellar disc formation enabled by removal of small dust grains. *Month. Notices RAS* 460, 2050–2076. doi: 10.1093/mnras/stw1124

Zhao, B., Li, Z.-Y., Nakamura, F., Krasnopolsky, R., and Shang, H. (2011). Magnetic flux expulsion in star formation. *Astrophys. J.* 742:10. doi: 10.1088/0004-637X/742/1/10

Conflict of Interest Statement: The authors declare that the research was conducted in the absence of any commercial or financial relationships that could be construed as a potential conflict of interest.

frontiers in Astronomy and Space Sciences

REVIEW
published: 31 July 2019
doi: 10.3389/fspas.2019.00054

The Role of Magnetic Fields in Protostellar Outflows and Star Formation

Ralph E. Pudritz[1]* *and Tom P. Ray*[2]

[1] Department of Physics and Astronomy, McMaster University, Hamilton, ON, Canada, [2] School of Cosmic Physics, Dublin Institute for Advanced Studies, Dublin, Ireland

The role of outflows in the formation of stars and the protostellar disks that generate them is a central question in astrophysics. Outflows are associated with star formation across the entire stellar mass spectrum. In this review, we describe the observational, theoretical, and computational advances on magnetized outflows, and their role in the formation of disks and stars of all masses in turbulent, magnetized clouds. The ability of torques exerted on disks by magnetized winds to efficiently extract and transport disk angular momentum was developed in early theoretical models and confirmed by a variety of numerical simulations. The recent high resolution Atacama Large Millimeter Array (ALMA) observations of disks and outflows now confirm several key aspects of these ideas, e.g., that jets rotate and originate from large regions of their underlying disks. New insights on accretion disk physics show that magneto-rotational instability (MRI) turbulence is strongly damped, leaving magnetized disk winds as the dominant mechanism for transporting disk angular momentum. This has major consequences for star formation, as well as planet formation. Outflows also play an important role in feedback processes particularly in the birth of low mass stars and cluster formation. Despite being almost certainly fundamental to their production and focusing, magnetic fields in outflows in protostellar systems, and even in the disks, are notoriously difficult to measure. Most methods are indirect and lack precision, as for example, when using optical/near-infrared line ratios. Moreover, in those rare cases where direct measurements are possible—where synchrotron radiation is observed, one has to be very careful in interpreting derived values. Here we also explore what is known about magnetic fields from observations, and take a forward look to the time when facilities such as SPIRou and the SKA are in routine operation.

Keywords: outflows, magnetic fields, star formation, disks, planet formation

OPEN ACCESS

Edited by:
Christopher F. McKee, University of California, Berkeley, United States

Reviewed by:
Zhi-Yun Li, University of Virginia, United States
John Bally, University of Colorado Boulder, United States

***Correspondence:**
Ralph E. Pudritz
pudritz@mcmaster.ca

Specialty section:
This article was submitted to Stellar and Solar Physics, a section of the journal Frontiers in Astronomy and Space Sciences

Received: *20 March 2019*
Accepted: *11 July 2019*
Published: *31 July 2019*

Citation:
Pudritz RE and Ray TP (2019) The Role of Magnetic Fields in Protostellar Outflows and Star Formation. Front. Astron. Space Sci. 6:54. doi: 10.3389/fspas.2019.00054

1. INTRODUCTION

Of the many important roles that magnetic fields play in the formation of stars, perhaps none is more dramatic nor as full of consequence as is the launch and collimation of powerful outflows. It is now nearly 70 years since the first evidence for energetic outflows in star formation regions was discovered (Herbig, 1951; Haro, 1952) although not realized as such. In fact it would be many years later before these nebulous clouds (now known as Herbig-Haro objects) were correctly identified

as radiative shocks driven by an outflow from a young star (Schwartz, 1977). The availability of new technologies and telescopes over the subsequent decades has yielded discoveries of bipolar molecular outflows at millimeter wavelengths, high speed (hundreds of km s^{-1}) optical jets in permitted and forbidden line emission, and more recently even synchrotron emitting jets associated with low mass star formation. This extensive body of work shows that bulk flows ranging from several to hundreds of km s^{-1} are observed in these different tracers. Although first discovered to be associated with the birth of low mass T-Tauri stars, observations over the last two decades have shown outflows to be linked with the formation of objects across the entire mass spectrum: from brown dwarfs (Whelan et al., 2005) on up to O stars (Caratti o Garatti et al., 2017). These observations have made it clear that outflows are an essential component of star formation.

The first clues to the origin of protostellar jets emerged from studies of outflows from low mass stars, whose radiation pressures fail by orders of magnitude to drive them at the observed thrusts (see for example Wu et al., 2004; Vaidya et al., 2011 on the decollimating effects of radiation in the case of massive young stars). It was therefore natural to consider the possibility that T Tauri jets and outflows could be magnetized winds from rotating bodies. Two kinds of magnetized rotors are possible—rapidly spinning, magnetized protostars or magnetized accretions disks out of which all stars and their planetary systems form. While magnetic field measurements needed to confirm such a picture have been long in coming, direct observational evidence is now available using several approaches: the spectro-polarimetry of jet sources (Donati et al., 2010), synchrotron emission in outflows from some young stars and most recently the detection of polarization of the SiO line in a jet from a low mass star arising from the Goldreich-Kylafis effect (Lee et al., 2018). The observed fields range in strength from kilogauss close to the star to a fraction of a milligauss in distant parts for the outflow. Such values suggest that while magnetic forces dominate in the vicinity of the young stellar object (YSO), they are no longer dynamically important further out. This scenario is in agreement with numerical simulations (Hartigan et al., 2007).

The basic physics of how magnetized rotating stars drive winds and undergo magnetic braking as a consequence was developed by Chandrasekhar (1956) and Mestel (1961) before being applied by Weber and Davis (1967) who showed that the magnetized solar wind would spin down the Sun. Magnetic field lines threading a rotating star can enforce the co-rotation of gas out to some distance along the field line—the Alfvén radius r_A where the outflow speed equals the speed of a transverse Alfvén wave ($B/\sqrt{4\pi\rho}$). In so doing, the wind is able to extract the rotor's angular momentum which is then carried out by the rotating, accelerated outflow. The lever arm of the wind torque is, in effect, the Alfvén radius. It can extend to significant distances from the body making the magnetized outflow a highly efficient mechanism for extracting angular momentum. It is this point, more than any other, that makes magnetic fields so important in the physics of protostellar outflows and underpins their role in star formation. Moreover, the combination of magnetic fields and outflows, or more precisely winds, continue to be important in subsequent evolutionary phases as a means of removing angular momentum even when a star is on the Main Sequence (Reiners and Mohanty, 2012).

Linking magnetized winds to the physics of accretion disks was first suggested in the context of accreting black holes at the centers of radio galaxies (Blandford and Payne, 1982). It became clear that magnetized disk-wind torques, exerted by fields threading vertically through the disk and bending outwards beyond, extract some, if not most of the angular momentum from each annulus of the disk. This, in turn, could drive an accretion flow onto the central black hole. When applied to circumstellar disks around young stars, magnetized disk winds (D-winds), extending over most of the disk surface, could also provide the major driver of accretion onto the central forming star (Pudritz and Norman, 1983). In any event this theory led rather quickly to the prediction that outflows and accretion disks must be fundamentally linked in a structure that undergoes both accretion and ejection. In particular the ratio of the mass outflow rate to the wind driven accretion rate depends on the lever arm of the flow: the ratio of r_A to the footpoint radius r_o of field line at each disk radius. Observations of a wide variety of systems typically observe a wind mass flux to accretion flux ratio, $\dot{M}_w/\dot{M}_a \simeq 0.1$ (Watson et al., 2016) confirming theoretical predictions (Pudritz and Norman, 1986). Another key prediction of the theory is that jets rotate—a consequence of the fact that they carry off the disks's angular momentum. These predictions have been confirmed by a large number of 2 and 3D hydromagnetic simulations using a wide variety of initial setups (isolated cores, turbulent clumps, etc.) and numerical codes (ZEUS, FLASH AMR, RAMSES AMR, SPH MHD, etc.). A small sampling of these works starts from Shibata and Uchida (1985), Ouyed et al. (1997), Krasnopolsky et al. (1999), Banerjee and Pudritz (2006), Hennebelle and Ciardi (2009), Price et al. (2012), Stepanovs and Fendt (2014), Staff et al. (2015), and Tomida et al. (2015), to the appearance of high resolution zoom-in techniques in Kuffmeier et al. (2017).

While D-wind models are attractive, an alternative mechanism for generating outflows from disks was proposed in a series of papers starting with Shu et al. (1994) and which are comprehensively reviewed in Shu et al. (2000). According to the latter model, high velocity outflows arise not from the surface of the disk but instead from the narrow annulus where the star's magnetosphere interacts directly with the inner edge of the disk, at the so-called co-rotation radius[1]. Here the magnetic field of the young star is assumed to be strong and to clear out disk matter as far as the co-rotation radius. At this radius the magnetic field switches from its inner closed configuration (associated with the star's magnetosphere) to an open configuration. This constitutes a magnetic X-point or more precisely an X ring. Matter is then launched centrifugally from the disk along the open field lines in a flow known as an X-wind. It should be emphasized that both X-winds and D-winds are driven magneto-centrifugally along open field embedded within rotating disks. One of the key physical differences between the two models is that the

[1]The co-rotation radius is the region where the disk rotates, in angular terms, at the same rate as the star

X-wind only removes most of the Keplerian angular momentum from near the disk's inner edge defined by the magnetopause (where the magnetic field of the star truncates the disk). In contrast, the D-wind removes angular momentum from every disk radius. The D-wind model also allows the Keplerian angular momentum at the disk inner edge to be transported to the star via gas infall along the stellar field lines. Several mechanisms have been proposed to remove this from the star, including coupling to the disk, or by an accretion powered stellar wind. In terms of magnetic field geometries, the main differences (Shang et al., 2007) are where the field lines are anchored: near the co-rotation radius, the X-radius, for X-winds—or over a wide range of radii for D-winds starting from the inner disk edge.

One of the basic questions regarding the application of such magneto-hydrodynamic (MHD) wind models to protostellar disks is the degree to which magnetic fields are really coupled to the disks, given that the very low ionization of high column density disks implies that non-ideal effects are important (Königl, 2009). A great deal of effort has been expended in developing computer codes capable of simulating these effects over the last decade (Duffin and Pudritz, 2009; Seifried et al., 2012; Bai and Stone, 2014; Gressel et al., 2015; Hennebelle et al., 2016). The results of this work have now challenged the traditional idea of accretion disks as systems that are dominated by turbulent angular momentum transport, as we shall see.

At the time bipolar outflows were discovered, protostellar disks had not yet been directly detected although their presence had been inferred from the modeling of observed spectral energy distributions using the IRAS satellite (Rucinski, 1985). Moreover, very little was known about the spins of young stars, except for the fact that a few rotate very slowly (periods of approximately a week). The first optical images of protostellar disks, seen against the bright emission of the Orion Nebula Cluster by the Hubble Space Telescope (O'Dell and Wen, 1994), showed them to be at most $1''$ in size for the nearest star formation regions. The search for disks associated with outflows, having the signatures of Keplerian rotation, required both high spatial and spectral resolution. Such capability became available with mm interferometry and an early-known jet source, HL Tau, was shown to possess a rotating circumstellar disk, perpendicular to the jet, using CO as a tracer (Sargent and Beckwith, 1987). Such discoveries, in fact became one of the major science drivers for ALMA, i.e., to discover and map protostellar disks and undertake studies of both star and planet formation within them. The connection of outflows with disks is now being directly addressed as part of the "ALMA revolution" wherein disks around young Class I stars, and their associated outflows (observed at millimeter wavelengths), have been resolved down to scales of a few au in nearby sources. Recent efforts have also focused on studying the formation and growth of disks in the most deeply embedded, even earlier phases of star formation (Class 0 sources), see for example Tobin et al. (2013).

While it is generally acknowledged that magnetic fields likely play a central role in observed protostellar outflows, until recently the possibility that outflows might also control the physics of accretion disks has been largely ignored. One reason is observational. Magnetic fields in jets and disks are notoriously difficult to measure and the needed instruments have not been available. A second reason is theoretical. The seminal papers on accretion disk theory assumed that turbulence in disks would result in a viscous torque. This transports angular momentum radially outwards through the disk, driving most of the disk material to accrete onto the star as the outer disk spreads out to carry off the angular momentum, see for example Armitage (1998). The questions here are—what is the origin of turbulence? Is it of sufficient amplitude to support the large observed disk accretion rates? It took nearly two decades for an explanation to emerge. The Magneto-Rotational Instability (MRI), arising from weak magnetic fields, provided a sound physical basis for turbulence in perfectly conducting, so-called "ideal," disks (Balbus and Hawley, 1998). However, recent ALMA observations show that turbulence is not strong enough to carry away angular momentum in observed disks, at least at tens of au from a young star (Flaherty et al., 2015, 2017, 2018). While the observations are consistent with numerical simulations for the mid-plane, where MRI-driven turbulence will be strongly damped, they are inconsistent with expected turbulent velocities at the disk surface, $v_{turb} \simeq 0.1 - 1.0\, c_s$, required to drive the observed accretion rates (Simon et al., 2018). At the same time, numerical simulations of protostellar disks, that account for important non-ideal MHD effects, have discovered that the MRI is strongly suppressed in the expected dense, poorly ionized gas. It gives way instead to magnetized disk winds (Bai and Stone, 2014; Gressel et al., 2015). While further developments are needed—such as including the effects of grain evolution on non-ideal MHD process—progress in the field has been enormous. Thus, recent advances in observations and breakthroughs in difficult numerical simulations both seem to point toward the primacy of magnetized outflows rather than disk turbulence as the driver of accretion disk physics (Simon et al., 2018). Before exploring disk winds further, it should be pointed out that alternative ways of transporting angular momentum outwards in an accretion disk have been suggested. In particular, transport can be by spiral density waves although such waves only form in disks that are a significant fraction of the mass of the central star (Kratter and Lodato, 2016). Moreover embedded masses, e.g., newly formed massive planets, can drain angular momentum away from a disk and support accretion onto the young star; this however does not seem to be an important mechanism (Armitage, 2011).

There is also the question of what causes the surprisingly low angular momentum of many young stars. Early work suggested that one effect of the star's magnetosphere interacting with the disk is to spin-down the star, through magnetic braking, so that it is effectively locked to the same rotation period as the inner edge of the accretion disk (Koenigl, 1991). This would explain why young stars, which show evidence of disks, rotate slower on average than their disk-less counterparts of comparable age and mass (Cieza and Baliber, 2007). More recent work suggests that stellar spin may be controlled by magnetized stellar outflows that originate from the protostars themselves. Here, the accretion of material from the inner disk flows onto the star by falling down magnetospheric field lines. The gravitational energy released in this infall impacts the foot points of these field lines. This ultimately gives rise to a powerful flux of Alfvén

waves that heats the stellar corona giving rise to an accretion-powered wind (see for example Matt et al., 2012). As already mentioned, outflows have also been suggested to originate at the disk-magnetosphere boundary—the so-called X-wind—which are proposed to carry off the angular momentum of the inner disk before matter is accreted onto the star (Shu et al., 2000). In any event, as soon as the star loses its disk, it starts to spin-up as it radius shrinks while descending its Hayashi track. Observational advances in measuring both the magnetic field and spins of young stellar objects have opened up the possibility of formulating the complete spin history of a star, the evolution of which appears to be particularly important in the early phases of star formation (Bouvier et al., 2014).

Magnetically driven outflows have a large number of other important consequences for star formation. If outflows originate from disks then the process of disk formation during gravitational collapse in a magnetized medium must be deeply connected with magnetic braking in the early collapse phase and subsequent launching of MHD outflows as the disk, or first core, starts to materialize. Disks and outflows in this view are inseparable, both being tied to collapse in turbulent, clouds. Indeed, as has long been known, one of the central features of the observations is that outflows are most powerful during the most deeply embedded Class 0 stage when at least half the mass of the system is still in the envelope which is collapsing into the disk (Jørgensen et al., 2009). Recent analytic and numerical calculations indeed show that small disks of about 20 au in size should form in magnetized collapse wherein the magnetic field is not frozen into the gas but undergoes (ambipolar) diffusion (Hennebelle et al., 2016). This is very much in keeping with the sense of recent IRAM-PdBI observations which find that disks are typically smaller than expected from purely hydrodynamic models (Maury et al., 2019). Thus, magnetic braking and the launch of outflows early in the gravitational collapse and disk formation stages of star formation, respectively, control one of the most fundamental physical properties of the initial state of a disk—its radius.

Feedback processes arising from outflows have long been thought to play an important role in defining the mass of a star and the efficiency of star formation. Magnetized outflows carry significant amounts of angular momentum and thrust, and are powered by the gravitational potential energy released during the collapse. In this way, outflows can act as an important, and even dominant form of protostellar feedback during star formation. This feedback can cut off the supply of infalling gas to the disk, and thereby help to limit or determine stellar mass (Matzner and McKee, 2000). On physical scales beyond the molecular core radius (typically $\approx$ 0.04 pc), protostellar outflows could stir up the surrounding molecular cloud and drive turbulence. This would, to some degree, stave off the formation of too much dense, star forming gas as first suggested in the pioneering paper of Norman and Silk (1980), and is in agreement with many current MHD simulations (Federrath, 2016). Feedback from protostellar outflows would then help to reduce star formation rates and efficiencies in molecular clouds addressing one of the big questions of star formation—why is the process so inefficient?

This review examines these issues and questions from a modern perspective. We focus on recent rapid progress in the ALMA era that has been made in the physics and observations of outflows and their role in star formation. ALMA has provided a radically new capability to study disks and their outflows. Most of our attention is on observational and theoretical results that have arisen since 2014 post the publication of Protostars and Planets VI. We first review the observational advances in measuring magnetic fields in stars, jets, and disks, and the properties of outflows (shocks, rotation, etc.). We then go on to examine the theoretical and computational results on how outflows are launched, and their significance in various aspects of star formation. These latter angular momentum related topics include outflows and their effects on—gravitational collapse, disk formation, disk evolution, and protostellar spin. We then discuss the feedback properties of outflows including their effects on stellar mass and molecular cloud turbulence. We address these issues in the context of both low and high mass star formation. The latter subject brings up the difficult question of how powerful protostellar radiation combines with magnetic outflows to determine conditions in massive star forming regions. Finally, since stars and planets form in disks, both must be affected by outflow physics and so we address how planet formation could be affected by outflows. The reader may consult reviews of earlier material in Ray et al. (2007), Pudritz et al. (2007), Frank et al. (2014), Li et al. (2014b), and Bally (2016).

2. OBSERVATIONAL OVERVIEW

It is remarkable that although magnetic fields are thought to collimate YSO jets, very few observations of field strength or direction are known. In contrast, through optical and near-infrared emission line imaging and spectroscopic studies, many jet parameters can be derived, e.g., neutral density, ionization fraction, temperature, jet opening angle, radial velocity, etc. With the addition of multi-epoch imaging, quantities such as the tangential velocity of knots, post shock cooling times, etc., can also be found (Frank et al., 2014), allowing a full 3-D kinematic study of outflows. We begin our overview from the largest outflow scales, and gradually focus down to accretion and outflow from the protostellar surface.

2.1. Do the Magnetic Fields of the Parent Cloud or Cores Determine the Outflow Direction?

It is now known that outflows from young stars extend to parsec and even tens of parsec scales, i.e., lengths comparable to the size of their parent molecular cloud (Bally, 2016). This is not surprising when one considers that it takes approximately 1 million years (Evans et al., 2009) for a solar mass young star to go through its outflow phase (i.e., from Class 0 to Class 2) and that typical outflows have velocities of several hundreds of kms^{-1}. Therefore an obvious starting point is to consider whether outflows are somehow aligned, either directly or indirectly, with the magnetic field of their parent cloud. Conceivably this could be through some sort of guiding action by the cloud's magnetic

field or alternatively, since accretion disks and outflows are perpendicular, by the field determining the disk's orientation. We can immediately dismiss the first suggestion since outflows are not only highly supersonic with respect to their internal and external sound speeds but also jet velocities are much higher than their internal and external Alfvén speeds. The second idea however is worth exploring. Despite low ionization levels, neutral and ionized matter in a molecular cloud are strongly coupled through collisions, and thus matter is preferentially accreted along magnetic field lines. In turn one might naively expect disks to form in the perpendicular plane.

As described elsewhere in this volume, magnetic field directions in a cloud can be obtained either through polarized absorption of continuum light by dust grains, when the optical depth is low, or through polarized emission at infrared/mm wavelengths from dust grains, when depths are high. Pioneering studies by Strom and Strom (1987) suggested there might be a relationship in the sense that the directions of outflows could follow that of the magnetic field in the surrounding cloud. Number statistics at the time however were very poor and subsequent studies have suggested there is no such correlation (Ménard and Duchêne, 2004; Targon et al., 2011) or at best present only for the youngest protostars. Of course expecting such a correlation assumes disks form only by the collapse of material along the field lines and subsequent distortion of the field into the classical "hourglass" pattern as gravity draws material inwards. Many studies however have shown that magnetic braking in such a case is far too effective and that disks, at least of the large sizes observed, should not form even when non-ideal damping MHD effects are taken into account (Duffin and Pudritz, 2009; Krasnopolsky et al., 2012). Moreover we also have to be careful in looking for a correlation with the large scale (≈ 1 pc) magnetic field direction in the parent cloud and the outflow when perhaps we should be searching for a link with the magnetic field direction in the smaller parent core and envelope. As polarization in the latter can only been measured when the optical depth is sufficiently high, and the scales we wish to investigate are at most a few thousand au, one has to turn to millimeter interferometry of younger embedded protostars. Here initial results (Hull et al., 2014) do not suggest any correlation and, in fact, if anything a tendency for outflows and magnetic fields in the cores *to be orthogonal*. We note however that a smaller study that used a more carefully selected sample of disks, came to the opposite conclusion, namely that there is a good correlation between outflows and magnetic field geometry on the scale of cores in class 0 sources (Chapman et al., 2013). Overall, a lack of correlation is understandable in the context of more up-to-date MHD simulations which show that disks, similar in diameter to what is observed, are only formed if there is *misalignment* between the rotation axis of the core and the ambient magnetic field *providing the field is weak* (Joos et al., 2012; Krumholz et al., 2013). Moreover the effectiveness of magnetic braking is also in line with the recent study of Galametz et al. (2018) who has shown there is increased likelihood of alignment between the outflow direction and the orientation of the ambient magnetic field if there is no small-scale multiplicity and no large disks on > 100 au scales. In summary then we do not expect, or find, any strong correlation between outflow orientation and the direction of the ambient magnetic field on scales of several hundred au to parsecs.

2.2. What Do Observations Tell Us About Magnetic Fields in Jets Far From the Young Star?

It is well known that most of the radiation emitted by jets from young stars comes from the cooling zone behind shocks. The properties of such shocks, in the absence of a magnetic field, have been modeled for a number of years and depending on the shock velocity various emission lines and relationships between the fluxes of such lines, are expected in the post shock zone. At optical wavelengths for example, we expect to see both lines from neutral, e.g., from H, O, and singly ionized species, e.g., S^+. As jets from young stars, or more precisely their atomic/ionized component, typically travel at hundreds of kms^{-1}, we would also predict the presence of highly ionized species, for example O^{++}, in the post shock cooling zone if most of the outflow energy is converted into radiation at a single shock. In reality, except for the tip of the largest bow shock shaped features (e.g., in HH 34) such emission is not observed. This is because the shock fronts seen in jets are so-called "working surfaces" in which the shock velocity is determined by *the difference in velocity* between consecutive flows from the young star (Raga et al., 2002). The line emission in this case is then consistent with a shock velocity of several tens of kms^{-1} rather than a few hundred kms^{-1}, i.e., in line with the velocity differences. Recent 3-D simulations, with realistic cooling, show the rich structure that such variations can lead to, see for example Hansen et al. (2017). What is important to emphasize is that the results of such simulations are in very good agreement with what is found through observations, for example, with HST.

Of course in a standard, i.e., adiabatic, strong shock the density of the flow increases by a factor of 4 and the velocity correspondingly decreases by the same factor. Here we are referring to velocities in the shock frame and by the term strong shock, we mean one in which the incoming velocity $V_s \gg c_s$ where c_s is the sound speed. In other words $M_s \gg 1$ where $M_s = V_s/c_s$ is the Mach number of the shock. In a radiative shock, due to the loss in energy, gas in the post shock zone is compressed over and above that expected for an adiabatic shock. The increased density leads to further collisional excitation and strong line emission is produced from oxygen, hydrogen, sulfur, etc. Gas density is then increased further in order to maintain pressure and effectively these lines act as thermostats keeping the temperature around 10^4 K.

Unfortunately the presence of a magnetic field in a jet cannot be determined in a straightforward manner through, for example, observable Zeeman splitting of its emission lines. If a magnetic field is present however, in particular one parallel to the shock front, or with a significant component that is parallel, then clearly the field will resist compression in the cooling zone and, in turn, this will have an impact on the shock's emission properties, e.g., observed line ratios. However, as pointed out many years ago by Hartigan et al. (1994), interpreting the results is complicated. This

is because observable line ratios are degenerate with respect to the field's strength as spectra from low velocity shocks, without a magnetic field, resemble those from higher density, higher velocity shocks with a field. Breaking this degeneracy requires additional information which may be present. For example if the shock is well resolved spatially and is bow shaped, then the extent of the [O III] emission near its tip, can be used directly to infer the shock velocity at the apex. In addition the Hα flux from the bow, assuming it is clearly separated from the cooling zone, and the [SII]λ 6716/λ 6731 line ratio can be used to determine both the pre-shock density and the post-shock compression, respectively. This in turn reveals the strength of the pre- and post-shock fields in the shock plane. In this way Morse et al. (1992, 1993) found weak fields, of around 30 μG, in the gas ahead of bow shocks in the HH 34 and HH 111 outflows. Compression of the field then resulted in around 1 mG in the cooling zone. It should be said that this equates to an Alfvén speed of around 10 kms^{-1} in most of the observed post-shock zone, i.e., comparable to the sound speed but orders of magnitude smaller than the velocity of the jet itself. Put another way, in these outer regions the magnetic field is no longer dynamically important although the situation may be very different close to the source.

A variation on the above method to measure the magnetic field using shock physics has been proposed by Hartigan and Wright (2015). Here the degeneracy is broken by measuring the extent of the cooling zone which is obtained from the distance, allowing for projection effects, between the Balmer emission lines and the forbidden lines. Applying the method to existing data for a bright knot in the HH 111 jet, they obtain a relatively low Alfvénic Mach number, $M_A = V_S/V_A$, indicative of super-magnetosonic velocity perturbations in the jet.

Another important effect that magnetic fields in jets have is on softening the effects of a shock. In a standard non-magnetic shock, the transition from pre- to post-shock gas conditions is sudden and the width of the shock is a few mean free paths. The presence of a magnetic field effectively allows energy to be transmitted upstream ahead of the shock, accelerating it, and giving rise to a gentler profile in which the heating of molecules and atoms is more gradual (Smith and Mac Low, 1997). Such shocks are known as C (Continuous) shocks as opposed to their non-magnetic J (Jump) shock counterparts. One effect of the more gradual changes in properties in a C-shock is that molecules, e.g., H_2, may not be dissociated even at shock velocities where this might be expected (Eislöffel et al., 2000)

The presence of magnetic fields can also be indirectly inferred from jet rotation. The theory is that the wind leaving the accretion disk is collimated into a jet and focused on scales comparable to the Alfvén radius. Up to such distances the ionized wind/jet material is forced to corotate with an angular velocity equal to that of its foot-point. Since the wind is expanding away from the star, along magnetic field lines, it gathers angular momentum as it does so. Through the magnetic field there is then a back reaction on the disk, forcing material in the disk to lose angular momentum and continue to spiral inwards. It is therefore possible for the wind/jet to carry away say 10% of the mass that flows through the disk but practically all of the angular momentum of the remainder. If this scenario is correct, then jets must rotate. The amount of rotation depends on where the jet is launched from. For example, if the X-wind model is correct and the jet comes from close to the disk's co-rotation radius (typically at a few stellar radii), then the expected spin of the jet should be small. If, on the other hand, most of the material comes from further out, say at ($\sim$ 1 au), then we expect any measured jet rotation to be corresponding higher. Here we are assuming that the magnetic level arm is similar in both cases, i.e., the ratio of mass outflow to mass accretion is the same.

The search for jet rotation initially used the Space Telescope Imaging Spectrograph (STIS) on the HST (Bacciotti et al., 2002; Coffey et al., 2007) either in the optical or UV. Here the high spatial resolution of this instrument, of order 0.1 arcs was particularly important. The reason for this is that if jets are launched within a few au of a young star, then one might expect a good place to look for signatures of rotation is close to the source, say within a few hundred au. In this region the jet has not had time to interact with its surroundings, an effect that might mask, or even mimic, rotation. In this region however, the jet width is at most a fraction of an arcsecond for the nearest young stars (Dougados et al., 2000). Thus, high spatial resolution, such as afforded by HST, is needed. Moreover, if a typical jet is launched with a velocity of a few hundred km s^{-1} then at most we expect differences in radial velocity of say a few tens of kms^{-1} from one side of the jet with respect to the other in a slice transverse to the outflow axis. As shown for example by Bacciotti et al. (2000), a transverse cut through a jet does not show a "top-hat" velocity profile, even in the absence of rotation. Instead such position velocity (PV) diagrams show a smoother decrease toward the jet edges, i.e., the poloidal velocity gradually decreases away from the jet axis. The search for a rotation signature is then a hunt for a lopsidedness, i.e., a lack of axisymmetry, in this profile.

These observations are extremely challenging however, even with STIS, given the angular widths of the nearest jets and the spectral resolution required. Nevertheless, observations of jet rotation in theory could help discriminate between different MHD jet wind launching models. One other obvious constraint that we might also reasonably impose is that any evidence for rotation must be consistent with the sense of rotation of the underlying accretion disk and that the opposing (red and blue-shifted) jets in a bipolar outflow must have opposing helicity. With these constraints in mind, results from optical/UV observations using HST have been something of a mixed bag. Moreover, even when rotation has been claimed, alternative explanations such as asymmetrical shocks (De Colle et al., 2016) and precession (Cerqueira et al., 2006) have been proposed to account for the observed effects.

An alternative observational approach in the search for rotation has however emerged in recent years. Instead of looking for a rotation signature in the atomic/partially ionized jet, studies are now being undertaken of the molecular outflow in the millimeter band using high spatial and spectral resolution interferometers such as ALMA. Although the available spatial resolution is not as good as HST (although resolutions of 0.02" have been achieved for ALMA observations of HH212, Lee et al., 2017), molecular jets tend to be wider than their atomic counterparts close to their source and the spectral resolution of

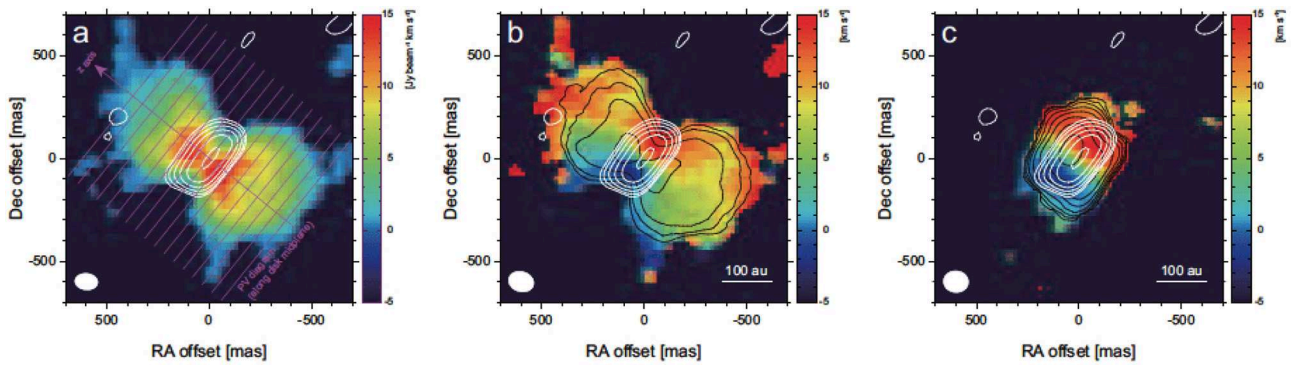

FIGURE 1 | ALMA observations of rotation in the bipolar outflow driven by Orion Source I, a high mass YSO candidate. White contours are 490 GHz continuum maps. **(a)** moment 0 (color; integrated intensity) map of 484 GHz emission in $Si^{18}O$; **(b)** moment 0 (black contours) and moment 1 (peak velocity; color) map of the 484 GHz Si18O line; **(c)** moment 0 (black) and moment 1 (color) maps of the 463 GHz H2O line. These latter two plots show rotational velocity gradients of the outflow- water line emission being more compact. From Hirota et al. (2017) reproduced with permission © Springer Nature.

an instrument like ALMA is much higher than STIS. Thus, it is possible to search amongst molecular jets for rotation signatures.

Figure 1 shows an outstanding example of a rotating, large scale molecular outflow observed by ALMA (Hirota et al., 2017)—a source whose rotating outflow was first discovered by SiO maser observations (Matthews et al., 2010). Observed at resolutions of about 50 au, observations were made in $Si^{18}O$ (484 GHz) and H_2 O (463 GHz) lines of an outflow from a region of massive star formation in the famous Orion nebula (KL region). The former traces emission from the outflow while the latter traces emission from a dense rotating disk. The outflow speed is $\sim$ 18 km s^{-1} on an outflow scale of 1000 au. We are afforded an almost edge-on view of the system. Using observations of the rotation curve of the gas in the disk, Ginsburg et al. (2018) were able to estimate the mass of the central star (SrC 1) to be $\sim (15) M_{\odot}$. Both these maps (**Figures 1b,c**) show velocity gradients along the disk plane.

The authors note that other possible explanations of this velocity gradient such as disk warping and other effects can be ruled out for this source making it likely to be an example of a rotating molecular outflow. The resolution is not sufficient to distinguish Keplerian vs. constant angular momentum ($v_\phi \propto r^{-1}$) for the disk. However the specific angular momentum of the outflow is approximately constant. With a measured value of this wind angular momentum of 400–600 km s^{-1} au, this corresponds to a source radius on the disk (where centrifugal and gravitational forces balance) of 21–47 au. The observations suggest that this is almost certainly evidence for a disk wind being accelerated off the disk far from the star or star-disk magnetosphere, and that the wind material is not swept up through entrainment by a narrow jet from the surrounding gas envelope. There are however a number of caveats worth pointing out about Source I and its immediate vicinity. First, like most massive stars, Source I is in a cluster that may not only be dynamically active, but which can cause confusion when trying to untangle the effects of one outflow from another. In particular, while previous work suggests a very young jet-like outflow from Source I in SiO and CO, this interpretation is less clear in recent ALMA data (Bally et al., 2017). Another point that should be stressed is that while our understanding of how high mass stars form seems, in the main, to resemble our picture for low mass star formation other physical processes must come into play. For example, as shown by simulations, increasing uv radiation and its ionizing effects, must be taken into account (Krumholz, 2015).

Figure 2 shows ALMA observations of an SiO jet in the famous class 0 outflow source HH 212, located in the Orion L1630 cloud at a distance of 400 pc. The importance of this source is that it allows us to probe the very earliest stages of the launch of outflows and their connection with disks. ALMA observations (Lee et al., 2017) reveal knots in the highly collimated jet within 120 au of the rotating disk (shown in red), down to 10 au scales. Of central importance is the 7σ detection of velocity gradients across these knots, perpendicular to the outflow. The sense of the gradient is the same for all of the knots, ruling out random fluctuations in the jet. The mean specific angular momentum in the jet is $l_j \sim 10.2 \pm 1.0$ au km s^{-1}. By assuming the conservation of angular momentum along streamlines, and projecting this back to a source radius on the disk (Anderson et al., 2003), one finds that the footpoint of this flow is $r_o \approx 0.05$ au, originating from the innermost regions of the disk. This is consistent with an origin from the innermost zones of the disk, from either a close-in disk wind, an X-wind or even a stellar magnetospheric wind.

A number of other rotating outflows have now been found, including sources such as DG Tau (Agra-Amboage et al., 2011), Orion BN/KL Source I (Chen et al., 2016), TMC 1A6 (Bjerkeli et al., 2016) with flows originating from extended disk scales, and the rotating and possibly precessing molecular outflow in HH30 (Louvet et al., 2018). In the case of the DG Tau source observed with the Plateau de Bure interferometer, the most likely explanation for the highly collimated jet seen in Fe lines is a quasi-steady centrifugal MHD disk wind ejected over 0.25–1.5 au and/or episodic magnetic tower cavities launched from the disk. The rotation seen in SMA observations of the outflow in Orion BN/KL suggests that the jet launching footpoint on the disk has

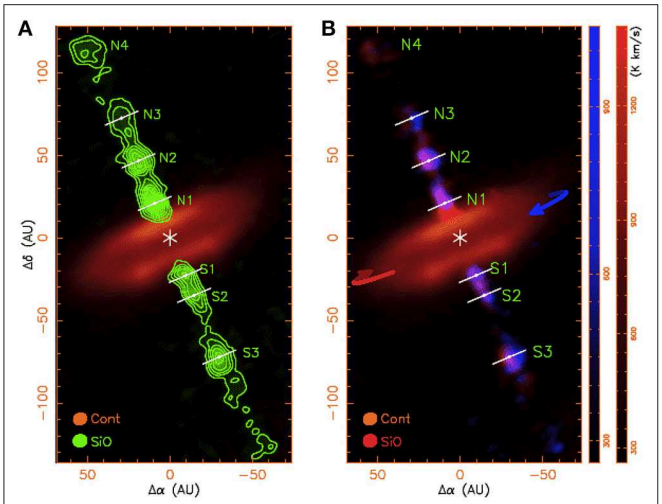

FIGURE 2 | ALMA observations of the rotating outflows of the class 0 protostar HH 212. Shown is a zoom-in to the innermost part of the jet in SiO within ≈ 120 au of the central source, at a resolution of ≈ 8 au on top of the continuum map of the disk. The maps show the intensity (in unit of K km s^{-1}) integrated over certain velocity range. **(A)** A chain of new knots trace the primary jet emanating from the disk, observed in SiO. **(B)** Blueshifted and redshifted SiO emission of the jet plotted with the continuum emission. Direction of rotation is shown with arrows. From Lee et al. (2017) reproduced with permission © Springer Nature.

a radius of 7.2–7.7 au. ALMA observations of the CO outflow in the TMC1A6 outflow indicate a source radius of 25 au from the disk, ruling out X-wind or stellar wind sources for this molecular outflow. In a similar vein, Zhang et al. (2018b) have observed the NGC 1333 IRAS 4C outflow in the Perseus Molecular Cloud with ALMA, tracing CCH and CS emission in an outflow cavity. Outflow rotation is detected from 120 to 1400 au above the disk, and its velocity is highly symmetric about the outflow axis. A flat distribution of specific angular momentum profile is observed in the outflow, with a mean value of 100 au km s^{-1}. Projecting this back onto the disk gives a launch radius of 5-15 au, indicating a wind originating from large portions of the disk. The wind may reach out to the centrifugal radius of the disk ($r_c \simeq 30$ au), so further high resolution observations are needed.

These various examples suffice to make the point that ALMA resolves rotating molecular outflows that originate from large sections of their disks, and perhaps out to their edges.

2.3. Outflows and Disk Formation

The observational evidence shows quite clearly that stars are born within surrounding disks or disk-like structures that, of course, are the birthplaces of planets. Nevertheless, there is still considerable debate in the theoretical models as to how and when protostellar disks first appear and what their basic physical properties are in these early phases (see the article by Würster and Li, this volume). Certainly multiplicity, across the stellar mass spectrum, is likely to be important in how disks evolve, and to effect outflow production. For example most class-0 low mass stars are in multiple systems and the level of multiplicity appears to decline as such systems evolve (Reipurth and Mikkola, 2012, 2015). This immediately suggests that dynamical, so-called N-body interaction, must be taken into account as it can lead to disk truncation and warping, precession of outflows, etc. Despite such complications, it is important to examine what effects magnetic fields might have on disk and outflow evolution. How influential magnetic fields are, can be gleamed from examining their structure, i.e., geometry, during the early stages of star formation.

The study of magnetic field structure in dense molecular clouds relies on the fact that elongated and spinning dust grains are aligned perpendicular to magnetic field lines. While radiation effects produce the spin needed for alignments by magnetic field, it is important to note that as asymmetric dust grains scatter or absorb photons they also undergo radiative torques which can be stochastic or regular (Hoang and Lazarian, 2009). These radiative torques leading to grain alignment would be minimal in regions of sufficiently high optical depths. Polarization observations of background star light passing through cores in molecular clouds are not possible at optical or infrared wavelengths because of the high column densities of such regions. However, thermal emission from these spinning grains can be detected at millimeter and submillimeter wavelengths and is weakly polarized in a direction perpendicular to the field lines (Matthews et al., 2009). Using these techniques, the relative orientation of bipolar outflows with magnetic field directions toward 16 class 0 and I outflows were measured (Hull et al., 2013). These high resolution submm observations were carried out at the CARMA. The results showed that magnetic fields on 1,000 AU scales are consistent with models in which outflows and magnetic fields are either randomly aligned, or preferentially perpendicular. These results may also be interpreted as the random alignment of disks with magnetic fields—as would arise if turbulence plays an important role in disk formation (see review by Hull and Zhang in this volume).

Probing the actual geometry of outflows and magnetic fields on disk scales is now possible with polarimetric observations at mm as well as mid-infrared wavelengths (Chuss et al., 2019; Jones et al., 2019). Observations of L1448 IRS 2 in ALMA band 6 were carried out by Kwon et al. (2019). Dust polarization can be affected by radiation anisotropy as well as self-scattering, but these it is argued may be minimal in this source. **Figure 3** shows that the magnetic field takes on the classic hour glass form expected for contracting magnetized disks threaded with an ordered field. The field is aligned with the outflow in the vertical direction, but switches to perpendicular alignment at the disk. The latter effect indicates the presence of a strong toroidal field at the disk. If this magnetic field interpretation is correct, then the field has been strongly wound up in the disk. The Davis-Chandrasekhar-Fermi (DCF) method was used to measure the field strength in the disk region of 720 μG, although some caution needs to be exercised in applying this to regions in which turbulence may not be strong. This strong field would brake the disk quickly; in 1,400 years. The ordered outflow and presence of a large disk perpendicular to it might suggest that magnetic braking effects have been minimized—perhaps by ambipolar diffusion. Chuss et al. (2019) present the best magnetic field map

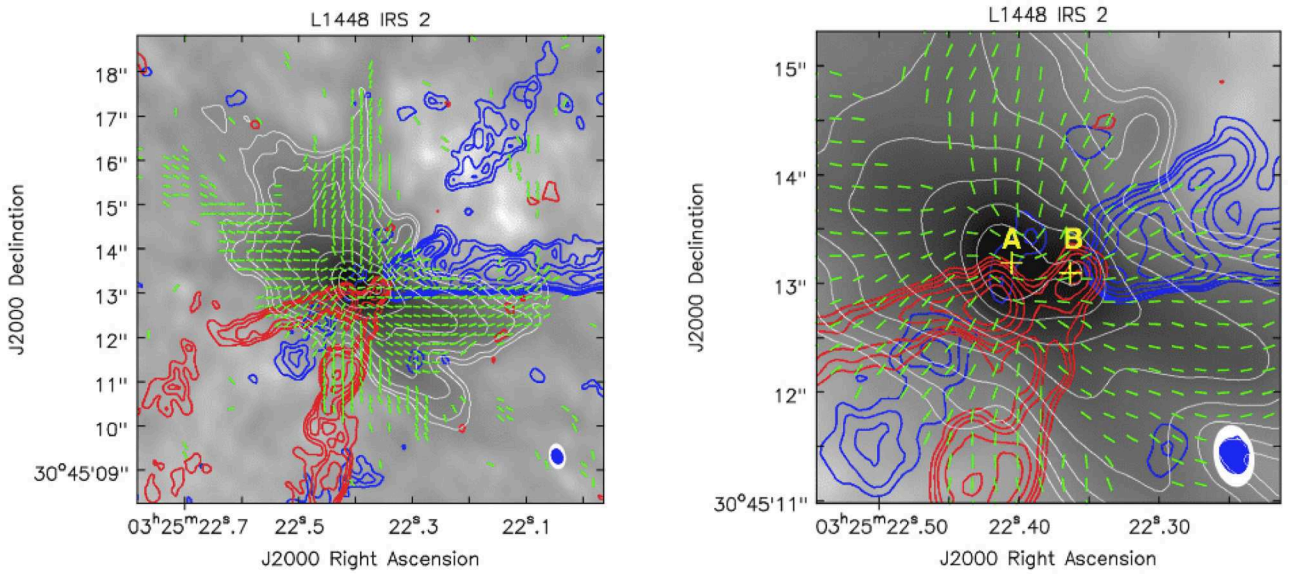

FIGURE 3 | Magnetic field morphology around L1448 IRS 2. (Left) The green vectors indicate the inferred magnetic field direction. The gray scales and white contours present the total intensity distribution with levels of 2 to 129 times 0.1 mJy beam. The blue and red contours are CO 2-1 intensity distributions integrated in velocity ranges of -8:0 to 2.0 and 7.5 to 16.0 km s^{-1}, respectively. (Right) Zoomed-in central region. The synthesized beams of the CO and the continuum data are marked in the bottom right corner in blue and white, respectively. From Kwon et al. (2019) reproduced with permission © AAS.

of the OMC1 core and outflow region to date. Again a classic hourglass pattern is seen.

Perhaps the largest sets of high resolution images that we now have of protostellar disks is a consequence of the Disk Substructures at High Angular Resolution Project (DSHARP) campaign at ALMA. The initial survey of 20 protostellar disks at a resolution of 5au FWHM provides the first look at the small-scale features in disks that are directly relevant to the planet formation process. It must be noted that this is a diverse collection of disks that are typically much larger than the bulk of disks now turning up in other surveys. They are images of Class II systems (ie disks well beyond the formation phase), and can be regarded as protolanetary disks (disks in earlier phases of star formation—the so called Class 0 and I phases, are denoted as protostellar disks). These images show a variety of rings and gaps, amplitudes, and disk sizes for targets with a range of stellar and disk properties (Andrews et al., 2018). The ubiquitous ring and gap structures have no obvious spacings that are connected with properties of the host star. The ring systems may arise through modulations of disk pressure that trap dust grains. Specifically, the observed system rings have been modeled as arising by dust trapping in axisymmetric pressure bumps (Dullemond et al., 2018). If the turbulence in disks is relatively weak, then dust can be strongly confined in pressure bumps, while strong turbulence compromises the trap. Theoretical modeling of the ALMA ring data suggests a lower limit to the turbulent amplitude expressed in the standard turbulent viscosity parameter (α) which takes a lower bound of $\alpha \geq 5 \times 10^{-4}$. Without this level of turbulence, the rings would be even sharper features than they already are. It is possible that these pressure bumps themselves are produced by planets. In any case, the model constraints on the turbulence level is of interest in comparing the relative role of turbulent vs. disk wind torques in disks.

2.4. What Radio Emission From Outflows Can Tell Us

Observations of YSO jets at radio wavelengths (around a few centimeters) have shown them to primarily emit thermal radiation (i.e., radiation with a positive spectral index α where the flux at frequency ν, $S_\nu \propto \nu^\alpha$). Moreover, typical flux densities are very low and usually less than 1 mJy (Anglada et al., 2018). Such emission is un-polarized and is often elongated in the direction of the known atomic/molecular outflow. Until recently the amount of information that could be obtained from radio maps was limited, primarily due to the lack of sensitivity of radio interferometers, nevertheless they provided upper limits to the diameter of jets and have proven that they must be collimated on scales less than 50 au in agreement with high spatial resolution HST data (Reipurth et al., 2004). In the past few years however radio astronomy has undergone a revolution that is having a major impact on our ability to image outflows from young stars. This revolution is akin to the replacement of photographic plates in optical astronomy (with quantum efficiencies (QE) of a few per cent) by the CCD (QE $\approx$ 70% or more). In the past traditional radio interferometers, such as the Very Large Array (VLA) in New Mexico and the high spatial resolution Multi-Element Radio Linked Interferometer (MERLIN) centered on Jodrell Bank, used microwave links between the various telescopes to transmit wavelength, amplitude and phase information. These links were of limited bandwidth and correspondingly only a narrow radio continuum could be observed at any one time. Such old links however have now been replaced by fiber,

allowing considerably larger observing bandwidths that are used in conjunction with much-improved correlators, lower noise amplifiers, and increased computer processing power. The net result is an enormous increase in radio continuum sensitivity (typically by an order of magnitude or more). For example the VLA in standard continuum observing mode had 4 sub-bands of 50 MHz each but the JVLA has 2 sub-bands 2 GHz wide! Of course this has a dramatic impact on radio studies of jets from young stars. Complete radio surveys of YSOs in nearby star formation regions, for example, have become possible for the first time (Dzib et al., 2015; Tychoniec et al., 2018).

A second strand to the radio astronomy "revolution" is the opening up of the low frequency radio spectrum with the advent of instruments such as the Low Frequency Array LOFAR (van Haarlem et al., 2013) radio telescope. LOFAR is allowing us to explore jets from young stars in a new band (at meter wavelengths) and, as described below, could reveal any non-thermal emission. A particular advantage of the radio band is that it can potentially provide very valuable information on magnetic fields in YSO jets. Theoretically we only expect magnetic fields to dominate the dynamics of an outflow close to the source, i.e., within 100 au, and in high velocity post-shock regions where the field is compressed and amplified (Hartigan and Morse, 2007). Thus we have a higher chance of measuring jet fields by studying the zone surrounding the young star at high angular resolution and the brightest knots (compressed zones) on more extended scales. But how might we do this? One powerful method is hinted at by the fact that a small number of jets/outflows have non-thermal radio spectra as demonstrated in the case of more massive young stars such as Herbig-Haro 80/81 (Carrasco-González et al., 2010) but also in their lower mass counterparts (Ainsworth et al., 2014). Such radiation appears to come from high-energy electrons (i.e., it is gyro-synchrotron or synchrotron emission) and, as discussed below, it may be common at very weak flux levels in "standard" low luminosity outflows but nevertheless detectable with the new suite of radio interferometers such as e-MERLIN, the Jansky VLA (JVLA) and at low frequencies (e.g., using LOFAR).

Figure 4 shows the radio continuum map of HH 80-81 (Carrasco-González et al., 2010). The analysis of the synchotron emission yields a field strength of $\sim$ 0.2 mG in the jet. The field is parallel to the jet axis, and the increase of polarized emission toward the limb of the jet is evidence for a collimating toroidal field. These characteristics are very similar to those of AGN jets, providing good evidence to support the idea that the jet mechanism is universal.

As stated previously, we primarily expect to detect free-free emission in the cm (1-010 GHz) band. However, non-thermal emission is observed on occasions and this opens up the intriguing possibility of directly measuring both the magnetic field's strength (using its intensity) and direction (using polarization). Such measurements, although difficult, could provide the "missing link" needed to properly evaluate the importance of magnetic fields in jets, as essentially all other parameters are known. The improved sensitivity and high resolution of e-MERLIN and the JVLA may allow us, in a systematic way, to study this type of emission as faint

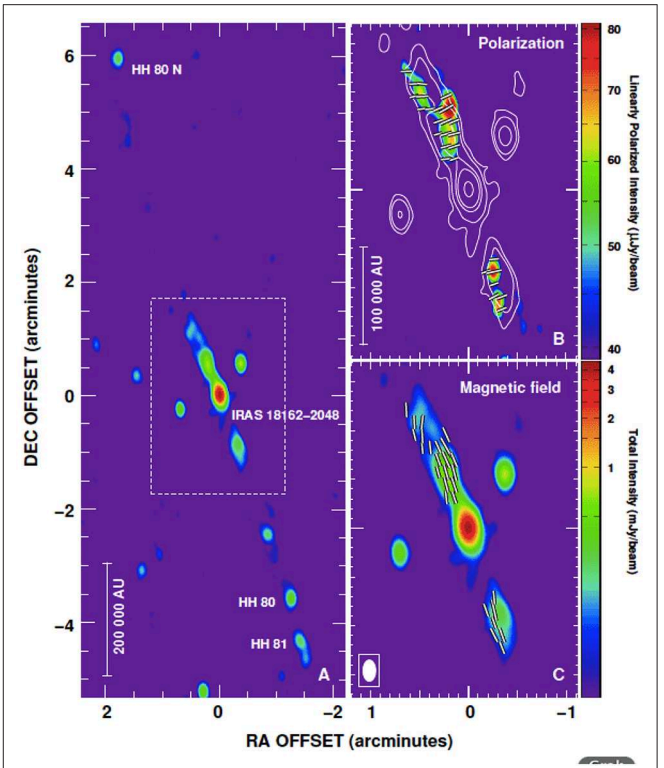

FIGURE 4 | High resolution, 6 cm radio continuum VLA images of the jet HH80-81. The knots, 0.5 pc from the source are linearly polarized indicating non-thermal synchotron emission from the jet. **(A)** Radio continuum image of the whole jet. **(B)** Linearly polarized continuum intensity image. **(C)** Apparent magnetic field directions superimposed on continuum map. From Carrasco-González et al. (2010) reproduced with permission © AAAS.

non-thermal radiation (arising from electrons being accelerated to relativistic speeds near shocks) mixed in with free-free emission (Rodríguez-Kamenetzky et al., 2016).

2.5. Magnetic Fields Close to Young Stars

Magnetic fields are thought to play a very important role in accretion onto young stars and the evolution of their outflows. In particular circumstellar magnetic fields are considered to be sufficiently strong to clear the central region of a young star's accretion disk and force the star to co-rotate with the disk's inner edge (Ferreira, 2013). Moreover, at the same time as they funnel material onto the star, they may also help remove excess angular momentum thereby allowing accretion to proceed and the star to contract to the main sequence. Magnetic fields may even play a role in planet formation since the inner gap they generate could allow hot Jupiters, which have already been discovered around T Tauri stars (Donati et al., 2016), to survive without them being accreted by their parent YSO (Adams et al., 2009).

It is only in recent years that we have been able to determine the geometry and strength of the fields in classical T Tauri stars (Johns-Krull, 2007; Donati et al., 2012). Such studies have revealed some surprises, including the fact that the weakest fields have the most complex geometries, i.e., they are not simple dipoles, and that these tend to be associated with the

development of a substantial radiative core (**Figure 5**, Left). Moreover these fields are found to vary, which with the addition of their complex geometry, suggests they are generated through dynamo action and are not fossil fields as has been assumed in the past. Determining the magnetic field direction and strength can be done using Zeeman Doppler Imaging or ZDI (Morin et al., 2011; Gregory et al., 2012), i.e., by spectro-polarimetry using instruments like HARPS-Pol at ESO. This involves measuring the circular polarization signal (Stokes V parameter) in both photospheric absorption lines and accretion dominated emission lines over several rotation cycles. The signal in accretion lines is usually so strong that measurements can be made using individual lines (e.g., He I 5876) although it should be stressed that this represents the field in the vicinity of an accretion "hotspot." In contrast the signal in magnetically sensitive photospheric lines is so weak that cross-correlation techniques over many lines have to be employed to get an average Zeeman signature (Gregory et al., 2012). Combining both sources of data together, and by monitoring how the Stokes V parameter changes as a function of rotational phase, it is then possible to map the magnetic field. While very few classical T Tauri star magnetic fields have been mapped in detail (Hussain and Alecian, 2014), application of the method has proven very successful including the case of AA Tau (Donati et al., 2010) a known jet source. The magnetic field of AA Tau is shown in **Figure 5**.

In addition to analyzing the magnetic field of the young stars, it may also be possible with the next generation near-infrared (NIR) spectro-polarimeters, such as SPIRou (Donati et al., 2018) to detect spectral features from the innermost regions of the accretion disks of high mass accretion rate stars (Class I and Class II). This could allow us to map both the "normal" disk poloidal and toroidal magnetic fields for the first time in an analogous way to what has been achieved for a CTTS disk in the more excited FU Ori state (Donati et al., 2005). A particular advantage of spectro-polarimeters like SPIRou is that not only do they operate in the NIR where disk emission can come from but also Zeeman splitting increases with λ^2, all else being equal, and this makes it easier to measure. Note also that this region of the disk is not accessible to ALMA. In addition, as SPIRou can measure radial velocity with exquisite precision it should be possible from the data to detect the presence of hot Jupiters.

2.6. Feedback: Outflow Interaction With Molecular Cores and Beyond

There is no doubt that the final mass of a young star can be influenced by a whole host of environmental factors. As pointed out earlier, stars are frequently born in multiple systems that are dynamically active. Interaction between the companions can, for example, truncate a star's growth at an early phase (Bate, 2018). Radiation pressure from the newly formed star itself, particularly in the high mass regime, can limit accretion (Sartorio et al., 2019) as can photo-evaporation from external sources such as supernovae and neighboring OB-stars (Haworth and Clarke, 2019). Nevertheless it is thought that outflows may be very important in limiting accretion and thus the final mass a star can attain. Clearly they drive away material from the core and the envelope once they start to operate. It is not immediately obvious however what fraction of the final mass is removed and deposited back into the parent cloud. A related problem is the effect of outflows on the molecular cloud itself. It has long been known that the lifetime of a molecular cloud should be shorter than observed if the only force acting against gravity is thermal energy. Instead an additional force must be present. In some cases this might come directly from the magnetic fields threading through a cloud. We also know however from observations that supersonic and super-Alfvénic turbulence are present although the latter may only exist in the denser regions (Heyer and Brunt, 2012). The presence of turbulence alone however does not resolve the issue as the timescale for turbulence to decay in a typical cloud is short: there must be some local source of turbulence. Can this be outflows from young stars?

Certainly outflows create cavities in their surroundings while at the same time ejecting momentum and energy into it. The net effect is to disperse the core (Arce and Sargent, 2006) and ultimately to terminate accretion. How efficiently outflows can do this determines the final stellar mass and also the fraction of the core's mass that is converted into a young star, i.e., the ratio between the so-called Core Mass Function (CMF) and stellar IMF (e.g., Offner and Arce, 2014). As a specific example, the core mass function of low mass, star forming cores in the Pipe Nebula, was measured by using infrared extinction of back ground stars (Alves et al., 2007). This showed that the IMF is the direct product of the dense core mass function and a uniform star formation efficiency of $30 \pm 10\%$. As already pointed out, both functions have similar profiles (see for example Cheng et al., 2018) the difference being the peak in the CMF is at roughly 3 times the mass of peak in the stellar IMF. Obviously if outflows typically remove 2/3 of the core mass, this could explain the observed relationship. A very good overview of the processes that can determine the relationship between the CMF and the IMF can be found in Offner et al. (2014).

In additon the expectation that outflows sweep away such a large fraction of the surrounding gas over their lifetime is supported by recent observations of the HH46/47 system using ALMA (Zhang et al., 2016). In carrying out such observations it is important to use optically thin tracers, e.g., ^{13}CO, to ensure the motion of the densest gas is not overlooked (Arce and Sargent, 2006).

Numerical simulations, for example by Offner and Chaban (2017), of the collapse and evolution of isolated dense cores now include the effects of turbulence, radiative transfer, and outflow feedback. These show that outflows can drive and maintain turbulence in the core environment even when magnetic fields are initially strong. Moreover, the final efficiencies are 15–40% in line with the observed values. Of course these are simulations at the individual star level: it should not be neglected that multiplicity can play a role in feedback not only in multiple systems but also on the larger cluster scale. In multiple systems, interaction between the components can lead to precession of the associated jets (Wu et al., 2009) thus broadening their impact on their surroundings. Moreover many stars are born in clusters, for example in regions such as NGC 1333 containing hundreds of stars and large numbers of criss-crossing outflows (Walawender

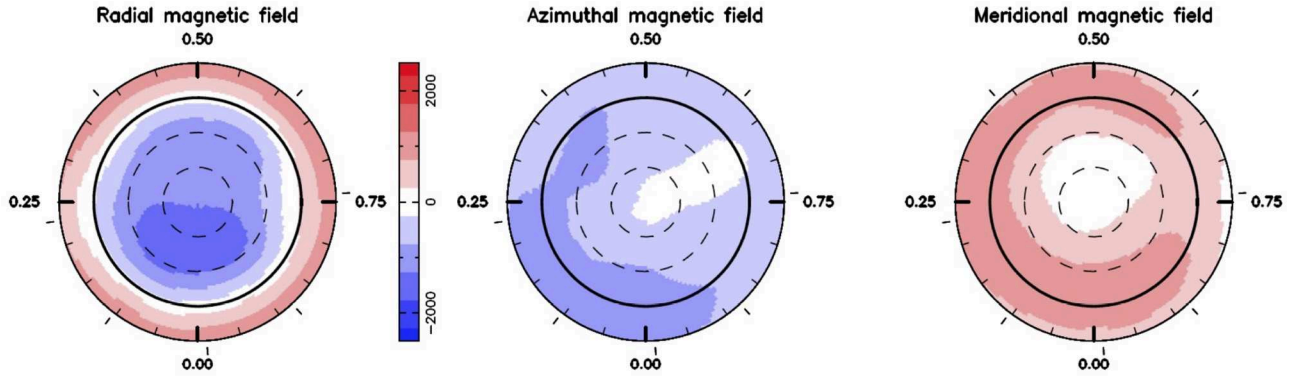

FIGURE 5 | Magnetic field map of the surface of the known jet source AA Tau. The field strength, shown by the colored scale, is in gauss for the radial, azimuthal and meridional components which are shown as a function of stellar phase. From Donati et al. (2010) reproduced with permission © OUP.

et al., 2008). This suggests we need to consider the ensemble to get a clearer picture of how outflows feedback into their environment. Whether magnetic fields or turbulence driven by stellar feedback ultimately control how molecular cloud material is converted into stars is still an open question (Li and Nakamura, 2006; Federrath, 2016).

3. THEORETICAL OVERVIEW

The last 5 years have also seen remarkable progress and new developments in the theory and simulations of magnetized outflows. The emergence of new computational tools and codes has played a leading role in these advances. These include time dependent radiation field and chemistry within MHD simulations (Gressel et al., 2015). On the horizon are new capabilities including zoom-in simulations in radiation MHD simulations using DISPATCH (Nordlund et al., 2018). Post-processing tools now available include Monte Carlo radiation transfer methods in RADMC3D. The ability to compute expected polarization maps from general MHD systems has recently appeared in the POLARIS code (Reissl et al., 2016) which has been applied to the polarimetry of outflows (Reissl et al., 2017).

3.1. Drivers for Outflows

There are several sources for magnetized outflows that are launched during the course of star formation, involving centrifugal or magnetic pressure drives from diverse sources such as forming disks in collapsing molecular cloud cores, the coronae of well established disks, magnetospheric boundaries, or the protostars themselves. Before getting into the details, we outline this general theory landscape.

(i) Magnetic braking and early outflows: As magnetized, pre-stellar cores begin to emerge from the filaments within turbulent clouds, magnetic braking begins to extract their angular momentum. The models of isolated, rotating molecular cloud cores with subsonic line widths that figure so prominently in many early theoretical and numerical studies are overly simplified pictures. In reality, hydrodynamic turbulence always contains small regions of non-zero angular momentum which, fed with enough mass, can produce disks—there is no need to assume that any coherently rotating object was present. In magnetized clouds in this earliest stage, turbulent MHD processes play a significant role in diluting the net braking torques on such pre-stellar cores, allowing disks to begin to form. The magnetic field geometry in these chaotic initial conditions likely become more ordered close to the disks as dissipative effects such as ambipolar diffusion take effect in higher density regions. Finally, at some point, collapsing magnetized cores reach their centrifugal balance radius. With the formation of this disk, or disk-like system, the pinching of field lines and/ or the accumulation of toroidal magnetic field results in the launch of the outflow. These are likely to global encompassing the entire eary disk. Class 0 ouflows likely have their origin in this event.

(ii) Magnetized disk winds: These will arise naturally during the evolution of magnetized accretion disks in their post formation phases. This has been shown by many authors, both theoretically and by means of numerical simulations using a variety of computer codes. These originate from disks that are both highly conducting, or in modern treatments, even from disks for which non-ideal effects dominate the physics of how fields are coupled to the gas and dust. Details of the launching mechanism likely involve a thermal component to the disk wind as it is launched from the upper layers of the disk or base of a disk corona. The large scale suppression of the MRI instability discovered in non-ideal MHD processes means that disk physics itself is not controlled so much by viscosity as it is by the outward transport of disk angular momentum by powerful winds.

(iii) Stellar spin and accretion powered stellar winds: The solution of the angular momentum problem for the protostar itself is another key aspect of star formation physics. If stars were to accrete the angular momentum from the inner edge of a Keplerian disk, they would spin up to break up speeds within a few hundred thousand years (the spin up torque of gas accreting from the magnetopause boundary r_{MP} onto the star is then $\dot{J} \sim \dot{M}_w \Omega_{Kep,MP} r_{MP}^2$, Matt and Pudritz, 2005). An early suggested solution for this dilemma proposed that magnetic field lines from the star, connect back into the disk such that flux penetrating the disk beyond the co-rotating orbit would effectively brake

the stellar spin by depositing angular momentum back into the disk (Koenigl, 1991). This "disk locking" picture has the problem that magnetic field lines would quickly shear out and reconnect, severing the connection between the star and disk. Centrifugally driven winds from the protostars can carry off angular momentum that is deposited by accreting gas streams flowing along magnetospheric field lines that connect the disk's inner edge, to the star (Matt and Pudritz, 2005). This work has met with considerable success in being a part of the rotational history of young stars (Bouvier et al., 2014). Earlier models of X-winds proposed that angular momentum from the disk inner edge is never accreted onto the star but is carried off in an X wind originating from the interface between the disk and the protostellar magnetosphere (Shu et al., 2000).

3.2. MHD Outflow Basics

To understand why magnetized outflows are so powerful and efficient in angular momentum extraction, we recall basic concepts of MHD flows from rotating bodies laid out in many papers and reviews (Konigl and Pudritz, 2000; Pudritz et al., 2007; Spruit, 2010). In the case of axisymmetric systems, we consider a rotating body threaded by magnetic field lines, with the footpoint of a field line located at a radial distance r_o from the rotation axis, along the rotor. The angular velocity of this footpoint at the base of the flow is Ω_o. The basic equations of stationary, axisymmetric MHD flows (e.g., Pelletier and Pudritz, 1992; Bai, 2016) tell us that the mass flux is conserved along streamlines of the outflow (from the continuity equation), as is the magnetic flux Φ. That is, the mass loss rate per unit area, along streamlines passing through an annular section flow of area dA, is $d\dot{M}_w/dA = \rho v_p$ (where v_p is the poloidal velocity along the field line) while the amount of poloidal magnetic flux through this same annulus is $d\Phi = B_p dA$. This means that the ratio of these two fluxes along a field line—the mass loss rate per unit magnetic flux, otherwise known as the mass loading of the flow—is also preserved: $k = d\dot{M}_w/d\Phi = const.$

The mass loading is determined by the physical conditions at the foot point of the flow, which is essentially at the slow magnetosonic point on each field line. As an example, if we consider the case of accretion disks as our basic rotors, the early 2D axisymmetric disk wind simulations of Ouyed et al. (1997) and Ouyed and Pudritz (1997) assumed that the flow originates at the base of a heated disk corona, whose heat source is not specified. Recent work takes the additional step of explicitly including FUV flux from the host star that heats the disk surface, feeding a disk corona (Bai, 2016). In any event, one needs to have a physical theory of how magnetic flux is distributed across the disk, and how mass is loaded onto it, in order to determine the mass loading function $k = k(r_o)$ which is a function of the conditions at the footpoint r_o (ie the slow magnetosonic point) of each field line on the rotor.

No theory that we are aware of has determined what this function is from basic first principles and so this remains one of the lingering uncertainties in the theory of MHD disk winds. Authors adopt some sort of "reasonable" scaling for the magnetic field distribution across the disk. As a specific example, consider outflows from magnetized Keplerian accretion disks. Suppose that the threading vertical field component is a power law $B_z \propto r_o^{\mu-1}$, the outflow speed at the footpoint scales with the local Kepler speed, and the base of the disk corona can be considered a polytrope (e.g., $\gamma = 5/3$). The mass load function then scales as $k \propto r_o^{-(\mu+1)}$. As an example, Blandford and Payne (1982) assume a self-similar model for disk winds which imposes a specific scaling for the field $B_{z,BP} \propto r_o^{-5/4}$, so that $\mu_{BP} = -1/4$ and hence $k_{BP} = r_o^{-3/4}$. The stable minimum energy jet structures investigated by Pelletier and Pudritz (1992) have $k_{PP} \propto r_o^{-1/2}$ (Pudritz et al., 2006). In general the power law index will also determine the degree to which poloidal magnetic field lines open up away from the footpoints. Recent global MHD models of outflows (Wang et al., 2018) assume that heating of the disk surface by stellar EUV photons provides thermal heating and provides thermal pressure that assists in driving an MHD disk wind. Here too, the initial distribution of magnetic field is assumed to follow a powerlaw distribution whose field lines initial structure is controlled by the choice of the power law exponent.

It is worth emphasizing that the concept of centrifugal acceleration of the flow arises naturally in the co-rotating frame of the footpoint of the flow (e.g., Spruit, 2010). There is no magnetic force driving the outflow in this frame that role being played by the centrifugal force. The flow in this region can be visualized as "beads on a wire." This is a very useful way to analyze the dynamics as long as the flow co-rotates with the rotor. This ends roughly at the Alfvén radius, where magnetic and inertial forces balance. The collimation of jets and outflows begins after the outflow passes through the Alfvén point on each field line. The reason is that the field lines now become increasingly toroidal. The degree of outflow collimation depends quite sensitively on the mass loading of field (Ouyed and Pudritz, 1999; Anderson et al., 2005). This is because it is the inertia of the material along the field line that causes the rotating field line to fall back from the rate of rotation of the footpoint, creating the toroidal field component. This is much like the behavior of a mass loaded whip. The solution of the induction equation specifically shows that the toroidal field B_ϕ in such an outflow depends on the mass loading. Since collimation of such rotationally driven outflows depends on the radial hoop stress exerted by the tension of the toroidal field line, mass loading must then control collimation properties of such winds. Specifically, magnetic fields in disks with power laws $\mu > -1/2$ will collimate to cylinders, while lower values will lead to wide-angle outflows that are parabolic at infinity (Pudritz et al., 2006).

As already noted, a central aspect of magnetized outflows is that they efficiently extract angular momentum from the rotor. How does this happen? Again, we first begin with ideal MHD since it allows us to see the basic physics quite simply. The conservation of angular momentum equation for our magnetized rotating system says that the conserved angular momentum per unit mass l of the fluid along a field line consists of two parts, the bulk rotation of the fluid itself rv_ϕ, and a component that is carried by the twisted mass -loaded field line, giving $l(r_o) = rv_\phi - (rB_\phi/4\pi k)$. For any theory of stationary winds, solutions are obtained by requiring that they flow smoothly through a

critical point on each field line (and for 2D flows, a critical line). Critical points are positions at which the outflow speed is equal to a signal speed in the flow. For purely hydrodynamic flows, the critical point occurs where the outflow speed equals the sound speed in the gas, $v_{p,hydro} = c_s$. For MHD flows, there are three MHD waves: the slow and fast magnetosonic waves (compressive modes) and the transverse Alfvén wave. The value of l on any field line is set by the condition that $v_p = V_A$, the Alfvén speed. If r_A is the radial distance of the field line from the outflow axis where this condition is met, then $l = r_A^2\Omega_o = (r_A/r_o)^2 l_o$ where $l_o = \Omega_o r_o^2$ is the specific angular momentum of the material at the footpoint of the flow.

This result reveals why outflows are so efficient. Each wind particle carries of a factor of $(r_A/r_o)^2$ more angular momentum per unit mass than its fellows rotating in the disk at the field line base. Thus, if the typical lever arm is $r_A/r_o \simeq 3$, then each wind particle can carry the angular momentum of ten particles in the underlying rotor. From this argument, it is also easy to see that in the limit that winds carry away all of the angular momentum of a disk that is accreting at the rate $\dot{M}_a$, the wind mass loss rate needed to drive this should simply scale as $\dot{M}_a \simeq (r_A/r_o)^2\dot{M}_w$. Indeed, this result follows from disk wind theory outlined in the following subsection.

The conservation of energy in ideal MHD, centrifugally driven winds is expressed by the Bernoulli equation for flow along the magnetic stream line. One finds that the terminal speed of the outflow is greater than the escape speed from flow at the base of any field line, specifically $v_\infty \simeq (r_A/r_o)v_{esc,o}$. It is this energy relation that ensures that hydromagnetic outflows scale with the depth of the gravitational well of the rotor. This is why star formation, from brown dwarfs to massive stars, is accompanied by jets and outflows. It is inevitably the efficient tapping of gravitational potential energy released during accretion by magnetized wind torques that is the main driver. This also implies that because the terminal speeds of outflows on each field line scale with the Kepler speed of the footpoint, then disk winds will have a wide range of terminal speeds—the highest (hundreds of km per sec) in the interior parts of the jet or outflow, the lowest on largest outflow scales that can be supported on the disk (10 km per sec or less). This is distinctly different than the prediction of X-wind models which really have only one velocity component originating from the innermost radius of the disk. Observations generally support the former velocity structure (recall however, the SiO observations of HH212, which are consistent with an inner disk-wind or an X-wind origin; Lee et al., 2017).

Another aspect of winds accelerated from disks is the launch angle at the footpoint of the flow. An intriguing aspect of such outflows is that they can be launched for completely cold gas—one only needs the field line to be bent by an angle of 30^o from vertical (Blandford and Payne, 1982). Of course, any additional heating of the outflow region near the surface of the disk will mean that radial thermal pressure gradients will increase this opening angle. As an example of this effect, polytropic models for the disk corona will have opening angles for field lines that increase with radial distance across the disk (e.g., Pudritz et al., 2006). Vertical pressure gradients can also lead to better acceleration along the field lines. Detailed heating models of disks by FUV irradiation from the star (Bai, 2016) will have their own prescriptions of field line opening.

Early numerical simulations of jets focused on initial axisymmetric setups, often focused on the launch region near to the disk. However, fully 3D simulations are needed to understand the complexity, stability, and asymmetries that can arise in jet dynamics in both the launch region and far from the disk.

In **Figure 6** we show a global, high resolution 3D simulation, (using ZEUSMP, Norman, 2000) of a collimating disk wind whose source is in the corona of a Keplerian disk threaded with magnetic field lines (Staff et al., 2015). This figure shows the toroidal velocity and magnetic field lines in a jet launched from the corona of a Keplerian disk. The magnetic geometry on the disk (and hence mass loading) follows that of Pelletier and Pudritz (1992). The jet is heated by shocks throughout its volume and the densities and temperature profiles are used to compute forbidden line emission in various lines in [CI IV], [S II], and Mg II transitions, whose critical densities are $n \approx 1, 10^4, 10^5$ cm^{-3}, respectively. The red and blue colors indicate Doppler shifts of rotating knots in the flow. The jet field has a strong poloidal field along the axis of the jet which acts as a "backbone" that helps preserve the jet against instabilities. Note that the toroidal field wraps around the jet, especially in the outer regions, giving rise to a highly collimated jet. This as noted, agrees with observations of field structures seen in discussed in the observations of H80-81 (see **Figure 4**). Other simulations with a less steep gradient of disk magnetic field did not collimate so well—as discussed above.

3.3. Early Phase: Gravitational Collapse, Outflows, and Disk Formation

A problem of critical importance for stellar birth is the formation and evolution of protostellar disks and the concomitant launch of outflows. These are highly nonlinear phenomena whose complexity arises from the interplay of gravity, turbulence, angular momentum, magnetic fields, radiation, thermodynamics and even chemical evolution. Despite this, the appearance of disks and outflows in the earliest stages of star formation appears to be universal and this poses several important challenges for theory.

3.3.1. Idealized Models

The first theoretical treatments of star formation in magnetized clouds focused on magnetic braking of idealized, uniformly rotating gas spheres. This is enabled by a flux of a special wave: the torsional Alfven wave—first discussed in mathematical papers by Gillis et al. (1974) and Gillis et al. (1979). Subsequently analytic solutions in ideal MHD were found by Mouschovias and Paleologou (1980). The idea is simple to visualize. Consider the formation of a condensation that is threaded with a magnetic field in a medium of non-zero angular momentum. The ongoing condensation will generate a shear that twists the magnetic field, creating a toroidal field component. The resulting magnetic torque on the condensation, extracts its angular momentum which is transported away by a flux of torsional Alfvén waves. The angular momentum is transferred to the surrounding medium which is gradually brought into co-rotation with the slowing

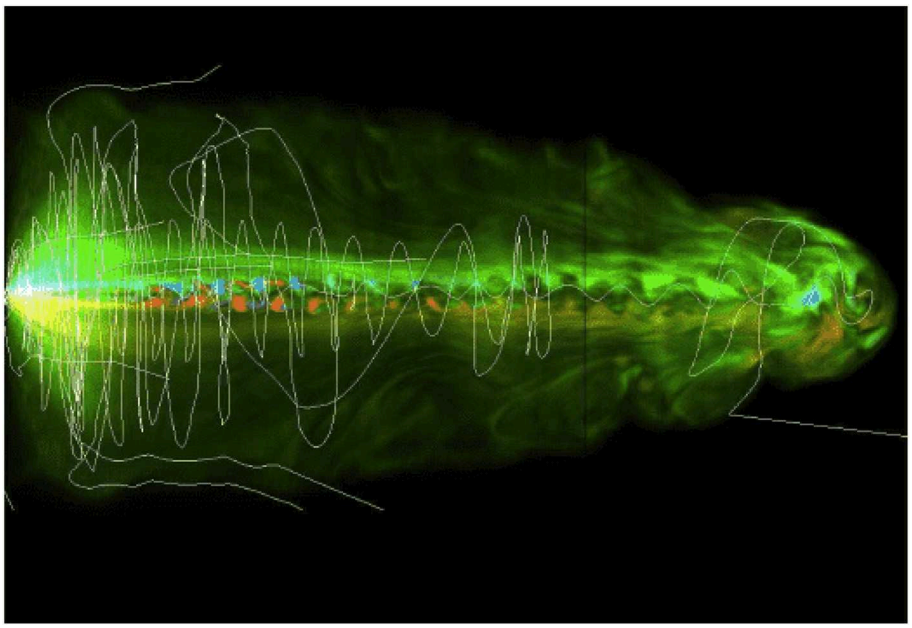

FIGURE 6 | 3D MHD simulations of a disk wind showing the toroidal velocity and magnetic field lines for a disk wind produced in the Pelletier and Pudritz (1992) model. The outflow source is the base of the corona of a Keplerian disk, shown on the left of the figure. The simulations are run on a grid extending out to 90 au along the jet axis, and 27 au on either side of the jet axis. Brightness indicates higher radiation intensity from shock-produced, forbidden line emission in the jet. The red and blue colors of the knots indicate red and blue shift due to jet rotation. Note also the recollimation of the jet half way down the flow. From Staff et al. (2015) reproduced with permission © OUP.

rotor. This braking picture suggests modest stirring of the environment around the forming star by a flux of these torsional waves. Given that the early stages of star formation are observed to be accompanied by vigorous outflows in the class 0 phase, this suggests that the braking phase occurs earlier, and sets the conditions for the first stages of disk formation.

This simple model, however, was later realized to create a problem for disk formation. Recent simulations have shown that braking in this picture is so efficient that disks fail to form. This has been dubbed as the magnetic braking catastrophe. How does this arise? First we recall that the exact condition for collapse to occur in the first place is that the ratio of the cloud's gravitational to magnetic energy densities exceed unity. The condition may be rephrased. The ratio of these energies can be written in terms of the mass to flux ratio of the cloud—which is equivalent to the ratio of the cloud's column density N to its field strength: $(M/\Phi) \propto (N/B)$. The critical condition is that the ratio λ of the cloud's mass to flux, to the critical mass to flux for stability, exceeds unit: $\lambda > 1$. The critical value $(N/B)_{crit} = 2.6$ must be exceeded (ie. becoming supercritical) for collapse to occur (Heiles and Troland, 2005). Li et al. (2015) performed MHD simulations of magnetized turbulent clumps and compared these to a variety of Zeeman and other observations and found that the typical molecular clump is supercritical with $\lambda \sim 3$. Thus, there is now a substantial body of observations confirmed by simulations, that places good limits on the origin and initial strength of magnetic fields in star forming cores—and therefore on the field that is available to drive outflows.

A substantial body of work on collapse calculations focuses on the consequences of the Mestel picture of idealized isolated, spherical magnetized clouds, wherein the MHD is treated as either ideal or non-ideal (Masson et al., 2016). One of the key processes that sets in on small scales of disk formation at higher gas density is non-ideal MHD. Magnetic fields will decouple from the gas at high densities, and this, it was hoped, would lead to substantial decoupling of the field from the collapsing gas. Non-ideal MHD processes such as ambipolar diffusion and Ohmic dissipation, which depend on how gas is ionized, and on grain sizes and charges at high densities, could play a role for the formation of protostellar disks. This has been investigated quite extensively by a number of groups.

As an example, Mellon and Li (2008) showed that braking can prevent the build-up of disks during the early phase of star formation for relatively week fields; $\lambda \leq 10$. Subsequent work established that even weakening the initial field by the process of ambipolar diffusion had little effect on this result (Mellon and Li, 2009). The basic point is that by the time densities at which AD becomes effective are reached, magnetic braking is still so effective that only small disks may form. Normal ambipolar diffusion and Ohmic dissipation are ineffective (Li et al., 2011). High spatial resolution RMHD simulations carried out by Tomida et al. (2015) on the other hand, find that nonideal MHD effects can resolve the magnetic braking catastrophe in the early phase of star formation—before a protostellar core is formed. These simulations (using different inner boundary conditions, and refraining from the use of a sink particle) find

the formation of a small rotationally supported (≈5 au) disk in the early phase. It is expected but not shown that the disk will grow later as larger angular momenta accrete.

One way out of this impasse for the classical model setup was suggested by Hennebelle and Ciardi (2009) who showed that by offsetting the magnetic and rotation axes of such rotors by even small angles of $\simeq 10^o$ centrifugally supported disks could form. They found that centrifugally supported disks cannot form for values of $\lambda \leq 3$ when the magnetic field and the rotation axis are perpendicular, and smaller than about $\lambda \simeq 5 - 10$ under perfect alignment. However, based on realistic distributions of magnetic field strengths and misalignment angles, Krumholz et al. (2013) showed that this would lead to a Keplerian disk fraction in the Class 0 stage of only 10 to at most 50 per cent, noticeably below the observed fraction of discs around Class I/II objects.

3.3.2. Realistic Initial Conditions: Turbulence

The magnetic braking catastrophe is really only a problem for the model of highly idealized initial conditions that it presupposes. With the benefit of Herschel and ALMA observations, we now have a far better picture. Molecular clouds are characterized by supersonic velocity dispersion, attributed to supersonic turbulence (Larson, 1981). Herschel observations show that stars typically form in filaments (André et al., 2010, 2014). This likely arises from some combination of gravitational fragmentation of filaments into discrete cores, or as members of small groups or clusters at the intersection of filament systems. However, examples of the theorist's dream model—fairly isolated, nearly spherical molecular cloud cores that are virtually identical to gravitationally unstable Bonner-Ebert spheres—do exist (Alves et al., 2001)! Magnetic field observations show that star formation occurs in cores in which gravitational dominates magnetic energy (Crutcher, 2012).

The strength of magnetic fields, and hence the role of outflows in star formation, is rooted in how star forming gas becomes supercritical in the first place. The intriguing point is that the cold neutral medium (CNM) out of which molecular clouds may ultimately form is highly subcritical (Heiles and Troland, 2005). For the CNM, with measured total fields of the order $B_{CNM} = 6\mu G$ (similar in value to the local Galactic component) these authors measure $\lambda = 0.42$—deep into the subcritical, magnetically dominated regime. Starting from this initial state of the ISM, an older approach to star formation in magnetized media supposed that the local mass-to-flux ratio is reduced by ambipolar diffusion until individual cloud cores become supercritical (see the review by Lizano and Galli, 2015). This process is far too slow to be important in quiescent regions of molecular clouds (e.g., star forming cores). However, some analytical models (Zweibel, 2002) and numerical simulations (Nakamura and Li, 2005) have suggested that this can be sped up in regions with supersonic turbulence.

In supersonic turbulence however, intersections of supersonic shocks create filamentary systems (see the review by Mac Low and Klessen, 2004). When magnetic fields are included, observations show that they tend to preserve their orientation at all scales that have been probed—from 100-pc scale down to sub-pc scale cloud cores. This suggests that both gravitational contraction and turbulent velocities should be anisotropic, due to the influence of dynamically important magnetic fields and this is in fact observed (Li et al., 2014a). Simulations do show that because gas is free to flow along magnetic field lines—supersonic turbulence can compress gas flows along field lines (Padoan and Nordlund, 1999). While it has been claimed that gas motions in the denser cores are super Alfvénic (the density has increased with little change in the field Padoan, 2018), the observations suggest that the field is strong enough that motions are trans-Alfvénic. The best studied low-mass cores of nearby star forming regions are typically subsonic.

Recent 3D global simulations of the initially subcritical ISM in a magnetized spiral galaxy show that long filamentary clouds form by the draining and compression of flows into long magnetic valleys of buckling field lines. This onset of such global Parker instabilities can create a system of kpc magnetized filamentary clouds of CNM. Subsequent filamentary flow along these long HI structures gather sufficient gas to quickly produce supercritical GMCs (Körtgen et al., 2018). The action of these global modes addresses the long standing question of how it is possible to gather enough gas from a collection region of the order of 1 kpc needed just to build GMCs (see review McKee and Ostriker, 2007).

The origin of the initial angular moment of pre-stellar cores is equally important. Given the fact the molecular clouds are turbulent, it is questionable to assume that angular momentum is coherently distributed. It is often assumed in analyzing the observations that cores have a uniform rotation and follow a rigid-body rotation law. Their angular velocity Ω is deduced from measurements of global velocity gradients in velocity maps (Myers and Benson, 1983; Goodman et al., 1993). By performing numerical simulations of turbulent, magnetized clouds in 3D, it has been found that the observations of the specific angular momentum of cores (which involve 2D projections) overestimate this quantity by a factor of approximately 10 (Dib et al., 2010). Hence, it is clear that protostellar disks are likely the result of *locally* generated angular momentum by turbulence (Jappsen and Klessen, 2004). In such situations, the link between the local angular momentum vector that will define the disk and the direction of the magnetic field at larger distances can be essentially random. This, as it turns out, is the clue to resolving disk formation.

The first simulations of disk formation in strongly magnetized, turbulent collapsing clouds were carried out using different numerical methods. Simulations using 3D MHD Adaptive Mesh Refinement (FLASH) simulations on the scale of individual turbulent clumps were carried out by Seifried et al. (2012) and Seifried et al. (2013). This work emphasized the inefficiency of magnetic torques in turbulent media. Another group focused on the role of turbulent reconnection of magnetic field lines in reducing the efficiency of magnetic braking (Santos-Lima et al., 2012). The former approach showed that Keplerian disks of extent 50–150 AU can be formed in the collapse of turbulent clouds with the typical initial cloud magnetic fields; $\lambda = 2.6$. Disks form even in turbulent clumps with initial zero total angular momentum. They arise as a consequences of the local angular momentum contained in the convergence of several

filaments in the turbulent flow. Disks formed for a range of initial core masses and turbulent settings, and for typical Mach numbers of the turbulence of $M = 5$, although disks formed in quite subsonic turbulence $M = 0.5$ as well (Seifried et al., 2015). In all cases, disks are formed by accretion out of discrete filaments and this is a fundamentally different picture than the collapse of idealized monoliths. The latter approach suggested that reconnection of tangled magnetic field lines plays a dominant role. Although the interpretations of the results differ, it appears that turbulence can aid disk formation in magnetized media.

Similar results have been found and extended by a number of different groups, using different numerical setups and codes. Joos et al. (2013) find disk formation in magnetized turbulence and interpret this as a consequence of the misalignment effect that turbulence imposes on the forming disks. Gray et al. (2018) ran simulations with similar initial conditions using their Orion 2 AMR, RMHD code, to the Seifried et al. (2013) setups—with a 300 $M_\odot$ initial clump, $\lambda = 2$, similar Mach number for turbulence, and most importantly, similar numerical resolution (1.2 AU). These simulations show, moreover, that rotationally supported disks don't form when the initial turbulent velocity field is aligned with the magnetic field.

An analysis of the statistical properties of such disks formed in purely hydrodynamic simulations of forming star clusters can be found in Bate (2018). Although, this study does not include magnetic fields, it confirms the general picture that initial velocity or density fluctuations are sufficient to provide locally the necessary angular momentum for the formation of protostellar disks.

Recent advances in computational techniques now allow, for the first time, multi-scale MHD simulations in turbulent Giant Molecular Cloud spanning scales from the cloud (40 pc) down to a few AU scale on the disk scale (Kuffmeier et al., 2017). The transport of angular momentum in the disks can be followed. The net inward mechanical transport is compensated for mainly by an outward-directed magnetic transport, with a contribution from gravitational torques by spiral waves that is less than the magnetic transport.

Figure 7 shows a selection of disks that form. One sees that disks are often associated with filaments. Because the most powerful parts of the jets are launched from the central regions of the disk, close to the (proto-)star, it is a numerical challenge to probe the efficiency of protostellar outflows in star cluster environments where spatial scale separation between the molecular cloud scale ($\sim$ 10 pc) and the inner disc scale ($\sim$ 1 au) spans more than six orders of magnitude. Attempts to probe self-consistently driven outflows out of turbulent cloud cores have been made. Those simulations don't yet probe the innermost disk scales where the most powerful parts of the jet are launched, but the results are most encouraging.

Figure 8 shows the evolution of the angle between the total angular momentum vector and the total magnetic field direction at 100 au around 8 different sink particles (stars) in the simulation. One sees that this distribution is essentially random, which is in good agreement with the observations.

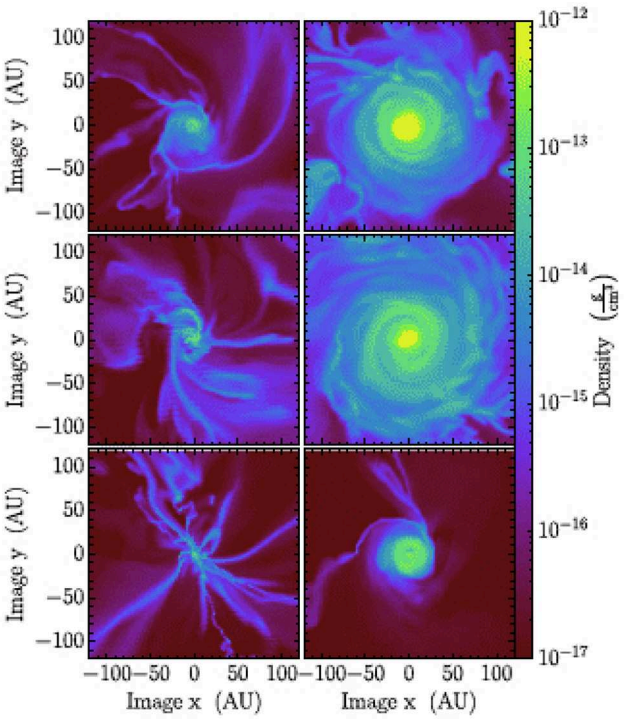

FIGURE 7 | Slices in the plane vertical to the mean angular momentum vector calculated for a sphere of 100 au at t = 50 kyr. First row: sink 1 (left), sink 4 (right); second row: sink 5 (left), sink 6 (right); third row: sink 7 (left), sink 9 (right). From Kuffmeier et al. (2017) reproduced with permission © AAS.

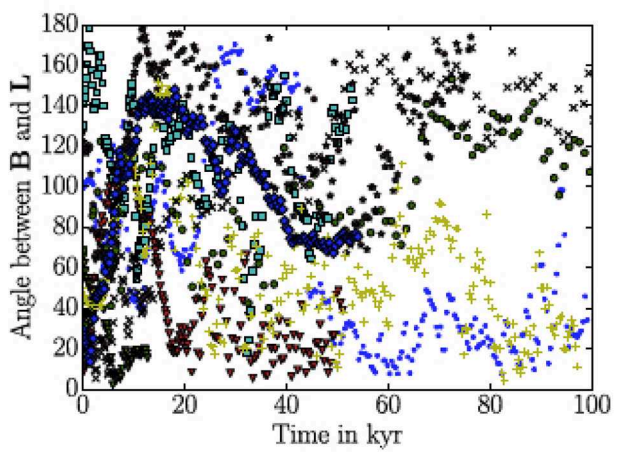

FIGURE 8 | Evolution of the angle between total angular momentum vector and total magnetic field direction within a sphere of 100 au around the eight different sinks. Note the high degree of random behavior. From Kuffmeier et al. (2017) reproduced with permission © AAS.

3.3.3. Non-ideal MHD: Effects of Grain Evolution

As already noted, for disks to form in ordered, laminar collapse, something must greatly accelerate the normal ambipolar diffusion time scale to reduce the field while gas is still at relatively

low density. This may be possible when one considers the fate of small dust grains in magnetized contracting cores.

The large population of very small dust grains (VSGs) of order 10 - a few 100Å dominates the coupling of magnetic field to gas at densities $n > 10^{10}$ cm^{-3}. The removal of this dust can lead to an increase of the ambipolar diffusion rate of the magnetic field out of the collapsing gas by two orders of magnitude. This allows 50-100 AU disks to form in well ordered collapses (Zhao et al., 2018). The depletion of VSGs arises as a natural consequence of their accretion of mantles (akin to molecular freeze-out) or coagulation. Grain coagulation has been shown to remove small grains $\leq 0.1\mu$m) within a few yr (Ossenkopf, 1993; Hirashita, 2012). The advantage of ambipolar diffusion driven by the loss of VSGs is that it occurs in the envelope of the forming disk which allows the formation of a large scale disk by avoiding catastrophic braking. 3D simulations of this picture show the presence of rings on scales of ~ 40 AU.

Since even subsonic turbulence allows for the formation of large disks in strong B fields, it is unclear at what stage this mechanism of grain removal in cores becomes important or competitive as subsonic conditions in cores are established.

3.3.4. The Earliest Outflows

With the collapse of a turbulent overdense region of a cloud, the magnetic field configuration winds up creating an ever stronger toroidal field. Angular momentum is extracted out of the region but since the collapse time scale becomes shorter than the time scale for the propagation of torsional Alfvén waves, the magnetized disk reaches its centrifugal balance radius r_c. Because of braking, this radius will be considerably smaller than one would predict solely using simple angular momentum conservation arguments for the initial state (Terebey et al., 1984). As r_c is reached, the winding of the field continues at a rate that is considerably faster than can be carried off by torsional wave braking. Pressure confinement by the infall leads to the accumulation of "magnetic twist." More precisely the building up of toroidal field creates an ever steepening vertical pressure gradient $\partial/\partial_z(B_\phi^2/8\pi)$ in the outer reaches of the forming disk out to the centrifugal radius. It is this magnetic pressure gradient force that ultimately launches a tower flow. The general idea of such flows was first derived theoretically by Lynden-Bell (2003).

The first numerical dynamical simulations of the early stages of disk formation and magneto-hydrodynamic launching of protostellar jets were performed soon after the theory of MHD disk winds had been proposed (Pudritz and Norman, 1983). In these simulations, magnetically threaded disks initially out of rotational balance, collapse inwards and launch outflows (Shibata and Uchida, 1985, 1986). This early work showed that strong transient outflows resembling tower flows were launched by collapsing rotating disks. Subsequent work included a magnetosphere around the central star, and showed that a polar jet would also emerge from the star (Uchida and Shibata, 1985).

Tower-like outflows were discovered and interpreted in magnetized collapse simulations by Banerjee and Pudritz (2006). The analytic solutions predict that the velocity of such towers is comparable to the rotation speed at the base. In the collapse case, this implies an outflow roughly comparable to the rotation speed of the disk at r_c. Banerjee and Pudritz (2006) showed that the inner regions of the disk, where Keplerian rotation is firmly established, would give rise to centrifugally driven winds. Thus, theory and simulations predict that disk winds at r_c and inwards accompany disk formation. This result corroborates the ALMA observations of large scale disk winds, shown in **Figure 1**.

Simulations of magnetized collapsing cores now also show that the formation of the hypothesized first hydrostatic core is accompanied by the launch of a magnetocentrifugal wind. Recent observations have found several candidates for these objects (Enoch et al., 2010; Pineda et al., 2011) and that these are accompanied by slow, well collimated outflows (Dunham et al., 2011). Price et al. (2012) have used an SPH MHD code to show that low-mass first cores produce tightly collimated jets (opening angles $\leq 10^0$) with speeds of $2-7$ km s^{-1}, consistent with some of the observed candidates.

3.4. Main Phase: Disk Evolution and Outflows

The vertically averaged angular momentum equation that governs a disk undergoing a total stress σ is (Pudritz and Norman, 1986; Bai, 2016),

$$\dot{M}_a \frac{d}{dr}(ru_\phi) = \frac{d}{dr}(2\pi r^2 < \sigma_{r,\phi} >) + 2\pi r^2 \sigma_{z,\phi}|_{-h}^{+h} \qquad (1)$$

where the accretion rate is $\dot{M}_a = 2\pi r \Sigma v_r$ for a radial inflow speed of the gas v_r, and the angle brackets in the first term indicate taking the vertical average of the torque by integrating over z. The total stress has contributions from both turbulence, and the Maxwell stress of threading magnetic fields. The first term on the right hand side denotes angular momentum flow in the radial direction, while the second term is angular momentum flow out in the vertical direction due to wind torques. In the case of shear turbulence, the stress is the average of the turbulent fluctuations, $\sigma_{r,\phi} = -\rho \delta v_r \delta v_\phi$. In the presence of a toroidal magnetic field B_ϕ in the disk, a radial field B_r can also contribute to flow in the radial direction through the Maxwell stress component; $\sigma_{r,\phi} = B_r B_\phi$. This possibility arises naturally in diffusive models due to field line dragging in the accretion flow. It also appears in recent models of non-ideal MHD wherein the Hall effect can produce an instability leading to a radial field component (Bai and Stone, 2014; Béthune et al., 2016; McNally et al., 2017). A threading vertical component of the field B_z however, exerts a torque on the disk with $\sigma_{z,\phi} = B_z B_\phi$ leading to an MHD disk wind, which is central to the action of the ubiquitous jets and outflows that accompany the formation of all young stars, regardless of their mass (Pudritz et al., 2007; Ray et al., 2007; Frank et al., 2014).

Physical models of accretion disks have focused heavily on the assumption that angular momentum is transported by turbulent viscosity, first addressed in the seminal papers by Shakura and Sunyaev (1973) and Lynden-Bell and Pringle (1974). Here, the turbulence is assumed to arise from the shearing Keplerian flow and takes the form $\sigma_{r,\phi} = \nu \Sigma r d\Omega/dr$. The effective viscosity of the disk ν can then be shown to scale with the disk scale height as $\nu = \alpha c_s h$ with the famous α parameter. Steady state disks

then have a radial accretion rate $\dot{M}_a$, which, away from the inner boundary of the disk can be written as

$$\dot{M}_a = 3\pi \nu \Sigma = const \quad (2)$$

In order to drive an accretion flow at the rate observed to fall onto T-Tauris stars, $\alpha \simeq 10^{-2} - 10^{-3}$. The angular momentum is carried out radially leading to the slow, outward radial spreading of the disk from its initial state. The high column densities of protoplanetary disks prevent much radiation from penetrating the disk, leaving it poorly ionized at the midplane. Thus non-ideal MHD processes such as Ohmic losses, ambipolar diffusion, and the Hall effect, all take their toll on the coupling of magnetic fields to gas. Each process dominates in a different vertical layer of the disk: Ohmic diffusivity in the mid plane, the Hall effect in the middle layer, and ambipolar diffusion (AD) in the surface regions. These diffusivities vary as a function of radius across the disk. As an example, the Ohmic diffusivity depends on both the temperature and electron fraction, both of which change with disk radius (e.g., Cridland et al., 2016). The damping of MRI instabilities occurs when the ratio of the growth rates to the damping rates predicted by these diffusivities is less than unity (e.g., review, Turner et al., 2014). These are the so-called Elsässer numbers for each effect: $A_m = v_A^2/(\eta_A \Omega)$, $\Lambda_H = v_A^2/(\eta_H \Omega)$, and $\Lambda_O = v_A^2/(\eta \Omega)$. At the disk midplane, where dust processes are important for building planets, Ohmic diffusivity generally dominates in the inner disk radii. However, ambipolar diffusion can start to dominate in the diffuse outer portions of the disk. Early work (Gammie, 1996) noted that whereas the MRI would be damped at the disk midplane by Ohmic dissipation, MRI driven accretion could still occur in an "active layer" in the disk surface regions. This idea known as the "dead zone" is an important region in the disk for many reasons, including issues of dust growth and planet formation. However, the inclusion of AD shows that the MRI instability is damped even in these surface layers (Bai and Stone, 2013). What does this say about outflows?

The launch of outflows requires a treatment of the mass loading of the flow. This demands a sensitive treatment of the microphysics of the gas at the magnetosonic point. Wind launch by a centrifugal mechanism requires that the field be sufficiently bent away from vertical. Vigorous outflow requires that the field be reasonably strong as well – near to equipartition value with thermal pressure in some models – making it difficult to bend the field as it emerges from the disk surface layers (Wardle and Koenigl, 1993; Ferreira and Pelletier, 1995), However AD effects allow bending to occur (Li, 1996). It was also noted that a strong vertical field would reduce the rotation of the disk to sub Keplerian rates too small to drive the wind (Ogilvie, 2012). Analytic treatments that included the full roster of non-ideal MHD effects seemed to suggest that MRI and centrifugal wind effects are mutually exclusive (Königl et al., 2010). Disk winds operate in weak MRI and field strengths near equipartition, while MRI requires weak fields at the midplane and would then not produce accretion rates high enough to match the observations.

Detailed simulations of the physics of these processes have led to a qualitative leap in our understanding. Bai and Stone (2013) simulated vertically stratified local shearing patches of disks threaded by weak vertical field lines, with a self consistent treatment of Ohmic and AD diffusivities based on detailed disk chemistry. They found that although MRI quickly develops in the initial weak disk field, the disk rapidly adjusts to a new equilibrium state in which the disk is laminar (the turbulence is almost completely damped) and a magnetocentrifugal outflow is formed. The viscous stress parameter was only $\alpha \simeq 3 \times 10^{-6}$ with viscous transport restricted to a narrow FUV heated surface layer. The angular momentum is carried off by the wind which drives disk accretion at rates sufficient to match the observations—but not so strong as to rapidly deplete the mass of the disk. All of the disk accretion flow takes place in a current layer of thickness $0.3h$ (where h is the disk scale height), at radial inflow speeds about $0.4c_s$. Disk evolution in these regions is unlikely to depend on turbulent viscous forces, although very low level turbulence may still be excited by various hydrothermal instabilities (Flock et al., 2012).

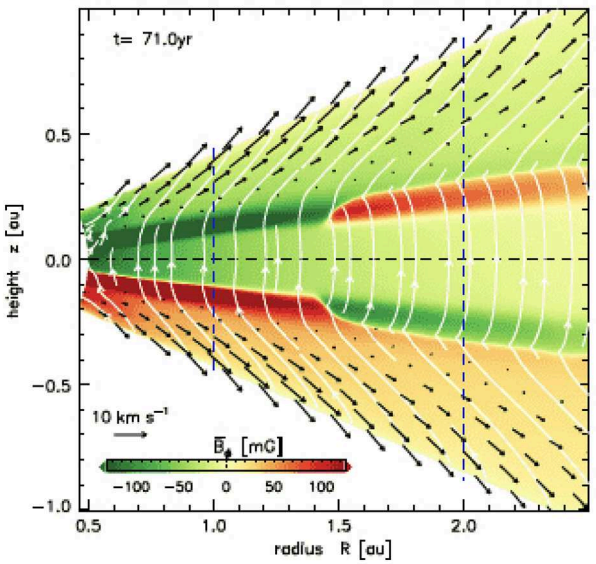

FIGURE 9 | Plot of the toroidal field (color) with peak values of a few hundred mG. The projected magnetic field lines (white) and velocity vectors (black) are indicated as is the position of the wind base (dot–dash). From Gressel et al. (2015) reproduced with permission © AAS.

Global simulations of non-ideal MHD effects in disk winds have been performed using different computational techniques. In **Figures 9**, **10** we compare results of the simulation of these effects from two different research groups (Gressel et al., 2015; Béthune et al., 2017). The global disk simulations of Gressel et al. (2015) include both Ohmic and AD terms and are shown in **Figure 9**. Their results are very similar to the shearing box simulations of Bai and Stone (2013). In particular—the inclusion of AD completely quenches the turbulence in the disk surface layers: without AD effects, MRI instabilities develop that transport angular momentum in the surface layers. In the full simulations, the field at the midplane is dominated by its poloidal component because the strength of the Ohmic dissipation effects prevents the appearance of currents that would create a toroidal

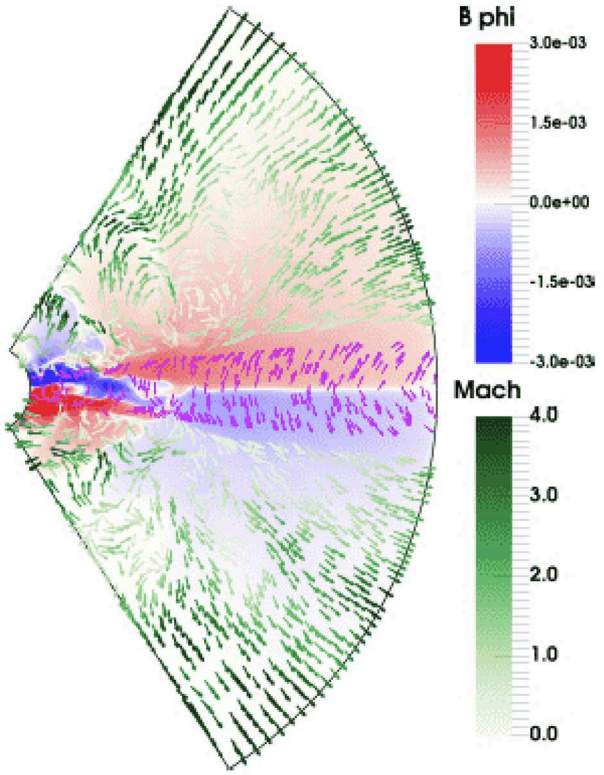

FIGURE 10 | A 2D, global non-ideal simulation of a disk and outflow showing: the toroidal magnetic field in color background (blue to red), the poloidal velocity field in units of local sound speed (Mach number)—green arrows in the corona, and the orientation of the angular momentum flux caused by magnetic stress (purple arrows in the disk). From Béthune et al. (2017) reproduced with permission © ESO.

field. As one moves away from the midplane, the field bends radially outwards. The reason for this is as follows (e.g., Konigl and Pudritz, 2000). The ions are braked directly by the magnetic torque and so move with slightly sub-Keplerian velocity. This is transmitted to the neutrals by the frictional drag (ambipolar diffusion), which slow down and lose their angular momentum to the field (the toroidal field increases). Thus the neutrals must move radially inwards in the disk. In so doing, the field is also dragged inwards, causing the field lines to begin to curve (in the R-z plane). The magnetic tension resulting from this field line curvature then balances the drag force.

The direction of the toroidal field in the inner part of the disk (inside 1.5 au) is in the same direction as that of field lines in the outflow. The poloidal field lines bend smoothly into the base of the outflow region. At disk radii $r \geq 1.5$ au, the polarity of the toroidal field reverses. Field lines now start to curve toward the star as the first steps in flow collimation start to take place. The change in toroidal and radial field components takes place in a narrow current layer concentrated at $z \simeq \pm 3.2$ h. These layers are found to be stable. Launch of the winds can be achieved with weak initial magnetic field strengths in the disk.

In **Figure 10**, the Hall term is also included within a full 3D global simulation of the disk (Béthune et al., 2017) although detailed chemistry and radiative transfer calculations are not included. There are similarities with the Gressel et al. (2015) results. The toroidal field changes sign across the midplane. It also changes sign at a disk radius ($2.5r_o$), largely an effect of the inner disk boundary conditions. An intriguing aspect of this model is that the disk can be accreting, or not, depending on the configuration of the large scale magnetic field. In this Figure, the inner region of the disk has a flow of angular momentum from the disk surface toward its midplane – while the outer regions have angular momentum flow away from the midplane. In general, angular momentum transport toward the mid plane results not in disk accretion, but rather large scale meridonal circulation. The non-accreting case is characterized by a meridional circulation, with accretion layers at the disk surface and decretion in the midplane. In the accreting case, vigorous disk winds drive radial accretion flows.

One of the intriguing aspects of the Hall effect is that the direction of transport of the magnetic flux in disks depends on the polarity of the threading poloidal field component $\mathbf{B_p}$ with respect to the disk rotation axis. If its direction is parallel to Ω , then flux transport is inwards, and if anti-aligned, outwards (Bai and Stone, 2017). Since the flux distribution affects the strength of the wind torques, these Hall effects could be significant for the physics of Type I migration (migration of low mass bodies that do not open gaps in the disk). In all situations, it appears that disks do not support MRI turbulence out to distances of 10 AU for standard conditions. This dead zone radius r_{DZ} must evolve with time as the disk thins out. It is particularly noteworthy that 10 AU scales corresponds to the planet forming region in most theoretical models of planet formation.

3.5. Stellar Spin and Outflows

At the earliest stages of their evolution, stars are in the process of contracting and are often accreting material with high specific angular momentum from a protostellar disk. It is surprising, therefore, that a large fraction of stars rotate more slowly than expected—approximately half of solar mass stars with ages of less than a few million years rotate at less than 10% of their breakup velocities (e.g., Rebull et al., 2004; Herbst et al., 2007; Scholz, 2009). In the absence of a significant spin-down torque, most stars should spin at near breakup speeds. Accretion disk signatures are more prevalent among slowly rotating pre main sequence stars, suggesting that accretion and rotation are connected.

The idea that protostellar winds could drive protostellar spin evolution has been suggested by a number of authors (Hartmann and MacGregor, 1982; Tout and Pringle, 1992; Paatz and Camenzind, 1996; Ferreira et al., 2000). Matt and Pudritz (2005) showed that as long as the mass loss rate in magnetized stellar winds is high enough, then these would dominate over disk-star coupling spin-equilibrium mechanisms. Specifically, they proposed that accretion onto the star would power a strong wind by the excitation of a large flux of Alfvén waves along the open field lines. They called this new class of stellar wind models—accretion powered stellar winds (APSW). This wave excitation mechanism was further explored by Cranmer (2008)

and Cranmer (2009), who showed that the predictions for X-ray luminosities from the shocks in these models are in general agreement with existing observations.

Theoretical studies of accretion powered stellar winds (with mass loss rate $\dot{M}_w$, stellar dipole magnetic field B_*, and radius R_*), derived the scaling of the Alvén radius, expressed as the lever arm of such a wind;

$$(r_A/R_*) = K(B_*^2 R_*^2/\dot{M}_w v_{esc})^m \quad (3)$$

where $K = 2.11$ and $m = 0.223$ are found by fits to numerical calculations (Matt and Pudritz, 2008). We note that this general scaling relation also holds in the context of disk winds, where from Pelletier and Pudritz (1992) one can deduce that $m = 1/3$.

The APSW model was applied to the study of spins of young stars undergoing evolution down the Hayashi track—up to 3 Myr in their evolution (Matt et al., 2012). The results were compared with X-wind and disk locking models. Overall, APSWs explain the observed distribution of young star spins in a similar way as the classical disk-locking picture, while at the same time avoiding the problem of magnetic field line opening it necessarily entails. When compared to the X-wind picture, it avoids the assumption of spin equilibrium and requirement of significant flux trapping. For the best fit to the observations, the APSWs are predicted to have mass loss rates that at least 1% of the disk accretion rate.

It is observationally challenging to clearly isolate an APSW from the fastest components of a disk wind originating at the innermost regions of the disk. However, it may be possible to identify the source regions of the flow predicted by the coronal wave- heating picture that it relies upon.

3.6. Outflow Feedback: Determining Stellar Masses and Star Formation Efficiency

Given the efficiency of magnetized outflows in tapping gravitational potential energy release and the angular momentum of disks, how is the surrounding core affected? Is stellar mass determined by this outflow feedback? And given that most stars form in clusters, do outflows control the star formation efficiency of clusters?

Most of the gravitational energy released during accretion originates from the inner disk. Disk winds scale with the local escape speed at the base of the footpoint of the flow, and hence with the escape speed from the central star. Since both low and high mass stars have approximately the same escape speeds, it follows that low mass stars are just as effective as high mass stars in their feedback effects (Matzner and McKee, 2000; Krumholz et al., 2018). This is unlike any other feedback mechanism (e.g., radiation fields) whose effects are strongly dependent on stellar mass.

The momentum per unit mass that can be delivered by these outflows is of the order 40 km s^{-1} which if spherically distributed, would disrupt cores. However outflows are well collimated and the interaction between outflows and the core material is mediated via a thin radiative shock in the Matzner and McKee (2000) model. This model also assumes that there is an escape polar angle θ_{esc} that separates the outflow from the region that accretes through the disk onto the star. The most important aspect of the collimation of the flow is that the thrust is concentrated in a mass that is less than the spherical case by a factor $1/ln(2\theta_o)$ where θ_o is the angular extent of the central outflow (typically $\theta_o \simeq 10^{-2}$).

This model assumes that accretion onto the star continues through the disk as the disk wind carves out a wind cavity. The ultimate mass of the star, therefore, is determined not by the outflow, but by having a finite mass reservoir (the core) out of which accretion proceeds. The prediction is that as long as low mass star formation dominates, true for clumps and clusters of $\leq 100 M_\odot$, that the efficiency of star formation $\epsilon = M_*/M_{clump,core} = (v_{esc}/v_w)ln(2\theta_o)/f_w \simeq 0.3 - 0.5$, where f_w is the ratio of the wind to star mass. This provides a theoretical explanation for the difference between the core mass function for the gas out of which stars form, and the initial mass function of stars, which are well known to differ by a factor of three in overall mass (e.g., review, André et al., 2014).

Recent numerical simulations allow a more comprehensive look at the complexities of this problem. High resolution computations down to the stellar surface have been done (Tomida et al., 2015), but the small time steps required limit these to only a small span of time (a few years). To overcome this, a number of simulations resort to building subgrid models that effectively prescribe the physics of an MHD outflow whose source region remains unresolved (Federrath et al., 2014). As already noted, Offner and Chaban (2017) find that the inclusion of real MHD effects in cores reduces the star formation efficiency—lower mass to flux ratios lead to a decrease in the star formation efficiency; ϵ drops from 0.4 to 0.15 as λ is decreased from hydro $\lambda \sim \infty$ to $\lambda = 1.5$. These simulations also find that ratio of launched outflow to the total (combined launched and entrained) outflow mass is 1:4.

The question of whether or not jets can drive turbulence has been addressed by several different methods and model setups. Maintaining turbulence can help delay gravitational collapse. The basic energetics of jets provides some interesting insights on this feedback (Banerjee et al., 2007). The lifetime of a jet can be estimated as $\tau_{jet} \simeq L/v_{jet}$ which for speeds of $\sim$ 300 km s^{-1} and a typical length scale of $L \sim 3$ pc is about 10^4 yrs—the typical duration of the early phase of star formation (class 0). The total mechanical luminosity of a jet $L = \dot{M}_{jet} v_{jet}^2/2$ is of the order 3×10^{33} ergs s^{-1} for a jet mass loss rate of $\simeq 10^{-8} M_\odot yr^{-1}$. Thus the total energy supplied to a cloud by a jet is $E_{jet} \simeq L_{jet}\tau_{jet}$, which is of the order 10^{44} ergs. For a cluster forming clump of $10^3 M_\odot$, the total turbulent energy given a typical velocity dispersion of $\simeq$ 1 km s^{-1} (Mach 5 turbulence) is $E_{turb} \simeq 10^{46}$ ergs. Thus, if f represents the coupling factor of converting outflow power into turbulence, the number of outflows needed to maintain turbulence in such a region is $N \sim 100/f$. The lifetime of the turbulence scales with the crossing time of the region L/v_{rms} and is of the order a few 10^6 years. Thus, if the coupling is reasonably strong, jets can power clump turbulence and this has an effect on star formation efficiency.

How efficiently does jet power convert to tubulence? Banerjee et al. (2007) found in 2 and 3D simulations that jets injected into quiescent cores do not develop instabilities (Kelvin-Helmholtz) and turbulence. The basic point here is that such instabilities are

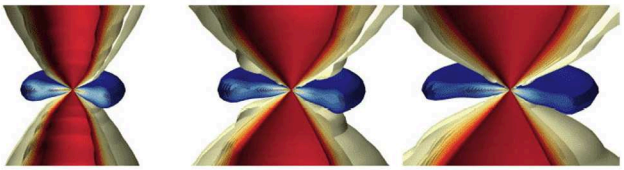

FIGURE 11 | Massive star formation and radiation feedback from jets and radiation fields. From left to right: accretion disk and protostellar outflow at times t = 20, 30, and 40 kyr of evolution. From Kuiper and Hosokawa (2018) reproduced with permission © ESO.

best excited for subsonic velocities. Jets, under these conditions, therefore have only very limited ability to drive supersonic turbulence. Other studies include multiple, highly collimated flows injected into an initially quiescent (Carroll et al., 2009) or turbulent medium (Offner and Chaban, 2017)) and these find that turbulence is excited. It is unclear what the reason is for such different results. Simulations of turbulence generated by jets in an initially turbulent clump suggest that it may be protostellar jet generated turbulence that sets the conditions for turbulent fragmentation into the IMF of stars in the cluster (Li and Nakamura, 2006).

3.6.1. Massive Star Formation and Feedback

Massive stars start to appear in clumps that exceed $100M_{\odot}$, and the nature of feedback related to radiation fields (photoionization and radiation pressure), massive stellar winds, and supernovae feedback are dependent on stellar mass (e.g., reviews, McKee and Ostriker, 2007; Tan et al., 2014). Fall et al. (2010) adopted semi-analytic arguments to compare the general effectiveness of protostellar outflows and other feedback mechanisms. Outflows are only effective at feedback for clumps with escape speeds below 7 km s^{-1}. In the context of highly idealized, spherical cloud models, radiation pressure is the dominant feedback process that controls star formation efficiency in massive star clusters ($\geq 10^4 M_{\odot}$). For lower clump masses, especially below $10^3 M_{\odot}$, protostellar outflows can play a significant role.

This leads to the question of whether magnetized disk winds play a role in the formation and feedback processes of massive stars. There is no consensus on the precise upper mass limit for stars, but the evidence to date suggests 150–300 $M_{\odot}$ (Figer, 2005; Crowther et al., 2010). Massive star formation likely involves the accretion of material from a massive disk which for a short time of 10–20 kyr, may be comparable to the mass of the star forming at its center. Because of accretion flows through massive disks, the limitation on stellar mass of $\simeq 40\,M_{\odot}$ set by the Eddington limit for spherical collapse is avoided by having radiation emitted through a radiatively driven cavity (Yorke and Bodenheimer, 1999). This anisotropic distribution of radiation due to the optical depth effects of the underlying flaring accretion disk is known as the "flashlight effect." The initial conditions for massive star formation resemble, to some degree, those for cluster formation. Many simulations often begin with an isolated clump mass of $\simeq 10^3\,M_{\odot}$.

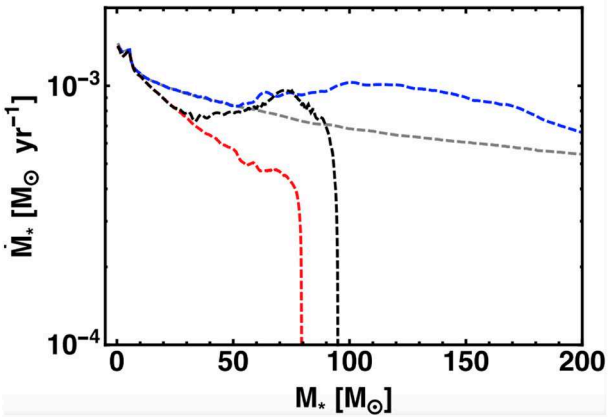

FIGURE 12 | The role of radiation and protostellar jet feedback in the formation of massive stars. Gray line is for outflow feedback only; blue line, outflow + photoionization feedback; red line, ouflow + radiation forces; black line, outflow + radiation forces + photoionization. From Kuiper and Hosokawa (2018) reproduced with permission © ESO.

Early simulations of photoionization effects from massive stars employed ray tracing methods within the FLASH AMR code (Peters et al., 2012). These simulations analyzed the role of photoionization and HII regions in driving observed molecular outflows from massive stars. Feedback from ionizing radiation was not sufficient to drive the observed massive CO outflows around massive stars. This suggests that magnetically driven outflows are important even around massive proto stars.

High spatial resolution, RHD simulations show that radiation pressure from the forming massive star pushes a bubble into the collapsing gas, while disk accretion continues through the disk (Krumholz et al., 2009; Kuiper et al., 2010; Klassen et al., 2016; Rosen et al., 2016). The details of the RHD simulations matter. Krumholz et al. (2009) used an Adaptive Mesh Refinement code (Orion) with radiative transfer handled only through flux limited diffusion, and found that the continued mass accretion onto the star proceeded by infall of cold gas produced by Rayleigh-Taylor "fingers" on an unstable bubble wall. Kuiper et al. (2010) used a high resolution, spherical fixed grid with a ray trace RHD method and found that such fall back did not occur, and that strong disk accretion flow built the star. The maximum stellar mass attained was $210M_{\odot}$. Klassen et al. (2016) combined an AMR approach with a hybrid approach to radiation transfer—combining ray tracing techniques with flux limited diffusion. These simulations found that indeed, the main mode of mass transfer to the star was by strong accretion flow, mediated by spiral waves excited in the self gravitating disk. The bottom line in these latter two studies is that by using only RHD, the mass of a star is limited only by the size of the mass reservoir. However, this group of studies did not include magnetic fields.

Because MHD disk winds are launched at the moment of disk formation, massive star forming disks should have already started to carve out a cavity before the radiation fields become important. In this regard, it is interesting to note that the best case for rotating disk winds is for the massive protostar in Orion as shown in **Figure 1**. Radiation, once it does become important,

will be able to escape through this outflow cavity—making the issue of the details of radiation blown bubbles a somewhat moot point (Krumholz et al., 2009). It is important therefore to have combined RMHD simulations of massive star formation. Will MHD outflows make it easier to form more massive stars?

Recent simulations (Kuiper and Hosokawa, 2018) include radiation forces from direct and dust-reprocessed radiation as well as photoionization. The effects of a magnetized disk wind were included: the outflow was injected into the computational domain at $t = 4kyr$ with an ejection-to-accretion efficiency of 10%, and a velocity of three times the local escape velocity with respect to the current protostellar mass. The evolution of the protostar was followed using evolutionary tracks by Hosokawa and Omukai (2009).

Figure 11 shows the resulting structure and evolution of the outflow and disk. The overpressure of the HII region fills the outflow cavity (left frame). This pressure acts on the surface of the disk below the cavity, serving to compress it and in the process, opening up the cavity even more. This enhanced pressure due to photoionization leads to the pile up of additional mass on the disk (middle frame) which shadows the disk beyond. This shadowing enables an enhanced accretion rates through the disk (the "scissor effect"). Other than this effect, photoionization does not seem to play a big role in this highly optical thick disks.

Figure 12 shows the accretion history and final masses of stars undergoing various combinations of feedback: outflow alone (gray), outflow + photoionzation (blue), outflow + radiation forces (red), and lastly all 4 feedback effects (black). We see that the magnetized outflows do not stop the accretion from the very large $1000M_{\odot}$ mass reservoir. Adding photoionization to the picture also does not shut off the infall. The addition of radiation pressure to the outflow, however, does lead to the truncation of accretion even from an effectively infinite mass reservoir (red and black curves). The final masses are 79 and 95 $M_{\odot}$ for the red and black curves, respectively. The photoionization scissor effect, present in the latter case, helps increase the accretion rate and final mass. In addition to the protostellar outflow, radiation forces are the dominant broadening mechanism of the bipolar region. These results suggest that, like low mass star formation, disk winds by themselves create feedback, but probably do not determine the masses of stars.

We also show a study that comes to different conclusions—as is shown in **Figure 13** (Tanaka et al., 2018). In this work, a semi-analytic treatment of radiative feedback and MHD disk winds is adopted. The latter input generalizes the Matzner and McKee (2000) model. An important new addition to the analysis is the dependence of disk accretion and final stellar masses on the metallicity. Radiation pressure is found to play a minor role in the feedback mechanism—MHD disk winds are the key player providing $\geq$ 90% of the outflow momentum. The novel insight in this work is that as the metallicity decreases, photoevaporation becomes stronger. This reduces the SFE because dust attenuation of ionizing photons is inefficient. In this analysis, there does not appear to be a firm upper limit to stellar mass.

The somewhat different conclusions that these studies reach likely arise from differences in their underlying modeling. The first is the different level of detail in the radiative transfer calculations, full RHD vs. semi-analytic theory. The second is that it may be useful to include the MHD wind explicitly. The subgrid modeling of the MHD disk wind itself, while capturing several of the key points, may still require more dynamic treatment. That said, it is clear that radiation and MHD disk winds are both important in massive star formation, and this is a tantalizing open problem.

Finally, we return to the question of the role of outflow feedback in cluster formation, as investigated by numerical simulations. Federrath et al. (2014) applied the MHD disk wind, sub grid model to turbulent, magnetized star cluster formation. The subgrid model features a disk wind opening angle of 30°—the minimum angle that gives rise to outflow for cold initial conditions (Blandford and Payne, 1982). The ratio of mass outflow to accretion rates is set to the standard value predicted by theory and numerical simulations of 0.3. The intial clump was taken to have a mass of $500M_{\odot}$ and diameter of 1 pc., with a typical turbulent velocity field and observed mass to flux ratio.

Figure 14 shows the results of these protostellar feedback simulations. In the left panel without outflows, the SFE reaches nearly 49% with a total of 23 stars formed. On the right, the simulation with outflows results in a SFE of 20% with 47 stars formed. The results show that jets and outflows eject about a quarter of their parent molecular clump in high-speed jets. These extend out to distances of more than a parsec from their disks. These outflows reduce the star formation rate by about a factor of two, and lead to the formation of $\sim$ 1.5 times as many stars compared to the no-outflow case. Perhaps the most important result is that MHD outflows reduce the average star mass by a factor of approximately three and may thus be essential for understanding the characteristic mass of the stellar initial mass function. These results show that indeed, outflow feedback plays a significant role in reducing SFE in low mass clusters, bringing them down in agreement with the observations.

3.7. Planet Formation and Outflows

Given that star and planet formation both depend on how angular momentum in disks is disposed of, MHD wind torques are likely to play an equally profound role in the question of planet formation (see review Pudritz et al., 2018). There are at least three aspects of disk winds that may matter for planet formation and migration.

The first is that braking and outflows lead to smaller disk radii, as noted in the observational section. This means that for a given disk mass, outflows produce disks with higher initial column densities. This in turn implies that the column density of solids in the disk will be greater and this is likely to have an important effect on planetary accretion time scales and mass distributions.

Secondly, outflows may connect with the presence of rings and gaps in disks. Early arguments suggested that gaps in the millimeter emission of disks could arise due to the enhanced growth of dust grains at opacity transitions (eg ice lines) at specific disk radii (Zhang et al., 2015). Surveys now show, however, that there is little correlation between such opacity transitions and the positions of the gaps (van der Marel et al., 2019). Much current work focuses on simulations that show that even a single, sufficiently massive planet can carve multiple gaps

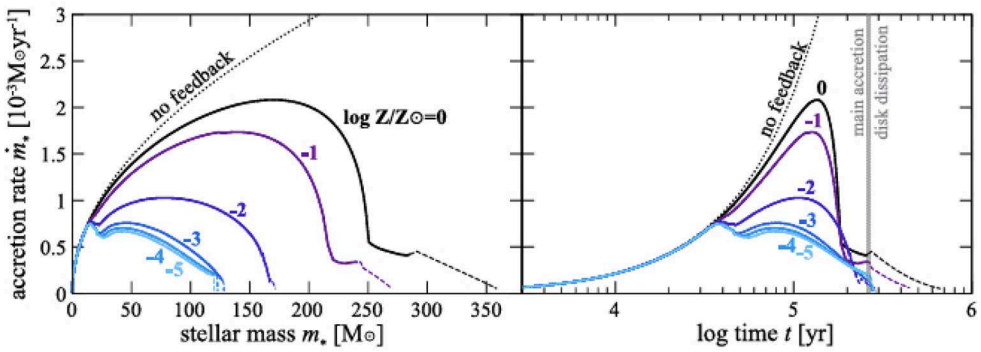

FIGURE 13 | The role of magnetized outflows in massive star formation as a function of metallicity. Accretion histories as functions of protostellar mass, $m_\star$ (Left) and time, t (Right) for stars forming from cores with initial masses of M_C=1000 $M_\odot$ and embedded in clump environments with Σ_{cl} = 1 g cm^{-2}. Results for metallicities log $Z/Z_\odot$ = -5, -4, -3, -2, -1, and 0 are shown as labeled. For each line, the solid part represents the main accretion phase and the dashed part is the disk dissipation phase (the gray vertical line in the right panel indicates the transition time). The black dotted lines show the no-feedback case. The accretion rate is lower at lower metallicity due to stronger total feedback. From Tanaka et al. (2018) reproduced with permission © AAS.

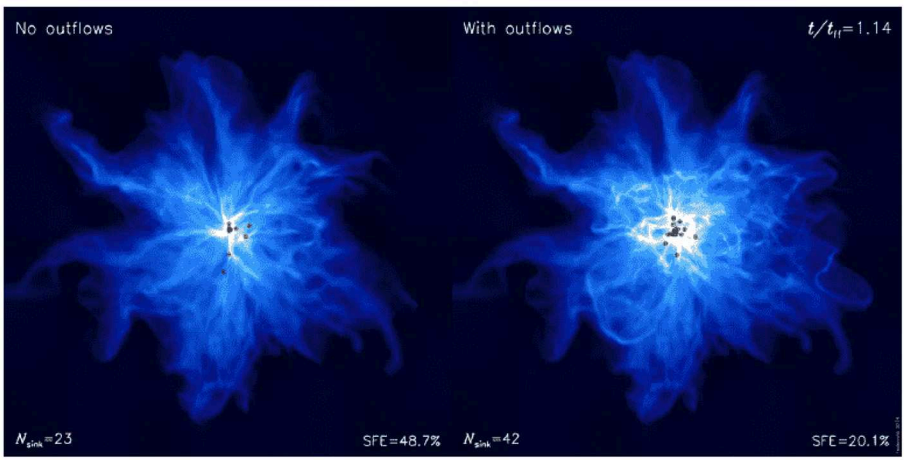

FIGURE 14 | Effects of feedback from protostellar outflows on star and cluster formation. The left frame shows the results of cluster formation without outflow feedback, and the right when feedback is included. Note the strong effect on the SFE and number of stars produced. From Federrath et al. (2014) reproduced with permission © AAS.

in inviscid ($\alpha \leq 10^{-4}$) disks as a consequence of the spiral shock waves induced by planet-disk interaction (e.g., Dong et al., 2017). This generally fits the ALMA observations of gaps and rings as well the origin of non-axisymmetric structures such as vortices, quite well (Zhang et al., 2018a). The formation of vortices requires low disk viscosity ($\alpha \simeq 10^{-4}$), which again suggests that low turbulence is necessary to explain key aspects of disk-planet interaction. This picture does not address how such planets may have formed but does provide observational constraints on the masses and orbital radii of forming planets. If disk winds drive disk accretion physics, then what specific effects might MHD disk winds have on creating these ring systems?

Only a few papers have addressed this issue so far. The launch of MHD (non-ideal limit) disk winds has been shown to also produce axisymmetric structures in the disks that could provide an explanation of the ring systems (Béthune et al., 2017). In these simulations, zonal flows can be established in the disk that lead to the creation of density peaks that are anti-correlated with peaks in the vertical field. It has also been shown that in the outer parts of disks beyond 10 AU, where ambipolar diffusion dominates the diffusivity of the disk magnetic field, that strong sharply defined current layers can develop. These drive fast flows that pinch the field, leading to their reconnection, which in turn leads slower gas accretion in these magnetically reduced regions. Neighboring regions have stronger fields and therefore undergo more rapid gas accretion—and it is here that gaps form (Suriano et al., 2018). This is demonstrated in both 2 and 3D non-ideal MHD simulations. Gas in such regions is preferentially removed by the wind compared to the dust, enhancing the local dust to gas ratio perhaps to the point that streaming instabilities are triggered. This would lead to rapid planetesimal formation, and perhaps planet formation. It

remains to be seen whether this model could predict planetary masses.

Finally, the migration of planets in disks is sensitive to the mechanism of angular momentum transfer in disks. In MHD wind-driven regions disks may be considered to be inviscid, and there, corotation torques on the gas will arise from MHD disk winds (McNally et al., 2017, 2018). In this situation, the shape of the horseshoe orbit region very near the planet can be modified by the winds, leading to a more history-dependent evolution of the horseshoe torque and its effects on planet migration. This may have important implications for how planets migrate when they are still low mass (so-called Type I migration).

In summary, it looks as if disk winds are not only central to disk formation, evolution, and star formation—but they may also play a key role in planet formation.

4. CONCLUSIONS

The role of magnetic fields in outflows and star formation has undergone a rapid change in its perceived importance by the astronomical community over the last 2 to 3 years. The combination of ALMA observations, the spatial resolution of outflows, and theoretical and observational advances on the nature of MRI turbulence in disks all point toward MHD disk winds as a primary agent in these processes. Our review then, comes to several important conclusions.

- Magnetized outflow is likely the dominant mechanism of disk angular momentum transport. The basic predictions of MHD disk wind theory and a large, diverse body of numerical simulations are born out by ALMA observations.
- The rotation of jets is now confirmed on several different scales. This most basic prediction of MHD disk wind theory indicates that we are actually now observing how accretion disks dispose of their angular momentum.
- The observations show that a wide range of outflow velocities are observed. The X-wind picture is "monochromatic" in that only a wind component originating at the magnetopause radius of the disk should be observed. While such a component may be present, it does not explain the wide range of data available.
- The observations support the universality of the MHD wind picture that is observed across all stellar masses. The connection with jets in AGNs and micro quasars is also becoming much clearer.
- Disk formation and observed disk properties arise from MHD turbulence conditions that dominate for the earliest pre-stellar states of forming cores. Even subsonic turbulence is sufficient to explain disk formation. While hour glass magnetic geometries are seen in some systems, many more have disordered magnetic geometries indicative of these initial conditions.
- The feedback effects of magnetized outflows play a key role in regulating the star formation efficiency and masses of low mass stars and star clusters. For massive star formation, the combination of MHD outflows and radiation pressure is central to massive star and massive cluster properties, but there are differences in the results. More work on RMHD theory and simulations is needed.

The next 5 years of ALMA observations, more powerful numerical simulations, and advances in theory are likely to result in a paradigm shift from turbulent viscosity to MHD outflows as the fundamental basis of accretion disk theory and star formation. This shift is already well underway. One of the most exciting consequences of this sea change may well be in our understanding of planet formation.

AUTHOR CONTRIBUTIONS

All authors listed have made a substantial, direct and intellectual contribution to the work, and approved it for publication.

FUNDING

RP was supported by a Discovery Grant from the Natural Sciences and Engineering Research Council (NSERC) of Canada. TR would like to acknowledge funding from the European Research Council under Advanced Grant No. 743029, Ejection, Accretion Structures in YSOs (EASY).

ACKNOWLEDGMENTS

We thank the Editors for their invitation to write this timely review, and in particular Chris McKee for his patience and ongoing support of this work. We are grateful to our referees, John Bally and Zi-Yun Li for their very useful and comprehensive reports. We also thank Robi Banerjee for insightful discussions and commentary at various phases of this project. Thanks also to Sylvie Cabrit, Gregory Lesur, Åke Nordlund, and Jake Simons for lively discussions.

REFERENCES

Adams, F. C., Cai, M. J., and Lizano, S. (2009). Migration of extrasolar planets: effects from X-wind accretion disks. *Astrophys. J. Lett.* 702, L182–L186. doi: 10.1088/0004-637X/702/2/L182

Agra-Amboage, V., Dougados, C., Cabrit, S., and Reunanen, J. (2011). Sub-arcsecond [Fe ii] spectro-imaging of the DG Tauri jet. Periodic bubbles and a dusty disk wind? *Astron. Astrophys.* 532:A59. doi: 10.1051/0004-6361/201015886

Ainsworth, R. E., Scaife, A. M. M., Ray, T. P., Taylor, A. M., Green, D. A., and Buckle, J. V. (2014). Tentative evidence for relativistic electrons generated by the jet of the young sun-like star DG tau. *Astrophys. J.* 792:L18. doi: 10.1088/2041-8205/792/1/L18

Alves, J., Lombardi, M., and Lada, C. J. (2007). The mass function of dense molecular cores and the origin of the IMF. *Astron. Astrophys.* 462, L17–L21. doi: 10.1051/0004-6361:20066389

Alves, J. F., Lada, C. J., and Lada, E. A. (2001). Internal structure of a cold dark molecular cloud inferred from the extinction of background starlight. *Nature* 409, 159–161. doi: 10.1038/35051509

Anderson, J. M., Li, Z.-Y., Krasnopolsky, R., and Blandford, R. D. (2003). Locating the launching region of T tauri winds: the case of DG tauri. *Astrophys. J.* 590, L107–L110. doi: 10.1086/376824

Anderson, J. M., Li, Z.-Y., Krasnopolsky, R., and Blandford, R. D. (2005). The structure of magnetocentrifugal winds. I. Steady mass loading. *Astrophys. J.* 630, 945–957. doi: 10.1086/432040

André, P., Di Francesco, J., Ward-Thompson, D., Inutsuka, S.-I., Pudritz, R. E., and Pineda, J. E. (2014). "From filamentary networks to dense cores in molecular clouds: toward a new paradigm for star formation," in *Protostars and Planets VI*, eds H. Beuther, R.S. Klessen, C. P. Dullemond, T. Henning (Tucson, AZ; Houston, TX: The University of Arizona Press; Lunar and Planetary Institute), 27–51. doi: 10.2458/azu_uapress_9780816531240-ch002

André, P., Men'shchikov, A., Bontemps, S., Könyves, V., Motte, F., Schneider, N., et al. (2010). From filamentary clouds to prestellar cores to the stellar IMF: initial highlights from the Herschel Gould Belt Survey. *Astron. Astrophys.* 518:L102. doi: 10.1051/0004-6361/201014666

Andrews, S. M., Huang, J., Pérez, L. M., Isella, A., Dullemond, C. P., Kurtovic, N. T., et al. (2018). The disk substructures at high angular resolution project (DSHARP). I. Motivation, sample, calibration, and overview. *Astrophys. J.* 869:L41. doi: 10.3847/2041-8213/aaf741

Anglada, G., Rodríguez, L. F., and Carrasco-González, C. (2018). Radio jets from young stellar objects. *Astron. Astrophys. Rev.* 26:3. doi: 10.1007/s00159-018-0107-z

Arce, H. G., and Sargent, A. I. (2006). The evolution of outflow-envelope interactions in low-mass protostars. *Astrophys. J.* 646, 1070–1085. doi: 10.1086/505104

Armitage, P. J. (1998). Turbulence and angular momentum transport in a global accretion disk simulation. *Astrophys. J.* 501, L189–L192. doi: 10.1086/311463

Armitage, P. J. (2011). Dynamics of protoplanetary disks. *Annu. Rev. Astron. Astrophys.* 49, 195–236. doi: 10.1146/annurev-astro-081710-102521

Bacciotti, F., Mundt, R., Ray, T. P., Eislöffel, J., Solf, J., and Camezind, M. (2000). Hubble space telescope STIS spectroscopy of the optical outflow from DG tauri: structure and kinematics on subarcsecond scales. *Astrophys. J.* 537, L49–L52. doi: 10.1086/312745

Bacciotti, F., Ray, T. P., Mundt, R., Eislöffel, J., and Solf, J. (2002). Hubble space telescope/STIS spectroscopy of the optical outflow from DG tauri: indications for rotation in the initial jet channel. *Astrophys. J.* 576, 222–231. doi: 10.1086/341725

Bai, X.-N. (2016). Towards a global evolutionary model of protoplanetary disks. *Astrophys. J.* 821:80. doi: 10.3847/0004-637X/821/2/80

Bai, X.-N., and Stone, J. M. (2013). Wind-driven accretion in protoplanetary disks. I. Suppression of the magnetorotational instability and launching of the magnetocentrifugal wind. *Astrophys. J.* 769:76. doi: 10.1088/0004-637X/769/1/76

Bai, X.-N., and Stone, J. M. (2014). Magnetic flux concentration and zonal flows in magnetorotational instability turbulence. *Astrophys. J.* 796:31. doi: 10.1088/0004-637X/796/1/31

Bai, X.-N., and Stone, J. M. (2017). Hall effect-mediated magnetic flux transport in protoplanetary disks. *Astrophys. J.* 836:46. doi: 10.3847/1538-4357/836/1/46

Balbus, S. A., and Hawley, J. F. (1998). Instability, turbulence, and enhanced transport in accretion disks. *Rev. Mod. Phys.* 70, 1–53. doi: 10.1103/RevModPhys.70.1

Bally, J. (2016). Protostellar Outflows. *Annu. Rev. Astron. Astrophys.* 54, 491–528. doi: 10.1146/annurev-astro-081915-023341

Bally, J., Ginsburg, A., Arce, H., Eisner, J., Youngblood, A., Zapata, L., et al. (2017). The ALMA view of the OMC1 explosion in orion. *Astrophys. J.* 837:60. doi: 10.3847/1538-4357/aa5c8b

Banerjee, R., Klessen, R. S., and Fendt, C. (2007). Can protostellar jets drive supersonic turbulence in molecular clouds? *Astrophys. J.* 668, 1028–1041. doi: 10.1086/521097

Banerjee, R., and Pudritz, R. E. (2006). Outflows and jets from collapsing magnetized cloud cores. *Astrophys. J.* 641, 949–960. doi: 10.1086/500496

Bate, M. R. (2018). On the diversity and statistical properties of protostellar discs. *Month. Notices RAS* 475, 5618–5658. doi: 10.1093/mnras/sty169

Béthune, W., Lesur, G., and Ferreira, J. (2016). Self-organisation in protoplanetary discs. Global, non-stratified Hall-MHD simulations. *Astron. Astrophys.* 589:A87. doi: 10.1051/0004-6361/201527874

Béthune, W., Lesur, G., and Ferreira, J. (2017). Global simulations of protoplanetary disks with net magnetic flux. I. Non-ideal MHD case. *Astron. Astrophys.* 600:A75. doi: 10.1051/0004-6361/201630056

Bjerkeli, P., van der Wiel, M. H. D., Harsono, D., Ramsey, J. P., and Jørgensen, J. K. (2016). Resolved images of a protostellar outflow driven by an extended disk wind. *Nature* 540, 406–409. doi: 10.1038/nature20600

Blandford, R. D., and Payne, D. G. (1982). Hydromagnetic flows from accretion discs and the production of radio jets. *Month. Notices RAS* 199, 883–903. doi: 10.1093/mnras/199.4.883

Bouvier, J., Matt, S. P., Mohanty, S., Scholz, A., Stassun, K. G., and Zanni, C. (2014). "Angular momentum evolution of young low-mass stars and brown dwarfs: observations and theory," in *Protostars and Planets VI*, eds H. Beuther, R. S. Klessen, C. P. Dullemond, and T. Henning (Tucson, AZ; Houston, TX: The University of Arizona Press; Lunar and Planetary Institute), 433.

Caratti o Garatti, A., Stecklum, B., Garcia Lopez, R., Eislöffel, J., Ray, T. P., Sanna, A., et al. (2017). Disk-mediated accretion burst in a high-mass young stellar object. *Nat. Phys.* 13, 276–279. doi: 10.1038/nphys3942

Carrasco-González, C., Rodríguez, L. F., Anglada, G., Martí, J., Torrelles, J. M., and Osorio, M. (2010). A magnetized jet from a massive protostar. *Science* 330:1209. doi: 10.1126/science.1195589

Carroll, J. J., Frank, A., Blackman, E. G., Cunningham, A. J., and Quillen, A. C. (2009). Outflow-driven turbulence in molecular clouds. *Astrophys. J.* 695, 1376–1381. doi: 10.1088/0004-637X/695/2/1376

Cerqueira, A. H., Velázquez, P. F., Raga, A. C., Vasconcelos, M. J., and de Colle, F. (2006). "Radial velocity asymmetries from jets with variable velocity profiles," in *Plasma and Fusion Science: 16th IAEA Technical Meeting on Research using Small Fusion Devices*, volume 875 of *American Institute of Physics Conference Series*, ed J. J. E. Herrera-Velázquez (Cairns, QLD: IOP Publishing), 285–288. doi: 10.1063/1.2405950

Chandrasekhar, S. (1956). Axisymmetric magnetic fields and fluid motions. *Astrophys. J.* 124:232. doi: 10.1086/146217

Chapman, N. L., Davidson, J. A., Goldsmith, P. F., Houde, M., Kwon, W., Li, Z.-Y., et al. (2013). Alignment between flattened protostellar infall envelopes and ambient magnetic fields. *Astrophys. J.* 770:151. doi: 10.1088/0004-637X/770/2/151

Chen, X., Arce, H. G., Zhang, Q., Launhardt, R., and Henning, T. (2016). Rotating bullets from A variable protostar. *Astrophys. J.* 824:72. doi: 10.3847/0004-637X/824/2/72

Cheng, Y., Tan, J. C., Liu, M., Kong, S., Lim, W., Andersen, M., et al. (2018). The core mass function in the massive protocluster G286.21+0.17 revealed by ALMA. *Astrophys. J.* 853:160. doi: 10.3847/1538-4357/aaa3f1

Chuss, D. T., Andersson, B. G., Bally, J., Dotson, J. L., Dowell, C. D., Guerra, J. A., et al. (2019). HAWC+/SOFIA multiwavelength polarimetric observations of OMC-1. *Astrophys. J.* 872:187. doi: 10.3847/1538-4357/aafd37

Cieza, L., and Baliber, N. (2007). Testing the disk regulation paradigm with spitzer observations. II. A clear signature of star-disk interaction in NGC 2264 and the Orion Nebula cluster. *Astrophys. J.* 671, 605–615. doi: 10.1086/522080

Coffey, D., Bacciotti, F., Ray, T. P., Eislöffel, J., and Woitas, J. (2007). Further indications of jet rotation in new ultraviolet and optical hubble space telescope STIS spectra. *Astrophys. J.* 663, 350–364. doi: 10.1086/518100

Cranmer, S. R. (2008). Turbulence-driven polar winds from T tauri stars energized by magnetospheric accretion. *Astrophys. J.* 689, 316–334. doi: 10.1086/592566

Cranmer, S. R. (2009). Testing models of accretion-driven coronal heating and stellar wind acceleration for T tauri stars. *Astrophys. J.* 706, 824–843. doi: 10.1088/0004-637X/706/1/824

Cridland, A. J., Pudritz, R. E., and Alessi, M. (2016). Composition of early planetary atmospheres - I. Connecting disc astrochemistry to the formation of planetary atmospheres. *Month. Notices RAS* 461, 3274–3295. doi: 10.1093/mnras/stw1511

Crowther, P. A., Schnurr, O., Hirschi, R., Yusof, N., Parker, R. J., Goodwin, S. P., et al. (2010). The R136 star cluster hosts several stars whose individual masses greatly exceed the accepted 150M_{solar} stellar mass limit. *Month. Notices RAS* 408, 731–751. doi: 10.1111/j.1365-2966.2010.17167.x

Crutcher, R. M. (2012). Magnetic fields in molecular clouds. *Annu. Rev. Astron. Astrophys.* 50, 29–63. doi: 10.1146/annurev-astro-081811-125514

De Colle, F., Cerqueira, A. H., and Riera, A. (2016). Transverse velocity shifts in protostellar jets: rotation or velocity asymmetries? *Astrophys. J.* 832:152. doi: 10.3847/0004-637X/832/2/152

Dib, S., Hennebelle, P., Pineda, J. E., Csengeri, T., Bontemps, S., Audit, E., et al. (2010). The angular momentum of magnetized molecular cloud cores: a two-dimensional-three-dimensional comparison. *Astrophys. J.* 723, 425–439. doi: 10.1088/0004-637X/723/1/425

Donati, J.-F., Gregory, S. G., Alencar, S. H. P., Hussain, G., Bouvier, J., Dougados, C., et al. (2012). Magnetometry of the classical T Tauri star GQ Lup: non-stationary dynamos and spin evolution of young Suns. *Month. Notices RAS* 425, 2948–2963. doi: 10.1111/j.1365-2966.2012.21482.x

Donati, J.-F., Skelly, M. B., Bouvier, J., Gregory, S. G., Grankin, K. N., Jardine, M. M., et al. (2010). Magnetospheric accretion and spin-down of the prototypical classical T Tauri star AA Tau. *Month. Notices RAS* 409, 1347–1361. doi: 10.1111/j.1365-2966.2010.17409.x

Donati, J. F., Kouach, D., Lacombe, M., Baratchart, S., Doyon, R., Delfosse, X., et al. (2018). "SPIRou: a NIR spectropolarimeter/high-precision velocimeter for the CFHT," in *Handbook of Exoplanets*, eds H. J. Deeg and J. A. Belmonte (Cham: Springer Nature), 107.

Donati, J. F., Moutou, C., Malo, L., Baruteau, C., Yu, L., Hébrard, E., et al. (2016). A hot Jupiter orbiting a 2-million-year-old solar-mass T Tauri star. *Nature* 534, 662–666. doi: 10.1038/nature18305

Donati, J. F., Paletou, F., Bouvier, J., and Ferreira, J. (2005). Direct detection of a magnetic field in the innermost regions of an accretion disk. *Nature* 438, 466–469. doi: 10.1038/nature04253

Dong, R., Li, S., Chiang, E., and Li, H. (2017). Multiple disk gaps and rings generated by a single super-earth. *Astrophys. J.* 843:127. doi: 10.3847/1538-4357/aa72f2

Dougados, C., Cabrit, S., Lavalley, C., and Ménard, F. (2000). T Tauri stars microjets resolved by adaptive optics. *Astron. Astrophys.* 357, L61–L64.

Duffin, D. F., and Pudritz, R. E. (2009). The early history of protostellar disks, outflows, and binary stars. *Astrophys. J.* 706, L46–L51. doi: 10.1088/0004-637X/706/1/L46

Dullemond, C. P., Birnstiel, T., Huang, J., Kurtovic, N. T., Andrews, S. M., Guzmán, V. V., et al. (2018). The disk substructures at high angular resolution project (DSHARP). VI. Dust trapping in thin-ringed protoplanetary disks. *Astrophys. J.* 869:L46. doi: 10.3847/2041-8213/aaf742

Dunham, M. M., Chen, X., Arce, H. G., Bourke, T. L., Schnee, S., and Enoch, M. L. (2011). Detection of a bipolar molecular outflow driven by a candidate first hydrostatic core. *Astrophys. J.* 742:1. doi: 10.1088/0004-637X/742/1/1

Dzib, S. A., Loinard, L., Rodríguez, L. F., Mioduszewski, A. J., Ortiz-León, G. N., Kounkel, M. A., et al. (2015). The gould's belt very large array survey. IV. The taurus-auriga complex. *Astrophys. J.* 801:91. doi: 10.1088/0004-637X/801/2/91

Eislöffel, J., Smith, M. D., and Davis, C. J. (2000). Spectroscopy of molecular hydrogen in outflows from young stars. *Astron. Astrophys.* 359, 1147–1161.

Enoch, M. L., Lee, J.-E., Harvey, P., Dunham, M. M., and Schnee, S. (2010). A candidate detection of the first hydrostatic core. *Astrophys. J. Lett.* 722, L33–L38. doi: 10.1088/2041-8205/722/1/L33

Evans, N. J., Dunham, M. M., Jørgensen, J. K., Enoch, M. L., Merín, B., van Dishoeck, E. F., et al. (2009). The spitzer c2d legacy results: star-formation rates and efficiencies; evolution and lifetimes. *Astrophys. J. Ser.* 181, 321–350. doi: 10.1088/0067-0049/181/2/321

Fall, S. M., Krumholz, M. R., and Matzner, C. D. (2010). Stellar feedback in molecular clouds and its influence on the mass function of young star clusters. *Astrophys. J. Lett.* 710, L142–L146. doi: 10.1088/2041-8205/710/2/L142

Federrath, C. (2016). "The role of turbulence, magnetic fields and feedback for star formation," in *Journal of Physics Conference Series*, volume 719 of *Journal of Physics Conference Series* (Avignon), 012002. doi: 10.1088/1742-6596/719/1/012002

Federrath, C., Schrön, M., Banerjee, R., and Klessen, R. S. (2014). Modeling jet and outflow feedback during star cluster formation. *Astrophys. J.* 790:128. doi: 10.1088/0004-637X/790/2/128

Ferreira, J. (2013). "Braking down an accreting protostar: disc-locking, disc winds, stellar winds, X-winds and Magnetospheric Ejecta," in *EAS Publications Series*, volume 62 of *EAS Publications Series*, eds P. Hennebelle and C. Charbonnel (EDP Sciences), 169–225. doi: 10.1051/eas/1362006

Ferreira, J., and Pelletier, G. (1995). Magnetized accretion-ejection structures. III. Stellar and extragalactic jets as weakly dissipative disk outflows. *Astron. Astrophys.* 295:807.

Ferreira, J., Pelletier, G., and Appl, S. (2000). Reconnection X-winds: spin-down of low-mass protostars. *Month. Notices RAS* 312, 387–397. doi: 10.1046/j.1365-8711.2000.03215.x

Figer, D. F. (2005). An upper limit to the masses of stars. *Nature* 434, 192–194. doi: 10.1038/nature03293

Flaherty, K. M., Hughes, A. M., Rose, S. C., Simon, J. B., Qi, C., Andrews, S. M., et al. (2017). A Three-dimensional View of Turbulence: constraints on turbulent motions in the HD 163296 protoplanetary disk using DCO^+. *Astrophys. J.* 843:150. doi: 10.3847/1538-4357/aa79f9

Flaherty, K. M., Hughes, A. M., Rosenfeld, K. A., Andrews, S. M., Chiang, E., Simon, J. B., et al. (2015). Weak turbulence in the HD 163296 protoplanetary disk revealed by ALMA CO observations. *Astrophys. J.* 813:99. doi: 10.1088/0004-637X/813/2/99

Flaherty, K. M., Hughes, A. M., Teague, R., Simon, J. B., Andrews, S. M., and Wilner, D. J. (2018). Turbulence in the TW Hya disk. *Astrophys. J.* 856:117. doi: 10.3847/1538-4357/aab615

Flock, M., Henning, T., and Klahr, H. (2012). Turbulence in weakly ionized protoplanetary disks. *Astrophys. J.* 761:95. doi: 10.1088/0004-637X/761/2/95

Frank, A., Ray, T. P., Cabrit, S., Hartigan, P., Arce, H. G., Bacciotti, F., et al. (2014). "Jets and outflows from star to cloud: observations confront theory," *Protostars and Planets VI*, eds H. Beuther, R.S. Klessen, C. P. Dullemond, T. Henning (Tucson, AZ; Houston, TX: The University of Arizona Press; Lunar and Planetary Institute), 451–474. doi: 10.2458/azu_uapress_9780816531240-ch020

Galametz, M., Maury, A., Girart, J. M., Rao, R., Zhang, Q., Gaudel, M., et al. (2018). SMA observations of polarized dust emission in solar-type Class 0 protostars: magnetic field properties at envelope scales. *Astron. Astrophys.* 616:A139. doi: 10.1051/0004-6361/201833004

Gammie, C. F. (1996). Layered accretion in T tauri disks. *Astrophys. J.* 457:355. doi: 10.1086/176735

Gillis, J., Mestel, L., and Paris, R. B. (1974). Magnetic braking during star formation, I. *Astrophys. Space Sci.* 27, 167–194. doi: 10.1007/BF00641596

Gillis, J., Mestel, L., and Paris, R. B. (1979). Magnetic braking during star formation. II. *Month. Notices RAS* 187, 311–335. doi: 10.1093/mnras/187.2.311

Ginsburg, A., Bally, J., Goddi, C., Plambeck, R., and Wright, M. (2018). A keplerian disk around orion SrCI, a 15 $M_\odot$ YSO. *Astrophys. J.* 860:119. doi: 10.3847/1538-4357/aac205

Goodman, A. A., Benson, P. J., Fuller, G. A., and Myers, P. C. (1993). Dense cores in dark clouds. VIII - Velocity gradients. *Astrophys. J.* 406, 528–547. doi: 10.1086/172465

Gray, W. J., McKee, C. F., and Klein, R. I. (2018). Effect of angular momentum alignment and strong magnetic fields on the formation of protostellar discs. *Month. Notices RAS* 473, 2124–2143. doi: 10.1093/mnras/stx2406

Gregory, S. G., Donati, J.-F., Morin, J., Hussain, G. A. J., Mayne, N. J., Hillenbrand, L. A., et al. (2012). Can we predict the global magnetic topology of a pre-main-sequence star from its position in the hertzsprung-russell diagram? *Astrophys. J.* 755:97. doi: 10.1088/0004-637X/755/2/97

Gressel, O., Turner, N. J., Nelson, R. P., and McNally, C. P. (2015). Global simulations of protoplanetary disks with ohmic resistivity and ambipolar diffusion. *Astrophys. J.* 801:84. doi: 10.1088/0004-637X/801/2/84

Hansen, E. C., Frank, A., Hartigan, P., and Lebedev, S. V. (2017). The shock dynamics of heterogeneous YSO jets: 3D simulations meet multi-epoch observations. *Astrophys. J.* 837:143. doi: 10.3847/1538-4357/aa5ca8

Haro, G. (1952). Herbig's nebulous objects near NGC 1999. *Astrophys. J.* 115:572. doi: 10.1086/145576

Hartigan, P., Frank, A., Varniére, P., and Blackman, E. G. (2007). Magnetic fields in stellar jets. *Astrophys. J.* 661, 910–918. doi: 10.1086/513499

Hartigan, P., and Morse, J. (2007). Collimation, proper motions, and physical conditions in the HH 30 jet from hubble space telescope slitless spectroscopy. *Astrophys. J.* 660, 426–440. doi: 10.1086/513015

Hartigan, P., Morse, J. A., and Raymond, J. (1994). Mass-loss rates, ionization fractions, shock velocities, and magnetic fields of stellar jets. *Astrophys. J.* 436:125. doi: 10.1086/174887

Hartigan, P., and Wright, A. (2015). A new diagnostic of magnetic field strengths in radiatively-cooled shocks. *Astrophys. J.* 811:12. doi: 10.1088/0004-637X/811/1/12

Hartmann, L., and MacGregor, K. B. (1982). Protostellar mass and angular momentum loss. *Astrophys. J.* 259, 180–192. doi: 10.1086/160158

Haworth, T. J., and Clarke, C. J. (2019). The first multidimensional view of mass loss from externally FUV irradiated protoplanetary discs. *Month. Notices RAS* 485, 3895–3908. doi: 10.1093/mnras/stz706

Heiles, C., and Troland, T. H. (2005). The millennium arecibo 21 centimeter absorption-line survey. IV. Statistics of magnetic field, column density, and turbulence. *Astrophys. J.* 624, 773–793. doi: 10.1086/428896

Hennebelle, P., and Ciardi, A. (2009). Disk formation during collapse of magnetized protostellar cores. *Astron. Astrophys.* 506, L29–L32. doi: 10.1051/0004-6361/200913008

Hennebelle, P., Commerçon, B., Chabrier, G., and Marchand, P. (2016). Magnetically self-regulated formation of early protoplanetary disks. *Astrophys. J.* 830:L8. doi: 10.3847/2041-8205/830/1/L8

Herbig, G. H. (1951). The spectra of two nebulous objects near NGC 1999. *Astrophys. J.* 113, 697–699. doi: 10.1086/145440

Herbst, W., Eislöffel, J., Mundt, R., and Scholz, A. (2007). "The rotation of young low-mass stars and brown dwarfs," in *Protostars and Planets V*, eds B. Reipurth, D. Jewitt, and K. Keil (Tucson, AZ; Houston, TX: The University of Arizona Press; Lunar and Planetary Institute), 297–311.

Heyer, M. H., and Brunt, C. M. (2012). Trans-Alfvénic motions in the Taurus molecular cloud. *Month. Notices RAS* 420, 1562–1569. doi: 10.1111/j.1365-2966.2011.20142.x

Hirashita, H. (2012). Dust growth in the interstellar medium: how do accretion and coagulation interplay? *Month. Notices RAS* 422, 1263–1271. doi: 10.1111/j.1365-2966.2012.20702.x

Hirota, T., Machida, M. N., Matsushita, Y., Motogi, K., Matsumoto, N., Kim, M. K., et al. (2017). Disk-driven rotating bipolar outflow in Orion Source I. *Nat. Astron.* 1:0146. doi: 10.1038/s41550-017-0146

Hoang, T., and Lazarian, A. (2009). Grain alignment induced by radiative torques: effects of internal relaxation of energy and complex radiation field. *Astrophys. J.* 697, 1316–1333. doi: 10.1088/0004-637X/697/2/1316

Hosokawa, T., and Omukai, K. (2009). Evolution of massive protostars with high accretion rates. *Astrophys. J.* 691, 823–846. doi: 10.1088/0004-637X/691/1/823

Hull, C. L. H., Plambeck, R. L., Bolatto, A. D., Bower, G. C., Carpenter, J. M., Crutcher, R. M., et al. (2013). Misalignment of magnetic fields and outflows in protostellar cores. *Astrophys. J.* 768:159. doi: 10.1088/0004-637X/768/2/159

Hull, C. L. H., Plambeck, R. L., Kwon, W., Bower, G. C., Carpenter, J. M., Crutcher, R. M., et al. (2014). TADPOL: a 1.3 mm survey of dust polarization in star-forming cores and regions. *Astrophys. J. Suppl. Ser.* 213:13. doi: 10.1088/0067-0049/213/1/13

Hussain, G. A. J., and Alecian, E. (2014). "The role of magnetic fields in pre-main sequence stars," in *Magnetic Fields throughout Stellar Evolution*, volume 302 of *IAU Symposium*, eds P. Petit, M. Jardine, and H. C. Spruit (Biarritz: Cambridge University Press), 25–37. doi: 10.1017/S1743921314001653

Jappsen, A.-K., and Klessen, R. S. (2004). Protostellar angular momentum evolution during gravoturbulent fragmentation. *Astron. Astrophys.* 423, 1–12. doi: 10.1051/0004-6361:20040220

Johns-Krull, C. M. (2007). The magnetic fields of classical T tauri stars. *Astrophys. J.* 664, 975–985. doi: 10.1086/519017

Jones, T. J., Dowell, C. D., Lopez Rodriguez, E., Zweibel, E. G., Berthoud, M., Chuss, D. T., et al. (2019). SOFIA Far-infrared Imaging Polarimetry of M82 and NGC 253: exploring the Supergalactic Wind. *Astrophys. J.* 870:L9. doi: 10.3847/2041-8213/aaf8b9

Joos, M., Hennebelle, P., and Ciardi, A. (2012). Protostellar disk formation and transport of angular momentum during magnetized core collapse. *Astron. Astrophys.* 543:A128. doi: 10.1051/0004-6361/201118730

Joos, M., Hennebelle, P., Ciardi, A., and Fromang, S. (2013). The influence of turbulence during magnetized core collapse and its consequences on low-mass star formation. *Astron. Astrophys.* 554:A17. doi: 10.1051/0004-6361/201220649

Jørgensen, J. K., van Dishoeck, E. F., Visser, R., Bourke, T. L., Wilner, D. J., Lommen, D., et al. (2009). PROSAC: a submillimeter array survey of low-mass protostars. II. The mass evolution of envelopes, disks, and stars from the Class 0 through I stages. *Astron. Astrophys.* 507, 861–879. doi: 10.1051/0004-6361/200912325

Klassen, M., Pudritz, R. E., Kuiper, R., Peters, T., and Banerjee, R. (2016). Simulating the formation of massive protostars. I. Radiative feedback and accretion disks. *Astrophys. J.* 823:28. doi: 10.3847/0004-637X/823/1/28

Koenigl, A. (1991). Disk accretion onto magnetic T Tauri stars. *Astrophys. J. Lett.* 370, L39–L43. doi: 10.1086/185972

Königl, A. (2009). Theory of wind-driving protostellar disks. *Astrophys. Space Sci. Proc.* 13, 67–76. doi: 10.1007/978-3-642-00576-3_8

Konigl, A., and Pudritz, R. E. (2000). "Disk winds and the accretion-outflow connection," in *Protostars and Planets IV*, eds V. Mannings, A. P. Boss, and S. S. Russell (Tucson, AZ: The University of Arizona Press), 759.

Königl, A., Salmeron, R., and Wardle, M. (2010). Wind-driving protostellar accretion discs - I. Formulation and parameter constraints. *Month. Notices RAS* 401, 479–499. doi: 10.1111/j.1365-2966.2009.15664.x

Körtgen, B., Banerjee, R., Pudritz, R. E., and Schmidt, W. (2018). The origin of filamentary star forming clouds in magnetized galaxies. *Month. Notices RAS* 479, L40–L44. doi: 10.1093/mnrasl/sly094

Krasnopolsky, R., Li, Z.-Y., and Blandford, R. (1999). Magnetocentrifugal launching of jets from accretion disks. I. Cold axisymmetric flows. *Astrophys. J.* 526, 631–642. doi: 10.1086/308023

Krasnopolsky, R., Li, Z.-Y., Shang, H., and Zhao, B. (2012). Protostellar accretion flows destabilized by magnetic flux redistribution. *Astrophys. J.* 757:77. doi: 10.1088/0004-637X/757/1/77

Kratter, K., and Lodato, G. (2016). Gravitational instabilities in circumstellar disks. *Annu. Rev. Astron. Astrophys.* 54, 271–311. doi: 10.1146/annurev-astro-081915-023307

Krumholz, M. R. (2015). "The formation of very massive stars," in *Very Massive Stars in the Local Universe*, volume 412 of *Astrophysics and Space Science Library*, ed J. S. Vink (Springer Nature), 43.

Krumholz, M. R., Crutcher, R. M., and Hull, C. L. H. (2013). Protostellar disk formation enabled by weak, misaligned magnetic fields. *Astrophys. J.* 767:L11. doi: 10.1088/2041-8205/767/1/L11

Krumholz, M. R., Klein, R. I., McKee, C. F., Offner, S. S. R., and Cunningham, A. J. (2009). The formation of massive star systems by accretion. *Science* 323:754. doi: 10.1126/science.1165857

Krumholz, M. R., McKee, C. F., and Bland-Hawthorn, J. (2018). Star Clusters Across Cosmic Time. *arXiv e-prints*. doi: 10.1146/annurev-astro-091918-104430

Kuffmeier, M., Haugbølle, T., and Nordlund, Å. (2017). Zoom-in simulations of protoplanetary disks starting from GMC scales. *Astrophys. J.* 846:7. doi: 10.3847/1538-4357/aa7c64

Kuiper, R., and Hosokawa, T. (2018). First hydrodynamics simulations of radiation forces and photoionization feedback in massive star formation. *Astron. Astrophys.* 616:A101. doi: 10.1051/0004-6361/201832638

Kuiper, R., Klahr, H., Beuther, H., and Henning, T. (2010). Circumventing the radiation pressure barrier in the formation of massive stars via disk accretion. *Astrophys. J.* 722, 1556–1576. doi: 10.1088/0004-637X/722/2/1556

Kwon, W., Stephens, I. W., Tobin, J. J., Looney, L. W., Li, Z.-Y., van der Tak, F. F. S., et al. (2019). Highly ordered and pinched magnetic fields in the class 0 protobinary system L1448 IRS 2. *Astrophys. J.* 879:25. doi: 10.3847/1538-4357/ab24c8

Larson, R. B. (1981). Turbulence and star formation in molecular clouds. *Month. Notices RAS* 194, 809–826. doi: 10.1093/mnras/194.4.809

Lee, C.-F., Ho, P. T. P., Li, Z.-Y., Hirano, N., Zhang, Q., and Shang, H. (2017). A rotating protostellar jet launched from the innermost disk of HH 212. *Nat. Astron.* 1:0152. doi: 10.1038/s41550-017-0152

Lee, C.-F., Hwang, H.-C., Ching, T.-C., Hirano, N., Lai, S.-P., Rao, R., et al. (2018). Unveiling a magnetized jet from a low-mass protostar. *Nat. Commun.* 9:4636. doi: 10.1038/s41467-018-07143-8

Li, H.-B., Goodman, A., Sridharan, T. K., Houde, M., Li, Z.-Y., Novak, G., et al. (2014a). "The link between magnetic fields and cloud/star formation," in *Protostars and Planets VI* (Tucson, AZ; Houston, TX: The University of Arizona Press; Lunar and Planetary Institute), 101–123.

Li, P. S., McKee, C. F., and Klein, R. I. (2015). Magnetized interstellar molecular clouds - I. Comparison between simulations and Zeeman observations. *Month. Notices RAS* 452, 2500–2527. doi: 10.1093/mnras/stv1437

Li, Z.-Y. (1996). Magnetohydrodynamic disk-wind connection: magnetocentrifugal winds from ambipolar diffusion-dominated accretion disks. *Astrophys. J.* 465:855. doi: 10.1086/177469

Li, Z.-Y., Krasnopolsky, R., and Shang, H. (2011). Non-ideal MHD effects and magnetic braking catastrophe in protostellar

disk formation. *Astrophys. J.* 738:180. doi: 10.1088/0004-637X/738/2/180

Li, Z.-Y., and Nakamura, F. (2006). Cluster formation in protostellar outflow-driven turbulence. *Astrophys. J.* 640, L187–L190. doi: 10.1086/503419

Li, Z. Y., Banerjee, R., Pudritz, R. E., Jørgensen, J. K., Shang, H., Krasnopolsky, R., et al. (2014b). "The earliest stages of star and planet formation: core collapse, and the formation of disks and outflows," in *Protostars and Planets VI*, eds H. Beuther, R. S. Klessen, C. P. Dullemond, and T. Henning (Tucson, AZ; Houston, TX: The University of Arizona Press; Lunar and Planetary Institute), 173.

Lizano, S., and Galli, D. (2015). "Gravitational collapse and disk formation in magnetized cores," in *Magnetic Fields in Diffuse Media*, volume 407 of *Astrophysics and Space Science Library*, eds A. Lazarian, E. M. de Gouveia Dal Pino, and C. Melioli (Springer Nature), 459.

Louvet, F., Dougados, C., Cabrit, S., Mardones, D., Ménard, F., Tabone, B., et al. (2018). The HH30 edge-on T Tauri star. A rotating and precessing monopolar outflow scrutinized by ALMA. *Astron. Astrophys.* 618:A120. doi: 10.1051/0004-6361/201731733

Lynden-Bell, D. (2003). On why discs generate magnetic towers and collimate jets. *Month. Notices RAS* 341, 1360–1372. doi: 10.1046/j.1365-8711.2003.06506.x

Lynden-Bell, D., and Pringle, J. E. (1974). The evolution of viscous discs and the origin of the nebular variables. *Month. Notices RAS* 168, 603–637. doi: 10.1093/mnras/168.3.603

Mac Low, M.-M., and Klessen, R. S. (2004). Control of star formation by supersonic turbulence. *Rev. Mod. Phys.* 76, 125–194. doi: 10.1103/RevModPhys.76.125

Masson, J., Chabrier, G., Hennebelle, P., Vaytet, N., and Commerçon, B. (2016). Ambipolar diffusion in low-mass star formation. I. General comparison with the ideal magnetohydrodynamic case. *Astron. Astrophys.* 587:A32. doi: 10.1051/0004-6361/201526371

Matt, S., and Pudritz, R. E. (2005). Accretion-powered stellar winds as a solution to the stellar angular momentum problem. *Astrophys. J. Lett.* 632, L135–L138. doi: 10.1086/498066

Matt, S., and Pudritz, R. E. (2008). Accretion-powered Stellar Winds. II. Numerical Solutions for Stellar Wind Torques. *Astrophys. J.* 678, 1109–1118. doi: 10.1086/533428

Matt, S. P., Pinzón, G., Greene, T. P., and Pudritz, R. E. (2012). Spin evolution of accreting young stars. II. Effect of accretion-powered stellar winds. *Astrophys. J.* 745:101. doi: 10.1088/0004-637X/745/1/101

Matthews, B. C., McPhee, C. A., Fissel, L. M., and Curran, R. L. (2009). The legacy of SCUPOL: 850 μm imaging polarimetry from 1997 to 2005. *Astrophys. J. Suppl.* 182, 143–204. doi: 10.1088/0067-0049/182/1/143

Matthews, L. D., Greenhill, L. J., Goddi, C., Chand ler, C. J., Humphreys, E. M. L., and Kunz, M. W. (2010). A feature movie of SiO emission 20-100 AU from the massive young stellar object orion source I. *Astrophys. J.* 708, 80–92. doi: 10.1088/0004-637X/708/1/80

Matzner, C. D., and McKee, C. F. (2000). Efficiencies of low-mass star and star cluster formation. *Astrophys. J.* 545, 364–378. doi: 10.1086/317785

Maury, A. J., André, P., Testi, L., Maret, S., Belloche, A., Hennebelle, P., et al. (2019). Characterizing young protostellar disks with the CALYPSO IRAM-PdBI survey: large Class 0 disks are rare. *Astron. Astrophys.* 621:A76. doi: 10.1051/0004-6361/201833537

McKee, C. F., and Ostriker, E. C. (2007). Theory of star formation. *Annu. Rev. Astron. Astrophys.* 45, 565–687. doi: 10.1146/annurev.astro.45.051806.110602

McNally, C. P., Nelson, R. P., and Paardekooper, S.-J. (2018). Low-mass planet migration in magnetically torqued dead zones - II. Flow-locked and runaway migration, and a torque prescription. *Month. Notices RAS* 477, 4596–4614. doi: 10.1093/mnras/sty905

McNally, C. P., Nelson, R. P., Paardekooper, S.-J., Gressel, O., and Lyra, W. (2017). Low mass planet migration in magnetically torqued dead zones - I. Static migration torque. *Month. Notices RAS* 472, 1565–1575. doi: 10.1093/mnras/stx2136

Mellon, R. R., and Li, Z.-Y. (2008). Magnetic braking and protostellar disk formation: the ideal MHD limit. *Astrophys. J.* 681, 1356–1376. doi: 10.1086/587542

Mellon, R. R., and Li, Z.-Y. (2009). Magnetic braking and protostellar disk formation: ambipolar diffusion. *Astrophys. J.* 698, 922–927. doi: 10.1088/0004-637X/698/1/922

Ménard, F., and Duchêne, G. (2004). On the alignment of Classical T Tauri stars with the magnetic field in the Taurus-Auriga molecular cloud. *Astron. Astrophys.* 425, 973–980. doi: 10.1051/0004-6361:20041338

Mestel, L. (1961). A note on equatorial acceleration in a magnetic star. *Month. Notices RAS* 122:473. doi: 10.1093/mnras/122.6.473

Morin, J., Donati, J.-F., Petit, P., Albert, L., Auriére, M., Cabanac, R., et al. (2011). "Exploring the magnetic topologies of cool stars," in *Physics of Sun and Star Spots*, volume 273 of *IAU Symposium*, eds D. Prasad Choudhary and K. G. Strassmeier (Cambridge University Press), 181–187. doi: 10.1017/S1743921311015213

Morse, J. A., Hartigan, P., Cecil, G., Raymond, J. C., and Heathcote, S. (1992). The bow shock and mach disk of HH 34. *Astrophys. J.* 399:231. doi: 10.1086/171919

Morse, J. A., Heathcote, S., Cecil, G., Hartigan, P., and Raymond, J. C. (1993). The bow shock and mach disk of HH 111V. *Astrophys. J.* 410:764. doi: 10.1086/172793

Mouschovias, T. C., and Paleologou, E. V. (1980). Magnetic braking of an aligned rotator during star formation - an exact, time-dependent solution. *Astrophys. J.* 237, 877–899. doi: 10.1086/157936

Myers, P. C., and Benson, P. J. (1983). Dense cores in dark clouds. II - NH3 observations and star formation. *Astrophys. J.* 266, 309–320. doi: 10.1086/160780

Nakamura, F., and Li, Z.-Y. (2005). Quiescent cores and the efficiency of turbulence-accelerated, magnetically regulated star formation. *Astrophys. J.* 631, 411–428. doi: 10.1086/432606

Nordlund, Å., Ramsey, J. P., Popovas, A., and Küffmeier, M. (2018). DISPATCH: a numerical simulation framework for the exa-scale era - I. Fundamentals. *Month. Notices RAS* 477, 624–638. doi: 10.1093/mnras/sty599

Norman, C., and Silk, J. (1980). Clumpy molecular clouds - A dynamic model self-consistently regulated by T Tauri star formation. *Astrophys. J.* 238, 158–174. doi: 10.1086/157969

Norman, M. L. (2000). "Introducing ZEUS-MP: a 3D, parallel, multiphysics code for astrophysical fluid dynamics," in *Revista Mexicana de Astronomia y Astrofisica Conference Series*, volume 9 of *Revista Mexicana de Astronomia y Astrofisica Conference Series*, eds S. J. Arthur, N. S. Brickhouse, and J. Franco (Instituto de Astronomia of the National Autonomous University of Mexico (UNAM)), 66–71.

O'Dell, C. R., and Wen, Z. (1994). Postrefurbishment mission hubble space telescope images of the core of the Orion Nebula: proplyds, herbig-haro objects, and measurements of a circumstellar disk. *Astrophys. J.* 436:194. doi: 10.1086/174892

Offner, S. S. R., and Arce, H. G. (2014). Investigations of protostellar outflow launching and gas entrainment: hydrodynamic simulations and molecular emission. *Astrophys. J.* 784:61. doi: 10.1088/0004-637X/784/1/61

Offner, S. S. R., and Chaban, J. (2017). Impact of protostellar outflows on turbulence and star formation efficiency in magnetized dense cores. *Astrophys. J.* 847:104. doi: 10.3847/1538-4357/aa8996

Offner, S. S. R., Clark, P. C., Hennebelle, P., Bastian, N., Bate, M. R., Hopkins, P. F., et al. (2014). "The origin and universality of the stellar initial mass function," in *Protostars and Planets VI*, eds H. Beuther, R. S. Klessen, C. P. Dullemond, and T. Henning (Tucson, AZ; Houston, TX: The University of Arizona Press; Lunar and Planetary Institute), 53.

Ogilvie, G. I. (2012). Jet launching from accretion discs in the local approximation. *Month. Notices RAS* 423, 1318–1324. doi: 10.1111/j.1365-2966.2012.20958.x

Ossenkopf, V. (1993). Dust coagulation in dense molecular clouds: the formation of fluffy aggregates. *Astron. Astrophys.* 280, 617–646.

Ouyed, R., and Pudritz, R. E. (1997). Numerical simulations of astrophysical jets from keplerian disks. I. Stationary models. *Astrophys. J.* 482, 712–732. doi: 10.1086/304170

Ouyed, R., and Pudritz, R. E. (1999). Numerical simulations of astrophysical jets from Keplerian discs - III. The effects of mass loading. *Month. Notices RAS* 309, 233–244. doi: 10.1046/j.1365-8711.1999.02828.x

Ouyed, R., Pudritz, R. E., and Stone, J. M. (1997). Episodic jets from black holes and protostars. *Nature* 385, 409–414. doi: 10.1038/385409a0

Paatz, G., and Camenzind, M. (1996). Winds and accretion flows around T Tauri stars. *Astron. Astrophys.* 308, 77–90.

Padoan, P. (2018). The magnetic field of molecular clouds. *Contribut. Astron. Observat. Skalnate Pleso* 48, 32–39.

Padoan, P., and Nordlund, Å. (1999). A super-Alfvénic model of dark clouds. *Astrophys. J.* 526, 279–294. doi: 10.1086/307956

Pelletier, G., and Pudritz, R. E. (1992). Hydromagnetic disk winds in young stellar objects and active galactic nuclei. *Astrophys. J.* 394, 117–138. doi: 10.1086/171565

Peters, T., Klaassen, P. D., Mac Low, M.-M., Klessen, R. S., and Banerjee, R. (2012). Are molecular outflows around high-mass stars driven by ionization feedback? *Astrophys. J.* 760:91. doi: 10.1088/0004-637X/760/1/91

Pineda, J. E., Arce, H. G., Schnee, S., Goodman, A. A., Bourke, T., Foster, J. B., et al. (2011). The enigmatic core L1451-mm: a first hydrostatic core? or a hidden VeLLO? *Astrophys. J.* 743:201. doi: 10.1088/0004-637X/743/2/201

Price, D. J., Tricco, T. S., and Bate, M. R. (2012). Collimated jets from the first core. *Month. Notices RAS* 423, L45–L49. doi: 10.1111/j.1745-3933.2012.01254.x

Pudritz, R. E., Cridland, A. J., and Alessi, M. (2018). "Connecting planetary composition with formation," in *Handbook of Exoplanets*, eds H. J. Deeg and J. A. Belmonte (Cham: Springer Nature), 144.

Pudritz, R. E., and Norman, C. A. (1983). Centrifugally driven winds from contracting molecular disks. *Astrophys. J.* 274, 677–697. doi: 10.1086/161481

Pudritz, R. E., and Norman, C. A. (1986). Bipolar hydromagnetic winds from disks around protostellar objects. *Astrophys. J.* 301, 571–586. doi: 10.1086/163924

Pudritz, R. E., Ouyed, R., Fendt, C., and Brandenburg, A. (2007). "Disk winds, jets, and outflows: theoretical and computational foundations," in *Protostars and Planets V*, eds B. Reipurth, D. Jewitt, and K. Keil (Tucson: The University of Arizona Press; Tucson; Houston: Lunar and Planetary Institute), 277–294.

Pudritz, R. E., Rogers, C. S., and Ouyed, R. (2006). Controlling the collimation and rotation of hydromagnetic disc winds. *Month. Notices RAS* 365, 1131–1148. doi: 10.1111/j.1365-2966.2005.09766.x

Raga, A. C., Noriega-Crespo, A., Reipurth, B., Garnavich, P. M., Heathcote, S., Böhm, K. H., et al. (2002). Kinematics of the HH 111 jet from the space telescope imaging spectrograph. *Astrophys. J.* 565, L29–L33. doi: 10.1086/338910

Ray, T., Dougados, C., Bacciotti, F., Eislöffel, J., and Chrysostomou, A. (2007). "Toward resolving the outflow engine: an observational perspective," in *Protostars and Planets V*, eds B. Reipurth, D. Jewitt, and K. Keil (Tucson, AZ; Houston, TX: The University of Arizona Press; Lunar and Planetary Institute), 231.

Rebull, L. M., Wolff, S. C., and Strom, S. E. (2004). Stellar rotation in young clusters: the first 4 million years. *Astron. J.* 127, 1029–1051. doi: 10.1086/380931

Reiners, A., and Mohanty, S. (2012). Radius-dependent angular momentum evolution in low-mass stars. I. *Astrophys. J.* 746:43. doi: 10.1088/0004-637X/746/1/43

Reipurth, B., and Mikkola, S. (2012). Formation of the widest binary stars from dynamical unfolding of triple systems. *Nature* 492, 221–224. doi: 10.1038/nature11662

Reipurth, B., and Mikkola, S. (2015). Brown dwarf binaries from disintegrating triple systems. *Astron. J.* 149:145. doi: 10.1088/0004-6256/149/4/145

Reipurth, B., Rodríguez, L. F., Anglada, G., and Bally, J. (2004). Radio continuum jets from protostellar objects. *Astron. J.* 127, 1736–1746. doi: 10.1086/381062

Reissl, S., Seifried, D., Wolf, S., Banerjee, R., and Klessen, R. S. (2017). The origin of dust polarization in molecular outflows. *Astron. Astrophys.* 603:A71. doi: 10.1051/0004-6361/201730408

Reissl, S., Wolf, S., and Brauer, R. (2016). Radiative transfer with POLARIS. I. Analysis of magnetic fields through synthetic dust continuum polarization measurements. *Astron. Astrophys.* 593:A87. doi: 10.1051/0004-6361/201424930

Rodríguez-Kamenetzky, A., Carrasco-González, C., Araudo, A., Torrelles, J. M., Anglada, G., Martí, J., et al. (2016). Investigating particle acceleration in protostellar jets: the triple radio continuum source in serpens. *Astrophys. J.* 818:27. doi: 10.3847/0004-637X/818/1/27

Rosen, A. L., Krumholz, M. R., McKee, C. F., and Klein, R. I. (2016). An unstable truth: how massive stars get their mass. *Month. Notices RAS* 463, 2553–2573. doi: 10.1093/mnras/stw2153

Rucinski, S. M. (1985). IRAS observations of T Tauri and post-T Tauri stars. *Astron. J.* 90, 2321–2330. doi: 10.1086/113937

Santos-Lima, R., de Gouveia Dal Pino, E. M., and Lazarian, A. (2012). The role of turbulent magnetic reconnection in the formation of rotationally supported protostellar disks. *Astrophys. J.* 747:21. doi: 10.1088/0004-637X/747/1/21

Sargent, A. I., and Beckwith, S. (1987). Kinematics of the circumstellar gas of HL tauri and R monocerotis. *Astrophys. J.* 323:294. doi: 10.1086/165827

Sartorio, N. S., Vandenbroucke, B., Falceta-Goncalves, D., Wood, K., and Keto, E. (2019). Massive star formation via torus accretion: the effect of photoionization feedback. *Month. Notices RAS* 486, 5171–5183. doi: 10.1093/mnras/stz1187

Scholz, A. (2009). "Stellar spindown: from the ONC to the sun," in *15th Cambridge Workshop on Cool Stars, Stellar Systems, and the Sun*, volume 1094 of *American Institute of Physics Conference Series*, ed E. Stempels (AIP Publishing), 61–70.

Schwartz, R. D. (1977). Evidence of star formation triggered by expansion of the Gum Nebula. *Astrophys. J. Lett.* 212, L25–L26. doi: 10.1086/182367

Seifried, D., Banerjee, R., Pudritz, R. E., and Klessen, R. S. (2012). Disc formation in turbulent massive cores: circumventing the magnetic braking catastrophe. *Month. Notices RAS* 423, L40–L44. doi: 10.1111/j.1745-3933.2012.01253.x

Seifried, D., Banerjee, R., Pudritz, R. E., and Klessen, R. S. (2013). Turbulence-induced disc formation in strongly magnetized cloud cores. *Month. Notices RAS* 432, 3320–3331. doi: 10.1093/mnras/stt682

Seifried, D., Banerjee, R., Pudritz, R. E., and Klessen, R. S. (2015). Accretion and magnetic field morphology around Class 0 stage protostellar discs. *Month. Notices RAS* 446, 2776–2788. doi: 10.1093/mnras/stu2282

Shakura, N. I., and Sunyaev, R. A. (1973). Black holes in binary systems. Observational appearance. *Astron. Astrophys.* 24, 337–355. doi: 10.1007/978-94-010-2585-0_13

Shang, H., Li, Z. Y., and Hirano, N. (2007). "Jets and bipolar outflows from young stars: theory and observational tests," in *Protostars and Planets V*, eds B. Reipurth, D. Jewitt, and K. Keil (Tucson, AZ; Houston, TX: The University of Arizona Press; Lunar and Planetary Institute), 261.

Shibata, K., and Uchida, Y. (1985). A magnetodynamic mechanism for the formation of astrophysical jets. I - Dynamical effects of the relaxation of nonlinear magnetic twists. *Publ. ASJ* 37, 31–46.

Shibata, K., and Uchida, Y. (1986). A magnetodynamic mechanism for the formation of astrophysical jets. II - Dynamical processes in the accretion of magnetized mass in rotation. *Publ. ASJ* 38, 631–660.

Shu, F., Najita, J., Ostriker, E., Wilkin, F., Ruden, S., and Lizano, S. (1994). Magnetocentrifugally driven flows from young stars and disks. I. A generalized model. *Astrophys. J.* 429:781. doi: 10.1086/174363

Shu, F. H., Najita, J. R., Shang, H., and Li, Z. Y. (2000). "X-winds theory and observations," in *Protostars and Planets IV*, eds V. Mannings, A. P. Boss, and S. S. Russell (Tucson, AZ: The University of Arizona Press), 789–814.

Simon, J. B., Bai, X.-N., Flaherty, K. M., and Hughes, A. M. (2018). Origin of weak turbulence in the outer regions of protoplanetary disks. *Astrophys. J.* 865:10. doi: 10.3847/1538-4357/aad86d

Smith, M. D., and Mac Low, M. M. (1997). The formation of C-shocks: structure and signatures. *Astron. Astrophys.* 326, 801–810.

Spruit, H. C. (2010). "Theory of magnetically powered jets," in *Lecture Notes in Physics, Berlin Springer Verlag*, volume 794 of *Lecture Notes in Physics*, ed T. Belloni (Berlin: Springer Verlag) 233.

Staff, J. E., Koning, N., Ouyed, R., Thompson, A., and Pudritz, R. E. (2015). Hubble space telescope scale 3D simulations of MHD disc winds: a rotating two-component jet structure. *Month. Notices RAS* 446, 3975–3991. doi: 10.1093/mnras/stu2392

Stepanovs, D., and Fendt, C. (2014). Modeling MHD accretion-ejection—from the launching area to propagation scales. *Astrophys. J.* 793:31. doi: 10.1088/0004-637X/793/1/31

Strom, S. E., and Strom, K. M. (1987). "Mass outflows associated with young stellar objects," in *Star Forming Regions*, volume 115 of *IAU Symposium*, eds M. Peimbert and J. Jugaku (Tokyo), 255–272.

Suriano, S. S., Li, Z.-Y., Krasnopolsky, R., and Shang, H. (2018). The formation of rings and gaps in magnetically coupled disc-wind systems: ambipolar diffusion and reconnection. *Month. Notices RAS* 477, 1239–1257. doi: 10.1093/mnras/sty717

Tan, J. C., Beltrán, M. T., Caselli, P., Fontani, F., Fuente, A., Krumholz, M. R., et al. (2014). "Massive star formation," in *Protostars and Planets VI,* eds H. Beuther, R.S. Klessen, C. P. Dullemond, T. Henning (Tucson, AZ; Houston, TX: The University of Arizona Press; Lunar and Planetary Institute), 149–172. doi: 10.2458/azu_uapress_9780816531240-ch007

Tanaka, K. E. I., Tan, J. C., Zhang, Y., and Hosokawa, T. (2018). The impact of feedback in massive star formation. II. Lower star formation efficiency at lower metallicity. *Astrophys. J.* 861:68. doi: 10.3847/1538-4357/aac892

Targon, C. G., Rodrigues, C. V., Cerqueira, A. H., and Hickel, G. R. (2011). Correlating the interstellar magnetic field with protostellar jets and its sources. *Astrophys. J.* 743:54. doi: 10.1088/0004-637X/743/1/54

Terebey, S., Shu, F. H., and Cassen, P. (1984). The collapse of the cores of slowly rotating isothermal clouds. *Astrophys. J.* 286, 529–551. doi: 10.1086/162628

Tobin, J. J., Hartmann, L., Chiang, H.-F., Wilner, D. J., Looney, L. W., Loinard, L., et al. (2013). Modeling the resolved disk around the class 0 protostar L1527. *Astrophys. J.* 771:48. doi: 10.1088/0004-637X/771/1/48

Tomida, K., Okuzumi, S., and Machida, M. N. (2015). Radiation magnetohydrodynamic simulations of protostellar collapse: nonideal magnetohydrodynamic effects and early formation of circumstellar disks. *Astrophys. J.* 801:117. doi: 10.1088/0004-637X/801/2/117

Tout, C. A., and Pringle, J. E. (1992). Spin-down of rapidly rotating, convective stars. *Month. Notices RAS* 256, 269–276. doi: 10.1093/mnras/256.2.269

Turner, N. J., Fromang, S., Gammie, C., Klahr, H., Lesur, G., Wardle, M., et al. (2014). "Transport and accretion in planet-forming disks," in *Protostars and Planets VI*, eds H. Beuther, R.S. Klessen, C. P. Dullemond, T. Henning (Tucson, AZ; Houston, TX: The University of Arizona Press; Lunar and Planetary Institute), 411–432.

Tychoniec, Ł., Tobin, J. J., Karska, A., Chandler, C., Dunham, M. M., Harris, R. J., et al. (2018). The VLA nascent disk and multiplicity survey of perseus protostars (VANDAM). IV. Free-Free emission from protostars: links to infrared properties, outflow tracers, and protostellar disk masses. *ArXiv e-prints*. doi: 10.3847/1538-4365/aaceae

Uchida, Y., and Shibata, K. (1985). Magnetodynamical acceleration of CO and optical bipolar flows from the region of star formation. *Publ. ASJ* 37, 515–535.

Vaidya, B., Fendt, C., Beuther, H., and Porth, O. (2011). Jet formation from massive young stars: magnetohydrodynamics versus radiation pressure. *Astrophys. J.* 742:56. doi: 10.1088/0004-637X/742/1/56

van der Marel, N., Dong, R., di Francesco, J., Williams, J. P., and Tobin, J. (2019). Protoplanetary disk rings and gaps across ages and luminosities. *Astrophys. J.* 872:112. doi: 10.3847/1538-4357/aafd31

van Haarlem, M. P., Wise, M. W., Gunst, A. W., Heald, G., McKean, J. P., Hessels, J. W. T., et al. (2013). LOFAR: the lOw-frequency ARray. *Astron. Astrophys.* 556:A2.

Walawender, J., Bally, J., Francesco, J. D., Jørgensen, J., and Getman, K. . (2008). "NGC 1333: a nearby burst of star formation," in *Handbook of Star Forming Regions, Volume I: The Northern Sky*, ed B. Reipurth, Vol. 4 (ASP Monograph Publications), 346.

Wang, L., Bai, X.-N., and Goodman, J. (2018). Global Simulations of Protoplanetary Disk Outflows with Coupled Non-ideal Magnetohydrodynamics and Consistent Thermochemistry. *arXiv e-prints*. doi: 10.3847/1538-4357/ab06fd

Wardle, M., and Koenigl, A. (1993). The structure of protostellar accretion disks and the origin of bipolar flows. *Astrophys. J.* 410, 218–238. doi: 10.1086/172739

Watson, D. M., Calvet, N. P., Fischer, W. J., Forrest, W. J., Manoj, P., Megeath, S. T., et al. (2016). Evolution of mass outflow in protostars. *Astrophys. J.* 828:52. doi: 10.3847/0004-637X/828/1/52

Weber, E. J., and Davis, Leverett, J. (1967). The angular momentum of the solar wind. *Astrophys. J.* 148, 217–227. doi: 10.1086/149138

Whelan, E. T., Ray, T. P., Bacciotti, F., Natta, A., Testi, L., and Randich, S. (2005). A resolved outflow of matter from a brown dwarf. *Nature* 435, 652–654. doi: 10.1038/nature03598

Wu, P.-F., Takakuwa, S., and Lim, J. (2009). Multiple bipolar molecular outflows from the L1551 IRS5 protostellar system. *Astrophys. J.* 698, 184–197. doi: 10.1088/0004-637X/698/1/184

Wu, Y., Wei, Y., Zhao, M., Shi, Y., Yu, W., Qin, S., et al. (2004). A study of high velocity molecular outflows with an up-to-date sample. *Astron. Astrophys.* 426, 503–515. doi: 10.1051/0004-6361:20035767

Yorke, H. W., and Bodenheimer, P. (1999). The formation of protostellar disks. III. The influence of gravitationally induced angular momentum transport on disk structure and appearance. *Astrophys. J.* 525, 330–342. doi: 10.1086/307867

Zhang, K., Blake, G. A., and Bergin, E. A. (2015). Evidence of fast pebble growth near condensation fronts in the HL tau protoplanetary disk. *Astrophys. J.* 806:L7. doi: 10.1088/2041-8205/806/1/L7

Zhang, S., Zhu, Z., Huang, J., Guzmán, V. V., Andrews, S. M., Birnstiel, T., et al. (2018a). The disk substructures at high angular resolution project (DSHARP). VII. The planet-disk interactions interpretation. *Astrophys. J.* 869:L47. doi: 10.3847/2041-8213/aaf744

Zhang, Y., Arce, H. G., Mardones, D., Cabrit, S., Dunham, M. M., Garay, G., et al. (2016). ALMA cycle 1 observations of the HH46/47 molecular outflow: structure, entrainment, and core impact. *Astrophys. J.* 832:158. doi: 10.3847/0004-637X/832/2/158

Zhang, Y., Higuchi, A. E., Sakai, N., Oya, Y., López-Sepulcre, A., Imai, M., et al. (2018b). Rotation in the NGC 1333 IRAS 4C outflow. *Astrophys. J.* 864:76. doi: 10.3847/1538-4357/aad7ba

Zhao, B., Caselli, P., Li, Z.-Y., and Krasnopolsky, R. (2018). Decoupling of magnetic fields in collapsing protostellar envelopes and disc formation and fragmentation. *Month. Notices RAS* 473, 4868–4889. doi: 10.1093/mnras/stx2617

Zweibel, E. G. (2002). Ambipolar drift in a turbulent medium. *Astrophys. J.* 567, 962–970. doi: 10.1086/338682

Conflict of Interest Statement: The authors declare that the research was conducted in the absence of any commercial or financial relationships that could be construed as a potential conflict of interest.

frontiers in Astronomy and Space Sciences

REVIEW
published: 24 July 2019
doi: 10.3389/fspas.2019.00051

Numerical Methods for Simulating Star Formation

Romain Teyssier[1]* *and Benoît Commerçon*[2]

[1] *Centre for Theoretical Astrophysics and Cosmology, Institute for Computational Science, University of Zurich, Zurich, Switzerland,* [2] *CNRS, Centre de Recherche Astrophysique de Lyon UMR5574, Univ Lyon, Ens de Lyon, Univ Lyon1, Lyon, France*

We review the numerical techniques for ideal and non-ideal magneto-hydrodynamics (MHD) used in the context of star formation simulations. We outline the specific challenges offered by modeling star forming environments, which are dominated by supersonic and super-Alfvénic turbulence in a radiative, self-gravitating fluid. These conditions are rather unique in physics and engineering and pose particularly severe restrictions on the robustness and accuracy of numerical codes. One striking aspect is the formation of collapsing fluid elements leading to the formation of singularities that represent point-like objects, namely the proto-stars. Although a few studies have attempted to resolve the formation of the first and second Larson's cores, resolution limitations force us to use sink particle techniques, with sub-grid models to compute the accretion rates of mass, momentum and energy, as well as their ejection rate due to radiation and jets from the proto-stars. We discuss the most popular discretisation techniques used in the community, namely smoothed particle hydrodynamics, finite difference and finite volume methods, stressing the importance to maintain a divergence-free magnetic field. We discuss how to estimate the truncation error of a given numerical scheme, and its importance in setting the magnitude of the numerical diffusion. This can have a strong impact on the outcome of these MHD simulations, where both viscosity and resistivity are implemented at the grid scale. We then present various numerical techniques to model non-ideal MHD effects, such as Ohmic and ambipolar diffusion, as well as the Hall effect. These important physical ingredients are posing strong challenges in term of resolution and time stepping. For the latter, several strategies are discussed to overcome the limitations due to prohibitively small time steps. An important aspect of star formation simulations is the radiation field. We discuss the current state-of-the-art, with a variety of techniques offering pros and cons in different conditions. Finally, we present more advanced strategies to mitigate the adverse effect of finite numerical resolution, which are very popular in the context of supersonic, self-gravitating fluids, namely adaptive mesh refinement, moving meshes, Smoothed Particle Hydrodynamics and high-order methods. Advances in these three directions are likely to trigger immense progress in the future of our field. We then illustrate the different aspects of this review by presenting recent results on supersonic MHD turbulence and magnetized collapse calculations.

Keywords: star formation, numerical techniques, MHD: ideal, MHD: non-ideal, astrophysical fluid dynamics, radiation fields, sink particles

OPEN ACCESS

Edited by:
Christopher F. McKee, University of California, Berkeley, United States

Reviewed by:
Christoph Federrath, Australian National University, Australia
Richard Klein, University of California, Berkeley, United States

***Correspondence:**
Romain Teyssier
romain.teyssier@uzh.ch

Specialty section:
This article was submitted to Stellar and Solar Physics, a section of the journal Frontiers in Astronomy and Space Sciences

Received: *22 January 2019*
Accepted: *02 July 2019*
Published: *24 July 2019*

Citation:
Teyssier R and Commerçon B (2019) Numerical Methods for Simulating Star Formation. Front. Astron. Space Sci. 6:51. doi: 10.3389/fspas.2019.00051

1. INTRODUCTION

Star formation is one of the main unsolved problems in astrophysics. Although our view of this fundamental process, at the nexus of galaxy formation, planetary science and stellar evolution, has considerably changed over the past decades, thanks to new observations and theoretical progress, many dark corners remain to be explored. One of the reasons why the true origin of stars still eludes us is the highly non-linear nature of the governing equations, describing self-gravitating, compressible, magnetized dust, and gas fluids interacting with radiation. In this review, we present these main governing equations, focusing on ideal magneto-hydrodynamics, radiation hydrodynamics, non-ideal effects and sink particle techniques. We describe the most popular discretisation schemes, focusing on possible sources of errors and their consequences on clouding our conclusions. We finally give a short description of the landscape in term of star formation simulations, with different set-up strategies addressing particular scales in this fundamentally multi-scale problem.

Star formation is believed to be the consequence of the collapse of mildly supersonic or transonic to subsonic molecular cores emerging out of supersonic turbulent flows in the interstellar medium (Mac Low and Klessen, 2004; McKee and Ostriker, 2007). The source of turbulence is probably to be found on large scales, as a consequence of large galactic shearing or colliding flows, but also on small scales, because of various sources of stellar feedback (McKee, 1989; Federrath et al., 2017). In this context, gravitational or thermal instabilities lead to the formation of dense gas clumps that undergo a more or less violent gravitational collapse, leading to the formation of a proto-star surrounded by a proto-stellar disk. Describing these processes using only simple analytical methods is almost impossible. Moreover, the traditional engineering methods in Computational Fluid Dynamics (CFD) are usually not robust enough to sustain highly supersonic and super-Alfvénic flows. Self-gravity, magnetic fields and radiation fields, taken together, define a very unique system of equations that has no equivalent in the industry. This has led astrophysicists to develop their own methods, largely inspired by traditional methods designed in the applied mathematics community, but significantly adapted to the specific problem at hand. In this context, Smoothed Particle Hydrodynamics (SPH) and Adaptive Mesh Refinement (AMR) techniques turned out to be particularly suitable to the problem of star formation. Both techniques have their own pros and cons, and comparing the two allows us to assess the robustness of our numerical results. New techniques have also been developed, that are specific to star formation, such as sink particles, a commonly adopted recipe to replace an otherwise collapsing fluid element by a collision-less particle, saving computational times and increasing the realism of the simulation.

In this review, we pay attention to the description of the equations, without necessarily discussing their physical foundations, such as the ideal MHD limit or the non-ideal diffusion processes. We describe the various numerical techniques, from low-order schemes to modern high-order methods, as well as from non-zero divergence schemes to exact divergence-free methods, etc. We refer to the corresponding literature, including all references that are relevant to the historical description of the discipline and that give a fair snapshot of the present state of the field. We apologize in advance for not having included all possible references on the topic.

2. IDEAL MHD: NUMERICAL TECHNIQUES

Developing new computational methods for solving the ideal MHD equations has generated a lot of interest within the applied mathematics and computational physics communities. Quite naturally, because of their success in solving the Euler equations, grid-based methods with flux upwinding, also known as Godunov's method, were applied to the MHD equations in the framework of finite-volume discretisation. In parallel, Smoothed Particle Hydrodynamics (SPH) generated a lot of interest in the astrophysics community because of its strict Galilean invariance. Both methods, however, quickly ran into difficulties trying to maintain the divergence-free property of the MHD equations.

2.1. The Ideal MHD Equations

Before we review the various improvements of MHD numerical solvers over the past decades, we briefly recall the ideal MHD equations, shown here in conservative form. We have first the mass conservation equation,

$$\frac{\partial \rho}{\partial t} + \nabla \cdot (\rho \mathbf{v}) = 0, \tag{1}$$

where ρ is the mass density and $\mathbf{v}$ is the fluid velocity vector. We also have the momentum conservation equation

$$\frac{\partial}{\partial t}(\rho \mathbf{v}) + \nabla \cdot \left(\rho \mathbf{v} \otimes \mathbf{v} + P_{\rm tot} \mathbb{I} - \frac{1}{4\pi} \mathbf{B} \otimes \mathbf{B} \right) = \rho \mathbf{g}, \tag{2}$$

where $\mathbf{B}$ is the magnetic field vector and $P_{\rm tot}$ is the total pressure, defined as the sum of the thermal pressure and the magnetic pressure

$$P_{\rm tot} = P + \frac{1}{8\pi} B^2. \tag{3}$$

Note that we work here in *cgs* units, hence the presence of the 4π term in these equations. We have also included the gravitational acceleration vector $\mathbf{g}$ as a source term on the right-hand side of the momentum conservation equation. Finally, we have the total energy conservation equation

$$\frac{\partial E_{\rm tot}}{\partial t} + \nabla \cdot \left((E_{\rm tot} + P_{\rm tot}) \mathbf{v} - \frac{1}{4\pi} \mathbf{B} (\mathbf{B} \cdot \mathbf{v}) \right) = \rho \mathbf{g} \cdot \mathbf{v}, \tag{4}$$

where the total fluid energy is the sum of the kinetic energy, the internal energy and magnetic energy

$$E_{\rm tot} = \frac{1}{2} \rho v^2 + e + \frac{1}{8\pi} B^2. \tag{5}$$

In order to close the system, we need the fluid equation of state, usually given be the ideal gas equation of state

$$P = (\gamma - 1) e, \tag{6}$$

and the induction equation for the evolution of the magnetic field

$$\frac{\partial \mathbf{B}}{\partial t} = -\nabla \times \mathbf{E} \quad \text{with} \quad \mathbf{E} = -\mathbf{v} \times \mathbf{B}, \tag{7}$$

where we have introduced the electric field **E** (also known as the electromotive force, emf). We need to add to these equations the most important property of the magnetic field, namely

$$\nabla \cdot \mathbf{B} = 0, \tag{8}$$

also known as the solenoidal constraint or the divergence-free condition. Since we consider now in this section ideal MHD conditions, we have no dissipation terms in the induction equation, as well as in the fluid equations.

2.2. Some Important Mathematical Properties

The fluid equations appear to be in conservative form, which naturally calls for a finite volume representation, which will ensure exact conservation of mass, momentum and total energy, by construction, owing to the divergence theorem

$$\int_V \nabla \cdot \mathbf{F} \mathrm{d}V = \int_S \mathbf{F} \cdot \mathbf{n} \mathrm{d}S, \tag{9}$$

where the vector **F** can be the flux of mass, momentum or energy. Designing a numerical scheme boils down to computing the flux through the surface of the volume elements. On the other hand, the induction equation naturally calls for a finite surface representation, owing to the Stoke's theorem

$$\frac{\partial}{\partial t} \int_S \mathbf{B} \cdot \mathbf{n} \mathrm{d}S = \int_S \nabla \times \mathbf{E} \cdot \mathbf{n} \mathrm{d}S = \int_L \mathbf{E} \cdot \mathrm{d}\mathbf{l}. \tag{10}$$

Similarly, the divergence-free condition, written in integral form as

$$\int_V \nabla \cdot \mathbf{B} \mathrm{d}V = \int_S \mathbf{B} \cdot \mathbf{n} \mathrm{d}S, \tag{11}$$

also calls for defining the magnetic field as a surface averaged quantity. This naturalness argument, together with the fact that the divergence-free condition can be maintained to machine precision accuracy, has led to the design of the *constrained transport* scheme (Evans and Hawley, 1988). This very popular method for grid-based techniques comes however with a price: the flow variables are not all co-located at cell centers, like volume-weighted fluid variables, but also at face centers, for the magnetic field components, and at edge centers for the electric field components.

A very important mathematical property of the magnetic field that emerges from the divergence-free condition is that the normal component of the field should be continuous across cell faces. The x-component of the field, for example, can be discontinuous in the y and z-directions, but has to vary smoothly in the x-direction. This property also naturally holds in the constrained transport method. It can be written as

$$\int_S [\mathbf{B} \cdot \mathbf{n}] \, \mathrm{d}S = 0, \tag{12}$$

where the operator $[A] = A^+ - A^-$ denotes the jump of a quantity A across the surface element.

2.3. Preserving the Divergence-Free Condition

Historically, one of the first ideal MHD, general purpose codes, is ZEUS-2D developed specifically for astrophysics by Stone et al. (1992b). It is a finite-difference code using constrained transport and artificial viscosity to handle shocks, The continuity and divergence-free conditions are therefore satisfied by construction, but since artificial viscosity is used to handle shocks, instabilities can occur in fast rarefaction waves (Falle, 2002).

The other popular strategy for grid-based methods is to maintain all MHD variables as volume-averaged quantities, allowing for discontinuities across all cell faces. In the late 90s, a series of papers presented finite-volume MHD codes with proper upwinding of numerical fluxes using Riemann solvers (Dai and Woodward, 1994; Ryu et al., 1995; Tóth, 1996; Balsara, 1998; Lee and Deane, 2009). These methods are very powerful, because they are strictly conservative and because they satisfy the so-called *entropy condition*, meaning the entropy can only increase, a key property to maintain the stability of the numerical solution. These finite-volume codes all considered the magnetic field as a volume-averaged, piecewise-constant, cell-centered quantity, which violates the continuity condition of the normal component of the field. The resulting schemes are therefore not necessarily divergence-free anymore. In order to maintain the divergence as small as possible, an additional step is required that modifies the magnetic field components and decreases or nullifies the divergence: this operation is called *divergence cleaning*. In a seminal paper, Tóth (2000) has compared various schemes and showed that they all passed with mixed success a variety of MHD test problems. We will now review these grid-based methods that are using divergence cleaning.

The first method we discuss here is the *projection scheme*, introduced by Brackbill and Barnes (1980). The idea is to measure the spurious divergence after the main update of the MHD variables, and solve for a Poisson equation defined as

$$\Delta \phi = \nabla \cdot \mathbf{B}^*. \tag{13}$$

where ϕ is a scalar potential. The new magnetic field is then corrected as

$$\mathbf{B}^{n+1} = \mathbf{B}^* - \nabla \phi, \tag{14}$$

so that by construction the divergence is now zero. This method works very well in many applications. It suffers however from two main issues: first, it is quite expensive as it requires to solve for a Poisson equation. Another consequence is that the correction is non-local: very localized divergence errors can be instantaneously transported across the grid to enforce the solenoidality condition. Second, the correction process modifies the magnetic field, without modifying the total energy. As a consequence, the resulting temperature can be modified, and the entropy condition might be violated. An easy fix is to remove the magnetic energy before the correction step and add the new

magnetic energy after the correction, but the resulting scheme is not conservative anymore.

The second popular method is the so-called 8-waves formulation or Powell's method (Powell et al., 1999). The idea is to write more general ideal MHD equations *allowing for the presence of magnetic monopoles*. This results in the following non-conservative form

$$\frac{\partial}{\partial t}(\rho \mathbf{v}) + \nabla \cdot \left(\rho \mathbf{v} \otimes \mathbf{v} + P_{\rm tot} \mathbb{I} - \frac{1}{4\pi} \mathbf{B} \otimes \mathbf{B} \right) = -(\nabla \cdot \mathbf{B}) \mathbf{B} + \rho \mathbf{g}, \quad (15)$$

$$\frac{\partial E_{\rm tot}}{\partial t} + \nabla \cdot \left((E_{\rm tot} + P_{\rm tot}) \mathbf{v} - \frac{1}{4\pi} \mathbf{B} (\mathbf{B} \cdot \mathbf{v}) \right) = -(\nabla \cdot \mathbf{B}) \mathbf{B} \cdot \mathbf{v} + \rho \mathbf{g} \cdot \mathbf{v}, \quad (16)$$

$$\frac{\partial \mathbf{B}}{\partial t} - \nabla \times (\mathbf{v} \times \mathbf{B}) = -(\nabla \cdot \mathbf{B}) \mathbf{v}. \quad (17)$$

This method proved very useful and robust for many applications. It is still widely used in astrophysics nowadays. The success of the method originates from the property that the spurious $\nabla \cdot \mathbf{B}$ is advected away with the flow, using the so-called eighth MHD wave, so that divergence errors do not accumulate. There are however two problems: First, in stagnation points[1], the divergence errors will accumulate because the flow trajectories are converging. Second, the scheme is not strictly conservative. Shock waves lead to solutions that do not converge to the correct conservation laws anymore.

A very elegant solution to the first problem was proposed in Dedner et al. (2002) using the so-called hyperbolic-parabolic divergence cleaning technique, also known as a Generalized Lagrange Multiplier (GLM) formulation of the ideal MHD equations, in short, *Dedner's scheme*. The idea is to add a ninth wave to the previous Powell's modified MHD equations, introducing the cleaning field ψ that satisfies

$$\frac{\partial \psi}{\partial t} + \mathbf{v} \cdot \nabla \psi + c_h^2 \nabla \cdot \mathbf{B} = -\frac{\psi}{\tau}, \quad (18)$$

and is used as a source term in the induction equation.

$$\frac{\partial \mathbf{B}}{\partial t} - \nabla \times (\mathbf{v} \times \mathbf{B}) = -\nabla \psi. \quad (19)$$

In the first equation, c_h is the divergence wave speed and τ is the divergence damping time scale. The latter is chosen equal to (or larger than) the fast magnetosonic wave speed, while the former is usually equal to (or larger than) the fast magnetosonic cell crossing time. At first sight, this new nine waves scheme can be seen as a combination of advection and damping of divergence errors, thus a clever combination of the projection method and the Powell's scheme. As shown recently by Derigs et al. (2017), it is in fact much more than that: this new divergence field ψ allows to restore the entropy condition, as this field can be interpreted as a divergence cleaning energy which stores temporarily the magnetic energy lost during the damping step. It is also conservative in a general sense, but still violates the Rankine-Hugoniot shock relations locally.

In parallel, accurate and stable MHD solvers have been the topics of many studies in the SPH framework. Probably because of its strict Galilean invariance, early SPH MHD solvers were quite oscillatory (see e.g., Dolag et al., 1999). Truncation errors associated to the non-zero divergence cannot be damped by numerical diffusion as they are advected away, as in the case of grid-based codes. Many regularization techniques have been proposed to provide stable SPH solvers for the ideal MHD equations: using the vector potential (e.g., Kotarba et al., 2009) or using artificial diffusivity (Price and Monaghan, 2005; Dolag and Stasyszyn, 2009). Interestingly, the work of Price and Monaghan (2005) was based on exploring various divergence cleaning methods used in grid-based codes for SPH. The authors concluded that this works in most cases, but in difficult cases, such as supersonic turbulent flows, this can lead to spurious effects, such as the violation of the entropy condition or wrong shock relations. More worrysome, these authors noticed that divergence cleaning can lead to an increase of the local magnetic energy, a price to pay to redistribute the truncation errors in the divergence. This results in *spurious dynamo effects*. Recently, however, Tricco and Price (2012) revisited the Dedner's scheme for SPH and found a formulation that guarantees that divergence cleaning leads to a decrease of the magnetic energy and an increase of the entropy, in the spirit of Derigs et al. (2017) for grid-based codes.

In light of these rather complex developments of divergence cleaning methods, the constrained transport (CT) approach we have introduced already seems quite appealing. Note however that this approach requires to have well defined cell-interfaces, which is not necessarily the case for SPH or the recently developed moving-mesh AREPO code (Springel, 2010). The CT scheme, introduced for astrophysical fluid flows by Evans and Hawley (1988) and used in the ZEUS-2D code (Stone et al., 1992b), features the nice property that the divergence of the magnetic field, defined in integral form as the net magnetic flux across the 6 faces of each cell, will always remain constant, So if it is initially zero, it will remain equal to zero within numerical round-off errors. This however requires to define the electric field on the cell edges, and this is the main difficulty of this approach (see **Figure 1**). Indeed, in the Godunov methodology, fluxes, defined at cell faces, are computed as the solution to the Riemann problem of the two neighboring cells meeting at their common cell interface. For the electric field, defined at cell edges, 4 neighboring cells meet and in order to properly upwind the electric field, we need to solve a *two-dimensional Riemann problem*, a rather daunting task (see Teyssier et al., 2006, for a discussion). Several solutions have been found to design 2D MHD Riemann solvers (Londrillo and del Zanna, 2004; Balsara et al., 2014), and this has been the main characteristic of several simulations codes with proper upwinding of both fluxes and electric fields, using the CT scheme within the Godunov

[1]Stagnation points are regions where the flow is brought to rest in the frame of the system under study. More generally, even if the velocity does not vanish, stagnation points are regions in the flow where the streamlines are converging and the flow becomes compressive.

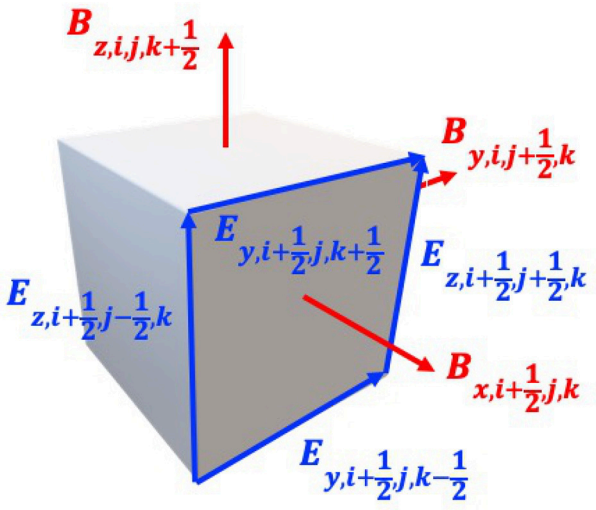

FIGURE 1 | Schematic showing the geometry of a Cartesian cell in the Constrained Transport approach. The finite volume cell is shown as a gray cube. It is labeled i, j, k. The magnetic field components are defined perpendicular to the faces of the cube. The are shown in red, only in the rightermost face in all three directions. The electric field components are defined on the cell edges. They are shown in blue and only in one face for sake of simplicity.

methodology (Londrillo and del Zanna, 2004; Fromang et al., 2006; Stone et al., 2008; Li et al., 2012; Mocz et al., 2014a).

2.4. Minimizing Numerical Errors: Higher Order vs. Mesh Refinement

When performing self-gravitating magnetized fluid simulations, it is of primary importance to quantify and understand numerical errors. These errors are often called *truncation errors* because they arise as leading order terms in the Taylor expansion of the adopted discrete numerical method. Usually, this Taylor expansion leads to the so-called *modified equation*, which encodes how the original ideal MHD equations have been transformed into a new set of equations with additional terms coming from the truncation errors. For first-order schemes, these terms are identical to a diffusion process, and are therefore called *numerical viscosity* or *numerical diffusivity*. In SPH, quite often, these terms are added explicitly to the equations as *artificial viscosity* and *artificial diffusivity*, while for grid-based Godunov solvers, these terms are only implicitly present, through this Taylor expansion of the discrete scheme. In both cases, however, these diffusion processes control how shock heating and magnetic reconnection proceed in the solution. They play a fundamental role in preserving the entropy condition, and in regulating the flow close to the grid scale. Unfortunately, many complex MHD processes, such as the small scale dynamo (Brandenburg and Subramanian, 2005) or the magneto-rotational instability (Balbus and Hawley, 1991) depend crucially on the so-called Prandtl number (Fromang et al., 2007; Federrath et al., 2014a), which is the ratio of the real magnetic diffusivity to the viscosity. In most case, this ratio is always close to 1 if one uses the numerical Prandtl number (Fromang et al., 2007; Federrath et al., 2011b), while in nature, it can vary widely. It is therefore crucial to adopt in some cases explicit viscosity and diffusivity coefficients and model the flow including these non-ideal processes (Fromang et al., 2007; Federrath, 2016).

As explained in the next section, in order to model these non-ideal effects, it is crucial to control and minimize the numerical diffusion as much as possible. There are two possible strategies to achieve this: refine the grid or increase the order of accuracy of the method. The first approach leads to the so-called Adaptive Mesh Refinement method, a very popular and successful technique in the context of star and galaxy formation. Popular AMR codes are available to the star formation community, such as RAMSES (Teyssier, 2002; Fromang et al., 2006), ORION (Klein, 1999; Krumholz et al., 2007b), ENZO (Bryan et al., 2014), or FLASH (Fryxell et al., 2000). Other codes, that used to be only unigrid, now propose an adapted grid or an adaptive grid extension, such as PLUTO (Mignone et al., 2007) and ATHENA (Stone et al., 2008). In all these codes, cells are adaptively refined according to various refinement criteria. In the context of star formation, the most popular approach is to always resolve the local Jeans length with 4 cells or more, the so-called Truelove criterion (Truelove et al., 1997)

$$\text{If } \lambda_J = \frac{c_s}{\sqrt{4\pi G\rho}} < 4\Delta x_\ell \quad \text{then refine to level } \ell + 1. \tag{20}$$

This corresponds to a level-dependent density threshold that triggers new refinements. SPH methods are Lagrangian in nature, so they cannot refine as much as grid-based codes. Usually, much more SPH particles are needed in the initial conditions to reach a certain target Jeans mass, corresponding to the maximum resolution level of the corresponding AMR simulation. Particle splitting is an interesting alternative to classical SPH but is still under development (Kitsionas and Whitworth, 2002; Chiaki and Yoshida, 2015), the difficulty being to handle sharp transitions in particle mass and its interaction with the smoothing kernel. Note that if similar resolution requirements are met, AMR and SPH methods largely agree on the quantitative predictions on how the collapse proceeds (Commerçon et al., 2008). For magnetized flows, the Jeans length-based refinement strategy has to be more conservative, of the order of 30 cells per Jeans length, in order to capture properly the magnetic field amplification in collapsing cores (Sur et al., 2010; Federrath et al., 2011c; Turk et al., 2012).

A difficulty arises when one uses AMR for Constrained Transport. In this case, it is mandatory to be able to interpolate the magnetic field from the coarser level to the finer level and still satisfy the divergence-free condition. For this, divergence preserving interpolation schemes have been developed (Balsara, 2001; Tóth and Roe, 2002) and play an important role in the viability of the CT approach in the context of AMR.

To reduce truncation errors, the other option is to use higher order schemes. The solution inside each cell is not piecewise constant as in the traditional first-order Godunov method, but it is reconstructed using high-order polynomials of degree p as

$$\rho(x) = \sum_{i=0,p} \alpha_i \psi_i(x). \tag{21}$$

The $\psi_i(x)$ are usually an orthonormal basis of polynomials of degree at most p. The coefficients α_i are computed using two different philosophies. The first option, the WENO approach computes the coefficients α_i at each time step using neighboring cells. The higher the polynomial degree, the more neighbors must be included in the stencil of the method (Jiang and Wu, 1999; Boscheri and Dumbser, 2014). The second option, the Discontinuous Galerkin (DG) approach, considers that the α_i are new variables, defined for each MHD variables, and updated using a projection of the ideal MHD equation onto the polynomial basis (Li and Xu, 2012; Mocz et al., 2014b; Klingenberg et al., 2017; Guillet et al., 2018). In the WENO case, one needs to access neighboring but possibly distant cells to compute the α_i, while in the DG case, one needs to store permanently the α_i and solve for their evolution at each time step. Note that other high-order methods are also being developed that do not strictly correspond to neither WENO nor DG (Felker and Stone, 2018).

In the context of high-order methods, the divergence free condition is particularly challenging. One can either implement high-order version of one of the above mentioned divergence cleaning techniques (Derigs et al., 2016), or one can try to preserve the divergence-free constraint within the method. The second approach could be seen as a generalization of the CT scheme to higher order. The key ingredients are: 1- the use of a divergence-free polynomial basis for the magnetic field (Li and Shu, 2005; Guillet et al., 2018), 2- enforcing the continuity of the normal field across cells boundaries (Li and Xu, 2012). Although some very promising solutions have been found recently, this is still a very active field of research. Interestingly, the traditional CT scheme with face-centered magnetic field variables can be re-interpreted as a DG scheme where each magnetic field component is piecewise-linear and continuous in the normal direction and piecewise constant in the transverse direction, so that two cell-centered coefficients are required (instead of one) for each field component.

3. NON-IDEAL MHD: NUMERICAL TECHNIQUES

3.1. Equations and Basic Concepts

Star formation takes place in molecular clouds, which are made of a mixture of dust and gas, implying dust and gas collisions, and both constituents are far from being fully ionized. In the previous section, we presented the work done in the ideal MHD framework, which do not appear to be well suited to the ionization state in collapsing cores, in particular at the onset of disk formation. Recent works have emphasized the imperfect coupling of the dust and gas mixture with the magnetic fields at the transition between the envelop and the disk in collapsing cores (see the review by Wurster and Li, 2018 for the work done in the context of protostellar disk formation) and a lot of effort has been devoted over the past 10 years to include the so called non-ideal effects: the ambipolar diffusion, the Ohmic diffusion, and the Hall effect. The ambipolar diffusion is the common name to describe the interaction between neutrals and charged particles. It can be seen as a friction term, it enables the neutral field to respond to the magnetic forces, via collisions with charged particles. The Ohmic diffusion results from the collision of electrons with the neutrals. Last, the Hall effect is due to the drift between the positively and negatively charged species. As shown in Marchand et al. (2016) and Tsukamoto et al. (2015a), *all* these three terms can be dominant over the others at different scales within the envelop of collapsing dense cores. For a classical dust size distribution (Mathis et al., 1977), Marchand et al. (2016) find that amipolar diffusion and the Hall effect dominate at densities $< 10^{12}$ cm^{-3} and that Ohmic diffusion is the stronger resistive effect at higher densities.

The exact scale and density at which these resistive effects become dominant over the other dynamical processes depend on the chemistry, the ionization intensity and the dust grain size distribution (Zhao et al., 2016, 2018a; Zhao et al., 2018b; Dzyurkevich et al., 2017). Hennebelle et al. (2016) have shown that ambipolar diffusion regulates the flow dynamics over the other dynamical processes (induction, rotation and free-fall) at scale of a few 10s AU, which sets the initial size of protostellar disks. In addition, Masson et al. (2016) have shown that scales of a few 10s AU exhibit magnetic Reynolds numbers less than unity (see also Tomida et al., 2013; Tomida et al., 2015; Vaytet et al., 2018 for studies including the Ohmic diffusion). Recently, Koga et al. (2019) performed a similar analysis considering the Hall effect only and found coherent results as for ambipolar diffusion.

Before we describe the numerical implementation for the three aforementioned resistive effects, let us recall the main equations and define the necessary quantities. Ideally, the system should account for the different behavior of the neutrals, as well as negatively and positively charged particles. Among them the different constituents that participate to the ionization balance, we have neutral (molecule, atoms, dust grains), ions (molecular and atomic), electrons, and charged dust grains. The latter can be positively or negatively charged, and can hold multiple charges (Draine and Sutin, 1987). Most current works follow a one-fluid approximation to describe the evolution of this complex mixture, where the Ohm's law accounts for the non-ideal effects with some assumptions. In the following, we focus on the work done in the single and two-fluid approximations. We review briefly the work done toward a multi-fluid treatment of the charged and neutral particles in section 3.6.

In the low ionization limit, each kind of charged particle is scarce, so that the pressure terms, the gravity, and the inertia term can be neglected in their momentum evolution equation in comparison to the Lorentz force and the frictional force exerted by the neutrals. The generalized Ohm's law reads

$$\mathbf{E_{NIMHD}} = \mathbf{v}\times\mathbf{B} - \eta_\Omega \mathbf{J} - \frac{\eta_\mathrm{H}}{||\mathbf{B}||}\mathbf{J}\times\mathbf{B} + \frac{\eta_\mathrm{AD}}{||\mathbf{B}||^2}\mathbf{J}\times\mathbf{B}\times\mathbf{B}, \quad (22)$$

where $\mathbf{J} = \nabla\times\mathbf{B}$ is the current, η_Ω, η_H, and η_AD are the Ohmic, Hall, and ambipolar resistivities, respectively (in units of cm^2 s^{-1}), and $\mathbf{v}$ is the velocity of the neutrals. The notation $||\mathbf{B}||$ represents the norm of the magnetic field vector $\mathbf{B}$. The electric field is then replaced in Equation (7). It is worth noticing that all the resistive terms lead to parabolic partial differential equations

to discretise. We note that only the Ohmic term can lead to reconnection here. It can be rewritten as a Laplacian operator $\eta_\Omega \Delta \mathbf{J}$, whereas the two others cannot. The ambipolar diffusion and the Hall effect can be assimilated to drift velocities of the magnetic fields with respect to the neutral speed $\mathbf{v}$. The total energy equation has to be modified accordingly, to account for the heating resulting from the friction terms, i.e., the ambipolar diffusion and the Ohmic diffusion

$$\frac{\partial E_{\rm tot}}{\partial t} + \nabla \cdot \left((E_{\rm tot} + P_{\rm tot})\,\mathbf{v} - \frac{1}{4\pi}\mathbf{B}(\mathbf{B}\cdot\mathbf{v}) \right) = \rho \mathbf{g}\cdot\mathbf{v} + \eta_\Omega ||\mathbf{J}||^2 + \eta_{\rm AD} \frac{||\mathbf{J}\times\mathbf{B}||^2}{||\mathbf{B}||^2}. \tag{23}$$

We refer readers to Shu et al. (1987), Nakano et al. (2002), and Balbus (2009) for more details on the derivation of the generalized Ohm's law in the one-fluid approximation. In the context of star formation, where a huge dynamical range has to be considered, the estimate of the resistivities is challenging. It requires to know the ionization state of the gas and dust mixture. The coupled chemistry of gas and dust has to be considered, which involves a huge variety of physical processes: gas phase and gas-dust chemistry, cosmic ray ionization, UV radiation, (in-)elastic collisions, grain growth. This domain remains the subject of intense research works that we do not detail in this review. We refer readers to section 4.0.1 in the review by Wurster and Li (2018) for a scan of the works that tackle the resistivity calculations.

Ambipolar diffusion and Ohmic diffusion were the first to be considered in star formation applications. Indeed, these two terms do not introduce new MHD waves in the system (they do not change the spectral properties of the hyberpoblic system), so that they do not require heavy modifications of the MHD solver. The induction equation integration is most of the time splitted in two steps: first the ideal MHD and second the resistive terms. If an energy equation is considered, the heating terms due to resistive effect in Equation (23) are integrated as source terms in most numerical implementations.

3.2. Ohmic Diffusion

The Ohmic diffusion is perhaps the simplest resistive term to introduce because of its diffusive nature, similar to the introduction of artificial viscosity and artificial resistivity to prevent any numerical artifact due to numerical diffusion. Assuming a constant resistivity, the Ohmic term can be rewritten as a Laplacian (which preserves the solenoidal constraint), leading to the following stability condition

$$\Delta t_\Omega = \frac{\Delta x^2}{\eta_\Omega}. \tag{24}$$

It corresponds to the stability condition required in numerical schemes integrating parabolic equations such as the heat equation with an explicit scheme.

Numerous implementations for the Ohmic diffusion have been developed in the past 10 years, in all different kind of codes. Masson et al. (2012) present a fully explicit implementation in the AMR code RAMSES, where they update the emf to account for the resistive terms and then use the CT scheme as for ideal MHD. Because of the restrictive stability condition for the resistive term which can be smaller that the MHD one, some authors considered schemes that enable to relax the time step constraint. For SPH, Bonafede et al. (2011) implemented Ohmic diffusion with a constant resistivity in GADGET following the method used for artificial dissipation (e.g., Price and Monaghan, 2005; Dolag and Stasyszyn, 2009). Tomida et al. (2013) implemented an explicit scheme in a nested-grid code following the implementation of Matsumoto (2011) in the AMR code SFUMATO. They adopt the Super-Time-Stepping (STS) algorithm proposed by Alexiades et al. (1996) to accelerate the integration of the diffusion term and to relax the stringent explicit CFL condition. The STS consists in a discretisation as a classical explicit scheme, which does not require to satisfy the stability in every step but after a series of integration cycles which are made of $N_{\rm STS}$ sub-timesteps $\Delta t_{\rm STS}$ which are based on Chebyshev polynomials to guarantee the stability conditions over the super-timestep $\Delta t_{\rm tot} = \sum_1^{N_{\rm STS}} \Delta t_{\rm STS}$. We also note the work of Mignone et al. (2007) and O'Sullivan and Downes (2006) where Ohmic diffusion is also integrated using the STS technique. Similarly, Tsukamoto et al. (2013) proposes a SPH discretisation of Ohmic dissipation using STS. Wurster et al. (2016) and Price et al. (2017) (in the PHANTOM code) use similar implementations on different SPH codes. Last, Marinacci et al. (2018) propose two implementations in AREPO: one using Powell divergence cleaning and another using CT. Both implementations can be integrated using an explicit or implicit scheme. Almost all the implementations mentioned so far for the Ohm diffusion are combined with ambipolar diffusion (see below).

Apart from resistive MHD, the STS technique is becoming increasingly popular in the computational astrophysics community to accelerate parabolic timestepping advancements in the context of radiation hydrodynamics with the FLD (Commerçon et al., 2011) and anisotropic diffusion (Meyer et al., 2012; Vaidya et al., 2017).

3.3. Ambipolar Diffusion

Ambipolar diffusion is not as straightforward to include since the associated term in the induction equation can not be rewritten as a Laplacian (Brandenburg and Zweibel, 1994). For the diffuse ISM, the drift between ions and neutrals is the effect of the ambipolar diffusion, that can be written as a friction force

$$\mathbf{F_{in}} = \rho_{\mathbf{i}} \rho_{\mathbf{n}} \gamma_{\rm AD} (\mathbf{v} - \mathbf{v_i}), \tag{25}$$

where ρ_i (resp. $\mathbf{v_i}$) and ρ_n ($\mathbf{v}$) are the mass density (resp. velocity) of ions and neutrals, and $\gamma_{\rm AD}$ is the collisional coupling constant, with $\gamma_{\rm AD} \sim 3 \times 10^{13}$ cm^3 s^{-1} g^{-1} in ISM mixture (Draine et al., 1983). In the one-fluid and strong coupling limit, the inertia of ions is neglected, as well as the pressure and gravitational forces (the ionization degree is very low). As a consequence, the Lorentz force equals the drag force so that the ion drift velocity is

$$\mathbf{v_d} \equiv \mathbf{v_i} - \mathbf{v} = \frac{\mathbf{1}}{\rho_{\mathbf{i}} \rho_{\mathbf{n}} \gamma_{\rm AD}} (\nabla \times \mathbf{B}) \times \mathbf{B}. \tag{26}$$

The induction equation thus reads

$$\frac{\partial \mathbf{B}}{\partial t} = \nabla \times [\mathbf{v_i} \times \mathbf{B}] = \nabla \times \left[\mathbf{v} \times \mathbf{B} + \frac{\mathbf{1}}{\rho_\mathbf{i} \rho_\mathbf{n} \gamma_{\rm AD}} (\nabla \times \mathbf{B}) \times \mathbf{B} \times \mathbf{B} \right]. \quad (27)$$

From Equation (22), we have $\eta_{\rm AD} = ||\mathbf{B}||^2/\rho_\mathbf{i}\rho_\mathbf{n}\gamma_{\rm AD}$. In the dense ISM, the heavy charged particles are ions and charged dust grains, and the expression of the resistivity is more complex (Marchand et al., 2016). In the two-fluid approximation, the ion inertia is not neglected and the system of equation accounts for both the ions and the neutrals momenta equation.

The first implementation of ambipolar diffusion in a grid code was presented in Black and Scott (1982) using a two-fluid approximation. They integrated the induction equation using the ion velocity and treated the collision between neutrals and ions as a friction force in the momenta equations. Mac Low et al. (1995) present a first 3D implementation of one-fluid ambipolar diffusion in the ZEUS code using a fully explicit scheme as well as CT. They propose to subcycle the magnetic fields evolution in the case when ambipolar diffusion timestep is much shorter than the dynamical one. The first SPH implementation can be found in Hosking and Whitworth (2004), where they used a two-fluid approximation, but their scheme did not preserve the solenoidal constraint. Duffin and Pudritz (2008) present a one-fluid implementation in the FLASH code using Powell's method (Powell et al., 1999). Masson et al. (2012) also implemented a one-fluid scheme for ambipolar diffusion in RAMSES with the same philosophy as for the Ohmic diffusion. A similar implementation using CT, operator splitting, and STS in the ATHENA code can be found in Bai and Stone (2011) and Chen and Ostriker (2014). Last, Wurster et al. (2014) propose a one-fluid implementation for SPH codes, which they implemented with success in PHANTOM.

Other one-fluid implementations in the strong coupling approximation can be found in Padoan et al. (2000) in a 3D explicit, finite difference grid code, Choi et al. (2009) in the MHD TVD code using a flux-interpolated CT scheme (Ryu et al., 1998; Balsara and Spicer, 1999), Christie et al. (2017) in the ENZO's Dedner MHD solver. Oishi and Mac Low (2006) and Li et al. (2006) present two simultaneous but independent implementations in the ZEUS code of a two-fluid solver in the heavy ion approximation.

For star formation applications, most of these methods are usually second-order accurate and at best second-order accurate in time (with a few exceptions though e.g., Meyer et al., 2014). Clearly, further work needs to be done to improve the accuracy of resistive MHD solvers. Alongside, multi-fluid approaches are also needed to account for more detailed physics (see section 3.6).

3.4. Hall Effect

The last resistive effect that has been implemented in star formation models is becoming increasingly popular. The Hall effect originates from the drift between ions and electrons, or, more generally the positively and negatively charged particles. The derivation of the generalized Ohm law (22) is not as straightforward as in the case of ambipolar diffusion only. We shall consider the momentum equations of ions and electrons, accounting for the Lorentz force as well as collisions between ions, electrons, and neutrals. If we restrict the resistive effects to the Hall effect only, the induction equation reads

$$\frac{\partial \mathbf{B}}{\partial t} = \nabla \times \left[\mathbf{v} \times \mathbf{B} - \frac{\eta_{\rm H}}{||\mathbf{B}||} \mathbf{J} \times \mathbf{B} \right] = \nabla \times \left[(\mathbf{v} + \mathbf{v}_{\rm H}) \times \mathbf{B} \right], \quad (28)$$

where we introduce the "Hall speed" $\mathbf{v}_{\rm H} = \frac{\eta_{\rm H}}{||\mathbf{B}||}\mathbf{J}$. Contrary to the two previous resistive terms, the Hall effect introduces new waves in the MHD systems: the *whistler* waves. The dispersion relation for whistler waves reads (Balbus and Terquem, 2001)

$$\omega = \pm \frac{\eta_{\rm H} k^2}{2} + \sqrt{\left(\frac{\eta_{\rm H} k^2}{2} \right)^2 + k^2 c_{\rm A}^2}. \quad (29)$$

The whistler waves are dispersive, the phase speed $c_{\rm w} = \omega/k$ depends on the wavenumber k and tends to infinity as the wavenumber tends to infinity. Since any discrete formulation cannot extend to infinity, a numerical solver cannot follow the whistler waves with very high frequencies. In practice, the whistler wave speed is chosen to be the one at the grid scale

$$c_{\rm w} = \left| \frac{\eta_{\rm H} \pi}{2\Delta x} \right| + \sqrt{\left(\frac{\eta_{\rm H} \pi}{2\Delta x} \right)^2 + c_{\rm A}^2}. \quad (30)$$

The time step is then constrained as

$$\Delta t \leq \frac{\Delta x}{c_{\rm w}} \approx \frac{\Delta x^2}{\eta_{\rm H}}. \quad (31)$$

The first way to implement the Hall effect is to use an operator split method, similarly to the Ohm and ambipolar diffusion. A pioneer implementation is presented in Sano and Stone (2002) in a second-order Godunov finite-difference code (Miyama et al., 1999), in the local shearing box framework. They use the CT method to update the induction equation with emf computed with the Hall term. The method has been implemented in 3D in ZEUS in Krasnopolsky et al. (2011). Falle (2003) presents an implicit scheme for multi-fluid MHD which alleviates the stringent time step conditions, where the time step goes to zero as the strength of the Hall effect increases. O'Sullivan and Downes (2006) designed a Hall Diffusion Scheme (HDS) in an explicit 3D code for multi-fluid MHD. They split the Hall diffusion in two parts, where the first part uses the STS time integration up to a critical value of the Hall resistivity (i.e., to satisfy the stability condition), and the second part, the HDS, diffuses the excess Hall resistivity with a different discretisation scheme. The balance between the ambipolar diffusion and the Hall resistivity determines the excess Hall resistivity. The HDS integrates the induction equation for the excess Hall using a dimensional splitting which is explicit for the first dimension, i.e., the x component B_x^{n+1} of the magnetic fields is given by B_y^n and B_z^n at time n, explicit-implicit for the second dimension, B_y^{n+1} is given by B_x^{n+1} and B_z^n, and finally implicit for third dimension, B_z^{n+1} is given by B_x^{n+1} and B_y^{n+1}. Both STS and HDS can be subcycled to reach the time step limit given by the hyperbolic system. The HDS

scheme has been also implemented in ATHENA by Bai (2014) using CT.

An alternative for finite volume methods is to include the Hall effect into the conservative integration scheme. Tóth et al. (2008) proposed a first implementation in the AMR code BATSRUS (Tóth et al., 2006). It uses block-adaptive grids with both explicit and implicit time discretisation, and various methods to control numerical errors in $\nabla \cdot \mathbf{B}$ (8-waves scheme with diffusion, projection scheme). They achieve spatial second-order convergence by using symmetric slope limiters (like *monotonized central*) instead of asymmetric limiters (like *minmod*). In addition, they show that the first-order Lax-Friedrich Riemann solver is inconsistent for the Hall MHD equations. This comes from the fact that the whistler wave speed is proportional to the grid spacing, which makes a one order loss in space in the truncation errors of the scheme. The same applies for MUSCL schemes and asymmetric slope limiters which are only first-order accurate. Lesur et al. (2014) built upon Tóth et al. (2008) a Hall MHD solver in PLUTO for protoplanetary disc evolution studies. They implement a HLL solver to estimate the flux and then update the magnetic fields using CT. When written in a conservative form, the Hall induction equation reads

$$\frac{\partial \mathbf{B}}{\partial t} - \nabla \cdot \left[\mathbf{vB} - \mathbf{Bv} - \frac{\eta_{\rm H}}{||\mathbf{B}||}(\mathbf{JB} - \mathbf{BJ}) \right] = 0. \qquad (32)$$

The current $\mathbf{J} = \nabla \times \mathbf{B}$ involves spatial derivatives of the magnetic fields, so that the flux depends on the conserved quantities, and on its derivative. This leads to a ill-defined Riemann problem. Lesur et al. (2014) solved this issue by assuming that $\mathbf{J}$ is an external parameter, which is computed at the cell interfaces using the predicted states. The left and right fluxes take this unique value as an input, with the predicted $\mathbf{B}$. The Godunov fluxes are then computed using a whistler-modified HLL solver, which accounts for the whistler waves speed (30) in the characteristics speeds.

Last, Marchand et al. (2018) recently extended the Lesur et al. (2014) implementation to the CT scheme of RAMSES, which uses 2D Riemann solver to integrate the induction equation. They designed a 2D whistler-modified HLL solver to estimate the emf on cell border, assuming a uniform current in the 2D Riemann solver, again computed from the predicted states.

In SPH codes, the Hall effect has been implemented and used with success for star formation applications in Wurster et al. (2016), Tsukamoto et al. (2017), and Price et al. (2017). The standard method is based on an operator splitting and either a full explicit or a STS scheme based on the implementation for ambipolar diffusion (Wurster et al., 2014).

To date, only (Krasnopolsky et al., 2011; Wurster et al., 2016; Tsukamoto et al., 2017; Marchand et al., 2018) applied their methods for protostellar collapse. While the SPH methods seem to lead to a relatively accurate conservation of the angular momentum, the grid-based methods using CT are suffering from severe non-conservation of the angular momentum. The origin of this non-conservation is unclear. Krasnopolsky et al. (2011) invoked Alfvén waves going out of the simulation volume, while Marchand et al. (2018) did not find evidence of this. Instead, they propose that the non-conservation takes place after the accretion shock formation. Shocks indeed generate strong gradients and thus large Hall velocities. Further investigation is clearly needed to cope with this fundamental issue.

3.5. Full Resistive Implementation

Currently, a handful of 3D codes benefit of a full implementation of the three resistive terms: PLUTO (Lesur et al., 2014), ATHENA (Bai, 2014), RAMSES (Masson et al., 2012; Marchand et al., 2018), the SPH code by Tsukamoto et al. (2017), PHANTOM (Price et al., 2017), ZeusTW (Li et al., 2011), and GIZMO (Hopkins, 2017). A very recent full implementation for solar physics can be found in González-Morales et al. (2018) in the MANCHA3D grid code. It combines STS for ambipolar and ohmic diffusion, and HDS for the Hall effect.

Currently, the ATHENA, PLUTO, RAMSES, and ZeusTW implementations rely on CT algorithms for the resistive MHD equations integration. All other works use divergence cleaning algorithms. Given the variety of the methods developed in the literature, a quantitative comparison (in standard tests as well as in star formation applications) of all these implementations would be welcome in the coming years.

Last but not least, it is not clear which non-ideal process dominates over the others. The physical conditions in star-forming regions are so wide that there is room for regions where all three effects dominate. In addition, every effect needs to be tested and quantified before any conclusions on the relative importance of each of these effects (see the review by Wurster and Li, 2018).

3.6. Multifluid Approach

Multifluid approaches are designed to describe multiphase or multifluid flows. In the context of star formation, different fluids or phases are at stack: neutrals, ions, electrons, and dust grains. A few attempts have been made to describe all or a part of these components using multi-fluid approach. In this section, we consider only the approaches which do account for N momentum equations, where N is the number of phases or fluids. For instance, a popular two-fluid framework considers ions and neutrals and describes the friction between these two fluids, i.e., the ambipolar diffusion. Toth (1994) presented a first 2D implementation of two-fluid ions and neutrals dynamics, which is based on a flux-corrected transport finite difference method. Inoue and Inutsuka (2008) propose an unconditionally stable numerical method to solve the coupling between two fluids ions-neutrals (frictional forces/heatings, ionization, and recombination, Draine, 1986) for an ISM gas subject to the thermal instability. They split time integration as follows: 1/ the ideal hydrodynamical part for neutrals, 2/ the ideal MHD part for ions. The first part is integrated using a second-order Godunov scheme. The ideal MHD part is solved in two steps, similarly to what is done for one-fluid ideal MHD solvers, i.e., Stone et al. (1992b): the magnetic pressure terms are solved using a second-order Godunov method, and the magnetic tension term and the induction equation are solved using the method of characteristics for Alfvèn waves with the CT algorithm. Tilley and Balsara (2008) present a semi-implicit method for two-fluid ion-neutral

ambipolar drift in the RIEMANN code (Balsara, 2001, 2004). Their scheme is second-order accurate in space and time and uses a mixed implicit-explicit formulation to deal with strong friction regimes. Pinto et al. (2008) consider a system composed of three fluids: positively-charged particles, negatively-charged particles, and neutrals. The charged particles include ions, electrons, as well as charged dust grains, depending on the main charge carrier. The self-consistent set of equations they designed remains to be implemented in 3D codes.

Last but not least, a complete multi-fluid approach should include dust grains dynamics on top of the neutrals, ions, and electrons. Falle (2003) presented a scheme for multi-fluid hydrodynamics in the limit of small mass densities of the charged particles, i.e., where the inertia of the charged particles are neglected. This is a similar to the heavy ion approximation but for neutrals, ions, electrons, and dust grains of various sizes. The HD equations are first integrated for the neutrals using a second-order Godunov scheme, and then the induction equation and the charged species velocities are updated using an implicit scheme. This scheme captures the three non-ideal effects and can deal with regime where the Hall effect dominates. We note that similar approaches were introduced in Ciolek and Roberge (2002) and O'Sullivan and Downes (2006).

The most complete work on multi-fluid designed for star formation was presented in Kunz and Mouschovias (2009). They considered a six-fluid set of equations (neutrals, electrons, molecular and atomic ions, positively charged, negatively charged, and neutral grains) and implemented it in a 2D version of the radiation-MHD ZEUS-MP code (Hayes et al., 2006). They modified the MHD solver to account for non-ideal effects (Ohmic dissipation and ambipolar diffusion). The abundances of the 6 species are calculated using a reduced chemical-equilibrium network. They applied their methods to protostellar collapse in Kunz and Mouschovias (2010). Unfortunately, the CPU cost of such a complete set of physics is prohibitive for 3D models, and no work has taken over since this first application.

3.7. What Is Next? Dust and Gas Mixture Dynamics

Currently, numerous studies report on the effect of non-ideal MHD in the star formation process. The wide majority of these works use the single-fluid approximation, assuming furthermore that the dust grains are perfectly coupled to the gas via collisions. Nevertheless, dust grains are observed to cover a wide range of sizes, from nanometer to micrometer in the ISM (Mathis et al., 1977) and even millimeter in protostellar disks environments (Chiang et al., 2012). Generally, it assumes that dust grains of different sizes coexist and follow a power-law dust distribution. Grains react to changes in the gas velocity via a drag force. For a given dust grain of mass m_g, the force is

$$\mathbf{F}_{\rm drag} = -\frac{m_g}{t_s}(\mathbf{v}_g - \mathbf{v}), \tag{33}$$

where $\mathbf{v}_g$ is the dust grain velocity, $\mathbf{v}$ the gas velocity, and t_s the stopping time, i.e., the characteristic decay timescale for the dust grain velocity relative to the gas. In star forming regions, the mean free path of the gas molecules is larger than the dust particles radius and the stopping time depends linearly on the dust grain size $t_s \sim s$ (Epstein, 1924). The Stokes number $\mathrm{St} \equiv t_s/t_{\rm dyn}$ characterizes the coupling of the dust grain relative to the gas, where well coupled dust grains follow $\mathrm{St} < 1$. $t_{\rm dyn}$ represents a characteristic dynamical time, e.g., the eddy turbulent crossing time for molecular clouds or the orbital time for prostostellar discs. The Stokes number thus depends on the dust grain size so that part of the dust grains of a given dust size distribution will be coupled to the gas and the other part will be decoupled.

Several implementations of dust and gas mixtures have been developed in the literature to deal with the various Stokes regime. For $\mathrm{St} > 1$, the bi-fluid formalism seems to be the most adapted (e.g., Bai and Stone, 2010; Laibe and Price, 2012; Meheut et al., 2012; Lorén-Aguilar and Bate, 2014; Booth et al., 2015). However, bi-fluid algorithms encounter sever limitations in the strong drag regime (small stopping time) (Laibe and Price, 2012), where prohibitive spatial and time discretisations may be required. In recent years, Laibe and Price (2014a) proposed a monofluid formalism for the dust and gas mixture which is well adapted to regimes with $\mathrm{St} \leq 1$. This monofluid formalism has been implemented with success in SPH and grid-based codes in the past 5 years (Laibe and Price, 2014b; Lebreuilly et al., 2019). Last, Price and Laibe (2015), Lin and Youdin (2017) present methods for simulating the dynamics of small grains with only one additional equation on the dust concentration on top of the Euler equations. These last methods have been recently implemented with success in PHANTOM (Price et al., 2017), as well as in PLUTO (Chen and Lin, 2018) and in RAMSES (Lebreuilly et al., 2019).

Recent works have emphasized the possible decoupling of micrometer dust grains in molecular clouds (Hopkins and Lee, 2016; Tricco et al., 2017) as well as of millimeter grains in collapsing dense cores (Bate and Lorén-Aguilar, 2017, see **Figure 2**). This decoupling is at the origin of a dynamical sorting which changes the dust size distribution. Other mechanisms may also affect the size distribution: coagulation, fragmentation, sublimation, etc. Further work should investigate the relative importance of each of these processes on the dust size distribution. In addition, the shape of the dust size distribution plays a critical role in the calculations of the resistivity as well as of the opacity. We can anticipate that coupled dust and gas dynamics will consider the evolution of the dust size distribution, coupled to non-ideal MHD and RHD algorithms. Last but not least, all current works on this field only account for the hydrodynamical (the pressure gradient) and gravitational forces. Adding the dynamics of charged dust grains is the natural next step.

4. RADIATIVE TRANSFER: NUMERICAL TECHNIQUES

4.1. A Poor's Man Approach: The Polytropic Equation of State

Radiative transfer plays a fundamental role in star formation and cannot be ignored, even for a review on magnetic fields. The

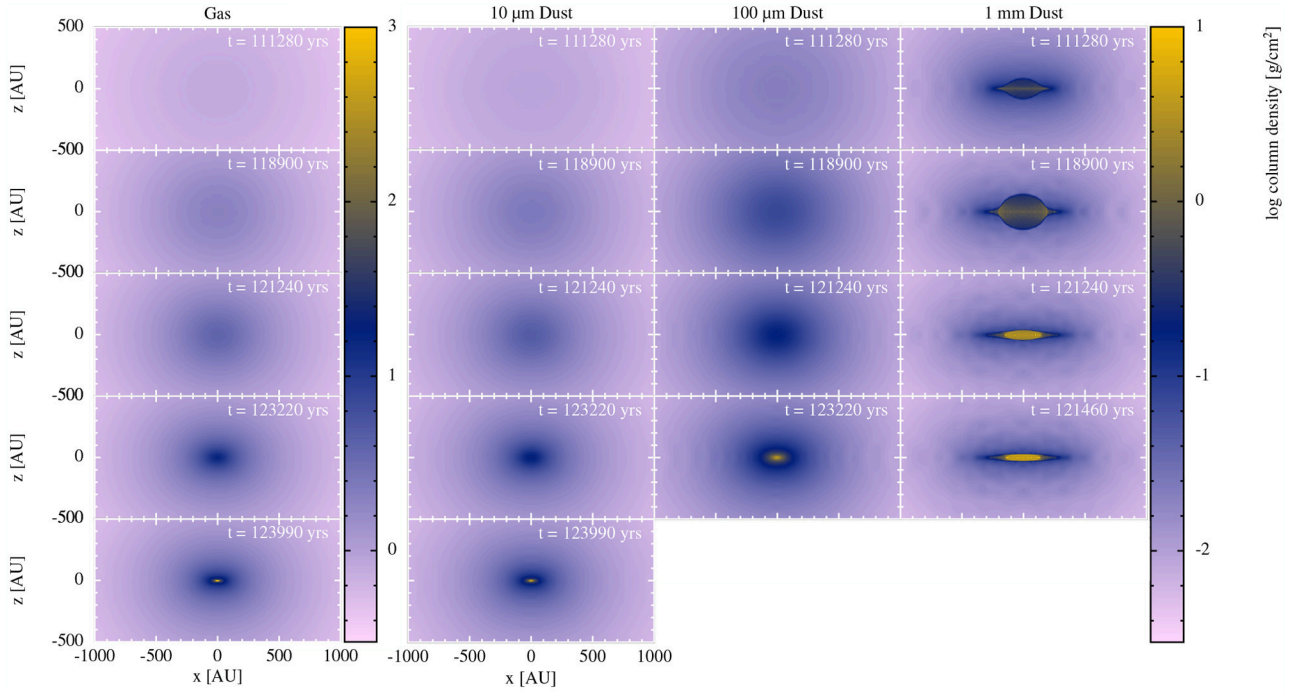

FIGURE 2 | SPH calculations of dust dynamics during the collapse of a 1 $M_\odot$ dense core. The left column shows the gas column density (edge-on view) and from left to right, the three other columns show the dust column density for dust grain sizes of 10 μm, 100 μm, and 1 mm. Large dust grains decouple from the gas and settle in the mid-plane faster into a large dusty disc with larger dust-to-gas ratio than in the envelop. Figure adapted from Bate and Lorén-Aguilar (2017) with permission from the authors.

importance of radiation fields is 2-fold. First, when the molecular cores collapse and reach a high enough density, the dust opacity becomes large enough to absorb the cooling radiation and the gas becomes optically thick. The traditional value for the dust opacity is

$$\kappa_{\rm dust} \simeq 0.1 \ {\rm cm}^2/{\rm g} \quad {\rm at} \quad T \simeq 10{\rm K}. \tag{34}$$

Requiring that the Jeans length of the gas becomes optically thick to infrared radiation leads to

$$\rho \kappa_{\rm dust} \lambda_{\rm J} > 1 \quad {\rm or} \quad \rho > \rho_{\rm crit} = \frac{G}{\pi \kappa_{\rm dust}^2 c_{\rm s}^2} \simeq 10^{-14} \ {\rm g/cm}^3. \tag{35}$$

Many MHD simulations use this critical density to define a polytropic equation of state of the form

$$T(\rho) = 10{\rm K} \left(1 + \left(\frac{\rho}{\rho_{\rm crit}} \right)^{2/3} \right), \tag{36}$$

to capture the transition from an optically thin, isothermal gas at low density to an optically thick, adiabatic gas at high density. Although this simplified approach is very useful for many already expensive simulations of collapse of turbulent clouds, this does not model properly the physics of radiative transfer (e.g., Commerçon et al., 2010). More importantly, once protostars have formed, higher energy radiation will emerge from the accretion shocks on the surface of the protostars, or from the main sequence stars after they ignited nuclear reactions. This high energy radiation in the optical or UV bands will then interact with the parent cloud, providing *radiation feedback* and influence the formation of the next generation of stars (Krumholz et al., 2007a; Myers et al., 2013). In conclusion, radiation plays a central role during the formation and the evolution of the first Larson core (see section 5), but later on acts as a self-regulating mechanism for star formation.

4.2. Ray Tracing and Long Characteristic Methods

The radiative transfer equation written in full generality using the radiation specific intensity $I_\nu(\mathbf{x}, \mathbf{n}, t)$

$$\frac{1}{c} \frac{\partial}{\partial t} I_\nu + \mathbf{n} \cdot \nabla I_\nu = j_\nu - \alpha_\nu I_\nu. \tag{37}$$

where j_ν is the emission coefficient and α_ν is the absorption coefficient. Note that the radiative transfer equation is written here in the laboratory frame. The absorption and emission coefficients are however defined in the comoving frame. Properly introducing the relativistic corrections to the radiative transfer equation and its various moments is a very important aspect of the problem we will only briefly touch upon in this review.

The most natural numerical technique to solve the radiative transfer equation is *ray-tracing*. The idea is to shoot a discrete set of light rays from a point source, solving the previous equation

along the path of the light ray using the curvilinear coordinate s defined as $\mathrm{d}s = c\mathrm{d}t$. The equation of radiative transfer can be written as a Lagrangian time derivative following the trajectory of the photons as

$$\frac{\mathrm{d}}{\mathrm{d}s} I_\nu = j_\nu - \alpha_\nu I_\nu. \tag{38}$$

The light ray is discretised along its path, matching the underlying gas distribution, whether it is a grid or a set of SPH particles. The difficulty is then to choose the appropriate number of rays, so that the angular distribution of the radiation field is properly sampled, but also so that enough light rays intersect the gas elements. In Abel and Wandelt (2002), an adaptive method was proposed, that splits or merges light rays adaptively, using the Healpix tessellation to sample the sphere. This method was first developed for the ENZO code (Wise and Abel, 2011) and used with success to describe photo-ionization regions at the Epoch of Reionization (Wise et al., 2012), as well as in turbulent molecular clouds (Shima et al., 2017). A similar scheme based on the Monte-Carlo approach has been developed for SPH in Altay et al. (2008) and Pawlik and Schaye (2008).

A similar approach is provided by the long characteristics method. This method can describe light rays emanating from a single point source like the ray-tracing method, but also diffuse radiation by adopting for each direction a set of parallel rays whose spacing matches the local grid resolution. This method has been implemented in the FLASH AMR code by Rijkhorst et al. (2006), with however an important addition we will discuss later. Diffuse radiation using long characteristics was included later by Buntemeyer et al. (2016) in the FLASH code, with an emphasis of describing both the optically thin and optically thick regimes. These methods exploit the particular property of the AMR implementations of FLASH and ENZO, namely large rectangular patches of various sizes and resolution. The long characteristic method has been developed for the graded octree AMR code RAMSES only recently by Frostholm et al. (2018).

4.3. Monte Carlo and Short Characteristic Methods

Although long characteristics offer the advantage of solving the exact attenuation along light rays, an especially accurate approach for point sources, they are tricky to parallelise because light rays propagate over multiple MPI domains. An alternative technique is the short characteristics method, for which light rays as short as the hydrodynamics cell size are considered. The radiation intensity from neighboring light rays is interpolated between neighboring cells, avoiding the use of long characteristics. Rijkhorst et al. (2006) use an hybrid long- and short-characteristics method in the FLASH code to overcome the difficulty to parallelise the long characteristics method. The short characteristic method also offers better scaling properties. The short characteristics method has also been used in the ATHENA code to solve the stationary radiative transfer equation by Davis et al. (2012) and in the C2-ray code for ionization problems (Mellema et al., 2006).

A third method which shares with the two previous ones the property of being accurate and able to capture complex radiation geometry is the Monte Carlo method. The Monte Carlo approach samples the radiation field with photon packets carrying information such as angle of propagation and frequency. This is as close as one can be from true photons propagating in the fluid and allows for complex scattering processes to be included in the models (Ercolano et al., 2003; Altay et al., 2008; Harries, 2011; Roth and Kasen, 2015). The method can be however quite expensive, as large particle numbers are required to avoid that the Poisson noise dominates the computed signal. In the diffusion limit, the mean free path becomes much smaller than the length scale of the system and the number of interactions becomes prohibitively large: It scales as the square of the optical depth (Nayakshin et al., 2009). It has also been mostly developed for stationary problems but many codes able to deal with non-stationary problems are now emerging (Nayakshin et al., 2009; Harries, 2011; Lomax and Whitworth, 2016).

4.4. Two Moments Methods

The common aspect in these three methods is that they can be quite expensive. This is probably not true for the short characteristics method, although the number of angular domains adopted plays a role in the final accuracy of the solution, and affects the cost. An alternative approach, called moment-based radiative transfer, can potentially solve this cost problem by integrating the radiative transfer equation over the angles. We obtain the radiation energy and the radiation momentum equation as

$$\frac{\partial}{\partial t} E_\nu + \nabla \cdot \mathbf{F}_\nu = 4\pi j_\nu - \alpha_\nu c E_\nu, \tag{39}$$

$$\frac{1}{c}\frac{\partial}{\partial t} \mathbf{F}_\nu + c\nabla \cdot \mathbb{P}_\nu = -\alpha_\nu \mathbf{F}_\nu, \tag{40}$$

where E_ν is the radiation energy, $\mathbf{F}_\nu$ is the radiation flux and $\mathbb{P} = \mathbb{D}E_\nu$ is the radiation pressure tensor and $\mathbb{D}$ is the Eddington tensor. For slowly varying spectral absorption and emission coefficients, for which one has

$$\nu \frac{\partial \alpha_\nu}{\partial \nu} \ll \alpha_\nu \quad \text{and} \quad \nu \frac{\partial j_\nu}{\partial \nu} \ll j_\nu, \tag{41}$$

one can write relativistic correction to first order in (v/c) as

$$\alpha_\nu(\mathbf{n}) = \alpha_\nu^0 - (\mathbf{n}\cdot\mathbf{v}/c)\alpha_\nu^0, \tag{42}$$

$$j_\nu(\mathbf{n}) = j_\nu^0 + 2(\mathbf{n}\cdot\mathbf{v}/c) j_\nu^0, \tag{43}$$

where superscript 0 refers to quantities measured in the comoving frame (see Mihalas and Klein, 1982; Mihalas and Mihalas, 1984; Krumholz et al., 2007b, for a detailed discussion). Injecting this in the radiative transfer equation and taking the moments over the angles leads to new terms accounting for the relativistic corrections

$$\frac{\partial}{\partial t} E_\nu + \nabla \cdot \mathbf{F}_\nu = 4\pi j_\nu^0 - \alpha_\nu^0 c E_\nu + \alpha_\nu^0 \mathbf{F}_\nu \cdot \frac{\mathbf{v}}{c}, \tag{44}$$

$$\frac{1}{c}\frac{\partial}{\partial t} \mathbf{F}_\nu + c\nabla \cdot \mathbb{P}_\nu = -\alpha_\nu^0 \mathbf{F}_\nu + \alpha_\nu^0 \mathbb{P}\,\mathbf{v} + 4\pi j_\nu^0 \frac{\mathbf{v}}{c}. \tag{45}$$

Since E_ν and $\mathbf{F}_\nu$ are still expressed in the laboratory frame but α^0_ν and j^0_ν are expressed in the comoving frame, these equations are often called *mixed frame* radiation moments equations. We can also Lorentz-transform the radiation moments from the laboratory frame to the comoving frame, which gives, to first order in (v/c)

$$E^0_\nu = E_\nu - \frac{2}{c}\mathbf{F}_\nu \cdot \frac{\mathbf{v}}{c}, \quad (46)$$

$$\mathbf{F}^0_\nu = \mathbf{F}_\nu - E_\nu \mathbf{v} - \mathbb{P}\,\mathbf{v}. \quad (47)$$

Injecting these relations *only in the right-hand side* of the moments equations and neglecting all (v/c) terms gives the simpler form

$$\frac{\partial}{\partial t}E_\nu + \nabla\cdot\mathbf{F}_\nu = \left(4\pi j^0_\nu - \alpha^0_\nu c E^0_\nu\right) - \alpha^0_\nu \mathbf{F}^0_\nu \cdot \frac{\mathbf{v}}{c}, \quad (48)$$

$$\frac{1}{c}\frac{\partial}{\partial t}\mathbf{F}_\nu + c\nabla\cdot\mathbb{P}_\nu = -\alpha^0_\nu \mathbf{F}^0_\nu + \left(4\pi j^0_\nu - \alpha^0_\nu c E^0_\nu\right)\frac{\mathbf{v}}{c}, \quad (49)$$

where all right-hand side terms are now expressed in the comoving frame. In practice, after the radiation transport step, encoded in the left-hand side, one then converts the laboratory frame radiation variables into the comoving frame and solve the thermo-chemistry encoded in the right-hand side in the comoving frame. Local thermodynamical equilibrium conditions can then be reached in the comoving frame, eventually reaching the diffusion limit (see below). At the end of the thermo-chemistry step, one finally converts back the radiation variables into the laboratory frame before entering the next transport step (see Rosdahl and Teyssier, 2015, for a detailed implementation).

These equations are quite handy because of their simplicity: We have no angular dependence anymore. There is a catch however, since everything depends on the Eddington tensor, for which we have no equation at this order of the moment's hierarchy. At this point, two different strategies have been explored in the star formation literature: (1) compute an accurate Eddington tensor by solving exactly the stationary radiative transfer equation using one of the methods presented above (short or long characteristics, ray-tracing or Monte Carlo), (2) compute an approximate form of the Eddington tensor based on a particular closure of the moment's hierarchy.

The first approach is often referred to a the Variable Eddington Tensor (VET) method. In Gnedin and Abel (2001), the authors developed a moment-based solver coupled to a cosmological hydrodynamics code, called Optically Thin Variable Eddington Tensor or OTVET. A similar technique has also been implemented for the SPH code GADGET (Petkova and Springel, 2011). The idea is to solve the stationary radiative transfer equation in the full domain assuming an optically thin medium, so that the problem boils down to a collection of $1/r^2$ sources combined together. This can be achieved efficiently using any gravity solver. Once the corresponding Eddington tensor is computed, the moments equations are solved using a finite difference scheme. In Jiang et al. (2012), on the other hand, the authors developed a moment-based solver for the ATHENA MHD code, using VET together with the short characteristic method of Davis et al. (2012) to compute the Eddington tensor. Obviously, this leads to significantly more accurate results in optically thicker environments. An intermediate solution has been implemented in the TreeCol code (Clark et al., 2012), for which a gravity tree code is used to collect column densities between particles.

The second approach relies on simple but approximate models for the Eddington tensor. The simplest one, called M0, assumes the Eddington tensor is isotropic, with

$$\text{M0 closure}: \quad \mathbb{D} = \frac{1}{3}\mathbb{I}, \quad (50)$$

as it is the case for example in the diffusion limit (see below). A slightly more elaborate model is called the M1 closure (Dubroca and Feugeas, 1999; Ripoll et al., 2001). It assumes that the radiation intensity can be fitted by a Lorentz-boosted Planckian distribution, in other words an ellipse in angular space. The parameters of this distribution are determined by matching the radiation energy and the radiation flux. This leads to

$$\text{M1 closure}: \quad \mathbb{D} = \frac{1-\chi}{2}\mathbb{I} + \frac{3\chi-1}{2}\mathbf{n}\otimes\mathbf{n}. \quad (51)$$

This closure captures the optically thick regime, but also optically thin conditions, in case there is one dominant source of radiation. Indeed, in this case, one gets the free-streaming regime for radiation with $\mathbb{D} \simeq \mathbf{n}\otimes\mathbf{n}$. The unit vector $\mathbf{n}$ and the parameter χ are determined using the radiation energy and the radiation flux as

$$\mathbf{n} = \frac{\mathbf{F}_\nu}{|\mathbf{F}_\nu|}, \quad \chi(f) = \frac{3+4f^2}{5+2\sqrt{4-3f^2}}, \quad f = \frac{|\mathbf{F}_\nu|}{cE_\nu} \quad (52)$$

A particularly interesting property of the M1 model is that it leads to a system of hyperbolic conservation laws, that can be numerically integrated using Godunov schemes. The M1 model has also some major caveats, such as radiation shocks, in case multiple strong sources are present, or incorrect radiation geometry, in case of sharp shadows. This model was introduced for the first time in astrophysics by González et al. (2007) in the HERACLES code. It was then adapted to cosmic reionization by Aubert and Teyssier (2008) in the ATON code, and ported to GPU into the RAMSES-CUDATON code (Aubert and Teyssier, 2010), used now routinely for simulations of the Epoch of Reionization (EoR) (e.g., Ocvirk et al., 2016). Later on, the M1 method has been ported to the AMR code RAMSES, leading to the design of the RAMSES-RT solver (Rosdahl et al., 2013; Rosdahl and Teyssier, 2015). The M1 method has also been ported to ATHENA by Skinner and Ostriker (2013) and recently to AREPO by Kannan et al. (2018), the latter based on a new higher-order implementation of the M1 closure.

4.5. Flux-Limited Diffusion Methods

A definitive advantage of moment-based radiative transfer methods is the possibility to model both optically thin and optically thick regimes. For optically thick conditions, the radiation field follows the diffusion limit of the radiative transfer

equation. In that limit, the radiation field *in the comoving frame* is quasi-isotropic, so that $\mathbb{D} \simeq \frac{1}{3}\mathbb{I}$ and the radiation flux can be approximated by

$$\mathbf{F}_\nu^0 \simeq -\frac{c}{3\alpha_\nu^0}\nabla E_\nu^0. \tag{53}$$

Since now the flux in the comoving frame is a direct function of the energy density in the comoving frame, we do not need the radiation flux equation anymore and we are left with only the radiation energy equation. The Lorentz transform can be written to leading order as

$$E_\nu \simeq E_\nu^0 \tag{54}$$

$$\mathbf{F}_\nu \simeq -\frac{c}{3\alpha_\nu^0}\nabla E_\nu^0 + \frac{4}{3}E_\nu^0\mathbf{v}. \tag{55}$$

Injecting these into the radiation energy equation leads to a fully covariant formulation in the diffusion limit

$$\frac{\partial}{\partial t}E_\nu^0 + \nabla\cdot\left(\frac{4}{3}E_\nu^0\mathbf{v}\right) - \nabla\cdot\left(\frac{c}{3\alpha_\nu^0}\nabla E_\nu^0\right) = \left(4\pi j_\nu^0 - \alpha_\nu^0 c E_\nu^0\right) + \frac{1}{3}\nabla E_\nu^0\cdot\mathbf{v}, \tag{56}$$

which can be written in the familiar form

$$\frac{\partial}{\partial t}E_\nu^0 + \nabla\cdot\left(E_\nu^0\mathbf{v}\right) + \frac{1}{3}E_\nu^0\nabla\cdot\mathbf{v} = \nabla\cdot\left(\frac{c}{3\alpha_\nu^0}\nabla E_\nu^0\right) + \left(4\pi j_\nu^0 - \alpha_\nu^0 c E_\nu^0\right). \tag{57}$$

This is the radiation energy equation in the diffusion limit using only comoving radiation variables. If one wants to extend this equation outside its validity range (high optical depth), then one can use Flux Limited Diffusion (FLD), for which the flux function is modified as

$$\mathbf{F}_\nu^0 \simeq -\frac{c\lambda(R)}{\alpha_\nu^0}\nabla E_\nu^0 \quad \text{and} \quad R = \frac{\left|\nabla E_\nu^0\right|}{\alpha_\nu^0 E_\nu^0}, \tag{58}$$

where $\lambda(R)$ is the flux limiter, a function that has to connect the diffusion limit with $\lambda \simeq 1/3$ for $R \simeq 0$ to the free-streaming regime where $\lambda \simeq 1/R$ for $R \to +\infty$. A possible form for the flux limiter has been proposed by Minerbo (1978) and reads

$$\lambda = \frac{2}{3+\sqrt{9+12R^2}} \quad \text{for} \quad 0 \le R \le \frac{3}{2}, \tag{59}$$

$$\lambda = \frac{1}{1+R+\sqrt{1+2R^2}} \quad \text{for} \quad \frac{3}{2} \le R \le +\infty. \tag{60}$$

while the Levermore (1984) flux limiter reads

$$\lambda = \frac{1}{R}\left(\coth R - \frac{1}{R}\right) \tag{61}$$

Historically, FLD has been the first method implemented in radiation hydrodynamics codes. Here again, the ZEUS 2D code was a precursor (Stone et al., 1992a). For AMR, the ORION code was developed specifically for FLD in collapsing star forming core by Krumholz et al. (2007b), using the mixed frame formulation outlined above or in Mihalas and Klein (1982). A version of the RAMSES code with FLD was developed later by Commerçon et al. (2011), with a particular emphasis on adaptive time stepping together with implicit time integration described in Commercon et al. (2014). Because of its simplicity, FLD has been used for many detailed studies of gravitational collapse with the effect of radiation included. The current frontier for FLD is probably the multigroup treatment of radiation, allowing for more accurate models of the full spectral energy distribution (Shestakov and Offner, 2008; Zhang et al., 2013; González et al., 2015). In the context of multifrequency radiative transfer, hybrid solutions have also been proposed, with ray-tracing techniques dedicated to the high-energy radiation field, and FLD for the infrared, dust-absorbed radiation field (Kuiper et al., 2010b; Klassen et al., 2014).

FLD has also been developed for SPH by Whitehouse and Bate (2004), Whitehouse et al. (2005), and Mayer et al. (2007), where most of the difference with the many grid-based versions lies in the radiation energy gradient that uses the SPH kernel. A simplified version based on a local estimate of the column density has also been proposed by Stamatellos et al. (2007) which avoids entirely the need for an implicit radiation solver. This method can be considered as an intermediate solution between the polytropic equation of state that we introduced at the beginning of this section and FLD. The main caveat here is the complete lack of any proper transport mechanism for radiation. In a similar spirit, Dale et al. (2007) also developed an approximate method for ionizing radiation, with Stromgren sphere iteratively grown around each star to locate photo-ionized, photo-heated gas.

5. SECOND COLLAPSE

From first principles, the ultimate goal of star formation is the formation of the protostar itself. The major difficulty sits in the huge dynamical range in physical and temporal scales that have to be described: protostars with radii of about 1 $R_\odot$ form within dense cores of sizes $\simeq$ 0.1 pc. So there are two ways to deal with protostars in star formation. The first one is to try to follow the collapse down to the stellar scales with the best numerical model accounting for the complex physical processes at stack combined with a very high numerical resolution at a cost of very short horizon of predictability. The second is the opposite: the physics and numerical resolutions are degraded, but the models are integrated over longer dynamical timescales to study the impact of protostellar feedback on the ISM dynamics. In the next three sections, we review the work that has been done using these two approaches, as well as attempts to account for protostellar evolution in large-scale models.

5.1. Historical Work and 1D Studies

Contemporary numerical star formation studies started in the late 60s with the outstanding pioneering work of Larson (1969) who first computed numerically the collapse of a dense core down to the formation of the protostar. He used a 1D spherically symmetric model, accounting for coupled gas dynamics and radiative transfer in a modified Eulerian scheme. Larson identified two distinct stages during the protostellar collapse, called the first and the second collapse. Each of these two stages are followed by the formation of a hydrostatic object,

commonly referred to as the first and second Larson cores in post (Larson, 1969) studies. Larson's work established an empirical evolutionary sequence as follows. Dense cores first collapse isothermally because dust thermal emission is very efficient at radiating away the gas compression energy (dust and gas are thermally coupled within dense cores, see for instance Galli et al., 2002). The first collapse stops at densities of the order of $\simeq 10^{-13}$ g cm^{-3} at which dust grains become opaque to their own radiation so that the gas begins to heat up quasi-adiabatically. This is the formation of the first Larson core. The first collapse lasts roughly a free-fall time. The first core accretes matter and its temperature increases up about 2000K where H_2 dissociation starts. This endothermic reaction enables the gas to behave as a fluid with an effective polytropic index smaller than the critical value 4/3 for collapse. The second collapse thus starts at typical densities of $\simeq 10^{-8}$ g cm^{-3} until stellar densities are reached within $\simeq$ 100 yr to form the second core, i.e., the protostar. The typical properties of first Larson cores at the start of the second collapse are a size $\simeq$ 10 AU, a mass $\simeq$ 0.01 $M_\odot$, and a lifetime $\simeq$ 1000 yr. We note that first Larson cores are predicted by theoretical and numerical studies, but there is no observational confirmation of such objects even though a few sources are considered as good candidates (Tsitali et al., 2013; Gerin et al., 2015; Maureira et al., 2017).

Since Larson's work numerous 1D calculations using spherical symmetry have been conducted. We note the work in the 80s by Stahler et al. (1980) and Winkler and Newman (1980) in which Larson predictions were confirmed to establish the current empirical evolution sequence of collapsing low-mass dense cores. This evolutionary picture is still currently the commonly admitted scenario for low-mass star formation. For massive star formation, recent work indicates that first cores may not have time to form because of the large accretion rates (Bhandare et al., 2018). Note that in the reminder of the section dedicated to second collapse, we mention only the work which is consistent with the Larson evolutionary picture, i.e., where the gas thermal and chemical budgets are taken into account, and we do not mention the work that has been done using an isothermal approximation.

Modern studies began with the calculations performed in Masunaga and Inutsuka (2000) who incorporated a more accurate radiation transport scheme as well as a realistic gas equation of state which accounts for H_2 dissociation. Masunaga and Inutsuka (2000) integrated their models throughout the Class 0 and Class I phases up to an age of 1.3×10^5 yr. Nowadays, 1D models are still used either as a first step toward describing more accurately the physics of the protostellar collapse, e.g., with multigroup radiative transfer (Vaytet et al., 2013, 2014) or with a view to provide quantitative predictions for the first and second Larson core properties (Vaytet and Haugbølle, 2017; Bhandare et al., 2018). These models are not pushed in time as far as the ones by Masunaga and Inutsuka (2000).

5.2. From 1D to 3D

Pioneered studies acknowledged up front that 1D spherical models were limited because the effect of rotation, turbulence, and magnetic fields cannot be taken into account. Three decades after Larson work, the first 3D numerical simulation able to describe the formation of the protostar was performed by Bate (1998) using SPH. The model accounted for initial rotation, but magnetic fields were neglected and radiative transfer was crudely mimicked by a piecewise polytropic equation of state. It is worth to notice at this point that grid-based codes took some time to reproduce (Bate, 1998) results for almost one decade. SPH is indeed naturally well-suited to collapse problems thanks to its Lagrangian nature while innovative techniques, such as AMR and nested grids, were not mature enough to capture the entire dynamical range and to cover eight orders of magnitude in physical length given the computer capabilities at that time. As mentioned in the section 2, ideal MHD was introduced early in protostellar collapse models using grid-based codes (e.g., Dorfi, 1982; Phillips and Monaghan, 1985). The first calculations of second collapse incorporating magnetic fields were thus done on a grid-based code by Tomisaka (2002) using a nested grid with cylindrical coordinates assuming axisymmetry (Tomisaka and Bregman, 1993). Tomisaka (2002) code solved the ideal MHD equations using a second-order "monotonic scheme" (van Leer, 1977; Winkler and Norman, 1986), a constrained transport scheme for the induction equation (Evans and Hawley, 1988), as well as an angular momentum preserving scheme. To capture the huge range in spatial scales, Tomisaka (2002) used up to 16 levels of refinement. He found that two different types of outflows were launched at the first and second cores scales. He suggested that the second core outflow corresponds to the optical jets observed in young stellar objects (YSOs), while the first core outflow corresponds to the molecular bipolar outflow. The first full 3D MHD models were presented in Machida et al. (2006) using nested grid with Cartesian coordinates and 21 levels of refinement. They compared the results obtained with resistive (Ohmic diffusion) and ideal MHD. They confirmed the results of Tomisaka (2002) even with non-ideal MHD included. After Machida et al. (2006) work, the numerical challenge of forming a protostar in 3D with MHD was faced, but the horizon of predictability remained very short since they had to stop their calculations 20 days after the protostar formation because of extremely small timesteps resulting from the high velocity of the jet propagating from the finest level. Banerjee and Pudritz (2006) also performed 3D collapse calculations down to stellar scales, using ideal MHD as well as molecular cooling, and they confirmed the results of Tomisaka (2002) and Machida et al. (2006).

All the multidimensional studies we mentioned so far were done assuming a piecewise polytropic equation of state to mimic the thermal behavior of the gas throughout the evolutionary sequence. Such barotropic equation of states are parameterized using the results of 1D spherical symmetry simulations previously mentioned, so that they cannot account for multidimensional effects such as the optical depth drop in the vertical direction that allows efficient cooling of the nascent protostellar disks and thus leads to incorrect results for the fragmentation (e.g., Boss et al., 2000; Commerçon et al., 2010; Tomida et al., 2010). The next level of complexity is to add a more accurate model for the thermal balance of the gas and dust mixture, i.e., to model radiative transfer (see section 4). The

addition of a more accurate model for radiation transport can be crudely resumed to an additional heating/cooling term in the gas internal energy equation due to matter/radiation interactions. For the models which are restricted to the first collapse and first core formation, i.e., for temperatures less than $\simeq$ 2000 K, the addition is conceptually straightforward for the gas evolution equations. An usual ideal gas equation of state can be used, with the only modification on the adiabatic index γ which varies with the temperature. At low temperature ($T \lesssim 150$ K), the H_2 molecule behaves like a monoatomic gas ($\gamma = 5/3$) because only the vibrational degrees of freedom are excited. At higher temperature, the rotational degrees start to be excited and the adiabatic index decreases to $\gamma = 7/5$. Accounting for this non-constant adiabatic index is important regarding the fragmentation properties (Commerçon et al., 2010) and the first core properties (Tomida et al., 2010; Lee and Hennebelle, 2018b). The driver of the second collapse is the endothermic dissociation of the H_2 molecule, which modifies considerably the gas equation of state. Currently, there are two ways to integrate non-ideal EOS in second collapse calculations. The first one is to compute on-the-fly the thermodynamic quantities from equilibrium chemical abundances and to use an ideal gas equation of state, including the effects of dissociation and ionization, to compute the gas pressure and the internal energy (Black and Bodenheimer, 1975). Most of the second-collapse including RHD are done with this approximation (Masunaga and Inutsuka, 2000; Whitehouse and Bate, 2006; Stamatellos et al., 2007; Forgan et al., 2009; Tomida et al., 2013; Bhandare et al., 2018). The second one consists in using tabulated EOS table coming from detailed studies to account for non-ideal effects (e.g., ionization by pressure, interaction between particles) which are important at high density/pressure (Saumon et al., 1995). Saumon et al. (1995) EOS is used in the work by Vaytet et al. (2013), Vaytet et al. (2014), Vaytet and Haugbølle (2017), and Vaytet et al. (2018), and also in the SPH public code PHANTOM (Price et al., 2017). We note that these developments imply that the dependency of the specific heat capacity as a function of the physical conditions has to be taken into account. Caution should thus be taken within the radiation solvers which are often integrated using implicit schemes. The most common and simple way to deal with it is to compute a heat capacity-like factor, $\tilde{C_V} \equiv e/T$ where e is the gas internal energy density, which is kept constant in the radiation solve. Readers can refer to Tomida et al. (2013) for a detailed implementation. Unfortunately, details on the numerical implementations are usually not reported in the literature. The first full 3D RHD calculations of the second collapse of an initial 1 $M_\odot$ dense core were performed by Whitehouse and Bate (2006) using the FLD approximation in a SPH code, followed by Stamatellos et al. (2007) who used a local radiative cooling approximation and SPH. Bate (2010) extended the work of Whitehouse and Bate (2006) beyond the formation of the stellar core for about 50 yr, using 3×10^6 equal-mass SPH particles to satisfy the Bate and Burkert (1997) mass resolution criterion throughout the entire collapse. Interestingly, there is to date no 3D RHD calculations of the second collapse, i.e., without magnetic field, performed with a grid-based code.

Last but not least, it has been demonstrated in Commerçon et al. (2010) that the interplay between magnetic fields and radiative transfer is of primary importance for the thermal budget of the collapsing gas and of the first and second core accretion shocks (Commerçon et al., 2011a; Vaytet et al., 2012; Vaytet et al., 2013, 2018). The infall velocity is indeed greatly modified in the presence of magnetic fields which tends to focus the collapsing gas on a smaller area compared to the case without magnetic fields (Commerçon et al., 2011b; Myers et al., 2013). The magnetic braking mechanism transports angular momentum from the inner parts of the collapsing cloud to the envelop. As a consequence, the infall velocity increases along with the incident kinetic energy, which then modifies the thermal budget through the accretion shocks. The next step in the increasing complexity is to perform full 3D RMHD calculations. The first SPH RMHD calculations of protostellar core formation were performed in Bate et al. (2014), extending their previous work to ideal MHD. Tomida et al. (2013) and Tomida et al. (2015) performed the first 3D full RMHD calculations using a grid-based code, extending the work of Machida et al. (2006) to account for radiative transfer with the FLD approximation, as well as the Ohmic dissipation and the ambipolar diffusion. They used a finite-volume nested-grid code with standard MUSCL predictor-corrector scheme to achieve second-order accuracy.More details on Tomida et al. (2015) implementation for non-ideal MHD are given in section 3. For the implicit radiation update, they used a linear system solver with a combination of the BiCGStab solver and the incomplete LU decomposition preconditionner. Tomida et al. (2013) used a nested-grid constructed to ensure that the Jeans length is always resolved by at least 16 cells, with typical spatial resolution at the maximum level of refinement of $\Delta x \simeq 6.6 \times 10^{-5}$ AU (23 levels). When this resolution condition cannot be satisfied, they stopped the calculations. This is particularly the case when discs form and grow with time to spread over different level of refinements. As a consequence, they cannot follow the second collapse in their model with ambipolar diffusion since a large disc is formed. More flexible refinement techniques, such as AMR or SPH are thus required to continue the calculations with a reasonable numerical resolution. Currently, the state-of-the-art includes 3D RMHD calculations with resistive effects, done with both SPH (Tsukamoto et al., 2015b; Wurster et al., 2018) and AMR (Vaytet et al., 2018). The typical resolution in SPH calculations currently achievable with limited CPU resources is of 3×10^6 equal-mass particles per $M_\odot$. In AMR, Vaytet et al. (2018) used a coarse grid of 64^3 with 21 additional levels of refinement, and a refinement criterion of 32 points per Jeans length. While the SPH calculations are able to integrate the three non-ideal effects (Wurster et al., 2018) down to stellar scales, there is no AMR work describing the Hall effect in second collapse calculations (Vaytet et al., 2018 accounts for the ambipolar diffusion and the Ohmic diffusion). The calculations by Wurster et al. (2018) were integrated 17 yr after the stellar core formation, while Vaytet et al. (2018) could only integrate for 24 days. Beside the major achievement which represents the formation of a protostar on a computer, we must admit that these kind of studies are not yet capable to give long term predictability. In addition, the CPU time required to integrate full 3D RMHD

models is relatively big. Clearly, second collapse study cannot be done on a frame covering a large parameter space. In addition, even at the first core scale, the integration timestep becomes so short in the adiabatic fragments that long time evolution calculations becomes prohibitive. In that view, the sink particles are a good alternative to reach a long horizon of predictability and to cover a wide parameter space.

6. SINK PARTICLES

Sink particles are Lagrangian particles, and can accrete matter as well as angular momentum in order to ensure mass and angular momentum conservation. Sink particles should not be confounded with sink cells which are usually introduced in grid-based codes which use a spherical grid to deal with the singularity in the center (e.g., Boss and Black, 1982; Kuiper et al., 2010a; Li et al., 2011). The differences between sink particles and sink cells are discussed in section 6.4. Sink particles are often erroneously referred as protostars or stars in the literature whereas the resolution at which they are introduced is generally much larger than the stellar scales, typically 1−10 AU for collapse calculations, and a few 100 AU for cluster formation and ISM evolution calculations. Multiple systems (small clusters, binaries), as well as systems made of a disk around a star can thus be encompassed within a single sink particle depending on the resolution.

6.1. Standard Implementations

Sink particles were introduced in star formation calculations by Bate et al. (1995) to enable long time integration to study the fragmentation of collapsing clouds. Sink particles were introduced to mimic the second collapse and the protostars at scales that could not be reached in numerical simulations. They are treated as accreting non-collisional point masses and enable one to follow the evolution through the main accretion phase, with a view to compare with observations of clusters in which most of the gas has been accreted. Their original implementation was done in a SPH code, with three main parts in the algorithm: (i) sink particle creation, (ii) sink particle accretion, (iii) boundary conditions for sink particles. A SPH gaseous particle is tagged for sink particle creation if its density exceeds a specific density threshold (defined by the user) and satisfied a number of tests. First, the smoothing length of the SPH particle that is a candidate for sink particle creation has to be less than half the accretion radius $r_{\rm acc}$ of the sink particle. This ensures that the sink particle is formed from at least $N_{\rm neigh}$. $r_{\rm acc}$ is defined before the calculations start and remains fixed. Its value is chosen by the user depending on the required level of resolution. It sets the smallest scale that can be resolved in the calculations. The knowledge of the flow within $r_{\rm acc}$ is lost and the gas is assumed to collapse beyond this scale to form protostars. Then, a series of tests is performed on the system composed of the particle and its neighbors to decide if it should create a sink particle. The tests ensure that the gas particles would continue to collapse if the sink particle was not created. First, the ratios α and β of the thermal energy and rotational energy to the gravitational energy must satisfy

$$\alpha \leq 1/2; \alpha + \beta \leq 1. \tag{62}$$

Additionally, the total energy must be negative, and finally, the system must be contracting ($\nabla \cdot \vec{v} < 0$). If all the tests are passed, a sink particle is formed from the system at the center of mass. Initially, the sink particle has thus a mass of $\sim N_{\rm neigh}$ times the standard SPH particle mass. Afterwards, sink particles interact only with the gas particles via gravity. The sink particle is allowed to accrete mass at each integration timestep if a gas particle enters $r_{\rm acc}$ and passes several criteria: the particle must be the most bound to the sink particle (and not to another more distant but more massive sink particle), and the particle must have a moderate specific angular momentum. When a gas particle is accreted, its mass and linear momentum are added to the sink particle, as well as the angular momentum which modifies the spin of the sink particle. The sink particle is moved to the center of mass of the sink and the accreted gas particle. Sink particles also contribute to the computation of the total gravitational potential in the same way as standard gaseous particles. Bate et al. (1995) pointed out that the introduction of sink particles in SPH calculations may affect the gas outside the accretion radius, in particular because there is a discontinuity in the number of particles across the accretion radius. They proposed different types of boundary conditions to account for missing neighbors. Note that the use of boundary conditions in modern sink particles implementation is not used anymore thanks to the improvements that have been made, in particular in the case of optically thick flows (e.g., Hubber et al., 2013).

Sink particles were introduced in Eulerian calculations for star formation purposes by Krumholz et al. (2004) in the AMR code ORION. They introduce a Jeans length criterion for sink creation, based on the resolution study of Truelove et al. (1997). A sink is created within a cell at the maximum level of refinement if the density ρ exceeds the maximum Jeans density $\rho_{\rm J}$ that can be resolved

$$\rho_{\rm J} < J^2 \frac{\pi c_{\rm s}^2}{G \Delta x_{\rm min}^2}, \tag{63}$$

where $J < 0.25$ is the Jeans length resolution criterion, $c_{\rm s}$ the gas sound speed, and $\Delta x_{\rm min}$ the minimum cell size. The initial mass of the sink is $m_{\rm sink} = (\rho - \rho_{\rm J}) \Delta x_{\rm min}^3$. In Krumholz et al. (2004), no additional checks are performed to validate the sink creation. Their algorithm is coupled to a sink merging scheme based on a friends-of-friends (FOF) algorithm to handle situations where a block of contiguous cells create sink particles in a single time step. The FOF is performed after each time step to group all the sink particles (old and new), with a linking length equal to $r_{\rm acc}$. All the groups of sink particles found by the FOF are then merged and replaced by a single particle at the center of mass of the group. All the merged sink particles quantities (mass, momentum, angular momentum) are also added conservatively to the new sink particle. Krumholz et al. (2004) sink accretion scheme was designed to handle situations where the flow onto the sink particle is subsonic (which is analogous to the case where boundary conditions have to be introduced in standard

SPH implementation). They set the accretion rate using an approximate formula from Bondi-Hoyle accretion which handles also the regime where the flow is supersonic. The accretion rate is estimated using average properties in the region within $r_{\rm acc}$. An important point in Krumholz et al. (2004) implementation is the description of the accretion zone. The mass accreted by the sink particle comes from all the cells in this accretion zone. Based on their experiments, Krumholz et al. (2004) use a value of $r_{\rm acc} = 4\Delta x$. In the case where the Bondi-Hoyle radius is smaller than the accretion zone, it is incorrect to estimate the accretion rate from all the cells in the entire accretion zone. Krumholz et al. (2004) thus use an accretion kernel where each cell within $r_{\rm acc}$ is assigned a weight from a Gaussian-like function. The kernel is used to compute the average quantities to determine the mass accretion rate. The mass to be accreted is redistributed within the accretion zone onto virtual cloud particles (each cell in the accretion zone is divided into 8^3 cloud particles). Additional checks can be then performed to avoid to accrete gas that has for instance too much angular momentum to be gravitationally bound. When a parcel of gas is accreted, it also transfers its linear and angular momentum to the sink. An absolute mass cap is also used to limit to 25% the amount of mass accreted from a unique cell in a single time step. After accretion, the position of the sink particle is changed in two steps according to its momentum after gas accretion and through gravity. First the momentum is updated to account for the gravitational interaction with the gas. The total force on a sink particle is computed by a direct summation over all the cells in the computational domain, except the ones in the accretion zone. This method remains practicable as long as the number of sink particles created remains limited. For the accretion zone, the interaction is computed between the sink and the cloud particles created during the accretion step. A Plummer law is used to soften the gravitational interaction at short distance, i.e., $F_{\rm grav} \sim 1/(r^2+\epsilon^2)$ where $\epsilon = 2\Delta x_{\rm min}$ is the softening length. Second, the acceleration due to particle-particle interaction is added to the sink particle momentum using a Bulirsch-Stoer algorithm with adaptive time step and error control. Note that the stability of the temporal discretisation scheme required that the sink particle velocity satisfies a CFL-like condition ($v_{\rm sink}\Delta t < C\Delta x$, with $C < 1$).

Sink particles algorithms have been complemented in the past 10 years to improve their versatility, in particular in the transition between the sub- and super-sonic regimes. All newer implementations have been built upon these two pioneering works.

6.2. Contemporary Implementations

In all current implementations, the sink creation and accretion are the most sensitive algorithms. Of course, the sink particles can be introduced in the initial conditions. Otherwise, they are created after the creation checks.

Each of the commonly used codes in star formation has its own implementation of sink particles. For the grid-based codes, we note the work of Wang et al. (2010) in the ENZO code, which is very similar to Krumholz et al. (2004) but with a different merging scheme which involves a maximum mass sink mass for merging. Federrath et al. (2010) presented an implementation in the AMR code FLASH, where the creation checks were similar to the ones by Bate et al. (1995) for SPH with two additional checks: the cell tagged for sink creation should be at the maximum level of refinement, and it should sit in a local gravitational potential minimum. They also account for magnetic energy in the energy budget done in the check algorithm. The checks are performed on a spherical region of radius $r_{\rm acc}$ around the cell candidate for sink creation. Their scheme for accretion is also different from the previous grid-based works. If a cell i within $r_{\rm acc}$ exceeds the density threshold $\rho_{\rm res}$ for sink creation, the mass increment $\Delta M = (\rho_i - \rho_{\rm res})\Delta x_i^3$ is considered for accretion onto the sink particle. The mass increment has to be gravitationally bound to the sink, and in the case of overlapping sink particles, it is accreted to the most gravitationally bound sink particle, the latter being moved to the center of mass of the particle-gas configuration before the accretion step. They also improve the treatment of the gas-sink gravitational interaction. Similarly to Krumholz et al. (2004), the sink-sink interaction is done by direct summation over all the sink particles. The gravitational acceleration of the sink due to the gas is estimated from the gravitational potential of the gas which is handled by the Poisson solver of FLASH to handle the gas-gas interaction. The acceleration is interpolated using a first-order cloud-in-cell method for each sink particle. Last, the acceleration of the gas due to the sink is done by a direct summation. Each sink particle contributes to the acceleration of each cell in the computational domain. The direct summations for the sink-sink and sink-gas interactions requires a gravitational softening. Federrath et al. (2010) use a cubic spline softening similar to what is used in SPH, which is less aggressive within the softening length than a simple Plummer profile. Federrath et al. (2011a) updated their first implementation to ensure exact momentum conservation using a direct summation between all cells and sink particles for the gas-sink interaction as well.

In addition, Federrath et al. (2010) performed a quantitative comparison between their implementation and the one by Bate et al. (1995) by comparing the results of two star formation calculations performed with FLASH and with a SPH code. They find a good quantitative agreement which was quite encouraging given the fundamental differences between SPH and AMR sink implementations.

Hubber et al. (2013) presented an improved algorithm for the sink particles in SPH, which can handle situations where sinks are introduced after the gas has become adiabatic. They propose a different combination of creation criteria which are based on the studies we just mentioned: (i) density threshold, (ii) no overlapping with another sink accretion volume, (iii) the gaseous particle flagged for sink creation sits in a minimum of gravitational potential (on a volume defined by its neighbors), (iv) the gaseous particle is outside the Hill sphere of fragments harboring another already formed sink.

Last, Bleuler and Teyssier (2014) presented an innovative sink creation scheme based on a clump finder algorithm used on-the-fly in the RAMSES code. The clump finder is performed in a first step to identify peaks and their associated regions. Second, the peaks are considered for sink creation. A virial theorem type analysis is performed on the clumps, accounting for surface

pressure as well as tidal forces. The virial check is passed if the second derivative of the moment of inertia in the center of mass frame is negative. Then a collapse check is performed, which corresponds to the contraction check of Krumholz et al. (2004) and Federrath et al. (2010), but adapted according to the virial analysis. Last, the final check is a proximity check. We also note that Bleuler and Teyssier (2014) offer also the possibility to use the alternative sink creation and accretion schemes reported in the literature. They provided an excellent review of the different creation checks, accretion, sink merging and trajectories schemes. In particular, they tested different schemes to perform sink accretion: Bondi-Hoyle accretion, flux accretion, and density threshold accretion. They show that all methods give good results for spherical Bondi accretion (i.e., when the flow is supersonic). In the subsonic regime, only the Bondi formula gives a correct accretion rate. They recommend to automatically adapt the accretion scheme depending on the surrounding flow properties.

A number of other sink particle implementations have been reported in the literature that we cannot detail in this review. We give in the following a non-exhaustive list, restricted to the field of star formation. In SPH, sink particles have been implemented in the codes GADGET (Jappsen et al., 2005), DRAGON (Goodwin et al., 2004), and SEREN (Hubber et al., 2011). For grid-based codes, sink particle are used in the uniform grid code ATHENA by Gong and Ostriker (2013), in RAMSES by Padoan and Nordlund (2011), and in the ORION2 code by Lee et al. (2014). Last, Greif et al. (2011) also proposed a sink particle algorithm within the AREPO moving-mesh code. Their implementation is very similar to the one used in SPH codes. We also note that sink particle merging is now widely used in most of the implementations.

Twenty years after their introduction, sink particles remain a sensible subject in the community. It is commonly accepted that an accreting sink particle should have a minimal impact on the collapsing gas around it. The easiest way to deal with it is to create the sink particle during the (quasi-) isothermal phases of the collapse (either the first or the second collapse), when the gas velocity is supersonic. The perturbation created by the sink particles on the gas dynamics cannot propagate since the CFL timestep is limited by the supersonic motions. An example of bad behaviors observed in protostellar collapse SPH calculations using sink particles introduced in the vicinity of the first cores can be found in appendix D of Commerçon et al. (2008). When a barotropic law is used to mimic the gas thermal budget, a simple method used to introduce sink particles in the vicinity of hydrostatic object can be found in Price and Bate (2008). They artificially change the gas equation of state to isothermal at an arbitrary density (e.g., 10^{-11} g cm^{-3}) and set the density threshold for sink creation to a value of more than two orders of magnitudes larger.

6.3. Sink Particles and Magnetic Fields

In the previous section, we did not discuss the sink particle algorithms in the presence of magnetic fields. We try to describe here some attempts done to provide a good description of MHD flows for sink creation and accretion. Sink particles can of course be introduced in MHD calculations, but the implementation is not as straightforward as in the hydrodynamical case. While it is relatively easy to accrete gas and momentum, magnetic flux accretion cannot bypass the solenoidal constraint $\nabla \cdot \vec{B} = 0$.

Price and Bate (2008) and Wang et al. (2010) performed star formation calculations in turbulent and magnetized clouds, but do not account for any contribution of the magnetic fields in their sink algorithms. Federrath et al. (2010) have introduced the magnetic energy in their negative total energy check for sink creation, but not in the accretion scheme. Lee et al. (2014) have extended the work of Krumholz et al. (2004) to deal with magnetized flows. For sink creation, they follow the work of Myers et al. (2013) who derived a magnetic Truelove criterion. They derive simple steady state accretion rates as a function of the plasma beta β and the Mach number $\mathcal{M}$.

In all implementations, gas is accreted by the sink particles but not magnetic flux. It stays the gas in the surrounding of the sink particles, and magnetic flux accumulates as collapse goes on. While at scales of a few 10-100s AU this flux accumulation is not problematic (Federrath and Klessen, 2012; Li et al., 2018), it eventually leads to a magnetic explosion and magnetic flux redistribution in the surrounding of the sink (Zhao et al., 2011) due to the development of an interchange instability (Spruit and Taam, 1990; Spruit et al., 1995; Li and McKee, 1996), which is also observed in high resolution models without sink particles and ideal MHD (Li et al., 2014; Masson et al., 2016). In addition, since density stays roughly constant while magnetic intensity increases in the sink accretion zone, the Alfvén speed increases significantly, leading to non-physical accretion rates, as well as short integration time steps. Lee et al. (2014) proposes to cap the accretion rate at a maximum value corresponding to a constant Alfvén speed after mass accretion. This trick tempers the accumulation of magnetic flux as well.

In the recent years, resistive MHD calculations have shown that all non-ideal effects leads to a decrease of the magnetic flux at the first core scale. Magnetic fields decouple from the gas and dust mixture dynamics. The magnetic flux does not accumulate at the first core border, but rather at a larger distance which corresponds to the radius at which non-ideal effects start to dominate (Hennebelle et al., 2016; Masson et al., 2016). Matter is accreted but leaves its associated magnetic flux outside the decoupling region. Adding sink particles in restive MHD calculations with resolution capable of resolving the decoupling region has not yet been investigated in detail (Machida et al., 2009; Matsumoto et al., 2017; Tomida et al., 2017), but one can foresee that introducing a sink within the decoupling region should prevent magnetic flux accumulation. It is expected that non-ideal MHD can alleviate the conditions of interchange instability, but is then necessary to resolve the decoupling scale, i.e., the disk. To date, the most detailed study of sink particles introduction in MHD calculations can be found in Machida et al. (2014).

6.4. Sink Particles vs. Sink Cells

A fundamental difference between sink cells and sink particles is that sink cells are fixed in position and have physical boundaries. There are pros and cons for the two methods, which we briefly summarize in the following.

First, the sink cell can be considered as a boundary in codes using a spherical grid. In collapse calculations, a sink cell is most often introduced as a passive boundary with zero gradients, or also called outflow (Yorke et al., 2002; Kuiper et al., 2010a; Li et al., 2011). The mass flux across the boundary is added to the central point mass of the sink cell and used to compute the gravitational acceleration. The sink cell enables one to make more detailed models for the magnetic field configuration at the boundary, as for instance in star-disk interaction studies (e.g., Mellon and Li, 2008; Takasao et al., 2018). In principle, this is a quite powerful numerical set-up to overstep the issue of time integration after the second core formation. The current state-of-the-art is not yet mature to design such numerical studies, but this should certainly be the purpose of future works.

On the other hand, a major inconvenience of sink cells resides in their fixed position in time, which forces the center of mass to be equal to the geometrical center of the disk. As a consequence, the development of non-axisymmetric azimuthal low wave-number modes may be artificially damped, which alters the development of eccentric gravitational instabilities (Adams et al., 1989; Shu et al., 1990). This effect can be particularly problematic in the case of young stellar objects with disks of mass comparable to the stellar mass, $M_{\rm disk}/M_{\rm star} > 1/3$ (Krumholz et al., 2007a; Kuiper et al., 2011; Sigalotti et al., 2018).

Last, the use of "outflow" boundary conditions for the mass accretion on the sink cell is very different from the algorithms we just presented for the sink particles. Machida et al. (2014) have shown that applying similar criteria for the sink accretion than the ones employed in studies with a sink cell (Li et al., 2011) may lead to very different results, i.e., no disk formation, compared to the same calculations done with a classical sink particle algorithm, i.e., formation of a disk.

7. SUB-GRID MODELS FOR SINK PARTICLES

Beyond the practical advantage of saving computational time, the sink particle has been shown to be very useful in works where (proto-)stellar feedback is considered. Similar to cosmological and galactic evolution studies, the sub-grid models can be associated to the sink particle evolution. We distinguish two types of sub-grid physics, depending on the feedback origin: radiative (luminosity, accretion shock, ionization), and dynamical (jets/outflow, winds). In any case, the source terms introduced by sub-grid physics are treated using operator splitting schemes.

7.1. Radiative Feedback

The first class of sub-grid models were designed to account for the radiative feedback of the nascent protostars. The radiative feedback term includes the accretion, the internal, and the ionization luminosities. When integrating over discrete timesteps, the luminosity is an energy or radiative flux input. Radiative feedback was introduced early in 2D models (e.g., Bodenheimer et al., 1990). They used a 2D axisymmetric hydrodynamical code (Rozyczka, 1985), which was primarily designed for stellar winds. Bodenheimer et al. (1990) used the gray FLD approximation for the radiation transport. They combined the evolution of their central zone, or sink cell, with a pre-main sequence evolution model based on Maclaurin spheroids in hydrostatic equilibrium. They computed the structure of the protostar according to the central (ρ, T) path tracks reported by Winkler and Newman (1980) from 1D spherical calculations. The protostar mass $M_\star$ and equatorial radius $R_\star$ were then used to compute the accretion luminosity $L_{\rm acc} = 0.5GM_\star\dot{M}/R_\star$, where $\dot{M}$ is the mass flux crossing the inner boundary. Bodenheimer et al. (1990) further assumed that the radiative energy input $L\Delta t$ was only due to the accretion luminosity and that all the infall kinetic energy was converted into radiation at the stellar core accretion shock. They found that most of the energy that went for heating in the envelope comes from this protostellar luminosity. Yorke and Bodenheimer (1999) and Yorke et al. (2002) used a more sophisticated protostellar evolution model which accounts for the intrinsic luminosity of the protostar $L_{\rm int}$. They realized that the central luminosity evolution sets the thermal budget within the envelop, but could not resolve the innermost regions of the star-disk system. They designed a protostellar accretion luminosity model which accounts for the luminosity coming from Keplerian motion of the disk being converted into heat and radiated away at the disk-core boundary layer following (Adams and Shu, 1986)

$$L_{\rm tot} = L_{\rm int} + \frac{3GM_\star\dot{M}}{4R_\star}, \tag{64}$$

where they assume that a fourth of the total potential energy of the accreted material is released into heat within the disk, the remaining being radiated away within the unresolved inner disk region and at the accretion shock. In addition, Yorke and Bodenheimer (1999) and Yorke et al. (2002) followed radiation transport using a frequency dependent ray-tracing algorithm (with 64 frequency bins). In particular, Yorke et al. (2002) demonstrated the importance to handle the protostellar irradiation using a frequency dependent irradiation scheme in the context of massive star formation. The flashlight effect, i.e., radiation escapes in the vertical direction and the radiative acceleration is reduced within the disk to allow accretion, is enhanced compared to a simple gray model. In addition, Krumholz et al. (2005) showed how protostellar outflows allow radiation to escape in the outflow cavities to allow a continued accretion onto the central massive stars. These results have been further confirmed by 3D dynamical simulations of Krumholz et al. (2007a), Kuiper et al. (2011, 2016), and Rosen et al. (2016).

Currently, most 3D numerical RHD calculations include stellar radiative feedback sub-grid models attached to sink particles/cells evolution. Most of the implementations account for both the internal and the accretion luminosities, with some modulation factors on the amount of potential energy radiated away and on the efficiency of the mass transfer for the sink accretion radius to the protostar. The simpler sub-grid models use a gray FLD model for the radiation transport where the protostellar luminosity is simply a source term in the radiative

energy equation (Krumholz et al., 2007a; Offner et al., 2009; Stamatellos et al., 2011; Fontani et al., 2018; Jones and Bate, 2018). Frequency dependent protostellar irradiation modules have been developed using ray-tracing to compute the radiation fields, combined with moment models for radiation hydrodynamics (Kuiper et al., 2010a; Wise and Abel, 2011; Klassen et al., 2014; Ramsey and Dullemond, 2015; Buntemeyer et al., 2016; Rosen et al., 2017). These frequency dependent modules have been used primarily in the context of massive star formation (Klassen et al., 2016; Rosen et al., 2016).

Last, we note the developments made to capture ionizing radiation feedback from massive stars: Dale et al. (2007) used a Strömgren volume method in SPH, Peters et al. (2010) ray tracing in the FLASH code, Kuiper and Hosokawa (2018) an hybrid ray-tracing and FLD irradiation module in the PLUTO code, Geen et al. (2015) the M1 moment method in the RAMSES code, and Harries (2015) Monte Carlo radiative transfer in the AMR code TORUS. These schemes are applied first in isolated collapse calculations (Kuiper and Hosokawa, 2018) and, mostly, in cluster formation studies (Dale and Bonnell, 2011; Peters et al., 2011; Dale et al., 2012; Geen et al., 2015, 2018; Ali et al., 2018).

7.2. Dynamical Feedback

The most advanced MHD collapse calculations have shown that outflows and jets naturally develop at different scales during the collapse (Tomisaka, 2002; Banerjee and Pudritz, 2006; Machida et al., 2006; Hennebelle and Fromang, 2008; Ciardi and Hennebelle, 2010; Commerçon et al., 2010; Tomida et al., 2010; Price et al., 2012). In addition, outflows and jets are commonly observed in YSO's (it is for instance a selection criterion for Class 0 sources, Andre et al., 1993) and they are considered as possible sources of turbulence driving in star forming clouds and participate in the regulation of the star formation rate (Matzner, 2007; Nakamura and Li, 2007; Krumholz, 2014; Federrath, 2015). Outflows and jets launching scales are nevertheless not captured in most studies because it requires a very high numerical resolution to reach sub-AU scales. Besides, studies neglecting magnetic fields cannot generate MHD winds driven centrifugally or by toroidal magnetic pressure. Consequently, very few numerical calculations have been able to launch self-consistently MHD outflows (e.g., Hennebelle et al., 2011). Sub-grid models have thus been developed to account for outflows/jets in numerical works with unresolved launching scales and missing physics, similarly to what has just been presented for the radiative feedback. The numerical implementation are based on analytical works dedicated to MHD wind launching (Blandford and Payne, 1982; Pelletier and Pudritz, 1992; Shu et al., 1994; Ferreira, 1997; Matzner and McKee, 1999).

The first works on sub-grid models have been reported in Li and Nakamura (2006) and Nakamura and Li (2007) who employed ideal MHD and self-gravity. They attached a protostellar outflow model on sink particles following (Matzner and McKee, 2000) because they were unable to describe the self-consistent launch of outflows with the crude resolution they use (128^3 for a ≈ 2 pc box). Each star injects in the ambient medium a momentum that is proportional to the stellar mass $M_\star$ with a two-component outflow model. The volume of injection is given by the sink accretion volume (which they refer to as "supercell"). A fraction η of the total outflow momentum is put in a conical collimated jet component to facilitate the transport of energy and momentum at large distances. The rest of the momentum is put into a spherical component around the protostar. The direction of the jet is given by the orientation of the magnetic field in the central cell, and they assume an opening angle of 30° about this direction.

Most of the implementation of outflows and jets have a similar construction, with flavors depending on the sink particle algorithm. Wang et al. (2010) implemented in the MHD ENZO code a simplified version for protostellar outflows where they only account for the collimated jet component. They adopt a continuous momentum injection $\Delta P = P_\star \Delta M$ where $P_\star$ is a proportionality constant which depends on the stellar mass $\sim M_\star^{1/2}$). If the momentum injection occurs in a cell with a too low density, they take 10% of ΔM out of the sink particle and redistribute it evenly between the injection cells in order to avoid too large outflow speeds (and too small integration timestep). Along the same line, Cunningham et al. (2011), Hansen et al. (2012) extended the work of Krumholz et al. (2005) and Krumholz et al. (2007a) and presented for the first time a combined sub-grid model which includes protostellar outflows (Matzner and McKee, 1999) and protostellar radiative heating (Offner et al., 2009), ignoring magnetic fields though. Their sub-grid model accounts for pre-main sequence evolution as in Offner et al. (2009) and the calculated protostellar radius is used in the outflow and radiative heating models. They parameterized their outflow model with dimensionless parameters which, for instance, sets the fraction of mass accreted by the protostar or launched in the outflow, and the ejection velocity as a function of the Kepler speed at the surface. Contrary to the case of radiative heating where energy is put within the accretion volume, they inject outflows at a distance comprised between $4\Delta x$ and $8\Delta x$ from the sink particle, and used angular dependency from Matzner and McKee (1999). We note that they not only inject momentum, but also mass and thermal energy. They set the wind temperature to 10^4 K, which is appropriate for an ionized wind. Using the same tool, Myers et al. (2014) added magnetic field in their simulations with ORION, but because of the low resolution they used (> 20 AU), they where not able to launch self-consistent outflows and used the sub-grid model we just mentioned. The outflows they produce may form strong shocks at very high temperature, higher than the dust sublimation temperature so that the dust opacity drops. Their radiative transfer scheme, primarily designed for dust thermal emission does not allow the gas to cool efficiently. They thus needed to add a line cooling function for the thermal budget of the gas.

Federrath et al. (2014b) implemented a sub-grid-scale outflow model upon the sink particles algorithm they implemented in FLASH (Federrath et al., 2010) for MHD collapse. Their model combines different features of the Li and Nakamura (2006), Nakamura and Li (2007), and Cunningham et al. (2011) implementations. They used a normalized velocity profile for momentum injection, which reproduces the two components outflow/jet with opening angles of 30° and 5°, respectively.

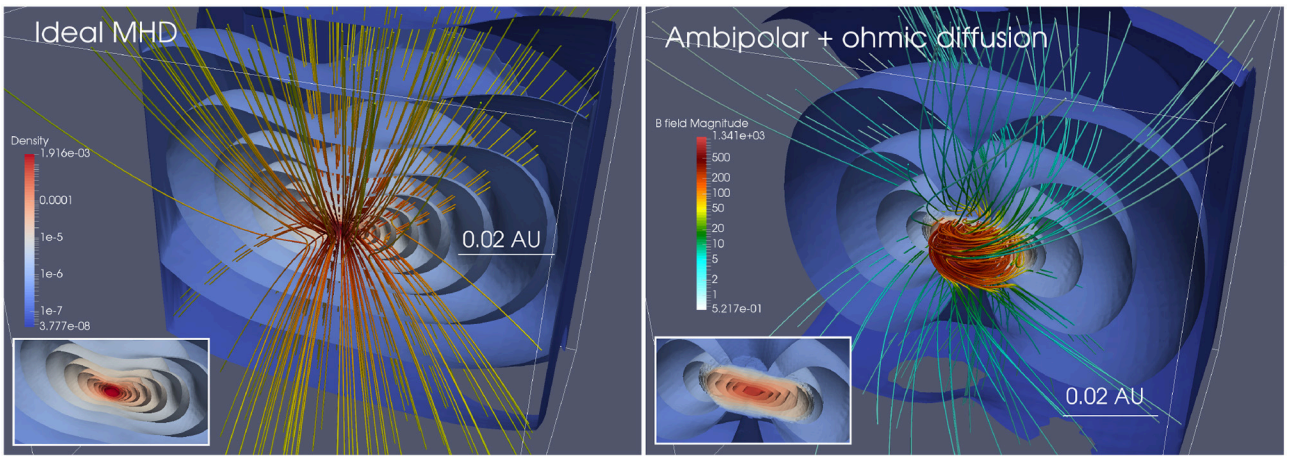

FIGURE 3 | Volume rendering from collapsing 1 $M_\odot$ dense cores at the protostellar core scale. The left panel shows the results of an ideal MHD 3D simulations, and the right panel the comparison with non-ideal MHD including ambipolar diffusion and Ohmic diffusion. The color lines indicate the 3D magnetic field lines, and the color coding the magnetic field amplitude. Figure reproduced from Vaytet et al. (2018) with permission of A&A.

They also improved the algorithm for the outflow orientation by recording the angular momentum transfer from the accreted gas to the sink particle. Their algorithm also conserves mass and momentum exactly in the sink accretion step. Murray et al. (2018) proposed a similar implementation in RAMSES. They follow (Offner et al., 2009; Cunningham et al., 2011; Federrath et al., 2014b; Myers et al., 2014) for the outflow injection as well as the protostellar evolution. Outflows are there injected within a conical volume about the spin axis of the sink particle in a radial extent comprised between 4 and 8 cells (at the highest refinement level) away from the sink particle. Federrath et al. (2014b) performed a parameter study on the number of cells for the radial outflow direction and found that convergence on the maximum outflow velocity requires 16 cells per outflow radius. Convergence on the mass, linear and angular momentum of the outflow is achieved though with 8 cells.

All these protostellar outflow sub-grid models are currently widely used in the community for astrophysical applications on the star formation rate/efficiency (e.g., Federrath, 2015; Kuiper et al., 2016; Offner and Chaban, 2017; Murray et al., 2018), stellar initial mass function (Krumholz et al., 2012), origin of turbulence driving (Nakamura and Li, 2011; Offner and Liu, 2018), as well as cluster and massive star formation (Wang et al., 2010; Cunningham et al., 2011; Kuiper et al., 2015; Li et al., 2018).

In the context of massive star formation, another class of outflows models are based on the luminosity and ionization. Sub-grids models of outflows generated by massive star luminosity have been developed (e.g., Krumholz et al., 2005; Peters et al., 2014), but the physical mechanisms driving this type of outflows are not yet well understood. No work in the context of massive star formation has accounted for the combined effects of magnetic fields and radiative force with a resolution sufficient to resolve the magnetic outflow launch. There is certainly a combination of magneto-centrifugal process and from radiative pressure, depending on the mass of the forming protostar.

7.3. Second Collapse and Pre-main Sequences

Ideally, the sub-grid models should be designed to reproduce the results of high resolution studies, which resolve the protostar scales. The short time integration after stellar core formation, dominated by the adiabatic evolution, does not allow to design sub-grid models for protostellar feedback from full 3D RMHD calculations with a high level of confidence. For these reason, all recent works mostly rely on the results of 1D spherical symmetry results to set their protostellar core evolution models. For instance, Kuiper and Yorke (2013) use the pre-main sequence evolution code STELLAR (Bodenheimer et al., 2007; Beuther et al., 2008) to determine the protostellar luminosity of the non-resolved protostars. Pelupessy et al. (2013) developed the open source Astrophysical Multi-purpose Software Environment (AMUSE), a component library of simulations involving different physical domains and scales. For instance, it enables one to couple hydrodynamical codes (GADGET, ATHENA, AMRVAC) with pre-main sequence and binary evolution codes such as MESA (Paxton et al., 2011). Recently, Wall et al. (2019) used AMUSE to perform a star cluster formation model that includes individual star formation from self-gravitating, magnetized gas, coupled to collisional stellar dynamics. It couples different tools: the AMR code FLASH (Fryxell et al., 2000), the N-body code ph4 (Capuzzo-Dolcetta et al., 2012), and the stellar evolution code SeBa (Portegies Zwart and Verbunt, 1996). We anticipate to see more works using this strategy of coupling tools and scales in the near future.

Recent work from Vaytet et al. (2018) have managed to resolve the second core formation with non-ideal MHD (Ohm diffusion and ambiploar diffusion) from collapse 1 $M_\odot$ dense core (see **Figure 3**). Interestingly, they show that the magnetic field lines topology is very different at the first and second core scales. Ambipolar diffusion is dominating at the first core scale. The magnetic fields direction is essentially vertical and the magnetic

fields and the gas evolution are decoupled. At the second core scale, the ionization rises due to high temperature and the system is back to ideal MHD, but with a high plasma beta $\beta = P_{\rm therm}/P_{\rm mag}$. The weak magnetic field is efficiently wrapped up by the gas rotation and the resulting fields direction is essentially toroidal. On the opposite, when ideal MHD is preserved all the way from the dense core to the stellar core, the magnetic fields lines are strongly pinched and the field remains poloidal at the second core scale. The energy balance at the first and second core accretion shocks is also different. While the accretion shock at the first core has been classified as a radiative supercritical shock, with *all* the incident kinetic energy radiated away (or often referred to as cold accretion), in 1D spherical core collapse studies (Commerçon et al., 2011a; Vaytet et al., 2012), recent 3D works have shown that the first core accretion experiences both cold and hot accretion at the same time at its surface, depending on the accretion flows morphology. On the surface of the stellar core, the accretion shock has been found to be subcritical (Vaytet et al., 2012; Vaytet et al., 2018; Tomida et al., 2013) with a significant part of the incident kinetic energy transferred to the protostars. Although these results have been investigated only for the very first stages of the protostar evolution (only 1 month in Vaytet et al., 2018), they indicate that it is not easy to derive general properties of small scales phenomena to design robust sub-grid models. In particular, Wurster et al. (2018) show that the magnetic fields evolution of the protostars they formed in their SPH models is largely affected by numerical diffusion. Last, the radiative efficiency of the stellar accretion shock has been shown to be a key process for the pre-main sequence evolution and sets the radius of the young protostars (Baraffe et al., 2012). We recall that the sub-grids models designed for the radiative and dynamical feedback take the protostellar radius as an input. The launching speed of the protostellar jets as well as the accretion luminosity depends on $R_\star^{-1}$.

8. DISCUSSION

We have described almost all the numerical methods that are required to model the star formation process within the turbulent interstellar medium. These discretised equations must now be solved for a given set of initial and boundary conditions, over some prescribed time. This defines the numerical set up and the overall simulation strategy. Obviously, given the wide range of spatial and temporal scales involved, one cannot realistically model an entire galaxy all the way down to the formation of brown dwarves and proto-planetary disks. Unfortunately, given the complexity of the star formation process, and the fact that large and small scales are strongly coupled, this is required by the physics of the problem. Indeed, supersonic turbulence is seeded on large scales, where kinetic energy is injected through shearing or colliding flows induced by galactic rotation, spiral waves and extra-galactic accretion flows. Moreover, turbulence and gas ejection can be triggered by stellar feedback processes occurring on very small scales, such as radiation driven flows, jets and ultimately supernovae explosions.

Modeling star formation is therefore fundamentally a multi-scale, multi-physics problem, and a very difficult one. Past or present day simulations always rely on some compromises. We can decompose them into several categories, corresponding roughly to the adopted box size and initial conditions. First, full galaxy simulations, where spiral waves and spiral shocks are used as the seed for turbulence. The box size must be of several tens of kiloparsecs to contain the entire rotating disk and possibly the galactic corona. The gas is compressed through the spiral shocks or various colliding flows. Thermal and gravitational instabilities fragment the gas into small molecular clouds. The spatial resolution never really drops below 0.1 or 1 pc in these simulations, so that stars cannot be modeled individually, at least for massive galaxies like the Milky Way (see **Figure 4** for illustration). Simulators rely on simplified, sub-grid star formation recipes based on stochastically spawning star cluster particles of the same mass, or on the sink particle technique where in this case sink particles represent a star cluster, rather than a single star. Bournaud et al. (2010) studied the properties the ISM substructure and turbulence in galaxy simulations with resolutions up to 0.8 pc and 5×10^3 $M_\odot$ with RAMSES. Renaud et al. (2013) and Kraljic et al. (2014) were able to capture the transition from turbulence-supported to self-gravitating gas with resolution up to 0.05 pc in simulations of Milky Way-like galaxies using RAMSES. Hopkins et al. (2012) presented SPH simulations dwarfs galaxies and Milky Way (MW) analogs to massive star-forming galactic discs with pc-scale resolution. Later, Hopkins et al. (2014) wrapped their implementation of feedback in the FIRE (Feedback In Realistic Environments) simulations suite, aiming, among others objectives, at resolving the formation of giant molecular clouds and the multi-phase interstellar medium (ISM). More recently, Hopkins et al. (2018) updated the FIRE implementation in the GIZMO code and performed sub-parsec resolution simulations of galactic discs. We also refer readers to the work of Dobbs et al. (2018) using SPH, Tasker (2011) using ENZO, and Smith et al. (2018) using AREPO. In addition, we note that for dwarf galaxies, it becomes possible to model much smaller scales so that at least massive stars can be modeled individually: Hu et al. (2016), Hu (2019) using SPH and a resolution of $1 - 5$ $M_\odot$ by gas particle, Emerick et al. (2018) and Emerick et al. (2019) using ENZO with a maximum resolution of 1.8 pc.

The second approach relies on simulating only a small portion of vertically stratified galactic disks. The box size is usually around 1 kilo-parsec, with periodic boundary conditions in the direction of the disk plane and outflow conditions in the direction perpendicular to the disk plane. The geometry is clearly heavily constrained by this elongated, vertical and stratified layer of gas but it captures most of the phenomenon at work locally in the disk. Using the shearing box technique, one can also add more realistic shearing conditions, so that turbulence can be maintained both by stellar feedback and a large scale galactic shearing flow (Kim et al., 2002). In this case, the resolution can drop significantly below 0.1 parsec, may be 0.01 parsec or even less for the highest resolution simulations. Unfortunately, it is still impossible to model individual stars at this resolution so that here again most papers are based on the sink particle techniques for representing star clusters. It is however almost possible to resolve massive molecular cores (and their associated sink particles) individually, so that individual supernovae and HII regions can be resolved. These simulations are probably the

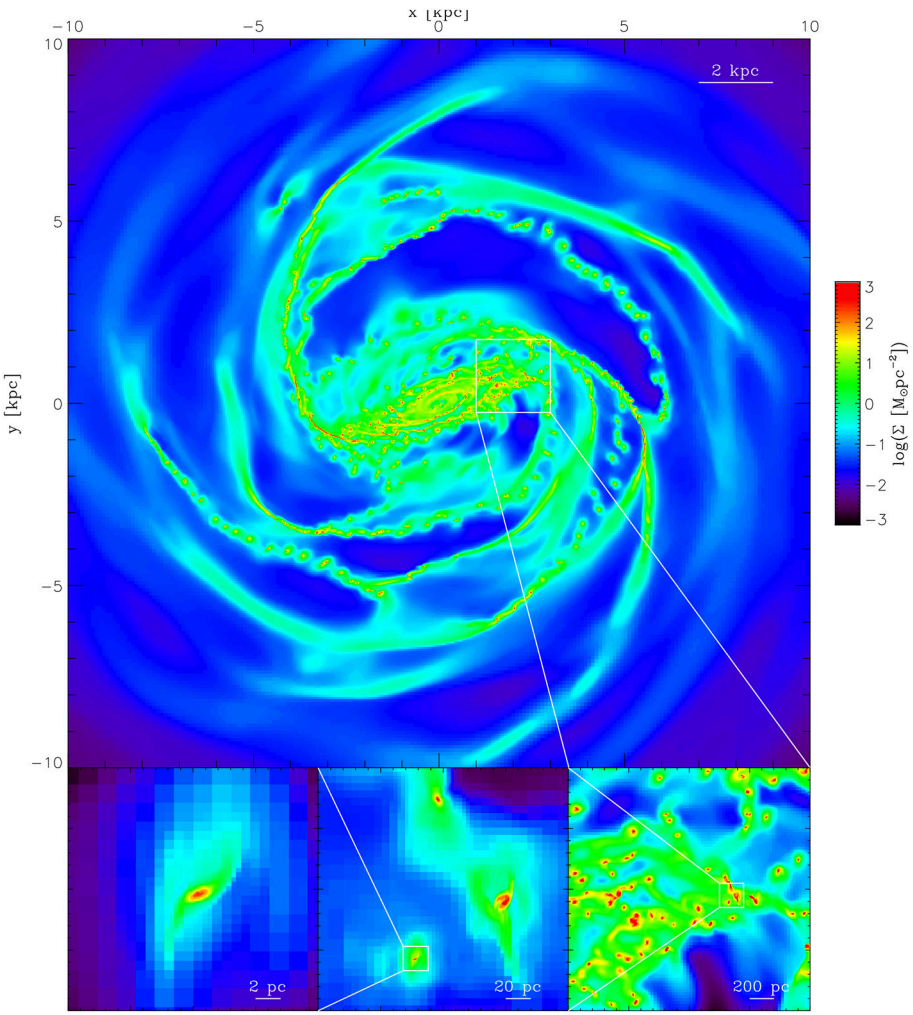

FIGURE 4 | Simulation of the Milky Way: column density of the gas disc in a sub-parsec resolution simulation. The color table only applies to the main panel: the table has been changed in each zoom-in view to enhance contrast. Figure adapted from Renaud et al. (2013) with permission from the authors.

most realistic models of the interstellar medium of the Galaxy, although still far from resolving the entire stellar population. In standard setups, the models account for the thermal instability and feedback (mechanical by SN and radiative by massive stars). First grid-based models were presented in Korpi et al. (1999) and included magnetic fields, SN heating and radiative cooling. 3D MHD AMR models of a kpc-scale ISM driven by SNe were presented in de Avillez and Breitschwerdt (2005) and Joung and Mac Low (2006). Currently, numerous studies and projects are based on a similar setup, with increasing physics put on over several years (SNe, radiative feedback, cosmic-rays, shear, etc.): the series of papers by Hennebelle and Iffrig (2014), Iffrig and Hennebelle (2017), and Colling et al. (2018) as well as the work of Martizzi et al. (2016) and Butler et al. (2015, 2017) using RAMSES, by Kim et al. (2011), Kim et al. (2013), Kim and Ostriker (2015), Kim and Ostriker (2017), and Kim and Ostriker (2018) using ATHENA, the SILCC project papers using FLASH (Walch et al., 2015; Girichidis et al., 2016, 2018; Gatto et al., 2017; Peters et al., 2017).

The third approach aims at simulating individual molecular cores. The box size ranges from 100 parsec down to 0.1 parsec for the highest resolution simulations. The mass typically ranges from 50 to a few 10^3 $M_\odot$. Boundary conditions are either periodic or isolated. In the latter case, the cloud as a whole can collapse, while the former set of simulations represents a more uniform background with collapsing regions only at very small scales. The smallest box sizes represents internal regions of larger clouds and are the only simulations for which the entire star population, down to the brown dwarf limit, can be modeled. These simulations are directly tackling the origin of the stellar IMF, and the formation of proto-planetary disks. We mention in the following a non-exhaustive list of the work done in this intense field of research. The series of papers by Bate & collaborators have investigated the collapse of molecular clouds

of mass ranging from 50 to 500 $M_\odot$ with increasing physics and numerical resolution since their pioneer work (Bate et al., 2003) using SPH. In particular, they have investigated the effect of radiative transfer (Bate, 2009, 2012) and magnetic fields (Price and Bate, 2008; Price and Bate, 2009). The work of Dale et al. (2007), Dale and Bonnell (2011), and Dale et al. (2012) have also used SPH simulations to study the effect of ionizing radiation from the forming massive stars. AMR codes have also been widely used in this context, accounting for a lot of physics and initial and boundary conditions. We note the work of Girichidis et al. (2011), Girichidis et al. (2012b), and Girichidis et al. (2012a) using FLASH who studied the importance of isolated initial conditions in isothermal cloud core collapse (without stellar feedback). Federrath et al. (2014b) also used FLASH to perform simulations of isolated cores with protostellar feedback (jets). Krumholz et al. (2007a), Krumholz et al. (2012), Hansen et al. (2012), Myers et al. (2013), Myers et al. (2014), Cunningham et al. (2011), Li et al. (2018), and Offner and Chaban (2017) presented 3D collapse models using ORION with radiative transfer and/or ideal MHD, as well as protostellar feedback (luminosity, outflows). RAMSES has also been extensively used in this approach: Hennebelle et al. (2011) and Commerçon et al. (2011b) for 100 $M_\odot$ isolated core collapse models with (R)MHD, Lee and Hennebelle (2018a), Lee and Hennebelle (2018b), and Lee and Hennebelle (2018c) focused on the peak of the IMF using (M)HD 1000 $M_\odot$ isolated core collapse models, Geen et al. (2015), Geen et al. (2016), and Gavagnin et al. (2017) studied the effect of ionizing radiation using the M1 moment method for radiative transfer. Last, we note the work of Wang et al. (2010) using ENZO with isolated boundary conditions, ideal MHD and protostellar jets. This non-exhaustive list of works done using this approach demonstrates the importance and the utility of such models. These simulations, however, rarely follow the formation of the second Larson core. They still rely on the sink particle technique, and on sub-grid models as well, when it comes to modeling proto-stellar jet launching, energy budget at accretion shocks and their associated radiation.

The last category of simulations deals with isolated collapsing low-mass dense cores, with the goal of following the formation of protostellar disks and ultimately the entire second collapse without relying on any sub-grid model. This ambitious strategy has already been discussed at length in the previous sections,

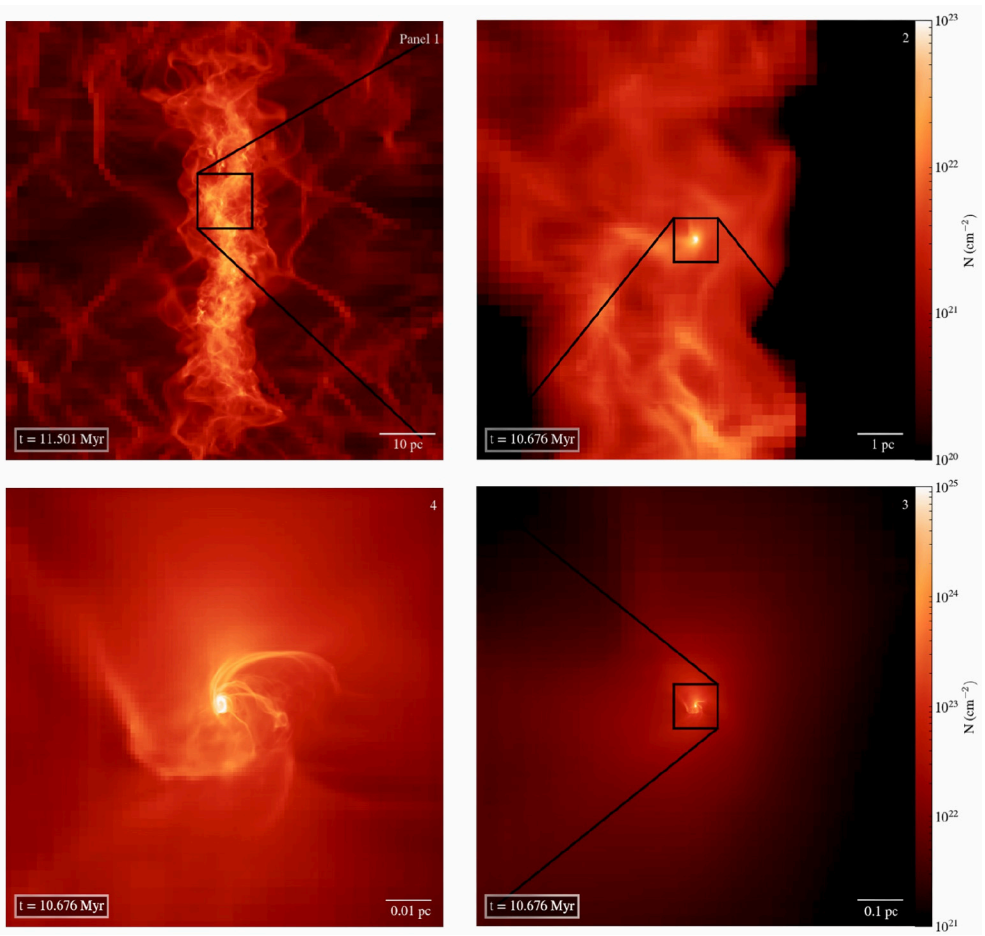

FIGURE 5 | Simulation of protostellar disk formation within molecular clouds. The column density maps show the entire molecular (upper left panel) and successive zoom within a star-forming dense core. Figure adapted from Zhang et al. (2018) with permission from the authors.

so we will not describe it here again. We also refer the reader to the review by Wurster and Li (2018) on the formation of protostellar disks.

An interesting intermediate strategy has been developed recently with the zoom-in technique. This method is used now routinely in galaxy formation simulations, for which only a single dark matter halo can be re-simulated at much higher resolution, keeping the entire cosmological environment alive but at a coarser resolution. Here, the idea is to model the turbulent molecular cloud on large scales, say with a box of size 100 parsecs, to identify a single collapsing core, and to zoom-in on the core with much higher resolution and follow the first and possibly the second collapse and the formation of the proto-planetary disk. For instance, Kuffmeier et al. (2017) and Kuffmeier et al. (2018) presented RAMSES AMR zoom-in calculations from an outer scale of 40 pc down to cell sizes of 2 au to study the effect of the environment on the formation and the evolution of protoplanetary disks. Zhang et al. (2018) performed high resolution calculations of the formation and evolution of a star-forming core, obtained by running larger scale calculations of molecular cloud formation (Zamora-Avilés et al., 2018). They used FLASH with a maximum resolution of 25 AU and were able to cover scales from 256 pc to 25 AU (see **Figure 5**). Mocz et al. (2017) performed moving mesh AREPO calculations from a box size of about 5 pc down to a maximum resolution of $\simeq$ 4 AU ($\simeq 5 \times 10^{-5}$ pc) to study the magnetic fields morphology from large to dense core scales. At larger scale, Padoan et al. (2017) performed a simulation of supernova-driven turbulence using RAMSES, with a box size of 250 pc and a maximum resolution of 0.0076 pc. At kpc scales, Hennebelle (2018) (FRIGG project with RAMSES, simulation of the formation of self-gravitating cores) and Seifried et al. (2017) (SLICC-Zoom project with FLASH, simulations of the formation of molecular clouds) presented zoom calculations of stratified Galactic disks down to resolution of $10^{-2} - 10^{-3}$ pc. Thanks to the steady increase in CPU power, we expect to see more and more work using the zoom-in technique in the coming years.

These different strategies are all in different ways very ambitious and address different problems in the theory of star formation. In addition, a compromise needs to be found between physical realism and computational efficiency. On one hand, we need to include magnetic fields, radiation fields and complex chemistry, but on the other hand, we need many small resolution elements and many time steps. Moreover, in the context of high performance computing, modern supercomputers are very hard to use at full efficiency when complex grid geometries is used in conjunction with expensive and demanding algorithms. There is a clear tendency for simulation projects deployed on the largest supercomputers in the world to use simple grid geometry, like Cartesian meshes and periodic boxes, with a highly simplified physical model. These large scale simulations are however very interesting to explore statistical aspects and large inertial range for turbulent flows. For example, Federrath (2013) performed 4096^3 hydrodynamic isothermal turbulence simulations using FLASH with periodic boundary condition for more than 40,000 time-steps on 32,768 CPU cores. In the framework of the magnetorotational turbulence, Fromang (2010), Ryan et al. (2017) performed high resolution simulations of isothermal shearing boxes using, respectively, ZEUS and a GPU version of RAMSES.

In conclusion, all simulations of star formation published in the literature, many of which have been discussed here, explore various corners of the numerical parameter space: resolution vs. box size, statistics vs. internal structure, physical realism vs. computational speed. It is interesting that at the smallest scales of interest here, a "first principle" approach is in principle possible and pursued by several groups. At larger scales, however, star formation simulations share the same kind of limitations as galaxy formation simulations, or climate models and weather forecasting simulations, namely a strong dependence of the results on small, unresolved scales. Although bigger computers with more efficient, higher order codes and more realistic models will certainly help shed light of the mysteries of star formation, a robust methodology to implement sub-grid models and couple them properly to the fluid equations still needs to be invented in our field. Various attempts have been proposed in the context of unresolved turbulence and star formation from analytical works (Krumholz and McKee, 2005; Hennebelle and Chabrier, 2011; Padoan and Nordlund, 2011; Federrath and Klessen, 2012) but the methodology, in the context of the full spectrum of required physical processes, is still at its infancy.

AUTHOR CONTRIBUTIONS

RT has written the introduction, the ideal MHD part and the radiative transfer part, as well as the discussion. BC has written the non-ideal MHD part, the second collapse part, the sink particle part and the subgrid models part.

ACKNOWLEDGMENTS

We would like to warmly thank our two referees, Richard Klein and Christoph Federrath, for their help in reviewing the manuscript. We thank Matthew Bate, Florent Renaud, and Shangjia Zhang for providing adapted figures from their work.

REFERENCES

Abel, T., and Wandelt, B. D. (2002). Adaptive ray tracing for radiative transfer around point sources. *Month. Notices R. Astron. Soc.* 330, L53–L56. doi: 10.1046/j.1365-8711.2002.05206.x

Adams, F. C., Ruden, S. P., and Shu, F. H. (1989). Eccentric gravitational instabilities in nearly keplerian disks. *Astrophys. J.* 347:959. doi: 10.1086/168187

Adams, F. C., and Shu, F. H. (1986). Infrared spectra of rotating protostars. *Astrophys. J.* 308:836. doi: 10.1086/164555

Alexiades, V., Amiez, G., and Gremaud, P. A. (1996). Super-time-stepping acceleration of explicit schemes for parabolic problems. *Commun. Numer. Methods Eng.* 12, 31–42.

Ali, A., Harries, T. J., and Douglas, T. A. (2018). Modelling massive star feedback with Monte Carlo radiation hydrodynamics: photoionization and radiation

pressure in a turbulent cloud. *Month. Notices R. Astron. Soc.* 477, 5422–5436. doi: 10.1093/mnras/sty1001

Altay, G., Croft, R. A. C., and Pelupessy, I. (2008). SPHRAY: a smoothed particle hydrodynamics ray tracer for radiative transfer. *Month. Notices R. Astron. Soc.* 386, 1931–1946. doi: 10.1111/j.1365-2966.2008.13212.x

Andre, P., Ward-Thompson, D., and Barsony, M. (1993). Submillimeter continuum observations of rho ophiuchi A: the candidate protostar VLA 1623 and prestellar clumps. *Astrophys. J.* 406:122. doi: 10.1086/172425

Aubert, D., and Teyssier, R. (2008). A radiative transfer scheme for cosmological reionization based on a local Eddington tensor. *Month. Notices R. Astron. Soc.* 387, 295–307. doi: 10.1111/j.1365-2966.2008.13223.x

Aubert, D., and Teyssier, R. (2010). Reionization simulations powered by graphics processing units. I. On the structure of the ultraviolet radiation field. *Astrophys. J.* 724, 244–266. doi: 10.1088/0004-637X/724/1/244

Bai, X.-N. (2014). Hall-effect-Controlled Gas Dynamics in Protoplanetary Disks. I. Wind Solutions at the Inner Disk. *Astrophys. J.* 791:137. doi: 10.1088/0004-637X/791/2/137

Bai, X.-N., and Stone, J. M. (2010). Particle-gas dynamics with athena: method and convergence. *Astrophys. J. Suppl. Ser.* 190, 297–310. doi: 10.1088/0067-0049/190/2/297

Bai, X.-N., and Stone, J. M. (2011). Effect of ambipolar diffusion on the nonlinear evolution of magnetorotational instability in weakly ionized disks. *Astrophys. J.* 736:144. doi: 10.1088/0004-637X/736/2/144

Balbus, S. A. (2009). Magnetohydrodynamics of protostellar disks. *arXiv:0906.0854*.

Balbus, S. A., and Hawley, J. F. (1991). A powerful local shear instability in weakly magnetized disks. I - Linear analysis. II - Nonlinear evolution. *Astrophys. J.* 376, 214–233. doi: 10.1086/170270

Balbus, S. A., and Terquem, C. (2001). Linear analysis of the hall effect in protostellar disks. *Astrophys. J.* 552, 235–247. doi: 10.1086/320452

Balsara, D. S. (1998). Total variation diminishing scheme for adiabatic and isothermal magnetohydrodynamics. *Astrophys. J. Suppl. Ser.* 116, 133–153. doi: 10.1086/313093

Balsara, D. S. (2001). Divergence-free adaptive mesh refinement for magnetohydrodynamics. *J. Comput. Phys.* 174, 614–648. doi: 10.1006/jcph.2001.6917

Balsara, D. S. (2004). Second-order-accurate schemes for magnetohydrodynamics with divergence- free reconstruction. *Astrophys. J. Suppl. Ser.* 151, 149–184. doi: 10.1086/381377

Balsara, D. S., Dumbser, M., and Abgrall, R. (2014). Multidimensional HLLC Riemann solver for unstructured meshes - With application to Euler and MHD flows. *J. Comput. Phys.* 261, 172–208. doi: 10.1016/j.jcp.2013.12.029

Balsara, D. S., and Spicer, D. S. (1999). A staggered mesh algorithm using high order godunov fluxes to ensure solenoidal magnetic fields in magnetohydrodynamic simulations. *J. Comput. Phys.* 149, 270–292. doi: 10.1006/jcph.1998.6153

Banerjee, R., and Pudritz, R. E. (2006). Outflows and jets from collapsing magnetized cloud cores. *Astrophys. J.* 641, 949–960. doi: 10.1086/500496

Baraffe, I., Vorobyov, E., and Chabrier, G. (2012). Observed luminosity spread in young clusters and FU Ori stars: a unified picture. *Astrophys. J.* 756:118. doi: 10.1088/0004-637X/756/2/118

Bate, M. R. (1998). Collapse of a molecular cloud core to stellar densities: the first three-dimensional calculations. *Astrophys. J.* 508, L95–L98. doi: 10.1086/311719

Bate, M. R. (2009). The importance of radiative feedback for the stellar initial mass function. *Month. Notices R. Astron. Soc.* 392, 1363–1380. doi: 10.1111/j.1365-2966.2008.14165.x

Bate, M. R. (2010). Collapse of a molecular cloud core to stellar densities: the radiative impact of stellar core formation on the circumstellar disc. *Month. Notices R. Astron. Soc.* 404, 79–83. doi: 10.1111/j.1745-3933.2010.00839.x

Bate, M. R. (2012). Stellar, brown dwarf and multiple star properties from a radiation hydrodynamical simulation of star cluster formation. *Month. Notices R. Astron. Soc.* 419, 3115–3146. doi: 10.1111/j.1365-2966.2011.19955.x

Bate, M. R., Bonnell, I. A., and Bromm, V. (2003). The formation of a star cluster: predicting the properties of stars and brown dwarfs. *Month. Notices R. Astron. Soc.* 339, 577–599. doi: 10.1046/j.1365-8711.2003.06210.x

Bate, M. R., Bonnell, I. A., and Price, N. M. (1995). Modelling accretion in protobinary systems. *Month. Notices R. Astron. Soc.* 277, 362–376. doi: 10.1093/mnras/277.2.362

Bate, M. R., and Burkert, A. (1997). Resolution requirements for smoothed particle hydrodynamics calculations with self-gravity. *Month. Notices R. Astron. Soc.* 288, 1060–1072. doi: 10.1093/mnras/288.4.1060

Bate, M. R., and Lorén-Aguilar, P. (2017). On the dynamics of dust during protostellar collapse. *Month. Notices R. Astron. Soc.* 465, 1089–1094. doi: 10.1093/mnras/stw2853

Bate, M. R., Tricco, T. S., and Price, D. J. (2014). Collapse of a molecular cloud core to stellar densities: stellar-core and outflow formation in radiation magnetohydrodynamic simulations. *Month. Notices R. Astron. Soc.* 437, 77–95. doi: 10.1093/mnras/stt1865

Beuther, H., Linz, H., and Henning, T. (2008). "Massive star formation: observations confront theory," in *ASP Conference Series*, Vol. 387 (San Francisco, CA: Astronomical Society of the Pacific), 189.

Bhandare, A., Kuiper, R., Henning, T., Fendt, C., Marleau, G.-D., and Kölligan, A. (2018). First core properties: from low- to high-mass star formation. *arXiv:1807.06597*. doi: 10.1051/0004-6361/201832635

Black, D. C., and Bodenheimer, P. (1975). Evolution of rotating interstellar clouds. I - Numerical techniques. *Astrophys. J.* 199, 619–632. doi: 10.1086/153729

Black, D. C., and Scott, E. H. (1982). A numerical study of the effects of ambipolar diffusion on the collapse of magnetic gas clouds. *Astrophys. J.* 263, 696–715. doi: 10.1086/160541

Blandford, R. D., and Payne, D. G. (1982). Hydromagnetic flows from accretion discs and the production of radio jets. *Month. Notices R. Astron. Soc.* 199, 883–903. doi: 10.1093/mnras/199.4.883

Bleuler, A., and Teyssier, R. (2014). Towards a more realistic sink particle algorithm for the RAMSES CODE. *Month. Notices R. Astron. Soc.* 445, 4015–4036. doi: 10.1093/mnras/stu2005

Bodenheimer, P., Laughlin, G. P., Rózyczka, M., and Yorke, H. W. (eds). (2007). *Astronomy and Astrophysics. Numerical Methods in Astrophysics: An Introduction*. Boca Raton, FL: Taylor & Francis Group.

Bodenheimer, P., Yorke, H. W., Rozyczka, M., and Tohline, J. E. (1990). The formation phase of the solar nebula. *Astrophys. J.* 355:651. doi: 10.1086/168798

Bonafede, A., Dolag, K., Stasyszyn, F., Murante, G., and Borgani, S. (2011). A non-ideal magnetohydrodynamic GADGET: simulating massive galaxy clusters. *Month. Notices R. Astron. Soc.* 418, 2234–2250. doi: 10.1111/j.1365-2966.2011.19523.x

Booth, R. A., Sijacki, D., and Clarke, C. J. (2015). Smoothed particle hydrodynamics simulations of gas and dust mixtures. *Month. Notices R. Astron. Soc.* 452, 3932–3947. doi: 10.1093/mnras/stv1486

Boscheri, W., and Dumbser, M. (2014). A direct Arbitrary-Lagrangian-Eulerian ADER-WENO finite volume scheme on unstructured tetrahedral meshes for conservative and non-conservative hyperbolic systems in 3D. *J. Comput. Phys.* 275, 484–523. doi: 10.1016/j.jcp.2014.06.059

Boss, A. P., and Black, D. C. (1982). Collapse of accreting, rotating, isothermal, interstellar clouds. *Astrophys. J.* 258, 270–279. doi: 10.1086/160077

Boss, A. P., Fisher, R. T., Klein, R. I., and McKee, C. F. (2000). The jeans condition and collapsing molecular cloud cores: filaments or binaries? *Astrophys. J.* 528, 325–335. doi: 10.1086/308160

Bournaud, F., Elmegreen, B. G., Teyssier, R., Block, D. L., and Puerari, I. (2010). ISM properties in hydrodynamic galaxy simulations: turbulence cascades, cloud formation, role of gravity and feedback. *Month. Notices R. Astron. Soc.* 409, 1088–1099. doi: 10.1111/j.1365-2966.2010.17370.x

Brackbill, J. U., and Barnes, D. C. (1980). The effect of nonzero product of magnetic gradient and B on the numerical solution of the magnetohydrodynamic equations. *J. Comput. Phys.* 35, 426–430. doi: 10.1016/0021-9991(80)90079-0

Brandenburg, A., and Subramanian, K. (2005). Astrophysical magnetic fields and nonlinear dynamo theory. *Phys. Rep.* 417, 1–209. doi: 10.1016/j.physrep.2005.06.005

Brandenburg, A., and Zweibel, E. G. (1994). The formation of sharp structures by ambipolar diffusion. *Astrophys. J.* 427:L91. doi: 10.1086/187372

Bryan, G. L., Norman, M. L., O'Shea, B. W., Abel, T., Wise, J. H., Turk, M. J., et al. (2014). ENZO: an adaptive mesh refinement code for astrophysics. *Astrophys. J. Suppl.* 211:19. doi: 10.1088/0067-0049/211/2/19

Buntemeyer, L., Banerjee, R., Peters, T., Klassen, M., and Pudritz, R. E. (2016). Radiation hydrodynamics using characteristics on adaptive decomposed domains for massively parallel star formation simulations. *New Astron.* 43, 49–69. doi: 10.1016/j.newast.2015.07.002

Butler, M. J., Tan, J. C., Teyssier, R., Rosdahl, J., Van Loo, S., and Nickerson, S. (2017). Kiloparsec-scale simulations of star formation in disk galaxies. IV. regulation of galactic star formation rates by stellar feedback. *Astrophys. J.* 841:82. doi: 10.3847/1538-4357/aa7054

Butler, M. J., Tan, J. C., and Van Loo, S. (2015). Kiloparsec-scale simulations of star formation in disk galaxies III. Structure and dynamics of filaments and clumps in giant molecular clouds. *Astrophys. J.* 805:1. doi: 10.1088/0004-637X/805/1/1

Capuzzo-Dolcetta, R., Limongi, M., and Tornambè, A. (2012). "Advances in computational astrophysics: methods, tools, and outcome," in *ASP Conference Proceedings,* Vol. 453 (San Francisco, CA: Astronomical Society of the Pacific), 129.

Chen, C.-Y., and Ostriker, E. C. (2014). Formation of magnetized prestellar cores with ambipolar diffusion and turbulence. *Astrophys. J.* 785:69. doi: 10.1088/0004-637X/785/1/69

Chen, J.-W., and Lin, M.-K. (2018). Dusty disc-planet interaction with dust-free simulations. *Month. Notices R. Astron. Soc.* 478, 2737–2752. doi: 10.1093/mnras/sty1166

Chiaki, G., and Yoshida, N. (2015). Particle splitting in smoothed particle hydrodynamics based on Voronoi diagram. *Month. Notices R. Astron. Soc.* 451, 3955–3963. doi: 10.1093/mnras/stv1227

Chiang, H.-F., Looney, L. W., and Tobin, J. J. (2012). The envelope and embedded disk around the class 0 protostar L1157-mm: dual-wavelength interferometric observations and modeling. *Astrophys. J.* 756:168. doi: 10.1088/0004-637X/756/2/168

Choi, E., Kim, J., and Wiita, P. J. (2009). An explicit scheme for incorporating ambipolar diffusion in a magnetohydrodynamics code. *Astrophys. J.* 181, 413–420. doi: 10.1088/0067-0049/181/2/413

Christie, D., Wu, B., and Tan, J. C. (2017). GMC collisions as triggers of star formation. IV. The role of ambipolar diffusion. *Astrophys. J.* 848:50. doi: 10.3847/1538-4357/aa8a99

Ciardi, A., and Hennebelle, P. (2010). Outflows and mass accretion in collapsing dense cores with misaligned rotation axis and magnetic field. *Month. Notices R. Astron. Soc.* 409, L39–L43. doi: 10.1111/j.1745-3933.2010.00942.x

Ciolek, G. E. L. E. C., and Roberge, W. A. G. R. (2002). Time-dependent, multifluid, magnetohydrodynamic shock waves with grain dynamics I. Formulation and numerical tests. *Astrophys. J.* 567, 947–961. doi: 10.1086/338591

Clark, P. C., Glover, S. C. O., and Klessen, R. S. (2012). TreeCol: a novel approach to estimating column densities in astrophysical simulations. *Month. Notices R. Astron. Soc.* 420, 745–756. doi: 10.1111/j.1365-2966.2011.20087.x

Colling, C., Hennebelle, P., Geen, S., Iffrig, O., and Bournaud, F. (2018). Impact of galactic shear and stellar feedback on star formation. *Astron. Astrophys.* 620:A21. doi: 10.1051/0004-6361/201833161

Commerçon, B., Audit, E., Chabrier, G., and Chièze, J.-P. (2011a). Physical and radiative properties of the first-core accretion shock. *Astron. Astrophys.* 530:A13. doi: 10.1051/0004-6361/201016213

Commercon, B., Debout, V., and Teyssier, R. (2014). A fast, robust, and simple implicit method for adaptive time-stepping on adaptive mesh-refinement grids. *Astron. Astrophys.* 563:A11. doi: 10.1051/0004-6361/201322858

Commerçon, B., Hennebelle, P., Audit, E., Chabrier, G., and Teyssier, R. (2008). Protostellar collapse: a comparison between smoothed particle hydrodynamics and adaptative mesh refinement calculations. *Astron. Astrophys.* 482:371. doi: 10.1051/0004-6361:20078591

Commerçon, B., Hennebelle, P., Audit, E., Chabrier, G., and Teyssier, R. (2010). Protostellar collapse: radiative and magnetic feedbacks on small-scale fragmentation. *Astron. Astrophys.* 510:L3. doi: 10.1051/0004-6361/200913597

Commerçon, B., Hennebelle, P., and Henning, T. (2011b). Collapse of massive magnetized dense cores using radiation magnetohydrodynamics: early fragmentation inhibition. *Astrophys. J. Lett.* 742:L9. doi: 10.1088/2041-8205/742/1/L9

Commerçon, B., Teyssier, R., Audit, E., Hennebelle, P., and Chabrier, G. (2011). Radiation hydrodynamics with adaptive mesh refinement and application to prestellar core collapse. I. Methods. *Astron. Astrophys.* 529:A35. doi: 10.1051/0004-6361/201015880

Cunningham, A. J., Klein, R. I., Krumholz, M. R., and McKee, C. F. (2011). Radiation-hydrodynamic simulations of massive star formation with protostellar outflows. *Astrophys. J.* 740:107. doi: 10.1088/0004-637X/740/2/107

Dai, W., and Woodward, P. R. (1994). Extension of the piecewise parabolic method to multidimensional ideal magnetohydrodynamics. *J. Comput. Phys.* 115, 485–514. doi: 10.1006/jcph.1994.1212

Dale, J. E., and Bonnell, I. (2011). Ionizing feedback from massive stars in massive clusters: fake bubbles and untriggered star formation. *Month. Notices R. Astron. Soc.* 414, 321–328. doi: 10.1111/j.1365-2966.2011.18392.x

Dale, J. E., Ercolano, B., and Bonnell, I. A. (2012). Ionizing feedback from massive stars in massive clusters - II. Disruption of bound clusters by photoionization. *Month. Notices R. Astron. Soc.* 424, 377–392. doi: 10.1111/j.1365-2966.2012.21205.x

Dale, J. E., Ercolano, B., and Clarke, C. J. (2007). A new algorithm for modelling photoionizing radiation in smoothed particle hydrodynamics. *Month. Notices R. Astron. Soc.* 382, 1759–1767. doi: 10.1111/j.1365-2966.2007.12486.x

Davis, S. W., Stone, J. M., and Jiang, Y.-F. (2012). A radiation transfer solver for athena using short characteristics. *Astrophys. J. Suppl.* 199:9. doi: 10.1088/0067-0049/199/1/9

de Avillez, M. A., and Breitschwerdt, D. (2005). Global dynamical evolution of the ISM in star forming galaxies. I. High resolution 3D simulations: effect of the magnetic field. *Astron. Astrophys.* 436, 585–600. doi: 10.1051/0004-6361:20042146

Dedner, A., Kemm, F., Kröner, D., Munz, C. D., Schnitzer, T., and Wesenberg, M. (2002). Hyperbolic divergence cleaning for the MHD equations. *J. Comput. Phys.* 175, 645–673. doi: 10.1006/jcph.2001.6961

Derigs, D., Winters, A. R., Gassner, G. J., and Walch, S. (2016). A novel high-order, entropy stable, 3D AMR MHD solver with guaranteed positive pressure. *J. Comput. Phys.* 317, 223–256. doi: 10.1016/j.jcp.2016.04.048

Derigs, D., Winters, A. R., Gassner, G. J., Walch, S., and Bohm, M. (2017). Ideal GLM-MHD: about the entropy consistent nine-wave magnetic field divergence diminishing ideal magnetohydrodynamics equations. *arXiv*, 420–467. doi: 10.1016/j.jcp.2018.03.002

Dobbs, C. L., Pettitt, A. R., Corbelli, E., and Pringle, J. E. (2018). Simulations of the flocculent spiral M33: what drives the spiral structure? *Month. Notices R. Astron. Soc.* 478, 3793–3808. doi: 10.1093/mnras/sty1231

Dolag, K., Bartelmann, M., and Lesch, H. (1999). SPH simulations of magnetic fields in galaxy clusters. *Astron. Astrophys.* 348, 351–363.

Dolag, K., and Stasyszyn, F. (2009). An MHD GADGET for cosmological simulations. *Month. Notices R. Astron. Soc.* 398, 1678–1697. doi: 10.1111/j.1365-2966.2009.15181.x

Dorfi, E. (1982). 3D models for self-gravitating, rotating magnetic interstellar clouds. *Astron. Astrophys.* 114, 151–164.

Draine, B. T. (1986). Multicomponent, reacting MHD flows. *Month. Notices R. Astron. Soc.* 220, 133–148. doi: 10.1093/mnras/220.1.133

Draine, B. T., Roberge, W. G., and Dalgarno, A. (1983). Magnetohydrodynamic shock waves in molecular clouds. *Astrophys. J.* 264, 485–507. doi: 10.1086/160617

Draine, B. T., and Sutin, B. (1987). Collisional charging of interstellar grains. *Astrophys. J.* 320, 803–817. doi: 10.1086/165596

Dubroca, B., and Feugeas, J. (1999). Etude théorique et numérique d'une hiérarchie de modèles aux moments pour le transfert radiatif. *Academie des Sciences Paris Comptes Rendus Serie Sciences Mathematiques* 329, 915–920. doi: 10.1016/S0764-4442(00)87499-6

Duffin, D. F., and Pudritz, R. E. (2008). Simulating hydromagnetic processes in star formation: introducing ambipolar diffusion into an adaptive mesh refinement code. *Month. Notices R. Astron. Soc.* 391, 1659–1673. doi: 10.1111/j.1365-2966.2008.14026.x

Dzyurkevich, N., Commerçon, B., Lesaffre, P., and Semenov, D. (2017). Magnetic diffusivities in 3D radiative chemo-hydrodynamic simulations of protostellar collapse. *Astron. Astrophys.* 603:A105. doi: 10.1051/0004-6361/201628995

Emerick, A., Bryan, G. L., and Mac Low, M.-M. (2018). Stellar radiation is critical for regulating star formation and driving outflows in low-mass dwarf galaxies. *Astrophys. J.* 865:L22. doi: 10.3847/2041-8213/aae315

Emerick, A., Bryan, G. L., and Mac Low, M.-M. (2019). Simulating an isolated dwarf galaxy with multichannel feedback and chemical yields

from individual stars. *Month. Notices R. Astron. Soc.* 482, 1304–1329. doi: 10.1093/mnras/sty2689

Epstein, P. S. (1924). On the resistance experienced by spheres in their motion through gases. *Phys. Rev.* 23, 710–733. doi: 10.1103/PhysRev.23.710

Ercolano, B., Barlow, M. J., Storey, P. J., and Liu, X. W. (2003). MOCASSIN: a fully three-dimensional Monte Carlo photoionization code. *Month. Notice R. Astron. Soc.* 340, 1136–1152. doi: 10.1046/j.1365-8711.2003.06371.x

Evans, C. R., and Hawley, J. F. (1988). Simulation of magnetohydrodynamic flows - A constrained transport method. *Astrophys. J.* 332, 659–677. doi: 10.1086/166684

Falle, S. (2003). A numerical scheme for multifluid magnetohydrodynamics. *Month. Notices R. Astron. Soc.* 344, 1210–1218. doi: 10.1046/j.1365-8711.2003.06908.x

Falle, S. A. E. G. (2002). Rarefaction shocks, shock errors, and low order of accuracy in ZEUS. *Astrophys. J.* 577, L123–L126. doi: 10.1086/344336

Federrath, C. (2013). On the universality of supersonic turbulence. *Month. Notices R. Astron. Soc.* 436, 1245–1257. doi: 10.1093/mnras/stt1644

Federrath, C. (2015). Inefficient star formation through turbulence, magnetic fields and feedback. *Month. Notices R. Astron. Soc.* 450, 4035–4042. doi: 10.1093/mnras/stv941

Federrath, C. (2016). Magnetic field amplification in turbulent astrophysical plasmas. *J. Plasma Phys.* 82:535820601. doi: 10.1017/S0022377816001069

Federrath, C., Banerjee, R., Clark, P., and Klessen, R. (2010). Modeling collapse and accretion in turbulent gas clouds: implementation and comparison of sink particles in AMR and SPH. *Astrophys. J.* 713, 269–290. doi: 10.1088/0004-637X/713/1/269

Federrath, C., Banerjee, R., Seifried, D., Clark, P. C., and Klessen, R. S. (2011a). "Implementing and comparing sink particles in AMR and SPH," in *Computational Star Formation, Proceedings of the International Astronomical Union, IAU Symposium*, vol. 270, 425–428. doi: 10.1017/S1743921311000755

Federrath, C., Chabrier, G., Schober, J., Banerjee, R., Klessen, R. S., and Schleicher, D. R. (2011b). Mach number dependence of turbulent magnetic field amplification: solenoidal versus compressive flows. *Phys. Rev. Lett.* 107:114504. doi: 10.1103/PhysRevLett.107.114504

Federrath, C., and Klessen, R. S. (2012). The star formation rate of turbulent magnetized clouds: comparing theory, simulations, and observations. *Astrophys. J.* 761:156. doi: 10.1088/0004-637X/761/2/156

Federrath, C., Rathborne, J. M., Longmore, S. N., Kruijssen, J. M. D., Bally, J., Contreras, Y., et al. (2017). The link between solenoidal turbulence and slow star formation in G0.253+0.016. *Multi-Messenger Astrophys. Galactic Centre* 322, 123–128. doi: 10.1017/S1743921316012357

Federrath, C., Schober, J., Bovino, S., and Schleicher, D. R. G. (2014a). The turbulent dynamo in highly compressible supersonic plasmas. *Astrophys. J. Lett.* 797:L19. doi: 10.1088/2041-8205/797/2/L19

Federrath, C., Schrön, M., Banerjee, R., and Klessen, R. S. (2014b). Modeling jet and outflow feedback during star cluster formation. *Astrophys. J.* 790:128. doi: 10.1088/0004-637X/790/2/128

Federrath, C., Sur, S., Schleicher, D. R. G., Banerjee, R., and Klessen, R. S. (2011c). A new jeans resolution criterion for (M)HD simulations of self-gravitating gas: application to magnetic field amplification by gravity-driven turbulence. *Astrophys. J.* 731:62. doi: 10.1088/0004-637X/731/1/62

Felker, K. G., and Stone, J. M. (2018). A fourth-order accurate finite volume method for ideal MHD via upwind constrained transport. *J. Comput. Phys.* 375, 1365–1400. doi: 10.1016/j.jcp.2018.08.025

Ferreira, J. (1997). Magnetically-driven jets from Keplerian accretion discs. *Astron. Astrophys.* 319, 340–359.

Fontani, F., Commerçon, B., Giannetti, A., Beltrán, M. T., Sánchez-Monge, Á., Testi, L., et al. (2018). Fragmentation properties of massive protocluster gas clumps: an ALMA study. *Astron. Astrophys.* 615:A94. doi: 10.1051/0004-6361/201832672

Forgan, D., Rice, K., Stamatellos, D., and Whitworth, A. (2009). Introducing a hybrid radiative transfer method for smoothed particle hydrodynamics. *Month. Notices R. Astron. Soc.* 394, 882–891. doi: 10.1111/j.1365-2966.2008.14373.x

Fromang, S. (2010). MHD simulations of the magnetorotational instability in a shearing box with zero net flux: the case Pm = 4. *Astron. Astrophys.* 514:L5. doi: 10.1051/0004-6361/201014284

Fromang, S., Hennebelle, P., and Teyssier, R. (2006). A high order Godunov scheme with constrained transport and adaptive mesh refinement for astrophysical magnetohydrodynamics. *Astron. Astrophys.* 457, 371–384. doi: 10.1051/0004-6361:20065371

Fromang, S., Papaloizou, J., Lesur, G., and Heinemann, T. (2007). MHD simulations of the magnetorotational instability in a shearing box with zero net flux. *Astron. Astrophys.* 476, 1123–1132. doi: 10.1051/0004-6361:20077943

Frostholm, T., Haugbølle, T., and Grassi, T. (2018). Lampray: multi-group long characteristics ray tracing for adaptive mesh radiation hydrodynamics. *arXiv:1809.05541*.

Fryxell, B., Olson, K., Ricker, P., Timmes, F. X., Zingale, M., Lamb, D. Q., et al. (2000). FLASH: an adaptive mesh hydrodynamics code for modeling astrophysical thermonuclear flashes. *Astrophys. J. Suppl. Ser.* 131, 273–334. doi: 10.1086/317361

Galli, D., Walmsley, M., and Gonçalves, J. (2002). The structure and stability of molecular cloud cores in external radiation fields. *Astron. Astrophys.* 394, 275–284. doi: 10.1051/0004-6361:20021125

Gatto, A., Walch, S., Naab, T., Girichidis, P., Wünsch, R., Glover, S. C. O., et al. (2017). The SILCC project - III. Regulation of star formation and outflows by stellar winds and supernovae. *Month. Notices R. Astron. Soc.* 466, 1903–1924. doi: 10.1093/mnras/stw3209

Gavagnin, E., Bleuler, A., Rosdahl, J., and Teyssier, R. (2017). Star cluster formation in a turbulent molecular cloud self-regulated by photoionization feedback. *Month. Notices R. Astron. Soc.* 472, 4155–4172. doi: 10.1093/mnras/stx2222

Geen, S., Hennebelle, P., Tremblin, P., and Rosdahl, J. (2015). Photoionization feedback in a self-gravitating, magnetized, turbulent cloud. *Month. Notices R. Astron. Soc.* 454, 4484–4502. doi: 10.1093/mnras/stv2272

Geen, S., Hennebelle, P., Tremblin, P., and Rosdahl, J. (2016). Feedback in Clouds II: UV photoionization and the first supernova in a massive cloud. *Month. Notices R. Astron. Soc.* 463, 3129–3142. doi: 10.1093/mnras/stw2235

Geen, S., Watson, S. K., Rosdahl, J., Bieri, R., Klessen, R. S., and Hennebelle, P. (2018). On the indeterministic nature of star formation on the cloud scale. *Month. Notices R. Astron. Soc.* 481, 2548–2569. doi: 10.1093/mnras/sty2439

Gerin, M., Pety, J., Fuente, A., Cernicharo, J., Commerçon, B., and Marcelino, N. (2015). Nascent bipolar outflows associated with the first hydrostatic core candidates Barnard 1b-N and 1b-S. *Astron. Astrophys.* 577:L2. doi: 10.1051/0004-6361/201525777

Girichidis, P., Federrath, C., Allison, R., Banerjee, R., and Klessen, R. S. (2012a). Importance of the initial conditions for star formation - III. Statistical properties of embedded protostellar clusters. *Month. Notices R. Astron. Soc.* 420, 3264–3280. doi: 10.1111/j.1365-2966.2011.20250.x

Girichidis, P., Federrath, C., Banerjee, R., and Klessen, R. S. (2011). Importance of the initial conditions for star formation - I. Cloud evolution and morphology. *Month. Notices R. Astron. Soc.* 413, 2741–2759. doi: 10.1111/j.1365-2966.2011.18348.x

Girichidis, P., Federrath, C., Banerjee, R., and Klessen, R. S. (2012b). Importance of the initial conditions for star formation - II. Fragmentation-induced starvation and accretion shielding. *Month. Notices R. Astron. Soc.* 420, 613–626. doi: 10.1111/j.1365-2966.2011.20073.x

Girichidis, P., Seifried, D., Naab, T., Peters, T., Walch, S., Wünsch, R., et al. (2018). The SILCC project - V. The impact of magnetic fields on the chemistry and the formation of molecular clouds. *Month. Notices R. Astron. Soc.* 480, 3511–3540. doi: 10.1093/mnras/sty2016

Girichidis, P., Walch, S., Naab, T., Gatto, A., Wünsch, R., Glover, S. C. O., et al. (2016). The SILCC (SImulating the lifeCycle of molecular Clouds) project - II. Dynamical evolution of the supernova-driven ISM and the launching of outflows. *Month. Notices R. Astron. Soc.* 456, 3432–3455. doi: 10.1093/mnras/stv2742

Gnedin, N. Y., and Abel, T. (2001). Multi-dimensional cosmological radiative transfer with a Variable Eddington Tensor formalism. *New Astron.* 6, 437–455. doi: 10.1016/S1384-1076(01)00068-9

Gong, H., and Ostriker, E. C. (2013). Implementation of sink particles in the athena code. *Astrophys. J. Suppl. Ser.* 204:8. doi: 10.1088/0067-0049/204/1/8

González, M., Audit, E., and Huynh, P. (2007). HERACLES: a three-dimensional radiation hydrodynamics code. *Astron. Astrophys.* 464, 429–435. doi: 10.1051/0004-6361:20065486

González, M., Vaytet, N., Commercon, B., and Masson, J. (2015). Multigroup radiation hydrodynamics with flux-limited diffusion and adaptive mesh refinement. *Astron. Astrophys.* 578:A12. doi: 10.1051/0004-6361/201525971

González-Morales, P., Khomenko, E., Downes, T., and De Vicente, A. (2018). MHDSTS: a new explicit numerical scheme for simulations of partially ionised solar plasma. *Astron. Astrophys.* 615:67. doi: 10.1051/0004-6361/201731916

Goodwin, S. P., Whitworth, A. P., and Ward-Thompson, D. (2004). Astronomy & Astrophysics Simulating star formation in molecular cloud cores I. The influence of low levels of turbulence on fragmentation and multiplicity. *Astron. Astrophys.* 414, 633–650. doi: 10.1051/0004-6361:20031594

Greif, T. H., Springel, V., White, S. D., Glover, S. C., Clark, P. C., Smith, R. J., et al. (2011). Simulations on a moving mesh: the clustered formation of population III protostars. *Astrophys. J.* 737:75. doi: 10.1088/0004-637X/737/2/75

Guillet, T., Pakmor, R., Springel, V., Chandrashekar, P., and Klingenberg, C. (2018). High-order magnetohydrodynamics for astrophysics with an adaptive mesh refinement discontinuous galerkin scheme. *arXiv*. doi: 10.1093/mnras/stz314

Hansen, C. E., Klein, R. I., McKee, C. F., and Fisher, R. T. (2012). Feedback effects on low-mass star formation. *Astrophys. J.* 747:22. doi: 10.1088/0004-637X/747/1/22

Harries, T. J. (2011). An algorithm for Monte Carlo time-dependent radiation transfer. *Month. Notices R. Astron. Soc.* 416, 1500–1508. doi: 10.1111/j.1365-2966.2011.19147.x

Harries, T. J. (2015). Radiation-hydrodynamical simulations of massive star formation using Monte Carlo radiative transfer - I. Algorithms and numerical methods. *Month. Notices R. Astron. Soc.* 448, 3156–3166. doi: 10.1093/mnras/stv158

Hayes, J. C., Norman, M. L., Fiedler, R. A., Bordner, J. O., Li, P. S., Clark, S. E., et al. (2006). Simulating radiating and magnetized flows in multiple dimensions with ZEUS-MP. *Astrophys. J. Suppl. Ser.* 165, 188–228. doi: 10.1086/504594

Hennebelle, P. (2018). The FRIGG project: from intermediate galactic scales to self-gravitating cores. *Astron. Astrophys.* 611:A24. doi: 10.1051/0004-6361/201731071

Hennebelle, P., and Chabrier, G. (2011). Analytical star formation rate from gravoturbulent fragmentation. *Astrophys. J.* 743:L29. doi: 10.1088/2041-8205/743/2/L29

Hennebelle, P., Commerçon, B., Chabrier, G., and Marchand, P. (2016). Magnetically self-regulated formation of early protoplanetary disks. *Astrophys. J. Lett.* 830:L8. doi: 10.3847/2041-8205/830/1/L8

Hennebelle, P., Commerçon, B., Joos, M., Klessen, R. S., Krumholz, M., Tan, J. C., et al. (2011). Collapse, outflows and fragmentation of massive, turbulent and magnetized prestellar barotropic cores. *Astron. Astrophys.* 528:A72. doi: 10.1051/0004-6361/201016052

Hennebelle, P., and Fromang, S. (2008). Magnetic processes in a collapsing dense core. I. Accretion and ejection. *Astron. Astrophys.* 477, 9–24. doi: 10.1051/0004-6361:20078309

Hennebelle, P., and Iffrig, O. (2014). Simulations of magnetized multiphase galactic disc regulated by supernovae explosions. *Astron. Astrophys.* 570:A81. doi: 10.1051/0004-6361/201423392

Hopkins, P. F. (2017). Anisotropic diffusion in mesh-free numerical magnetohydrodynamics. *Month. Notices R. Astron. Soc.* 466, 3387–3405. doi: 10.1093/mnras/stw3306

Hopkins, P. F., Kereš, D., Oñorbe, J., Faucher-Giguère, C.-A., Quataert, E., Murray, N., et al. (2014). Galaxies on FIRE (feedback in realistic environments): stellar feedback explains cosmologically inefficient star formation. *Month. Notices R. Astron. Soc.* 445, 581–603. doi: 10.1093/mnras/stu1738

Hopkins, P. F., and Lee, H. (2016). The fundamentally different dynamics of dust and gas in molecular clouds. *Month. Notices R. Astron. Soc.* 456, 4174–4190. doi: 10.1093/mnras/stv2745

Hopkins, P. F., Quataert, E., and Murray, N. (2012). The structure of the interstellar medium of star-forming galaxies. *Month. Notices R. Astron. Soc.* 421, 3488–3521. doi: 10.1111/j.1365-2966.2012.20578.x

Hopkins, P. F., Wetzel, A., Kereš, D., Faucher-Giguère, C.-A., Quataert, E., Boylan-Kolchin, M., et al. (2018). FIRE-2 simulations: physics versus numerics in galaxy formation. *Month. Notices R. Astron. Soc.* 480, 800–863. doi: 10.1093/mnras/sty1690

Hosking, J. G., and Whitworth, a. P. (2004). Modelling ambipolar diffusion with two-fluid smoothed particle hydrodynamics. *October* 1000, 994–1000. doi: 10.1111/j.1365-2966.2004.07273.x

Hu, C.-Y. (2019). Supernova-driven winds in simulated dwarf galaxies. *Month. Notices R. Astron. Soc.* 483, 3363–3381. doi: 10.1093/mnras/sty3252

Hu, C.-Y., Naab, T., Walch, S., Glover, S. C. O., and Clark, P. C. (2016). Star formation and molecular hydrogen in dwarf galaxies: a non-equilibrium view. *Month. Notices R. Astron. Soc.* 458, 3528–3553. doi: 10.1093/mnras/stw544

Hubber, D. A., Batty, C. P., McLeod, A., and Whitworth, A. P. (2011). SEREN - a new SPH code for star and planet formation simulations. Algorithms and tests. *Astron. Astrophys.* 529:A27. doi: 10.1051/0004-6361/201014949

Hubber, D. A., Walch, S., and Whitworth, A. P. (2013). An improved sink particle algorithm for SPH simulations. *Month. Notices R. Astron. Soc.* 430, 3261–3275. doi: 10.1093/mnras/stt128

Iffrig, O. and Hennebelle, P. (2017). Structure distribution and turbulence in self-consistently supernova-driven ISM of multiphase magnetized galactic discs. *arXiv* 70, 1–22. doi: 10.1051/0004-6361/201630290

Inoue, T., and Inutsuka, S. (2008). Two-fluid magnetohydrodynamic simulations of converging H I flows in the interstellar medium. I. Methodology and basic results. *Astrophys. J.* 687, 303–310. doi: 10.1086/590528

Jappsen, A. K., Klessen, R. S., Larson, R. B., Li, Y., and Mac Low, M. M. (2005). The stellar mass spectrum from non-isothermal gravoturbulent fragmentation. *Astron. Astrophys.* 435, 611–623. doi: 10.1051/0004-6361:20042178

Jiang, G.-S., and Wu, C.-c. (1999). A high-order WENO finite difference scheme for the equations of ideal magnetohydrodynamics. *J. Comput. Phys.* 150, 561–594. doi: 10.1006/jcph.1999.6207

Jiang, Y.-F., Stone, J. M., and Davis, S. W. (2012). A godunov method for multidimensional radiation magnetohydrodynamics based on a variable eddington tensor. *Astrophys. J. Suppl.* 199:14. doi: 10.1088/0067-0049/199/1/14

Jones, M. O., and Bate, M. R. (2018). Sink particle radiative feedback in smoothed particle hydrodynamics models of star formation. *Month. Notices R. Astron. Soc.* 480, 2562–2577. doi: 10.1093/mnras/sty1969

Joung, M. K. R., and Mac Low, M.-M. (2006). Turbulent structure of a stratified supernova-driven interstellar medium. *Astrophys. J.* 653, 1266–1279. doi: 10.1086/508795

Kannan, R., Vogelsberger, M., Marinacci, F., McKinnon, R., Pakmor, R., and Springel, V. (2018). AREPO-RT: radiation hydrodynamics on a moving mesh. *arXiv:1804.01987*. doi: 10.1093/mnras/stz287

Kim, C.-G., Kim, W.-T., and Ostriker, E. C. (2011). Regulation of star formation rates in multiphase galactic disks: numerical tests of the thermal/dynamical equilibrium model. *Astrophys. J.* 743:25. doi: 10.1088/0004-637X/743/1/25

Kim, C.-G., and Ostriker, E. C. (2015). Vertical equilibrium, energetics, and star formation rates in magnetized galactic disks regulated by momentum feedback from supernovae. *Astrophys. J.* 815:67. doi: 10.1088/0004-637X/815/1/67

Kim, C.-G., and Ostriker, E. C. (2017). Three-phase interstellar medium in galaxies resolving evolution with star formation and supernova feedback (TIGRESS): algorithms, fiducial model, and convergence. *Astrophys. J.* 846:133. doi: 10.3847/1538-4357/aa8599

Kim, C.-G., and Ostriker, E. C. (2018). Numerical simulations of multiphase winds and fountains from star-forming galactic disks. I. Solar neighborhood TIGRESS model. *Astrophys. J.* 853:173. doi: 10.3847/1538-4357/aaa5ff

Kim, C.-G., Ostriker, E. C., and Kim, W.-T. (2013). Three-dimensional hydrodynamic simulations of multiphase galactic disks with star formation Feedback. I. Regulation of star formation rates. *Astrophys. J.* 776:1. doi: 10.1088/0004-637X/776/1/1

Kim, W.-T., Ostriker, E. C., and Stone, J. M. (2002). Three-dimensional simulations of parker, magneto-jeans, and swing instabilities in shearing galactic gas disks. *Astrophys. J.* 581, 1080–1100. doi: 10.1086/344367

Kitsionas, S., and Whitworth, A. P. (2002). Smoothed particle hydrodynamics with particle splitting, applied to self-gravitating collapse. *Month. Notices R. Astron. Soc.* 330, 129–136. doi: 10.1046/j.1365-8711.2002.05115.x

Klassen, M., Kuiper, R., Pudritz, R. E., Peters, T., Banerjee, R., and Buntemeyer, L. (2014). A general hybrid radiation transport scheme for star formation simulations on an adaptive grid. *Astrophys. J.* 797:4. doi: 10.1088/0004-637X/797/1/4

Klassen, M., Pudritz, R., Kuiper, R., Peters, T., and Banerjee, R. (2016). Simulating the formation of massive protostars. I. Radiative feedback and accretion disks. *Astrophys. J.* 823:28. doi: 10.3847/0004-637X/823/1/28

Klein, R. I. (1999). Star formation with 3-D adaptive mesh refinement: the collapse and fragmentation of molecular clouds. *J. Comput. Appl. Math.* 109, 123–152. doi: 10.1016/S0377-0427(99)00156-9

Klingenberg, C., Pörner, F., and Xia, Y. (2017). An efficient implementation of the divergence free constraint in a discontinuous galerkin method for magnetohydrodynamics on unstructured meshes. *Commun. Comput. Phys.* 21, 423–442. doi: 10.4208/cicp.180515.230616a

Koga, S., Tsukamoto, Y., Okuzumi, S., and Machida, M. N. (2019). Dependence of Hall coefficient on grain size and cosmic ray rate and implication for circumstellar disc formation. *Month. Notices R. Astron. Soc.* 484, 2119–2136. doi: 10.1093/mnras/sty3524

Korpi, M. J., Brandenburg, A., Shukurov, A., Tuominen, I., and Nordlund, Å. (1999). A supernova-regulated interstellar medium: simulations of the turbulent multiphase medium. *Astrophys. J.* 514, L99–L102. doi: 10.1086/311954

Kotarba, H., Lesch, H., Dolag, K., Naab, T., Johansson, P. H., and Stasyszyn, F. A. (2009). Magnetic field structure due to the global velocity field in spiral galaxies. *Month. Notices R. Astron. Soc.* 397, 733–747. doi: 10.1111/j.1365-2966.2009.15030.x

Kraljic, K., Renaud, F., Bournaud, F., Combes, F., Elmegreen, B., Emsellem, E., et al. (2014). The role of turbulence in star formation laws and thresholds. *Astrophys. J.* 784:112. doi: 10.1088/0004-637X/784/2/112

Krasnopolsky, R., Li, Z. Y., and Shang, H. (2011). Disk formation in magnetized clouds enabled by the hall effect. *Astrophys. J.* 733, 1–6. doi: 10.1088/0004-637X/733/1/54

Krumholz, M. R. (2014). The big problems in star formation: the star formation rate, stellar clustering, and the initial mass function. *Phys. Rep.* 539, 49–134. doi: 10.1016/j.physrep.2014.02.001

Krumholz, M. R., Klein, R. I., and McKee, C. F. (2007a). Radiation-hydrodynamic simulations of collapse and fragmentation in massive protostellar cores. *Astrophys. J.* 656, 959–979. doi: 10.1086/510664

Krumholz, M. R., Klein, R. I., and McKee, C. F. (2012). Radiation-hydrodynamic simulations of the formation of orion-like star clusters. II. The initial mass function from winds, turbulence, and radiation. *Astrophys. J.* 754:71. doi: 10.1088/0004-637X/754/1/71

Krumholz, M. R., Klein, R. I., McKee, C. F., and Bolstad, J. (2007b). Equations and algorithms for mixed-frame flux-limited diffusion radiation hydrodynamics. *Astrophys. J.* 667, 626–643. doi: 10.1086/520791

Krumholz, M. R., and McKee, C. F. (2005). A general theory of turbulence-regulated star formation, from spirals to ultraluminous infrared galaxies. *Astrophys. J.* 630, 250–268. doi: 10.1086/431734

Krumholz, M. R., McKee, C. F., and Klein, R. I. (2004). Embedding lagrangian sink particles in eulerian grids. *Astrophys. J.* 611, 399–412. doi: 10.1086/421935

Krumholz, M. R., McKee, C. F., and Klein, R. I. (2005). How protostellar outflows help massive stars form. *Astrophys. J.* 618, L33–L36. doi: 10.1086/427555

Kuffmeier, M., Frimann, S., Jensen, S. S., and Haugbølle, T. (2018). Episodic accretion: the interplay of infall and disc instabilities. *Month. Notices R. Astron. Soc.* 475, 2642–2658. doi: 10.1093/mnras/sty024

Kuffmeier, M., Haugbølle, T., and Nordlund, Å. (2017). Zoom-in simulations of protoplanetary disks starting from GMC scales. *Astrophys. J.* 846:7. doi: 10.3847/1538-4357/aa7c64

Kuiper, R., and Hosokawa, T. (2018). First hydrodynamics simulations of radiation forces and photoionization feedback in massive star formation. *Astron. Astrophys.* 616:A101. doi: 10.1051/0004-6361/201832638

Kuiper, R., Klahr, H., Beuther, H., and Henning, T. (2010a). Circumventing the radiation pressure barrier in the formation of massive stars via disk accretion. *Astrophys. J.* 722, 1556–1576. doi: 10.1088/0004-637X/722/2/1556

Kuiper, R., Klahr, H., Beuther, H., and Henning, T. (2011). Three-dimensional simulation of massive star formation in the disk accretion scenario. *Astrophys. J.* 732:20. doi: 10.1088/0004-637X/732/1/20

Kuiper, R., Kuiper, R., Klahr, H., Klahr, H., Dullemond, C., Dullemond, C., et al. (2010b). Fast and accurate frequency-dependent radiation transport for hydrodynamics simulations in massive star formation. *Astron. Astrophys.* 511:81. doi: 10.1051/0004-6361/200912355

Kuiper, R., Turner, N. J., and Yorke, H. W. (2016). Protostellar outflows and radiative feedback from massive stars. II. Feedback, star-formation efficiency, and outflow broadening. *Astrophys. J.* 832:40. doi: 10.3847/0004-637X/832/1/40

Kuiper, R., and Yorke, H. (2013). On the simultaneous evolution of massive protostars and their host cores. *Astrophys. J.* 772:61. doi: 10.1088/0004-637X/772/1/61

Kuiper, R., Yorke, H. W., and Turner, N. J. (2015). Protostellar outflows and radiative feedback from massive stars. *Astrophys. J.* 800:86. doi: 10.1088/0004-637X/800/2/86

Kunz, M. W., and Mouschovias, T. C. (2009). The nonisothermal stage of magnetic star formation. I. Formulation of the problem and method of solution. *Astrophys. J.* 693, 1895–1911. doi: 10.1088/0004-637X/693/2/1895

Kunz, M. W., and Mouschovias, T. C. (2010). The non-isothermal stage of magnetic star formation - II. Results. *Month. Notices R. Astron. Soc.* 408, 322–341. doi: 10.1111/j.1365-2966.2010.17110.x

Laibe, G., and Price, D. J. (2012). Dusty gas with smoothed particle hydrodynamics - I. Algorithm and test suite. *Month. Notices R. Astron. Soc.* 420, 2345–2364. doi: 10.1111/j.1365-2966.2011.20202.x

Laibe, G., and Price, D. J. (2014a). Dusty gas with one fluid. *Month. Notices R. Astron. Soc.* 440, 2136–2146. doi: 10.1093/mnras/stu355

Laibe, G., and Price, D. J. (2014b). Dusty gas with one fluid in smoothed particle hydrodynamics. *Month. Notices R. Astron. Soc.* 440, 2147–2163. doi: 10.1093/mnras/stu359

Larson, R. B. (1969). Numerical calculations of the dynamics of collapsing proto-star. *Month. Notices R. Astron. Soc.* 145:271. doi: 10.1093/mnras/145.3.271

Lebreuilly, U., Commerçon, B., and Laibe, G. (2019). Small dust grain dynamics on adaptive mesh refinement grids I. Methods. *Astron. Astrophys.* 626:96. doi: 10.1051/0004-6361/201834147

Lee, A. T., Cunningham, A. J., McKee, C. F., and Klein, R. I. (2014). Bondi-Hoyle accretion in an isothermal magnetized plasma. *Astrophys. J.* 783:50. doi: 10.1088/0004-637X/783/1/50

Lee, D., and Deane, A. E. (2009). An unsplit staggered mesh scheme for multidimensional magnetohydrodynamics. *J. Comput. Phys.* 228, 952–975. doi: 10.1016/j.jcp.2008.08.026

Lee, Y.-N., and Hennebelle, P. (2018a). Stellar mass spectrum within massive collapsing clumps. I. Influence of the initial conditions. *Astron. Astrophys.* 611:A88. doi: 10.1051/0004-6361/201731522

Lee, Y.-N., and Hennebelle, P. (2018b). Stellar mass spectrum within massive collapsing clumps. II. Thermodynamics and tidal forces of the first Larson core. A robust mechanism for the peak of the IMF. *Astron. Astrophys.* 611:A89. doi: 10.1051/0004-6361/201731523

Lee, Y.-N., and Hennebelle, P. (2018c). Stellar mass spectrum within massive collapsing clumps III. Effects of temperature and magnetic field. *arXiv:1812.05508*. doi: 10.1051/0004-6361/201834428

Lesur, G., Kunz, M. W., and Fromang, S. (2014). Thanatology in protoplanetary discs. The combined influence of Ohmic, Hall, and ambipolar diffusion on dead zones. *Astron. Astrophys.* 566:A56. doi: 10.1051/0004-6361/201423660

Levermore, C. D. (1984). Relating Eddington factors to flux limiters. *J. Quant. Spectrosc. Radiat. Transfer* 31, 149–160. doi: 10.1016/0022-4073(84)90112-2

Li, F., and Shu, C.-W. (2005). Locally divergence-free discontinuous galerkin methods for MHD equations. *J. Sci. Comput.* 22–23, 413–442. doi: 10.1007/s10915-004-4146-4

Li, F., and Xu, L. (2012). Arbitrary order exactly divergence-free central discontinuous Galerkin methods for ideal MHD equations. *J. Comput. Phys.* 231, 2655–2675. doi: 10.1016/j.jcp.2011.12.016

Li, P. S., Klein, R. I., and McKee, C. F. (2018). Formation of stellar clusters in magnetized, filamentary infrared dark clouds. *Month. Notices R. Astron. Soc.* 473, 4220–4241. doi: 10.1093/mnras/stx2611

Li, P. S., Martin, D. F., Klein, R. I., and McKee, C. F. (2012). A stable, accurate methodology for high mach number, strong magnetic field MHD turbulence with adaptive mesh refinement: resolution and refinement studies. *Astrophys. J.* 745:139. doi: 10.1088/0004-637X/745/2/139

Li, P. S., McKee, C. F., and Klein, R. I. (2006). The heavy-ion approximation for ambipolar diffusion calculations for weakly ionized plasmas. *Astrophys. J.* 653, 1280–1291. doi: 10.1086/508977

Li, Z.-Y., Krasnopolsky, R., and Shang, H. (2011). Non-ideal Mhd effects and magnetic braking catastrophe in protostellar disk formation. *Astrophys. J.* 738:180. doi: 10.1088/0004-637X/738/2/180

Li, Z.-Y., Krasnopolsky, R., Shang, H., and Zhao, B. (2014). On the role of pseudodisk warping and reconnection in protostellar disk formation in turbulent magnetized cores. *Astrophys. J.* 793:130. doi: 10.1088/0004-637X/793/2/130

Li, Z.-Y., and McKee, C. F. (1996). Hydromagnetic accretion shocks around low-mass protostars. *Astrophys. J.* 464:373. doi: 10.1086/177329

Li, Z.-Y., and Nakamura, F. (2006). Cluster formation in protostellar outflow-driven turbulence. *Astrophys. J.* 640, L187–L190. doi: 10.1086/503419

Lin, M.-K., and Youdin, A. N. (2017). A thermodynamic view of dusty protoplanetary disks. *Astrophys. J.* 849:129. doi: 10.3847/1538-4357/aa92cd

Lomax, O., and Whitworth, A. P. (2016). SPAMCART: a code for smoothed particle Monte Carlo radiative transfer. *Month. Notices R. Astron. Soc.* 461, 3542–3551. doi: 10.1093/mnras/stw1568

Londrillo, P., and del Zanna, L. (2004). On the divergence-free condition in Godunov-type schemes for ideal magnetohydrodynamics: the upwind constrained transport method. *J. Comput. Phys.* 195, 17–48. doi: 10.1016/j.jcp.2003.09.016

Lorén-Aguilar, P., and Bate, M. R. (2014). Two-fluid dust and gas mixtures in smoothed particle hydrodynamics: a semi-implicit approach. *Month. Notices R. Astron. Soc.* 443, 927–945. doi: 10.1093/mnras/stu1173

Mac Low, M.-M., and Klessen, R. S. (2004). Control of star formation by supersonic turbulence. *Rev. Mod. Phys.* 76, 125–194. doi: 10.1103/RevModPhys.76.125

Mac Low, M.-M., Norman, M. L., Konigl, A., and Wardle, M. (1995). Incorporation of ambipolar diffusion into the ZEUS magnetohydrodynamics code. *Astrophys. J.* 442:726. doi: 10.1086/175477

Machida, M. N., Inutsuka, S.-i., and Matsumoto, T. (2006). Second core formation and high-speed jets: resistive magnetohydrodynamic nested grid simulations. *Astrophys. J. Lett.* 2, 151–154. doi: 10.1086/507179

Machida, M. N., Inutsuka, S.-I., and Matsumoto, T. (2009). First direct simulation of brown dwarf formation in a compact cloud core. *Astrophys. J.* 699, L157–L160. doi: 10.1088/0004-637X/699/2/L157

Machida, M. N., Inutsuka, S.-i., and Matsumoto, T. (2014). Conditions for circumstellar disc formation: effects of initial cloud configuration and sink treatment. *Month. Notices R. Astron. Soc.* 438, 2278–2306. doi: 10.1093/mnras/stt2343

Marchand, P., Commerçon, B., and Chabrier, G. (2018). Impact of the Hall effect in star formation and the issue of angular momentum conservation. *arXiv:1808.08731*, 37. doi: 10.1051/0004-6361/201832907

Marchand, P., Masson, J., Chabrier, G., Hennebelle, P., Commerçon, B., and Vaytet, N. (2016). Chemical solver to compute molecule and grain abundances and non-ideal MHD resistivities in prestellar core-collapse calculations. *Astron. Astrophys.* 592:A18. doi: 10.1051/0004-6361/201526780

Marinacci, F., Vogelsberger, M., Kannan, R., Mocz, P., Pakmor, R., and Springel, V. (2018). Non-ideal magnetohydrodynamics on a moving mesh. *Month. Notices R. Astron. Soc.* 476, 2476–2492. doi: 10.1093/mnras/sty397

Martizzi, D., Fielding, D., Faucher-Giguère, C.-A., and Quataert, E. (2016). Supernova feedback in a local vertically stratified medium: interstellar turbulence and galactic winds. *Month. Notices R. Astron. Soc.* 459, 2311–2326. doi: 10.1093/mnras/stw745

Masson, J., Chabrier, G., Hennebelle, P., Vaytet, N., and Commerçon, B. (2016). Ambipolar diffusion in low-mass star formation. I. General comparison with the ideal magnetohydrodynamic case. *Astron. Astrophys.* 587:A32. doi: 10.1051/0004-6361/201526371

Masson, J., Teyssier, R., Mulet-Marquis, C., Hennebelle, P., and Chabrier, G. (2012). Incorporating ambipolar and ohmic diffusion in the AMR MHD code RAMSES. *Astrophys. J. Suppl.* 201:24. doi: 10.1088/0067-0049/201/2/24

Masunaga, H., and Inutsuka, S.-i. (2000). A radiation hydrodynamic model for protostellar collapse. II. The second collapse and the birth of a protostar. *Astrophys. J.* 531, 350–365. doi: 10.1086/308439

Mathis, J. S., Rumpl, W., and Nordsieck, K. H. (1977). The size distribution of interstellar grains. *Astrophys. J.* 217, 425–433. doi: 10.1086/155591

Matsumoto, T. (2011). An implicit scheme for ohmic dissipation with adaptive mesh refinement. *Publ. Astron. Soc. Jpn.* 63, 317–323. doi: 10.1093/pasj/63.2.317

Matsumoto, T., Machida, M. N., and ichiro Inutsuka, S. (2017). Circumstellar disks and outflows in turbulent molecular cloud cores: possible formation mechanism for misaligned systems. *Astrophys. J.* 839:69. doi: 10.3847/1538-4357/aa6a1c

Matzner, C. D. (2007). Protostellar outflow-driven turbulence. *Astrophys. J.* 659, 1394–1403. doi: 10.1086/512361

Matzner, C. D., and McKee, C. F. (1999). Bipolar molecular outflows driven by hydromagnetic protostellar winds. *Astrophys. J.* 526, L109–L112. doi: 10.1086/312376

Matzner, C. D., and McKee, C. F. (2000). Efficiencies of low-mass star and star cluster formation. *Astrophys. J.* 545, 364–378. doi: 10.1086/317785

Maureira, M. J., Arce, H. G., Dunham, M. M., Pineda, J. E., Fernández-López, M., Chen, X., et al. (2017). Kinematics of a young low-mass star-forming core: understanding the evolutionary state of the first-core candidate L1451-mm. *Astrophys. J.* 838:60. doi: 10.3847/1538-4357/838/1/60

Mayer, L., Lufkin, G., Quinn, T., and Wadsley, J. (2007). Fragmentation of gravitationally unstable gaseous protoplanetary disks with radiative transfer. *Astrophys. J.* 661, L77–L80. doi: 10.1086/518433

McKee, C. F. (1989). Photoionization-regulated star formation and the structure of molecular clouds. *Astrophys. J.* 345, 782–801. doi: 10.1086/167950

McKee, C. F., and Ostriker, E. C. (2007). Theory of star formation. *Annu. Rev. Astro. Astrophys.* 45, 565–687. doi: 10.1146/annurev.astro.45.051806.110602

Meheut, H., Meliani, Z., Varniere, P., and Benz, W. (2012). Dust-trapping Rossby vortices in protoplanetary disks. *Astron. Astrophys.* 545:A134. doi: 10.1051/0004-6361/201219794

Mellema, G., Iliev, I. T., Alvarez, M. A., and Shapiro, P. R. (2006). C 2-ray: a new method for photon-conserving transport of ionizing radiation. *New Astron.* 11, 374–395. doi: 10.1016/j.newast.2005.09.004

Mellon, R. R., and Li, Z. (2008). Magnetic braking and protostellar disk formation: the ideal MHD limit. *Astrophys. J.* 681, 1356–1376. doi: 10.1086/587542

Meyer, C. D., Balsara, D. S., and Aslam, T. D. (2012). A second-order accurate Super TimeStepping formulation for anisotropic thermal conduction. *Month. Notices R. Astron. Soc.* 422, 2102–2115. doi: 10.1111/j.1365-2966.2012.20744.x

Meyer, C. D., Balsara, D. S., and Aslam, T. D. (2014). A stabilized Runge-Kutta-Legendre method for explicit super-time-stepping of parabolic and mixed equations. *J. Comput. Phys.* 257, 594–626. doi: 10.1016/j.jcp.2013.08.021

Mignone, A., Bodo, G., Massaglia, S., Matsakos, T., Tesileanu, O., Zanni, C., and Ferrari, A. (2007). PLUTO: a numerical code for computational astrophysics. *Astrophys. J. Suppl. Ser.* 170, 228–242. doi: 10.1086/513316

Mihalas, D., and Klein, R. I. (1982). On the solution of the time-dependent inertial-frame equation of radiative transfer in moving media to O(vc). *J. Comput. Phys.* 46, 97–137. doi: 10.1016/0021-9991(82)90007-9

Mihalas, D., and Mihalas, B. W. (1984). *Foundations of Radiation Hydrodynamics*. New York, NY: Oxford University Press.

Minerbo, G. N. (1978). Maximum entropy Eddington factors. *J. Quant. Spectr. Radiat. Transf.* 20, 541–545. doi: 10.1016/0022-4073(78)90024-9

Miyama, S. M., Tomisaka, K., and Hanawa, T. (1999). "Numerical astrophysics," in *Proceedings of the International Conference on Numerical Astrophysics 1998 (NAP98)* (Boston, MA: Kluwer Academic), 383.

Mocz, P., Burkhart, B., Hernquist, L., McKee, C. F., and Springel, V. (2017). Moving-mesh Simulations of Star-forming Cores in Magneto-gravo-turbulence. *Astrophys. J.* 838:40. doi: 10.3847/1538-4357/aa6475

Mocz, P., Vogelsberger, M., and Hernquist, L. (2014a). A constrained transport scheme for MHD on unstructured static and moving meshes. *Month. Notices R. Astron. Soc.* 442, 43–55. doi: 10.1093/mnras/stu865

Mocz, P., Vogelsberger, M., Sijacki, D., Pakmor, R., and Hernquist, L. (2014b). A discontinuous Galerkin method for solving the fluid and magnetohydrodynamic equations in astrophysical simulations. *Month. Notices R. Astron. Soc.* 437, 397–414. doi: 10.1093/mnras/stt1890

Murray, D., Goyal, S., and Chang, P. (2018). The effects of protostellar jet feedback on turbulent collapse. *Month. Notices R. Astron. Soc.* 475, 1023–1035. doi: 10.1093/mnras/stx3153

Myers, A. T., Klein, R. I., Krumholz, M. R., and McKee, C. F. (2014). Star cluster formation in turbulent, magnetized dense clumps with radiative and outflow feedback. *Month. Notices R. Astron. Soc.* 439, 3420–3438. doi: 10.1093/mnras/stu190

Myers, A. T., McKee, C. F., Cunningham, A. J., Klein, R. I., and Krumholz, M. R. (2013). The fragmentation of magnetized, massive star-forming cores with radiative feedback. *Astrophys. J.* 766:97. doi: 10.1088/0004-637X/766/2/97

Nakamura, F., and Li, Z.-Y. (2007). Protostellar turbulence driven by collimated outflows. *Astrophys. J.* 662, 395–412. doi: 10.1086/517515

Nakamura, F., and Li, Z.-Y. (2011). Clustered star formation in magnetic clouds: properties of dense cores formed in outflow-driven turbulence. *Astrophys. J.* 740:36. doi: 10.1088/0004-637X/740/1/36

Nakano, T., Nishi, R., and Umebayashi, T. (2002). Mechanism of magnetic flux loss in molecular clouds. *Astrophys. J.* 573, 199–214. doi: 10.1086/340587

Nayakshin, S., Cha, S.-H., and Hobbs, A. (2009). Dynamic Monte Carlo radiation transfer in SPH: radiation pressure force implementation. *Month. Notices R. Astron. Soc.* 397, 1314–1325. doi: 10.1111/j.1365-2966.2009.15091.x

Ocvirk, P., Gillet, N., Shapiro, P. R., Aubert, D., Iliev, I. T., Teyssier, R., et al. (2016). Cosmic Dawn (CoDa): the first radiation-hydrodynamics simulation of reionization and galaxy formation in the local universe. *Month. Notices R. Astron. Soc.* 463, 1462–1485. doi: 10.1093/mnras/stw2036

Offner, S. S. R., and Chaban, J. (2017). Impact of protostellar outflows on turbulence and star formation efficiency in magnetized dense cores. *Astrophys. J.* 847:104. doi: 10.3847/1538-4357/aa8996

Offner, S. S. R., Klein, R. I., McKee, C. F., and Krumholz, M. R. (2009). The effects of radiative transfer on low-mass star formation. *Astrophys. J.* 703, 131–149. doi: 10.1088/0004-637X/703/1/131

Offner, S. S. R., and Liu, Y. (2018). Turbulent action at a distance due to stellar feedback in magnetized clouds. *Nat. Astron.* 2, 896. doi: 10.1038/s41550-018-0566-1

Oishi, J. S., and Mac Low, M.-M. (2006). The inability of ambipolar diffusion to set a characteristic mass scale in molecular clouds. *Astrophys. J.* 638, 281–285. doi: 10.1086/498818

O'Sullivan, S., and Downes, T. P. (2006). An explicit scheme for multifluid magnetohydrodynamics. *Month. Notices R. Astron. Soc.* 366, 1329–1336. doi: 10.1111/j.1365-2966.2005.09898.x

Padoan, P., Haugbølle, T., Nordlund, Å., and Frimann, S. (2017). Supernova driving. IV. The star formation rate of molecular clouds. *Astrophys. J.* 840:48. doi: 10.3847/1538-4357/aa6afa

Padoan, P., and Nordlund, Å. (2011). The star formation rate of supersonic magnetohydrodynamic turbulence. *Astrophys. J.* 730:40. doi: 10.1088/0004-637X/730/1/40

Padoan, P., Zweibel, E., and Nordlund, Å. (2000). Ambipolar drift heating in turbulent molecular clouds. *Astrophys. J.* 540, 332–341. doi: 10.1086/309299

Pawlik, A. H., and Schaye, J. (2008). TRAPHIC - radiative transfer for smoothed particle hydrodynamics simulations. *Month. Notices R. Astron. Soc.* 389, 651–677. doi: 10.1111/j.1365-2966.2008.13601.x

Paxton, B., Bildsten, L., Dotter, A., Herwig, F., Lesaffre, P., and Timmes, F. (2011). Modules for experiments in stellar astrophysics (MESA). *Astrophys. J. Suppl. Ser.* 192:3. doi: 10.1088/0067-0049/192/1/3

Pelletier, G., and Pudritz, R. E. (1992). Hydromagnetic disk winds in young stellar objects and active galactic nuclei. *Astrophys. J.* 394, 117–138. doi: 10.1086/171565

Pelupessy, F. I., van Elteren, A., de Vries, N., McMillan, S. L. W., Drost, N., and Portegies Zwart, S. F. (2013). The astrophysical multipurpose software environment. *Astron. Astrophys.* 557:A84. doi: 10.1051/0004-6361/201321252

Peters, T., Banerjee, R., Klessen, R. S., and Mac Low, M.-M. (2011). The interplay of magnetic fields, fragmentation, and ionization feedback in high-mass star formation. *Astrophys. J.* 729:72. doi: 10.1088/0004-637X/729/1/72

Peters, T., Banerjee, R., Klessen, R. S., Mac Low, M.-M., Galván-Madrid, R., and Keto, E. R. (2010). H II regions: witnesses to massive star formation. *Astrophys. J.* 711, 1017–1028. doi: 10.1088/0004-637X/711/2/1017

Peters, T., Klaassen, P. D., Mac Low, M.-M., Schrön, M., Federrath, C., Smith, M. D., et al. (2014). Collective outflow from a small multiple stellar system. *Astrophys. J.* 788:14. doi: 10.1088/0004-637X/788/1/14

Peters, T., Naab, T., Walch, S., Glover, S. C. O., Girichidis, P., Pellegrini, E., et al. (2017). The SILCC project - IV. Impact of dissociating and ionizing radiation on the interstellar medium and Hα emission as a tracer of the star formation rate. *Month. Notices R. Astron. Soc.* 466, 3293–3308. doi: 10.1093/mnras/stw3216

Petkova, M., and Springel, V. (2011). A novel approach for accurate radiative transfer in cosmological hydrodynamic simulations. *Month. Notices R. Astron. Soc.* 415, 3731–3749. doi: 10.1111/j.1365-2966.2011.18986.x

Phillips, G. J., and Monaghan, J. J. (1985). A numerical method for three-dimensional simulations of collapsing, isothermal, magnetic gas clouds. *Month. Notices R. Astron. Soc.* 216, 883–895. doi: 10.1093/mnras/216.4.883

Pinto, C., Galli, D., and Bacciotti, F. (2008). Three-fluid plasmas in star formation. I. Magneto-hydrodynamic equations. *Astron. Astrophys.* 484, 1–15. doi: 10.1051/0004-6361:20078818

Portegies Zwart, S. F., and Verbunt, F. (1996). Population synthesis of high-mass binaries. *Astron. Astrophys.* 309, 179–196.

Powell, K. G., Roe, P. L., Linde, T. J., Gombosi, T. I., and De Zeeuw, D. L. (1999). A solution-adaptive upwind scheme for ideal magnetohydrodynamics. *J. Comput. Phys.* 154, 284–309. doi: 10.1006/jcph.1999.6299

Price, D. J., and Bate, M. R. (2008). The effect of magnetic fields on star cluster formation. *Month. Notices R. Astron. Soc.* 385, 1820–1834. doi: 10.1111/j.1365-2966.2008.12976.x

Price, D. J., and Bate, M. R. (2009). Inefficient star formation: the combined effects of magnetic fields and radiative feedback. *Month. Notices R. Astron. Soc.* 398, 33–46. doi: 10.1111/j.1365-2966.2009.14969.x

Price, D. J., and Laibe, G. (2015). A fast and explicit algorithm for simulating the dynamics of small dust grains with smoothed particle hydrodynamics. *Month. Notices R. Astron. Soc.* 451, 813–826. doi: 10.1093/mnras/stv996

Price, D. J., and Monaghan, J. J. (2005). Smoothed particle magnetohydrodynamics — III. multidimensional tests and the div B= 0 constraint. *Month. Notices R. Astron. Soc.* 364, 384–406. doi: 10.1111/j.1365-2966.2005.09576.x

Price, D. J., Tricco, T. S., and Bate, M. R. (2012). Collimated jets from the first core. *Month. Notices R. Astron. Soc.* 423, L45–L49. doi: 10.1111/j.1745-3933.2012.01254.x

Price, D. J., Wurster, J., Tricco, T. S., Nixon, C., Toupin, S., Pettitt, A., et al. (2017). Phantom: a smoothed particle hydrodynamics and magnetohydrodynamics code for astrophysics. *arXiv:1702.03930*. doi: 10.1017/pasa.2018.25

Ramsey, J. P., and Dullemond, C. P. (2015). Radiation hydrodynamics including irradiation and adaptive mesh refinement with AZEuS. I. Methods. *Astron. Astrophys.* 574:A81. doi: 10.1051/0004-6361/201424954

Renaud, F., Bournaud, F., Emsellem, E., Elmegreen, B., Teyssier, R., Alves, J., et al. (2013). A sub-parsec resolution simulation of the Milky Way: global structure of the interstellar medium and properties of molecular clouds. *Month. Notices R. Astron. Soc.* 436, 1836–1851. doi: 10.1093/mnras/stt1698

Rijkhorst, E. J., Plewa, T., Dubey, A., and Mellema, G. (2006). Hybrid characteristics: 3D radiative transfer for parallel adaptive mesh refinement hydrodynamics. *Astron. Astrophys.* 452, 907–920. doi: 10.1051/0004-6361:20053401

Ripoll, J. F., Dubroca, B., and Duffa, G. (2001). Modelling radiative mean absorption coefficients. *Combust. Theory Model.* 5, 261–274. doi: 10.1088/1364-7830/5/3/301

Rosdahl, J., Blaizot, J., Aubert, D., Stranex, T., and Teyssier, R. (2013). RAMSES-RT: radiation hydrodynamics in the cosmological context. *Month. Notices R. Astron. Soc.* 436, 2188–2231. doi: 10.1093/mnras/stt1722

Rosdahl, J., and Teyssier, R. (2015). A scheme for radiation pressure and photon diffusion with the M1 closure in RAMSES-RT. *Month. Notices R. Astron. Soc.* 449, 4380–4403. doi: 10.1093/mnras/stv567

Rosen, A. L., Krumholz, M. R., McKee, C. F., and Klein, R. I. (2016). An unstable truth: how massive stars get their mass. *Month. Notices R. Astron. Soc.* 463, 2553–2573. doi: 10.1093/mnras/stw2153

Rosen, A. L., Krumholz, M. R., Oishi, J. S., Lee, A. T., and Klein, R. I. (2017). Hybrid adaptive ray-moment method (HARM^2): a highly parallel method for radiation hydrodynamics on adaptive grids. *J. Comput. Phys.* 330, 924–942. doi: 10.1016/j.jcp.2016.10.048

Roth, N., and Kasen, D. (2015). Monte Carlo radiation-hydrodynamics with implicit methods. *Astrophys. J. Suppl.* 217:9. doi: 10.1088/0067-0049/217/1/9

Rozyczka, M. (1985). Two-dimensional models of stellar wind bubbles. I - Numerical methods and their application to the investigation of outer shell instabilities. *Astron. Astrophys.* 143, 59–71.

Ryan, B. R., Gammie, C. F., Fromang, S., and Kestener, P. (2017). Resolution dependence of magnetorotational turbulence in the isothermal stratified shearing box. *Astrophys. J.* 840:6. doi: 10.3847/1538-4357/aa6a52

Ryu, D., Jones, T. W., and Frank, A. (1995). Numerical magnetohydrodynamics in astrophysics: algorithm and tests for multidimensional flow. *Astrophys. J.* 452:785. doi: 10.1086/176347

Ryu, D., Miniati, F., Jones, T. W., and Frank, A. (1998). A divergence-free upwind code for multidimensional magnetohydrodynamic flows. *Astrophys. J.* 509, 244–255. doi: 10.1086/306481

Sano, T., and Stone, J. M. (2002). The effect of the hall term on the nonlinear evolution of the magnetorotational instability. I. Local axisymmetric simulations. *Astrophys. J.* 570, 314–328. doi: 10.1086/339504

Saumon, D., Chabrier, G., and van Horn, H. M. (1995). An equation of state for low-mass stars and giant planets. *Astrophys. J. Suppl. Ser.* 99:713. doi: 10.1086/192204

Seifried, D., Walch, S., Girichidis, P., Naab, T., Wünsch, R., Klessen, R. S., et al. (2017). SILCC-Zoom: the dynamic and chemical evolution of molecular clouds. *Month. Notices R. Astron. Soc.* 472, 4797–4818. doi: 10.1093/mnras/stx2343

Shestakov, A. I., and Offner, S. S. R. (2008). A multigroup diffusion solver using pseudo transient continuation for a radiation-hydrodynamic code with patch-based AMR. *J. Comput. Phys.* 227, 2154–2186. doi: 10.1016/j.jcp.2007.09.019

Shima, K., Tasker, E. J., and Habe, A. (2017). Does feedback help or hinder star formation? The effect of photoionization on star formation in giant molecular clouds. *Month. Notices R. Astron. Soc.* 467, 512–523. doi: 10.1093/mnras/stw3279

Shu, F., Najita, J., Ostriker, E., Wilkin, F., Ruden, S., and Lizano, S. (1994). Magnetocentrifugally driven flows from young stars and disks. 1: a generalized model. *Astrophys. J.* 429, 781–796. doi: 10.1086/174363

Shu, F. H., Adams, F. C., and Lizano, S. (1987). Star formation in molecular clouds: observation and theory. *Annu. Rev. Astron. Astrophys.* 25, 23–81. doi: 10.1146/annurev.aa.25.090187.000323

Shu, F. H., Tremaine, S., Adams, F. C., and Ruden, S. P. (1990). SLING amplification and eccentric gravitational instabilities in gaseous disks. *Astrophys. J.* 358:495. doi: 10.1086/169003

Sigalotti, L. D. G., Cruz, F., Gabbasov, R., Klapp, J., and Ramírez-Velasquez, J. (2018). From large-scale to protostellar disk fragmentation into close binary stars. *Astrophys. J.* 857:40. doi: 10.3847/1538-4357/aab619

Skinner, M. A., and Ostriker, E. C. (2013). A Two-moment radiation hydrodynamics module in athena using a time-explicit godunov method. *Astrophys. J. Suppl.* 206:21. doi: 10.1088/0067-0049/206/2/21

Smith, M. C., Sijacki, D., and Shen, S. (2018). Supernova feedback in numerical simulations of galaxy formation: separating physics from numerics. *Month. Notices R. Astron. Soc.* 478, 302–331. doi: 10.1093/mnras/sty994

Springel, V. (2010). E pur si muove: galilean-invariant cosmological hydrodynamical simulations on a moving mesh. *Month. Notices R. Astron. Soc.* 401, 791–851. doi: 10.1111/j.1365-2966.2009.15715.x

Spruit, H. C., Stehle, R., and Papaloizou, J. C. B. (1995). Interchange instability in and accretion disc with a poloidal magnetic field. *Month. Notices R. Astron. Soc.* 275, 1223–1231. doi: 10.1093/mnras/275.4.1223

Spruit, H. C., and Taam, R. E. (1990). Mass transport in a neutron star magnetosphere. *Astron. Astrophys.* 229, 475–493.

Stahler, S. W., Shu, F. H., and Taam, R. E. (1980). The evolution of protostars. I - Global formulation and results. *Astrophys. J.* 241, 637–654. doi: 10.1086/158377

Stamatellos, D., Whitworth, A., Bisbas, T., and Goodwin, S. (2007). Radiative transfer and the energy equation in SPH simulations of star formation. *Astron. Astrophys.* 475, 37–49. doi: 10.1051/0004-6361:20077373

Stamatellos, D., Whitworth, A. P., and Hubber, D. A. (2011). The importance of episodic accretion for low-mass star formation. *Astrophys. J.* 730:32. doi: 10.1088/0004-637X/730/1/32

Stone, J. M., Gardiner, T. A., Teuben, P., Hawley, J. F., and Simon, J. B. (2008). Athena: a new code for astrophysical MHD. *Astrophys. J. Suppl. Ser.* 178, 137–177. doi: 10.1086/588755

Stone, J. M., Mihalas, D., and Norman, M. L. (1992a). ZEUS-2D: a radiation magnetohydrodynamics code for astrophysical flows in two space dimensions. III - The radiation hydrodynamic algorithms and tests. *Astrophys. J. Suppl. Ser.* 80, 819–845. doi: 10.1086/191682

Stone, J. M., Stone, J. M., and Norman, M. L. (1992b). ZEUS-2D: a radiation magnetohydrodynamics code for astrophysical flows in two space dimensions. II. The magnetohydrodynamic algorithms and tests. *Astrophys. J. Suppl.* 80:791. doi: 10.1086/191681

Sur, S., Schleicher, D. R. G., Banerjee, R., Federrath, C., and Klessen, R. S. (2010). The generation of strong magnetic fields during the formation of the first stars. *Astrophys. J. Lett.* 721, L134–L138. doi: 10.1088/2041-8205/721/2/L134

Takasao, S., Tomida, K., Iwasaki, K., and Suzuki, T. K. (2018). A three-dimensional simulation of a magnetized accretion disk: fast funnel accretion onto a weakly magnetized star. *Astrophys. J.* 857:4. doi: 10.3847/1538-4357/aab5b3

Tasker, E. J. (2011). Star formation in disk galaxies. II. The effect Of star formation and photoelectric heating on the formation and evolution of giant molecular clouds. *Astrophys. J.* 730:11. doi: 10.1088/0004-637X/730/1/11

Teyssier, R. (2002). Cosmological hydrodynamics with adaptive mesh refinement. A new high resolution code called RAMSES. *Astron. Astrophys.* 385, 337–364. doi: 10.1051/0004-6361:20011817

Teyssier, R., Fromang, S., and Dormy, E. (2006). Kinematic dynamos using constrained transport with high order Godunov schemes and adaptive mesh refinement. *J. Comput. Phys.* 218, 44–67. doi: 10.1016/j.jcp.2006.01.042

Tilley, D. A., and Balsara, D. S. (2008). A two-fluid method for ambipolar diffusion. *Month. Notices R. Astron. Soc.* 389, 1058–1073. doi: 10.1111/j.1365-2966.2008.13636.x

Tomida, K., Machida, M. N., Hosokawa, T., Sakurai, Y., and Lin, C. H. (2017). Grand-design spiral arms in a young forming circumstellar disk. *Astrophys. J.* 835:L11. doi: 10.3847/2041-8213/835/1/L11

Tomida, K., Okuzumi, S., and Machida, M. N. (2015). Radiation magnetohydrodynamic simulations of protostellar collapse: nonideal magnetohydrodynamic effects and early formation of circumstellar disks. *Astrophys. J.* 801:117. doi: 10.1088/0004-637X/801/2/117

Tomida, K., Tomisaka, K., Matsumoto, T., Hori, Y., Okuzumi, S., Machida, M. N., et al. (2013). Radiation magnetohydrodynamic simulations of protostellar collapse: protostellar core formation. *Astrophys. J.* 763:6. doi: 10.1088/0004-637X/763/1/6

Tomida, K., Tomisaka, K., Matsumoto, T., Ohsuga, K., MacHida, M. N., and Saigo, K. (2010). Radiation magnetohydrodynamics simulation of proto-stellar collapse: two-component molecular outflow. *Astrophys. J. Lett.* 714(1 Pt 2):58–63. doi: 10.1088/2041-8205/714/1/L58

Tomisaka, K. (2002). Collapse of rotating magnetized molecular cloud cores and mass outflows. *Astrophys. J.* 575, 306–326. doi: 10.1086/341133

Tomisaka, K., and Bregman, J. N. (1993). Extended hot-gas halos around starburst galaxies. *Publ. Astron. Soc. Jpn.* 45, 513–528.

Toth, G. (1994). Numerical study of two-fluid C-type shock waves. *Astrophys. J.* 425, 171–194. doi: 10.1086/173973

Tóth, G. (1996). A general code for modeling MHD flows on parallel computers: versatile advection code. *Astrophys. Lett. Commun.* 34:245. doi: 10.1007/978-94-009-0315-9_101

Tóth, G. (2000). The div B=0 constraint in shock-capturing magnetohydrodynamics codes. *J. Comput. Phys.* 161, 605–652. doi: 10.1006/jcph.2000.6519

Tóth, G., De Zeeuw, D. L., Gombosi, T. I., and Powell, K. G. (2006). A parallel explicit/implicit time stepping scheme on block-adaptive grids. *J. Comput. Phys.* 217, 722–758. doi: 10.1016/j.jcp.2006.01.029

Tóth, G., Ma, Y., and Gombosi, T. I. (2008). Hall magnetohydrodynamics on block-adaptive grids. *J. Comput. Phys.* 227, 6967–6984. doi: 10.1016/j.jcp.2008.04.010

Tóth, G., and Roe, P. L. (2002). Divergence- and curl-preserving prolongation and restriction formulas. *J. Comput. Phys.* 180, 736–750. doi: 10.1006/jcph.2002.7120

Tricco, T. S., and Price, D. J. (2012). Constrained hyperbolic divergence cleaning for smoothed particle magnetohydrodynamics. *J. Comput. Phys.* 231, 7214–7236. doi: 10.1016/j.jcp.2012.06.039

Tricco, T. S., Price, D. J., and Laibe, G. (2017). Is the dust-to-gas ratio constant in molecular clouds? *Month. Notices R. Astron. Soc.* 471, L52–L56. doi: 10.1093/mnrasl/slx096

Truelove, J. K., Klein, R. I., McKee, C. F., Holliman, J. H. I., Howell, L. H., and Greenough, J. A. (1997). The jeans condition: a new constraint on spatial resolution in simulations of isothermal self-gravitational hydrodynamics. *Astrophys. J. Lett.* 489:L179. doi: 10.1086/310975

Tsitali, A. E., Belloche, A., Commerçon, B., and Menten, K. M. (2013). The dynamical state of the first hydrostatic core candidate Chamaeleon-MMS1. *Astron. Astrophys.* 557:A98. doi: 10.1051/0004-6361/201321204

Tsukamoto, Y., Iwasaki, K., and Inutsuka, S.-i. (2013). An explicit scheme for ohmic dissipation with smoothed particle magnetohydrodynamics. *Month. Notices R. Astron. Soc.* 434, 2593–2599. doi: 10.1093/mnras/stt1205

Tsukamoto, Y., Iwasaki, K., Okuzumi, S., Machida, M. N., and Inutsuka, S. (2015a). Bimodality OF circumstellar disk evolution induced by the hall current. *Astrophys. J. Lett.* 810:L26. doi: 10.1088/2041-8205/810/2/L26

Tsukamoto, Y., Iwasaki, K., Okuzumi, S., Machida, M. N., and Inutsuka, S. (2015b). Effects of Ohmic and ambipolar diffusion on formation and evolution of first cores, protostars, and circumstellar discs. *Month. Notices R. Astron. Soc.* 452, 278–288. doi: 10.1093/mnras/stv1290

Tsukamoto, Y., Okuzumi, S., Iwasaki, K., Machida, M. N., and Inutsuka, S.-I. (2017). The impact of the Hall effect during cloud core collapse: implications for circumstellar disk evolution. *Publ. Astron. Soc. Jpn.* 69:95. doi: 10.1093/pasj/psx113

Turk, M. J., Oishi, J. S., Abel, T., and Bryan, G. L. (2012). Magnetic fields in population III star formation. *Astrophys. J.* 745:154. doi: 10.1088/0004-637X/745/2/154

Vaidya, B., Prasad, D., Mignone, A., Sharma, P., and Rickler, L. (2017). Scalable explicit implementation of anisotropic diffusion with Runge- Kutta-Legendre super-time stepping. *Month. Notices R. Astron. Soc.* 472, 3147–3160. doi: 10.1093/mnras/stx2176

van Leer, B. (1977). Towards the ultimate conservative difference scheme. IV. A new approach to numerical convection. *J. Comput. Phys.* 23:276. doi: 10.1016/0021-9991(77)90095-X

Vaytet, N., Audit, E., Chabrier, G., Commerçon, B., and Masson, J. (2012). Simulations of protostellar collapse using multigroup radiation hydrodynamics: I. the first collapse. *Astron. Astrophys.* 543:60. doi: 10.1051/0004-6361/201219427

Vaytet, N., Chabrier, G., Audit, E., Commerçon, B., Masson, J., Ferguson, J., et al. (2013). Simulations of protostellar collapse using multigroup radiation hydrodynamics. II. The second collapse. *Astron. Astrophys.* 557:A90. doi: 10.1051/0004-6361/201321423

Vaytet, N., Commerçon, B., Masson, J., González, M., and Chabrier, G. (2018). Protostellar birth with ambipolar and ohmic diffusion. *Astron. Astrophys.* 615:A5. doi: 10.1051/0004-6361/201732075

Vaytet, N., and Haugbølle, T. (2017). A grid of one-dimensional low-mass star formation collapse models. *Astron. Astrophys.* 598:A116. doi: 10.1051/0004-6361/201628194

Vaytet, N., Tomida, K., and Chabrier, G. (2014). On the role of the H_2 ortho: para ratio in gravitational collapse during star formation. *Astron. Astrophys.* 563:A85. doi: 10.1051/0004-6361/201322855

Walch, S., Girichidis, P., Naab, T., Gatto, A., Glover, S. C. O., Wünsch, R., et al. (2015). The SILCC (SImulating the LifeCycle of molecular Clouds) project - I. Chemical evolution of the supernova-driven ISM. *Month. Notices R. Astron. Soc.* 454, 238–268. doi: 10.1093/mnras/stv1975

Wall, J. E., McMillan, S. L. W., Mac Low, M.-M., Klessen, R. S., and Portegies Zwart, S. (2019). Collisional N-body dynamics coupled to self-gravitating magnetohydrodynamics reveals dynamical binary formation. *arXiv:1901.01132*.

Wang, P., Li, Z.-Y., Abel, T., and Nakamura, F. (2010). Outflow feedback regulated massive star formation in parsec-scale cluster-forming clumps. *Astrophys. J.* 709, 27–41. doi: 10.1088/0004-637X/709/1/27

Whitehouse, S. C., and Bate, M. R. (2004). Smoothed particle hydrodynamics with radiative transfer in the flux-limited diffusion approximation. *Month. Notices R. Astron. Soc.* 353, 1078–1094. doi: 10.1111/j.1365-2966.2004.08131.x

Whitehouse, S. C., and Bate, M. R. (2006). The thermodynamics of collapsing molecular cloud cores using smoothed particle hydrodynamics with radiative transfer. *Month. Notices R. Astron. Soc.* 367, 32–38. doi: 10.1111/j.1365-2966.2005.09950.x

Whitehouse, S. C., Bate, M. R., and Monaghan, J. J. (2005). A faster algorithm for smoothed particle hydrodynamics with radiative transfer in the flux-limited diffusion approximation. *Month. Notices R. Astron. Soc.* 364, 1367–1377. doi: 10.1111/j.1365-2966.2005.09683.x

Winkler, K. A., and Norman, M. L. (1986). "Astrophysical radiation hydrodynamics," in *NATO Advanced Research Workshop on Astrophysical Radiation Hydrodynamics* (Dordrecht; Holland; Boston, MA: D. Reidel Publishing Co.), 187.

Winkler, K. H. A., and Newman, M. J. (1980). Formation of solar-type stars in spherical symmetry. I - The key role of the accretion shock. *Astrophys. J.* 236, 201–211. doi: 10.1086/157734

Wise, J. H., and Abel, T. (2011). ENZO+MORAY: radiation hydrodynamics adaptive mesh refinement simulations with adaptive ray tracing. *Month. Notices R. Astron. Soc.* 414, 3458–3491. doi: 10.1111/j.1365-2966.2011.18646.x

Wise, J. H., Turk, M. J., Norman, M. L., and Abel, T. (2012). The birth of a galaxy: primordial metal enrichment and stellar populations. *Astrophys. J.* 745:50. doi: 10.1088/0004-637X/745/1/50

Wurster, J., Bate, M. R., and Price, D. J. (2018). On the origin of magnetic fields in stars. *Month. Notices R. Astron. Soc.* 481, 2450–2457. doi: 10.1093/mnras/sty2438

Wurster, J., Bate, M. R., and Price, D. J. (2018). The collapse of a molecular cloud core to stellar densities using radiation non-ideal magnetohydrodynamics. *Month. Notices R. Astron. Soc.* 475, 1859–1880. doi: 10.1093/mnras/stx3339

Wurster, J., and Li, Z.-Y. (2018). The role of magnetic fields in the formation of protostellar discs. *Front. Astron. Space Sci.* 5:39. doi: 10.3389/fspas.2018.00039

Wurster, J., Price, D., and Ayliffe, B. (2014). Ambipolar diffusion in smoothed particle magnetohydrodynamics. *Month. Notices R. Astron. Soc.* 444, 1104–1112. doi: 10.1093/mnras/stu1524

Wurster, J., Price, D. J., and Bate, M. R. (2016). Can non-ideal magnetohydrodynamics solve the magnetic braking catastrophe? *Month. Notices R. Astron. Soc.* 457, 1037–1061. doi: 10.1093/mnras/stw013

Yorke, H. W., and Bodenheimer, P. (1999). The formation of protostellar disks. III. The influence of gravitationally induced angular momentum transport on disk structure and appearance. *Astrophys. J.* 525, 330–342. doi: 10.1086/307867

Yorke, H. W., Yorke, H. W., Sonnhalter, C., and Sonnhalter, C. (2002). On the formation of massive stars. *Astrophys. J.* 569, 846–862. doi: 10.1086/339264

Zamora-Avilés, M., Vázquez-Semadeni, E., Körtgen, B., Banerjee, R., and Hartmann, L. (2018). Magnetic suppression of turbulence and the star formation activity of molecular clouds. *Month. Notices R. Astron. Soc.* 474, 4824–4836. doi: 10.1093/mnras/stx3080

Zhang, S., Hartmann, L., Zamora-Avilés, M., and Kuznetsova, A. (2018). On estimating angular momenta of infalling protostellar cores from observations. *Month. Notices R. Astron. Soc.* 480, 5495–5503. doi: 10.1093/mnras/sty2244

Zhang, W., Howell, L., Almgren, A., Burrows, A., Dolence, J., and Bell, J. (2013). Castro: a new compressible astrophysical solver. III. Multigroup radiation hydrodynamics. *Astrophys. J. Suppl. Ser.* 204:7. doi: 10.1088/0067-0049/204/1/7

Zhao, B., Caselli, P., and Li, Z.-Y. (2018a). Effect of grain size on differential desorption of volatile species and on non-ideal MHD diffusivity. *Month. Notices R. Astron. Soc.* 478, 2723–2736. doi: 10.1093/mnras/sty1165

Zhao, B., Caselli, P., Li, Z.-Y., Krasnopolsky, R., Shang, H., and Nakamura, F. (2016). Protostellar disc formation enabled by removal of small dust grains. *Month. Notices R. Astron. Soc.* 460, 2050–2076. doi: 10.1093/mnras/stw1124

Zhao, B., Caselli, P., Li, Z. Y., and Krasnopolsky, R. (2018b). Decoupling of magnetic fields in collapsing protostellar envelopes and disc formation and fragmentation. *Month. Notices R. Astron. Soc.* 473, 4868–4889. doi: 10.1093/mnras/stx2617

Zhao, B., Li, Z.-Y., Nakamura, F., Krasnopolsky, R., and Shang, H. (2011). Magnetic flux expulsion in star formation. *Astrophys. J.* 742:10. doi: 10.1088/0004-637X/742/1/10

Conflict of Interest Statement: The authors declare that the research was conducted in the absence of any commercial or financial relationships that could be construed as a potential conflict of interest.

Advantages of publishing in Frontiers

OPEN ACCESS
Articles are free to read for greatest visibility and readership

FAST PUBLICATION
Around 90 days from submission to decision

HIGH QUALITY PEER-REVIEW
Rigorous, collaborative, and constructive peer-review

TRANSPARENT PEER-REVIEW
Editors and reviewers acknowledged by name on published articles

Frontiers
Avenue du Tribunal-Fédéral 34
1005 Lausanne | Switzerland

Visit us: www.frontiersin.org
Contact us: info@frontiersin.org | +41 21 510 17 00

REPRODUCIBILITY OF RESEARCH
Support open data and methods to enhance research reproducibility

DIGITAL PUBLISHING
Articles designed for optimal readership across devices

FOLLOW US
@frontiersin

IMPACT METRICS
Advanced article metrics track visibility across digital media

EXTENSIVE PROMOTION
Marketing and promotion of impactful research

LOOP RESEARCH NETWORK
Our network increases your article's readership